

*The*  
**MOCVD**  
*Challenge*

---

*Volume 2:*  
*A survey of GaInAsP–GaAs  
for photonic and electronic  
device applications*

**Manijeh Razeghi**

The MOCVD Challenge  
Volume 2: A survey of  
GaInAsP–GaAs for photonic and  
electronic device applications



Taylor & Francis  
Taylor & Francis Group  
<http://taylorandfrancis.com>

# **The MOCVD Challenge**

## **Volume 2:**

### **A survey of GaInAsP–GaAs for photonic and electronic device applications**

**Manijeh RAZEGHI**

McCormick School of Engineering  
Center for Quantum Devices/EECS Department  
Northwestern University  
Evanston, Illinois 60208

Institute of Physics Publishing  
Bristol and Philadelphia

© IOP Publishing Ltd 1995

All rights reserved. No part of this publication may be reproduced, stored in a retrieval system or transmitted in any form or by any means, electronic, mechanical, photocopying, recording or otherwise, without the prior permission of the publisher. Multiple copying is permitted in accordance with the terms of licences issued by the Copyright Licensing Agency under the terms of its agreement with the Committee of Vice-Chancellors and Principals.

*British Library Cataloguing-in-Publication Data*

A catalogue record for this book is available from the British Library.

ISBN 0 7503 0309 3

*Library of Congress Cataloging-in-Publication Data*

(Revised for volume 2)

Metallorganic chemical vapour deposition growth of  
photonic and electronic materials.

Vol. 2 title: The MOCVD challenge.

Includes index.

Bibliography: p.

Contents: v. 1. InP and related compounds -- v. 2.

A survey of GaInAsP-GaAs for photonic and  
electronic applications.

1. Vapor-plating. I. Razeghi, M.

TS695.M47 1989 671.7'32 88-28466

ISBN 0-8527-4161-8 (v. 1)

ISBN 0-7503-0309-4 (v. 2)

IOP Publishing Ltd and the author have attempted to trace the copyright holders of all the material reproduced in this publication and apologize to copyright holders if permission to publish in this form has not been obtained.

Consultant Editor: **Professor Greg Stillman**, University of Chicago, IL, USA

Published by Institute of Physics Publishing, wholly owned by The Institute of Physics, London

Institute of Physics Publishing, Techno House, Redcliffe Way, Bristol BS1 6NX,  
UK

US Editorial Office: Institute of Physics Publishing, The Public Ledger Building,  
Suite 1035, Independence Square, Philadelphia, PA 19106, USA

Typeset in Te<sub>X</sub> using the IOP Bookmaker Macros

Printed in the UK by J W Arrowsmith Ltd, Bristol

To my parents, my educators, my family,  
and my past, present, and future students



Taylor & Francis  
Taylor & Francis Group  
<http://taylorandfrancis.com>

# Contents

---

<b>Preface</b>	<b>xi</b>
<b>Foreword</b>	<b>xiii</b>
<b>Introduction</b>	<b>xv</b>
<b>1 Introduction to Semiconductor Compounds</b>	<b>1</b>
1.1 III–V semiconductor alloys	1
1.2 III–V semiconductor devices	4
1.3 Technology of multilayer growth	8
References	19
<b>2 MOCVD Growth Technique</b>	<b>22</b>
2.1 MOCVD growth systems	22
2.2 The MOCVD growth mechanism and growth process	29
2.3 Gas flow patterns and reactor design	34
2.4 MOCVD starting materials	42
2.5 Low-pressure MOCVD and MOMBE	47
References	49
<b>3 In situ Characterization during MOCVD</b>	<b>54</b>
3.1 Introduction	54
3.2 Reflectance anisotropy and ellipsometry	57
3.3 Optimization of the growth of III–V binaries by RDS	64
3.4 RDS investigation of III–V lattice-matched heterojunctions	71
3.5 RDS investigation of III–V lattice-mismatched structures	88
3.6 Insights on the growth process	108
References	111
<b>4 Ex situ Characterization Techniques</b>	<b>114</b>
4.1 Chemical bevel revelation	114
4.2 Deep-level transient spectroscopy	118
4.3 X-ray diffraction	129

4.4	Photoluminescence	143
4.5	Electrochemical capacitance–voltage and photovoltage spectroscopy	149
4.6	Resistivity and Hall measurement	155
4.7	Thickness measurement	166
	References	168
<b>5</b>	<b>MOCVD Growth of GaAs Layers</b>	<b>170</b>
5.1	Introduction	170
5.2	GaAs and related compounds band structure	170
5.3	MOCVD growth mechanism of GaAs and related compounds	179
5.4	Experimental details	182
5.5	Incorporation of impurities in GaAs grown by MOCVD	188
	References	197
<b>6</b>	<b>Growth and Characterization of the GaInP–GaAs System</b>	<b>199</b>
6.1	Introduction	199
6.2	Growth details	200
6.3	Structural order in $\text{Ga}_x\text{In}_{1-x}\text{P}$ alloys grown by MOCVD	202
6.4	Defects in GaInP layers grown by MOCVD	204
6.5	Doping behaviour of GaInP	207
6.6	GaAs–GaInP heterostructures	214
6.7	Growth and characterization of GaInP–GaAs multilayers by MOCVD	248
6.8	Optical and structural investigations of GaAs–GaInP quantum wells and superlattices grown by MOCVD	252
6.9	Characterization of GaAs–GaInP quantum wells by Auger analysis on chemical bevels	260
6.10	Evaluation of the band offsets of GaAs/GaInP multilayers by electoreflectance (Razeghi <i>et al</i> 1992)	264
6.11	Intersubband hole absorption in GaAs–GaInP quantum wells	275
	References	279
<b>7</b>	<b>Optical Devices</b>	<b>283</b>
7.1	Electro-optical Modulators	283
7.2	GaAs-based infrared photodetectors grown by MOCVD	293
7.3	Solar cells and GaAs solar cells	308
	References	313
<b>8</b>	<b>GaAs-based Lasers</b>	<b>317</b>
8.1	Introduction	317
8.2	Basic physical concepts	318
8.3	Laser structures	326

8.4	New GaAs-based materials for lasers	336
	References	365
<b>9</b>	<b>GaAs-based heterojunction electron devices grown by MOCVD</b>	<b>369</b>
9.1	Introduction	369
9.2	Heterostructure field-effect transistors (HFETs)	371
9.3	Heterojunction bipolar transistors (HBTs)	391
	References	400
<b>10</b>	<b>Optoelectronic Integrated Circuits (OEICs)</b>	<b>403</b>
10.1	Introduction	403
10.2	Material considerations	404
10.3	OEICs on Si substrate	405
10.4	The role of optoelectronic integration in computing	409
10.5	Examples of optoelectronic integration by MOCVD	414
	References	417
<b>Appendices</b>		
<b>A</b>	<b>Effect of Substrate Miscut on the Measured Superlattice Period</b>	<b>419</b>
<b>B</b>	<b>Optimization of Thickness and In Composition of InGaAs Well for 980 nm Lasers</b>	<b>422</b>
	References	425
<b>C</b>	<b>Energy Levels and Laser Gains in a Quantum Well (GaInAsP): the ‘Effective Mass Approximation’</b>	<b>426</b>
<b>D</b>	<b>Luttinger–Kohn Hamiltonian</b>	<b>429</b>
D.1	<i>k</i> · <i>p</i> theory	429
D.2	Luttinger–Kohn Hamiltonian	429
	References	430
<b>E</b>	<b>Infrared Detectors</b>	<b>431</b>
E.1	Classification	431
E.2	General theory of photodetectors	431
	References	435
<b>Index</b>		<b>437</b>



Taylor & Francis  
Taylor & Francis Group  
<http://taylorandfrancis.com>

## Preface

---

This volume is the second in a series with MOCVD-based photonics as its theme. The first volume started with an in-depth overview of the growth, characterization and applications of InP and its related compounds. Many publishers had asked me to write a book about MOCVD; however, it was Dr Cyril Hilsum, then a Consultant Editor of Institute of Physics Publishing, who was most persistent. In short, I relented and wrote volume 1 of *The MOCVD Challenge*. Towards the end of this work Dr Hilsum asked about GaAs and its related compounds, saying that it was impossible to write a book on MOCVD without including GaAs. I told him that as I had only just started working with this material system, I was leaving this for volume 2 because I wanted to gain further insight and experience before writing about it.

In volume 2, similarly to volume 1, the research reported charts much of the pioneering work that I completed in the growth of GaAs–(Ga,In)(As,P) in collaboration with and with the encouragement of many excellent scientists from around the world, especially Klaus von Klitzing's group. The aim of volume 2 is to provide insight, detail and an overview of the MOCVD growth process for GaAs and its related compounds. The GaAs–GaInP heterojunction has been of particular strategic interest as a robust and powerful alternative to GaAs–AlGaAs for devices with improved performance and reliability. Much of this volume focuses on the growth of a sophisticated quaternary material system, (Ga,In)(As,P), addressing such issues as crystal quality, optical properties and composition control. The driving force of my work has been the reliable growth of high-quality phosphorus-based materials for low-dimensional electronic, photonic and optoelectronic integrated circuit (OEIC) devices. Naturally, a key element of this work is the application of GaAs and its related compounds. It is through the development of these material systems and those described in volume 1 that MOCVD has appeared as the technique of choice for industrial mass production as well as for cutting-edge research.

In volume 2, Chapter 1 is devoted to an introduction to semiconductor compounds and Chapter 2 describes the MOCVD growth process. Chapter 3 discusses the use of reflection difference spectroscopy (RDS) for *in situ* monitoring during growth. This technique is important because it is a direct analogue of the RHEED technique for MBE growth. The RDS technique

has proved critical in the optimization of reactor design and improving the quality of the material and understanding the properties of heterojunction interfaces. Chapter 4 discusses *ex situ* characterization techniques not described in volume 1. Chapter 5 covers the specifics of the growth of GaAs as the basis for Chapter 6 which covers the growth and characterization of the GaAs–GaInP system. Chapter 7 describes optical devices based on GaAs and related compounds whereas Chapter 8 details the specifics of GaAs-based laser diode structures. Chapter 9 discusses electronic devices, and finally Chapter 10 provides an overview of optoelectronic integrated circuits.

Achieving the results reported in this book, as those in volume 1, would have been impossible without my excellent groups at Thomson-CSF in the Exploratory Material Laboratory and, more recently, at the Center for Quantum Devices at NWU. I would like to thank all of my students and colleagues: this book is for them, and all of my future students and colleagues.

I am indebted to Dr Hilsum, who reviewed and edited volume 1 of *The MOCVD Challenge* and large parts of this volume, for being the driving force behind this series. In addition, I am also grateful to Dr Clivia Sotomayor Torres and Professor Greg Stillman who also reviewed and edited the manuscript. Their suggestions made an invaluable contribution to this work.

Since I joined Northwestern University in 1991 I have had the support and encouragement of many scientists, in particular Drs Leo Esaki, Lester Eastman, George Wright, Yoon-Soo Park, Max Yoder, L N Durvasula, Ray Balcerak, Henry Everitt, Gail Brown, G Witt, W Mitchel, R Burnham, John Fan, Mark Spitzer, R Bredhauer, E Spitz, G Nuzillat, D Kaplan and J P Duchemin. Moreover, the Center for Quantum Devices would not have come into existence except for the original vision of Northwestern University. I am grateful to Drs A Weber, H Bienen, D Cohen, W Kern, W Fischer and A Haddad for their unequivocal support since I joined Northwestern University. I am particularly indebted to Dean J Cohen for convincing me that Northwestern University is the place to do research, for facilitating my move from Thomson-CSF and for his continuing support and encouragement.

**Manijeh Razeghi**

McCormick School of Engineering  
Northwestern University  
Evanston, Illinois

April 1995

## Foreword

---

History has often marked its progress in terms of materials, starting with the stone age, then the iron age, then the bronze age and on to the present age. Indeed, materials continue to be a limiting factor in enabling many areas of technology even today. For example, the development of optical fibres for communications has been a key factor in constructing the information superhighway.

In the future when historians look back on our current stage of development they will probably describe it as the age of artificial materials, a period when we learned how to create new forms of materials tailored specifically to our needs, not found in nature or by refining nature. As a material scientist, I find that composites come to mind, but just as pervasive now is the development of layered semiconductors by those interested in electronic and optical devices. How marvellous it is to think that we are now able to build, atom by atom, different optoelectronic devices constructed of a whole series of materials many of which never existed before. Professor Manijeh Razeghi's efforts in this regard are almost legendary at this point; she has been one of a handful of pioneers in developing the techniques and the devices themselves.

For me, as an engineering Dean, it has been a distinct adventure—a ride into the future—to encourage Manijeh to leave Paris and to come to our University to join our Department of Electrical Engineering and Computer Science. In no time we have been able to help Manijeh to establish her new laboratory facilities and the Center for Quantum Devices. (Indeed help is the correct word, because often she had to look back and wait for some of us to catch up.)

Now many new things are coming from these laboratories, but Manijeh's life also now has a very new dimension beyond the research that she aggressively pursues. Generations of 'students', high-schoolers, undergraduates, graduates, postdocs and visitors are all being influenced by her philosophy and approach to work, an influence she could not fulfil in her previous roles.

Those of us who are in academic research have a secret: in our careers we may indeed discover something grand (and Manijeh has certainly done so and more can be expected) but most of all we have inspired and launched many young people on their way to successful careers. In many senses, this results in a greater satisfaction than our own splendid discoveries. Manijeh is

now firmly entrenched in academia and clearly enjoying both sides of such a career. This book is another example of her ability to do cutting-edge research and her desire to educate. It is a text of the fundamentals of semiconductor crystal growth and material characterization leading into many of the important concepts in advanced device design and fabrication.

**Jerome B Cohen**

Robert R McCormick School of Engineering and Applied Science  
Northwestern University  
Evanston, Illinois

April 1995

## Introduction

---

Professor Razeghi's *The MOCVD Challenge* volume 1 appeared in 1989 and was extremely well received by the scientific and engineering communities working on semiconductors. This volume complements volume 1 in that it has a focus on GaAs and other arsenides grown by MOCVD, whereas volume 1 covered mainly the phosphide-based materials.

Naturally this volume conveys much more than MOCVD growth of GaAs. Based on her world-class research work carried out at Thomson-CSF and more recently at Northwestern University, the author explores thoroughly the issue of *in situ* MOCVD growth monitoring of both arsenides and phosphides by means of differential reflectivity. This pioneering work is explained in detail supported by a solid theoretical analysis of its principles. The potentials for studying and understanding the initial stages of growth are clearly indicated and this will be extremely useful for future developments in, for example, self-organized growth of semiconductor nanostructures by MOCVD. Moreover, the author gives a clear example of the dynamic interaction between an *in situ* growth characterization technique, the following modifications of a reactor design and the impact of these on the resultant sample design and properties. A full cycle of improvements, which constitutes a marvellous example of how progress can be made in an experimental multi-variable problem.

Reflecting Manijeh Razeghi's trajectory in recent years, the book offers welcome perspectives from both industrial and academic points of view; whereas most topics covered are treated at the level of final year/graduate students in material sciences, there is a consistent treatment of the relevant science issues which have a bearing on device applications. This is most obviously exemplified by the chapter on *ex situ* characterization and the last four chapters on device application. Device-relevant issues are addressed from the very beginning of the book in the unique breathtaking style of the author.

Another fascinating aspect offered by Professor Razeghi's book is the journey offered, which starts by putting atoms together with MOCVD, via the growth and characterization of semiconductor layers, then through discrete devices and finally reaching an overview of an optoelectronic system. And at most stops there is the possibility of an in-depth study tour.

It is now almost three years since Professor Razeghi was appointed to a

prestigious chair at Northwestern University. Within two years her research team and laboratory achieved critical mass, with many projects flowing in and high-impact novel results on photonic devices physics and engineering coming out. Some of these are based on another family of promising materials, the antimonides, and I very much hope that in a few years' time we shall see volume 3 in which Manijeh Razeghi shows the continued power and flexibility of MOCVD as a major industrial semiconductor technological base.

**Clivia M Sotomayor Torres**  
Glasgow

---

## Introduction to Semiconductor Compounds

The first volume of this series is concentrated on MOCVD growth of InP–GaInAsP multilayers for photonic and electronic devices. In this volume, the MOCVD growth of GaAs and related alloys for photonic and electronic devices will be described.

### 1.1 III–V SEMICONDUCTOR ALLOYS

#### 1.1.1 III–V binary compounds

Most of the III–V semiconductor compounds have the zincblende structure. Table 1 shows the bandgap energy, lattice parameter, refractive index, dielectric constant, conduction band effective mass and valence band effective masses of some of the binary III–V compounds. These binary semiconductors are generally useful as substrates and some binary, ternary and quaternary alloys of these compounds have certain useful characteristics. Some of the ternary and quaternary alloys are lattice matched to certain binary compounds with different bandgap energies providing interesting physical properties.

#### 1.1.2 III–V ternary alloys

When more than one element from group III or group V is distributed randomly on group III or group V lattice sites, III–III–V or III–V–V ternary alloys can be achieved. The notation most frequently used is  $\text{III}_x\text{III}_{1-x}\text{V}$  or  $\text{IIIV}_y\text{V}_{1-y}$ . There are 18 possible ternary systems among the group III and group V elements of interest.

The bandgap energy  $E_g(x)$  of a ternary compound varies with the composition  $x$  as follows:

$$E_g(x) = E_g(0) + bx + cx^2 \quad (1.1)$$

where  $E_g(0)$  is the bandgap energy of the lower-bandgap binary compound and  $c$  is the bowing parameter. The bowing parameter  $c$  can be theoretically

**Table 1.1** Physical constants of some III–V binary compounds at 300 K.

III–V binary compound	Atomic number $\bar{Z}$	Lattice parameter (Å)	Bandgap energy (eV)	Refractive index ( $\bar{n}$ )	Effective mass ( $m_e/m_0$ )	Effective mass ( $m_{hh}/m_0$ )	Effective mass ( $m_{lh}/m_0$ )	Effective mass ( $m_{hh}/m_0$ )	Dielectric constant ( $\epsilon/\epsilon_0$ )	Electron affinity $\chi$ (eV)
InSb	50	6.479 37	0.17	4.0	0.0145	0.44	0.016	17.7	4.69	
InAs	41	6.058 4	0.36	3.520	0.022	0.41	0.025	14.6	4.45	
GaSb	41	6.095 93	0.73	3.820	0.044	0.33	0.056	15.7	4.03	
InP	32	5.868 75	1.35	3.450	0.078	0.8	0.012	12.4	4.4	
GaAs	32	5.653 21	1.424	3.655	0.065	0.45	0.082	13.1	4.5	
AlSb	32	6.133 5	1.58	3.400	0.39	0.5	0.11	14.4	3.64	
AlAs	23	5.662 2	2.16	3.178	0.11	—	0.22	10.1	—	
Gap	23	5.451 17	2.26	3.452	0.35	0.86	0.14	11.1	4.0	
AlP	14	5.451	2.45	3.027	—	0.63	0.20	—	—	

**Table 1.2** Compositional dependence of the energy gap in the III-V ternary solid solution at 300 K (Casey and Panish 1978).

Ternary	Direct energy gap $E_g$ (eV)
$\text{Al}_x\text{Ga}_{1-x}\text{As}$	$E_g(x) = 1.424 + 1.247x$
$\text{Al}_x\text{In}_{1-x}\text{As}$	$E_g(x) = 0.360 + 2.012x + 0.698x^2$
$\text{Al}_x\text{Ga}_{1-x}\text{Sb}$	$E_g(x) = 0.726 + 1.139x + 0.368x^2$
$\text{Al}_x\text{Ga}_{1-x}\text{Sb}$	$E_g(x) = 0.172 + 1.621x + 0.43x^2$
$\text{Ga}_x\text{In}_{1-x}\text{P}$	$E_g(x) = 1.351 + 0.643x + 0.786x^2$
$\text{Ga}_x\text{In}_{1-x}\text{As}$	$E_g(x) = 0.360 + 1.064x$
$\text{Ga}_x\text{In}_{1-x}\text{Sb}$	$E_g(x) = 0.172 + 0.139x + 0.415x^2$
$\text{GaP}_x\text{As}_{1-x}$	$E_g(x) = 1.424 + 1.15x + 0.176x^2$
$\text{GaAs}_x\text{Sb}_{1-x}$	$E_g(x) = 0.726 - 0.502x + 1.2x^2$
$\text{InP}_x\text{As}_{1-x}$	$E_g(x) = 0.36 + 0.891x + 0.101x^2$
$\text{InAs}_x\text{Sb}_{1-x}$	$E_g(x) = 0.18 - 0.41x + 0.58x^2$

determined (Van Vechten and Bergstresser 1970). It is especially helpful to estimate  $c$  when experimental data are unavailable. The lattice constant  $a$  of ternary compounds can be calculated using Vegard's law. According to Vegard's law the lattice constant of the ternary alloys can be expressed as follows:

$$a_{\text{alloy}} = x a_A + (1 - x) a_B \quad (1.2)$$

where  $a_A$  and  $a_B$  are the lattice constants of the binary alloys A and B. Vegard's law is obeyed quite well in most of the III-V ternary alloys. The compositional dependence of the energy gaps of various III-V ternary alloys at 300 K is given in table 1.2 (Casey and Panish 1978).

### 1.1.3 III-V quaternary compounds

The interest in quaternary alloys has centred on their use in conjunction with binary and ternary alloys to form lattice-matched heterojunction structures with different bandgaps. The reduction of stress in  $\text{Al}_x\text{Ga}_{1-x}\text{As}$  layers grown on GaAs substrates is illustrated by the introduction of small amounts of P to give the quaternary  $\text{Al}_x\text{Ga}_{1-x}\text{P}_y\text{As}_{1-y}$ . The InP/ $\text{Al}_x\text{Ga}_{1-x}\text{P}_y\text{As}_{1-y}$  heterojunction serves as a successful example of a binary-quaternary lattice-matched system.

Ilegems and Panish (1974) calculated quaternary phase diagrams with the solid decomposed into ternary alloys: ABC, ACD, ABD and BCD (where A and B are group III elements, and C and D are group V elements). Jordan and Ilegems (Jordan *et al* 1974) obtained equivalent formulations considering the solid as a mixture of binary alloys: AC, AD, BC and BD. Assuming a linear dependence on composition of lattice parameter  $a_{AC}$  for the binary AC,

**Table 1.3** Binary to quaternary III-V lattice-matched systems of multilayer heterostructures (Casey and Panish 1978).

Quaternary	Lattice-matched binary	Wavelength, $\lambda$ ( $\mu\text{m}$ )
$\text{Al}_x\text{Ga}_{1-x}\text{P}_y\text{As}_{1-y}$	GaAs	0.8–0.9
$\text{Al}_x\text{Ga}_{1-x}\text{As}_y\text{Sb}_{1-y}$	InP	1
$\text{Al}_x\text{Ga}_{1-x}\text{As}_y\text{Sb}_{1-y}$	InAs	3
$\text{Al}_x\text{Ga}_{1-x}\text{As}_y\text{Sb}_{1-y}$	GaSb	1.7
$\text{Ga}_x\text{In}_{1-x}\text{P}_y\text{As}_{1-y}$	GaAs, InP	1–1.7
$\text{Ga}_x\text{In}_{1-x}\text{P}_y\text{Sb}_{1-y}$	InP, GaSb, AlSb	2
$\text{In}(\text{P}_x\text{As}_{1-x})_y\text{Sb}_{1-y}$	AlSb, GaSb, InAs	2–4
$(\text{Al}_x\text{Ga}_{1-x})_y\text{In}_{1-y}\text{P}$	GaAs, $\text{Al}_x\text{Ga}_{1-x}\text{As}$	0.57
$(\text{Al}_x\text{Ga}_{1-x})_y\text{In}_{1-y}\text{As}$	InP	0.8–1.5
$(\text{Al}_x\text{Ga}_{1-x})_y\text{In}_{1-y}\text{Sb}$	AlSb	1.1–2.1

and similarly for the other lattice parameters, the lattice parameter of the alloy  $\text{A}_x\text{B}_{1-x}\text{C}_y\text{D}_{1-y}$  is

$$a_0 = xy a_{\text{AC}} + x(1-y) a_{\text{AD}} + (1-x)y a_{\text{BC}} + (1-x)(1-y) a_{\text{BD}}. \quad (1.3)$$

The bandgap energy determination is more complicated. However, if the bowing parameter ( $c$ ) is neglected, the bandgap energy may be approximated from the bandgap of the binaries, assuming linear variation:

$$E_g = xy E_{\text{AC}} + x(1-y) E_{\text{AD}} + (1-x)y E_{\text{BC}} + (1-x)(1-y) E_{\text{BD}}. \quad (1.4)$$

The binary to quaternary III-V lattice-matched systems for multilayer heterostructures are listed in table 1.3.

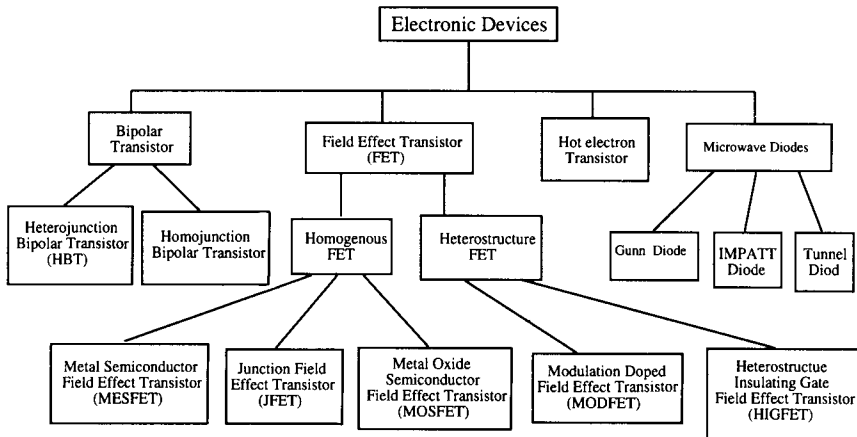
## 1.2 III-V SEMICONDUCTOR DEVICES

The most important semiconductor multilayer devices fall into two groups:

- (i) optoelectronic devices (table 1.4), and
- (ii) electronic devices (table 1.5).

**Table 1.4** Main optoelectronic devices.

Device	Operational principle
Light-emitting diodes (LEDs) and laser diodes (LDs)	Convert electrical energy into optical radiation
Solar cells	Convert optical radiation into electrical energy
Modulators	Convert electrical signals into optical signals
Photodetectors (PDs)	Convert optical signals into electric current or voltage

**Table 1.5** Most commonly used electronic devices.

### *Electronic devices*

(1) In bipolar devices both electrons and holes are involved in the transport processes. The bipolar transistor in which there is interaction between two closely coupled p–n junctions is one of the most important semiconductor devices. The thyristor, which basically comprises three closely coupled p–n junctions in the form of a multilayered p–n–p–n structure, exhibits bistable characteristics and can be switched between a high-impedance, low-current OFF state, and a low-impedance, high-current ON state.

(2) In unipolar devices only one type of carrier participates predominantly in the conduction mechanism. The junction field effect transistors (JFETs), and metal oxide–semiconductor devices (MOSFETs) are the most important devices for very large-scale integrated (VLSI) circuits.

(3) Microwave diodes can be made with operating frequencies covering the range from about 0.1 GHz to 1000 GHz with corresponding wavelengths from 300 cm to 0.3 mm.

*Tunnel diode* devices are associated with quantum tunnelling phenomena (a majority carrier effect). The tunnelling time of carriers through the potential energy barrier is very short, permitting the use of tunnel devices well into the millimetre-wave region (Esaki 1958).

The IMPATT (impact ionization avalanche transit time) diode is one of the most powerful solid state sources of microwave power (Sze and Ryder 1971). IMPATT diodes employ impact ionization and transit time properties of semiconductor structures to produce negative resistance at microwave frequencies. The Gunn diode discovered by Gunn (1963, 1964), is a transferred electron device. He found that a coherent microwave output was generated when a DC electric field in excess of a critical threshold value of several thousand volts per centimetre was applied across an n-type sample of GaAs or InP. Earlier, Hilsum (1962) and Ridley (Ridley and Watkins 1961) had proposed a theory

of negative differential resistance, which is due to a field-induced transfer of conduction band electrons from a low-energy, high-mobility valley to higher-energy, low-mobility satellite valleys that could result in microwave oscillation. The transferred electron effect has been referred to as the Gunn effect or as the Hilsum–Ridley effect.

#### *Optoelectronic devices*

Optoelectronic and photonic devices are those in which photons play a major role. These devices can detect, generate and convert optical energy to electrical energy (photodetectors, PD) or vice versa (light-emitting diodes (LEDs) and laser diodes (LDs)). Optoelectronic and photonic devices can be divided into several groups: solar cells, photodetectors, semiconductor light-emitting diodes, laser diodes and optical modulators.

(a) *Solar cells* convert optical radiation into electrical energy. As worldwide energy demand increases, natural resources of fossil fuels will become exhausted. The solar cell can be considered as a major candidate for obtaining energy from the sun. The solar cell was first developed by Chapin *et al* (1954) using a diffused silicon p–n junction. To date, solar cells have been made from many III–V semiconductors.

(b) *Photodetector devices* convert the received optical power into an electrical current or voltage which is amplified and processed to deliver information in a useful form. In general, the performance of a photodetector depends on two parameters: the quantum efficiency (the number of electron–hole pairs collected per incident photon), and the energy gap of the material with a high absorption coefficient ( $\simeq 10^3 \text{ cm}^{-1}$ ). Above the band gap, III–V multilayer photodiodes can absorb efficiently in a layer only a few micrometres thick, leading to a small device structure and a short carrier transit time.

(c) *The semiconductor light-emitting diode and laser diode devices* convert electrical energy into optical radiation. The demonstration of the injection laser and continuous wave (CW) operation at room temperature had to await not only the basic invention of the laser and the advances in semiconductor physics of the 1950s, but also the development of suitable materials technology for the growth of several new semiconductors. Semiconductor lasers are considered to be the most important light sources for optical fibre communication systems.

The principal materials for semiconductor lasers were the direct energy gap compounds and alloys between elements of group III and group V of the periodic table. In a series of binary III–V compounds like InP, GaAs and GaP, increasing the atomic weight of the group III or group V element in general decreases the energy gap ( $E_g$ ) and increases the refractive index  $\bar{n}$  with exception of GaAs–AlAs and GaP–AlP, where the lattice parameter  $a$  increases. The crystalline solid solutions between these binary compounds, i.e. alloys, usually have properties intermediate between the end components as described in equations (1.3) and (1.4).

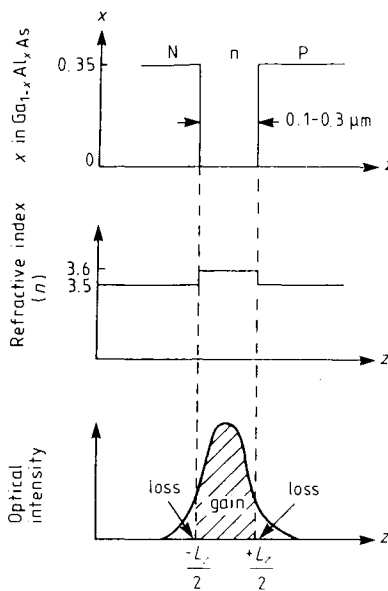


**Figure 1.1** Alloy composition, the refractive index and the confinement of light in the GaAs–GaAlAs double-heterostructure lasers.

Heterostructure lasers are layered semiconductor structures in which the lattice parameter is usually held constant from layer to layer while  $E_g$  and  $\bar{n}$  are varied. The quaternary solid solution systems provide continuously variable  $E_g$  and  $\bar{n}$  for various compositions at constant  $a_0$  and permit additional possible heterostructure laser semiconductors.

The active layer in a double heterostructure (DH) laser is the region where the light is generated (figure 1.1). The ratio of the optical intensity within the active layer to the total optical intensity is the confinement factor, and is used to represent the effect of the waveguide parameters on the threshold current density (figure 1.2). The DH laser provides a well defined dielectric waveguide and was the first injection laser structure to permit CW operation at room temperature.

Virtually all lasing semiconductors have direct bandgaps. This is to be expected since the radiative transition in a direct-bandgap semiconductor is a first-order process, and the transition probability is high. Some of the binary–ternary and binary–quaternary III–V lattice-matched systems for DH laser applications are listed in tables 1.6 and 1.7. The bandgap energy of the recombination region (active layer) controls the emission wavelength

$$\lambda (\mu\text{m}) = \frac{hc}{E_g} = \frac{1.24}{E_g (\text{eV})} \quad (1.5)$$

where  $E_g$  is the energy gap,  $c$  is the velocity of light in vacuum and  $h$  is Planck's constant.

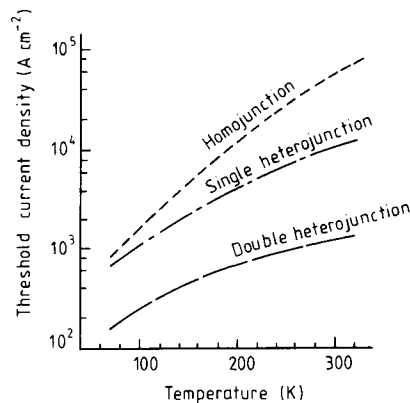


**Figure 1.2** Variation of threshold current density ( $J_{\text{th}}$ ) versus temperature for a homojunction, single heterojunction and double heterojunction of GaAs–GaAlAs lasers.

### 1.3 TECHNOLOGY OF MULTILAYER GROWTH

Here we consider some of the important materials for microwave and optoelectronic devices, i.e. GaAs,  $\text{Ga}_x\text{Al}_{1-x}\text{As}$  and  $\text{Ga}_x\text{In}_{1-x}\text{P}$ . In the GaAs–GaAlAs system, the lattice constant of GaAlAs is almost identical to that of the GaAs substrate so there is no lattice mismatch problem. In the  $\text{Ga}_x\text{In}_{1-x}\text{P}$  system, the lattice constants of GaInP can vary widely and the quality of the epilayer depends on how closely the lattice constant of the GaInP is matched to that of the GaAs substrate. However, the technology behind liquid phase epitaxy (LPE), vapour phase epitaxy (VPE), molecular beam epitaxy (MBE) and metallorganic chemical vapour phase deposition (MOCVD) provides the means to achieve multilayer structures in this III–V system. Devices such as diode lasers, LEDs, detectors, FETs, phototransistors and waveguides fabricated with these two material systems have been prepared by these four growth processes.

#### 1.3.1 Epitaxial technology

A wide range of semiconducting materials, particularly materials based on InP and GaAs, need to be grown as thin single-crystal films for a variety of applications. The discovery of quantum wells and superlattices has revolutionized the area of semiconductor technology in terms of new devices. These new devices require precise control and uniformity of thickness, excellent homogeneity, high purity, very sharp interfaces between the substrate and epitaxial layers, and low misfit dislocations in the epilayers. In the last few decades, epitaxial techniques have advanced to a level where such requirements can be easily met by a variety of growth techniques. Each technique has its own strengths and weaknesses.

**Table 1.6** Ternary III–V lattice matched to binary III–V systems for laser applications using multilayer heterostructures.

Ternary	Lattice-matching binary substrate	Bandgap $E_g$ (eV, 300 K)	Wavelength $\lambda$ ( $\mu\text{m}$ , 300 K)	DH for laser
Ga <sub>0.9</sub> In <sub>0.1</sub> Sb	AlSb (indirect)	0.633	2.0	AlSb/Ga <sub>0.9</sub> In <sub>0.1</sub> Sb/AlSb
InAs <sub>0.82</sub> Sb <sub>0.18</sub>	AlSb	0.23	0.59	AlSb/InAs <sub>0.82</sub> Sb <sub>0.18</sub> /AlSb
Ga <sub>1-x</sub> Al <sub>x</sub> As	GaAs	1.49–1.9	0.7–0.9	Ga <sub>1-x</sub> Al <sub>x</sub> As/GaAs/Ga <sub>1-x</sub> Al <sub>x</sub> As
G <sub>0.49</sub> In <sub>0.51</sub> P	GaAs	1.883	0.65	G <sub>0.49</sub> In <sub>0.51</sub> P/GaAs/G <sub>0.49</sub> In <sub>0.51</sub> P
Al <sub>0.49</sub> In <sub>0.51</sub> P	GaAs	2.3		Al <sub>0.49</sub> In <sub>0.51</sub> P/G <sub>0.49</sub> In <sub>0.51</sub> P/Al <sub>0.49</sub> In <sub>0.51</sub> P
AlAs <sub>0.08</sub> Sb <sub>0.92</sub>	Gasb	0.72	1.72	AlAs <sub>0.08</sub> Sb <sub>0.92</sub> /Gasb/AlAs <sub>0.08</sub> Sb <sub>0.92</sub>
InAs <sub>0.91</sub> Sb <sub>0.09</sub>	Gasb	0.287	4.3	Gasb/InAs <sub>0.91</sub> Sb <sub>0.09</sub> /Gasb
Ga <sub>0.47</sub> In <sub>0.53</sub> As	InP	0.75	1.7	InP/Ga <sub>0.47</sub> In <sub>0.53</sub> As/InP
Al <sub>0.47</sub> In <sub>0.53</sub> As	InP	1.46	0.85	Al <sub>0.47</sub> In <sub>0.53</sub> As/InP/Al <sub>0.47</sub> In <sub>0.53</sub> As
AlAs <sub>0.16</sub> Sb <sub>0.84</sub>	InAs	0.36	3.4	AlAs <sub>0.16</sub> Sb <sub>0.84</sub> /InAs/AlAs <sub>0.16</sub> Sb <sub>0.84</sub>
GaAs <sub>0.08</sub> Sb <sub>0.92</sub>	InAs	0.36		GaAs <sub>0.08</sub> Sb <sub>0.92</sub> /InAs/GaAs <sub>0.08</sub> Sb <sub>0.92</sub>

**Table 1.7** Quaternary III–V lattice matched to binary III–V systems for laser applications using multilayer heterostructures.

Substrate	Quaternary	Bandgap energy $E_g$ (eV)	Wavelength $\lambda$ ( $\mu\text{m}$ )
InAs	$\text{In}_x\text{Ga}_{1-x}\text{As}_y\text{Sb}_{1-y}$ $(1 - y) = 0.916(1 - x)$	0.35–0.7	3.5–1.77
InP	$\text{In}_x\text{Ga}_{1-x}\text{As}_y\text{P}_{1-y}$ $y = 2.16(1 - x)$	0.75–1.35	1.7–0.9
GaAs	$\text{In}_x\text{Ga}_{1-x}\text{As}_y\text{P}_{1-y}$ $(1 - y) = 2.04x$	1.42–1.9	0.87–0.65

*(a) Liquid phase epitaxy*

LPE involves precipitation of material from a supercooled solution onto an underlying substrate. The composition of the layers formed on the substrate depends mainly on the equilibrium phase diagram and, to a lesser extent, on the orientation of the substrate. There are basically three parameters that affect the growth in LPE. These are growth temperature, growth time and melt composition. The first LPE growth apparatus was developed by Nelson (1963). The LPE reactor consists of a horizontal furnace system and a sliding graphite boat. The LPE apparatus is quite simple and excellent quality layers and high purity levels can be achieved.

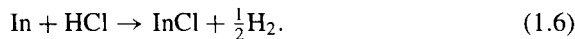
The advantages of LPE are the simplicity of equipment, higher deposition rates and the high-purity layers that can be obtained. Background elemental impurities are eliminated due to the availability of high-purity metals and the inherent purification process that occurs during the liquid to solid phase transition. For example, during the purification stage of Al-containing material, oxygen in the system forms highly stable  $\text{Al}_2\text{O}_3$  on the surface of the liquid which prevents oxygen incorporation into the epitaxial layer.

The limitations of LPE technology are the poor thickness uniformity of the epitaxial layers and difficulty in growing multilayer structures with extremely abrupt interfaces due to the high growth rate and meltback effect. Another limitation is the difficulty in growing certain materials. For example, in alloys containing both Al and In, the high Al distribution coefficient leads to much difficulty in growing alloys with a high composition of In.

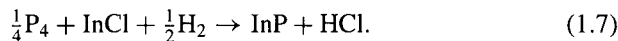
*(b) Vapour phase epitaxy*

VPE, like LPE, is a thermodynamic equilibrium growth technique. The growth of InP-based materials can be obtained in a fused-silica reactor composed of two zones set at different temperatures by using a multielement furnace that surrounds the reactor. Hydrogen or hydrogen chloride (HCl) are often used as a carrier gas, and arsine ( $\text{AsH}_3$ ) and phosphine ( $\text{PH}_3$ ) as arsenic (As) and phosphorus (P) sources, respectively. Pure indium and gallium metal can be

used as group III elemental sources. In the first zone of the reactor (source zone), which is held at 750 °C to 800 °C, the gaseous species to be transported are synthesized following the reaction



In the second zone (deposition zone), which has a temperature range 650–750 °C, growth occurs via the reaction



One of the major advantages of VPE over LPE is the possibility of localized epitaxy. This means that if one grows InP-based material on an InP substrate consisting of a stripe of SiO<sub>2</sub> or Si<sub>3</sub>N<sub>4</sub>, there is monocrystal growth on the substrate, but no growth on the dielectric (SiO<sub>2</sub> or Si<sub>3</sub>N<sub>4</sub>) surface, which could be important for monolithic integrated circuits on InP substrates.

The disadvantages of VPE include the potential for hillock and haze formation, and interfacial decomposition during the preheat stage. It is very difficult, if not impossible, to grow superlattice structures. Alternating layers are normally obtained by physically moving the substrate back and forth between reactor tubes. This approach is unattractive when compared with techniques such as MBE or MOCVD where the transport of source materials rather than the substrates is controlled.

### *(c) Molecular beam epitaxy*

The MBE process involves the evaporation of elemental sources at a controlled rate onto a crystalline substrate surface held at a suitable temperature under ultrahigh-vacuum (UHV) conditions. Therefore, it is a high-vacuum technique where beams of evaporated molecules or atoms are focused onto the substrate. The use of UHV introduces two advantages. Firstly, atoms and molecules reach the growth surface in a very clean condition. Secondly, the growth process can be monitored *in situ* by diagnostic techniques as the crystal grows one atomic layer at a time (Parker 1985). *In situ* diagnostic techniques such as reflection high-energy electron diffraction (RHEED), Auger electron spectroscopy (AES), x-ray photoelectron spectroscopy (XPS), low-energy electron diffraction (LEED), secondary-ion mass spectroscopy (SIMS) and ellipsometry are used.

MBE has attracted much interest as an excellent crystal growth technology for the production of complex and varied structures, especially for GaAs-based multilayer structures. This is due to its capability for extremely precise control over layer thickness and doping profile. However, the disadvantage of MBE is that it is expensive because of the need for UHV apparatus. Another major problem is the difficulty in growing phosphorus-containing materials such as InP and GaInAsP. Phosphorus is found to bounce around in the system, eventually collecting in the vacuum pumps. In addition, the growth of alloys containing both As and P is particularly difficult.

*(d) Metallorganic chemical vapour deposition*

Growth of III–V compounds from organometallic and hydride sources was first reported in 1960 by Didchenko *et al* (1960). In their experiment, deposition of InP from trimethylindium (TMIn) and phosphine (PH<sub>3</sub>) was obtained in a closed-tube system. Later, Manasevit (1968, 1971, Manasevit *et al* 1971) established the possibility of depositing many common compound semiconductors from organometallic materials and he coined the term metallorganic chemical vapour deposition (MOCVD). It is also called metallorganic vapour phase epitaxy (MOVPE). This technique for epitaxial growth of compound semiconductors using organometallic precursors has advanced rapidly during the past decades. In recent years, MOCVD has established itself as an important epitaxial crystal growth technique, yielding high-quality low-dimensional structures for fundamental semiconductor physics research and useful electronic and photonic semiconductor devices.

In MOCVD, chemically active species interact to produce a corresponding epitaxial layer either in the vapour phase or on a solid surface of the substrate. In particular, growth of semiconductor III–V compounds results from introducing metered amounts of group III alkyls and group V hydrides into a quartz tube which contains a substrate placed on an heated susceptor. The hot susceptor has a catalytic effect on the decomposition of the gaseous products and the growth therefore primarily takes place on this hot surface. MOCVD is attractive because of its relative simplicity compared to other growth methods. It can produce heterostructures, multiquantum wells and superlattices with very abrupt transitions in composition as well as in doping profiles in continuous growth by rapid changes of the gas composition in the reaction chamber.

The technique is also attractive because of its ability to grow uniform layers, low-background doping density, sharp interfaces and the potential for large-scale commercial applications. MOCVD can be used to prepare multilayer structures with thicknesses as thin as a few atomic layers. This allows the study and incorporation into device applications of the two-dimensional electron gas (2DEG) (Delahaye *et al* 1986, Guldner *et al* 1986, Razeghi *et al* 1986), two-dimensional hole gas (2DHG) (Razeghi *et al* 1986, Rogers *et al* 1986) and transport and quantum size effects (QSE) (Razeghi 1983) in a variety of III–V compound semiconductors, heterojunctions and multilayers (Razeghi *et al* 1986, Nicholas *et al* 1985). It also makes it possible to ‘engineer the bandgap’ by growing a predetermined alloy composition and doping profile (Razeghi *et al* 1986). As a result, an entirely new class of electronic and photonic devices is realized (Razeghi *et al* 1987). Another recent advance is the ability to grow strained-layer superlattices, in which the crystal lattices of the two materials are not very closely matched and there is a built-in strain in each layer (Osbourne 1982).

The main disadvantage of the MOCVD growth technique is the use of large quantities of poisonous gases such as AsH<sub>3</sub> and PH<sub>3</sub>. However, the recent development of less hazardous precursors for MOCVD has made it a very

powerful technique for epitaxial growth.

(e) *Metallorganic molecular beam epitaxy*

Low-pressure MOCVD techniques have been shown to provide high-quality films by eliminating the parasitic reactions normally observed in atmospheric reactors. This idea of low pressure was further extended to high vacuum to grow high-quality GaAs, GaAsP and GaInAs films (Fraas 1981).

Since conventional MBE has the disadvantage of difficulty in the growth of phosphide compounds, the solid sources for the group V element, usually As and P, are replaced with the gaseous sources AsH<sub>3</sub> and PH<sub>3</sub>, giving rise to gas source molecular beam epitaxy (GSMBE). In addition, even group III solid elements in MBE have been replaced by simple metallorganic compounds—metallorganic molecular beam epitaxy (MOMBE) (Vodjani 1982). It is also called chemical beam epitaxy (CBE) and metallorganic chemical beam deposition (MOCBD).

Compared to MOCVD growth, the MOCBD technique has the advantages of MBE, such as *in situ* surface diagnostic techniques which provide monitoring of *in situ* etching and the removal of oxides before growth, and is compatible with other high-vacuum thin-film processing.

GSMBE looks more promising since it uses lower quantities of phosphine and also it reduces the problem of using chemical waste disposal systems such as scrubbers normally used in MOCVD.

(f) *Atomic layer epitaxy*

Atomic layer epitaxy (ALE) is a new growth technique with control at the monolayer level. ALE was originally proposed by Suntola (Suntola *et al* 1980) as a novel mode of preparing thin films of ZnS by evaporative deposition. ALE operates by growing complete layers on top of each other, similarly to evaporative deposition. Thus there are two basic variants: heated elemental source materials and sequential surface exchange reactions between compound reactants. By definition, ALE is based on chemical reactions at the solid surface of a substrate, to which the reactants are transported alternately as pulses of neutral molecules or atoms, either as chopped beams in high vacuum or as switched streams of vapour possibly with an inert carrier gas. The incident pulse reacts directly and chemically only with the outermost atomic layer of the substrate. The film therefore grows stepwise, a single monolayer per pulse, provided that at least one complete monolayer coverage of a constituent element, or of a chemical compound containing it, is formed before the next pulse is allowed to react with the surface.

In metallorganic atomic layer epitaxy (MOALE) (Nishizawa and Kurabayashi 1986, Doi *et al* 1986) hydrides are used as the starting materials and instead of alkyls, chloride is used along with hydrides. The technique is called chloride atomic layer epitaxy (chloride-ALE) (Matsumoto and Usui 1986). Kobayashi *et al* (1985) introduced a small amount of AsH<sub>3</sub> during the TEGA exposure step in order to grow n-type GaAs films. They called this technique flow-rate modulation epitaxy (FME). The major advantages of ALE, especially digital

ALE, where the thickness grown is insensitive to any analogue quantities such as source gas pressure, growth temperature and growth time, is the ability to obtain large-area growth with monolayer control of thickness and composition.

*(g) Migration-enhanced epitaxy*

Rapid migration of the evaporated materials on the growing surface is essential to the growth of high-quality epitaxial layers. In conventional MBE growth of GaAs and AlAs layers, migrating materials on the growing surface are Ga–As and Al–As molecules rather than Ga and Al atoms, respectively, because these layers are grown under arsenic-stabilized conditions. The migration of these molecules on the surface is very slow, especially at low temperatures. Therefore, lowering the substrate temperature considerably deteriorates the crystal quality of grown layers.

Horikoshi proposed a new mode of MBE growth which makes it possible to grow high-quality GaAs and AlAs layers at very low substrate temperatures ( $\sim 200^\circ\text{C}$ ) by enhancing the migration of the materials evaporated on the growing surface (Horikoshi 1986). This method has been termed migration-enhanced epitaxy (MEE). It is based on the very rapid migration of Ga and Al atoms on the growing surface, and on the GaAs surface, much more rapidly than Ga–As and Al–As molecules, and the fact that they migrate very actively even at temperatures as low as  $200^\circ\text{C}$ . They showed that high-quality GaAs and AlAs could be grown at very low temperatures by alternately supplying Ga (Al) atoms and arsenic molecules to the substrate surface. Applying the MEE method,  $1\text{--}2\ \mu\text{m}$  thick GaAs layers were grown at a substrate temperature of  $200^\circ\text{C}$ . These layers showed efficient photoluminescence from the band-edge excitons at 4.2 K. AlAs–GaAs single-quantum-well structures with 3–6 nm widths were also grown at  $200^\circ\text{C}$  by MEE. These structures showed photoluminescence due to electronic transitions between quantized levels in the wells, indicating a reasonable quality of AlAs (Horikoshi 1986).

### 1.3.2 Review of III–V heterostructures grown by LPE, MBE and MOCVD

Table 1.8 shows recent achievements in the growth of modulation-doped structures and superlattices of  $\text{GaAs}-\text{Ga}_x\text{Al}_{1-x}\text{As}$  using different growth techniques. Similar information for the  $\text{Ga}_x\text{In}_{1-x}\text{As}_y\text{P}_{1-y}-\text{InP}$  lattice-matched system is presented in table 1.9.

The improvement of the threshold current density of injection in  $\text{GaAs}-\text{Ga}_x\text{Al}_{1-x}\text{As}$  lasers, using double-heterostructure and quantum well active layers is illustrated in table 1.10. Table 1.11 indicates the best threshold current density ( $J_{\text{th}}$ ) of  $\text{GaInAsP}-\text{InP}$  double-heterostructure lasers emitting at  $1.3\ \mu\text{m}$  produced by different growth techniques (MBE, LPE, VPE and LP-MOCVD). From the results illustrated in tables 1.8–1.11, one can draw the following conclusions.

*(a)  $\text{GaAs-GaAlAs}$  systems*

The smoothest and sharpest layers have been demonstrated by MBE (Gossard 1979) and MOCVD (Frijlink 1991). The highest mobilities have been achieved

**Table 1.8** Historical development of the growth of modulation-doped structures and superlattices in the GaAs–Ga<sub>x</sub>Al<sub>1-x</sub>As lattice-matched system.

Observation of quantum size effect in GaAs–GaAlAs multiquantum wells	1974 MBE	Dingle <i>et al</i> 1974
Experimental observation of 2DEG detected by Shubnikov–de Haas magnetoresistance oscillations of the conduction electrons in uniformly Sn-doped MBE-grown GaAs–GaAlAs superlattice	1977 MBE	Chang <i>et al</i> 1977
GaAs–GaAlAs heterostructures and superlattices with modulated silicon doping	1978 MBE	Dingle <i>et al</i> 1978
Observation of 2DEG in LPE-grown GaAs–GaAlAs heterojunctions	1979 LPE	Tsui and Logan 1979
Modulation-doped GaAs–GaAlAs heterojunctions by MBE with highest mobilities $\mu(2\text{ K}) = 11.7 \times 10^6 \text{ cm}^2 \text{ V}^{-1} \text{ s}^{-1}$	1988 MBE	Pfeiffer <i>et al</i> 1989 Foxon <i>et al</i> 1989
Modulation-doped GaAs–GaAlAs heterojunctions by MOCVD with highest mobilities $\mu(2\text{ K}) = 7 \times 10^5 \text{ cm}^2 \text{ V}^{-1} \text{ s}^{-1}$	1989 MOCVD	Frijkink <i>et al</i> 1991
GaAs with highest mobilities $\mu(40\text{ K}) = 3.35 \times 10^5 \text{ cm}^2 \text{ V}^{-1} \text{ s}^{-1}$	1989 LP-MOCVD	Razeghi <i>et al</i> 1989

with the MBE technique, but the mobility enhancement observed with LPE (Tsui and Logan 1979) and MOCVD (Hersee *et al* 1982) is also very appreciable.

For optoelectronic devices based on the GaAs–GaAlAs system, high-quality quantum well (QW) lasers, MQW lasers, graded index waveguides and separate confinement heterostructure (GRIN-SCH) lasers have been achieved by MBE and by MOCVD (Hersee *et al* 1982, Burnham *et al* 1983, Kasemset *et al* 1982). Both techniques showed extremely low threshold current densities,  $J_{\text{th}}$ , of 100 to 300 A cm<sup>-2</sup>. Consequently, MOCVD and MBE are potentially useful for the growth of high-quality multilayers (MQW and SL) of GaAs–GaAlAs for optoelectronic and microwave devices. Considerations of economics or convenience may determine the choice of crystal growth technique.

#### (b) GaAs–GaInP systems

The interest in Ga<sub>0.51</sub>In<sub>0.49</sub>P lattice matched to GaAs substrate is due to its potential for optoelectronic and microwave devices. Because of its wide direct bandgap ( $E_g = 1.9$  eV), this material provides a visible wavelength operation ( $\lambda = 0.65 \mu\text{m}$ ) for light-emitting and laser diodes at room temperature. The GaInP–GaAs system is very promising for high-speed circuit applications. The large valence band discontinuity ( $\Delta E_v = 0.24$  eV) offers good device performance for n–p–n heterojunction bipolar transistors (HBTs), and p-channel FETs. The most important feature of the Ga<sub>x</sub>In<sub>1-x</sub>P–GaAs heterostructure is that the crossover of its direct ( $\Gamma$ ) and indirect (X) conduction bands lies at  $x = 0.74$ ,

**Table 1.9** Historical development of the growth of modulation-doped structures and superlattices in the  $\text{Ga}_x\text{In}_{1-x}\text{As}_y\text{P}_{1-y}$  lattice-matched system.

Observation of quantum size effect (QSE) in the multiple thin layers of $\text{Ga}_x\text{In}_{1-x}\text{As}_y\text{P}_{1-y}$ ( $\lambda = 1.1 \mu\text{m}$ )	1977 LPE	Rezek <i>et al</i> 1977
Observation of 2DEG in modulation-doped $\text{Ga}_{0.47}\text{In}_{0.53}\text{As}-\text{InP}$	1982 LP-MOCVD	Razeghi <i>et al</i> 1982
Modulation-doped heterostructures of $\text{Ga}_{0.47}\text{In}_{0.53}\text{As}-\text{InP}$ superlattices	1983 LP-MOCVD	Razeghi <i>et al</i> 1983b
Observation of QSE in multilayered QW structures of $\text{Ga}_{0.47}\text{In}_{0.53}\text{As}-\text{InP}$ (with well width of GaInAs of 200, 100, 50 and 25 Å)	1983 LP-MOCVD	Razeghi <i>et al</i> 1983c
Observation of QSE and the 2DEG in heterojunctions of GaInAsP-InP $\lambda = 1.3 \mu\text{m}$	1984 LP-MOCVD	Razeghi and Duchemin 1984
Growth of $\text{Ga}_{0.25}\text{In}_{0.75}\text{As}_{0.5}\text{P}_{0.5}-\text{InP}$ superlattices (10 wells of GaInAsP of 75 Å with InP barrier of 75 Å)	1984 LP-MOCVD	Duchemin and Razeghi 1984
Growth of superlattices and modulation-doped GaInAs/InP	1983 VPE	Komeno <i>et al</i> 1983
GaInAs-InP heterostructure with highest mobilities ( $700\,000 \text{ cm}^2 \text{ V}^{-1} \text{ s}^{-1}$ )	1987 LP-MOCVD	Razeghi <i>et al</i> 1987

which is far from the lattice-matched composition ( $x = 0.51$ ). In the case of  $\text{Al}_x\text{Ga}_{1-x}\text{As}$ , the crossover of direct and indirect conduction bands is around  $x = 0.45$ . Donor-related deep traps, the so-called DX centres, were observed in  $\text{Al}_x\text{Ga}_{1-x}\text{As}$  and their presence was particularly important for  $x > 0.3$ , i.e. for a composition close to the  $x = 0.45$  crossover point. Trap activation energies were found to follow the minimum of the indirect L band. Figures 1.3(a) and (b) compare the composition dependence of direct and indirect gaps of GaInP and GaAlAs.

The presence of DX centres in highly n-doped GaInP-GaAs heterostructures will be smaller than that in GaAlAs-GaAs layers. The DX centre is a deep donor level related to the crystal lattice rather than a defect and its activation energies follow one of the indirect conduction bands in III-V compounds. Once the composition of a ternary compound is near or over the crossover point of the bandgap transition, DX centres will start to affect the device electrical properties. For those compositions below the crossover point, DX centres lie above the minimum of the conduction band and no deep trap effect will be observed. Since this type of deep trap is quite common in all III-V semiconductors, a large separation between the lattice-matched composition and that of the crossover point helps to eliminate the DX centre problems. Therefore,  $\text{Ga}_{0.51}\text{In}_{0.49}\text{P}$  allows operation without significant donor-related deep traps.

Studies by deep-level transient spectroscopy (DLTS) (Watanabe and Ohba

**Table 1.10** The improvement of  $J_{th}$  of injection in GaAs–Ga<sub>x</sub>Al<sub>1-x</sub>As lasers using DH and QW active layers.

Homostructure GaAs p–n junction laser $J_{th} \approx 10^5 \text{ A cm}^{-2}$	1968 LPE	Hayashi <i>et al</i> 1969
Single heterostructure of GaAs–GaAlAs p–n heterojunction lasers $J_{th} \approx 4 \times 10^3 \text{ A cm}^{-2}$	1969 LPE	Alferov <i>et al</i> 1969
Double heterostructure of Ga <sub>x</sub> Al <sub>1-x</sub> As/GaAs/Ga <sub>x</sub> Al <sub>1-x</sub> As lasers $J_{th} \approx 2 \times 10^3 \text{ A cm}^{-2}$	1970 LPE	Hayashi and Panish 1970
The use of a graded aluminium fraction ( $x$ ) in the Ga <sub>x</sub> Al <sub>1-x</sub> As optical cavity surrounding a thin active region (GRIN-SCH) lasers $J_{th} \approx 250 \text{ A cm}^{-2}$	1982 MOCVD	Tsang <i>et al</i> 1982
The lowest threshold current density of GRIN-SCH lasers $J_{th} \approx 120 \text{ A cm}^{-2}$	1982 MOCVD	Hersee <i>et al</i> 1982
Multiphoton well (MQW) of GaAs/Ga <sub>x</sub> Al <sub>1-x</sub> As lasers $J_{th} \approx 170 \text{ A cm}^{-2}$	1982 MOCVD MBE	Dupuis and Dapkus 1978 Burnham <i>et al</i> 1983 Hiyamizu 1982

**Table 1.11** The best  $J_{th}$  of GaInAsP–InP DH lasers emitting at 1.3  $\mu\text{m}$ .

Growth technique	$J_{th}$ (A cm <sup>-2</sup> )	Cavity length ( $\mu\text{m}$ )	Reference
LPE	770	1500	Itaya <i>et al</i> 1979
VPE	980	400	Mizutani <i>et al</i> 1980
MBE	1000	400	Tsang <i>et al</i> 1982
LP-MOCVD	430	400	Razeghi <i>et al</i> 1983a

1987) have shown that there are no detectable deep levels in n-doped GaInP layers, and that the concentration of electron traps is lower than  $10^{13} \text{ cm}^{-3}$ . In the absence of deep traps in doped GaInP layers, this material provides an option to replace the AlGaAs layer of HEMTs, HIGFETs and HBT in high-speed circuit applications (Chan *et al* 1989).

### (c) GaInAsP–InP systems

The first volume of this series concentrated on the survey of GaInAsP–InP for photonic and electronic applications. The smoothest and sharpest layers of GaInAsP–InP have been demonstrated by LP-MOCVD (Razeghi and Duchemin 1984). The highest mobilities for modulation-doped GaInAs–InP have been obtained from LP-MOCVD- and VPE-grown materials (Razeghi *et al* 1983a, Komeno *et al* 1983). The lowest threshold current density of a GaInAsP–InP

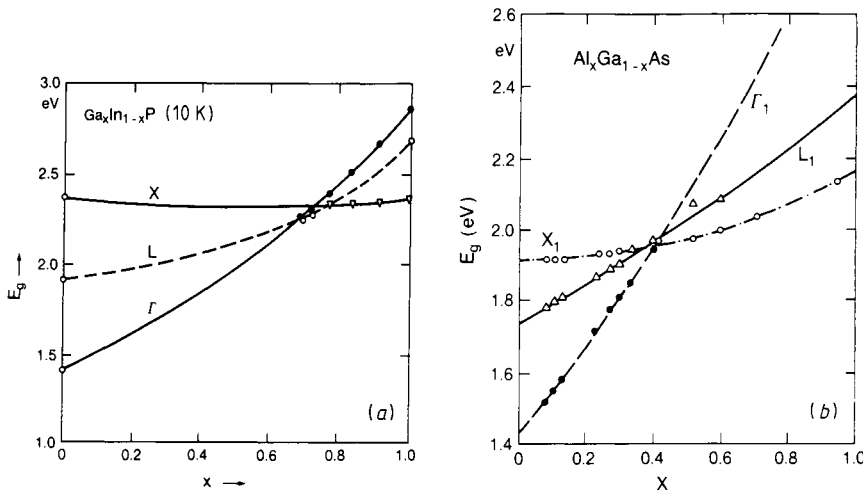


**Figure 1.3** (a)  $\text{Ga}_x\text{In}_{1-x}\text{P}$ : composition dependence of direct and indirect gaps of  $\text{Ga}_x\text{In}_{1-x}\text{P}$  at 10 K (full symbols: piezoresistance measurements for compositions near the band crossover; open circles: experimental values for InP and GaP). For the indirect edges the energy values correspond to  $E_{g-\text{ind}} - E_b + \hbar\omega_{\text{phonon}}$ , where  $E_b$  is the exciton binding energy. (b)  $\text{Al}_x\text{Ga}_{1-x}\text{As}$ : composition dependence of direct and indirect gaps of AlGaAs and of a deep donor level obtained by conductivity and Hall effect measurements.

double heterostructure emitting at  $1.3\ \mu\text{m}$  has been achieved with LP-MOCVD (Razeghi *et al* 1983c, Razeghi 1985).

For optoelectronic  $\text{GaInAsP-InP}$  DH lasers, LPE, VPE and LP-MOCVD are potentially useful for the growth of high-quality DH lasers emitting between  $1.2$  and  $1.6\ \mu\text{m}$ .

#### (d) $\text{GaInAlP-GaAs}$ systems

A useful material for short-wavelength optical devices is the quaternary alloy  $\text{Ga}_{1-x-y}\text{In}_y\text{Al}_x\text{P}$  lattice matched to GaAs. This alloy lattice matched to GaAs has a direct bandgap between  $1.9\ \text{eV}$  ( $x = 0$ ) and  $2.3\ \text{eV}$  ( $x = 0.7$ ). This system is important for the fabrication of visible-, red-light-emitting lasers ( $\lambda = 630\text{--}680\ \text{nm}$ ), and for heterojunction bipolar transistor applications.

Suzuki *et al* (1988a, b, c) have reported that the bandgap energy of  $(\text{Al}_x\text{Ga}_{1-x})_{0.5}\text{In}_{0.5}\text{P}$ , at a fixed value of  $x$  grown by MOCVD, exhibits a variation in energy gap of more than 100 meV, which can be related to the (111) ordering on the group III sublattice. They showed that the degree of ordering in this system is related to the MOCVD growth conditions such as growth temperature, growth rate, V/III ratio and GaAs substrate orientation. High-quality  $\text{Ga}_x\text{In}_y\text{Al}_{1-x-y}\text{P}/\text{GaAs}$  heterojunctions, quantum wells and superlattices have been grown by Valster *et al* (1991), Mpaskoutas *et al* (1991) and Watanabe and Ohba (1987).

Watanabe and Ohba (1987) studied the conduction-band discontinuity  $\Delta E_c$  and interface charge density  $\sigma$  for GaAs–In<sub>0.5</sub>(Ga<sub>1-x</sub>Al<sub>x</sub>)<sub>0.5</sub>P heterojunctions, grown by MOCVD. They investigated the dependence of  $\Delta E_c$  and  $\sigma$  on composition  $x$  for  $0 < x < 1$ . They also studied Ga<sub>0.5</sub>In<sub>0.5</sub>P/In<sub>0.5</sub>Al<sub>0.5</sub>P and found that the valence-band discontinuity  $\Delta E_v$  for GaAs/In<sub>0.5</sub>(Ga<sub>1-x</sub>Al<sub>x</sub>)<sub>0.5</sub>P is a linear function of  $x$  and is larger than  $\Delta E_c$ . They also found that  $\sigma$  for GaAs/In<sub>0.5</sub>(Ga<sub>1-x</sub>Al<sub>x</sub>)<sub>0.5</sub>P is one order of magnitude larger than that for In<sub>0.5</sub>Al<sub>0.5</sub>P/In<sub>0.5</sub>Ga<sub>0.5</sub>P and GaAs/GaAlAs. Kondo *et al* (1991) reported the MOCVD growth of (Al<sub>0.7</sub>Ga<sub>0.3</sub>)<sub>0.5</sub>In<sub>0.5</sub>P–Ga<sub>x</sub>In<sub>1-x</sub>P strained single-quantum-well structures on GaAs substrate. The growth temperature was 710°C and the growth pressure was 76 Torr. The V/III ratio was 200 and the growth rate was 1.3 μm h<sup>-1</sup>. By changing  $x$  between 0.38 and 0.68 the biaxial misfit strain ( $\varepsilon$ ) was varied between +1.0% and -1.24%. The photoluminescence (PL) microscopy showed that 100 Å thick GaInP layers are free of misfit dislocations at  $|\varepsilon| < 1.5\%$ . The PL linewidth of AlGaInP–GaInP strained single quantum wells (SSQWs) was as narrow as 9–12 meV at 4 K, independent of misfit strain, which confirms the structural perfection of SSQWs.

## REFERENCES

- Alferov Zh I, Andreev V M, Korol'kov V I and Portnoi E L 1969 *Sov. Phys.–Semicond.* **2** 843  
 Burnham R D, Streifer W, Paoli T L and Holonyak N Jr 1983 *IOOC-83 (Tokyo, 1983)*  
 Casey H C and Panish M B 1978 *Heterostructure Laser* (New York: Academic)  
 Chan Y J, Pavlidis D, Razeghi M and Omnes F 1989 *Gallium Arsenide and Related Compounds 1989 (Inst. Phys. Conf. Ser. 106)* ed T Ikoma and H Watanabe (Bristol: Institute of Physics) p 891  
 Chang L L, Sakaki M, Chang C A and Esaki L 1977 *Phys. Rev. Lett.* **38** 1489  
 Chapin D M, Fuller C S and Pearson G L 1954 *J. Appl. Phys.* **25** 676  
 Delahaye F, Dominguez D, Alexandre F, Andre J P, Hirtz J P and Razeghi M 1986 *Metrologia* **22** 103  
 Didchenko R, Alix J E and Toeniskoetter R H 1960 *J. Inorg. Nucl. Chem.* **14** 35  
 Dingle R, Stormer H, Gossard A C and Weigmann W 1978 *Appl. Phys. Lett.* **33** 665  
 Dingle R, Weigmann W and Henry C H 1974 *Phys. Rev. Lett.* **38** 1489  
 Doi A, Aoyagi Y and Namba S 1986 *Appl. Phys. Lett.* **48** 1787  
 Dupuis R D and Dapkus P D 1978 *Gallium Arsenide and Related Compounds (Inst. Phys. Conf. Ser. 45)* ed C M Wolfe (Bristol: Institute of Physics)  
 Esaki L 1958 *Phys. Rev.* **109** 603  
 Foxon C T, Harris J J, Hilton D, Hewett J and Roberts C 1989 *Semicond. Sci. Technol.* **4** 582  
 Fraas L M 1981 *J. Appl. Phys.* **52** 6939  
 Frijkink P M, Nicolas J L and Suchet P 1991 *J. Crystal Growth* **107** 166  
 Gossard A C 1979 *Thin Solid Films* **57** 3  
 Guldner Y, Vieren J P, Voos M, Delahaye F, Dominguez D, Hirtz J P and Razeghi M 1986 *Phys. Rev. B* **33** 3990  
 Gunn J B 1963 *Solid State Commun.* **1** 88  
 Gunn J B 1964 *IBM J. Res. Dev.* **8** 141  
 Hayashi I and Panish M B 1970 *Device Research Conf. (Seattle, WA, 1970)*

- Hayashi I, Panish M B and Foy P W 1969 *IEEE J. Quantum Electron.* **QE-5** 211  
 Hersee S D, Baldy M, Assenat P, de Cremoux B and Duchemin J P 1982 *Electron. Lett.* **18** 870  
 Hilsum C 1962 *Proc. IRE* **5** 185  
 Hiyamizu S 1982 *Oyo Buturi* **51** 942 (in Japanese)  
 Horikoshi L 1986 *The Physics and Fabrication of Microstructures*  
 Illegems M and Panish M B 1974 *J. Phys. Chem. Solids* **35** 409  
 Itaya Y, Katayama S and Sumatsu Y 1979 *Electron. Lett.* **15** 123  
 Jordan A S and Illegems M 1974 *J. Phys. Chem. Solids* **36** 329  
 Kasemset D, Mong C S, Patel N B and Dapkus P D 1982 *J. Appl. Phys. Lett.* **41** 912  
 Kobayashi N, Makimoto T and Horikoshi Y 1985 *Japan. J. Appl. Phys.* **24** L962  
 Komeno J, Takikawa M and Ozeki M 1983 *Electron. Lett.* **19** 473  
 Kondo M, Domen K, Anayama C, Tanahashi T and Nakajima K 1991 *J. Crystal Growth* **107** 578  
 Manasevit H M 1968 *Appl. Phys. Lett.* **12** 156  
 Manasevit H M 1971 *J. Electrochem. Soc.* **118** 647  
 Manasevit H M, Erdmann F M and Simpson W I 1971 *J. Electrochem. Soc.* **118** 1864  
 Matsumoto T and Usui A 1986 *Abstracts of 1986 Fall Meeting of Japan Soc. Appl. Phys.*  
 Mizutani T, Yoshida M, Usui A, Watanabe H, Yuasa T and Hayashi I 1980 *Japan. J. Appl. Phys.* **19** L113  
 Mpaskoutas M, Morhaim C, Patillon J N, Andre J P, Valster A and Rusch J J 1991  
*J. Crystal Growth* **107** 192  
 Nelson H 1963 *RCA Rev.* **19** 603  
 Nicholas R J, Brunel L C, Huant S, Karrai K, Portal J C, Brummell M A Razeghi M,  
 Chang K Y and Cho A Y 1985 *Phys. Rev. Lett.* **55** 8883  
 Nishizawa J and Kurabayashi T 1986 *J. Crystallogr. Soc. Japan* **28** 133  
 Osbourn G C 1982 *J. Vac. Sci. Technol.* **21** 469  
 Parker E H C 1985 *The Technology and Physics of Molecular Beam Epitaxy* (New York:  
 Plenum)  
 Pfeiffer L, West K W, Stormer H L and Baldwin K W 1989 *Appl. Phys. Lett.* **55** 1888  
 Razeghi M 1983 *Rev. Tech. Thomson-CSF* **15** 1  
 Razeghi M 1985 *Lightwave Technology for Communication* ed W T Tsang (New York:  
 Academic)  
 Razeghi M and Duchemin J P 1984 *J. Crystal Growth* **70** 145  
 Razeghi M, Duchemin J P, Portal J C, Dmowski L, Remeni G, Nicholas R J and Briggs  
 A 1986 *Appl. Phys. Lett.* **48** 712  
 Razeghi M, Hersee S, Blondeau R, Hirtz P and Duchemin J P 1983a *Electron. Lett.* **19**  
 336  
 Razeghi M, Hirtz P, Blondeau R and Duchemin J P 1983b *Electron. Lett.* **19** 481  
 Razeghi M, Hirtz J P, Ziemelis U D, Delagande C, Etienne B and Voos M 1983c *Appl.  
 Phys. Lett.* **43** 586  
 Razeghi M, Hosseini A, Vilcot J P and Decoster D 1987 *Gallium Arsenide and Related  
 Compounds 1987* (Bristol: Institute of Physics) p 625  
 Razeghi M, Omnes F, Nagle J, Defour M, Acher D and Bove P 1989 *Appl. Phys. Lett.*  
**55** 1677  
 Razeghi M, Poisson M A, Larivain J P, de Cremoux B and Duchemin J P 1982 *Electron.  
 Lett.* **18** 339  
 Rezek E A, Holonyak N Jr, Vojak B A, Stillman G E, Rossi J A and Keune D L 1977  
*Appl. Phys. Lett.* **31** 288  
 Ridley B K and Watkins T B 1961 *Proc. Phys. Soc. London* **78** 293  
 Rogers D C, Nicholas R J, Portal J C and Razeghi M 1986 *Semicond. Sci. Technol.* **1**  
 350

- Suntola T, Atron J, Pakkala A and Linfors S 1980 *SID 80 Digest* 108  
Suzuki T, Gomyo A, Hino I, Kobayashi K, Kawata S and Iijima S 1988a *Japan. J. Appl. Phys.* **27** L1549  
Suzuki T, Gomyo A and Iijima S 1988b *J. Crystal Growth* **93** 389  
Suzuki T, Gomyo A, Iijima S, Kobayashi K, Kawata S, Hino I and Yuasa T 1988c *Japan. J. Appl. Phys.* **27** 2098  
Sze S M and Ryder R M 1971 *Proc. IEEE* **59** 1140  
Tsang W T, Remhart F K and Ditzenberg J A 1982 *Electron. Lett.* **18** 75  
Tsui D C and Logan R A 1979 *Appl. Phys. Lett.* **35** 35  
Valster A, Liedenbaum C T, Finke M N, Severens A L, Boermans M J B,  
Vandenhoudt D E W and Bulle-Lieuwma C W T 1991 *J. Crystal Growth* **107** 403  
Van Vechten J A and Bergstresser T K 1970 *Phys. Rev. B* **1** 3361  
Vodjani N 1982 *These de Doctorat 3e Cycle* University Paris XI  
Watanabe M O and Ohba Y 1987 *Appl. Phys. Lett.* **50** 906

## MOCVD Growth Technique

### 2.1 MOCVD GROWTH SYSTEMS

The MOCVD growth of semiconductor III–V or II–VI compounds is achieved by introducing source materials and the radicals into a reactor chamber, which can be either a quartz tube or a stainless steel chamber, that contains a substrate placed on a heated susceptor. The hot susceptor has a catalytic effect on the decomposition of the gaseous products and growth therefore takes place primarily at this hot surface. A simplified schematic diagram of an MOCVD system is shown in figure 2.1.

A typical MOCVD system consists of four major parts:

- (1) gas handling system,
- (2) reactor chamber,
- (3) heating system for pyrolysis temperatures and
- (4) exhaust system and safety apparatus.

The gas handling system includes the sources of alkyls and hydrides, and all of the valves, pumps and instruments necessary to control the gas flows and mixtures. Details of the different source alkyls and hydrides are discussed in section 2.4. In order to grow high-quality layers the gas handling system has to be clean and leak tight. Stainless steel tubes are used to transport alkyls from the source to the reactor chamber and electronic mass flow controllers and a

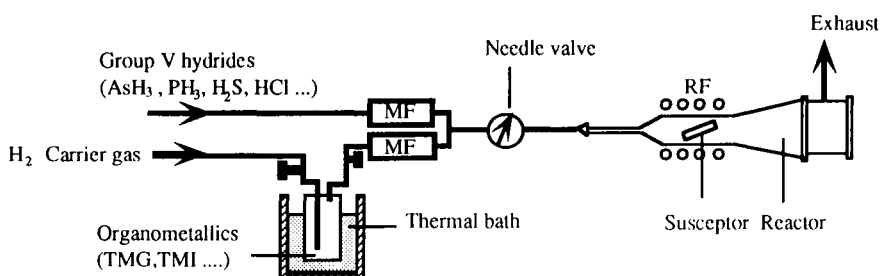


**Figure 2.1** Schematic diagram of an MOCVD reactor.

thermal bath system deliver precisely controlled amounts of gases to the reactor chamber.

Purity of the starting materials is one of the most important issues in modern semiconductor technology. Much effort is made to purify every source material used in an MOCVD reactor to avoid any kind of contamination. Gases used in MOCVD reactors can introduce contaminants in the semiconductor films. Hydrogen, nitrogen, and helium are the most common carrier gases used in the MOCVD growth process. The major impurities in H<sub>2</sub> gas are O<sub>2</sub> and H<sub>2</sub>O. Also, contaminants can be introduced during improper gas cylinder changes and from gas system components such as tubes, valves, etc. In order to avoid contaminants from gas system components, 316 stainless steel tubes with electropolished inner walls are often used (Callahan 1985). To avoid introducing contaminants during cylinder changes, many systems have gas cabinets with built-in purging gas systems.

### 2.1.1 Selection of tubing and valves

The appropriate selection of tubes, fittings and valves for MOCVD growth is essential for producing high-purity films. Since some of the organometallic sources and gases used in MOCVD growth are highly corrosive, it is important to select a suitable material resistant to these corrosives. For example, most MOCVD reactors use 316 seamless stainless steel tubes which are electropolished inside. More information regarding the selection of tubes and fittings is given in the Swagelok tube fitting and installation manual (Callahan 1985).

### 2.1.2 Hydrogen purifier

The hydrogen typically supplied by many gas companies is only 99.99% pure. This is not sufficient for high-quality semiconductor growth. These companies also supply high-purity, 99.9995% pure hydrogen, which is called research grade hydrogen, but since the research grade hydrogen is expensive, normally 99.99% pure hydrogen is used along with a hydrogen purifier.

In a hydrogen purifier, the impure hydrogen is passed through palladium alloy tubing, which is used as the diffusion medium. The palladium is inside a cell, which is heated to 400–425 °C. At this temperature, only hydrogen diffuses through the palladium tube and all other elements are blocked. In this way ultrapure hydrogen is delivered to the system.

### 2.1.3 Thermal bath

Metalloorganic sources are usually obtained in stainless steel cylinders. The partial pressure of the source vapour is regulated by precisely controlling the temperature of the metallorganic source bubbler. Commercial thermal baths are able to control the temperature to an accuracy of  $\pm 0.01$  °C and the temperatures can be varied in the range of –30 °C to 100 °C.

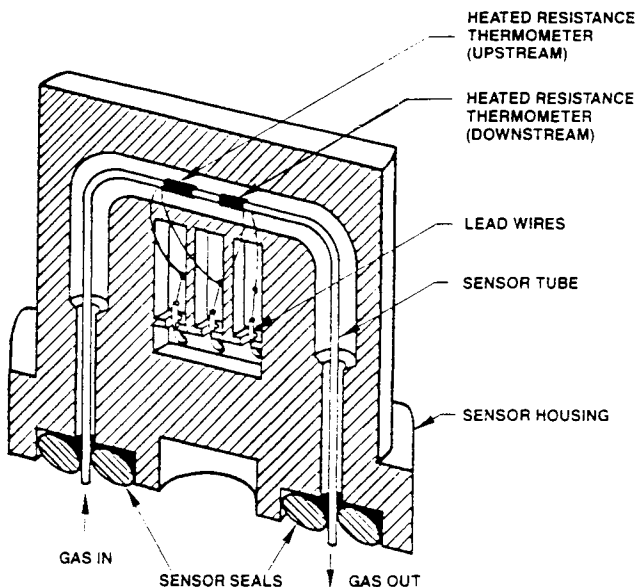


**Figure 2.2** Flow sensor for mass flow controller.

Electronic mass flow controllers are used to control the exact amount of carrier gas flowing through the bubbler and to maintain a constant vapour pressure of the source. Thus a controlled amount of source material can be transported to the reactor.

#### 2.1.4 Electronic mass flow controllers

Mass flow controllers accurately and reliably measure and/or control the mass flow rate of gases. They have been specifically designed to allow operation on any gas having a known molar specific heat. The accuracy of electronic mass flow controllers is  $\pm 1\%$  of the full scale. The flow controller is a self-contained, closed-loop control system which measures the mass rate of gaseous flow through the instrument, compares this with an externally commanded flow rate and adjusts the valve to control the flow to the commanded level. The flow controller consists of four basic elements which accomplish this function: flow sensor, flow splitter, control valve and the electronics which control the control valve.

The flow sensor (figure 2.2) consists of two self-heated resistance thermometers wound around the outside diameter of a thin-walled capillary tube. The coils are connected in a bridge circuit and supplied with a regulated current. The heat generated by the power dissipation in the coils raises the tube temperature and at no flow, the heat is uniformly distributed along the tube. As the flow through the tube increases, heat is carried down the tube from the

upstream coil to the downstream coil, producing a temperature difference and thus a resistance difference, that is directly proportional to the mass flow rate of the gas through the tube. The bridge output, being a direct function of the resistance difference, is amplified and further linearized by the electronics to give 0 to 5.0 V DC signal as a measure of flow rate.

Another important aspect of the mass flow controller is the gas conversion factor. Since different gases have different masses, the conversion factor is used to achieve accurate flow rates. The flow meters are normally calibrated for nitrogen. Using the conversion factors, the actual flow of a particular gas can be calculated. Usually the supplier provides the conversion factor table.

A significant advantage of electronic mass flow controllers is the ease of automation and programming for MOCVD processes.

### **2.1.5 Manifold**

In MOCVD processes, the gas mixing system is an important part. The gas mixing system is a clean, leak-free, stainless steel system designed to uniformly mix metallorganic and hydride sources prior to reaching the growth zone. The function of the gas mixing manifold is crucial for growing superlattices, quantum well structures and for reducing the memory effect (Hollan 1981) associated with some dopant sources. The gas mixing manifold first stabilizes the flow and then directs the flow to the reaction chamber. At other times the flow is sent directly to the vent. The gas handling manifold has air-pressure-controlled valves that can be opened or closed by computers.

### **2.1.6 Susceptor heating system**

There are three types of heating method that are used to heat the susceptor: radio frequency (RF) induction heating, radiative heating and resistance heating. In RF heating, the graphite or silicon-carbide graphite susceptor is inductively coupled to the RF coil. This type of heating is used in big industrial reactors and is usually very complex. In order to avoid the complexity of RF heating, radiative heating is used. Here the heat energy from a resistance element is transformed into radiant energy. The graphite susceptor absorbs this radiant energy and converts it back into heat energy. In that resistance heating method, heat energy is introduced by electric current flow through a metallic (aluminum or molybdenum) susceptor.

There are two methods used to measure temperature: thermocouples (chromel–alumel) and pyrometers.

### **2.1.7 Exhaust system**

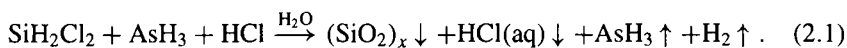
The exhaust system is the most critical part of the MOCVD system in terms of safety. This system serves two main functions: removing unreacted gases

and byproducts from the reaction chamber and providing a path for reactants to bypass the reaction zone. The products of unreacted gases can block the exhaust system, and great care has to be taken to remove such blockages. In addition, these blockages in the exhaust system can lead to sudden pressure changes in the reactor and back-diffusion of vented gas which affect the growth uniformity. The vented gas may contain unreacted sources which may be toxic, pyrophoric or flammable. A variety of exhaust systems are available, such as scrubbing systems, particle filters and burnboxes.

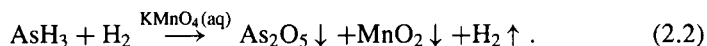
### 2.1.8 Scrubbing systems

The semiconductor wafer fabrication industry uses a variety of corrosive, toxic, pyrophoric and flammable chemicals. In order to control pollution of toxic materials, different types of scrubber are used. In the past, it was commonly believed that many chemicals could be released into the environment without hazard if they were diluted to a safe concentration level. The function of scrubbers was only to reduce the concentration of contaminants produced to 'safe concentration levels', which were determined by the regulating agency using the detection limits of the current instrumentation or based on a standard developed with concern for the worker's risk of exposure at the release site. As time went on, scientists demonstrated the negative impact of environmental contaminants at ever-diminishing levels. There has been a shift from scrubbers that simply dilute pollutants to a new type of scrubber which can capture, isolate and transform pollutants before allowing them to reach the environment (figures 2.3(a), (b) and (c)).

As an example, silicon epitaxy involves the deposition of SiO<sub>2</sub> and minute amounts of arsine dopants on an Si wafer. To remove unreacted arsine, the scrubber has two stages. In the first stage, water removes the unreacted dichlorosilane from the gas system by converting it to a complex mixture of solid silicon oxides. At the same time, HCl dissolves in the water and then exits the scrubber as aqueous HCl, which is neutralized. This reaction is summarized below:



In the second stage, an oxidizing agent such as potassium permanganate solution oxidizes the arsenic to a solid residue which can then be safely recovered for recycling and the reaction is shown in equation (2.2)



Since the solution used in removing toxic gases is expensive and hard to dispose of, scrubbers using solids have been developed (figure 2.3(c)). By utilizing activated carbon, the toxic compounds from the effluent stream of the

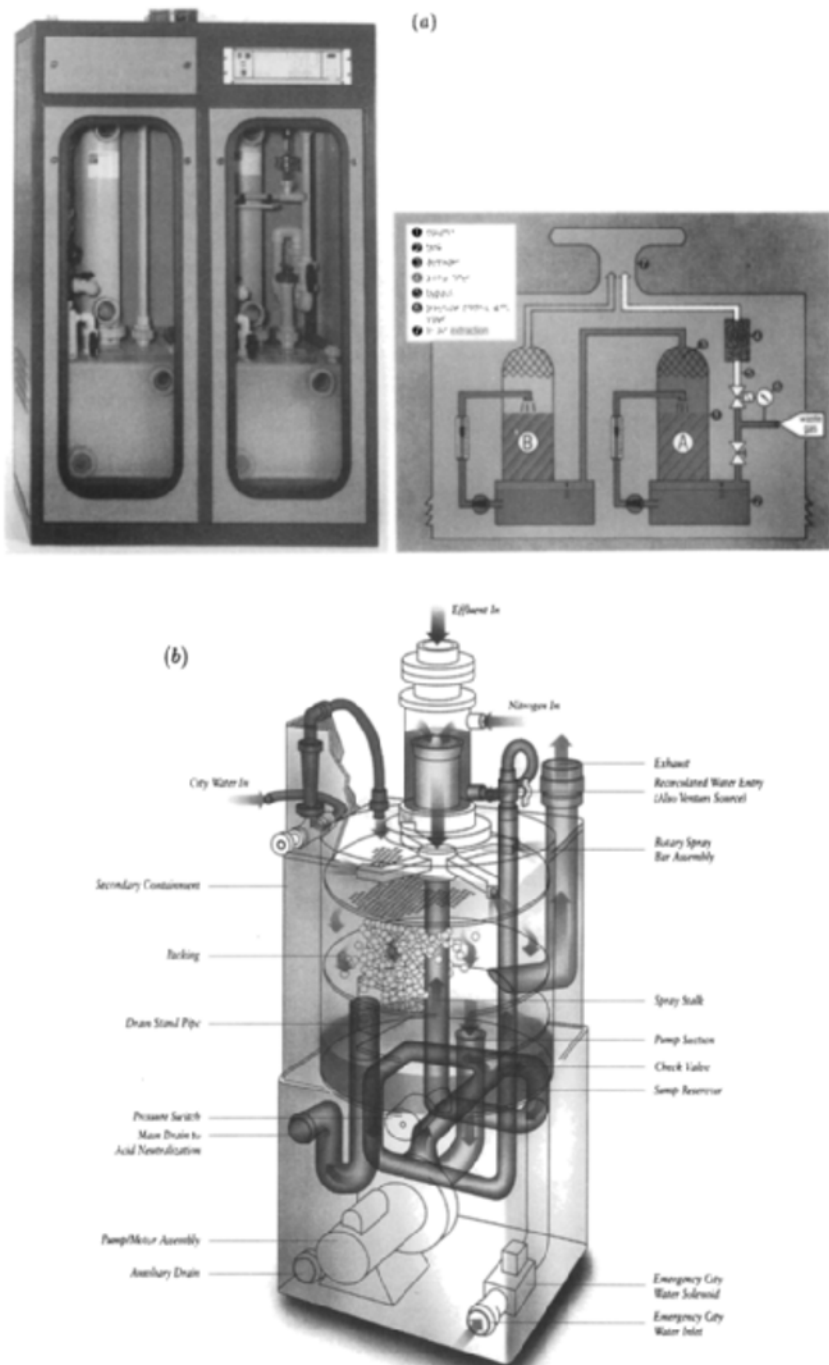


**Figure 2.3** (a) A liquid-based scrubber (courtesy of AIXTRON); (b) a liquid-based scrubber (courtesy of VECTOR).

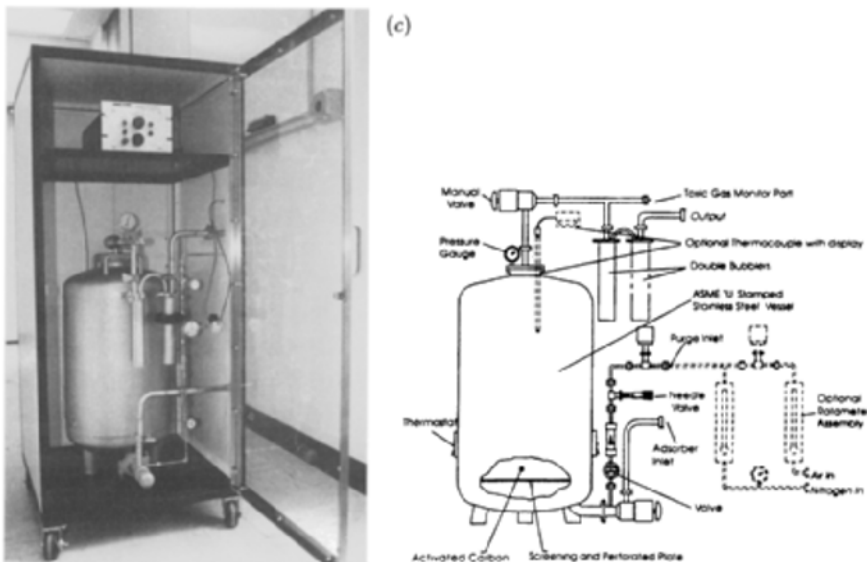


Figure 2.3 Continued. (c) A solid-based scrubber (courtesy of EMCORE).

MOCVD process are adsorbed. In addition, controlled oxidation turns potentially harmful gases into solid oxides which are safer and easier to dispose of. This solid scrubbing is preferable to many other methods such as liquid scrubbers, burnboxes and incinerators which may cause back-streaming problems, produce byproducts or be costly to dispose of.

### 2.1.9 Burnboxes

Another way to dispose of the unreacted materials from the exhaust is to use burnboxes. Burnboxes contain a furnace heated at very high temperatures (900 °C to 1000 °C). By maintaining the high temperature, the unreacted materials from the exhaust will be cracked and oxidized, therefore becoming harmless. The reaction product radicals condense on the wall of the quartz tubes. Thus wastes may be removed easily from the quartz tubes.

### 2.1.10 Particulate filters

Particulate filters are used in conjunction with burnboxes or before pumping systems in low-pressure MOCVD systems. They must meet the following requirements: (1) removal of the particulates, (2) immunity to clogging, (3) reading services without exposing the operator to As dust and (4) minimum internal outgassing.

### 2.1.11 Gas leak detector

#### *Arsine and phosphine detectors*

Toxic gas monitors are an essential part of any MOCVD system. Today, almost all III–V growth systems use toxic gases such as  $\text{AsH}_3$  and  $\text{PH}_3$ . The toxic gas monitoring system is used to quantitatively detect the presence of both  $\text{AsH}_3$  and  $\text{PH}_3$ . It provides an instantaneous readout of concentration and initiates both warn and alarm signals whenever the preprogrammed concentration level for a particular gas and location is exceeded.

Today, most laboratories commonly use solid state gas sensors. These contain a heated resistor, which is supplied with a certain voltage. Whenever the gas enters the sensor, the voltage across the resistor changes due to its resistance change. The voltage change is proportional to the concentration of detected gas. The voltage is precalibrated in the factory for different gases and corresponding concentrations. In this way toxic gases can be detected. Based on the safety level of each gas, the warn and alarm signal can be set by users.

#### *Hydrogen gas detector*

Another common type of gas leak detector is the portable gas leak detector for identifying the location of gas leaks. This gas leak detector is not only used to detect  $\text{H}_2$  gas but also for gases such as arsine and phosphine. It uses a solid state gas sensor with a sintered metallic block. The gas is drawn into the unit by the internal low-power drain micropump. The sample gas is then passed over the sensor and exhausted to the atmosphere. The detector is calibrated for different amounts of gases and a wheel setting is provided to determine the amount of gas leak.

## 2.2 THE MOCVD GROWTH MECHANISM AND GROWTH PROCESS

Fundamental processes occurring during crystal growth are commonly subdivided into thermodynamic and kinetic components. Thermodynamics determine the driving force for the overall growth process, and kinetics define the rates at which the various processes occur. Hydrodynamics and mass transport, which are intimately linked, control the rate of transport of material to the growing solid/vapour interface. The rates of the chemical reactions occurring during growth, either homogeneously in the gas phase, or heterogeneously at the growing interface, also play a role. Each of these factors will dominate some aspect of the overall growth process. Figure 2.4 shows a schematic outline of the fundamental processes involved in MOCVD (Stringfellow 1985a). A study of the dependence of a macroscopic quantity, such as growth rate, on external parameters, such as substrate temperature and input precursor (source) flow rates, gives insight into the overall growth mechanism.

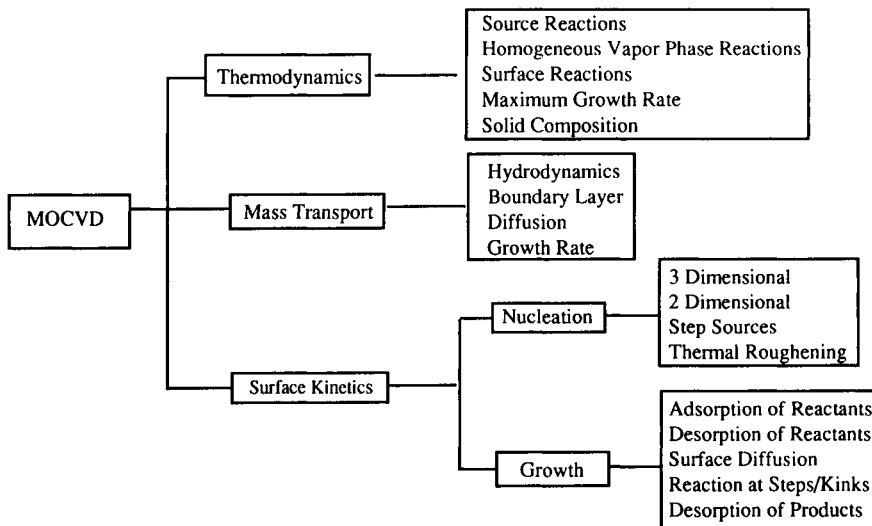


**Figure 2.4** Schematic outline of the fundamental processes involved in MOCVD (after Stringfellow 1985a).

### 2.2.1 Thermodynamics

Thermodynamic calculations are useful in obtaining information about the solid composition of a multicomponent system when vapour phase compositions are known. Furthermore, they are also useful in obtaining the phase diagram of a multicomponent system by calculating the compositions of the solid for different temperatures and pressures. The growth rate for an epitaxial process can also be obtained from thermodynamic calculations. Since thermodynamic calculations are elaborate, a basic idea of the calculations is described.

First of all, thermodynamic calculations are done for an equilibrium system. Although the MOCVD growth process is a non-equilibrium process, still thermodynamic calculations give a preliminary idea of the solid composition of a multicomponent system and its growth rate. Equilibrium is defined as the state when the Gibbs free energy is minimum. Gibbs free energy ( $G$ ) is related to enthalpy  $H$  and entropy  $S$  as

$$G = H - TS. \quad (2.3)$$

Here  $T$  is the temperature and  $H$  is defined as  $H = E + PV$ , where  $E$  is the internal energy,  $P$  is the pressure and  $V$  is the volume.

If two systems A and B are in equilibrium, there is no change in the total Gibbs free energy of these systems. Mathematically this can be expressed as

$$\left( \frac{\partial G_i}{\partial n_i} \right)_{T, P, n_j}^A - \left( \frac{\partial G_i}{\partial n_j} \right)_{T, P, n_i}^B = 0. \quad (2.4)$$

The term  $\partial G/\partial n$  is defined as the chemical potential ( $\mu$ ) of a system. Here  $n_i$  is the mole concentration of one of the components. For a single-ideal-gas system, the chemical potential is expressed as

$$\mu_i = \mu_i^0 + RT \ln \frac{P_i}{P_i^0} \quad (2.5)$$

where  $R$  is the gas constant,  $P_i$  is the partial pressure and  $P_i^0$  and  $\mu_i^0$  are the partial pressure and chemical potential of a standard state, respectively.

The above expression is slightly modified for non-ideal cases, as  $\mu_i = \mu_i^0 + RT \ln a_i$  where  $a_i$  is the activity coefficient and is defined as

$$a_i = \gamma_i x_i \quad (2.6)$$

where  $\gamma_i$  is the non-ideality factor and  $x_i$  is the mole fraction. The vapour phase is often considered as an ideal case, since source molecules are typically highly diluted so that there are no interreactions among the source molecules. Non-ideal cases are vapour–solid and solid–liquid phases.

When the system is not at equilibrium the thermodynamic *driving force* to restore equilibrium is

$$\Delta\mu = \mu_B - \mu_A. \quad (2.7)$$

This is the driving force for epitaxy and it specifies the maximum growth rate. Too large a driving force will cause rough growth surfaces and too small a driving force will lead to slow growth.

Since the MOCVD growth process involves vapour–solid phases, non-ideal expressions are used in thermodynamic calculations. Let us consider a simple binary system involving two molecules A and B. There are three possible nearest-neighbour interactions, AA, AB, BB. The equilibrium condition for the binary system is that the Gibbs free energy of this system should be minimum. In this case, the Gibbs free energy for mixing is written as

$$\Delta G^M = \Delta H^M - T \Delta S^M \quad (2.8)$$

where M corresponds to mixing. The entropy of mixing is (Kittel and Kroemer 1980)

$$\Delta S^M = -R(x \ln x + (1-x) \ln(1-x)) \quad (2.9)$$

and the enthalpy of mixing is

$$\Delta H^M = x(1-x)\Omega \quad (2.10)$$

where  $\Omega$  is the interaction parameter, which is related to the enthalpy of different bond energies, such as  $H_{AA}$ ,  $H_{AB}$  and  $H_{BB}$ , and  $x$  is the mole fraction. All of the above three equations provide the fundamental basis for phase diagrams.

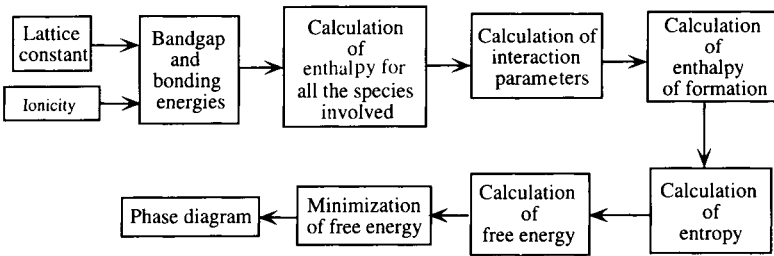


**Figure 2.5** Parameters involved in constructing a phase diagram.

Phase diagrams are constructed mainly using the above three equations. In order to give an idea of how many parameters are necessary to construct a phase diagram, a schematic diagram is shown in figure 2.5.

Most of the parameters are already available in the literature (see for example Barin and Knacke 1973). There are some commercial computer programs available such as SOLGASMIX to obtain phase diagrams. Also in the literature, phase diagrams of many multicomponent systems are available (Stringfellow 1985b, 1975, Razeghi 1989a). For MOCVD growth purposes, phase diagrams provide the initial growth parameters, such as partial pressures of gases and temperature, in order to get a preliminary idea of solid compositions. Thermodynamic analyses of solid composition against vapour composition have been published for the systems  $\text{GaAs}_{1-x}\text{P}_x$ ,  $\text{InAs}_{1-x}\text{P}_x$ ,  $\text{In}_{1-x}\text{Ga}_x\text{As}$  (Mullin and Hurle 1973) and the quaternary  $\text{Ga}_{1-x}\text{In}_x\text{As}_{1-y}\text{P}_y$  (Koukitu 1980). Generally, good agreement between calculated and experimental results is obtained.

Growth rate is another important parameter that can be determined from thermodynamic calculations and it provides the maximum growth rate. Usually, in the MOCVD growth process, the actual growth rate is much lower than that determined from thermodynamic calculations. This is because kinetics and hydrodynamic transport also play a role in determining the growth rate.

The growth rate is obtained from thermodynamic calculation by assuming that the growth rate is basically a diffusion-limited process. Then the growth rate is directly proportional to the flow of incoming atoms. The flux is related to the partial pressures of the incoming atoms and also to the diffusion coefficient of the atoms. In most cases, one of the species is the dominant species in determining the growth rate. For example, in GaAs, the As atom partial pressure is very high compared to Ga atoms and, hence, the Ga atom partial pressure is the critical one in determining the growth rate of GaAs.

### 2.2.2 Kinetics

Thermodynamic equilibrium concepts determine the state of a closed system given very long times. However, the MOCVD process is by definition not an equilibrium process. Thus, thermodynamics define only certain limits for the

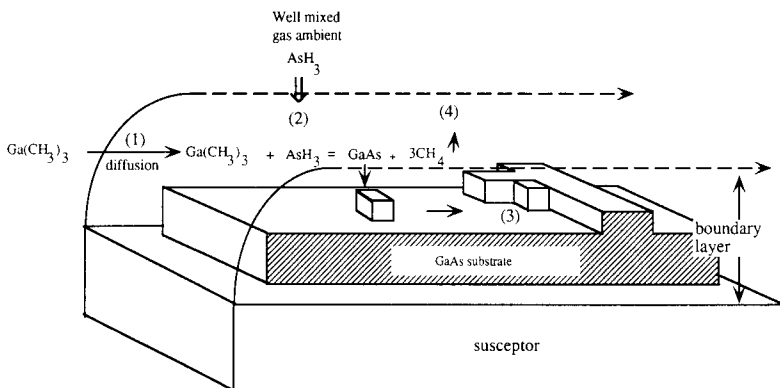


**Figure 2.6** A simplified schematic picture of the GaAs growth process involving different steps.

growth process, and is unable to provide any information about the time required to attain equilibrium, the actual steps involved in the pursuit of the lowest-energy state or the rates of the various processes occurring during the transition from the initial input gases to the final semiconductor solid. These problems can only be approached in terms of kinetics (Stringfellow 1989a).

Several types of reaction occur in MOCVD growth process. Reactions that occur entirely in the gas phase are termed *homogeneous* (reactions among gases) and those occurring at a solid surface are *heterogeneous* (reaction between gases and solids). Normally both types of reaction will be either unimolecular, a process undergone by an energetically activated species without interaction with other species, or bimolecular, which requires the collision of two species, producing an activated complex that may then undergo a unimolecular reaction.

MOCVD growth of GaAs has been studied most so far. TMGa is generally carried by H<sub>2</sub> gas. Studies on low-pressure MOCVD-grown GaAs by AsH<sub>3</sub> and (C<sub>2</sub>H<sub>5</sub>)<sub>3</sub>Ga on GaAs(100) surfaces (Pemble *et al.* 1991) have shown that the H<sub>2</sub> carrier gas did not play a major role in the growth process since the decomposition of AsH<sub>3</sub> will generate adsorbed hydrogen radicals. This has been confirmed by a number of studies involving the use of He, N<sub>2</sub> and D<sub>2</sub> as alternative carrier gases (Hoare 1990, Larsen *et al.* 1988, Yoshida *et al.* 1985). The growth ambient generally has a large excess of the group V constituent, arsine in this case, over the metal alkyl. This is because of the lower sticking coefficient and relatively inefficient decomposition of group V hydrides compared to the metal alkyl. A simplified description of the growth process for III-V compounds, such as the growth of GaAs by TMGa and arsine, occurring near and at the substrate surface is illustrated in figure 2.6.

There are several steps involved in the growth processes of GaAs. In the first step, both AsH<sub>3</sub> and Ga(CH<sub>3</sub>)<sub>3</sub> are carried by hydrogen diffusion through the boundary layer to reach the substrate. The second step involves the surface

reactions. The third step is the formation of GaAs and the final step is the removal of the reaction products. The above reaction is oversimplified. The exact surface reactions and nucleation of GaAs are much more complicated.

Recently a physicochemical model of the MOCVD process has been presented combining fluid flow and heat transfer models for a typical horizontal MOCVD reactor (Jensen *et al* 1991). Jensen's model simulates GaAs growth rates and carbon incorporation trends with temperature, pressure and V/III ratio. The mechanism given in table 2.1 reflects recent reports on the basic chemical reactions (Jensen *et al* 1991).

The exact chemical reaction pathway in MOCVD is not clearly understood. The surface reaction mechanism for growth is complicated by the large number of possible reactions. With reference to the above example, the general reaction pathway involves the following types of chemical reaction process: multiple steps of pyrolytic decomposition of organometallics and reactions with hydrogen radicals in gas phase (G1–G17) (Hebner *et al* 1989, Gaskill *et al* 1988, Larsen *et al* 1988, Yoshida *et al* 1985), heterogeneous decomposition (S1–S13), surface adsorption and desorption (S1–S13). The growth of the GaAs crystal occurs via reactions between Ga- and As-containing surface precursors (S22 and S26). Volatile reaction byproducts are removed from the surface by adsorption, colliding gas-phase radicals (S14–S17, S24) and by bimolecular surface recombination reactions (S18–S21, S23, S25). Carbon incorporation occurs following reactions S8–S10.

## 2.3 GAS FLOW PATTERNS AND REACTOR DESIGN

The gas velocities and temperature gradients in the vicinity of the hot susceptor play a significant role in the deposition process. The problems of reactor cell design and their solutions are best discussed in terms of the hydrodynamics of the reactant gas flowing into the cell, mainly concerned with bulk fluid properties (pressure, viscosity, volume and temperature changes).

### 2.3.1 Laminar and turbulent flow

Consider the case of steady fluid flow through a uniform pipe. The flow may start uniformly but will soon develop into a non-uniform flow. After traversing a distance  $z_V$ , the velocity entry length, the flow velocity  $V(r)$  attains a parabolic profile as shown in figure 2.7(a) (Stringfellow 1989a)

$$V(r) = -\frac{1}{4\eta} \frac{dp}{dz} (a^2 - r^2) \quad (0 \leq r \leq a) \quad (2.11)$$

$\sim dp/dz$  is the pressure gradient,  $a$  is the cross-section radius,  $r$  is the and  $\eta$  is the dynamic viscosity. The reason for the parabolic profile real gas moves against a boundary the gas sticks to the boundary

**Table 2.1** Gas-phase and surface reaction mechanism for growth of GaAs from TMGa and arsine. S<sub>A</sub> refers to an arsenic site, S<sub>G</sub> refers to a gallium site (after Jensen *et al.* 1991). (An asterisk refers to surface adsorption.)

	Gas-phase reactions	Surface reactions
(G1)	$\text{Ga}(\text{CH}_3)_3 \rightarrow \text{Ga}(\text{CH}_3)_2 + \text{CH}_3$	(S1) $\text{H} \cdot + \text{S}_G \rightarrow \text{H}_G^*$
(G2)	$\text{Ga}(\text{CH}_3)_2 \rightarrow \text{GaCH}_3 + \text{CH}_3$	(S2) $\text{H} \cdot + \text{S}_A \rightarrow \text{H}_A^*$
(G3)	$\text{CH}_3 \cdot + \text{AsH}_3 \rightarrow \text{AsH}_2 + \text{CH}_4$	(S3) $\text{CH}_3 \cdot + \text{S}_G \leftrightarrow (\text{CH}_3)_G^*$
(G4)	$\text{CH}_3 \cdot + \text{H}_2 \rightarrow \text{CH}_4 + \text{H}$	(S4) $\text{CH}_3 \cdot + \text{S}_A \leftrightarrow (\text{CH}_3)_A^*$
(G5)	$\text{H} \cdot + \text{H} \cdot + \text{M} \rightarrow \text{H}_2 + \text{M}$	(S5) $\text{GaCH}_3 + \text{S}_G \leftrightarrow \text{GaCH}_3^*$
(G6)	$\text{CH}_3 + \text{H} \cdot + \text{M} \rightarrow \text{CH}_2 + \text{M}$	(S6) $\text{Ga}(\text{CH}_3)_2 + \text{S}_G \rightarrow \text{Ga}(\text{CH}_3)_2 + 2\text{CH}_3$
(G7)	$\text{CH}_3 \cdot + \text{CH}_3 \cdot \rightarrow \text{C}_2\text{H}_6$	(S7) $\text{Ga}(\text{CH}_3)_3 + \text{S}_G \rightarrow \text{Ga}(\text{CH}_3)_3 + 2\text{CH}_3$
(G8)	$\text{GaCH}_3 \cdot + \text{CH}_3 \cdot \rightarrow \text{GaCH}_2 + \text{CH}_4$	(S8) $\text{GaCH}_2 + \text{S}_G + \text{S}_A \rightarrow \text{GaC} + \text{H}_2$
(G9)	$\text{GaCH}_2 + \text{H} \cdot \rightarrow \text{GaCH}_3$	(S9) $\text{Ga}(\text{CH}_3)\text{CH}_2 + \text{S}_G + \text{S}_A \rightarrow \text{GaC} + \text{CH}_3 \cdot + \text{H}_2$
(G10)	$\text{Ga}(\text{CH}_3)_3 + \text{CH}_3 \cdot \rightarrow \text{Ga}(\text{CH}_3)_2\text{CH}_2 + \text{CH}_4$	(S10) $\text{Ga}(\text{CH}_3)_2\text{CH}_2 + \text{S}_G + \text{S}_A \rightarrow \text{GaC} + 2\text{CH}_3 \cdot + \text{H}_2$
(G11)	$\text{Ga}(\text{CH}_3)_2\text{CH}_2 + \text{H} \cdot \rightarrow \text{Ga}(\text{CH}_3)_3$	(S11) $\text{AsH}_2 + \text{S}_A \leftrightarrow \text{AsH}^*$
(G12)	$\text{Ga}(\text{CH}_3)_2\text{CH}_2 \rightarrow \text{Ga}(\text{CH}_3)\text{CH}_2 + \text{CH}_3$	(S12) $\text{AsH}_2 + \text{S}_A \leftrightarrow \text{AsH}^* + \text{H}$
(G13)	$\text{Ga}(\text{CH}_3)\text{CH}_2 \rightarrow \text{GaCH}_2 + \text{CH}_3$	(S13) $\text{AsH}_3 + \text{S}_A \leftrightarrow \text{AsH}^* + \text{H}_2$
(G14)	$\text{Ga}(\text{CH}_3)_3 + \text{H} \cdot \rightarrow \text{Ga}(\text{CH}_3)_2 + \text{CH}_4$	(S14) $\text{CH}_3 \cdot + \text{H}_A^* \rightarrow \text{CH}_4 + \text{S}_G$
(G15)	$\text{Ga}(\text{CH}_3)_2 + \text{H} \cdot \rightarrow \text{Ga}(\text{CH}_3)_3 + \text{CH}_4$	(S15) $\text{CH}_3 \cdot + \text{H}_A^* \rightarrow \text{CH}_4 + \text{S}_A$
(G16)	$\text{Ga}(\text{CH}_3)_2 + \text{CH}_3 \cdot \rightarrow \text{Ga}(\text{CH}_3)\text{CH}_2 + \text{CH}_4$	(S16) $\text{H} \cdot + (\text{CH}_3)_G^* \rightarrow \text{CH}_4 + \text{S}_G$
(G17)	$\text{Ga}(\text{CH}_3)\text{CH}_2 + \text{H} \cdot \rightarrow \text{Ga}(\text{CH}_3)_2$	(S17) $\text{H}_G^* + (\text{CH}_3)_A^* \rightarrow \text{CH}_4 + \text{S}_A$
		(S18) $\text{H}_G^* + (\text{CH})_G^* \rightarrow \text{CH}_4 + \text{S}_A + \text{S}_G$
		(S19) $\text{H}_A^* + (\text{CH})_G^* \rightarrow \text{CH}_4 + \text{S}_A + \text{S}_G$
		(S20) $\text{H}_A^* + \text{H}_G^* \rightarrow \text{H}_2 + \text{S}_A + \text{S}_G$
		(S21) $(\text{CH}_3)_A^* + (\text{CH}_3)_G^* \rightarrow \text{C}_2\text{H}_6 + \text{S}_A + \text{S}_G$
		(S22) $\text{GaCH}_3^* + \text{AsH}^* \rightarrow \text{GaAs} + \text{CH}_4 + \text{S}_A + \text{S}_G$
		(S23) $\text{AsH}^* + \text{AsH}^* \rightarrow \text{As}_2 + \text{H}_2 + 2\text{S}_A$
		(S24) $\text{CH}_3 \cdot + \text{AsH}^* \rightarrow \text{As}^* + \text{CH}_4$
		(S25) $\text{As}^* + \text{As}^* \rightarrow \text{As}_2 + 2\text{S}_A$
		(S26) $\text{GaCH}_3^* + \text{As}^* \rightarrow \text{GaAs} + \text{CH}_3 \cdot + \text{S}_G + \text{S}_A$

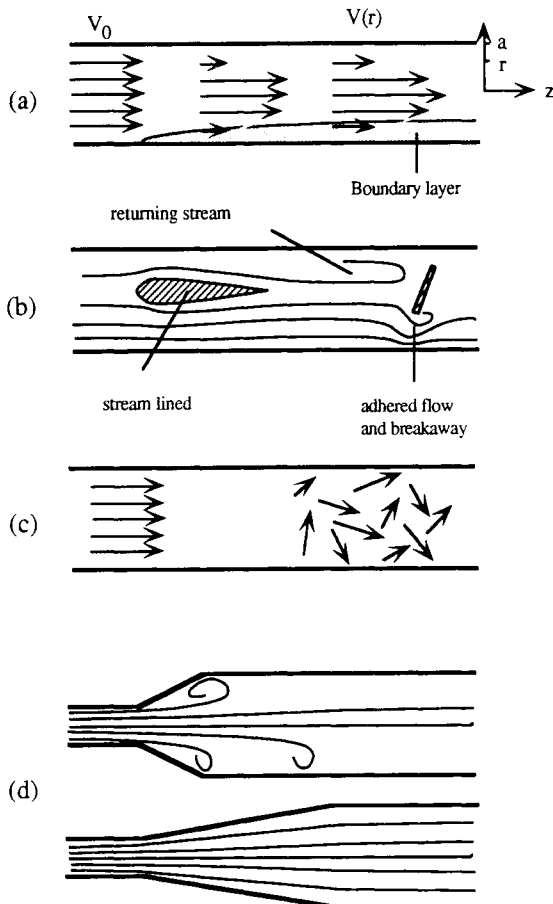


**Figure 2.7** (a) Boundary layer of a gas flowing in a pipe and its velocity distribution (Stringfellow 1989a). (b) Streamlines showing adhered flow and breakaway. (c) Turbulent regime of gas flow. (d) Flow patterns effected by expansion angle of tubes.

without slipping. The flow in figure 2.7(a) is steady, non-uniform and laminar. In laminar flow, the velocity at a fixed position is always the same. Each element of the reactive species travels smoothly along a simple well defined path and each element starting at the same place follows the same path.

The laminar pattern can easily be disturbed by putting a barrier in the flow path (figure 2.7(b)), or by changing the tube diameter (figure 2.7(d)). In figure 2.7(b), the breaking away or adhesion of gas molecules from the wall of a pipe is represented by another set of lines—streamlines—which are used to show the direction of motion of the molecules of a gas. The streamline touching the edge of the barrier does not touch the plate anywhere else and the flow breaks away from the surface at this point. The wave behind the breakaway may rotate

slowly, forming a stable eddy wave. In the case of a susceptor placed inside the reactor chamber at a large angle with respect to the flow direction, a return stream flow would occur.

In figure 2.7(d), a gas flowing in a pipe where the cross-sectional area changes suddenly, either increasing or decreasing, experiences either a decrease or an increase in pressure, respectively. Vortices can develop due to this kind of sudden momentum change. More importantly, vortex creation is due to too high flow velocities. As the mean velocity increases so do the velocity gradients. The friction between adjacent layers of flow can become so high that local velocity components normal to the flow direction are no longer smoothed out but instead will progressively develop into the onset of a turbulent or chaotic flow. The rate of change of decrease in pressure when a pipe expands determines whether or not the expansion is smooth or turbulent. The usual dividing line between laminar and turbulent flows of expansion is taken as a linear expansion angle ( $\theta$ ) of 7 degrees as shown in figure 2.7(d).

When the flow becomes turbulent, the flow develops a highly random character with rapid irregular fluctuations of velocity in both space and time. In this case, an element of gas flow follows a highly irregular distorted path as shown in figure 2.7(c). Different elements starting at the same place follow different paths, since the pattern of irregularities is changing all the time (Shapiro 1961). The irregular motions do not affect all the molecules at the same instant so that if the velocity is averaged out it can still be thought of as a steady flow with a steady average velocity. The criteria to establish whether a gas will be flowing in a turbulent or laminar regime are established by its Reynolds number and defined as

$$Re = \frac{\rho v d}{\eta} \quad (2.12)$$

where  $\rho$  is the density ( $\text{kg m}^{-3}$ ),  $v$  the average flow rate ( $\text{m s}^{-1}$ ),  $d$  the diameter of the tube (m). When  $Re$  is small (less than 100) the flow regime is laminar.

Consider the case of parallel flow over a flat plate. The velocity distribution in the fluid phase is shown in figure 2.8. The flow is uniform with velocity  $V_0$  before the plate is inserted into the system. After the plate is introduced into the system, a low-velocity boundary layer develops next to the plate. The resulting boundary layer width, for the condition  $z > \delta_0$ , is given by (Schlichting 1968)

$$\delta_0 \simeq 4.56 (Dz/V_0)^{1/2} \quad (2.13)$$

where  $D$  is the diffusion coefficient and  $V_0$  is the entry velocity. The boundary layer width is proportional to the square root of  $z$ , the distance measured from the leading edge.

### 2.3.2 The heat effect

Introducing heat into the pipe adds another dimension of complexity to the gas flow, since convection becomes important in the control of the gas flows along

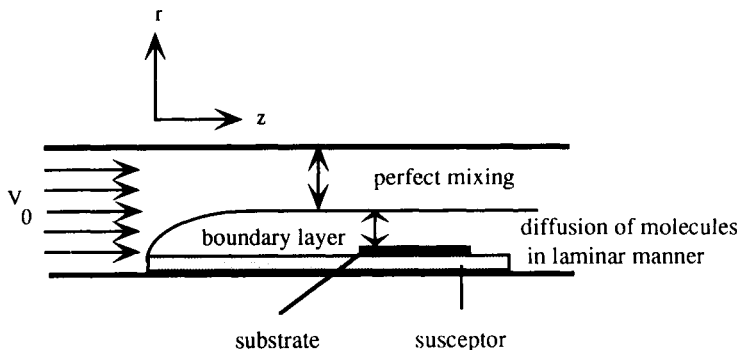


**Figure 2.8** Schematic diagram of reactor showing a gas flow.

the length of the pipe. In a horizontal reactor chamber the temperature differences from the chamber wall to the heated susceptor are enough to influence the flow of gas. When the thermal diffusivity is large and the temperature difference is small, the exchange of momentum on a microscopic scale is so fast that no real macroscopic gas density gradients can develop. Hence, no buoyancy will be observed and the gas is said to be metastable. For higher temperature gradients and smaller heat conductivities, the heavy cold gas moves downwards and the light hot gas near the susceptor moves upwards. The buoyancy forces are so large that free convection occurs. Similar to the Reynolds number, this is characterized by the Rayleigh number ( $Ra$ )

$$Ra = \frac{\alpha g C_p \rho^2 h^3 \Delta T}{\eta k} \quad (2.14)$$

where  $\alpha$  is the coefficient of thermal expansion ( $K^{-1}$ ),  $g$  the gravitational constant ( $9.81 \text{ m s}^{-2}$ ),  $C_p$  the specific heat ( $J \text{ kg}^{-1} \text{ K}^{-1}$ ),  $\rho$  the density ( $\text{kg m}^{-3}$ ),  $h$  the free height above the susceptor (m),  $\Delta T = T_{\text{susceptor}} - T_{\text{reactor wall}}$ ,  $\eta$  the dynamic viscosity ( $\text{kg m}^{-1} \text{ s}^{-1}$ ) and  $k$  the thermal conductivity ( $\text{J m}^{-1} \text{ s}^{-1} \text{ K}^{-1}$ ). When  $Ra \leq 1700$ , the gas is stable; for  $Ra > 1700$ , free convection occurs.

The flux ( $J_i$ ) of a chemical species  $i$  towards the susceptor surface now depends on the local temperature, the local temperature gradient and the creation or annihilation of molecules during the reaction (Giling 1985)

$$J_i = \frac{D_i}{RT} \left( \frac{P_t}{P_t + (n-1)P_i} \frac{\partial P_i}{\partial Z} + \alpha_i \frac{\partial T}{\partial z} \right) \quad (2.15)$$

where  $D_i(T) = D_0(T/T_0)^2$  is the binary diffusion coefficient of species  $i$  as a function of  $T$ ,  $P_t$  the total pressure,  $P_i$  the partial pressure of component  $i$ ,  $n$  the ratio of the number of molecules after and before the reaction,  $z$  the direction normal to the susceptor surface and  $\alpha_i$  the thermal diffusion factor for species  $i$ .

### 2.3.3 Modelling of gas flow pattern and applications to reactor design

There are two approaches to the study of gas flow patterns and the effect of reactor design on the flow patterns. The first approach is based on experimental observations and simulation. The second is numerical calculation.

#### (a) Flow visualization

Flow patterns can be studied by using smoke particles (Eversteijn 1974, Takahashi *et al* 1972, Ban 1978). Generally,  $\text{TiO}_2$  smoke is employed to visualize flow patterns in the reactor. These experiments provide information about the existence of a boundary layer adjacent to the susceptor, the presence of temperature gradients perpendicular to the flow, and evidence of a convection-caused gas motion. These flow visualization experiments also provide a qualitative insight into the momentum transfer in the gas phase. The problem of the smoke test is that it does not give a clear boundary layer thickness since the particles of smoke are heavier than the real gases.

#### (b) Holographic interference study of flow patterns

Giling used holographic interference techniques to investigate temperature gradients (Giling 1985). In this method, two light beams are compared to each other: the reference beam, which represents the original situation, and the sample beam, which contains the information about the changed situation. Small differences in the two light paths become visible as interference patterns. If the gas is turbulent all fringe lines will move around giving an incoherent image. When the gas is convective the isotherms will be curved such that an upward or downward flow is recognized, and when the gas is laminar and stable against convection, fringes parallel to the hot surface will be formed. Giling analysed the flow images for four carrier gases,  $\text{H}_2$ ,  $\text{N}_2$ ,  $\text{Ar}$  and  $\text{He}$ .

#### (c) Berkman *et al*'s model

Berkman *et al* (1977) have developed a detailed model of the flow dynamics, mass and thermal gradients in a horizontal cold-walled reactor that is heated from below. A set of readily usable engineering formulae are given which are derived from hydrodynamic flow theories and that are well correlated with experimental observations.

In a reactor there are two distinct zones above the susceptor. The gas near the susceptor flows in a nearly laminar manner. Above that, the gas flows in a turbulent manner with oscillations of 3–5 Hz. The turbulence is caused by both thermal entry effects and buoyancy forces originating at the leading edge of the hot susceptor. The model of Berkman treats the upper turbulent zone as a cold finger of well mixed gas which acts as a reservoir of reactants. The lower zone acts as a laminar boundary layer, with a velocity profile having average characteristics of both laminar and turbulent flow, through which the reactant is transported by diffusion. For a float susceptor, the growth rate decreases exponentially along the susceptor as  $\exp(-Az)$  where  $A = 2D_T/V_T b_0^2$ ;  $V_T$  is the temperature-corrected gas velocity,  $D_T$  is the reactant diffusion coefficient at temperature  $T$  and  $b_0$  is the initial channel height above the susceptor.

The exponential variation can be nullified by tilting the susceptor at an angle  $\theta_c$  (3–5°) such that

$$\sin(\theta_c) = (2D_0/b_0 V_0)(T_a/T_0)^{0.88} \quad (2.16)$$

where  $D_0$  is the diffusion coefficient of the precursor molecule measured at room temperature,  $T_0$ ;  $T_a$  is the average temperature of the gas above the susceptor,  $V_0$  is the initial horizontal gas velocity at  $T_0$  in front of the susceptor. Low-pressure MOCVD ( $\sim 0.1$  atm) increases  $V_0$ , allowing  $\sin(\theta_c)$  to approach zero.

*(d) Numerical simulation of flow patterns*

Modelling of mass transport problems in epitaxial systems involves solving the mass continuity equation, the Navier–Stokes equation (momentum conservation) and appropriate boundary conditions according to the geometry of the reactor, the heating method and gas inlet and outlet flow (Rosenberger 1979). With the rapid development in computational speed and memory over the last decade, numerical models have expanded from simple boundary-layer descriptions through two-dimensional models to three-dimensional descriptions of horizontal reactors (see Jensen *et al* 1991 and the references therein).

The effort on numerical modelling has been spent on studying different reactor cells, such as return cells (Visser *et al* 1989, Fotiadis *et al* 1990a), horizontal reactors (Quazzani and Rosenserger 1990, Moffat and Jensen 1988) and recirculation cells in the vertical reactor configuration (Patnaik *et al* 1989, Fotiadis *et al* 1990b), to study the influence of inlet flow rate, pressure and geometry on the flow pattern and to understand the origin and nature of mixed convection flows. Two-dimensional simulation flow pattern analyses have been carried out on both horizontal and vertical reactors (Jensen 1989, Patnaik *et al* 1989, Fotiadis *et al* 1990b).

Modelling of three-dimensional flow fields for growth of GaAs using trimethylgallium and arsine has been reported (Jensen 1991). Jensen's model describes processes and the incorporation of detailed chemical kinetic mechanisms into an accurate transport description. The following boundary conditions are assumed to solve the partial differential equations:

- (1) no slip at solid walls,
- (2) constant wall temperature or insulated side walls,
- (3) no flux on non-reacting surfaces or a flux balanced by the rate of incorporation of the species into the growing film.

Surface adsorptions are also considered in the boundary conditions.

This technique transformed the partial differential equations and the associated boundary conditions into a large set of non-linear algebraic equations of the order of 40 000–90 000 that was solved on a supercomputer using Newton's method.

### 2.3.4 Engineering considerations to improve growth uniformity

From Giling's study (Giling 1985) and practice of MOCVD growth (Razeghi

1989a), one can conclude that for the growth of high-quality III-V semiconductor materials, with sharp interfaces, and to avoid parasitic reactions in the gas phase and condensation at the inlet of the deposition zone of the reactor, giving variations from day to day and from system to system, the following considerations on reactor design are crucial.

- (1) Laminar flows free of convection should exist by:
  - (a) using a horizontal reactor,
  - (b) working at low pressure and
  - (c) decreasing the reactor diameter.
- (2) No temperature gradient should be present across the susceptor.
- (3) Eliminate the memory effect:
  - (a) the geometry of the reactor is such that no vortices can develop,
  - (b) no dead volumes are present inside the reactor.

Vortices will develop in sharp corners and behind the susceptor when the susceptor is placed at a large angle with respect to the horizontal level. Dead volumes should be avoided because both vortices and the dead volumes will act as sources of unwanted materials which cannot be removed easily.

There have been at least 60 publications over the last 20 years dealing with designs of reactor cells and configurations. The essential factors in the design of horizontal cells have been established over the last few years (Roberts *et al* 1984, Blaauw *et al* 1985, Landgren *et al* 1986, Thrush *et al* 1984, Griffiths *et al* 1983, Giling 1982). The ability to grow highly uniform compound semiconductors by MOCVD is influenced by a number of parameters in the gas handling manifold and the growth cell. Several modifications of reactor design have been reported to improve the uniformity of the films.

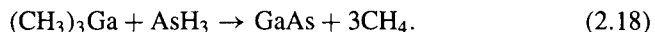
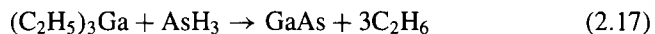
- (1) The manifold must incorporate pressure-balanced vent-run systems.
- (2) The gas mixing region must promote atomic level mixing to ensure good homogeneity across the susceptor. It has been shown that compositional non-uniformity can be eliminated by the use of a gas mixing device (Blaauw *et al* 1987), including vanes, meshes of various porosities, mixing jets, spray tubes, silica frits and orifices, and perforated plates which are either stationary or of variable rotation.
- (3) The expansion region must prevent flow separation from the cell walls which will lead to recirculation, upstream deposition and non-uniform layers (Giling 1982, van de Ven *et al* 1986a, b, Goodings *et al* 1989, Visser *et al* 1989, Makarov and Zhmakin 1989, Schmitz *et al* 1991).
- (4) The head height above the susceptor must be small enough to prevent rolls (Visser *et al* 1989).
- (5) Rotating the substrate (Frijink 1988, Woelk and Beneking 1988, Tompa *et al* 1988, Mircea *et al* 1988) to overcome gas phase depletion and geometrical effects has been reported. Another approach to this engineering problem is the use of a technique levitating the wafer carrier on a gas foil (Woelk and Beneking 1988).

(6) Use of reactors with two separate inlets avoids parasitic gas reactions and improves the quality of the layers (Mpaskoutas *et al* 1991).

The understanding of MOCVD growth mechanisms, including gas flow patterns and chemical reaction pathways, is still premature. The optimum growth parameters, such as growth temperature, reactor pressure, total carrier flow and III/V ratio, are still determined experimentally by both *in situ* and *ex situ* characterization results and determined by *in situ* monitoring of growth rather than solely by theoretical calculations.

## 2.4 MOCVD STARTING MATERIALS

Alkyls of the group II and III metals and hydrides of group V and VI elements are generally used as precursors in MOCVD. Dilute vapours of these chemicals are transported at or near room temperature to a hot zone where a pyrolysis reaction occurs. For example, gallium arsenide is formed by heating trimethylgallium ( $\text{CH}_3\text{)}_3\text{Ga}$  or triethylgallium ( $\text{C}_2\text{H}_5\text{)}_3\text{Ga}$  and arsine over a suitable substrate, usually a single crystal of GaAs or Si, at around 600 °C.



The reaction can be generalized for III–V compounds as:



where M is the group III metal (such as Ga, In, Al), E is the group V element (such as As, P, Sb) and R is the alkyl radical (either  $\text{CH}_3$  or  $\text{C}_2\text{H}_5$ ).

The criteria for the starting materials in MOCVD are:

- stable at room temperature and not subject to spontaneous decomposition or polymerization
- vaporize in  $\text{H}_2$ ,  $\text{N}_2$  or He without decomposing
- capable of purification to remove impurities
- lowest possible toxicity.

A list of suitable starting materials is given in table 2.2. They are used either to grow the III–V host lattices or to dope the crystals of n- or p-type.

### 2.4.1 Group III sources

Trimethyl and triethyl alkyls have been used exclusively in the early development of MOCVD. The trimethyl sources are most often used due to their higher vapour pressure and greater stability. TEAl, TEGa, and TEIn are marginally stable. TEIn has been observed to decompose in storage containers.

**Table 2.2** Starting materials for MOCVD.

Name of compound	Acronym	Purpose
Trimethylgallium	TMGa	III element
Triethylgallium	TEGa	III element
Trimethylaluminium	TMAI	III element
Triethylaluminium	TEAl	III element
Trimethylindium	TMIn	III element
Triethylindium	TEIn	III element
Ethyldimethylindium	EDMIn	III element
Trimethylantimony	TMSb	V element
Triethylantimony	TESb	V element
Trimethylarsine	TMA <sub>3</sub>	V element
Triethylarsine	TEAs	V element
Diethylarsinehydride	DEAs	V element
<i>tert</i> -Butylarsine	TBA <sub>3</sub>	V element
<i>tert</i> -Butylphosphine	TBP	V element
Arsine	AsH <sub>3</sub>	V element
Phosphine	PH <sub>3</sub>	V element
Hydrogen selenide	H <sub>2</sub> Se	n dopant
Hydrogen sulphide	H <sub>2</sub> S	n dopant
Silane	SiH <sub>4</sub>	n dopant
Disilane	Si <sub>2</sub> H <sub>6</sub>	n dopant
Tetramethyltin	TMSn	n dopant
Tetraethyltin	TESn	n dopant
Dimethylzinc	DMZn	p dopant
Diethylzinc	DEZn	p dopant
Diethylberyllium	DEBe	p dopant
Dimethylcadmium	DMCd	p dopant
Bis-cyclopentadienyl magnesium	BCP <sub>2</sub> Mg	p dopant

It has also been found that TEIn reacts with the group V hydrides AsH<sub>3</sub> and PH<sub>3</sub> to form non-volatile adducts upstream from the substrates (Stringfellow 1985b) in atmospheric-pressure MOCVD reactors. However, in low-pressure MOCVD reactors, using TEGa and TEAl significantly reduced carbon concentrations in GaAs and AlGaAs (Kuech *et al* 1986) since they pyrolyse without producing highly reactive CH<sub>3</sub> radicals, which are generally believed to be the main source of carbon in the epitaxial layers. Recently, triisobutylgallium (TIBGa), which has an even lower thermal stability than TEGa, has been used to grow GaAs (Plass *et al* 1988).

Trimethylindium (TMIn) is up to now the most widely used In source. The use of TMIn avoids the problems associated with the use of TEIn. Parasitic reactions are not observed in atmospheric-pressure MOCVD growth using TMIn. However, TMIn has problems such as non-uniform evaporation rate, since it is a solid at room temperature. It also has a tendency to explode. The non-uniform evaporation rate can be controlled by using liquid sources. Alternatively, In sources are required which are liquid below room temperature and at the same

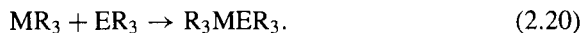
time still have adequate vapour pressure and good chemical stability properties.

Knauf *et al* (1988) tried to combine the advantages of TMIn (weak unwanted side reactions) with those of TEIn (liquid during use) in the new compound ethyldimethylindium (EDMIn). EDMIn is liquid at room temperature and has a vapour pressure of 0.85 Torr at 17 °C, which is similar to the value of 1 Torr for TMIn and an order of magnitude greater than the vapour pressure of TEIn. Early experiments showed that EDMIn was not as pure as the best TMIn. However, EDMIn in high-purity form is now available which makes it an attractive In source.

The growth of Al-containing semiconductors has always been difficult due to the fact that Al is so reactive that it readily incorporates carbon and oxygen into the solid (Stringfellow 1981). This is particularly problematic when TMAI is used, since it pyrolyzes to form aluminum carbide. Other alkyl sources such as TEAl and TIBAl, which decompose to Al metal, can be used to reduce carbon incorporation. However, they have low vapour pressures at room temperature which is a disadvantage for MOCVD, since heating the sources to above room temperature necessitates heating the gas lines and reactor tube as well. In addition, these compounds are not sufficiently stable to be effective sources. Kuech *et al* (1986) has reported reduced growth efficiency as compared with other sources. This indicates the occurrence of parasitic reactions, predominantly premature pyrolysis resulting in wall deposits upstream from the substrate. TIBAl is even less stable and decomposed in storage containers even at room temperature.

In order to solve the problems of Al precursor, the development of new molecules with the appropriate properties is necessary. DMAIH (Bhat *et al* 1986) has an acceptable vapour pressure of 2 Torr at 25 °C and is found to pyrolyze at temperatures as low as 250 °C. Auger electron spectroscopy and SIMS analysis of the films indicate little carbon contamination. It was found that DMAIH can produce excellent AlGaAs epitaxial layers. The only problem is that the layers were always n-type at a level of approximately  $2 \times 10^{18} \text{ cm}^{-3}$ . This was determined to be due to Si and S impurities in the DMAIH source. Preliminary photoluminescence data indicate that the carbon concentration is substantially lower than in AlGaAs layers grown using TMAI.

Alternative sources for MOCVD growth of III-V compounds are sources using adducts. An adduct is a compound formed between a group III alkyl such as  $\text{MR}_3$  which acts as an electron-acceptor molecule (Lewis acid), and a group V alkyl such as  $\text{ER}_3$ , which acts as an electron-donor molecule (Lewis base), according to the reaction



This was first proposed by Harrison and Tompkins (1962) for the growth of InSb and GaAs.

Since 1980, acid-base adducts, e.g., TMIn-TEP (Benz *et al* 1981) and TMIn-TMP, have been used as alternative metal sources (Bath *et al* 1987,

Lee *et al* 1988, Wolfram *et al* 1989) to solve the parasitic reaction problem encountered in atmospheric-pressure MOCVD growth of InP. The main reason for producing less parasitic reactions is their high chemical stability, avoiding unwanted side reactions in the gas phase during growth and enabling safe handling in production and purification processes. Today, fewer problems arise when using the trimethyl and triethyl alkyls due to their higher purity and the improved, safer handling facilities. Nevertheless, the adducts are still used in many laboratories, producing high-quality InP (Wolfram *et al* 1989, Laube *et al* 1985), GaInAs-InP quantum well structures (Streubel *et al* 1988) and even InP on Si layers (Lee *et al* 1988). The films have almost the same properties in terms of layer quality or background doping level as the alkyls under the same growth conditions. The main advantages of adducts are their low reactivity with oxygen and water vapour and the fact that they are already in liquid form at room temperature. The adduct TEGa-TEP is used at British Telecom Research Labs in place of TEGa because of its lower vapour pressure as compared to the Ga alkyls (Moss and Evans 1981). The In adducts, however, have rather low vapour pressures. They are normally used at temperatures above 60 °C and the gas lines of the MOVPE system must be heated to prevent condensation.

Only the first steps have been achieved in investigating new classes of organometallics and in tailoring physicochemical properties (vapour pressure, melting point, stability). Plass *et al* (1988) have employed triisobutylgallium (TIBGa) as a starting material, but due to impurities in the source, the resulting layers showed relatively high n-type conduction. Another type of alternative source has been investigated with the aim to have one source for both the metal and the group V element. Maury *et al* (Maury and Constant 1983, Maury *et al* 1984, 1986, Maury and El Hammadi 1988a, b) successfully grew GaAs layers using  $(\text{ClMe}_2\text{Ga}-\text{AsEt}_2)_2\text{CH}_2$  and  $(\text{C}_6\text{F}_5)_3\text{Ga}-\text{AsEt}_3$  without an additional As source. However, the importance of such compounds is limited to the growth of binary materials. For atomic layer epitaxy by MOVPE, Mori *et al* (1988) and Sasaoka *et al* (1988) used  $\text{Ga}(\text{C}_2\text{H}_5)_2\text{Cl}$  as a starting material. Such reactants have not previously been used in a normal MOCVD process.

#### 2.4.2 Group V sources

The chemical sources used for III-V epitaxial growth techniques are most often highly toxic or flammable. In particular, the hydrides such as arsine ( $\text{AsH}_3$ ) and phosphine ( $\text{PH}_3$ ) are highly toxic with threshold level values (TLV) of 0.05 and 0.3 ppm respectively. A summary of the effects on human exposure to As and P hydrides is given by Hess and Riccio (1966). In addition, they must be stored in high-pressure cylinders (the equilibrium vapour pressures at 20 °C are 14 and 41 bars for arsine and phosphine, respectively). Large quantities of these toxic materials may accidentally be released in a very short time. They must be handled very carefully, especially when changing containers. Thus, the utilization of arsine and phosphine requires costly and delicate equipment to

protect the operators and the environment from hazards and the products from atmospheric contamination. Less toxic and hazardous alternative materials are desired for safety reasons. A number of organometallic group V sources are less toxic than the hydrides. Another advantage of the organometallic sources is that they are moderate-vapour-pressure liquids. This results in a less hazardous working environment since computer study shows that the dispersion of these organometallic materials is approximately two orders of magnitude slower than for the release from a high-pressure cylinder.

Research work for starting materials alternative to the highly toxic  $\text{AsH}_3$  has been explored recently. Organoarsenic materials normally have much lower vapour pressures and higher TLV levels (Chiu *et al* 1987) which enables much safer handling. The commonly used reactants are trimethylarsenic (TMAs) (Brauers *et al* 1988, Fraas *et al* 1987) and triethylarsenic (TEAs) (Razeghi 1989a, Brauers *et al* 1988, Fraas *et al* 1987, Stringfellow 1989b, Lum *et al* 1988a, Fujita *et al* 1988). It is shown that TEAs is less stable than  $\text{AsH}_3$  at normal growth conditions, enabling lower V–III ratios in the MOCVD process. But, in most cases, a significant carbon incorporation, resulting in carbon concentrations higher than  $5 \times 10^{16} \text{ cm}^{-3}$  in the films (Blaauw *et al* 1985, Lum *et al* 1988b), is still a problem to be investigated. Also, it is found that the epitaxial layer morphology is far from perfect, probably due to the incorporation of other atomic or molecular impurities.

Other materials such as tertiarybutylarsine (TBAs) (Brauers *et al* 1988, 1989, Haacke *et al* 1989, Tanaka *et al* 1989), isobutylarsine (IBAs) (Chen *et al* 1987, Lum *et al* 1987), dimethylarsine (DMA<sub>3</sub>H) (Chen *et al* 1989), diethylarsine (DEAsH) (Bath *et al* 1987) and phenylarsine ( $\text{PhAsH}_2$ ) (Brauers *et al* 1988) have been used to overcome this problem. Some of them, especially TBAs and  $\text{PhAsH}_2$ , have shown promising results (Brauers *et al* 1989, Tanaka *et al* 1989). The use of elemental As (Bath 1985) seems not to be suitable for a reliable epitaxial process. Most of the organoarsenic compounds mentioned above are commercially available. In addition to the carbon problem, other disadvantages of these sources are the limited purity and the high prices.

Alternative P sources are also required due to toxic waste and safety problems. Initially experiments were carried out with trimethylphosphine (TMP) and triethylphosphine (TEP) (Benz *et al* 1982). Due to their high thermal stability, they have to be precracked before introducing into the growth chamber (Benz *et al* 1982). This is a rather irreproducible technique and therefore not suitable for MOVPE. The same holds true for elemental P sources which were applied by Naitoh *et al* (1988).

Larger organophosphorus molecules such as tertiarybutylphosphine (TBP) and isobutylphosphine (IBP) have shown better growth results (Chen *et al* 1986, Saxena *et al* 1988, Kellert *et al* 1989, Kurtz *et al* 1989). Especially TBP has a favourable vapour pressure and is found to be pyrolyzed several hundred degrees lower than  $\text{PH}_3$  (Chen *et al* 1986). This may be an advantage when growing quaternary compounds (e.g., InGaAsP) where As and P sources with comparable

thermal stability are required. Furthermore, the toxicity is lower than PH<sub>3</sub>. Thus TBP is a good candidate for future investigations (Stringfellow 1989b).

## 2.5 LOW-PRESSURE MOCVD AND MOMBE

Due to the specific limitations associated with both the conventional MBE and MOCVD growth processes, modifications to both of these techniques have been investigated in recent years.

To overcome the viscous effects that cause the problems of expansion and buoyancy in MOCVD, low-pressure MOCVD (LPMOCVD) operated in the pressure range of 0.1 to 76 Torr has been developed. The successful growth of high-quality epitaxial GaAs, GaAsP and InGaAs films by reacting combinations of TE<sub>2</sub>As, TEIn, arsine and phosphine in a high-vacuum chamber ( $\sim 10^{-3}$  Torr) has also been reported (Fraas *et al* 1987). This technique is called vacuum chemical epitaxy (VCE). Likewise, for MBE, the conventional group V solid sources are replaced by AsH<sub>3</sub> and PH<sub>3</sub> gas-cracking cells (Panish 1980), and the new process is called gas-source molecular beam epitaxy (GSMBE). Vodjani (1982) and Veuhoff *et al* (1981) have carried the GSMBE process one step further by replacing the group III MBE sources with organometallic group III sources and have named this technique metallorganic molecular beam epitaxy (MOMBE). The MOMBE reactor was based on a UHV MBE growth chamber and used a conventional MOCVD gas handling system. Some references named this UHV growth technique with organometallic and hydride sources chemical beam epitaxy (CBE) to separate its growth technology from that of elemental group III and hydride group V sources.

The main advantages of the MOMBE technique compared to conventional MBE are:

- capacity to grow high-purity InP-based materials, even at high growth rates
- improved flux uniformity and stability
- significant reduction in morphological defects, even at high growth rates
- improved flexibility for rapid controlled composition and doping changes
- source replenishment *ex vacuo*
- easier industrial scale-up and significant reduction in liquid nitrogen cooling requirements.

The significant advantages of MOMBE compared to conventional MOCVD are:

- use of one or two orders of magnitude less AsH<sub>3</sub> and PH<sub>3</sub> for the growth of GaAs- and InP-based materials
- elimination of the parasitic gas-phase reaction
- availability of *in situ* diagnostic and control techniques
- molecular-flow growth regime, hence MBE-like monolayer thickness control
- UHV background should lead to higher-quality Al-containing epilayers

- improvements in homogeneity, composition and reproducibility for large-area growth of InP-based materials
- selective-area growth capability
- reduction of p-type doping memory effects
- *in vacuo* oxide removal possible prior to III-V growth on silicon.

The first attempts to use MOMBE to grow GaAs epilayers using a TEGa source were seriously hampered by the high unintentional carbon-doping levels observed, which generated p-type carrier concentrations typically in the range  $10^{16}$ – $10^{21} \text{ cm}^{-3}$  (Putz *et al* 1985). However, significant improvements have since been obtained by using TMGa (which possesses a significantly weaker GaC bond) and has led to the observation of residual p-type doping levels in the low  $10^{14} \text{ cm}^{-3}$  range (Chiu *et al* 1987, Saito *et al* 1988), with corresponding room-temperature and 77 K Hall mobility values of 500 and  $5000 \text{ cm}^2 \text{ V}^{-1} \text{ s}^{-1}$  respectively. In addition, GaAs layers with a residual n-type background have also been grown using high III/V flux ratios, but the electron mobilities reported to date have been found to be limited to  $72\,000 \text{ cm}^2 \text{ V}^{-1} \text{ s}^{-1}$  by the unintentional incorporation of carbon (Putz *et al* 1986). The level of unintentional carbon contamination has been subsequently found to be even more serious for GaAlAs layers (typically  $p = 2 \times 10^{17} \text{ cm}^{-3}$  for  $x = 30\%$ ), and increase further with increasing aluminium concentration (Benehimol *et al* 1989). As a direct consequence, the highest 77 K two-dimensional electron gas mobility reported to date for MOMBE-grown GaAs/GaAlAs structures has been around  $60\,000 \text{ cm}^2 \text{ V}^{-1} \text{ s}^{-1}$ . It is clear that a detailed materials investigation is required to overcome this limitation.

On the other hand, the high level of carbon incorporation observed when using TEGa as the source material has allowed this source to be used as an intentional p-type doping source when growing GaAs/GaAlAs layers using TEGa. In this way, the highest p-type doping levels ever reported for GaAs (in excess of  $10^{21} \text{ cm}^{-3}$ ) have been achieved. Despite the importance of the GaAs/GaAlAs materials system, surprisingly little information has yet emerged with regard to MOMBE-grown GaAs/GaAlAs device characteristics. Chiu *et al* (1988) have reported a  $1 \mu\text{m}$  GaAs MESFET device with a maximum transconductance of  $177 \text{ mS mm}^{-1}$  occurring at 0.7 V, and also a double-heterostructure laser with low threshold current.

In the case of the MOMBE growth of lattice-matched GaInP on GaAs (Ozasa *et al* 1989), very few attempts have yet been made to study this material system and little information is available. In contrast to the GaAs/GaAlAs system, MOMBE-grown InP-based materials, in general, exhibit electrical and optical properties which are at least comparable to those obtained from corresponding materials grown using other state-of-the-art techniques. For example, the MOMBE growth of high-quality InP exhibiting a 77 K mobility of  $105\,000 \text{ cm}^2 \text{ V}^{-1} \text{ s}^{-1}$ , has already been reported. In addition, high-quality lattice-matched InGaAs epilayers on InP (electron mobilities 10 000–12 000 and  $40\,000$ – $67\,000 \text{ cm}^2 \text{ V}^{-1} \text{ s}^{-1}$  at 300 and 77 K respectively for carrier

concentration in the  $5 \times 10^{14} - 5 \times 10^{15} \text{ cm}^{-3}$  range) have also been produced for both long-wavelength optical communication and high-frequency FET device applications. The ability of MOMBE to provide MBE-like levels of monolayer thickness control and interface sharpness has also already been confirmed by the fabrication of high-quality GaInAs/InP quantum-well and superlattice structures. In addition, the MOMBE growth of high-quality quaternary GaInAsP epilayers, lattice matched to InP over the entire composition range, has also been demonstrated (Razeghi *et al* 1986b, c).

Rapid progress made with regard to the MOMBE growth of InP-based materials and heterostructures has already led to the successful application of a large variety of promising optoelectronic devices. For example, MOMBE-grown low-leakage-current GaInAs PIN photodiodes, 1.3 and 1.5 micron wavelength GaInAsP/InP waveguides, low-threshold-current ( $1.3 - 1.5 \text{ kA cm}^{-2}$ ) GaInAs/InP double-heterojunction and multiquantum well lasers (Amor *et al* 1989) and high-mobility GaInAs/InP HEMT structures have already been reported. Furthermore, the additional flexibility of MOMBE to grow very sophisticated structures has been clearly demonstrated following the fabrication of step-graded GaInAs/GaInAsP/InP DHBT devices with 150 Å InGaAs base regions p-type doped up to  $5 \times 10^{19} \text{ cm}^{-3}$ .

Despite the considerable progress already made in MOMBE-grown materials and device structures, there is now an important need for detailed physical and chemical information regarding MOMBE growth reactions if the potential of the MOMBE technique is to be realized. While reports of modulated beam mass spectrometry (Yalada *et al* 1989) and REED (Kimural *et al* 1987) are just beginning to appear, considerable work is required to perform a detailed study to identify reactant species, the possible formation of intermediate complexes and the nature of adsorbed and desorbing organic products as a function of growth conditions.

## REFERENCES

- Amor S B, Dmowski L, Portal J C, Pulsford N J, Nicholas R J, Singleton J and Razeghi M 1989 *J. Appl. Phys.* **65** 2756  
Ban V S 1978 *J. Electrochem. Soc.* **125** 317  
Barin I and Knacke O 1973 *Thermochemical Properties of Inorganic Substances* (Berlin: Springer)  
Bath R 1985 *J. Electron. Mater.* **14** 433  
Bath R, Koza M A and Skromme B J 1987 *Appl. Phys. Lett.* **50** 1386  
Benehimol J L, Alexandre F, Gao Y and Alaoui F 1989 *J. Crystal Growth* **95** 150  
Benz K W, Haspelko H and Bosch R 1982 *J. Physique Coll.* **43 C5** 393 (Suppl.)  
Benz K W, Renz H, Wiedlein J and Pilkuhn N H 1981 *J. Electron. Mater.* **10** 185  
Berkman S, Ban V S and Goldsmith N 1977 *Heterojunction Semiconductors for Electronic Devices* ed G W Cullen and C C Wang (New York: Springer) p 264  
Bhat R, Koza M A, Chang C C, Schwarz A and Harris T D 1986 *J. Crystal Growth* **77** 7  
Blaauw C, Emmerstorfer B and Spring Thorpe A T 1987 *J. Crystal Growth* **84** 431

- Blaauw C, Mincr C, Emmerstorfer B, Spring Thorpe A J and Gallant M 1985 *Can. J. Phys.* **63** 664
- Brauers A, Kaysor O, Kall R, Heinecke H, Balk P and Hofmann H 1988 *J. Crystal Growth* **93** 7
- Brauers A, Weyers M and Balk P 1989 *Chemtronics* **4** 8
- Callahan F J 1985 *Swagelok Tube Fitting and Installation Manual*
- Chen C H, Larsen C A and Stringfellow G B 1987 *Appl. Phys. Lett.* **50** 218
- Chen C H, Larsen C A, Stringfellow G B, Brown D W and Robertson A J 1986 *J. Crystal Growth* **77** 11
- Chen C H, Reihlen E H and Stringfellow G B 1989 *J. Crystal Growth* **96** 497
- Chiu T H, Tsang W T, Ditzenberger J A, Tu C W, Ren F and Wu C S 1988 *J. Electron. Mater.* **17** 217
- Chiu T H, Tsang W T, Schubert E F and Agyekum E 1987 *Appl. Phys. Lett.* **51** 1109
- Didchenko R, Alix J E and Toeniskoetter R H 1960 *J. Inorg. Nucl. Chem.* **14** 35
- Doi A, Aoyagi Y and Namba S 1986 *Appl. Phys. Lett.* **48** 1787
- Eversteijn F C 1974 *Philips Res. Rep.* **29** 45
- Fotiadis D I, Boekholt M, Jensen K F and Richter W 1990a *J. Crystal Growth* **100** 577
- Fotiadis D I, Kieda S and Jensen K F 1990b *J. Crystal Growth* **102** 441
- Fraas L M 1981 *J. Appl. Phys.* **52** 6939
- Fraas L M, McLeod P S, Weiss R E, Partain L D and Cape J A 1987 *J. Appl. Phys.* **62** 299
- Frijink P M 1988 *J. Crystal Growth* **93** 207
- Fujita S, Imaizumi M, Araki S, Takeda Y and Sasaki A 1988 *J. Crystal Growth* **93** 1
- Gaskill D K, Kolubeyev V, Bottka N, Sillmon R S and Butler J E 1988 *J. Crystal Growth* **93** 127
- Giling L J 1982 *J. Electrochem. Soc.* **129** 634
- Giling L J 1985 *Crystal Growth of Electronic Materials* ed E Kaldus (Amsterdam: North-Holland) p 83
- Goodings C, Mason N J, Walker P J and Jebb D 1989 *J. Crystal Growth* **96** 13
- Griffiths R J M, Chew N G, Cullis A G and Joyce G C 1983 *Electron. Lett.* **19** 319
- Haacke G, Watkins S P and Burnhard H 1989 *Appl. Phys. Lett.* **54** 2029
- Harrison B C and Tompkins E H 1962 *Inorg. Chem.* **1** 951
- Hebner G A, Kileen K P and Biefeld R M 1989 *J. Crystal Growth* **98** 293
- Hess K L and Riccio R J 1966 *J. Crystal Growth* **77** 95
- Hoare R D 1990 *PhD Thesis* University of Manchester Institute of Science and Technology
- Hollan L, Boulon M and Chane J P 1981 *J. Electron Mater.* **10** 193
- Horikoshi L 1986 *The Physics and Fabrication of Microstructures* (Les Houches)
- Jensen K F 1989 *J. Crystal Growth* **98** 148
- Jensen K F, Fotiadis D I and Mountzaris T J 1991 *J. Crystal Growth* **107** 1
- Kellert F G, Whelan J S and Chan K T 1989 *J. Electron. Mater.* **18** 355
- Kimural K, Horiguchi S, Kamn K, Mashata M, Mahara M and Tshii M 1987 *Japan. J. Appl. Phys.* **26** 419
- Kittel Ch and Kroemer H 1980 *Thermal Physics* (San Francisco: Freeman)
- Knauf J, Schmitz D, Strauch G, Jurgensen H and Heyen M 1988 *J. Crystal Growth* **93** 34
- Koukitu A and Seki H 1980 *J. Crystal Growth* **49** 325
- Kuech T F, Wu E, Kuan T S, Deline V and Potemski R 1986 *J. Crystal Growth* **77** 257
- Kurtz S R, Olson J M and Kibbler A 1989 *J. Electron. Mater.* **18** 15
- Landgren G, Anderson S G, Anderson J Y, Samuelson L, Silverberg P and Tolkien P 1986 *J. Crystal Growth* **77** 67
- Larsen C A, Buchan N I and Stringfellow G B 1988 *Appl. Phys. Lett.* **52** 480

- Laube G, Kohier U, Weidlein J, Schol F, Streubel K, Dieter R J, Karl N and Gerdon M 1985 *J. Crystal Growth* **93** 45
- Lee M K, Huang K C, Wuu D S, Tung H H and Yu K Y 1988 *J. Crystal Growth* **93** 539
- Lum R H, Klingert J K and Lamont M G 1987 *Appl. Phys. Lett.* **50** 284
- Lum R M, Klingert J K and Lamont M G 1988a *J. Crystal Growth* **89** 137
- Lum R M, Klingert J K, Wynn A S and Lamont M G 1988b *Appl. Phys. Lett.* **52** 1475
- Makarov Yu N and Zhmakina A I 1989 *J. Crystal Growth* **94** 537
- Manasevit H M 1971 *J. Electrochem. Soc.* **118** 647
- Manasevit H M and Simpson W I 1969 *J. Electrochem. Soc.* **116** 1725
- Matsumoto T and Usui A 1986 *Abstracts of 1986 Fall Meeting of Japan Soc. Appl. Phys.*
- Maury F and Constant G 1983 *J. Crystal Growth* **62** 568
- Maury F, Constant G, Fontaine P and Biberian J P 1986 *J. Crystal Growth* **78** 185
- Maury F and El Hammadi A 1988a *J. Crystal Growth* **91** 105
- Maury F and El Hammadi A 1988b *J. Crystal Growth* **91** 97
- Maury F, El Hammadi A and Constant G 1984 *J. Crystal Growth* **68** 88
- Mircea A, Ougazzaden A, Daste P, Gao Y, Kazmierski C, Bouley J C and Carencio A 1988 *J. Crystal Growth* **92** 235
- Moffat H K and Jensen K F 1988 *J. Electrochem. Soc.* **135** 459
- Mori K, Yoshida M and Usui A 1988 *Gallium Arsenide and Related Compounds 1987 (Inst. Phys. Conf. Ser. 91)* (Bristol: Institute of Physics) p 187
- Moss R H and Evans J S 1981 *J. Crystal Growth* **55** 129
- Mpaskoutas M, Morhaim C, Patillon J N and André J P 1991 *J. Crystal Growth* **107** 192
- Mullin J B and Hurle D T J 1973 *Luminesc. J.* **7** 176
- Naitoh M, Soga T, Jimbo T and Umeno M 1988 *J. Crystal Growth* **93** 52
- Nelson H 1963 *RCA Rev.* **19** 603
- Nicholas R J, Brunel L C, Huant S, Karrai K, Portal J C, Brummell M A, Razeghi M, Chang K Y and Cho A Y 1985 *Phys. Rev. Lett.* **55** 8883
- Nishizawa J and Kurabayashi T 1986 *J. Crystallogr. Soc. Japan* **28** 133
- Osbourne G C 1985 *Mater. Res. Soc. Symp. Proc.* **37** 220
- Ozasa K, Yuri M, Tanaka S and Matsunami H 1989 *J. Crystal Growth* **95** 171
- Panish M B 1980 *J. Electrochem. Soc.* **127** 2729
- Parker E H C 1985 *The Technology and Physics of Molecular Beam Epitaxy* (New York: Plenum)
- Patnaik S, Brown R A and Wang C A 1989 *J. Crystal Growth* **96** 153
- Pemble M E, Buhaenko D S, Francis S M, Goulding F P and Allen J T 1991 *J. Crystal Growth* **107** 44
- Plass C, Heinecke H, Kayser O, Luth H and Balk P 1988 *J. Crystal Growth* **88** 455
- Putz N, Heinecke H, Heyen M, Balk P, Weyers M and Luth H 1986 *J. Crystal Growth* **74** 292
- Putz N, Venhoff E, Meinecke H, Heyen M, Luth M and Balk P 1985 *J. Vac. Sci. Technol. B* **3** 671
- Quazzani J and Rosenberger F 1990 *J. Crystal Growth* **100** 545
- Razeghi M 1983 *Rev. Tech. Thomson-CSF* **15** 1
- Razeghi M 1985a *Lightwave Technology for Communication* ed W T Tsang (New York: Academic)
- Razeghi M 1985b *Semiconductors and Semimetals* vol 22 part A, ed W T Tsang (Orlando, FL: Academic) p 305
- Razeghi M 1989a *The MOCVD Challenge Volume 1: A Survey of GaInAsP-InP for Photonic and Electronic Applications* (Bristol: Hilger) p 14
- Razeghi M 1989b *Photonics, European Institute of Technology* p 49, Lectures presented at the Workshop on Photonics, Verona, November 1989, Banca Popolare Di Verona
- Razeghi M, Blondeau R, Bouley J C, Decremoux B and Duchemin J P 1984 *Proc. 9th*

- IEEE Int. Laser Conf.*
- Razeghi M, Defour M, Omnes F, Dobers M, Vieren J P and Guldner Y 1989a *Appl. Phys. Lett.* **55** 457
- Razeghi M, Duchemin J P, Portal J C, Dmowski L, Remeni G, Nicholas R J and Briggs A 1986a *Appl. Phys. Lett.* **48** 712
- Razeghi M, Hosseini A, Vilcot J P and Decoster D 1987 *Gallium Arsenide and Related Compounds* (Bristol: Institute of Physics) p 625
- Razeghi M, Maurel Ph, Omnes F, Ben Amor S, Dmowski L and Portal J C 1986b *Appl. Phys. Lett.* **48** 1267
- Razeghi M, Maurel Ph, Omnes F and Pochelle J P 1986c *Appl. Phys. Lett.* **49** 1110
- Razeghi M, Maurel Ph, Tardella A, Dimovsky L, Gauthier D and Portal J C 1986d *Appl. Phys. Lett.* **60** 2453
- Razeghi M, Omnes F, Nagle J, Defour M, Acher O and Bove P 1989b *Appl. Phys. Lett.* **55** 1677
- Roberts J S, Mason N J and Robinson M 1984 *J. Crystal Growth* **68** 422
- Rogers D C, Nicholas R J, Portal J C and Razeghi M 1986 *Semicond. Sci. Technol.* **1** 350
- Rosenberger F 1979 *Fundamentals of Crystal Growth* (Berlin: Springer)
- Saito J, Ono K, Nanbu K, Ishikawa T and Kondo K 1988 *Japan. J. Appl. Phys.* **127** L114
- Sasaoka C, Yoshida M and Usui A 1988 *Japan. J. Appl. Phys. Lett.* **27** L190
- Saxena R R, Fouquet J E, Sardi V M and Moon R L 1988 *Appl. Phys. Lett.* **53** 26
- Schlichting H 1968 *Boundary Layer Theory* 6th edn (New York: McGraw-Hill)
- Schmitz D, Strauch G, Jürgensen H and Heyen M 1991 *J. Crystal Growth* **107** 188
- Shapiro A H 1961 *Shape and Flow* (London: Heinemann)
- Streubel K, Scholz F, Laube G, Dieter R J, Zielinski E and Keppler F 1988 *J. Crystal Growth* **93** 347
- Stringfellow G B 1975 *International Review of Science, Inorganic Chemistry* Series 2, vol 10 (London: Butterworths) pp 111–45
- Stringfellow G B 1981 *J. Crystal Growth* **55** 42
- Stringfellow G B 1985a *Crystal Growth of Electronic Materials* ed E Kaldus (Amsterdam: Elsevier) p 247
- Stringfellow G B (1985b) *Semiconductors and Semimetals* vol 22 part A, ed W T Tsang (Orlando, FL: Academic) p 209
- Stringfellow G B 1989a *Organometallic Vapor-Phase Epitaxy: Theory and Practice* (New York: Academic) p 218
- Stringfellow G B 1989b *J. Electron. Mater.* **17** 327
- Suntola T 1984 *16th Int. Conf. on Solid State Devices and Materials* (Tokyo) Extended Abstracts 647
- Suntola T, Atron J, Pakkala A and Linfors S 1980 *SID 80 Digest* 108
- Takahashi R, Koga Y and Sugawara K 1972 *J. Electrochem. Soc.* **119** 1406
- Tanaka H, Kikkawa T, Kasai K and Komono J 1989 *Japan. J. Appl. Phys.* **28** L901
- Thrush E J, Whiteway J E A, Wale-Evans G, Wight D R and Cullis A G 1984 *J. Crystal Growth* **68** 412
- Tompa G S, McKee M A, Beckham C, Zawadski P A, Colabella J M, Reinert P D, Capuder K, Stall R A and Norris P E 1988 *J. Crystal Growth* **92** 220
- van de Ven J, Rutten G J M, Raaymakers M J and Giling L J 1986a *J. Crystal Growth* **76** 352
- van de Ven J, Schoot H G and Giling L J 1986b *J. Appl. Phys.* **60** 1648
- Veuhoff E, Pletschen W, Balk P and Luth H 1981 *J. Crystal Growth* **55** 30
- Visser E P, Kleijn C R, Govers C A M, Hoogendoorn C J and Giling L J 1989 *J. Crystal Growth* **95** 929
- Vodjani N 1982 *These de Doctorat 3e Cycle* University Paris XI

- Vodjani N, Lemarchand A and Paradan H 1982 *J. Physique Coll.* **43** C5 339  
Woelk E and Beneking H 1988 *J. Crystal Growth* **93** 216  
Wolfram P, Reier F W, Franke D and Schumann H 1989 *J. Crystal Growth* **96** 691  
Yalada T, Tokumitsu E, Saito K, Akasaka T, Miyauchi M, Kanagai M and Takahashi K  
1989 *J. Crystal Growth* **95** 145  
Yoshida M, Watanabe H and Uesugi F 1985 *J. Electrochem. Soc.* **132** 677

## In situ Characterization during MOCVD

### 3.1 INTRODUCTION

Molecular beam epitaxy (MBE) benefits from many *in situ* characterization techniques because of its high-vacuum environment. For instance, reflection high-energy electron diffraction (RHEED) is used for optimization of MBE growth conditions. Very few techniques are available for *in situ* characterization of MOCVD because the development of such techniques is hampered by a number of difficulties. These include reactor geometry considerations, inability to use ultrahigh-vacuum techniques, and the deposition of reaction products on the reactor walls during growth. In comparison with MBE and metallorganic MBE (MOMBE), the *in situ* control of growth parameters is still in a premature state.

The kinetic data needed to understand the first step in growth include measurements of precursor decomposition, the search for and measurement of new products generated in the reactions, the influence of operation conditions on these data and monitoring the growing surfaces as RHEED does in MOMBE.

Mass spectroscopy (Lee *et al* 1988, Mashita *et al* 1986) has been widely used to sample species from the reaction zone. The mass spectrometer is usually at some distance from the sampling region. Therefore the sampled gas volume is studied under different conditions (pressures and temperatures) than those prevailing in the reactor. The sampled molecules undergo a very large number of collisions between the sampling point and the detection chamber. This implies that short-lived reactive species, e.g. free radicals, are likely to be removed by wall reactions and gas-phase reactions before the sample is analysed. Thus mass spectrometry is not a true *in situ* characterization tool.

Since techniques with electron beams are not available in MOCVD, photons are used as probes. They can easily penetrate through the gas phase to the important regions near the substrate and can be chosen such that they do not modify the molecules studied.

For optical diagnostics, ultraviolet (UV), visible (VIS) (Haigh 1983) and near-infrared (NIR) probes are most often used to study the vibrational and electronic spectra of gas species respectively. IR laser absorption spectroscopy is applicable to a large number of molecular species, for example, to characterize gaseous

chemical intermediates (Gaskill *et al* 1988) and to monitor the vibrational frequencies of gaseous species (Butler *et al* 1986), but the technique is hampered by averaging over the probe volume. This can make interpretation difficult for MOCVD systems where there are generally considerable spatial variations in concentrations and temperature.

Opto-galvanic detection and laser-induced fluorescence (Donnelly and Karlicek 1982) spectroscopy require a tunable laser to tune into either a fluorescent or an ionizing transition. They provide very sensitive and selective detection. However, opto-galvanic detection has not been applied to MOCVD and the potential of laser-induced fluorescence has been shown only in a few cases (Richter *et al* 1991).

Raman scattering (RS), either linear (spontaneous) or non-linear, is experimentally elaborate. It always exhibits good temporal and spatial resolution. While spontaneous RS has a low sensitivity, the non-linear method coherent anti-Stokes Raman scattering (CARS) yields an adequate signal at typical MOCVD partial pressures.

All of the techniques mentioned above are applied in gas-phase diagnostics. They do not provide direct information about the growing surface. There is also a clear need for the development and use of diagnostic tools as monitoring devices in the routine growing equipment. In comparison with MBE and MOMBE, the on-line control and accurate presetting of growth parameters is still in a premature state. One of the techniques for monitoring the growth surface is quasielectric light scattering (QLS) which has been used to characterize surface defects and surface roughness (Olson and Kibbler 1986). It is particularly sensitive to extended, correlated surface roughness of the kind typically found in morphologically unstable crystal growth systems.

Optical second-harmonic generation has been applied to monitor the dynamic surface chemical processes for low-pressure MOCVD. Preliminary results showed that the measurements depend exclusively upon surface rather than gas-phase processes. This work illustrated the potential for a second-harmonic generation technique as a monitoring tool for real-time growth of MOCVD. In principle, real-time ellipsometry is an apparently well adapted technique for the purpose of monitoring the growing surface of MOCVD because it is non-destructive, compatible with high pressure and various reactor geometries (Aspnes 1988b, Drevillon 1989, Collins 1989). Ellipsometry analyses the polarization-dependent reflection properties of a light beam under oblique incidence and data are directly correlated to the dielectric function of the structure under investigation. Although it contains some information about the sample surface, it is very difficult to separate the surface contribution from the much larger bulk contribution. In order to yield information on the growing surface, UV light must be used to decrease the penetration depth to about 100 Å, thus the deposition on the reactor wall can prevent any prolonged real-time study.

The above limitations can be overcome using a technique called either reflectance anisotropy (RA) or reflectance difference spectroscopy (RDS) (Aspnes

1985, Aspnes and Studna 1985). RDS measures the optical anisotropy of a sample under normal incidence. More precisely, the technique involves illuminating the sample with polarization-modulated light, and detecting the polarization of the reflected light. Thus, RDS is analogous to ellipsometry, in that oblique incidence is used. Because of the cubic symmetry of the III-V semiconductors, the bulk is nearly isotropic, while the regions of lower symmetry, like the surface and interfaces, can be anisotropic. In the case of the (100) surfaces of III-V semiconductors, the contribution from the bulk is expected to vanish (Agranovich and Ginzburg 1984). Therefore, as compared to ellipsometry, RDS is expected to be directly sensitive to the surface (and interfaces) whatever the wavelength of the light. Also RDS is sensitive to both the chemical and structural state of the surface. Moreover the presence of a film deposited on the reactor walls does not affect RDS.

RDS has been adopted for real-time monitoring of MOCVD growth in several laboratories since 1985. A strong RDS 'chemical' peak related to Ga near 2.5 eV was observed (Colas *et al* 1989) in MOCVD growth of GaAs using arsine and trimethylgallium as the sources of As and Ga. It seems that the RDS can follow the relative surface coverages of Ga and As on (001) GaAs in MOCVD, and it was suggested that 2.5 eV (near the 2.41 eV, 514.5 nm Ar laser line) is a suitable energy to modify MOCVD growth processes with light (Aoyagi *et al* 1987). RDS has been applied to study, in real time, surface reconstruction changes, as well as catalytic effects of surfaces on the decomposition of adsorbed species from various reactants (Colas *et al* 1988). For example, Colas *et al* found a difference in the response of TMGa and TMAI and hence in the decomposition mechanisms of these two molecules. A Ga response is immediately visible during the TMGa pulse and increases during the interruption pulse in hydrogen, whereas an Al response from TMAI is only visible when arsine is supplied (Colas *et al* 1988). MOCVD processes are less characterized than MBE and are potentially more complex. Colas *et al* (1991) reported a quantitative study of the catalytic effect of the GaAs surface on the decomposition of TMGa and the growth process suggested that decomposition of an organic molecule occurs, e.g., TMGa in the case of GaAs. In addition, this decomposition may occur either on the surface or in the gas phase which contains both group III (TMGa) and group V (arsine) reactant molecules in conventional growth. Anisotropic changes at the growing surface can have a variety of origins including the surface roughness, which depends on sample history as well as growth conditions. It is possible to separate their individual surface-chemical effects and the difference pathways determining the kinetic limit of growth on (001) GaAs.

In 1990, Jonsson *et al* (1990) reported the first measurements of growth oscillations in high-vacuum metallorganic vapour phase epitaxy. They found that the frequency of the optically detected growth oscillations is proportional to the flux of TEGa and to the growth rate. By comparing the oscillations obtained by RDS with those seen in RHEED, it was found that RHEED and RDS oscillations had the same period. Since it is well known that the RHEED oscillations

correspond to the growth of exactly one monolayer, the RDS oscillations proved to be useful for the calibration of growth rates, for optimizing the buffer layer growth and for eliminating pressure transients which result in a varying growth rate at the initiation of growth. In a similar experiment, Samuelson *et al* (1991) reported the monolayer saturation phenomenon, when too much TEGa was injected into the chamber, and by using the oscillation periodicity, they measured the kinetics of regeneration of As-stabilized surfaces.

The RDS technique appears particularly attractive for a variety of new applications including the *in situ* study of crystal growth by MOCVD (Colas *et al* 1989, Acher *et al* 1990b, c, Koch *et al* 1990, 1991).

### 3.2 REFLECTANCE ANISOTROPY AND ELLIPSOMETRY

Despite its novelty, RDS belongs to the well known family of polarization-modulation techniques, like ellipsometry and dichroism. RDS is the determination of the difference between normal-incidence reflectance for light polarized along the two principal axes of the surface. Thus, an RDS instrument can be considered as a normal incidence ellipsometer. However, compared to the other polarization-modulation techniques, RDS measurements are only sensitive to the surface of the material, even though the light penetrates deep into the bulk. It was recently shown that, because of its lower symmetry, the surface of nominally isotropic crystals can display a measurable anisotropy (Aspnes 1985). In particular, the bulk contribution is expected to vanish in the case of (100) surfaces of III-V semiconductors (Agranovich and Ginzburg 1984, Acher 1990), however the surface anisotropy generally induces small contributions to the RDS signal. Relative surface anisotropy ranging from  $10^{-4}$  to  $10^{-3}$  has typically been reported. This can be a strong limitation when dealing with real-time measurements because of the presence of noise induced by the experimental environment (rotating pumps, vibrations). As a consequence, the most successful *in situ* applications are performed using a fast photoelastic modulator (40–50 kHz) (Aspnes *et al* 1988a, Paulsson *et al* 1990, Colas *et al* 1989, Acher *et al* 1990b, c, Koch *et al* 1990, 1991).

#### 3.2.1 Principles of RDS

The numerous similarities between ellipsometry and RDS will be emphasized in this section for a better understanding of the RDS technique. Consider the two optical eigenaxes of a sample,  $x$  and  $y$ . In general, the ellipsometric technique measures the ratio between the two corresponding complex reflectances  $r_x$  and  $r_y$  (Azzam and Bashara 1977)

$$\rho = r_x/r_y = \tan \Psi \exp(i\Delta) \quad (3.1)$$

where  $\Delta$  is the optical path difference between  $x$ - and  $y$ -direction light. Considering oblique incidence, the optical eigenaxes are the directions parallel

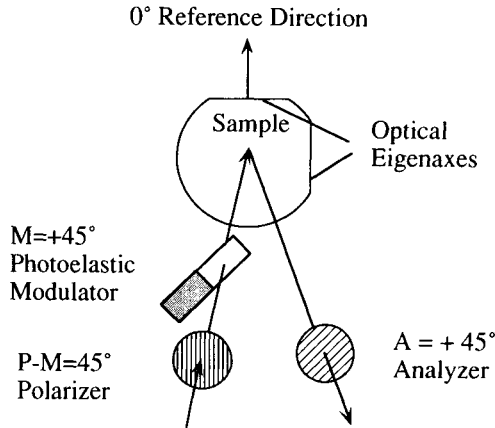


**Figure 3.1** Relative azimuths of the principal optical components of the RDS spectrometer (after Acher 1990).

(p) and perpendicular (s) to the plane of incidence. Thus ellipsometry is the measurement of  $r_p/r_s$ .

In the case of a crystal surface, the eigenaxes can be deduced from symmetry considerations. For instance [011] and [01̄] are the eigenaxes of the (100) surfaces of semiconductors and  $r_{011}$  and  $r_{01\bar{1}}$  are the reflectances associated with these directions. RDS consists in the measurement of the relative difference:

$$r_a = \frac{r_{001} - r_{01\bar{1}}}{r}. \quad (3.2)$$

In the case of small anisotropies, equation (3.2) can be approximated to

$$r_a \approx 2\Psi' + i\Delta' \quad (3.3)$$

where  $\Psi = \Psi' - \pi/4$  and  $\Delta' = \Delta - \pi$ . When large anisotropies are considered (Acher *et al* 1990b),  $r$  is generally replaced by  $r_{01\bar{1}}$  in the denominator of equation (3.2) and then

$$r_a = \tan \Psi \exp(i\Delta') - 1. \quad (3.4)$$

At this point, let us reconsider the various ellipsometry techniques. Phase-modulated ellipsometry (PME) is based on the use of a photoelastic modulator generating a periodic phase shift  $\delta(t) = A_m \sin \omega t$  ( $\omega = 50$  Hz) between orthogonal amplitude components of the transmitted beam. Finally, the detected intensity takes the general form (Jasperson and Schnatterly 1969, Drevillon *et al* 1982, Acher *et al* 1989):

$$I(t) = I[I_0 + I_s \sin \delta(t) + I_c \cos \delta(t)] \quad (3.5)$$

where  $I_0$ ,  $I_s$  and  $I_c$  are trigonometric functions of  $\Psi$  and  $\Delta$ . Particular configurations of the optical elements allow simple determination of  $\Psi$  and  $\Delta$ . In the case illustrated in figure 3.1, known in PME as configuration III, one obtains:

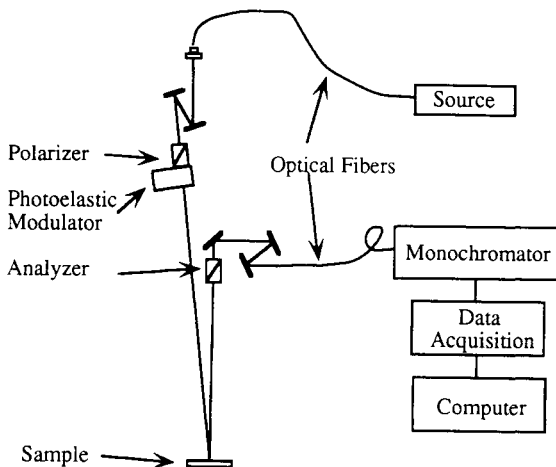


**Figure 3.2** Schematic diagram of the reflectance anisotropy spectrometer (after Acher 1990).

$$I_0 = 1$$

$$I_s = (\pm)_P (\pm)_A \sin 2\Psi \sin \Delta \approx -(\pm)_P (\pm)_A \Delta' \quad (3.6)$$

$$I_c = (\pm)_P (\pm)_M \cos 2\Psi \approx -(\pm)_P (\pm)_M 2\Psi'$$

which, in the small-anisotropy approximation, gives

$$I_s \approx -(\pm)_P (\pm)_A \Delta'$$

$$I_c \approx -(\pm)_P (\pm)_M 2\Psi'$$

where  $(\pm)A = 1$  if  $A = +45^\circ$ , and  $-1$  if  $A = -45^\circ$ , etc. Equations (3.3) and (3.6) show that  $I_s$  and  $I_c$  are related to the imaginary and real part of the RDS signal, respectively. The optical configuration corresponding to figure 3.1 is generally used in RDS measurements.

### 3.2.2 The optical set-up and data acquisition system

The optical set-up of the RDS spectrometer is presented in figure 3.2. The light source can be either a 75 W xenon lamp or a low-power laser. A mechanical shutter, included between the light source and the optical fibre, allows evaluation of the DC background. In order to increase the compactness of the spectrometer, optical fibres are used in both arms. Since the beam goes through a fixed polarizer before being modulated and through an analyser before being detected, PME is insensitive to any polarization effect due to the optical fibres (Drevillon *et al* 1989). The polarizer and the analyser are Glan-Taylor polarizers. The photoelastic modulator consists of a fused silica bar submitted to a periodical

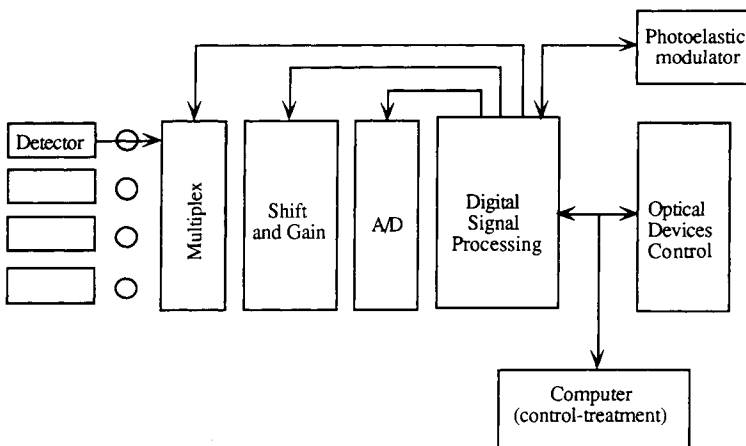


**Figure 3.3** Schematic diagram of the data acquisition system (after Acher 1990).

stress (50 kHz). The polarizer, the modulator and the analyser are mounted on 1 min precision rotators. The angle between the modulator and the polarizer is fixed at 45°. The modulator and the analyser can be automatically rotated by means of stepping motors. The spot size to the sample can be focused to less than 1 mm<sup>2</sup>. The energy of the light is analysed by a double-grating monochromator. In the simplest set-up, a photomultiplier is used as detector. In this case, the available wavelength range is 230 to 830 nm. However, this range can easily be extended towards near IR by using narrow-gap semiconductor detectors. More generally, it can be pointed out that this set-up is compatible with the simultaneous use of four detectors.

A data acquisition system is presented in figure 3.3. It can be considered as a new version of the numerical Fourier transform processing system previously used (Drevillon and Karlicek 1982). This new system is already used in phase-modulated ellipsometry (Drevillon *et al.* 1989). The read-out system consists of a gain-controlled amplifier and a 14-bit digital-analogue offset which are used to allow a correct matching between the detected signal and the analogue-digital converter (ADC). A fast ADC (12 bit, 1 MHz) is then used to synchronously convert the signal at a frequency of 16ω. The Fourier analysis of the signal is then performed using a digital signal processor specially dedicated to the fast Fourier transform computation. Finally, the DC component together with the four first harmonics of the signal ( $S_\omega$ ,  $S_{2\omega}$ ,  $S_{3\omega}$  and  $S_{4\omega}$ ) are continuously transmitted to a personal computer (PC) using a first-in-first-out register. The maximum data acquisition rate is fixed at 1 kHz. Moreover, the digital signal processor (DSP) allows on-line control of the modulation amplitude  $A_m$ , using the higher harmonics,  $S_{3\omega}$  or  $S_{4\omega}$ , following a calibration procedure described in detail elsewhere (Acher *et al.* 1989, Drevillon *et al.* 1989). Finally, the PC is devoted to the overall monitoring of the RDS spectrometer. In particular, it

controls the optical devices (shutter, detector power supply, monochromator and stepping motors).

The data acquisition system allows further external connections, as previously described (Drevillon *et al* 1989). In particular, the data acquisition system can easily deal with a second low-frequency modulation. This can be very useful for extension to infrared because of the presence of a chopper. This facility can also be used to record RDS measurements performed with rotating samples, as has been suggested recently (Aspnes *et al* 1990). Furthermore, as mentioned above, four analogue channels can be recorded simultaneously. These measurements can correspond to different light detectors or external parameters like control process information.

### 3.2.3 Experimental procedure

The analogy between RDS and PME allows a simple transposition of the calibration procedure used in ellipsometry. This procedure, based on the multiple-harmonic model, is described in detail by Acher *et al* (1989). In fact, the calibration procedure appears simpler in the case of RDS. In particular, the RDS optical set-up acts in a transmission configuration when isotropic samples are considered such as amorphous materials or (111) surfaces of semiconductors. Moreover, as compared to ellipsometry, RDS allows the use of reference samples with well known reflectances like polarizers and birefringent plates.

The determination of the angles  $\Psi$  and  $\Delta$  from the Fourier analysis is performed following the procedure used in PME. From equation (3.4), it can be easily shown that  $I_s$  and  $I_c$  are related to the ratios  $S_\omega/S_0$  and  $S_{2\omega}/S_0$ , respectively. Finally the useful quantities are deduced from equations (3.2) or (3.6).

In practical applications of RDS, the angle of incidence cannot strictly be zero (see figure 3.2). In the present case, the angle of incidence is found to be less than  $3^\circ$ . Nevertheless, a parasitic ellipsometric contribution cannot be ignored. The orientation of the incidence plane as referred to the sample eigenaxis is defined by an angle  $\Omega$ . The influence of the small angle of incidence can be evaluated from the general expressions for  $I_0$ ,  $I_s$  and  $I_c$  in PME. It can be shown that the ellipsometric contribution vanishes if  $\Omega = \pm 45^\circ$ .

Another imperfection of the RDS technique may be a possible misalignment of the sample eigenaxes,  $\theta$  as referred to the reference position. This effect can be evaluated from the general expressions for  $I_0$ ,  $I_s$  and  $I_c$ . In the case of small anisotropies, one obtains:

$$\begin{aligned} I_0 &= 1 + (\pm)_A 2\Psi' \sin 2\theta \\ I_s &= -(\pm)_P (\pm)_A \Delta' \cos 2\theta \\ I_c &= -(\pm)_P (\pm)_M \cos 2\Psi' \cos 2\theta. \end{aligned} \quad (3.7)$$

Equation (3.7) shows that a weak misalignment leads to second-order effects in  $S_\omega/S_0$  and  $S_{2\omega}/S_0$ . Moreover, equation (3.7) shows that the eigenaxes of

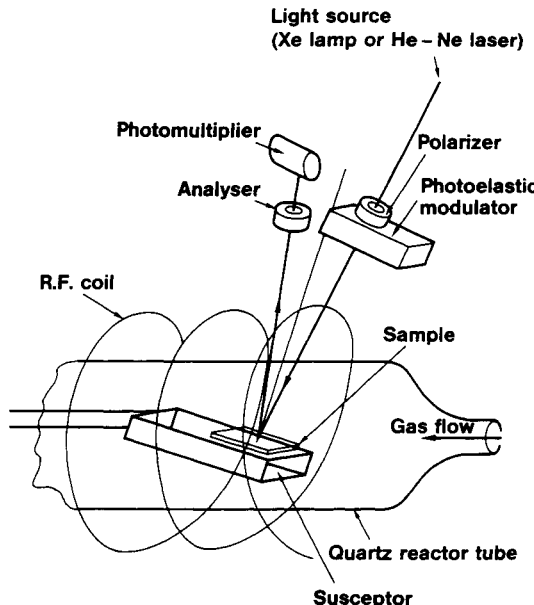


**Figure 3.4** The RDS spectrometer adapted to a MOCVD chamber (after Razeghi 1989).

any sample can be identified by the determination of the minima of  $S_\omega/S_0$  and  $S_{2\omega}/S_0$  as functions of  $\theta$ .

### 3.2.4 Adaptation to a MOCVD reactor

The RDS spectrometer can be directly adapted to various deposition chambers. Figure 3.4 shows the RDS spectrometer coupled to a low-pressure MOCVD (Razeghi 1989) reactor chamber for real-time III-V crystal growth investigations. This diagram reveals that this adaptation can be realized without any modification of the MOCVD reactor. The light beam is not affected by the presence of the RF heating system. Nevertheless the MOCVD quartz tube does not allow UV light transmission below 3400 Å.

In any *in situ* application of RDS, the reactor windows can be submitted to inhomogeneous strains inducing birefringence effects that perturb the RDS measurements. In the case of ultrahigh-vacuum applications, low-strain windows can be used to overcome this experimental problem (Studna *et al* 1989). However, such a solution cannot be extended to MOCVD reactors based on the use of a cylindrical quartz tube. In order to evaluate this effect, the tube can be considered as two birefringence plates (input and output of the optical beam) with orientations  $\theta_i$  (resp  $\theta_o$ ) and phase shifts  $\delta_i$  (resp  $\delta_o$ ). Considering small anisotropies, it can be shown from (3.7) that to the first order in  $\Delta$ ,  $\delta_i$  and  $\delta_o$

$$\begin{aligned} I_s &= (\pm)_P (\pm)_A [\Delta' + \delta_i \cos 2\theta_i + \delta_o \cos 2\theta_o] \\ I_c &= -(\pm)_P (\pm)_M 2\Psi'. \end{aligned} \quad (3.8)$$

Thus, the tube birefringence only affects the imaginary part of the RDS signal. This explains why during real-time investigations the noise level on  $\text{Re } r_a$  is generally lower than  $10^{-4}$  while it is one order of magnitude higher on  $\text{Im } r_a$ . Therefore, both the real and the imaginary part of the RDS signal can only be measured *in situ* when large anisotropies are investigated (Acher *et al* 1990b).

Finally, it has to be noted that in MOCVD reactors the substrate holder is slightly tilted ( $5\text{--}10^\circ$ ) as referred to the horizontal direction (Razeghi 1989). Thus the light beam penetrates into the quartz tube at an oblique angle of incidence  $\Phi$ . This induces a contribution to the real part of the RDS signal  $2\Phi^2[(n-l)/n]^2$  where  $\Phi$  is measured with respect to the normal incidence and  $n$  is the refractive index of the tube. This constant contribution is found to be  $4 \times 10^{-3}$  for  $\Phi = 8^\circ$ .

### 3.2.5 Comparison with other RDS techniques

The RDS system presented above can be compared to other RDS set-ups based upon modulation techniques. The first RDS measurements were performed using rotating samples (Aspnes 1985, Acosta-Ortiz and Lastras-Martinez 1987). The detected intensity was measured using a lock-in amplifier. This technique is not sensitive to the phase shift at the reflection of the sample as defined by (3.2) and (3.3). Moreover, this technique is incompatible with growth techniques involving fixed samples.

Then, the adoption of a rotating analyser ellipsometer to RDS was proposed for *in situ* applications with fixed samples (Aspnes *et al* 1987). It allows the determination of the real part of the RDS signal. In the case of real-time studies, the main limitation comes from the relatively low frequency of the mechanical rotation of the analyser (50–100 Hz). Nevertheless *in situ* measurements of anisotropies in the  $10^{-3}$  range were reported.

An RDS set-up based on the use of two detectors has also been successfully used (Briones and Horikoshi 1990). The sample is illuminated with polarized light tilted at  $45^\circ$  with respect to the optical eigenaxes. Then the two orthogonal polarizations are separated and detected. *In situ* measurements were performed. Nevertheless, the absence of modulation can be a limitation for more general real-time investigations.

Other normal-incidence RDS techniques have also been reported (Azzam 1977, 1981). They consist of strictly normal-incidence techniques, using semi-transparent plates. Signal processing allows the determination of  $\text{Re } r_a$  and  $\text{Im } r_a^2$ . Thus, they do not appear to be well adapted to small anisotropy measurements ( $\text{Im } r_a^2 \approx 10^{-7}, 10^{-8}$ ). Therefore these last techniques do not provide a crucial improvement as compared to the sample rotation set-up.

### 3.3 OPTIMIZATION OF THE GROWTH OF III-V BINARIES BY RDS

RDS has been used in InAs growth by MOCVD and has been operated under different growth conditions to optimize the growth parameters. The effects of growth rate, III/V ratio and substrate temperature on the RDS signal were investigated. The difference in the optical anisotropy between the growing and non-growing surface,  $\delta$ , was studied. This study also showed the possibility of monitoring transient flow perturbations on the growing surface due to the switching of gas flows.

The majority of the measurements were taken with light of energy 2.28 eV using a 0.5 mW He–Ne laser. A 75 W xenon lamp and a Jobin–Yvon H25 monochromator were used for the spectroscopic study. The fully digital acquisition system was set at an acquisition rate of 0.08 s per point, and the noise level of the measured signal using the laser was lower than  $10^{-4}$ .

The measurements were taken on a 1  $\mu\text{m}$  thick InAs buffer layer grown on either InAs or InP(100) substrates misoriented 2° toward [01 $\bar{1}$ ]; the results were identical on the different substrates. In all cases the wafer surface was mirror-like after the growth. Unless otherwise stated, the following growth parameters were used: a growth rate of 250  $\text{\AA min}^{-1}$ , a substrate temperature of 480 °C, a H<sub>2</sub> flow rate of 100  $\text{cm}^3 \text{min}^{-1}$  in the trimethylindium (TMI) bubbler and an AsH<sub>3</sub> flow rate of 10  $\text{cm}^3 \text{min}^{-1}$ .

#### 3.3.1 Effects of the MOCVD reactor design on the growth

For InAs growth under optimal conditions, a significant change in the RDS signal was observed when the TMI flow was switched on and off, while maintaining a constant AsH<sub>3</sub> flow rate; this is shown in figure 3.5. It is clear from the figure that the steady-state optical anisotropy levels of the InAs surface under AsH<sub>3</sub> or during growth are stable and reproducible. The time constant associated with the switching off is very fast (< 0.2 s), and then the signal stabilizes by approximately  $2 \times 10^{-3}$  with respect to the level of the growing surface. In contrast, when the TMI is switched on, the RDS signal exhibits a damped oscillation behaviour before reaching its steady-state value.

It is interesting to note that the 1.5 s period of these signal oscillations is independent of growth rate, so that it does not correspond to the deposition of one monolayer; it is also independent of temperature. These observations suggest that the oscillations are due to perturbations in gas flows in the reactor, rather than a growth phenomenon. After intentionally changing gas flows, this was indeed found to be the case. The oscillations were observed whenever the gas flow in the organometallic line was increased, whether by switching on the TMI flow or simply by increasing the hydrogen flow while maintaining a constant TMI flow. Figure 3.6 shows that oscillations are observed when the TMI flow is switched on, and also when an excess hydrogen flow in the organometallic line is switched on and off. This was found not to be due to the hydrogen itself,

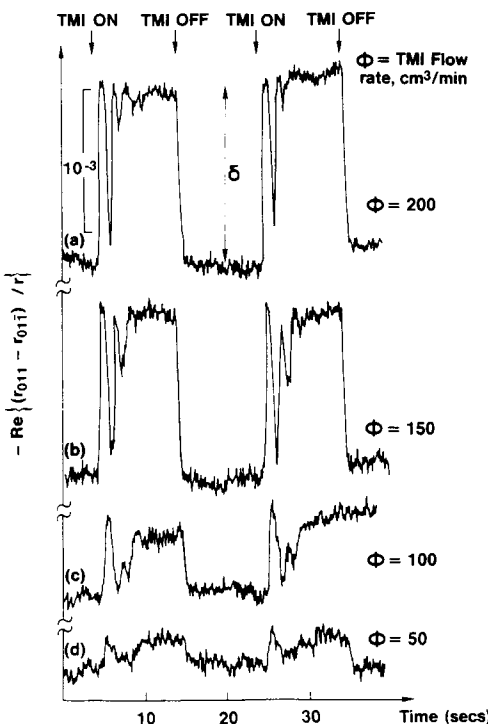


**Figure 3.5** RDS signals for InAs growth at 480 °C, where the TMI bubbler flow was switched on and off at the times indicated by the arrows. The different records were taken using the indicated TMI bubbler flows. The AsH<sub>3</sub> flow was maintained at 15 cm<sup>3</sup> min<sup>-1</sup> in each case (after Koch *et al* 1990).

since there was no effect on the RDS signal when the extra hydrogen was sent through the line used for hydrides. There is a difference between the hydride line and the organometallic line, however: the hydride line is not regulated by a valve whereas there is a needle valve between the organometallic line and the reactor tube, used to regulate the pressure in the organometallic line. Apparently this valve takes a few seconds to regulate a change in the pressure in the organometallic line; as the valve opens and closes during this transient period, more and less TMI is supplied to the reactor, even though the TMI flow set by the reactor control panel is kept fixed. Therefore the V/III ratio of the gas flows changes, and as described below, this gives rise to a measurable RDS signal change. Oscillations are therefore not seen when the TMI flow is stopped, consistent with this phenomenon. Razeghi and Acher (1989) showed that it was possible to cancel this effect by changing the flow rates of the various hydrogen flows used. These observations are important, because they show that RDS can be very useful in determining the effects of the MOCVD apparatus on growth, and therefore can aid in optimizing reactor design. In fact, RDS is the only

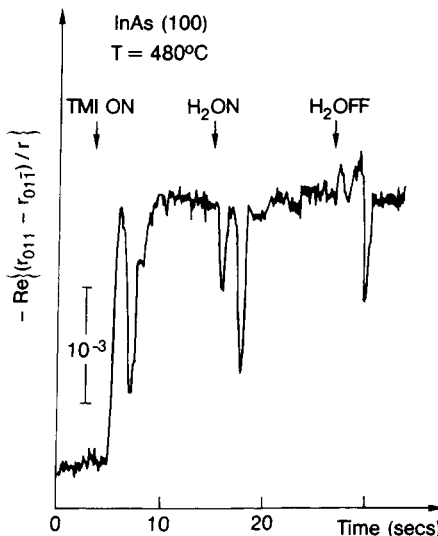


**Figure 3.6** RDS signal changes for InAs at 480 °C upon introduction of TMI and H<sub>2</sub> into the reactor, at the times indicated by the arrows (after Koch *et al* 1990).

method that can measure such reactor effects on the wafer surface. Particularly for the abrupt interfaces required in devices, especially quantum wells, this level of control during the first few seconds of growth is essential.

### 3.3.2 The III/V flux dependence of RDS signals

Figure 3.5 shows that the steady-state optical anisotropy level of the InAs surface under AsH<sub>3</sub> is significantly different from that during growth. This difference, referred to as  $\delta$ , was found to be very sensitive to the growth parameters, including the V/III ratio, growth rate and temperature. Figure 3.5 shows a series of such measurements for a variety of different TMI flow rates. The value of  $\delta$  clearly depends on the TMI flow rate.

Figure 3.7 shows a compilation of  $\delta$  values as a function of the V/III gas flow ratio; each curve shows the results for a given AsH<sub>3</sub> flow rate. It is clear that  $\delta$  increases with decreasing V/III ratio until it reaches a saturation level. At very high V/III ratios, only small  $\delta$  values can be measured. Other measurements show that  $\delta$  changes in the same manner when the V/III ratio is changed by reducing the AsH<sub>3</sub> flow while keeping the TMI flow constant. Clearly this reflects the change in ratio of the element III and element V species on the surface when the V/III ratio of the gas flows is changed. Comparison of the different curves shows that  $\delta$  depends not only on the V/III ratio, but also on the growth rate (for a fixed V/III ratio); it increases with TMI flow rate. It is interesting to note that, for a non-growing InAs surface at 480 °C under AsH<sub>3</sub>,

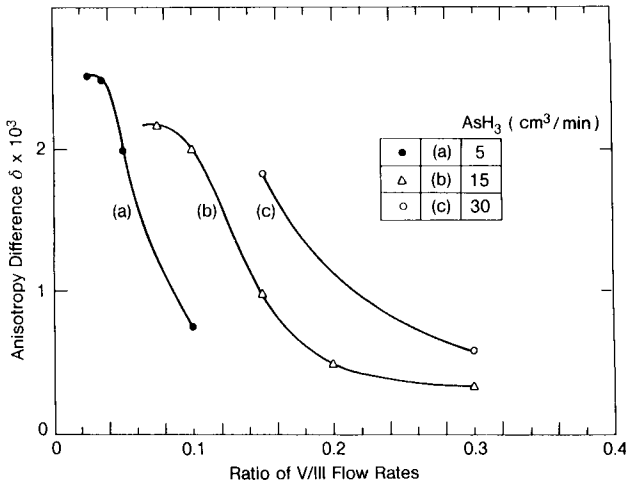


**Figure 3.7** A compilation of  $\delta$ , the difference between the RDS signals for the growing and the static  $\text{AsH}_3$ -stabilized surface, as a function of V/III flow ratio. The different curves were measured using the indicated  $\text{AsH}_3$  flow rates (after Koch *et al* 1990).

increasing the  $\text{AsH}_3$  flow rate from 2 to  $30\text{ cm}^3\text{ min}^{-1}$  had no effect on the RDS signal. This indicates that the non-growing surface is  $\text{AsH}_3$  stabilized.

### 3.3.3 The temperature dependence of RDS signals

The value of  $\delta$  is also temperature dependent. Figure 3.8 shows a compilation of  $\delta$  as a function of temperature for several sets of gas flow rates. In each case  $\delta$  is roughly constant at low temperatures (decreasing very slightly with decreasing temperature) and then drops to nearly zero by  $520^\circ\text{C}$ . Comparison of the curves shows that the curves shift to higher temperatures for lower V/III flux ratios, and also for higher growth rate with the same  $\text{AsH}_3$  flux. Also apparent from the figure is that the measured anisotropy difference in the lower temperature range is approximately  $2.5 \times 10^{-3}$ , regardless of the gas flow rates.

### 3.3.4 Discussion

These data show that the RDS signal is dependent on V/III ratio, TMI flow rate and temperature. The observed  $\delta$  means that the growing surface has a different optical anisotropy than the  $\text{AsH}_3$ -stabilized, non-growing surface. These observations raise interesting questions about the nature of the growing InAs surface. It is not known whether the surface is terminated by As, hydrogen, organometallic groups or molecular species containing In and As. Unlike RHEED, which is sensitive only to the structure of the surface reciprocal lattice, RDS can also distinguish among various chemical structures. There are a number

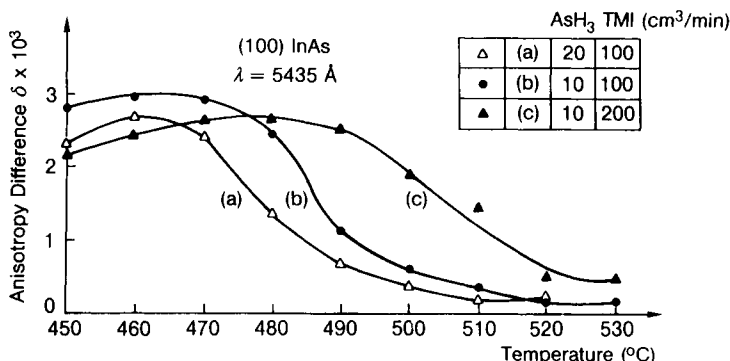


**Figure 3.8** The temperature dependence of  $\delta$ , the difference between the RDS signals for the growing and the static AsH<sub>3</sub>-stabilized surface. The different curves were measured using the indicated gas flow rates (after Koch *et al* 1990).

of different factors that influence the RDS signal, including surface roughness, surface reconstruction, surface stoichiometry and chemisorbed or physisorbed species on the surface.

'Islands' nucleating and coalescing for each monolayer formed have been used to explain RHEED oscillations during MBE (Harris *et al* 1981) and metallorganic molecular-beam epitaxy (MOMBE) (Tsang *et al* 1987) growth. However, they do not explain the RDS signals, as shown in figures 3.5 and 3.8. The surface may roughen in another manner during MOCVD growth. As Aspnes (1985) has shown, information about surface roughness can be obtained from the spectral dependence of the RDS signal. Figure 3.9 shows the value of  $\delta$  as a function of light energy, for InAs growth at 480 °C. There is a maximum in the range of 2.30–2.38 eV, and  $\delta$  then falls to zero at approximately 3.26 eV. The contribution of surface roughness is expected to be larger with UV light than with infrared (Aspnes 1985). Since this is not consistent with the results of figure 3.7, surface roughness as the dominant contribution to the RDS signal can be ruled out.

While surface roughness does not explain the measured  $\delta$ , another possibility is that  $\delta$  indicates a change in the surface reconstruction when the growth is stopped; since a change in surface reconstruction would change the surface symmetry, it could be detected by RDS. The optimal nucleation of InAs/GaAs by MBE occurs under In-rich conditions (Schaffer *et al* 1983). Although this cannot be verified in the case of MOCVD growth, the optimal growth conditions may also correspond to In-rich growth. In this case,  $\delta$  would be due to a change from an In-stabilized to an As-stabilized surface. However, the In-stabilized (4 × 2) to As-stabilized (2 × 4) transition seen in MBE growth of InAs (Schaffer *et al* 1983, Foxon and Joyce 1978, Sugiyama 1986) changes abruptly with temperature, all other factors being constant, whereas figure 3.7 shows a slower

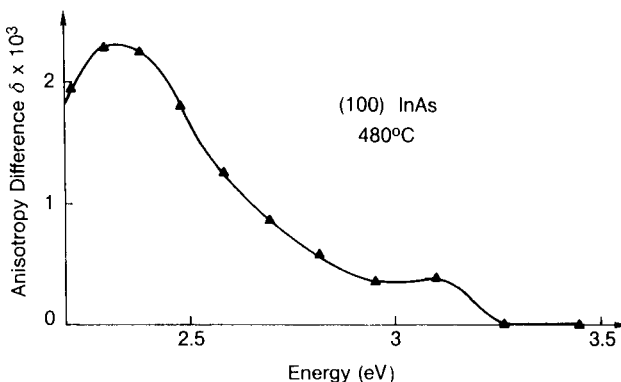


**Figure 3.9** The spectral dependence of the value of  $\delta$ , the difference between the RDS signals for the growing and non-growing  $\text{AsH}_3$ -stabilized surface for InAs growth at  $480^\circ\text{C}$ . The gas flow rates were  $100\text{ cm}^3\text{ min}^{-1}$  for the TMI bubbler and  $10\text{ cm}^3\text{ min}^{-1}$  for  $\text{AsH}_3$  (after Koch *et al* 1990).

temperature dependence. Therefore surface reconstruction changes cannot be the only contribution to the RDS signal observed.

The results of figure 3.6, which indicate a decrease in  $\delta$  with V/III ratio, suggest that In-related species or reaction products cause the change in optical anisotropy. The temperature dependence of  $\delta$ , shown in figure 3.7, could be explained by the change in the V/III ratio of the species at the surface of the wafer due to temperature effects. Less efficient  $\text{AsH}_3$  cracking in the lower-temperature range ( $450$ – $470^\circ\text{C}$ ) would lead to an increase in the density of In species on the surface and therefore a larger  $\delta$  would be observed. The shift of the curves to higher temperature with lower V/III ratio is consistent with this explanation as well. For the temperature range studied excess evaporation of As species should not be a problem.

It is not evident, however, what chemical species are on the surface, and also what gives rise to the optical anisotropy. It is quite likely that organometallic groups are present on the surface when the film is growing (Stringfellow 1989) which can give rise to optical anisotropy. The decrease in  $\delta$  at high temperature would then mean that the adsorbed species are no longer present on the surface, so that the surface optical anisotropy is the same during growth and without growth.

As Razeghi and Acher (1989) have reported, starting and stopping the flow of TMI changes the anisotropy of the surface under certain conditions. Starting and stopping the TMI and  $\text{AsH}_3$  flows, individually or in combination, gives further insight into the processes occurring at the surface. Figure 3.10 shows the result of an experiment of this type on an InAs surface at  $480^\circ\text{C}$  with different types of gas flow. The measurement at time  $t = 0$  is of the growing InAs surface with a TMI flow of  $100\text{ cm}^3\text{ min}^{-1}$  and an  $\text{AsH}_3$  flow of  $10\text{ cm}^3\text{ min}^{-1}$ .

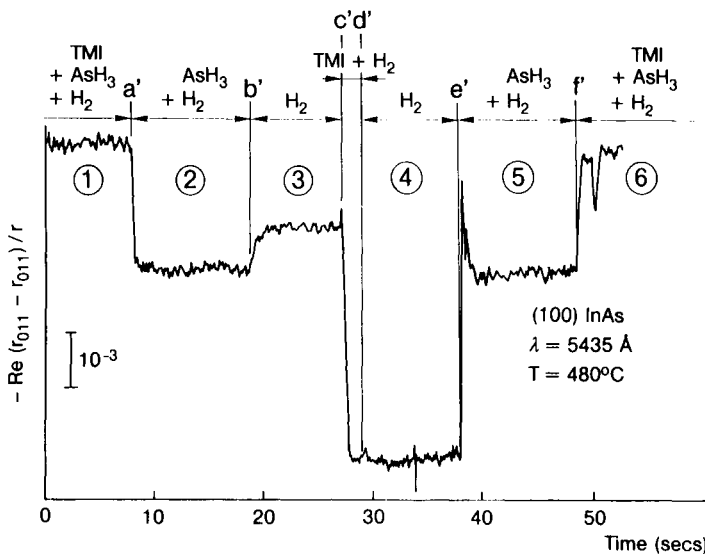


**Figure 3.10**  $r_a$  signal of InAs at  $480^\circ\text{C}$  under a variety of different gas flows in the reactor, as indicated (after Koch *et al* 1990).

When the TMI flow is cut at time  $a'$ , the signal changes abruptly by  $2 \times 10^{-3}$ . When the  $\text{AsH}_3$  flow is stopped the signal again changes, this time toward the level of the growing InAs surface. Unlike the abrupt changes at the start and stop of growth, the time dependence of this change is more gradual suggesting arsenic evaporation from the surface (Foxon and Joyce 1978). As a result, the surface would be more In rich. When TMI alone is switched on for 2 s at time  $c'$  (corresponding to approximately two or three monolayers by extrapolation from the measured growth rate), the signal again changes abruptly, but surprisingly toward the direction of the  $\text{AsH}_3$ -stabilized surface, rather than the expected change toward the growing surface level. When the TMI is stopped and only hydrogen flows through the reactor, the signal level is unchanged, indicative of a passivated surface; when  $\text{AsH}_3$  alone is switched on (time  $e'$ ), there is an initial transient and then the signal stabilizes at the same level as it was in region 2 of the figure, after the TMI flow had been stopped for the first time. This shows that the surface had not undergone an irreversible change when the  $\text{AsH}_3$  flow was cut, at least as far as can be determined by RDS. Finally, when the growth is resumed, the signal returns to its original level.

The RDS signal changes in figure 3.10 can be explained as follows. At time  $b'$ , arsenic presumably desorbs from the surface. The resulting change in optical anisotropy may be due to a surface reconstruction change or simply a change in the surface stoichiometry without further structural changes. When the surface under hydrogen is exposed to TMI without  $\text{AsH}_3$  at time  $c'$ , the signal changes in the direction toward that of the  $\text{AsH}_3$ -stabilized surface rather than that of

the surface with both  $\text{AsH}_3$  and TMI. This means that the signal is due to other factors than simply the relative quantities of indium and arsenic on the surface; the most likely contributions are chemisorbed species and/or surface reconstruction changes. By using atomic layer epitaxy (ALE) for the MOMBE growth of GaAs, Chiu (1989) found that after the deposition of a Ga monolayer, the surface reconstructs in a manner different from the  $4 \times 2$  Ga-stabilized surface of GaAs:  $4 \times 6$  and  $4 \times 8$  reconstructions can appear. Analogous changes may account for this observation. The signal ‘spikes’ at time  $e'$  as shown in figure 3.10, when  $\text{AsH}_3$  is again sent to the reactor. This is suggestive of  $\text{AsH}_3$  reacting with the In species on the surface. The signal then stabilizes when the growth is complete.

### 3.4 RDS INVESTIGATION OF III-V LATTICE-MATCHED HETEROJUNCTIONS

#### 3.4.1 RDS observations of heterojunction growth

When heterojunctions are grown by MOCVD, the RDS signal changes abruptly at the onset of the growth of the new material as shown in figure 3.11 for the growth of two different  $\text{Ga}_x\text{In}_{1-x}\text{As}_y\text{P}_{1-y}$  materials on InP using light of wavelength  $5435 \text{ \AA}$ . The signal recorded during the beginning of the measurement is that of the growing InP surface: at  $t = 2.8 \text{ s}$  the InP growth was stopped and the quaternary growth was simultaneously started. The subsequent signal is that of the growing quaternary relative to the initial InP signal level. Each heterojunction is lattice matched, but the compositions and bandgaps are different. For  $\text{Ga}_{0.25}\text{In}_{0.75}\text{As}_{0.5}\text{P}_{0.5}$ , the bandgap is  $\lambda = 1.3 \mu\text{m}$  whereas for  $\text{Ga}_{0.5}\text{In}_{0.5}\text{As}_{0.9}\text{P}_{0.1}$ ,  $\lambda = 1.5 \mu\text{m}$ . In each case, there is an abrupt signal change upon growth of the quaternary followed by a rise to a maximum. The signal then undergoes various changes before reaching a final level after about 10 s. Note that the signal changes do not correspond to the time to grow a monolayer, as in the case of RHEED oscillations.

There are a number of differences between the RDS signals of the two samples. The slope of the initial transient is the same in the two cases, but the time to reach the first maximum is  $0.6 \text{ s}$  for the  $1.5 \mu\text{m}$  alloy and  $1.3 \text{ s}$  for the  $1.3 \mu\text{m}$  alloy. The subsequent signal changes occur somewhat more rapidly for the  $1.5 \mu\text{m}$  quaternary which also has a higher growth rate than that of the  $1.3 \mu\text{m}$  quaternary. The signal for the  $1.3 \mu\text{m}$  alloy oscillates around the value of approximately  $-6 \times 10^{-4}$  with respect to the InP signal level. In contrast, the signal for the  $1.5 \mu\text{m}$  alloy changes sign from negative to positive and then approaches a level near that of InP.

For the reverse sequence, the growth of InP on each of the two quaternaries, the signal evolution is quite different. This is shown in figure 3.12, again using  $5435 \text{ \AA}$  light. In this case, each signal changes abruptly by a value of the order

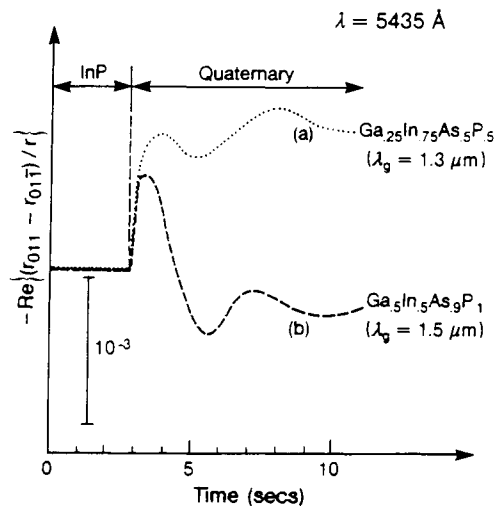


**Figure 3.11** RDS records of two different lattice-matched  $\text{Ga}_x\text{In}_{1-x}\text{As}_y\text{P}_{1-y}$ /InP heterojunctions using light of wavelength  $5435 \text{ \AA}$  (after Koch *et al* 1991).

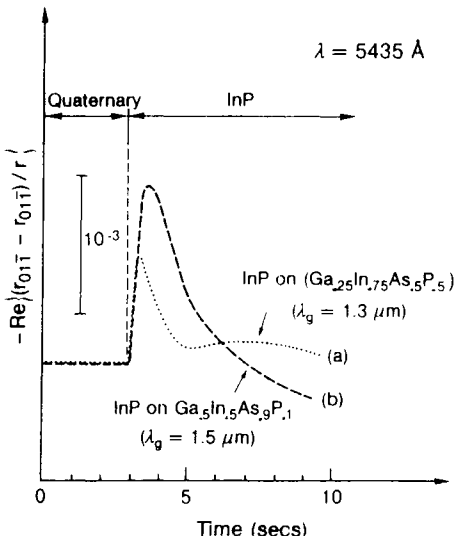


**Figure 3.12** RDS records of two different lattice-matched InP/ $\text{Ga}_x\text{In}_{1-x}\text{As}_y\text{P}_{1-y}$  heterojunctions using light of wavelength  $5435 \text{ \AA}$  (after Koch *et al* 1991).

of  $-5 \times 10^{-4}$  and then returns toward the  $\text{Ga}_x\text{In}_{1-x}\text{As}_y\text{P}_{1-y}$  level. Only one large peak is observed in each case. The peak height for the  $1.5 \mu\text{m}$  alloy is consistently larger than that of the  $1.3 \mu\text{m}$  alloy even though the same material, InP, is growing during the time measurement. This is due to the fact that the RDS

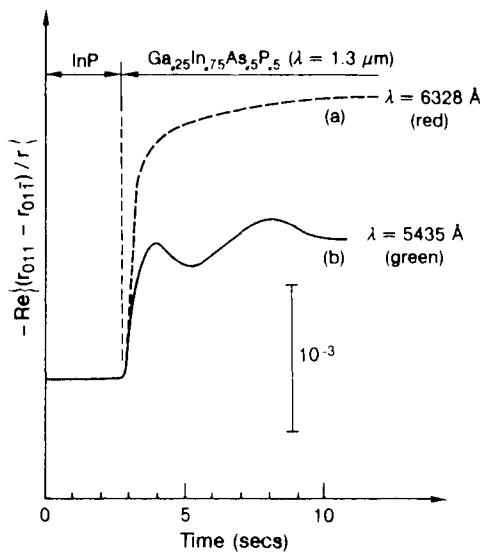


**Figure 3.13** A comparison of the RDS signatures for  $\text{Ga}_{0.25}\text{In}_{0.75}\text{As}_{0.5}\text{P}_{0.5}/\text{InP}$  growth using light of wavelength (a)  $\lambda = 6328 \text{ \AA}$  and (b)  $\lambda = 5435 \text{ \AA}$  (after Koch *et al* 1991).

signal is measuring the optical anisotropy of both the surface and heterointerface, the latter being different in the two cases.

The form of each RDS record shown in figures 3.11 and 3.12 is reproducible: the time of the initial signal transient, the changes in the following few seconds and the final level reached after these changes were found to be characteristic of the wide variety of lattice-matched heterojunctions studied by Koch *et al* (1991). One can therefore refer to these characteristic signal changes as the RDS ‘signature’ of each heterojunction.

The RDS signature of heterojunctions depends on the light wavelength used for the measurement. Figure 3.13 shows a comparison between the RDS signatures taken with a green ( $5435 \text{ \AA}$ ) and a red ( $6328 \text{ \AA}$ ) laser for the  $\text{InP} \rightarrow \text{Ga}_{0.25}\text{In}_{0.75}\text{As}_{0.5}\text{P}_{0.5}$  transition. While in both cases an abrupt change in the signal level is observed at the onset of the quaternary growth there are a number of differences between the two signatures. The most important one is that the signal changes resembling oscillations, observed using green light, are not seen with red light. In addition, the difference between the signal levels of InP and  $\text{Ga}_{0.25}\text{In}_{0.75}\text{As}_{0.5}\text{P}_{0.5}$  after 10 s is roughly twice as large with the red laser as with the green laser.

Although the RDS signals appear to stabilize after several seconds, in fact they slowly evolve over the course of several minutes. This is shown in figure 3.14 for  $\text{GaInP}$  growth on  $\text{GaAs}$ . The signal exhibits a damped oscillation behaviour, with amplitude changes of the order of  $10^{-3}$ . This is in contrast to lattice-mismatches (Acher *et al* 1990b) where signal changes of the order of

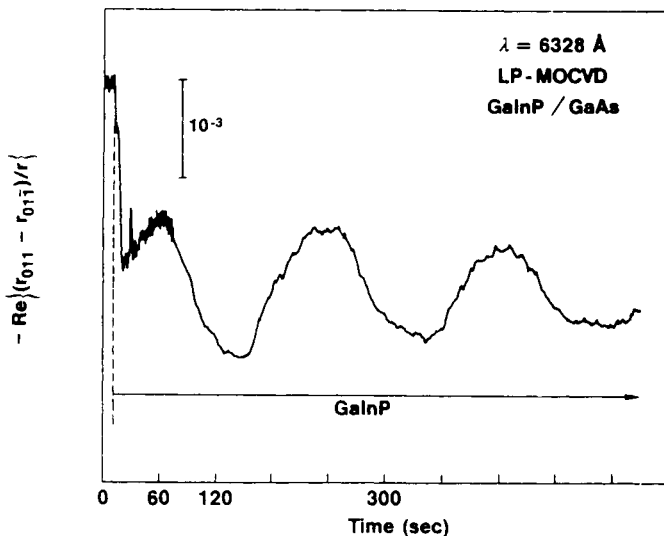


**Figure 3.14** The RDS record for GaInP/GaAs epitaxy during several minutes of growth using light of wavelength 6328 Å (after Koch *et al* 1991).

several tenths are observed during the first few minutes of growth. As will be discussed, the damped oscillation behaviour seen in figure 3.14 is most likely due to interference effects; this continues until the epilayer is sufficiently thick that light reaching the interface is absorbed in the film. Therefore, the signal level reached after the buried interface oscillations have been damped out is the surface anisotropy of the second layer relative to that of the first layer; this level is different from the apparent steady-state level reached after the first few seconds of growth.

### 3.4.2 Interpretations of the experimental observations

There may be a variety of structural and chemical contributions to the RDS signals during heterojunction growth. The origins of optical anisotropy of materials have been investigated by Aspnes (Aspnes 1985, Aspnes and Studna 1985, Aspnes *et al* 1988a, 1989) and others (Acosta-Ortiz and Lastras-Martinez 1987, Manghi *et al* 1989, Berkovits *et al* 1987). Contributions to surface and interface anisotropy include chemical bonding at the surface and interface, anisotropic roughness and the presence of chemi- and physisorbed species on the surface.

The optical anisotropy of interfaces may depend on the bonding sequence that occurs. In the case of a perfectly abrupt InAlAs/InP interface, for example, the atomic sequence in the growth direction may be either ...P-In-P-/(In, Al)-As... or ...-P-In-/-As-(Al, In)-As; the associated RDS contribution is expected to be different for the two cases. In addition, the electric field at the

interface, screening effects or interfacial roughness can contribute to the signal. Thus, RDS is expected to be sensitive to interface quality as will be discussed subsequently.

At the beginning of growth, both the surface and interfacial anisotropy are measured and gradually the interfacial contribution becomes negligible for thick films. Surface processes at the very beginning of growth can be different from those after several seconds. Thus, the contributions to the RDS signal vary, depending on the growth time.

(a) *Short-time-scale changes (less than two seconds)*

The nature of the RDS signature can be analysed by comparing the normal growth sequence with the effect of the group-V gas change alone. This is shown in figure 3.15. Each part of the figure shows the standard RDS signature of a heterojunction (stopping the first-layer growth while simultaneously beginning the second-layer growth) compared with the signal change when the first-layer growth is stopped and only the group-V gas of the second material is sent to the reactor. In each case the signal change is in the same sense (negative) for both the growth and for the group-V change. The comparison between GaInAs grown on InP and AsH<sub>3</sub> alone over InP is shown in figure 3.15(a). The two signatures are clearly different, because there are signal changes resembling oscillations for the growing material, but not for the case of AsH<sub>3</sub> alone over InP. However, the initial transient time to reach the first feature in the GaInAs/InP signature, 0.1 s, is identical to the time to reach the steady-state value in the AsH<sub>3</sub>-only signature.

In figure 3.15(b) for InP/GaInAs and PH<sub>3</sub>/GaInAs, the time to reach the maximum is nearly the same in the two cases and the signal maxima roughly occur at the same amplitude. RDS signatures at  $\lambda = 5435$  and  $6328\text{ \AA}$  for GaInP/GaAs as a function of PH<sub>3</sub>/GaAs also show similar behaviour: comparable initial transient times, but differences after this transient. These results suggest that during heterojunction growth the change in the group-V species on the surface causes the initial RDS transient, and the subsequent signal oscillations are due to processes occurring during the growth.

Another rapid RDS signal change can occur when the group-V gas flow is stopped over a non-growing surface. Figure 3.16 shows the RDS signal change occurring when the PH<sub>3</sub> flow ( $500\text{ cm}^3\text{ min}^{-1}$ ) over a non-growing InP surface is stopped; the substrate temperature is maintained at  $540^\circ\text{C}$ . In 1.5 s, the signal amplitude changes by  $10^{-3}$ , followed by a slower change and then the signal remains fairly constant. Upon restarting the PH<sub>3</sub> flow after 1 min there is an abrupt (0.3 s) return to the former signal level where the signal remains. The initial signal change is most likely phosphorus loss from the surface. The fact that the signal returns to its former level once the PH<sub>3</sub> flow is restarted indicates that the surface has not been damaged by the lack of PH<sub>3</sub>, at least according to the detection sensibility of RDS. The origin of these signal changes can be both the stoichiometry change and the reconstruction change that is likely to

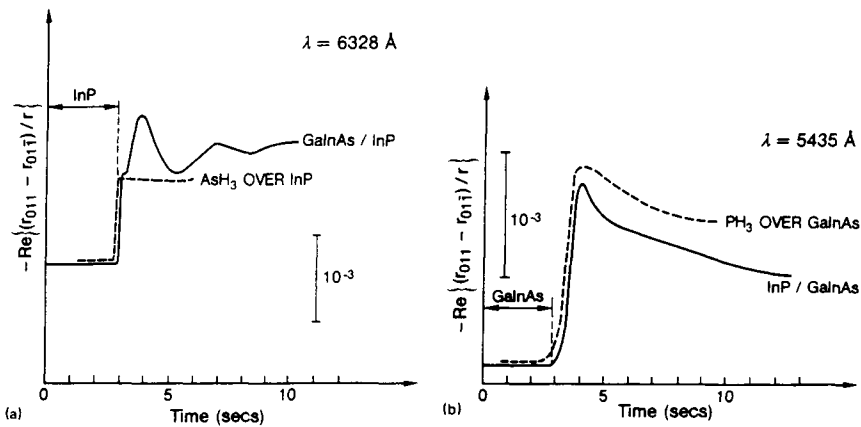


**Figure 3.15** Comparisons of the RDS signals between the standard heterojunction growth and the change in the group-V species only. (a) GaInAs/InP as a function of AsH<sub>3</sub> over InP and (b) InP/GaInAs as a function of PH<sub>3</sub> over GaInAs (after Koch *et al* 1991).

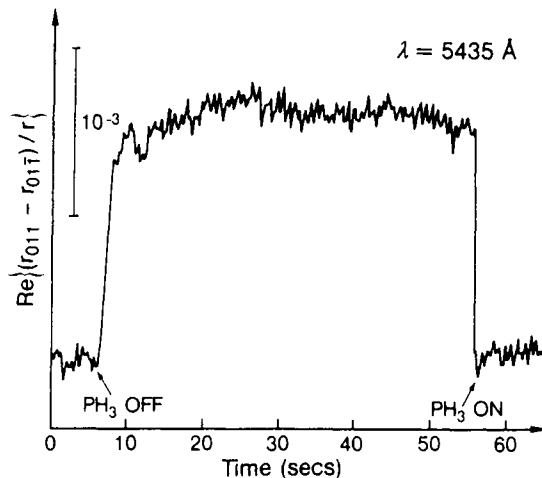


**Figure 3.16** RDS signal change occurring when the PH<sub>3</sub> flow over a non-growing InP surface is stopped and restarted. The substrate temperature is 540 °C. (After Koch *et al* 1991.)

occur, although this cannot be established with the present understanding of RDS without RHEED.

The last measurement suggests that an important application of RDS can be determining whether the surface is stabilized by the element III or V species. This is done with RHEED for MBE and MOMBE, where the majority of III-

V compounds are grown under group-V-rich conditions. RHEED is used to determine what temperature and group-V flux are needed to maintain a V-rich surface; this is judged by the reconstruction change from  $4 \times 2$  (Ga rich) to  $2 \times 4$  (As rich) in GaAs, for example. By repeating the process shown in figure 3.16 for a variety of different growth conditions, RDS may also be used in this manner.

Another factor which affects the first two seconds of a heterojunction signature is the manner in which the interface growth is done. Acher *et al* (1991) found that slight delays in gas arrival to the substrate, for example, can affect the signature; this was done intentionally in order to study the different effects of the group-III and -V species on the initial RDS signal change. This is shown in figure 3.17 for the InP $\rightarrow$ GaInAs transition. Figure 3.17(a) shows the standard RDS signature for the normal growth procedure, whereas figure 3.17(b) shows the effect of stopping the PH<sub>3</sub> gas flow for 1 s before starting the GaInAs growth while maintaining a TMI flow. An extra peak appears in the RDS signal. This signal change is positive, in contrast to the negative signal change seen for the standard InP/GaInAs transition. When the PH<sub>3</sub> gas flow is stopped while introducing AsH<sub>3</sub> and TMI into the reactor for 1 s, figure 3.17(c), the extra dip in the signal is in the negative direction. Other similar experiments, such as briefly switching on the group-III gases of the second layer before the group-V gas, show the same effect: changing the group-V species causes a signal change in the same sense as that observed for the normal growth procedure, while inducing a group-III-rich surface by changing the group-III gas causes the opposite sign change.

These observations again support the idea that the initial rapid signal change is due to changes associated with the group-V species on the surface. The transient time is typically less than 1 s and shorter than the time for the growth of one monolayer. Therefore, the signal change is not simply due to the change in optical anisotropy when going from one group-V-terminated material to another. Instead, a rapid process is occurring, such as the replacement of P atoms on the surface by As atoms for the case of AsH<sub>3</sub> flow over InP, as shown in figure 3.15(a). This possibility is supported by the results of an experiment similar to that shown in figure 3.16. In that case, Acher *et al* (Acher 1990, Acher *et al* 1990b) introduced an AsH<sub>3</sub> flow instead of only H<sub>2</sub> over the non-growing InP surface for several seconds. They observed RDS signal changes that were much larger than those in figure 3.16; in addition, the reflectivity changed significantly.

#### (b) RDS changes occurring from two to 10 seconds of growth

An interesting feature of RDS signatures are the signal changes that are typically observed for about 10 s before the signal reaches an apparently stabilized level. Acher *et al* (1991) found that although these signal changes do not correspond to monolayer growth, the characteristic times of the signal changes depend on the growth rate. Figure 3.18 shows a series of RDS signatures for Ga<sub>0.47</sub>In<sub>0.53</sub>As/InP

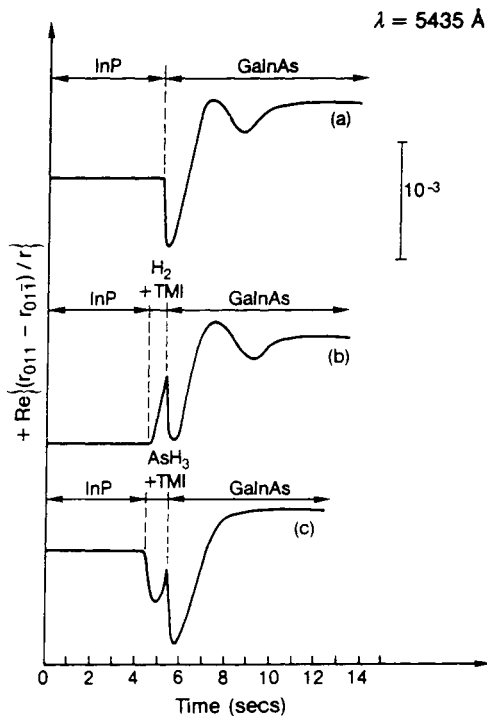


**Figure 3.17** Effects of slight delays in switching the gas during GaInAs/InP heterojunction growth. (a) Standard RDS signature. (b) The effect of stopping the  $\text{PH}_3$  gas flow for 1 s before starting the GaInAs growth while maintaining a TMI flow. (c) The effect of stopping the  $\text{PH}_3$  gas flow while introducing  $\text{AsH}_3$  and TMI into the reactor for 1 s (after Koch *et al.* 1991).

lattice-matched growth for different growth rates and  $\text{AsH}_3$  flow rates. The signatures obtained with normal gas flow rates, the growth rate divided by two and the growth rate divided by three are shown in figures 3.18(a), (b) and (c) respectively. In figure 3.18(c), both the growth rate and the  $\text{AsH}_3$  flow rate are divided by two from the standard conditions. In all cases, the initial signal transient time is 0.4 s. The characteristic times for the subsequent signal changes, however, are longer when using lower gas flow rates. The time between the first minimum and the first maximum compared to that of the standard (curve (a)) is inversely proportional to the group-III gas flow. The times between the other 'oscillations' also increase with decreasing flow rate although not by exact factors of two or three. In contrast, there is only a slight difference between the RDS signals where group-III as well as group-V gas flows were reduced by half (figure 3.18(c)) compared to when only the group-III gas flows were reduced by half (figure 3.18(b)). The growth of GaInP/GaAs was also investigated in the same manner, and again signal changes were found to be inversely proportional

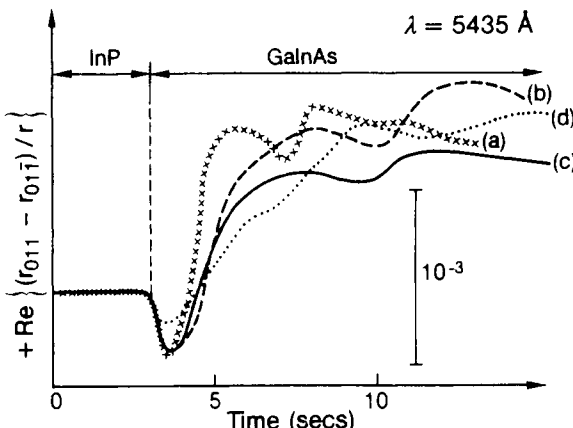


**Figure 3.18** A series of RDS signatures for  $\text{Ga}_{0.47}\text{In}_{0.53}\text{As}/\text{InP}$  lattice-matched growth using different growth rates and group-V flow rates. The growth runs were performed with (a) the standard flow rates, (b) group-III flow rates divided by two, (c) both group-III and -V flow rates divided by two and (d) group-III flow rates divided by three (after Koch *et al* 1991).

to the group-III gas flow rate. These results, as well as those of figure 3.15, suggest that the signal changes are related to the growth process. However, since the RDS signal depends on the thickness of the material, the results in figure 3.18 may indicate that the optical anisotropy is due to volume effects, such as the electric field in the bulk originating from the interface.

The signal changes occurring during the first few seconds are not related to oscillations previously observed (Koch *et al* 1990) when beginning the growth of a film on a non-growing substrate. As shown for the case of InAs growth (Koch *et al* 1990), the valve regulating the pressure in the organometallic line fluctuates at the beginning of the growth, and this causes a fluctuation in the quantity of organometallic species reaching the substrate surface; in this case, damped sinusoidal signal changes are seen, with a period that is independent of the gas flow rates.

For the  $\text{Ga}_{0.47}\text{In}_{0.53}\text{As} \rightarrow \text{InP}$  transition, figure 3.19, signal oscillations are not observed after the initial signal change and the signature shows essentially no effect arising from the change in gas flows. As for the  $\text{InP} \rightarrow \text{Ga}_{0.47}\text{In}_{0.53}\text{As}$  transition, the initial transient time is the same regardless of growth rate.

Koch *et al* (1991) also compared Al- and Ga-containing materials which have nearly identical lattice constants. Figure 3.20 shows the signatures for  $\text{GaInAs}/\text{InP}$  and  $\text{AlInAs}/\text{InP}$  growth. As expected, the initial signal transient times are nearly identical for the two types of material both for red (figure 3.20(a)) and green (figure 3.20(b)) light as expected since the group-V species used are the same in both cases. In addition, although  $\text{GaInAs}$  and  $\text{AlInAs}$

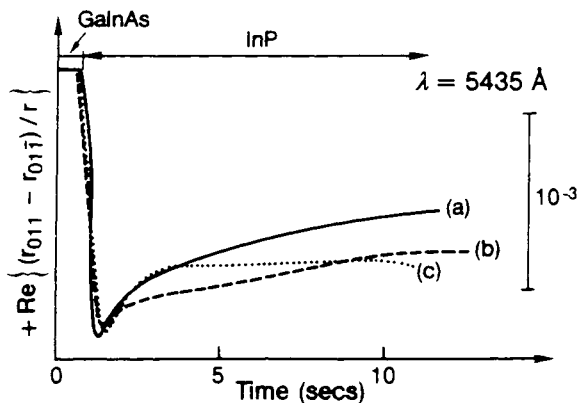


**Figure 3.19** A series of RDS signatures for InP/Ga<sub>0.47</sub>In<sub>0.53</sub>As lattice-matched growth using different growth rates and group-V flow rates. The growths were performed with (a) the standard flow rates, (b) the group-III flow rates divided by two and (c) the group-III flow rates divided by three (after Koch *et al.* 1991).

have quite different optical and electrical properties, the RDS signatures for the two are fairly similar especially when using green light. This again suggests that the optical anisotropy is due to surface effects, such as reconstruction and chemisorbed species, rather than volume.

The origins of these signal changes are not clear. The signal level reached after about 10 s is a measure of the surface anisotropy of the GaInP, combined with the effects of the GaInP/GaAs interface anisotropy relative to the value of the GaAs signal level at time  $t = 0$ . The fact that there is no observation of a change from the GaAs level to the GaInP level, but rather signal oscillations, suggests that some sort of transient processes occur at the beginning of the heterojunction growth. One possibility is that the sticking coefficients of the different group-III species in a ternary or quaternary may be significantly different on the surface of the 'substrate' than during the steady-state growth of the layer. For example, for GaInAs/InP growth, the flow rates of TEGa and TMi are adapted to give a lattice-matched GaInAs layer. However, the relative sticking coefficients of the two species may be different on a P-terminated surface compared to an As-terminated surface, so that the material grown for the first few monolayers may be rich in one of the group-III species. Such a situation may be possible, because the use of organometallic sources leads to complicated reactions in the gas phase and at the surface: there may be a number of intermediate reaction species on the surface during the growth and desorption of group-III species at each step of the reaction. RHEED oscillation and modulated-beam mass spectrometry measurements of MOMBE growth, for example, show that gallium incorporation in GaAs (Martines and Whitehouse 1989) is quite different from that in GaP (Maurel *et al.* 1990). Clearly, further

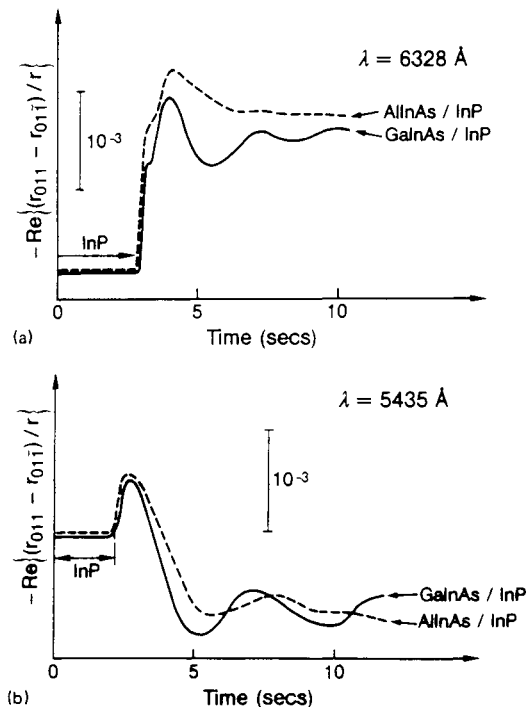


**Figure 3.20** A comparison between the RDS signatures of AlInAs/InP and GaInAs/InP using (a)  $\lambda = 6328 \text{ \AA}$  and (b)  $\lambda = 5435 \text{ \AA}$  (after Koch *et al* 1991).

studies of surface kinetics and the interfacial structure are necessary.

Slight differences in the arrival rates between the two gases due to reactor geometry, for instance, may also affect the first few monolayers but not the thick-layer growth. Such explanations are consistent with the fact that Acher *et al* (1991) did not observe signal oscillations during the growth of binary material on an alloy as shown in figure 3.12. However, it is possible that oscillations may be observed for binaries when using other light wavelengths, based on the data in figure 3.13 which show that the heterojunction signatures depend on the light wavelength. Another possibility, arising from photoluminescence data (Razeghi *et al* 1990), is that the growth rate changes during the first few seconds of growth. Any of these explanations would mean that the signal oscillations are due to non-optimal growth. This would not be the case if the signal changes were due to volume effects but such contributions as will be shown later are negligible. Clearly further understanding of the RDS signatures can yield important information about heterojunction optimization.

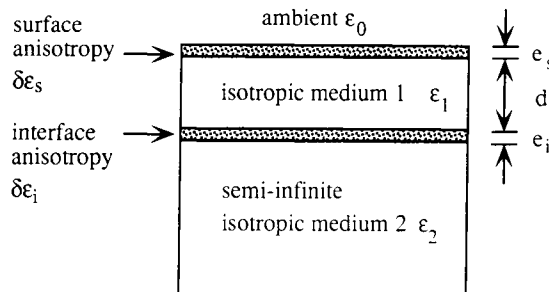


**Figure 3.21** Schematic diagram of the heterojunction model used in the calculations of the interference effects (after Koch *et al* 1991).

(c) *Long-time-scale changes*

As was shown in figure 3.14 the RDS signal shows a damped oscillation behaviour over the course of several minutes. A model for this behaviour has been developed ascribing the damped oscillations to light interference upon the growing layer, as well as the anisotropy of the buried interface. The model is based on the following facts. The growing layer acts as a Fabry-Pérot cavity. The reflection and transmission coefficients of the surface and interface are slightly anisotropic, and so the conditions of constructive and destructive interference depend slightly on the polarization. For Fabry-Pérot effects, the pseudoperiod  $\tau$  can be related to the growth rate  $v$  by writing that the optical path length increases by  $\lambda$  during a pseudoperiod:

$$\frac{v\tau}{2n} = \lambda. \quad (3.9)$$

The material is modelled as a thin epilayer on a substrate as shown in figure 3.21, and  $2 \times 2$  matrices are used to consider the reflection and transmission of the polarized light at the surface and interface using the method of Abeles (Azzam and Bashara 1977). The surface and interface are treated as films with a very small thickness  $e$  compared to the light wavelength  $\lambda$ , and their optical properties are calculated to first-order development in  $e/\lambda$  as in McIntyre and Aspnes (1971). The epilayer and substrate 'bulk' materials are assumed to be isotropic. The surface and interface are assumed to have the same optical eigenaxes [011] and [011]. The calculation leads to

$$\begin{aligned} \frac{r_{01\bar{1}} - r_{011}}{r} &= \frac{4j\pi}{\lambda} \frac{N_0}{\epsilon_1 - \epsilon_0} e_s \delta\epsilon_s + \frac{16j\pi}{\lambda} \frac{N_0 \epsilon_1}{(\epsilon_1 - \epsilon_0)(N_1 + N_2)^2} \\ &\times \frac{X}{[1 + (r_{12}/r_{01})X](1 + r_{12}r_{01}X)} \left( e_i \delta\epsilon_i + \frac{\epsilon_1 - \epsilon_2}{\epsilon_1 - \epsilon_0} e_c \delta\epsilon_c \right) \end{aligned} \quad (3.10)$$

with

$$X = \exp \left( -\frac{4j\pi N_1 d}{\lambda} \right)$$

where  $X$  is a damped oscillating function,  $\delta\epsilon_s$  is the difference between the surface dielectric constant associated with the direction of the two eigenaxes, the product  $\epsilon_s\delta\epsilon_s$  characterizes the surface anisotropy and  $\epsilon_i\delta\epsilon_i$  characterizes the interface anisotropy. The effective media model used for the interface and surface is somewhat simplistic since it neglects inhomogeneities. However, more detailed calculations on the optical properties of surfaces (Del Sole 1981) yield essentially the same results. In the present approach,  $N_0$ ,  $N_1$  and  $N_2$  are the indices of refraction for the ambient, epilayer and substrate, respectively.  $\epsilon_0$ ,  $\epsilon_1$  and  $\epsilon_2$  are the dielectric constants of the ambient, epilayer and substrate, respectively.  $d$  is the thickness of the epilayer.  $r_{01}$  and  $r_{12}$  are the reflection coefficients of the surface and interface, respectively.  $t_{01}$  and  $t_{12}$  are the transmission coefficients of the surface and interface respectively. They can be expressed as a function of the index using the Fresnel relations (Azzam and Bashara 1977).

The real part of  $\delta r/r$  gives the evolution of the RDS signal. The signal is the sum of three terms as shown in (3.10). The first term is due to surface anisotropy without buried interface effects. The second and third terms indicate that the oscillations are due to the anisotropy of both the interface and surface with oscillations disappearing when layer thicknesses are large compared to the light penetration depth.

Experimentally, Acher *et al* (1991) measured only variations and the real part of the anisotropy. Therefore one cannot determine  $\epsilon_s\delta\epsilon_s$  and  $\epsilon_i\delta\epsilon_i$  separately using (3.10). However, for InP and AlInAs at the wavelength now used,  $\epsilon_1 \approx \epsilon_2$ , and so the prefactor  $(\epsilon_1 - \epsilon_2)/(\epsilon_1 - \epsilon_0)$  of (3.10) is small. Therefore the oscillatory behaviour is dominated by the interface anisotropy. This also means that  $N_1 = N_2$  and  $r_{12} \approx 0$ . Equation (3.10) then simplifies to

$$\frac{r_{01} - r_{011}}{r} = \frac{4j\pi}{\lambda} \frac{N_0}{\epsilon_1 - \epsilon_0} (\epsilon_s\delta\epsilon_s + X\epsilon_i\delta\epsilon_i). \quad (3.11)$$

$\epsilon_i\delta\epsilon_i$  therefore can be determined from the amplitude and phase of the observed oscillations.

Using these results, the different features of the RDS signal of heterojunctions can be explained in the following manner. During the first few seconds of heterojunction growth ( $X \approx 1$ ), the RDS signal is governed by changes in surface chemistry and hence by changes of the properties of the surface and interface. Then, the surface is expected to reach its steady-state level of anisotropy and the interface properties should stay the same. The RDS signal is then governed by the damped oscillation behaviour described by (3.11). When the epilayer is sufficiently thick the light does not penetrate enough to be sensitive to interface effects, and the RDS signal is related simply to the surface anisotropy.

Calculations of this effect are in good agreement with experimental measurements using both green and red light as shown in figures 3.22(a) and (b) for the growth of InAlAs on InP. Using green light (figure 3.22(a)), the pseudoperiod of the damped oscillations is 131 s ( $\pm 6$  s) (Acher *et al* 1991).

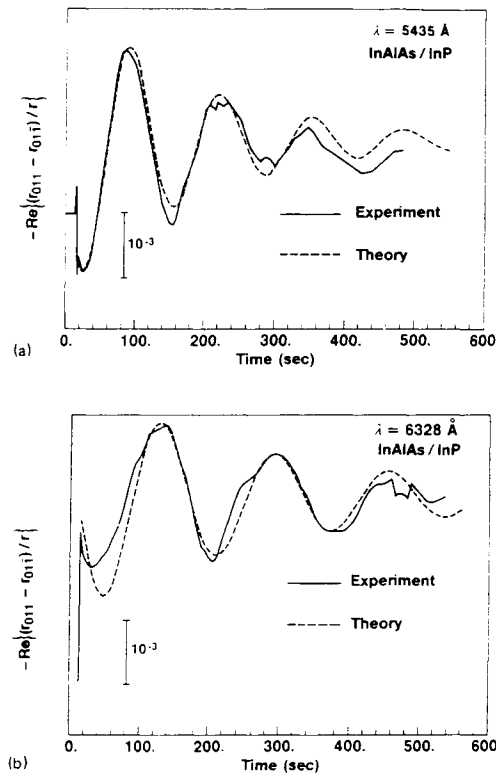


**Figure 3.22** A comparison between the theory and experimental observations for RDS records of InAlAs/InP growth over several minutes. (a)  $\lambda = 5435 \text{ \AA}$  and (b)  $\lambda = 6328 \text{ \AA}$  (after Koch *et al* 1991).

Assuming the index of refraction of InAlAs is equal to that of InP, using equation (3.2) one finds that  $v = 340 \text{ \AA min}^{-1}$  ( $\pm 16 \text{ \AA min}^{-1}$ ), which is in excellent agreement with *ex situ* thickness measurements.

For  $\lambda = 5435 \text{ \AA}$ , figure 3.22(a), the theoretical curve was obtained using an index of refraction of  $N_1 = N_2 = 3.66 - 0.4j$  (Palik 1985), and one finds that the value of the buried interface anisotropy is

$$e_i \delta_i = (-3 + 11j) \text{ \AA}. \quad (3.12)$$

The difference between the surface anisotropy of InAlAs and InP is simply the real part of the difference between equation (3.11) for the two materials:

$$\text{Re} \{ \exp(1.8j) [ (e_s \delta e_s)_{\text{InAlAs}} - (e_s \delta e_s)_{\text{InP}} ] \} = 7 \text{ \AA}. \quad (3.13)$$

For  $\lambda = 6328 \text{ \AA}$  (figure 3.22(b)), the theoretical curve was obtained with an index of refraction of  $N_1 = N_2 = 3.53 - 0.3j$ , and one finds that the value of

the buried interface anisotropy is

$$e_i \delta_i = (-9 + 4j) \text{ \AA}. \quad (3.14)$$

The difference between the surface anisotropy of InAlAs and InP is

$$\text{Re} \{ \exp(1.75j) [ (e_s \delta e_s)_{\text{InAlAs}} - (e_s \delta e_s)_{\text{InP}} ] \} = 16 \text{ \AA}. \quad (3.15)$$

The results show that the theoretical calculation agrees well with the experimental measurement. However, the presence of bulk anisotropy will lead to similar signal oscillations. For the semiconductor (100) surface, the bulk is optically isotropic due to symmetry considerations. However, the electric field originating at the surface or interface may extend over quite long distances in the material relative to the light wavelength. This will give rise to bulk anisotropy (Acosta-Ortiz and Lastras-Martinez 1987). If such an effect exists, the oscillation amplitude would first increase as the epilayer thickness increases (because there is more and more anisotropic material), and then decrease as less light penetrates to the interface. The bulk anisotropic effects will become more obvious when the difference between the optical indices of the epilayer and substrate is relatively large and when the absorption of the epilayer is not too strong. Calculations have shown that bulk effects are negligible.

### 3.4.3 Applications of RDS for growth monitoring

#### (a) Optimizing the MOCVD reactor geometry

One important goal of RDS is the assessment of interface quality during MOCVD growth. Figure 3.23 shows the RDS signature of two GaAs–GaInP heterojunctions which differ significantly. The electron Hall mobilities at 77 K ( $30\,000$  and  $90\,000 \text{ cm}^2 \text{ V}^{-1} \text{ s}^{-1}$ ) show that the two interfaces are quite different in quality (Razeghi *et al.* 1988b). The growth conditions for these two GaInP/GaAs samples were the same except for the fact that the samples were in different reactor chambers. The higher-quality film was grown after modifying the reactor geometry. A major difference in their RDS signatures is the time constant of the initial variation, 2 s for sample (a) and 0.2 s for sample (b). According to the previous study of different heterojunctions, the initial variation of the RDS signal is mainly due to the change in element V source on the surface. Here, the relatively long time constant observed in figure 3.23(a) suggests that the switch from arsine to phosphine was not abrupt enough. These results therefore led to a modification of the geometry of the group V section in the gas panel to obtain fast initial transients (figure 3.23(b)). Conversely, the quality of the GaInP/GaAs films improved significantly. The evolution of the RDS signal during the period following the initial transient is not yet understood. However, it was found to be very sensitive to film composition and growth rate. Any delay in the switching of the different gases will change the behaviour.

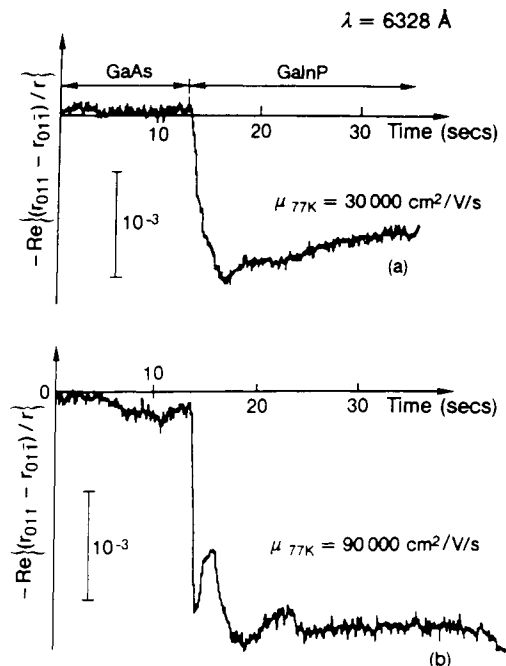


**Figure 3.23** RDS records during the MOCVD growth of GaInP/GaAs using two different reactor geometries. The Hall electron mobilities measured at 77 K are (a)  $30\ 000\ \text{cm}^2\ \text{V}^{-1}\ \text{s}^{-1}$ , (b)  $90\ 000\ \text{cm}^2\ \text{V}^{-1}\ \text{s}^{-1}$  (after Koch *et al.* 1991).

#### (b) Monitoring of superlattice growth

The sensitivity of RDS to small deviations from optimal conditions is extremely useful for monitoring complex structures. In the case of a quantum well or a superlattice, it is not possible to assess individually the quality of each interface using mobility measurements. However, observation of the RDS signature can be very useful. The RDS signature of the GaInP/GaAs interface was observed during the growth of several GaInP/GaAs/GaInP quantum wells (figure 3.24). For small GaAs thickness (10 s or less GaAs) the signature clearly departs from that of the high-quality interface of figure 3.23(b). This difference was greatly reduced by improving the switching sequence.

In figure 3.25, the RDS record of a GaInP/GaAs superlattice exhibits RDS features quite similar to figure 3.23(b). It also shows that the interfaces are reproducible. It is possible to compare the signatures of heterojunctions independently of the underlying structure only because RDS is not sensitive to bulk effects. This is an extremely useful feature of RDS when compared to other techniques like ellipsometry. Ellipsometric records of superlattices do not allow direct comparison of the different periods (Hottier *et al.* 1980).

Figures 3.26(a) and (b), respectively, show the RDS record for InP-GaInAs

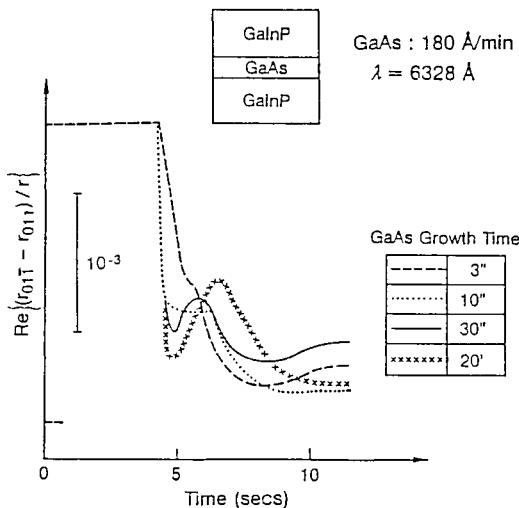


**Figure 3.24** RDS records of the GaInP/GaAs interface of quantum wells with different well thickness (after Acher *et al* 1990a).

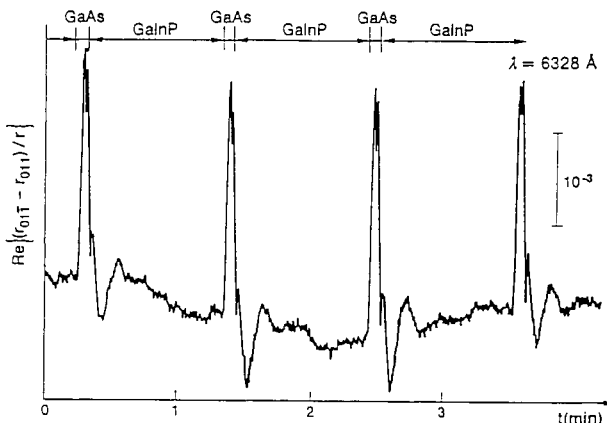


**Figure 3.25** RDS record of the growth of a GaInP-GaAs superlattice (after Acher *et al* 1990a).

superlattices grown on an InP/GaAs/Si structure at different stages of the InP growth. The superlattice shown in figure 3.26(a) was grown directly on the GaAs/Si substrate. The RDS signal varies irregularly with an amplitude as high as  $10^{-2}$  indicating that the quality of this superlattice is quite poor due to the rough surface of lattice-mismatched growth. In contrast, the InP-GaInAs superlattice grown on InP/GaAs/Si substrate, with  $3600 \text{ \AA}$  InP pre-grown first, shows a good periodic structure with amplitude as low as  $10^{-3}$ . As indicated in figure 3.26(b), the surface of InP has been smoothed. These figures show that,

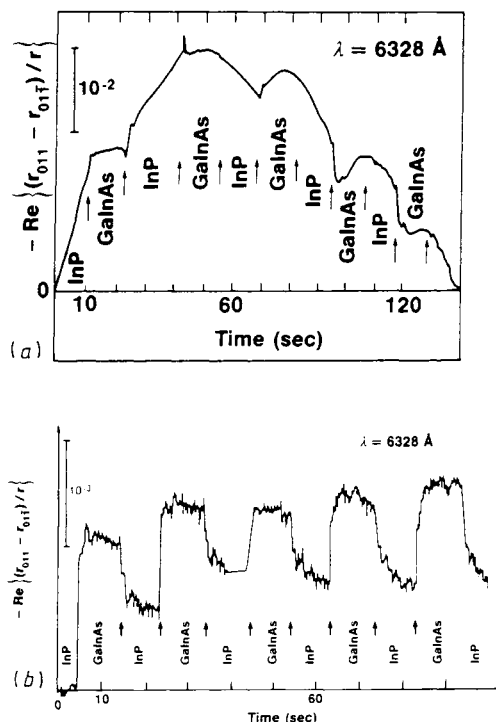


**Figure 3.26** RDS records of InP-GaInAs superlattices grown on InP/GaAs/Si. The superlattices were grown (a) immediately on GaAs/Si substrate, and (b) after growing 3600 Å of InP on GaAs/Si substrate (after Koch *et al* 1991).

in contrast to most *ex situ* measurements, RDS is sensitive to each period in the superlattice. RDS can also be used to detect changes in superlattice growth, such as degradation over a period of time.

### 3.5 RDS INVESTIGATION OF III-V LATTICE-MISMATCHED STRUCTURES

GaAs on silicon and InP on GaAs structures are very attractive for device applications. A number of devices using this material system have been reported such as a GaInAsP-InP on silicon substrate laser emitting at 1.3  $\mu\text{m}$  (Razeghi *et al* 1988a) and a GaInAs-InP on GaAs/silicon photodiode (Razeghi *et al* 1989). The growth of lattice-mismatched III-V layers on other III-V substrates also has important applications. For example, since semi-insulating InAs substrates are not commercially available, GaAs and InP semi-insulating substrates can be used for InAs growth.

The use of RDS for *in situ* monitoring of the growth of InAs/InP, InP/GaAs/Si, GaInP/GaAs and GaInP/InP will be illustrated. The results will show that

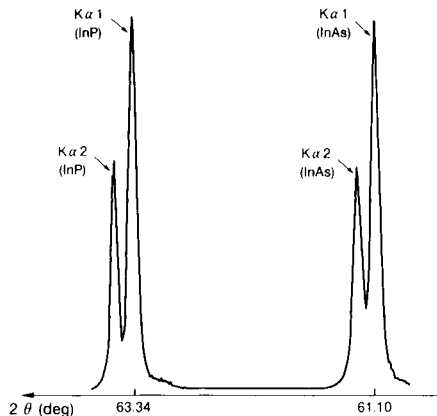


**Figure 3.27** X-ray diffraction pattern of a 1  $\mu\text{m}$  thick InAs layer grown on an InP substrate (after Acher *et al* 1990b).

the anisotropic three-dimensional growth is responsible for the RDS signal changes. The detailed growth procedure of InAs/InP and InP/GaAs/Si will be discussed below. A model will be proposed and will be shown to agree well with experimental observations of the first stages of growth. As the roughness dimensions increase, precise modelling is not possible, but the broad features of RDS behaviour are well understood.

### 3.5.1 Growth procedure of InAs/InP and InP/GaAs/Si

The lattice mismatch is 3.2% in the case of the InAs-InP system, and 3.8% for InP-GaAs. The growth of InAs was done directly on InP substrates. The substrate orientation was (100) with 2° off [011] unless otherwise stated. After introduction into the reactor, the substrates were heated under AsH<sub>3</sub> until they reached the growth temperature of 480 °C. The H<sub>2</sub> flow through the TMI bubbler was typically 100 cm<sup>3</sup> min<sup>-1</sup> and the AsH<sub>3</sub> flow was between 5 and 20 cm<sup>3</sup> min<sup>-1</sup>. Under these conditions, the growth rate of InAs, deduced from thickness measurements performed on thick layers, was about 270 Å min<sup>-1</sup>. Layer quality was assessed by x-ray diffraction. The x-ray diffraction pattern has well separated K<sub>α</sub>1 and K<sub>α</sub>2 diffraction peaks (figure 3.27) indicating a good structural quality. The typical Hall electron mobility at room temperature was about 11 500 cm<sup>2</sup> V<sup>-1</sup> s<sup>-1</sup>.

The growth of InP/GaAs/Si structures has been described in detail elsewhere (Razeghi *et al* 1988c). Some InP-GaInAs superlattices can be included in the InP to reduce threading dislocation propagation. Lasers emitting at 1.3  $\mu\text{m}$  in CW mode were fabricated using these structures, indicative of excellent material quality (Razeghi *et al* 1988a).

RDS records of InP-GaInAs superlattices grown on GaAs/Si are shown in

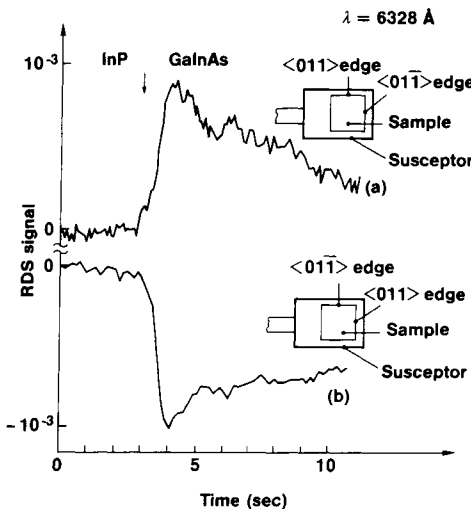


**Figure 3.28** RDS signal at  $\lambda = 6328\text{ \AA}$  recorded during the growth of a GaInAs/InP heterojunction on two differently orientated substrates. The RDS signal is  $\text{Re}[(r_{011} - r_{01\bar{1}})/r]$  for sample (a) and  $-\text{Re}[(r_{011} - r_{01\bar{1}})/r]$  for sample (b) (after Razeghi and Acher 1989).

figure 3.26. For both InAs/InP and InP/GaAs/Si, the sample becomes hazy during the first minutes of growth, which indicates a three-dimensional (3D) growth. If the growth is optimized, the haze disappears after 10 to 20 min. After 1 h of growth the sample surface is mirror-like.

In contrast with the cases of lattice-matched structure, for lattice-mismatched growth, the RDS signals are much larger. It is possible to record both the real and imaginary part of the reflectance anisotropy with a small level of noise. Because the perturbation due to the reactor tube adds an offset to the RDS signals, only the variations of optical anisotropy are measured. The offset is of the order of  $4 \times 10^{-3}$  which is large compared to surface chemistry changes, but negligible compared to typical variations during the growth of lattice-mismatched materials. There is a simple method to determine whether the measured RDS signals arise from parasitic effects. Depending on the substrate orientation, the measured signal is either  $(r_{011} - r_{01\bar{1}})/r$  or its opposite  $-(r_{011} - r_{01\bar{1}})/r$ . Two identical experiments with the substrate orientation differing by  $90^\circ$  should change the sign of the signal. Conversely, when a material system is well known, the measured sign of the RDS signal indicates the orientation (Acher *et al* 1990c). Figure 3.28 illustrates the effects of substrate orientation on RDS signal.

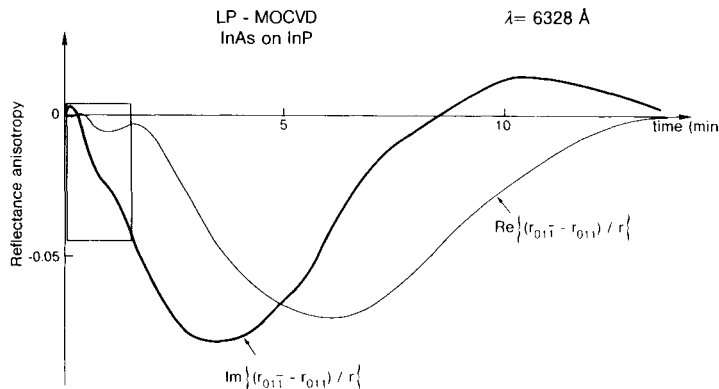
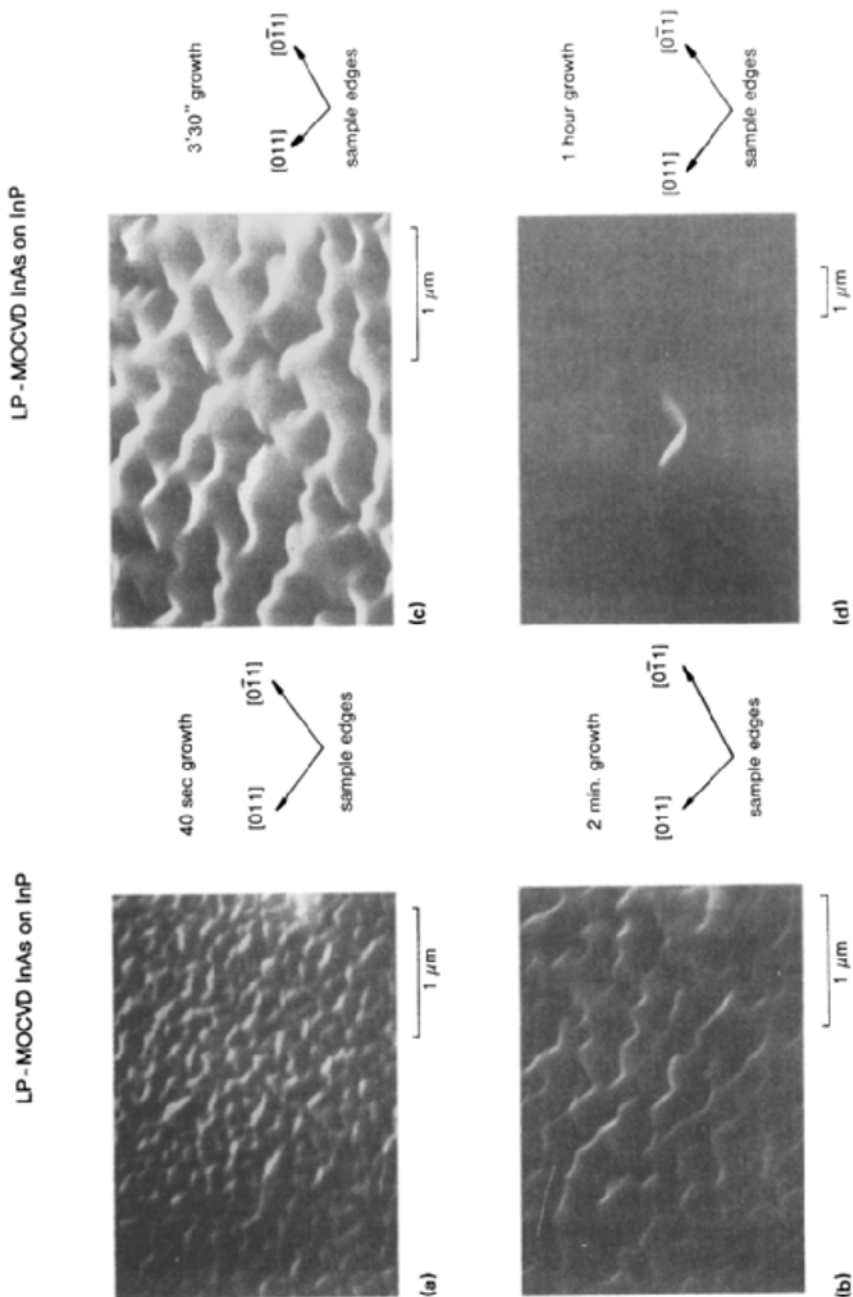


**Figure 3.29** RDS record of the growth of an InAs layer on an InP substrate using  $\lambda = 6328 \text{ \AA}$  light wavelength (Acher *et al* 1990b).

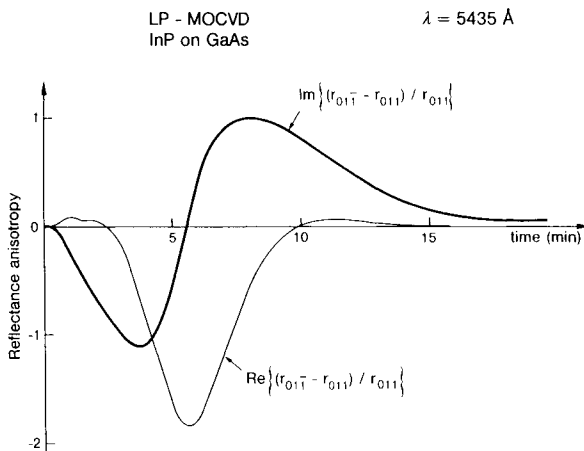
### 3.5.2 RDS records during real-time growth

Figure 3.29 shows the RDS record of the growth of InAs on an InP substrate for 15 min using a  $6328 \text{ \AA}$  light wavelength. The magnitude of the measured anisotropies is of the order of 5%. In contrast, the RDS signals measured for lattice-matched growth are generally about  $10^{-3}$  (Aspnes 1988a, Acher *et al* 1990c, Koch *et al* 1990). The occurrence of these large RDS signals is correlated with the occurrence of three dimensional (3D) growth, to a hazy surface appearance and a decrease in the measured reflectivity. The time scale of these anisotropy changes is also suggestive of structural evolution. By the end of 15 min growth, the RDS signal had returned to zero, the surface had smoothed and the reflectivity increased to a level comparable to the initial value. After 1 h, the growth was stopped, and the sample surface was mirror-like. Similar RDS records were obtained using different wavelengths, ranging from 3800 to  $6328 \text{ \AA}$ .

The surface morphology of InAs on InP was observed using a scanning electron microscope (SEM). The growth was interrupted after 40 s (figure 3.30(a)), 2 min (figure 3.30(b)), 3 min 30 s (figure 3.30(c)) and 1 h (figure 3.30(d)). All the pictures were taken with the electron beam coming from the top of the pictures, and the samples were tilted by about  $45^\circ$ . The resolution in figure 3.30(a) is not sufficient to distinguish clearly the shape of the roughness. The lateral dimension of the roughness increases with deposition time and its geometry appears clearly on the other photos. It consists mainly of rectangular holes of different sizes but all with their edges parallel to  $[011]$  and  $[0\bar{1}\bar{1}]$ . This observation is consistent with the prediction that they should be the preferred symmetry directions. The dispersion in size and shape is quite important in figures 3.30(a)–(c). These pictures do not reveal clear anisotropic patterns. The anisotropy may arise from the lateral dimensions of the holes, and also from



**Figure 3.30** Scanning electron microscope pictures of InAs on InP after: (a) 40 s growth, (b) 2 min growth, (c) 3 min and 30 s growth and (d) 1 h growth (after Acher *et al.* 1990b).



**Figure 3.31** RDS record of the growth of an InP layer on a GaAs on Si structure, using  $\lambda = 5435 \text{ \AA}$  light wavelength (after Acher *et al* 1990b).

their slope or their spacing. After 1 h growth, very few roughness patterns can be seen on the surface; one of these features is shown in figure 3.30(d). This is consistent with the fact that the sample is mirror-like after 1 h growth.

The dimensions of the roughness features increase with time (note the factor of three difference between the magnifications of figures 3.30(c) and (d)). One should point out that when the growth of the samples represented in figures 3.30(a)–(c) was stopped, the RDS signal continued to have an evolution as long as the sample was maintained at the growth temperature. This suggests that some mass transport occurs on the surface at that temperature. As a consequence, figures 3.30(a)–(c) may not show exactly the shape of the roughness under growth conditions. For the same reason, it is difficult to conduct spectroscopic studies on such samples. There is an evolution of properties determined through the RDS signal after stopping the growth which makes it difficult to compare kinetic and spectroscopic measurements. A fast cooling may be required to freeze the optical anisotropy.

Figure 3.31 shows the RDS record using  $5435 \text{ \AA}$  light of the growth of InP on a GaAs on silicon substrate. In this case the optical anisotropy is extremely large, sometimes with more than a factor of two difference between  $r_{011}$  and  $r_{01\bar{1}}$ . However, the broad features, the signs of the variations, are similar in figures 3.29 and 3.31. This suggests that the underlying mechanism responsible for the RDS signal evolution is the same, and is related to 3D growth, rather than effects associated with the specific material, such as chemical bonding.

For further discussion, it will be convenient to distinguish various stages in the RDS records. The initial transient corresponds to the first 5–10 s of growth. The experimental curve shown in figure 3.32 corresponds to the inset of figure 3.29, and it appears clearly that the initial behaviour of the RDS signal

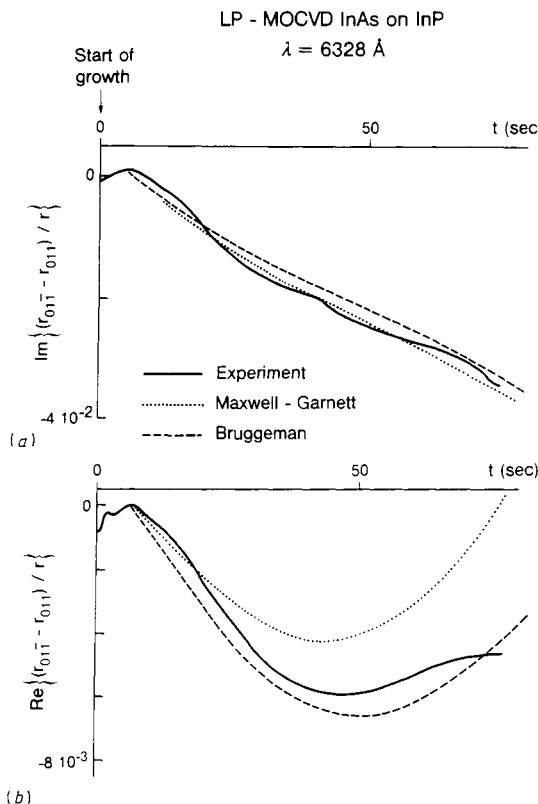


**Figure 3.32** Comparison between experiment (as per figure 3.29) and theory for the RDS record using  $\lambda = 6328 \text{ \AA}$  of the first minute of growth of InAs on InP. (a)  $\text{Im}\{[r_{01\bar{1}} - r_{01\bar{1}}]/r\}$ ; (b)  $\text{Re}\{[r_{01\bar{1}} - r_{01\bar{1}}]/r\}$ . Note the change in scale between the two figures. The Maxwell-Garnett fit was obtained with  $F \delta q de/dt = 17 \text{ \AA min}^{-1}$ . The Bruggeman fit corresponds to  $f = 0.7$ ,  $q = 0.5$ ,  $\delta q = 0.23$  and  $de/dt = 100 \text{ \AA min}^{-1}$  (after Acher *et al* 1990b).

differs from the behaviour after 10 s growth. During this initial transient, the dominant contribution to RDS does not arise from surface roughness, as will be discussed further. In the first stage, corresponding to the first minute, the RDS record exhibits a rapid, nearly linear variation of  $\text{Im}[r_{01\bar{1}} - r_{01\bar{1}}/r]$ . In contrast,  $\text{Re}[r_{01\bar{1}} - r_{01\bar{1}}/r]$  remains quite small. Figure 3.29 shows a kind of oscillation with a time constant clearly different from the rest of the variations. The second stage corresponds to the rest of the growth, where the reflectance anisotropy shows a kind of damped oscillation behaviour with large period and amplitude.

### 3.5.3 Optical models

It is clear from direct observation and SEM pictures (figure 3.30) that the surface of the growing lattice-mismatched layer is rough during the first stages of

growth. It is suspected that this roughness accounts for the large reflectance anisotropies observed.

Optical properties of rough surfaces are commonly treated using effective medium theories (EMTs). Briefly, a rough surface can be approximated as a homogeneous film, with a thickness corresponding to the height of the roughness, and with a dielectric constant between that of the dense medium and that of the ambient. Accordingly, a layer with a rough surface can be modelled as two layers: a dense layer covered by a rough layer. A rough InAs/InP sample can be described as a stack of three homogeneous layers: InP substrate, InAs dense layer and a rough layer. The reflection coefficients of such a multilayer structure and its associated optical anisotropy can easily be calculated using the Abeles formalism (Azzam and Bashara 1977), provided that the dielectric constant and thickness of all layers are known. The dielectric constants of GaAs, InP and InAs are tabulated (Palik 1985) and that of the rough layer evaluated using EMTs.

However, no reflectance anisotropy will arise from that model unless the shape of the roughness is anisotropic. It is well known that oblong particles may affect light polarization; this effect is known as form birefringence (Born and Wolf 1970). It is possible to get from EMTs a quantitative evaluation of the form of birefringence associated with the anisotropic roughness, as shown below.

All EMTs yield the following form for the dielectric function of the effective medium (Aspnes 1983)

$$\varepsilon_{\text{eff}} = \frac{q\varepsilon_0\varepsilon_1 + (1-q)\varepsilon_h[f\varepsilon_1 + (1-f)\varepsilon_0]}{(1-q)\varepsilon_h + q[f\varepsilon_1 + (1-f)\varepsilon_0]} \quad (3.16)$$

where  $\varepsilon_1$  is the dielectric function of the dense medium,  $\varepsilon_0$  is that of vacuum and  $f$  is the filling factor corresponding to the proportion of medium 1 making up this roughness. If  $f < 0.5$ , the roughness can be viewed as hills. If  $f > 0.5$ , the roughness can be viewed as a layer with depressions in it. The depolarization factor  $q$  is associated with the roughness shape, and accounts for the screening of the electric field within the effective medium. For anisotropic patterns,  $q$  depends on the orientation of the polarization, and one expects that  $q_{011} \neq q_{01\bar{1}}$ , leading to  $\varepsilon_{011,\text{eff}} \neq \varepsilon_{01\bar{1},\text{eff}}$ . If the roughness consists of long stripes,  $q = 0$  for light polarized along the stripes and  $q = 1$  for light polarization perpendicular to the stripes. The value of  $q$  associated with the main axes of ellipsoidal particles has been reported (Kittel 1976). There is no straightforward derivation of  $q$  for patterns like that shown in figure 3.30.  $\varepsilon_h$  is the dielectric function of the background or 'host' medium. In the Maxwell-Garnett theory (MG),  $\varepsilon_h = \varepsilon_1$  or  $\varepsilon_h = \varepsilon_0$ , depending on the choice of prevalent medium. The Bruggeman theory takes  $\varepsilon_h = \varepsilon_{\text{eff}}$ . It is often preferred to MG, because it is self-consistent and does not attribute a particular role to either medium 0 or medium 1.

The present approach (Aspnes 1983) leads to a description of a sample using four media: the ambient, a rough anisotropic layer, a dense layer and the

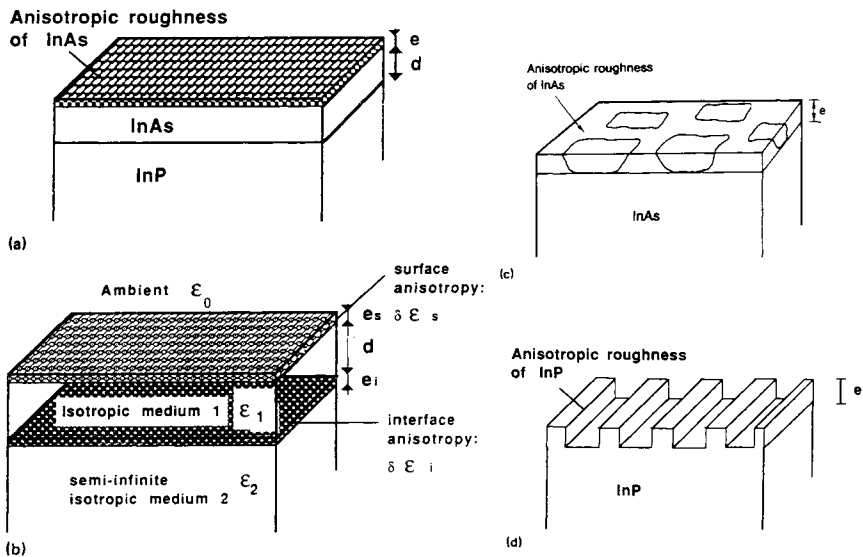


**Figure 3.33** Schematic view of the four models used to account for the observed RDS signal: (a) model with semi-infinite substrate, InAs dense layer and InAs rough anisotropic layer with thickness  $e \ll \lambda$ , (b) model with semi-infinite substrate, isotropic epilayer, anisotropic surface and interface, (c) model with semi-infinite InAs dense layer and InAs rough anisotropic layer and (d) model with semi-infinite layer and roughness consisting of infinite stripes. (d) corresponds to a particular case of model (c) (after Acher *et al* 1990b).

substrate. With the Abeles matrix formulation, it is very easy to calculate the optical properties of such multilayer systems numerically by computer. However, in order to get a better understanding of the observations, it is advantageous to use simpler models, if possible, with simple analytical solutions. The SEM observations and the thickness measurements suggest a growth process where both the dense layer and the top rough layer are growing.

To simplify the calculation, one can consider different models for different growth stages of the RDS records. During the first stage (figure 3.33(a)), the roughness thickness  $e$  is very small compared to the light wavelength  $\lambda$  allowing a first-order development in  $e/\lambda$ . In the second stage of growth (figure 3.33(c)), the roughness should be treated without the small-thickness approximation. The effect of the substrate is ignored, because the dense layer is thick enough to absorb the light before it reaches the layer/substrate interface. This assumption is fully valid provided that the dense-layer thickness exceeds the penetration depth of light of a fixed wavelength in the material.

#### (a) Optical model for small roughness thickness

The model related to the first stage of growth is developed as follows. Figure 3.33(b) shows schematically an isotropic layer growing on an isotropic

substrate, with anisotropic surface and interface. The surface and interface are modelled as anisotropic layers with respective thicknesses  $e_s, e_i \ll \lambda$ . The Abeles matrix formulation and a first-order development in  $e/\lambda$  yield the reflectance anisotropy as shown in equation (3.7):

$$\frac{r_{01\bar{1}} - r_{011}}{r} = \frac{4j\pi}{\lambda} \frac{N_0}{(\varepsilon_1 - \varepsilon_0)} e_s \delta\varepsilon_s + \frac{16j\pi}{\lambda} \frac{N_0 \varepsilon_1}{(\varepsilon_1 - \varepsilon_0)(N_1 + N_2)^2} X \left( e_i \delta\varepsilon_i + \frac{\varepsilon_1 - \varepsilon_2}{\varepsilon_1 - \varepsilon_0} e_c \delta\varepsilon_c \right) \quad (3.17)$$

with

$$X = \exp\left(-\frac{4j\pi N_1 d}{\lambda}\right) \quad r_{12} = \frac{N_1 - N_2}{N_1 + N_2} \quad r_{01} = \frac{N_0 - N_1}{N_0 + N_1} \quad (3.18)$$

and

$$\delta\varepsilon_s = (\varepsilon_{01\bar{1}} - \varepsilon_{011})_{\text{surface}} \quad \delta\varepsilon_i = (\varepsilon_{01\bar{1}} - \varepsilon_{011})_{\text{interface}}. \quad (3.19)$$

$N_0, N_1$  and  $N_2$  are the optical indices of the ambient, epilayer and substrate, respectively.  $d$  is the thickness of the layer.

When the epilayer thickness is large enough, the influence of the substrate can be ignored, because all the light is absorbed before it reaches the substrate-epilayer interface. This corresponds to  $X = 0$ . In this case, (3.18) yields the known expression for the reflectance anisotropy of the surface of a bulk sample (Aspnes *et al* 1989, McIntyre and Aspnes 1971, Del Sole and Selloni 1984). It should be noticed that equation (3.18) was established using a time dependence of electromagnetic waves of  $\exp(j\omega t)$  corresponding to a complex optical index given by  $N = n - jk$  where  $n$  is the real index and  $k$  is the extinction coefficient. If the  $\exp(j\omega t)$  convention is preferred, equation (3.18) should be replaced by its conjugate.

Figure 3.33(a) corresponds to the case where the interface anisotropy  $\delta\varepsilon_i$  is neglected and surface anisotropy is given by the EMTs. One can take surface roughness into account in the following way. For small anisotropies  $\delta q = (q_{01\bar{1}} - q_{011}) \ll 1$  and for  $\varepsilon_1 \gg \varepsilon_0 = 1$ , a first-order development of MG with  $\varepsilon_h = \varepsilon_1$  gives

$$\delta\varepsilon_s = -\delta q F \varepsilon_1 \quad (3.20)$$

where  $F$  is related to the roughness geometry by

$$F = f(1 - f)/(1 - qf)^2. \quad (3.21)$$

The RDS signal corresponding to the case in figure 3.33(a) with the Maxwell-Garnett description of roughness is obtained using equations (3.11) and (3.7), with  $\varepsilon_1 \gg \varepsilon_0$ .

$$\frac{r_{01\bar{1}} - r_{011}}{r} = -\frac{4j\pi}{\lambda} F e \delta q \left( 1 + \frac{4X'}{(1 - X')^2} \right) \quad (3.22)$$

with

$$X' = r_{12} \exp\left(-\frac{4j\pi N_1 d}{\lambda}\right) \quad r_{12} = \frac{N_1 - N_2}{N_1 + N_2}$$

where  $e$  is the roughness thickness,  $r_{12}$  is the reflection coefficient of the layer–substrate interface.

It is clear from equation (3.22) that the anisotropic roughness affects mainly the imaginary part of the reflectance anisotropy, as observed experimentally during the first stages of the growth shown in figures 3.29 and 3.32. The real part arises only from the term in  $X'$ , which is a perturbation. It corresponds to light reflected at the substrate–dense-layer interface. As the dense-layer thickness increases, interference conditions between the light reflected at the surface and at the interface are modified. This leads to an oscillating behaviour of  $\text{Re}[(r_{01\bar{1}} - r_{011})/r]$  as  $d$  increases. The characteristics of roughness appear in the factor  $Fe\delta q$ . It is clearly not possible to obtain independently values for  $f$ ,  $q$ ,  $e$ ,  $\delta q$  from the experimental data. Indeed, the product  $Fe\delta q$  is the only variable parameter that need be introduced in a fit of experimental measurement. It is important to emphasize that the relationship between the real and imaginary parts deduced from equation (3.22) is independent of roughness characteristics. For a given substrate and layer, if the growth rate of the dense layer is known, the model predicts the value of the real part of the reflectance anisotropy as a function of the imaginary part only. Therefore, the ability of the model to account for both components of the RDS signal is a good test of its validity.

If the Bruggeman theory is used instead of MG to calculate the value of  $\delta\epsilon_s$ , one no longer obtains a simple analytic expression similar to equation (3.20).  $\delta\epsilon_s$  has to be evaluated numerically using equation (3.16). The RDS signal is computed using equation (3.18). Bruggeman is expected to be more accurate but both theories lead to similar results (Acher *et al* 1991). The discussion based on equation (3.22) is expected to remain essentially valid.

### (b) Optical model for large roughness thickness

After both the rough and the dense layer have grown for some time, another model (figure 3.33(c)) should be used to describe the second stage. This is indeed a three-medium model, with an anisotropic intermediate medium treated using the MG or Bruggeman theory. The RDS signal associated with such a sample is easily computed as a function of roughness characteristics. The main features expected from such a model are the possibility to account for large anisotropies, and the interference-like features measured by RDS (figures 3.29 and 3.31). Clearly, the thicker the anisotropic medium, the greater the interaction with light, and therefore the larger the optical anisotropy. Constructive or destructive interference within this layer is possible only if the material is not too absorbing. Indeed, the effective medium described by the MG or Bruggeman theory is significantly less absorbing than the dense medium. The penetration depth of light in the rough layer exceeds the wavelength in this material. One can therefore expect to observe oscillating interference-like features on the RDS

signal when the thickness of the roughness increases, even for light wavelengths strongly absorbed in the dense medium.

One should point out that the validity of EMTs depends on the dimensions of the rough features compared to the light wavelength. If the roughness consists of a series of parallel stripes of infinite length (figure 3.33(d)), the ratio between the lateral dimensions (stripe width and spacing) and the wavelength is the relevant criterion. This ratio should be small in order for the theories to be valid; discrepancies appear when this ratio exceeds 0.1. However, SEM images (figure 3.30) show that in fact roughness dimensions are comparable with light wavelength after 4 min growth of InAs on InP. Even if EMTs are used somewhat outside of their range of validity, they can still give a qualitative idea of the optical properties of a rough layer. One cannot expect to get quantitative information from RDS measurements after a few minutes of growth.

### 3.5.4 The first stage of 3D growth

Figures 3.32, 3.34 and 3.35 present the RDS record of the first minute of InAs/InP growth and the corresponding fit using the model shown in figure 3.33(a). Figure 3.32 is a detail of figure 3.29. After an initial transient of 5–10 s,  $\text{Im}[(r_{01\bar{1}} - r_{011})/r]$  shows a nearly linear variation. This suggests that the roughness thickness  $e$  increases linearly with time. Equation (3.22) shows that the slope of the imaginary part of reflectance anisotropy is  $F \delta q de/dt$ . This is the only adjustable parameter used in the MG model to fit both the real and the imaginary part of  $(r_{01\bar{1}} - r_{011})/r$ . The evolution of the thickness  $d$  of the dense layer as a function of time has to be known in order to evaluate  $X'$  in equation (3.22). The growth rate of the dense InAs layer  $dd/dt$  was taken as  $250 \text{ \AA min}^{-1}$  for figures 3.32 and 3.34. This value was chosen to be slightly lower than the  $270 \text{ \AA min}^{-1}$  measured experimentally on thick samples. This is because only part of the growth contributes to the dense layer; another part contributes to increasing the roughness thickness. In the case of figure 3.35, where the growth rate was doubled,  $dd/dt$  was taken as  $500 \text{ \AA min}^{-1}$ . It can be noticed that a small error in the evaluation of  $dd/dt$  would slightly change the period of the oscillation of  $\text{Re}[(r_{01\bar{1}} - r_{011})/r]$  but would not significantly affect the agreement observed between the experiment and the model.

The simulations shown in figures 3.32, 3.34 and 3.35 using the Bruggeman theory were made using  $f = 0.7$ ,  $q = 0.5$ , and by varying the shape anisotropy  $\delta q$  and the roughness growth rate  $de/dt$ . No attempt was made to find the best fit by allowing all parameters to vary. As discussed previously, it is not possible to obtain reliable evaluations for each parameter individually, but only for combinations of them. Using the MG theory, the model yields  $17 \text{ \AA min}^{-1}$ ,  $19.5 \text{ \AA min}^{-1}$  and  $35.5 \text{ \AA min}^{-1}$  for the  $F \delta q de/dt$  product for figures 3.32, 3.34 and 3.35, respectively. The corresponding values using Bruggeman theory are  $11.5 \text{ \AA min}^{-1}$ ,  $14 \text{ \AA min}^{-1}$  and  $24 \text{ \AA min}^{-1}$ . This shows that the MG and Bruggeman theory yield comparable  $F \delta q de/dt$  product for a given sample.

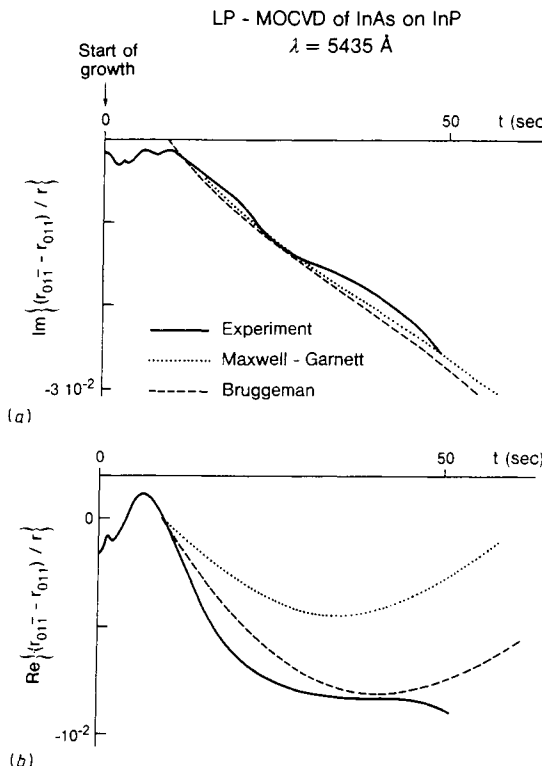


**Figure 3.34** A comparison between experiment and theory for the RDS record using  $\lambda = 5435 \text{ \AA}$  of the first minute of growth of InAs on InP. The Maxwell-Garnett fit was obtained with  $F \delta q de/dt = 19.5 \text{ \AA min}^{-1}$ . The Bruggeman fit corresponds to  $f = 0.7$ ,  $q = 0.5$ ,  $\delta q = 0.28$  and  $de/dt = 100 \text{ \AA min}^{-1}$  (after Acher *et al.* 1990b).

As seen from the figures, both models give comparable predictions. The model based on Bruggeman theory accounts very well for the behaviour of the real part of the reflectance anisotropy, and is of the order of one magnitude difference between the real and the imaginary parts. The model agrees well with the measurements both at  $\lambda = 5435 \text{ \AA}$  (figure 3.34) and at  $\lambda = 6328 \text{ \AA}$  (figure 3.32). The  $F \delta q de/dt$  products found in both cases are similar. Doubling the growth rate (figure 3.35) yields a nearly doubled  $F \delta q de/dt$  product. The period of the oscillation of  $\text{Re}[(r_{01\bar{i}} - r_{011})/r]$  is shorter, in accordance with the higher growth rate of the dense layer. Figures 3.32, 3.34 and 3.35 show that the model proposed gives a satisfactory description of experimental observations. The slope of  $\text{Im}[(r_{01\bar{i}} - r_{011})/r]$  gives a quantitative indication of the anisotropic thickness growth rate. The oscillatory behaviour of  $\text{Re}[(r_{01\bar{i}} - r_{011})/r]$ , as a function of dense-layer thickness predicted by equation (3.22), is actually observed. Other experiments have shown that this feature is observed also at the  $5000 \text{ \AA}$  wavelength but is no longer seen with UV light. This is because the

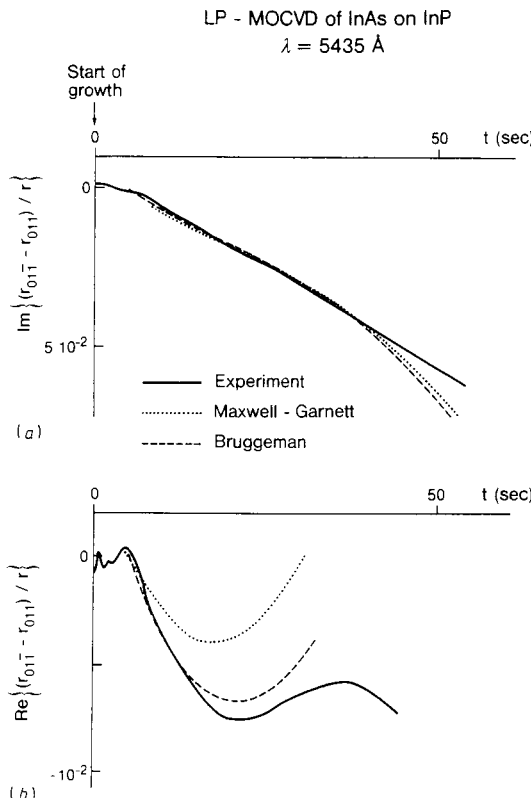


**Figure 3.35** Comparison between experiment and theory for the RDS record using  $\lambda = 5435 \text{ \AA}$  of the first minute of growth of InAs on InP, for twice the usual growth rate. The Maxwell-Garnett fit was obtained with  $F \delta q de/dt = 35.5 \text{ \AA min}^{-1}$ . The Bruggeman fit corresponds to  $f = 0.7$ ,  $q = 0.5$ ,  $\delta q = 0.8$  and  $de/dt = 170 \text{ \AA min}^{-1}$  (after Acher *et al.* 1990b).

InAs epilayer is too absorbing in the UV and the quantity  $X'$  in equation (3.22) vanishes even for small epilayer thickness.

The same model was also used for the growth of InP on GaAs. The sign of the reflection coefficient between InP and GaAs is the opposite of that of InAs on InP. Therefore, the sign of the initial variation of  $\text{Re}[(r_{01\bar{1}} - r_{011})/r]$  given by equation (3.22) should be opposite of that observed in the case of InAs on InP. This is indeed the case (figure 3.31). But the oscillatory behaviour visible especially in figures 3.33 and 3.35 is masked here by the variations of surface roughness. The assumption that  $e \ll \lambda$  breaks down very quickly for the InP/GaAs samples.

The model does not account for the initial stage, corresponding to the first 5–10 s of the growth. It takes between 4 (figures 3.32 and 3.35) and 9 s (figure 3.34) for the imaginary part of the reflectance anisotropy to begin its linear variation.

This shows that the variation of the RDS signal during this initial stage comes from a contribution other than anisotropic 3D growth.

### 3.5.5 Subsequent growth

After one minute of growth, the fit between the calculated and measured RDS signal evolution no longer holds for  $\text{Re}[(r_{01\bar{1}} - r_{011})/r]$ . This is expected, because the model displayed in figure 3.33(a) is valid only for small roughness thickness,  $e \ll \lambda$ . One should use the model developed for the second stage (figures 3.33(c) and (d)), which works for finite roughness thickness.

This is shown in figure 3.36, for InP/GaAs/Si growth, where the calculated reflectance anisotropy is plotted as a function of roughness thickness, and compared with the RDS versus time record of figure 3.31. The calculated curve is obtained by approximating the roughness to be stripes (figure 3.33(d)), which is the most anisotropic shape ( $\delta q = 1$ ). Both the MG and Bruggeman models are equivalent in that case. The filling factor was taken to  $f = 0.5$ . The theoretical curve as a function of roughness thickness  $e$  exhibits the same general features as the variations of measured signal as a function of time. There is agreement for the sign of the variation, the order of magnitude, the sign change of the imaginary part and the correspondence between the inflection points and the extrema of both components. This similarity between the theoretical curve as a function of  $e$  and the experimental record function of time suggests that roughness thickness  $e$  increases linearly with time. Differences exist between the observation and the model, but many reasons may account for this. The roughness shape, the filling factor and the growth rate of  $e$  may vary with time. Besides, as previously mentioned, the EMT is not used in its range of strict validity.

The growth of InAs on InP was investigated at different wavelengths, ranging from 3800 to 6328 Å. The broad features and the sign of the variations are the same at all wavelengths, except the initial oscillation of  $\text{Re}[(r_{01\bar{1}} - r_{011})/r]$  as mentioned before. This is consistent with a structural origin of the RDS behaviour. The model of figure 3.33(c) was used to account for an RDS record of InAs/InP. Figure 3.37 represents the calculated RDS signal for the growth of rough InAs/InP as a function of roughness thickness  $e$ . The roughness shape is kept constant ( $f = 0.7$ ,  $q = 0.5$ ,  $\delta q = 0.16$ ). The model agrees quite well with the experimental record of RDS signal as a function of time (same record as the one detailed in figure 3.34). While it was not possible to determine separately the value of  $de/dt$  and the shape of the anisotropy  $\delta q$  during the first minute of growth, these two parameters have quite different effects on the RDS features for longer time scale. As a rough indication, the period of the oscillations of the RDS signal corresponds to constructive or destructive interference conditions, and is therefore related to the roughness thickness  $e$ ; the magnitude of the signal at the extrema depends on the shape anisotropy  $\delta q$ .

The models used (figures 3.33(c) and (d)) assume that the influence of the substrate on the optical properties can be neglected. This assumption is valid

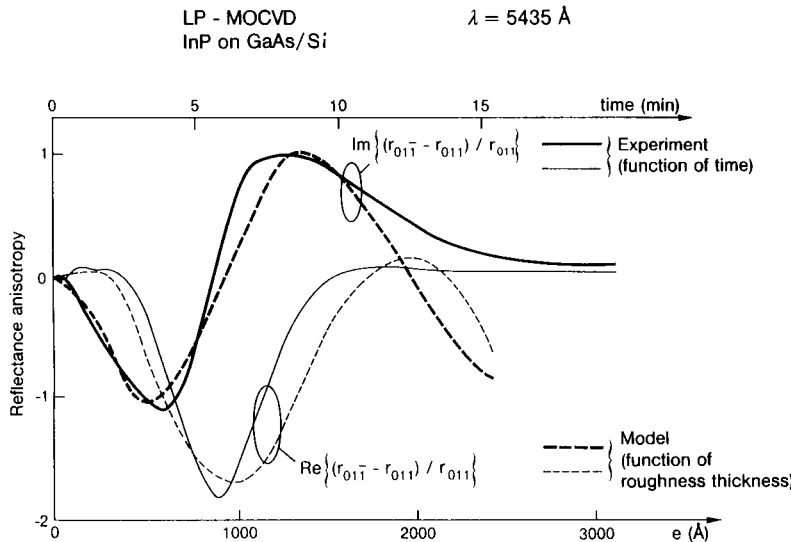


**Figure 3.36** Comparison between experimental RDS record as a function of time (same as figure 3.31), and theoretical prediction of model (figure 3.33(d)) as a function of roughness thickness. The filling factor was taken as  $f = 0.5$  (after Acher *et al* 1990b).

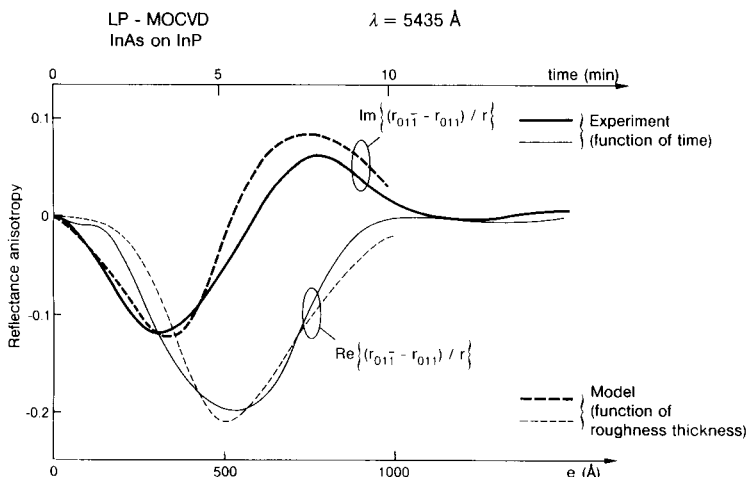


**Figure 3.37** Comparison between experimental RDS record as a function of time of InAs/InP, and theoretical prediction of the model (figure 3.33(c)) as a function of roughness thickness. The roughness was modelled using the Bruggeman theory, with  $f = 0.7$ ,  $\delta q = 0.16$  and  $q = 0.5$  (after Acher *et al* 1990b).

provided that the penetration length of light in the material is smaller than the dense-layer thickness. This is true after several minutes of deposition, depending on the wavelength and the growth rate, but does not hold after only one minute of growth for the wavelengths used. However, as discussed above, the effects due to light reflected by the substrate–layer interface are small. Taking this effect into account during the second stage of the RDS signal would bring only small corrections.

Figures 3.36 and 3.37 suggest that the roughness thickness keeps increasing with time. The corresponding growth rate of the roughness  $de/dt$  is  $160 \text{ \AA min}^{-1}$  in the case of InP/GaAs/Si (figure 3.36) and  $100 \text{ \AA min}^{-1}$  in the case of InAs/InP (figure 3.37). However, after 10 or 15 min growth, the surface improves, leading to a mirror-like surface after one hour of growth. This is consistent with the fact that the RDS signal returns to zero, instead of exhibiting more oscillations as the models would predict. The mechanisms that could lead to an increase both in apparent roughness thickness and in the inhibition of roughness have not been investigated. They are beyond the scope of the present modelling.

Various details of the models will now be considered in more depth. The anisotropy has been described only with the screening parameter anisotropy  $\delta q$ , and we shall try to relate this quantity to the shape of the roughness and to its anisotropy in the lateral dimension. The difficulty in finding a more accurate description for the optical properties of roughness with large dimensions will be emphasized. With our present understanding, RDS observations give some insights into the growth process. Information concerning the critical thickness of strained layers and the orientation of the anisotropic 3D patterns can be obtained. The influence of substrate misorientation as evidence of mass transport during annealing can be measured. With our present understanding, the information obtained using RDS can be of use for the optimization of the growth of lattice-mismatched semiconductors.

### 3.5.6 Discussion of optical models

The first stages of growth have been described successfully using the model of figure 3.33(a), and the agreement between experiment and theory is shown in figures 3.32, 3.34 and 3.35. The roughness features are small, and EMTs are clearly used within their range of validity. It is possible to give an idea of the correspondence between this parameter and the shape of the roughness in some cases. The sign of  $\delta q$  indicates that the screening is less effective along the [011] direction than along [0\bar{1}\bar{1}]. This suggests that the roughness patterns are elongated in the [011] direction. For oblate spheroids,  $\delta q$  depends on the ratio between axial lengths  $c/a$  (Kittel 1976); for example,  $\delta q = 0.3$  corresponds to  $c/a \approx 1.4$ . This elongation is moderate but can account for the RDS behaviour observed for InAs on InP (figure 3.37). The determination of the depolarization factor associated with a given particle shape is not straightforward, and no attempt was made to relate  $\delta q$  to SEM observations. The dispersion of roughness

shape has not been taken into account in this calculation. It is possible to include it in a model (Borensztein *et al* 1988), but this would add more parameters.

In all the calculations, instead of high-temperature values of the optical index of InAs and InP, room-temperature values have been used. The main parameter affected by this simplification is the reflection coefficient at the substrate-layer interface  $r_{12}$ , which relates the variation of the real part of RDS signal to the variation of the imaginary part (equation (3.22)). However,  $r_{12}$  depends mainly on the difference between the indices, and should not be affected greatly by temperature, since the indices of both InAs and InP are expected to have similar variations with temperature.

No effects other than the structural contribution have been taken into account in this model. The contribution of chemisorbed species to the RDS signal is known to be in the  $10^{-3}$  range, in particular for InAs. It may account for the variations of the RDS signal in the first seconds of growth, but clearly not for the larger variations observed afterwards. However, the effect of the strain should be considered. It is known that a lattice-mismatched layer is very strained at the beginning of growth, and gradually relaxes. If the deformation of the epilayer is purely tetragonal, no RDS contribution is expected to arise from the strain. If the relaxation process is different in the [011] and [01 $\bar{1}$ ] directions, as has been reported in the case of GaAs on silicon (Koch 1988), it is expected to have an influence on the RDS signal. The effect of strain on the optical properties of semiconductors has been studied using piezoreflectance measurements (Sell 1973, Camassel *et al* 1975); the effect is extremely wavelength dependent, increases by one order of magnitude, and has a sign change near the critical points  $E_0$  and  $E_1$ . This probably rules out anisotropic strain as a major contribution to the RDS records of lattice-mismatched materials, because the observed features are essentially similar for two wavelengths. The influence of strain may be a key feature in understanding the evolution of the RDS signal in the first 5 or 10 s. Using available data on GaAs (Sell 1973) a strain anisotropy in the growth plane of  $10^{-3}$  would lead to an RDS contribution less than  $10^{-3}$  far below  $E_1$ . It would reach  $5 \times 10^{-3}$  in the  $E_1$ ,  $E_1 + \Delta_1$  region. Spectroscopic measurements would be necessary to assess this effect.

As previously mentioned, EMTs are based on the assumption that the dimensions of the roughness are very small compared to the light wavelength. This assumption clearly holds during the first minute, but is no longer true after 5 min. The use of EMTs to account for RDS behaviour after 5 min of growth (figures 3.36 and 3.37) requires some further discussion. The reflectivity of the sample decreases by a factor of two to six after 10 min of 3D growth, before returning to a level comparable to its original value. EMTs fail to account for this evolution of the reflectivity. One reason is that they do not take into account light diffusion. When the typical size of roughness patterns approaches the light wavelength, part of the light is diffused, leading to a decrease in reflectivity and to a hazy appearance. But the reflectance anisotropy is not expected to be much affected by the diffused light since it contributes to decrease both  $r_{011}$  and  $r_{01\bar{1}}$ .

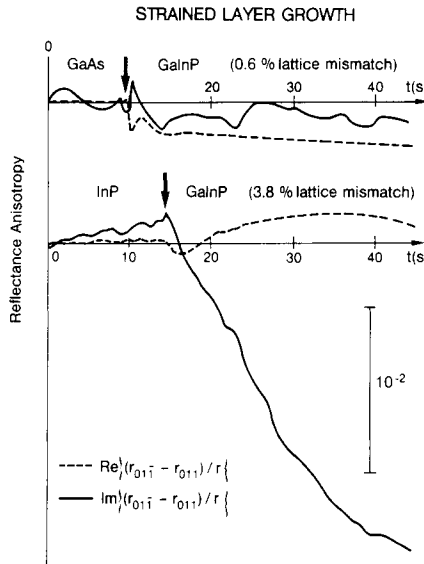
Another important assumption which is no longer valid for thick roughness is the homogeneity along the growth direction. These factors may explain why EMTs account quite well for the behaviour of the RDS signal  $(r_{01\bar{1}} - r_{011})/r$ , but completely fail to describe  $r_{011}$  and  $r_{01\bar{1}}$  individually.

A more accurate model would be able to account for the optical properties of roughness with characteristic dimensions comparable to the wavelength. Much effort has been devoted to the study of scattering by anisotropic particles (Asano and Yamamoto 1975, Asano 1979, Barber and Wang 1978, Uzunoglu *et al* 1976) leading very often to numerical solutions requiring long computations. The modelling of anisotropic patterns on a surface may be more difficult than that of isolated particles (Berreman 1970). Besides, SEM pictures show that the roughness is not uniform, and a distribution of roughness characteristics should be used. This inhomogeneity may also induce partial depolarization of reflected light. A model based on the Fresnel–Kirchoff theory of diffraction accounts for the decrease in reflectivity of rough surfaces with lateral roughness dimensions that are large compared to the wavelength, and small roughness thickness (Ohlidal and Lucks 1972). This model is only valid if the slope of the roughness features is very small, which does not seem to hold in the present case, and is unable to account for reflectance anisotropy under normal incidence. The difficulty in finding a model that would account both for reflectance measurements and characterization in polarized light has often been mentioned (Pickering *et al* 1989).

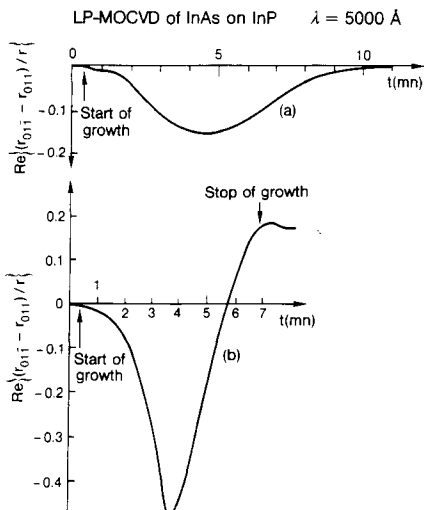
### 3.5.7 RDS monitoring of growth of GaInP/GaAs and GaInP/InP

Figure 3.38 shows the RDS records of growth of GaInP on two different substrates. In the case (*a*), the composition of GaInP is adjusted so that there is 0.6% compression stress in the epilayer. The variation of the imaginary part is in the  $10^{-3}$  range, and is mainly due to noise. No anisotropic roughness is detected on the surface. In the case (*b*), the GaInP epilayer exhibits a 3.8% lattice mismatch with the InP substrate. The evolution of  $\text{Im}[(r_{01\bar{1}} - r_{011})/r]$  shows that the growth is three dimensional from the very first seconds of epilayer growth. The real part  $\text{Re}[(r_{01\bar{1}} - r_{011})/r]$  is not affected significantly by 3D growth, as expected from equation (3.13) because  $r_{12}$  is quite small. The thickness of the roughness is expected to increase at a rate  $de/dt$  with  $F \delta q de/dt \approx 24 \text{ \AA min}^{-1}$ .

On a larger time scale, the roughness thickness can increase so that the assumption  $e \ll \lambda$  no longer holds. Then, both real and imaginary parts of  $(r_{01\bar{1}} - r_{011})/r$  attain large values, sometimes larger than 0.1. However, if a proper growth procedure is followed, a smooth surface can be obtained and, as a consequence, the optical anisotropy returns to zero. RDS can give indications of whether the surface cures or not and at what rate. This information is particularly important since surface morphology is very sensitive to a slight perturbation of growth conditions. Figure 3.39 illustrates this point. Two InAs layers were grown on InP substrates. Growth conditions were identical in both cases. The



**Figure 3.38** RDS records of two strained layers, showing both the real and imaginary parts of the anisotropy: (a) GaInP on GaAs, with a lattice mismatch of 0.6% (compressive stress); (b) GaInP on InP, with a lattice mismatch of 3.8% (tensile stress) (after Acher *et al* 1990a).



**Figure 3.39** RDS records of the growth of InAs on InP substrate (% lattice mismatch). Growth conditions are the same in both cases, but the heating procedure was faster in (b) than in (a) (after Acher *et al* 1990a).

only difference consisted in the heating procedure, which was faster in (b) than in (a). It is clear from the RDS records that the roughness cures better in (a) than in (b). Therefore, the growth was stopped in the second case.

### 3.6 INSIGHTS ON THE GROWTH PROCESS

Using this understanding of the RDS technique, it is now possible to discuss the aspects of growth. Among the crystal-growth issues that can be dealt with is the assessment of critical thickness where 3D growth begins. During the initial stage of growth, RDS behaviour does not correspond to anisotropic 3D growth. This could mean that the growth is two dimensional during the first 5–10 s. This corresponds to Stranski–Krastanov growth: growth of several layers of a complete InAs film, followed by island formation. After this initial stage, both the dense and the rough part of the film grow. The RDS signal evolution observed during the initial transient, corresponding to the first seconds of growth, may arise from a variety of contributions. The contribution of chemisorbed and physisorbed species are expected to be different in the case of InP or in the case of growing InAs. Atomic rearrangements at the surface or interface can affect the signal. Another contribution may arise from anisotropic strain in the layer, as discussed later.

The magnitude of the RDS signal for InAs/InP is very dependent on growth conditions, substrate cleaning and the heating procedure. It makes the quantitative RDS assessment of  $F \delta q \, de/dt$  more suitable for *in situ* monitoring. The small difference between the values deduced from figures 3.32 and 3.34 corresponding to two different growths monitored using two different wavelengths may not arise from an unexpected spectroscopic dependence, but simply because the growth conditions were slightly different between the two experiments. The choice of wavelength for performing such *in situ* studies is not crucial. The same broad features are found at all wavelengths except the oscillation on  $\text{Re}[(r_{01\bar{1}} - r_{011})/r]$  during the first minute. It is not detectable for wavelengths too strongly absorbed in the dense medium.

The observations show that during the growth of both InAs/InP and InP/GaAs/Si, anisotropic 3D growth occurs. The magnitude of this effect is different for the two systems. Modelling suggests that roughness patterns are more anisotropic and grow faster in the case of InP/GaAs than in the case of InAs/InP.

In a preliminary study, the growth of InAs and InP was stopped while keeping the  $\text{AsH}_3$  flux and temperature constant. Figure 3.40 reports the RDS record of a 3 min 30 s growth of InAs on InP followed by about 1 min under  $\text{AsH}_3$  without growth at the same temperature. This is the same sample as that used in figure 3.30(c). The RDS signal changes significantly during this annealing, suggesting that there was mass transport and a change in roughness characteristics. The change during the first 30 s is about 5%

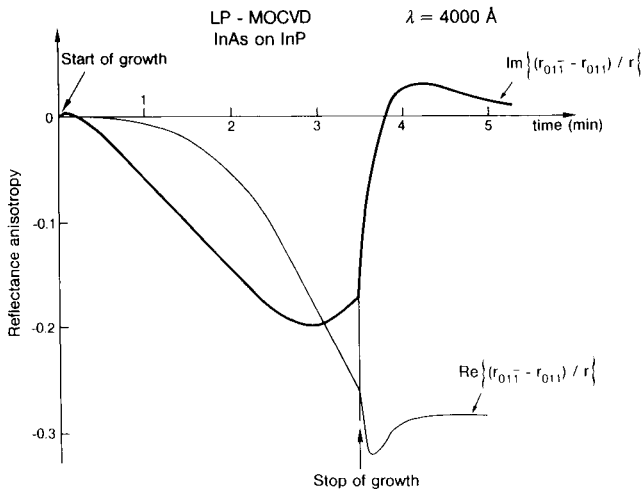


**Figure 3.40** RDS record of the growth of an InAs layer on an InP substrate, using  $\lambda = 4000 \text{ \AA}$ . The growth is stopped after 3 min and 30 s, the  $\text{AsH}_3$  flux and temperature being unchanged. Note the important change of RDS signal in the seconds following the growth interruption (after Acher *et al* 1990b).

for  $\text{Re}\{r_{01\bar{1}} - r_{011}\}/r$ , and 20% for  $\text{Im}\{(r_{01\bar{1}} - r_{011})/r\}$ , which corresponds to a variation rate larger than during growth. Then the optical anisotropy reaches a steady-state value. The change in RDS is expected to come from a change in roughness shape and characteristics since only structural contributions can account for this order of magnitude. The mechanism for such structural evolutions has not been investigated. It is important to note that stopping the growth and keeping the sample at the same temperature does not stop surface evolution. As previously mentioned, it makes a comparison between kinetic RDS data and spectroscopic RDS recorded after growth has been stopped more difficult. This is because the evolution of the optical properties of a sample during the process of stopping the growth and cooling down is not negligible.

The models proposed for the first and second stages of the RDS records of roughness suggest that the roughness thickness continuously increases with time. It is also clear that after some time the roughness contribution disappears, indicating that the surface has smoothed. These two aspects are not contradictory if one supposes that the roughness thickness increases while its filling factor increases toward unity. Figures 3.30(a)–(d) are consistent with roughness features increasing in size but becoming less and less numerous as a function of time. The mechanism needs further investigation.

Two factors contribute to the difference in optical properties of the [011] and [01̄1] directions. One is the chemical asymmetry between the two directions: the dangling bonds of the group-V element are aligned along the [011] direction.

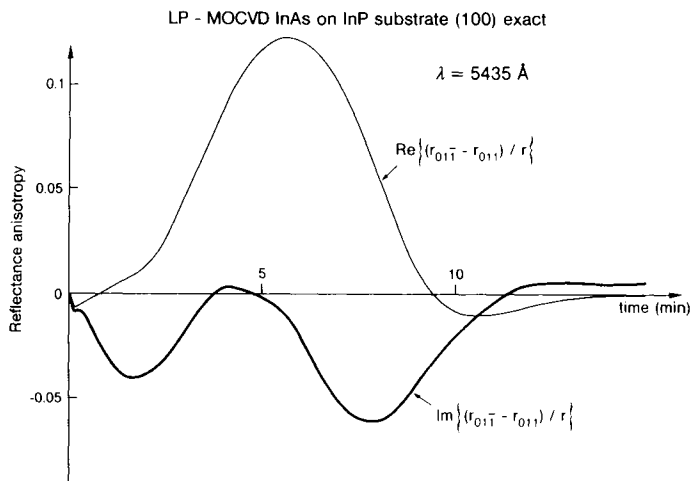


**Figure 3.41** RDS record of the growth of an InAs layer on an InP substrate with (100) exact surface orientation using  $\lambda = 5435 \text{ \AA}$  (after Acher *et al* 1990b).

The other is the structural asymmetry due to the presence of steps on the surface. The steps are due to the slight tilt of the surface of the substrate relative to (100). For the samples misoriented toward [01̄1] that were used for this study, the steps are along the [011] direction. Steps are known to play an important role in the first stages of the growth of GaAs/Si (Koch 1988): nucleation occurs at the step edges and GaAs islands are elongated along the step. In the present study, the sign of  $\delta q$  tells us that roughness is elongated along [011] which is also the direction of the steps. Preliminary experiments were conducted with (100) exact substrates, in order to assess the importance of the structural asymmetry of the substrate on the RDS behaviour (figure 3.41). The RDS features related to 3D growth are quite different from those observed on substrates with 2° misorientation toward [01̄1]. This suggests that structural rather than chemical anisotropy of the surface of the substrate determines the privileged directions of anisotropic 3D growth. It shows the importance of substrate misorientation for the growth of lattice-mismatched materials. With our present understanding, the RDS record of figure 3.41 is difficult to comment on in more detail. It is not even clear that [011] and [01̄1] are the optical eigenaxes. The orientation of the commercially available substrates is not specified with a precision better than 0.5°, and optical eigenaxes may correspond to the orientation of the residual tilt. Further studies with different substrate misorientations are required to separate the influence of the chemical and structural asymmetry of the substrate on the roughness characteristics.

## REFERENCES

- Acher O 1990 *These de Doctorat* Universite Paris-Sud
- Acher O, Benferhat R, Drevillon B and Razeghi M 1990a *Proc. SPIE* **1361** 1156
- Acher O, Bigan E and Drevillon B 1989 *Rev. Sci. Instrum.* **60** 65
- Acher O, Koch S M, Omnes F, Defour M, Razeghi M and Drevillon B 1990b *J. Appl. Phys.* **68** 3564
- Acher O, Omnes F, Koch S M, Razeghi M, Drevillon B and Bigan E 1991 *Revue Technique Thomson-CSF* (Paris: Gauthier-Villars)
- Acher O, Omnes F, Razeghi M and Drevillon B 1990c *Mater. Sci. Eng. B* **5** 223
- Acosta-Ortiz S E and Lastras-Martinez A 1987 *Solid State Commun.* **64** 809
- Agranovich V M and Ginzburg V L 1984 *Spatial Dispersion in Crystal Optics and Theory of Excitons* (Berlin: Springer)
- Aoyagi Y, Doi A, Iwai S and Namba S 1987 *J. Vac. Sci. Technol. B* **5** 1460
- Asano S 1979 *Appl. Opt.* **18** 712
- Asano S and Yamamoto G 1975 *Appl. Opt.* **14** 29
- Aspnes D E 1983 *J. Physique Coll. C* **10** 3
- Aspnes D E 1985 *J. Vac. Sci. Technol. B* **3** 1498
- Aspnes D E 1988a *Appl. Phys. Lett.* **52** 957
- Aspnes D E 1988b *Proc. SPIE* **946** 84
- Aspnes D E, Chang Y C, Studna A A, Florez L T, Farrell H H and Harbison J P 1990 *Phys. Rev. Lett.* **64** 192
- Aspnes D E, Colas E, Studna A A, Bhat R, Koza M A and Keramidas V G 1988a *Phys. Rev. Lett.* **61** 2782
- Aspnes D E, Harbison J P, Studna A A and Florez L T 1987 *Phys. Rev. Lett.* **59** 1687
- Aspnes D E, Harbison J P, Studna A A, Florez L T and Kelly M K 1988b *J. Vac. Sci. Technol. B* **6** 1127
- Aspnes D E and Studna A A 1985 *Phys. Rev. Lett.* **54** 1956
- Aspnes D E, Studna A A, Florez L T, Chang Y C, Harbison J P, Kelly M K and Farrell H H 1989 *J. Vac. Sci. Technol. B* **7** 901
- Azzam R M A 1977 *Opt. Commun.* **20** 405
- Azzam R M A 1981 *J. Opt. (Paris)* **12** 317
- Azzam R M and Bashara N M 1977 *Ellipsometry and Polarized Light* (Amsterdam: North-Holland)
- Barber P W and Wang D S 1978 *Appl. Opt.* **17** 797
- Berkovits V L, Ivantsov L F, Makarenko I V, Minashvili T A and Safarov V I 1987 *Solid State Commun.* **64** 767
- Berreman D W 1970 *J. Opt. Soc. Am.* **60** 499
- Borensztein Y, Jebari M, Lopez-Rios T and Vuye G 1988 *Europhys. Lett.* **7** 617
- Born M and Wolf E 1970 *Principles of Optics* (New York: Pergamon)
- Briones F and Horikoshi Y 1990 *J. Appl. Phys.* **29** 1014
- Butler J F, Bottka N, Sillmon R S and Gaskill D K 1986 *J. Crystal Growth* **77** 163
- Camassel J, Auvergne D and Mathieu H 1975 *J. Appl. Phys.* **46** 2683
- Chiu T H 1989 *Appl. Phys. Lett.* **55** 1244
- Colas E, Aspnes D E, Bhat R, Studna A A, Harbison J P, Florez L T, Koza M A and Keramidas V G 1991 *J. Crystal Growth* **107** 47
- Colas E, Aspnes D E, Bhat R, Studna A A, Koza M A and Keramidas V G 1988 *J. Crystal Growth* **93** 931
- Colas E, Aspnes D E, Bhat R, Studna A A, Koza M A and Keramidas V G 1989 *J. Crystal Growth* **94** 613
- Collins R W 1989 *Advances in Disordered Semiconductors* vol I (Singapore: World Scientific)

- Del Sole R 1981 *Solid State Commun.* **37** 537
- Del Sole R and Selloni A 1984 *Solid State Commun.* **9** 825
- Donnelly V M and Karlicek R F 1982 *J. Appl. Phys.* **53** 6399
- Drevillon B 1989 *J. Non-Cryst. Solids* **114** 139
- Drevillon B, Parey J Y, Stchakovsky M, Benferhat R, Josserand T and Schlayen B 1989 *Proc. SPIE* **1188** 174
- Drevillon B, Perrin J, Marbot R, Violet A and Dalby J L 1982 *Rev. Sci. Instrum.* **53** 969
- Foxon C T and Joyce B A 1978 *J. Crystal Growth* **44** 75
- Gaskill D K, Kolubayev V, Bottka N, Sillmon R S and Butler J E 1988 *J. Crystal Growth* **93** 127
- Haigh J 1983 *J. Mater. Sci.* **18** 1072
- Harris J J, Joyce B A and Dobson P J 1981 *Surf. Sci.* **103** L90
- Hottier F, Hallais J and Simonet F 1980 *J. Appl. Phys.* **51** 1599
- Jasperson S N and Schnatterly S E 1969 *Rev. Sci. Instrum.* **40** 761
- Jonsson J, Deppert K, Jeppesen S, Paulsson G, Samuelson L and Schmit P 1990 *Appl. Phys. Lett.* **56** 2414
- Kittel C 1976 *Introduction to Solid State Physics* (New York: Wiley)
- Koch S M 1988 *PhD Thesis* Stanford University
- Koch S M, Acher O, Omnes F, Defour M, Drevillon B and Razeghi M 1990 *J. Appl. Phys.* **68** 3364
- Koch S M, Acher O, Omnes F, Defour M, Drevillon B and Razeghi M 1991 *J. Appl. Phys.* **69** 1389
- Lee P W, Omstead T R, McKenna D R and Jensen K F 1987 *J. Crystal Growth* **85** 165
- Lee P W, Omstead T R, McKenna D R and Jensen K F 1988 *J. Crystal Growth* **93** 134
- Manghi F, Del Sole R, Molinari E and Selloni A 1989 *Surf. Sci.* **211/212** 518
- Martines T and Whitehouse C R 1989 *Proc. 2nd Int. CBE Conf. (Houston)*
- Mashita M, Origuchi S, Shimazu M, Kamon K, Mihara M and Ishii M 1986 *J. Crystal Growth* **77** 194
- Maurel P, Bove P, Garcia J C and Razeghi M 1990 *Semicond. Sci. Technol.* **5** 638
- McIntyre J D E and Aspnes D E 1971 *Surf. Sci.* **24** 417
- Ohlidal I and Lucks F 1972 *Opt. Acta* **19** 817
- Olson J M and Kibbler A 1986 *J. Crystal Growth* **77** 182
- Palik E D 1985 *Handbook of Optical Constants of Solids* (New York: Academic)
- Paulsson K, Deppert S, Jeppeson S, Jonsson J, Samuelson L and Schmidt P 1990 *J. Crystal Growth* **105** 312
- Pickering C, Greef R and Hodge A M 1989 *Semicond. Sci. Technol.* **4** 574
- Razeghi M 1989 *The MOCVD Challenge: Volume 1: A Survey of GaInAsP-InP for Photonic and Electronic Applications* (Bristol: Hilger)
- Razeghi M and Acher O 1989 *Proc. NATO Studies 1989*
- Razeghi M, Defour M, Blondeau R, Omnes F, Maurel P, Acher O, Brilouet F, Fan J C and Salerno J 1988a *Appl. Phys. Lett.* **53** 2389
- Razeghi M, Defour M, Omnes F, Maurel P, Bigan E, Acher O, Nagle J, Brilouet F and Portal J C 1988b *J. Crystal Growth* **93** 776
- Razeghi M, Defour M, Omnes F, Maurel P, Chazelas J and Brilouet F 1988c *Appl. Phys. Lett.* **53** 725
- Razeghi M, Defour M, Omnes F, Nagle J, Maurel P, Acher O, Huber A and Mijuin D 1988d *Mater. Res. Soc. Symp. Proc.* **126** 143
- Razeghi M, Machado A, Koch S M, Acher O, Omnes F and Defour M 1990 *SPIE Conf. (Aachen, 28 October–2 November 1990)*
- Razeghi M, Omnes F, Blondeau R, Maurel Ph, Defour M, Acher O, Vassilakis E, Mesquida G, Fan J C and Salerno J 1989 *Appl. Phys. Lett.* **65** 4066
- Richter W, Kurpas P, Lückerath R and Motzkus M 1991 *J. Crystal Growth* **107** 13

- Samuelson L, Deppert K, Jeppesen S, Jonsson J, Paulsson G and Schmidt P 1991  
*J. Crystal Growth* **107** 68
- Schaffer W J, Lind M D, Kowalczyk S P and Grant R W 1983 *J. Vac. Sci. Technol. B* **1**  
688
- Sell D D 1973 *Surf. Sci.* **37** 876
- Studna A A, Aspnes D E, Florez L T, Wilkens B J, Harbison J P and Ryan R E 1989 *J.  
Vac. Sci. Technol. A* **7** 3291
- Sugiyama K 1986 *J. Crystal Growth* **75** 435
- Tsang W T, Chiu T H, Cunningham J E and Robertson A 1987 *Appl. Phys. Lett.* **50** 1376
- Uzunoglu N, Evans B G and Holt A R 1976 *Electron. Lett.* **12** 312

## ***Ex situ* Characterization Techniques**

*Ex situ* measurements are very important to characterize material quality for predicting device performance and for optimizing growth conditions. This chapter introduces the most commonly used *ex situ* characterization techniques for routine measurement. Chemical bevel revelation and DLTS are used to obtain information about defects in the material. X-ray diffraction is a powerful tool for structural characterization. Photoluminescence is an optical characterization technique which provides information about optical properties such as bandgap energy, quantum-well energies, and deep-level energies. Electrochemical capacitance–voltage, photovoltage spectroscopy and Hall measurements can be used to obtain information about electrical properties, such as carrier concentration profiles, mobility and compensation ratis. Various thickness-measurement techniques can be used to measure the thickness of epilayers or steps.

### **4.1 CHEMICAL BEVEL REVELATION**

The bevel revelation technique is a structural characterization tool developed for interface characterization of heterostructures and multilayers. It performs this task by magnifying and revealing the defect distribution of any grown layer using a combination of apparatus, that can create a bevel of a fraction of a degree, and chemical revelation baths. The system is simple to use and quick enough that it is viable as a standard characterization to complement Hall, photoluminescence and x-ray diffraction measurements.

The bevel revelation technique is capable of tracing any build-up of dislocations to its origins as well as detecting crystal breakdown through mismatch or other growth parameters. It is also used for determining substrate problems from polishing or cleaning deficiencies.

#### **4.1.1 Principle of magnification**

The idea behind magnification is that by creating a bevel, the effective distance between interfaces can be increased. As an example, if we take two layers of

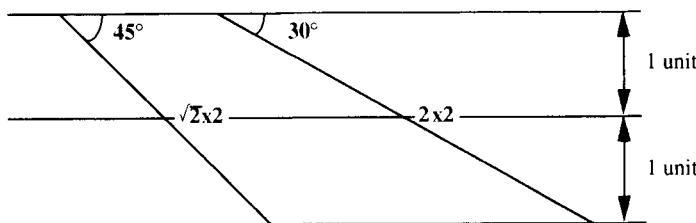


**Figure 4.1** Principle of magnification in bevel revelation.

unit thickness, the distance between interfaces is increased by a factor of  $\sqrt{2}$  and two by making a bevel of angle  $45^\circ$  and  $30^\circ$  respectively, as shown in figure 4.1.

Taking this to the limit, angles of  $0.005^\circ$  or less, which equate to a magnification factor of 10 000, can be achieved. This makes investigation of the fine layers much easier. To produce such slight gradients, a chemical etch is necessary since mechanical polishing will introduce extrinsic defects.

#### 4.1.2 Description

These fine bevels are achieved using a special apparatus as shown in figure 4.2. The apparatus consists of a simple etch system with a sophisticated gas controlling system. Two vertically mounted, gas-tight Pyrex tubes are connected by a three-way tap capable of connecting either chamber with a drain or connecting the two chambers directly. A precisely regulated gas pumping system is used to pump the solutions from the right to the left chamber at a constant rate. The constant rate is assured by use of a mass flow controller. This is complemented by a switching manifold comprising pneumatic three-way valves, which are able to very rapidly reverse or stop the gas feed, minimizing the changeover time when the flow direction is reversed. The pumping gas is nitrogen which assures that sample oxidation is kept to a minimum.

Prior to carrying out the experiment, it is sometimes necessary to put the samples through rigorous cleaning and deoxidation procedures for reproducible results. If a sample has an oxide layer on its surface the chemical attack will be uneven and unpredictable. As a result it gives a meaningless result.

Bromine/methanol solution is used as the etching solution for most III-V semiconductors and is placed in the chamber on the right. The sample is vertically attached on the holder of the chamber on the left above a protective layer of methanol. A protective resin is used to attach the sample and also cover half of its surface so as to leave a reference layer. The sample can be as small as 1 cm in length and 4 mm in width. The ability to use such small-size samples is an important factor in the basic research, where growth runs are made using substrate fragments of not greater than  $10\text{ cm}^2$  on which four or five destructive or non-destructive characterizations will be made and possibly

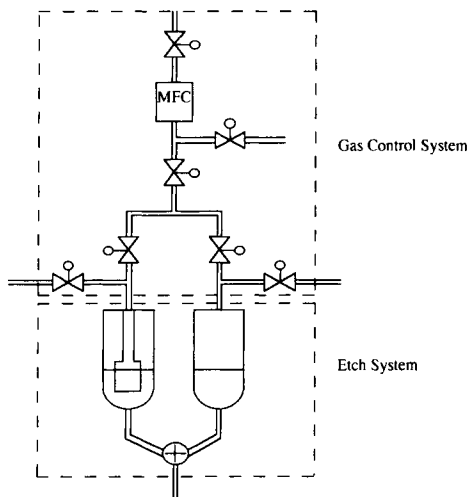


**Figure 4.2** Chemical bevel apparatus.

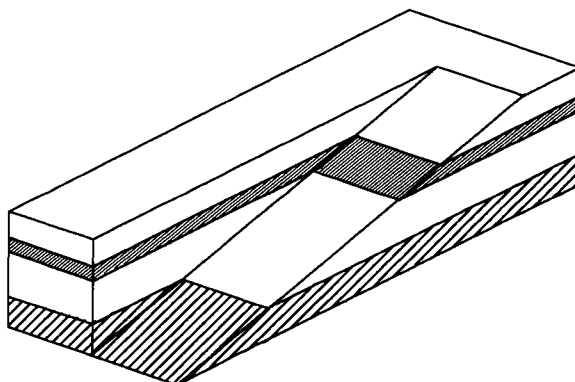


**Figure 4.3** A typical beveled sample with a reference layer.

devices processed.

By pumping the bromine solution in and out of the left-hand reservoir, a bevel is formed as a result of the bromine solution being in contact with the sample for longer at its base than at its head. A typical bevel of constant gradient with a parallel reference level is shown in figure 4.3. In this condition, the different refractive indices of the III–V compounds make it possible to see clearly the material interfaces. Changes in material appear as changes in brightness.

The angle of the bevel can be controlled by varying the concentration of bromine/methanol solution and pumping speed. An increased concentration of bromine will produce a stronger attack and a greater bevel angle (smaller magnification). On the other hand, the pumping speed works in the opposite

sense in that an increase in speed produces a shallower attack since the sample would remain in the dissolution mixture for a shorter time (larger magnification). Of the two, the pumping speed offers a more precise control of the bevel angle mainly because the mass flow controller gives a very precise control of the pumping speed.

The etched samples are then studied under optical microscopes for more detail. Two microscopes are generally used to carry out the investigation. An ordinary contrast microscope is used when differentiating areas of different brightness and obvious features on the surface such as steps. A Nomarski-type microscope is used in situations where greater sensitivity to surface texture changes is required. A typical magnification is 250, which coupled with the bevel magnification will give an effective magnification factor in excess of a million. One advantage of this technique is that, by adjusting the magnification, an overall view as well as a small part of the material can be examined.

#### 4.1.3 Bath revelation

Defects are revealed using a variety of baths and etching conditions. Revelation baths have a preferential rate of attack for certain crystal faces/planes. If a crystal structure is subjected to an environment which removes atoms from its surface, then the rate of removal around the defect may be different from that of the perfect surrounding matrix. The possible causes of this difference can be attributed to lattice distortion and strain field of the defect geometry of planes associated with the defect and the concentration of impurity atoms at the dislocations and defects, which change the chemical composition of the material in that region.

The type of etch feature formed depends on the attack of the bath. For those where material removal in the defect is more rapid than the surroundings, etch pits result, while if etching is slower in the defect, hillocks will become apparent. Therefore, the defects are prominent and the level of dislocations due to the growth conditions or substrate deficiencies can be assessed. In addition, each bath requires that a certain thickness of the layer is etched away before these growth features are revealed. This thickness varies with the material to be characterized and the bath used. Through the use of a variety of baths and etching conditions, the weakness in the system can be reduced and even the finest layers can be characterized.

The baths currently being used most widely are AB, H, L and DSL baths. The properties and composition of these baths are as follows:

- AB bath (Abrahams and Buiocchi 1965) is a chemical mixture between  $H_2O/AgNO_3/HF$  and  $H_2O/CrO_3$ . It preferentially attacks GaAs material but also etches related compounds at a slower rate. It is, however, not particularly suitable for the purpose of GaAs materials because of its high etch rate and the need for a strong light source for preferential etching.

- DSL bath (Weyher and Van de Ven 1983, 1986, 1988), a HF/CrO<sub>3</sub>/H<sub>2</sub>O mixture, is being widely used as the replacement bath to AB.
- H bath (Huber *et al* 1984), which consists of one volume of HBr and two volumes of H<sub>3</sub>PO<sub>4</sub>, attacks only InP and as it has an etch rate of about 1 μm min<sup>-1</sup>, it can make successful revelations of very thin layers (Huber *et al* 1983).
- L bath (Lourenco 1984), consisting of 200 cm<sup>3</sup> H<sub>2</sub>O, 16 g KOH, and 1 g K<sub>3</sub>Fe(CN)<sub>6</sub>, is a relatively recent bath which preferentially attacks {110} GaInAsP. It has also been found to be effective for InP, GaInAs and GaInP revelation. Due to its very low etch rate and strong preferentiality, when used under illumination, it is ideal for this characterization.

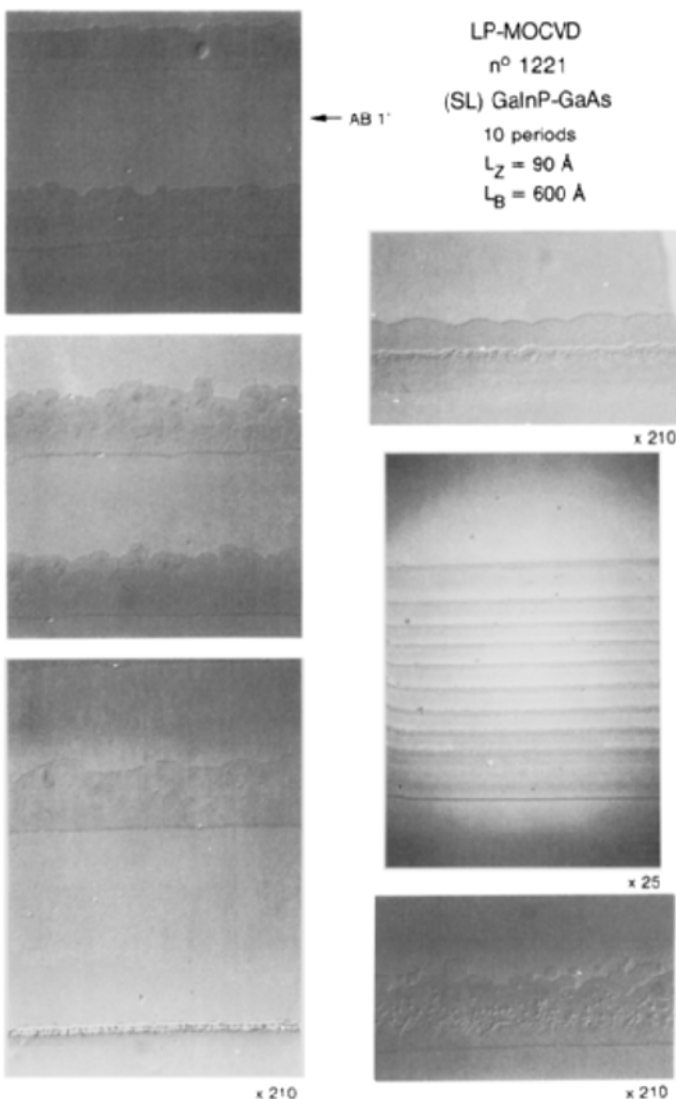
For all but H bath, a strong white light illumination is used to promote the preferential nature of the bath allowing the same degree of revelation with a much smaller attack.

Figure 4.4 shows the final result of a GaAs/GaInP sample after using chemical bevel revelation. For this specific experiment, DSL bath was used for 4 min. A detailed defect distribution profile is obtained and interfaces are easily distinguishable. Figure 4.4 also shows the overall view of the sample but with higher optical magnification a small specific part of the sample can also be studied.

Such powerful, flexible and yet simple qualities of the bevel revelation technique have led to many research uses. Huber *et al* (1987) used the technique to study the influence of As content on InP layer perfection. From the experiment, it was concluded that improvement of crystal quality seems to be critical in the case of LP-MOCVD if the As concentration is above  $3 \times 10^{19}$  cm<sup>-3</sup>. Huber *et al* (1984) also assessed the substrate quality by studying the depth of polishing damage as well as studying the quality of several quantum well (MQW) and superlattice (SL) structures such as GaInAs/InP MQW and Si δ-doped GaAs/AlGaAs SL. In the experiment with Si δ-doped GaAs/AlGaAs SL it was observed that the generation of some new defects occurs particularly in the δ-doped region of GaAs. This result was attributed to the formation of a small Si lattice when As vapour pressure is in excess, resulting in a locally disordered crystal.

## 4.2 DEEP-LEVEL TRANSIENT SPECTROSCOPY

Deep levels play a vital role in semiconductor technology. They may be intentionally added to control material and device characteristics, but in many cases they are undesirable defects. Deep-level transient spectroscopy (DLTS), originally proposed by Lang (1974), is a capacitance transient thermal scanning characterization method used to identify such deep levels in semiconductors. The technique exploits the properties of a potential barrier such as a Schottky



**Figure 4.4** View of GaAs/GaInP structure following chemical bevel revelation.

diode or p-n junction for the detection of these deep levels and it is on this fact that the high sensitivity and flexibility of DLTS is based.

DLTS displays the spectrum of traps as a function of temperature and this spectrum is used to extract information on energy, density and thermal emission properties of traps. The presence of each trap is indicated by a positive or negative peak as a function of temperature. The sign of each peak determines whether it is due to a majority- or minority-carrier trap and the height of the

peaks indicates the respective trap concentration. The positions of the peaks are determined by the integrator gate settings and the thermal emission properties of the traps. With a suitable choice of experimental parameters, the thermal emission rate, activation energy, concentration profile, and capture rate of each trap can be measured. In addition, it is also capable of detecting both radiative and non-radiative recombination centres over a wide range of depths within the bandgap.

In the following section, the basic concepts of the DLTS technique and the underlying semiconductor physics are presented.

#### 4.2.1 Deep levels

The electrical characteristics of semiconductors are controlled by foreign atoms or crystal defects sited within the regular semiconductor lattice. On a representative energy level diagram these atoms form discrete energy levels positioned in the forbidden bandgap. A certain amount of energy has to be gained or lost by a carrier positioned in a deep level in order to be excited to or from the bands.

Commonly, dopant atoms are intentionally added in order to make the semiconductor more conducting. These dopant atoms give rise to shallow levels positioned near to a band edge (within 0.1 eV) and are readily thermally ionized. The origin of deep levels is more complicated. They lie between 0.1 eV and mid-bandgap and are due to impurities and defects. Defect deep levels are the result of crystal imperfections, such as dislocations, stacking faults, precipitates, vacancies or interstitials. These imperfections may arise from: dopant atoms positioned substitutionally or interstitially, vacancies, host atoms on the wrong site in compound semiconductors (antisite defect) or damage induced by irradiation or ion-implantation. Impurity atoms may be contaminants from material growth or processing, oxygen or transition metals, for instance.

Deep levels may behave as carrier traps or as generation–recombination centres if they are near mid-bandgap. As traps, they can capture free carriers, thus compensating the shallow levels and reducing the effective doping density. This increases the resistivity of the material and could therefore have a detrimental effect. However, for very high levels of compensation the material acquires intrinsic-like properties. For example, III–V semiconductors may have resistivities greater than  $10^7 \Omega \text{ cm}$  and are said to be semi-insulating. Semi-insulating materials are essential for device substrates and therefore deep levels are deliberately introduced occasionally: chromium atoms are added to GaAs and Fe atoms are added to InP for this purpose.

Deep levels behaving as recombination centres may also be either beneficial or detrimental. They provide a path for the generation and recombination of electron–hole pairs across the entire bandgap. The performance of devices such as light emitting diodes (LEDs) and lasers requires radiative recombination; however, this process is degraded when deep levels form a parallel non-

radiative recombination path. On the other hand, such paths also provide a means of controlling minority carrier lifetimes. Gold, for example, is commonly intentionally added to silicon for this purpose. In these cases, the deep levels are desirable and beneficial.

Deep levels may be characterized by three properties: the activation energy ( $E_T$ ) which is related to the position of the level in the bandgap, its concentration ( $N_T$ ) and its capture cross-section ( $\sigma$ ) which provides a measure of the ability of the deep level to trap carriers. DLTS measures all of these properties directly.

#### 4.2.2 Generation of capacitance transients

In order to obtain information about an impurity level in a depletion region, the capacitance transient, associated with the transition from thermal equilibrium of the trap level occupation following an initial non-equilibrium condition, is used. The change in capacitance is a result of applying a bias pulse to introduce carriers and therefore change the electron occupation of a trap from the steady-state condition. As the system returns to its equilibrium, the capacitance returns to its quiescent value.

The change in capacitance transient can be explained in more detail using an example involving a metal–semiconductor (Schottky) barrier. When a metal comes into contact with a semiconductor to form a Schottky barrier there is a transfer of free charge from the region of semiconductor next to the barrier to regions away from it. This results in a depletion (space charge) region,  $W$ , which is given by

$$W = \sqrt{\frac{2\epsilon(V_D - V)}{qN}} \quad (4.1)$$

where  $\epsilon$  is the permittivity of the semiconductor,  $q$  the electronic charge,  $V_D$  the flat-band potential,  $V$  the applied potential across the barrier and  $N$  the effective doping density which should equal the shallow-level concentration compensated by any deep levels present.

The depletion region acts as a parallel plate capacitor of capacitance  $C$  given by

$$C = \epsilon A / W \quad (4.2)$$

where  $A$  is the area of the Schottky contact. The width of the depletion region and hence its capacitance as a function of the applied bias  $V$  is then given by

$$C = \sqrt{\frac{q\epsilon N A^2}{2(V_D - V)}} \quad (4.3)$$

Figure 4.5(a) shows a Schottky barrier under reverse biased quiescent state. The Fermi level, the statistical energy level which governs the probability of any other level being empty or full, remains flat across the barrier. The semiconductor

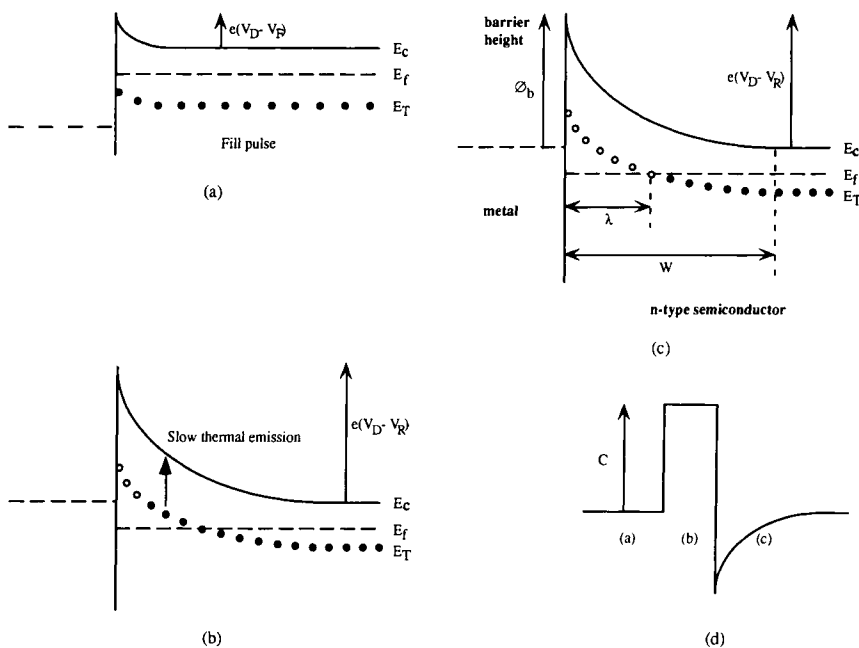


**Figure 4.5** Capacitance variation corresponding to when (a) a quiescent reverse bias  $V_R$  is applied across the Schottky barrier, (b) a forward bias pulse  $V_F$  fills all the traps and (c) the reverse bias pulse  $V_R$  slowly emits the trapped electrons in the deep levels.

is assumed to be an n-type semiconductor with a single deep level behaving as a donor electron trap. The trap is empty and positively charged above the Fermi level and full and neutral below the Fermi level. The transient is produced in a controlled manner by applying a forward bias  $V_F$  to fill intentionally all the traps through the capture process shown in figure 4.5(b). The forward bias decreases the depletion width and so increases the capacitance as given by equation (4.2). When a reverse bias  $V_R$  is then applied, the depletion width instantaneously readjusts back to the quiescent width and as a result the capacitance decreases. In this new position some of the full deep levels find themselves above the Fermi level but the trapped electrons do not emit instantaneously because the response time of trapped electrons in the deep level is relatively slow and very temperature sensitive unlike free electrons. Therefore, the capacitance does not immediately return to its original value. The trapped electrons above the Fermi level are released by thermal emission at temperatures where sufficient excitation energy is present as shown in figure 4.5(c). The steady-state condition is reached when all deep levels above the Fermi level have lost their electrons. Figure 4.5(d) shows the variation of the observed capacitance in figures 4.5(a), (b), and (c).

The usual method for measuring the capacitance transient is the boxcar

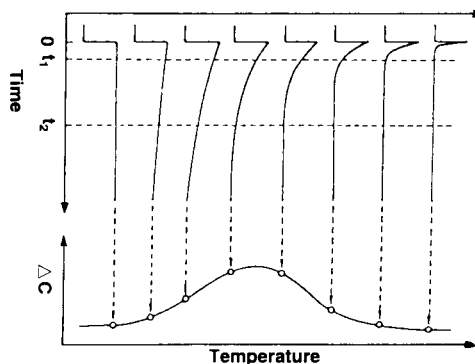


**Figure 4.6** The temperature development of a capacitance transient observed through a rate window produces a DLTS peak (Lang 1974).

technique. The transient is measured conventionally between two sampling points at times  $t_1$  and  $t_2$ . The time period between the sampling points is referred to as the rate window. Because deep-level emission is thermally activated, the time constant of the transient will change with temperature. As a result, as the temperature increases, the shape of the transient changes in a manner characteristic of a particular trap.  $\Delta C$  will be small at high temperature since all the traps are readily ionized and small at low temperatures since few will be ionized. However, when the rate window matches the maximum thermal emission rate of the deep level,  $\Delta C$  will be at a maximum. Hence an output of  $\Delta C$  against temperature will show a DLTS peak (figure 4.6), which is characteristic of the trap being studied. The peak occurs at

$$\frac{1}{e_n} = \frac{t_1 - t_2}{\ln(t_1/t_2)}. \quad (4.4)$$

Figures 4.7 and 4.8 also illustrate, in four steps, how the capacitance transients vary between a majority- and minority-carrier trap. For simplicity of explanation, only those traps in the low-doped p side of an asymmetric n<sup>+</sup>p diode will be considered and in both figures the band bending due to the junction electric field is omitted. Furthermore, only one emission rate will be considered for a given trap since for most centres one emission rate usually dominates. Generally, the electron emission rate for trap levels in the upper half of the bandgap is much higher than the hole emission rate, and similarly the hole emission rate is much higher than the electron emission rate for trap levels in the lower half of the bandgap.

Figure 4.7 shows an electron (minority-carrier) trap, which is normally empty of electrons and thus capable of capturing them. Step I shows the reverse-biased quiescent state of the diode and in step II, an injection pulse is applied which momentarily injects electrons into the region of observation. At the same time, the injection pulse allows filling of the electron trap through the capture process.

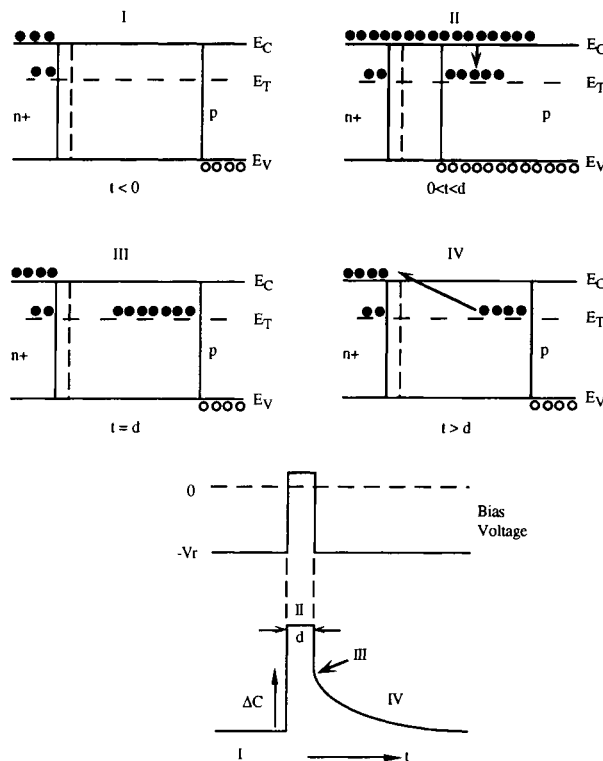


**Figure 4.7** Schematic summary of the emission and capture processes of an electron (minority-carrier) trap in p-type material and the resulting capacitance transient.

After a reverse-biased pulse is applied, as in step III, the trapped electrons are released by thermal emission as shown in step IV. The steady-state condition is reached when all deep levels within the depletion region have lost their electrons. Figure 4.7 also shows the typical time dependence involved in pulsed bias capacitance transients for minority-carrier traps.

Figure 4.8 shows the analogous majority-carrier pulse sequence for a hole (majority-carrier) trap. A hole trap is a trap which is normally full of electrons and is capable of capturing holes, i.e. recombination. The four processes previously discussed are shown. In this case, the pulse momentarily reduces the diode bias and introduces only holes (majority carriers) into the region of observation. The appropriate time dependence involved in pulse bias capacitance transients for majority-carrier traps is also shown in figure 4.8. It is therefore possible to distinguish from the capacitance transients whether the deep level is a minority- or a majority-carrier trap.

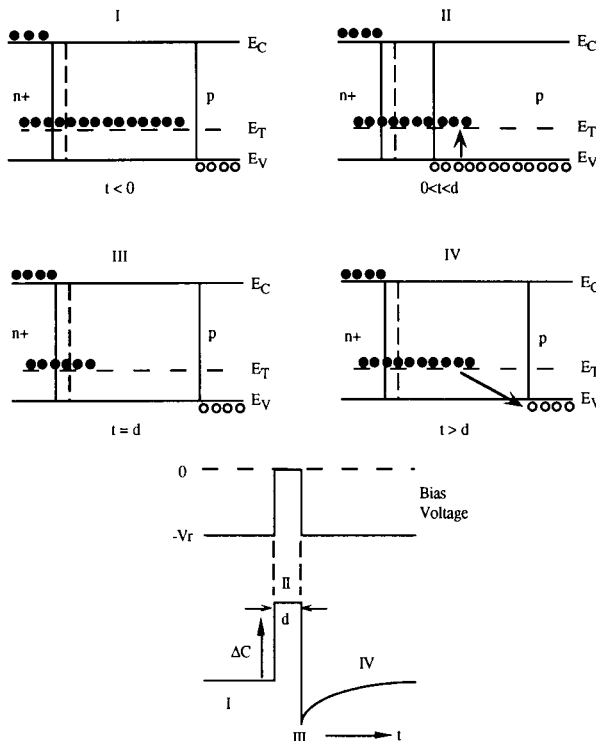


**Figure 4.8** Schematic summary of the emission and capture processes of a hole (majority-carrier) trap in p-type material and the resulting capacitance transient.

#### 4.2.3 Determination of trap parameters

As mentioned before, the DLTS is capable of determining a number of trap parameters such as activation energy, concentration of traps, capture cross-section and capture rates. These are very important parameters in determining the quality of a material and performance of a device. Therefore, the principle behind the use of DLTS for determining these specific parameters will be covered in the following section.

##### (a) Trap activation energy

The most unique and essential quality of DLTS is the strong temperature dependence of the thermal emission rates. DLTS can observe a response peak of a transient only at the temperature where the trap emission rate is within an emission rate window. The transients are processed with the help of a signal average to provide an output signal, as a function of temperature.

To determine the energy level, different emission rate windows are selected for each thermal scan which moves the peak to different temperatures. Figure 4.9 shows these multiple DLTS peaks of a silicon sample using a Polaron 4600 DLTS system. The emission rate is proportional to a Boltzmann factor  $k$ , and thus

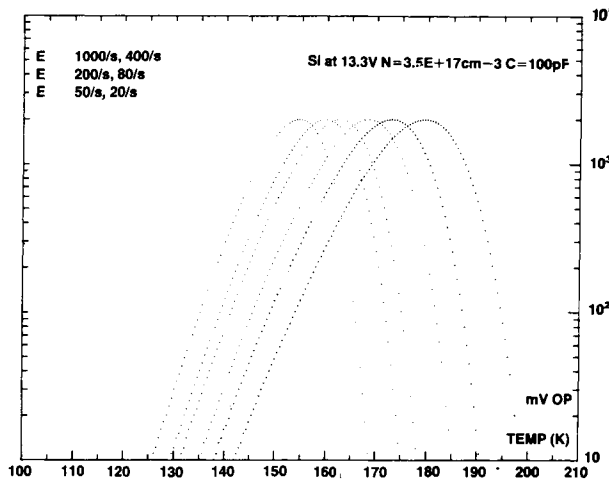


**Figure 4.9** An example of DLTS peaks acquired from a silicon sample.

depends exponentially on the energy difference between the trap level and the conduction band, in the case of electron emission, and the trap level and the valence band, in the case of hole emission. The exact emission rate is given by

$$e = \frac{N_0 \sigma V_{th}}{g} \exp\left(\frac{\Delta E}{kT}\right) \quad (4.5)$$

where  $N_0$  is the effective density of states in the band associated with the trapped carriers,  $\sigma$  is the capture cross-section,  $V_{th}$  is the thermal velocity and  $g$  is the degeneracy of the level. If  $\sigma$  is independent of temperature, then the activation energy  $\Delta E$  represents the energy of the trap from the band edge to which carriers are emitted.

In equation (4.5) the product  $N_0 V_{th}$  is proportional to  $T^2$ , therefore the peak shift is used to construct an Arrhenius plot of  $\ln(e/T^2)$  versus  $1/T$  to calculate the activation energy from the slope of the plot. The activation energy  $\Delta E$  is used to identify the trap present.  $\Delta E$  can be viewed as the deep level's 'label'. However, there is no theoretical method of relating measured activation energies to any particular deep level. Therefore, in most cases, the deep level is identified by referring to published data. Figure 4.10 shows an Arrhenius plot of the silicon sample of figure 4.9 and its comparison with the library of known deep levels.

#### (b) Trap concentration

The concentration of the trap ( $N_T$ ) can be obtained directly from the capacitance change corresponding to completely filling the trap with a large enough pulse. The relationship for an electron trap in an  $n^+$ p step junction is

$$N_T = \frac{2\Delta C}{C} (N_A - N_D) \quad (4.6)$$

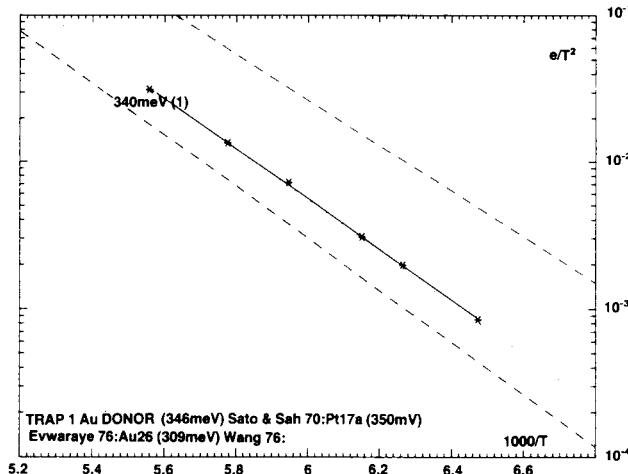


**Figure 4.10** The activation plot of the peaks in figure 4.9 and its comparison with the library of known deep levels.

where  $N_T$  is the trap concentration,  $\Delta C$  is the capacitance change due to a saturating injection pulse,  $C$  is the capacitance of the diode under quiescent reverse-biased conditions and  $N_A - N_D$  is the net acceptor concentration on the p side of the junction where the trap is observed. It should be stressed that these relationships apply accurately only under the following conditions:

- the trap and the doping density are uniformly distributed, with a field-independent emission rate
- only a single emission process occurs at the deep level
- $N_T \ll N_A - N_D$ .

### (c) Capture cross-section

The third important parameter to be derived is the capture cross-section of the traps,  $\sigma_n$  or  $\sigma_p$ . The widespread practice is to extrapolate the Arrhenius plot to  $T = \infty$  and calculate  $\sigma_n$  from the y-axis intercept. However, this method can give an apparent capture cross-section which is normally very different from the true cross-section. Taking a thermodynamic approach, the effective capture cross-section  $\sigma_{n,\text{eff}}$  can be given by (Schroder 1990)

$$\sigma_{n,\text{eff}} = \sigma_n X_n \quad (4.7)$$

where  $\sigma_n$  is the true capture cross-section and  $X_n$  is defined as

$$X_n = \left( \frac{g_0}{g_1} \right) \exp \left( \frac{\Delta S_{na}}{k} \right) \quad (4.8)$$

where  $g_0$  is the degeneracy of the deep level unoccupied by an electron,  $g_1$  is the degeneracy of the deep level occupied by one electron and  $\Delta S_{na}$  is

the entropy change due to atomic vibrational changes. As a result, effective cross-sections larger by factors of 50 or more than true cross-sections are not uncommon (Lang *et al* 1980). Further inaccuracies are introduced if  $\sigma$  is temperature or electric-field dependent. A good discussion of energy levels, enthalpies, entropies, capture cross-section, etc, can be found in the work of Lang *et al* (1980) and further thermodynamic derivations can be found in the work of Thurmond (1975) and Van Vechten and Thurmond (1976).

A more accurate method of determining the capture cross-section is through the filling pulse method. The idea behind this method is that the capture rate varies depending on  $\sigma_n$ . If a Schottky barrier is under forward bias, all the majority-carrier traps are available for filling but for a certain time of the forward pulse only some of the traps will actually fill. Traps with a large capture cross-section are more likely to fill within a short pulse than those with a small capture cross-section.

To calculate  $\sigma_n$  the standard DLTS temperature scan is repeated at a fixed rate window, but with a varying fill pulse width. As the pulse width increases, the peak height also increases until it eventually reaches a maximum. At this point all the traps are able to fill within one pulse length (saturation). The final DLTS plot consists of peaks displaced vertically. In this manner the capture cross-section is determined from a capture, not an emission, process. The measurement is more difficult to implement because capture times are much shorter than emission times and the instrumentation is more demanding.

Standard DLTS processing is performed on the transient. The peak height is related to the fill pulse by

$$(1 - f) = \exp(-t/\tau) \quad (4.9)$$

where  $f$  is the peak height for one pulse width/saturated peak height,  $\tau$  is the characteristic filling time and  $t$  is the pulse width. The capture cross-section is then calculated from the slope of  $\ln(1 - f)$  plotted against  $t$  since the slope is  $1/\tau$  and

$$\sigma_n = 1/\tau V_{th} n \quad (4.10)$$

where  $n$  is the effective doping density.

#### (d) Capture rate

Using the same filling pulse method as used for capture cross-section, the capture rate can be determined. The capture process into an initially empty trap is described by (Miller *et al* 1977)

$$N(t) = N_T [1 - \exp(-ct)] \quad (4.11)$$

where  $N(t)$  is the density of traps filled by a bias pulse of width  $t$ ,  $N_T$  is the total trap density and  $c$  is the capture rate of the trap.  $N(t)$  values are obtained from the peak heights at different widths of the filling pulse.  $N_T$  corresponds to the pulse width which saturates all the traps. The capture rate is then obtained from the plot of  $\ln[(N_T - N(t))/N_T]$  against  $t$ .

## 4.3 X-RAY DIFFRACTION

### 4.3.1 Introduction

X-ray diffraction is a well established and commonly used analytical tool for the non-destructive characterization of semiconductor structure. In principle, the interpretation of measured diffraction patterns is simple. Angular positions of the Bragg peaks of the epilayers and substrates are related to the lattice constant of the material. The alloy composition of the ternary alloy can be determined from the lattice constant by using Vegard's law.

An x-ray diffraction measurement, of course, can reveal a great deal of information about the structure of a compound semiconductor such as III–V or II–VI materials. In particular, the interference fringe structure accompanying the Bragg peak from a thin epilayer permits measurement of the layer thickness with an accuracy of one or two per cent, depending on the quality of the material itself and the precision of the diffraction data. In this section we describe related theories behind x-ray diffraction and the simple analysis used for interpretation of the measured diffraction data; moreover, a dynamical x-ray diffraction simulation method based on the solution of Tagaki–Taupin equations is presented. An example of the characterization of superlattices is also included in the last part to describe the importance of dynamical simulation.

### 4.3.2 Bragg's law

Due to W H Bragg and W L Bragg (1913a,b) an improved experimental technique contributed greatly to the development of knowledge in the fields of the wave nature of x-rays and the periodic structure of crystals.

Crystal lattices can be modelled as three-dimensional gratings. A linear diffraction grating can be regarded as a special case of a one-dimensional grating. Based on this point of view a three-dimensional grating may be defined as a spatial distribution of matter for which the scattering power is a periodic function of three-dimensional space, i.e.,  $\Psi(\mathbf{r}) = \Psi(\mathbf{r} + L_1\mathbf{a}_1 + L_2\mathbf{a}_2 + L_3\mathbf{a}_3)$ , where  $L_1$ ,  $L_2$  and  $L_3$  are integers. With grating spaces  $\mathbf{a}_1$ ,  $\mathbf{a}_2$  and  $\mathbf{a}_3$ , which are the periods of the different axes, the three-dimensional grating can thus be considered as consisting of three sets of one dimensional linear gratings. To find the diffraction maximum according to the three-dimensional case, the Laue vector equations are employed as follows for each of the one-dimensional linear gratings:

$$\begin{aligned}\mathbf{a}_1 \cdot (\mathbf{k}_{H_1 H_2 H_3} - \mathbf{k}_0) &= H_1 \\ \mathbf{a}_2 \cdot (\mathbf{k}_{H_1 H_2 H_3} - \mathbf{k}_0) &= H_2 \\ \mathbf{a}_3 \cdot (\mathbf{k}_{H_1 H_2 H_3} - \mathbf{k}_0) &= H_3\end{aligned}\quad (4.12)$$

where  $\mathbf{k}_0$  is the wavevector of the incident x-ray beam and  $\mathbf{k}_{H_1 H_2 H_3}$  is that of the diffracted beam. The quantities  $H_1$ ,  $H_2$  and  $H_3$ , being integers, are Miller

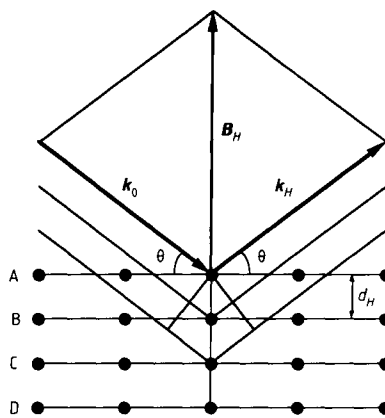


**Figure 4.11** Diffraction of x-rays by a section of a crystal with lattice planes spaced a distance  $d_H$  apart. The atoms are arranged on a set of parallel planes A, B, C, ... normal to the plane of the drawing.

indices of a family of lattice planes and are associated with each diffraction maximum. Equation (4.12) can be further simplified as a vector equation (Laue vector equation):

$$\mathbf{k}_H - \mathbf{k}_0 = \mathbf{B}_H. \quad (4.13)$$

In (4.13), the vector  $\mathbf{B}_H = \mathbf{B}_{H_1 H_2 H_3} = H_1 \mathbf{b}_1 + H_2 \mathbf{b}_2 + H_3 \mathbf{b}_3$  is normal to the  $(H_1 H_2 H_3)$  planes and its length is equal to the reciprocal of the spacing between planes, where  $\mathbf{b}_1, \mathbf{b}_2, \mathbf{b}_3$  is the reciprocal unit vector set of  $\mathbf{a}_1, \mathbf{a}_2, \mathbf{a}_3$ . Since  $|\mathbf{k}_H| = |\mathbf{k}_0| = 1/\lambda$ , the Laue vector equation expresses the fact that the only diffracted beam ( $\mathbf{k}_H$ ) formed is that shown in figure 4.11, namely one making a reflected angle  $\theta$  equal to the incident angle  $\theta$ . In other words, one may consider the diffracted beam to be produced by a reflection of the incident beam in the family of planes normal to  $\mathbf{B}_H$ . Equating the magnitude of the two sides of (4.13), the Bragg equation can be derived

$$2 \sin \theta_B / \lambda = 1/d_H = n/d_h \quad (4.14)$$

where  $\theta_B$  is thus complementary to the angle of incidence or reflection and is called the Bragg glancing angle. The magnitude of the right-hand side of (4.13) is  $1/d_{H_1 H_2 H_3}$  or  $n/d_{h_1 h_2 h_3}$  when  $H_1, H_2, H_3$  have a common integral factor  $n$ , and  $h_1, h_2, h_3$  are prime numbers and  $d_{h_1 h_2 h_3}$  is the spacing between two consecutive planes between  $(h_1 h_2 h_3)$  planes. The wavelength of the x-ray is of the order of  $10^{-8}$  cm, whereas the smallest lattice period lies in the range  $10^{-8} \sim 10^{-5}$  cm. Accordingly, it may be expected that the scattering angles for the diffraction maxima are large enough to be measured.

### 4.3.3 Bond's method

The Bond method (Bond 1960) presents a way to determine the lattice constant by measuring the Bragg angles at two complementary positions ( $180^\circ$  azimuthal angle difference), which cancel the errors due to the misorientation of the sample and the x-ray systems. Lattice constants can be determined up to a few parts in a million for highly perfect crystals. This accuracy is comparable to the accuracy with which wavelengths of x-rays were determined. In the measurement, the axis of crystal rotation ( $\theta$ ) must be perpendicular to the plane of incidence within a few arc seconds. This alignment criterion may be discussed in terms of the non-orthogonality of the incident beam with the crystal rotation axis  $\theta$  (or  $\omega$ ), called the beam tilt, and any lack of parallelism of the reflecting planes with the crystal rotation axis, called crystal tilt.

The main errors which may be caused by the system itself and non-optimized measurements include:

- angle reading error
- eccentricity error
- absorption error
- crystal tilt error
- axial divergence error (or beam tilt error).

Figure 4.12 shows the spatial configuration of the diffractometer and various movements. Based on Bond's description, optimization is necessary to bring the scattering vector into the scattering plane. The scattering vector of a particular set of lattice planes is perpendicular to these planes. In the Bragg condition (equation (4.14)), the scattering vector bisects the incident and diffracted beams. The scattering plane is in a plane which is perpendicular to the goniometer rotation axis (see figure 4.13). Non-optimization results in a serious drop in intensity and resolution. Rotating the sample around Phi or alternatively around R can bring the scattering vector into the scattering plane. The better the alignment the more accurate the measurement.

### 4.3.4 Simple analysis of x-ray diffraction

#### (a) Interface quality determination

The diffraction patterns for the accurate determination of alloy composition or lattice mismatch are usually obtained on a x-ray diffractometer. The process of measuring a lattice parameter is a very indirect one, and is fortunately of such a nature that high precision is fairly easily obtainable by x-ray diffraction. The parameter  $a$  of a cubic structure substance is directly proportional to the spacing  $d$  of any particular set of lattice planes. If we measure the Bragg angle  $\theta_B$  for this set of planes, we can use the Bragg law to determine  $d$  and, knowing  $d$ , we can calculate  $a$ .

The angular separation of the peaks can be related to the lattice mismatch through the differential form of the Bragg equation with respect to  $\theta$ . For

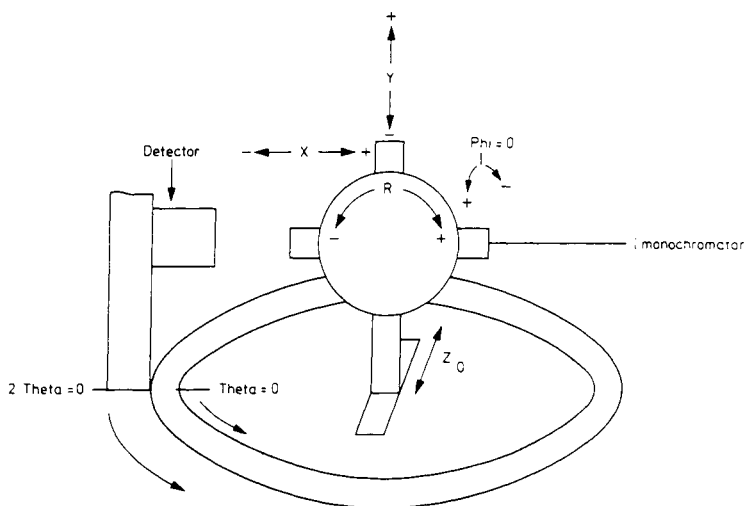


**Figure 4.12** Spatial configuration of the horizontal goniometer.

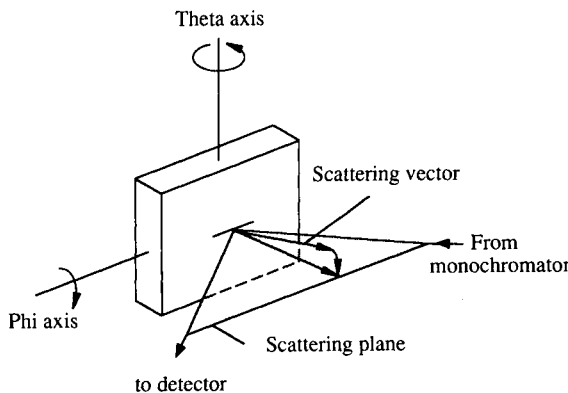


**Figure 4.13** Scattering geometry for a crystal with diffraction planes roughly parallel to the surface.

symmetric geometry, which is the case where the diffraction planes are parallel to the sample surface, we obtain

$$(\Delta a/a)_{\perp} = -\cot \theta_B \Delta\theta. \quad (4.15)$$

$(\Delta a/a)_{\perp}$  represents the lattice strain perpendicular to the crystal surface, which is related to the relaxed lattice mismatch  $(\Delta a/a)_r$  by

$$(\Delta a/a)_r = (\Delta a/a)_{\perp}[(1 - \nu)/(1 + \nu)] \quad (4.16)$$

provided the in-plane strain  $(\Delta a/a)_{\parallel}$  parallel to the surface is assumed to be zero and  $\nu$  is Poisson's ratio for the layer material. This relaxed mismatch can then

be related to the material composition, such as  $x$  in the ternary alloy  $\text{Ga}_x\text{In}_{1-x}\text{P}$ , by assuming Vegard's law

$$a_{\text{Ga}_x\text{In}_{1-x}\text{P}} = x a_{\text{GaP}} + (1 - x) a_{\text{InP}}. \quad (4.17)$$

By measuring the lattice constant  $a_{\text{Ga}_x\text{In}_{1-x}\text{P}}$ , the compositions  $x$  can be determined. Conversely, if we know the alloy compositions, the lattice constant of this ternary material can also be obtained precisely. Thus, once the angular separation between two peaks shown in the diffraction pattern is known, information on lattice mismatch, material quality and layer compositions can be acquired.

### (b) Pendellosung fringes

The hyperfine structure observed in diffraction patterns near the substrate and/or layer peaks may be attributed to the interaction between incident and reflected waves through the whole epitaxial layer. In the reflection case (Bragg case) of the dynamical diffraction theory, the beating of two wave fields inside a crystal occurs between wave points on the same branch of the dispersion surface (pendellosung). This type of wave interference is rarely observed and as such is more within the framework of a plane wave, rather than a spherical wave phenomenon. The known relation (Tapfer and Ploog 1986) between the angular spacing of the pendellosung fringes  $\Delta\theta$  and the thickness  $L$  of the whole epilayer is

$$L = \lambda |\gamma_h| / \Delta\theta \sin(2\theta_B) \quad (4.18)$$

where  $\gamma_h = \sin(\theta_B + \alpha)$  and  $\alpha$  is the angle between the sample surface and diffraction plane. Equation (4.18) can be simplified easily for symmetrical geometry

$$L = \lambda / (2\Delta\theta \cos\theta_B). \quad (4.19)$$

Equations (4.18) and (4.19) are also applicable to the period  $T$  of a superlattice, which is a periodic repeat of some layer structure with period  $T$ . The whole epilayer thickness is replaced by the superlattice period  $T$ , and the oscillation spacing is replaced by the angular distance between the satellite peaks which occur in x-ray diffraction curves from superlattices.

We conclude that, by using (4.18) or (4.19), the thickness of not only the superlattice periodicity but also some layer thickness of the multiquantum well can be determined; moreover, the thickness measurement can be carried out from measured symmetrical or asymmetrical diffraction patterns. These patterns can be simulated by using the dynamical x-ray diffraction theory described below.

### (c) X-ray reflectivity

The specular x-ray reflectivity, or (000) Bragg reflection, can be interpreted simply within the framework which was developed for x-ray diffraction. For other Bragg reflection geometries like (004) and (002), the role played by the dimensions defining the layer within the layer plane has been ignored, so this

implicitly assumes that the layer plane is infinitely extended in these directions. In the case of reflectivity, because of the low-angle geometry, information on the surface and interface roughness (Cowley and Ryan 1987) can be known, and, since this technique is independent of crystal periodicity and unit cells of materials, the dominant role is played by the shape of the area with different electron density as a function of depth. Therefore, x-ray reflectivity can be used to study liquids, amorphous or crystalline films. All that has to be considered is the electron density variation through layers. As mentioned before, although x-ray reflectivity can be explained within the framework developed there are some additional factors that must be considered, especially for superlattice structures, to understand the whole picture of this technique.

(i) *X-ray refraction.* Snell's law is the traditional approach used to relate the angle of incidence to the angle of refraction of electromagnetic waves travelling through media with different refractive indices  $n$ . For x-rays, the refractive index of most materials is slightly less than unity:

$$n_m = 1 - \delta - i\beta \quad (4.20)$$

where  $i$ , which relates to the x-ray absorption, indicates the imaginary component of a complex number. From Snell's law, if the refractive index of the air/vacuum is taken to be unity, for total external reflection the refractive index  $n_m$  of the material is equal to  $\cos \theta_c$ , where  $\theta_c$ , the incident angle between x-ray and interface, is the critical angle and is related to the density of the material and the wavelength of the x-rays. At  $\theta_c$ , the penetration of the x-rays into the sample is very limited. Typically the penetration depth will be around 50 Å. As the incident angle is increased, the x-rays rapidly penetrate deeper into the material.

(ii) *Effective layer thickness.* The layer thickness measured directly from the raw data of a reflectivity curve appears to be thinner than its real thickness, since, due to the x-ray refraction, the effective path length of the x-rays in the material will be increased.

(iii) *Scattered radiation effect.* Strong interaction (between incident beam and scattered radiation) of the x-rays with the sample will happen within and close to the area where total external reflection occurs. Due to this interaction effect the complete optical theory of reflectivity using Maxwell's equations and the Fresnel formula must be introduced to describe the full behaviour of x-ray reflectivity. Generally, within the range of twice the critical angle the strong interaction should be taken onto account to avoid making serious measurement errors.

#### 4.3.5 Dynamical x-ray diffraction theory simulation

The general basis and framework of the dynamical theory were developed soon after the discovery of x-ray diffraction in crystals. This theory, treated by Ewald (1916, 1917, 1920, 1921, 1924, 1925, 1958), took into account all

wave interactions within the crystal. The measured diffraction pattern must be simulated by means of the dynamical diffraction theory in order to have more accurate and unambiguous information about the structure properties of the sample. As a consequence, the dynamical theory of x-ray diffraction was developed to take into account normal absorption as well as the interaction between incident and scattered radiation.

*(a) The dynamical theory of x-ray diffraction*

Normal absorption occurs for all directions of incidence while extinction is important only when the incident wavevector has such a value that the Laue vector equation (equation (4.13)) is exactly or very nearly fulfilled for one or more reciprocal lattice vectors  $\mathbf{B}_H$ . The incident x-ray wave also suffers changes when it enters the crystal; that is to say, diffracted waves depend upon the internal incident wave which in turn depends upon the diffracted waves and both waves form a coupled system. Hence, the incident wave inside and outside the crystal material can be represented by the expression:

$$\mathbf{D}_I(\mathbf{r}) = \mathbf{D}_0(\mathbf{r}) \exp[i(\omega_0 t - 2\pi\beta_0 \cdot \mathbf{r})] \quad (4.21)$$

where  $\mathbf{r}$  is a point in the actual space,  $\mathbf{D}(\mathbf{r})$  the displacement vector and  $\beta_0 \cdot \mathbf{r}$  a plane wave with  $\beta_0$  constant. Outside the crystal, i.e. in the vacuum,  $\beta_0 = \mathbf{k}_0$  and  $\beta_0 \cdot \mathbf{r}$  and  $\mathbf{D}_0(\mathbf{r})$  are supposed to be real but space dependent, whereas the frequency  $\omega_0$  remains constant. On the contrary, inside the crystal the same function  $\beta_0 \cdot \mathbf{r}$  is maintained and  $\mathbf{D}_0(\mathbf{r})$  is introduced in perturbations originated in the wave by the crystalline medium, i.e.,  $|\beta_0|^2 = \epsilon |\mathbf{k}_0|^2$ , where the dielectric constant  $\epsilon$  is a complex quantity and is equal to  $n_m^2$ , the square of the refractive index. Therefore,  $\mathbf{D}_0(\mathbf{r})$  becomes, in general, a complex quantity. On the other hand, the wave corresponding to the sum of incident and diffracted waves in the interior of the crystal may be written as:

$$\mathbf{D}(\mathbf{r}) = \sum_H \mathbf{D}_H(\mathbf{r}) \exp[i(\omega_0 t - 2\pi\beta_H \cdot \mathbf{r})] \quad (4.22)$$

where  $\beta_H = \beta_0 + \mathbf{B}_H$  is the wavevector of a diffracted wave in the dynamical theory and the amplitude of this wave is expected to be negligibly small except when the Laue vector equation is satisfied. Obviously, the wave field represented in (4.22) is a set of coupled plane waves and  $H$  can take the value zero with  $\mathbf{B}_H = 0$ . In the dynamical theory, the case in which the incident beam produces just one diffracted beam at a time is specifically treated. In other words, for a reciprocal lattice vector  $\mathbf{B}_H$ , which lies relatively far away from where the Bragg geometry reflection should be, one may set the amplitude  $\mathbf{D}_H$  to be zero.

*(b) The fundamental equations for the general case*

As mentioned earlier, the dielectric constant  $\epsilon$  plays an important role in the dynamical theory of x-ray diffraction and may be expressed as follows:

$$\epsilon = 1 + \Psi = 1 + \Psi' + i\Psi''. \quad (4.23)$$

The dielectric constant, however, is not a constant but a function of position having the periodicity of the crystal lattice. Since  $\Psi$  is periodic, this distribution function may be expressed as a Fourier series

$$\Psi(\mathbf{r}) = \sum_H \Psi_H \exp(-i2\pi \mathbf{B}_H \cdot \mathbf{r}) \quad (4.24)$$

where

$$\Psi_H = V^{-1} \int_V \Psi(\mathbf{r}) \exp(i2\pi \mathbf{B}_H \cdot \mathbf{r}) dV$$

and where  $H$  can take also the value zero with  $\mathbf{B}_H = 0$ .  $\Psi_{0,H} = -(e^2/mc^2)(\lambda^2/\pi V)F_{0,H}$  are the coefficients of Fourier expansion, where  $F_{0,H}$  are the structure factors for the incident and diffracted beams and both include absorption,  $V$  is the unit cell volume and  $m$  the electron mass. Since the dielectric constant in the x-ray region is only slightly different from unity, the condition  $\Psi \ll 1$  can be assumed and the refractive index of crystal medium  $n_m$  can be expressed as:

$$n_m = 1 + \Psi/2 = 1 + (\Psi' + i\Psi'')/2. \quad (4.25)$$

This expression implies that the refractive index  $n_m$  becomes a complex and periodic function of position. Also, the imaginary part of equation (4.25) indicates that the scattering is accompanied by a true absorption corresponding to the emission of photoelectrons.

In addition to the assumption  $\Psi \ll 1$ , the following conditions are assumed: (i) the magnetic permeability is unity and (ii) the current density is zero. According to the above assumptions, the Maxwell equation gives:

$$\nabla \times [\nabla \times (1 - \Psi) \mathbf{D}] = -\frac{1}{c^2} \frac{\partial^2 \mathbf{D}}{\partial t^2} \quad (4.26)$$

where  $1/\varepsilon$  is set to be  $1 - \Psi$  and  $\mathbf{D}$  represents the sum of incident and diffracted waves and is actually the one expressed in (4.22). By substituting (4.22) into (4.26), an equation with an infinite number of unknowns  $\mathbf{D}_H$  is obtained. This equation can be further transformed into a system of an infinite number of equations with each one corresponding to the wave diffracted by the planes related to the reciprocal lattice vector  $\mathbf{B}_H$ . Therefore, when the Bragg condition is fulfilled for one reciprocal lattice vector  $\mathbf{B}_H$  only, the incident wave and one diffracted wave of appreciable amplitude exist.

### (c) Diffraction pattern simulation

Simulation of measured diffraction patterns can be accomplished through the use of a computer program developed by P F Fewster at Philips (Fewster and Curling 1987), which is based on the solution of the Takagi-Taupin equations (Takagi 1962, 1969, Taupin 1964) derived by the dynamical scattering approach described earlier with the introduction of a quantity  $\alpha_H(\omega) = -2(\theta - \theta_B) \sin 2\theta_B$

measuring the deviation from the Bragg condition at each point of the crystal, where  $\omega$  is the incident angle of the x-rays. The basic equations derived from (4.26) become

$$\begin{aligned} (i\lambda\gamma_H/\pi)(dD_H/dZ) &= \Psi_0 D_H + C\Psi_H D_0 - \alpha_H(\omega)D_H \\ (i\lambda\gamma_0/\pi)(dD_0/dZ) &= \Psi_0 D_0 + C\Psi_H D_H \end{aligned} \quad (4.27)$$

where  $D_{0,H}$  are complex amplitudes of the incident and diffracted beams, and  $Z$  is the depth into the crystal.  $\gamma_{0,H} = \mathbf{n} \cdot \mathbf{k}_{0,H}$  are direction cosines of incident and diffracted beams, where  $\mathbf{n}$  is the vector normal to the surface and  $\mathbf{k}_{0,H}$  are wavevectors of the incident and diffracted beams, and  $\lambda$  is the wavelength of the x-ray source. The polarization factor  $C$  is unity for  $\sigma$  polarization and  $\cos(2\theta_B)$  for  $\pi$  polarization. However, these two Laplacians are normally negligible as compared to the other terms of each equation of (4.27) once the curvature radius of the incident wave is larger than the absorption path through the crystal. Accordingly, if an amplitude ratio  $X(z, \omega) = D_H/D_0$  is defined, a differential equation can be derived as follows:

$$\frac{\partial X}{\partial Z} = \frac{i\pi}{\lambda\gamma_0} \left\{ \Psi_H X^2 + \left[ \left( 1 - \frac{\gamma_0}{|\gamma_H|} \right) \Psi_0 + \alpha_H(\omega) \frac{\gamma_0}{|\gamma_H|} \right] X - \frac{\gamma_0}{|\gamma_H|} \Psi_H \right\} \quad (4.28)$$

and a simplified form may be expressed as:

$$\partial X / \partial Z = iD(AX^2 + BX + C) \quad (4.29)$$

where  $A \simeq C$  for symmetrical reflections,  $B$  depends on  $\theta - \theta_B$  and  $A, C, D$  depend on direction cosines and structure factors. For a layer of constant composition, the solution  $X(z, \omega)$  can be obtained:

$$X(z, \omega) = \frac{[Sx(Z, \omega) + i(Bx(Z, \omega) + C) \tan(DS(Z - z))]}{(S - i(Ax(Z, \omega) + B) \tan(DS(Z - z)))} \quad (4.30)$$

with boundary condition  $X = x$  at  $z = Z$ , by solving a standard integral which comes from the integration after separating (4.28) into partial fractions, where  $S^2 = (B^2 - AC)$ . Since the diffracted wave deep inside the crystal is almost zero, the solution at the surface of a thick substrate is derived by using the boundary condition  $X = 0$  at  $Z = \infty$ . This amplitude ratio  $X$  can then be used as a boundary condition at the bottom of the first heteroepitaxial layer of depth  $Z$  and thickness  $t$  to calculate  $X(Z - t, \omega)$  at the top of the first layer. The procedure is iterated from the first layer until the top of the surface layer is reached. The reflectivity is thus given by:

$$R(\omega) = X(0, \omega)X^*(0, \omega) \quad (4.31)$$

and the angular range (from  $\omega_1$  to  $\omega_2$ ) for simulation is based on the range used in the experiment. From (4.31) the calculated diffraction pattern (the fitted data) can be obtained and may be compared to the measured diffraction profile (the raw data). Without using a simulation program, especially for those harmonics extending to several degrees, it is difficult to extract accurate information on structures only from measured data.

#### 4.3.6 Structural characterization of GaAs/GaInP superlattices

Many improvements have been made recently in understanding and controlling the purity, interface quality, optical and electronic properties of the GaAs/GaInP lattice-matched system grown by MOCVD.  $\text{Ga}_{0.51}\text{In}_{0.49}\text{P}$  lattice matched to GaAs shows a number of unique and interesting features. Also, high-quality GaAs/ $\text{Ga}_{0.51}\text{In}_{0.49}\text{P}$  heterostructures such as superlattices (SL) and multiquantum wells (MQW) have been grown by LP-MOCVD. Here, we describe the characterization of a superlattice structure by a high-resolution x-ray diffraction technique.

To attempt to fully characterize this GaAs/ $\text{Ga}_{0.51}\text{In}_{0.49}\text{P}$  sample with high-resolution x-ray diffraction, a set of three Bragg geometries (004), (002) and (000) is selected for detailed study. The (004) reflection is the most commonly studied reflection for (001)-oriented III-V structures, being the point where all atomic planes within the sample scatter in phase. As such, the (004) reflection will be the most intense, and will exhibit features from the whole sample structure. For superlattice materials containing GaAs it is often very revealing to study the (002) reflection in conjunction with the traditional (004). At the (002) point, alternate atomic planes within the sample will scatter out of phase. So for materials like GaAs, where the average electron density of each atomic plane is very similar, the (002) reflection will be almost absent. In the case of GaAs/GaInP superlattices, this implies that the (002) reflection will exhibit features predominantly from the GaInP aspect of the superlattice. As an independent validation of any conclusions drawn from the (002) and (004) reflections, the x-ray reflectivity (000) was also measured. The comparison of x-ray reflectivity with x-ray diffraction can often provide vital clues as to the detailed layer structure as each is sensitive to different aspects of the sample. X-ray reflectivity is a probe of macroscopic electron density fluctuations, while x-ray diffraction is a probe of fluctuations in the crystal structure.

##### *(a) Experimental results*

The sample studied here is a 10-period GaAs/ $\text{Ga}_x\text{In}_{1-x}\text{P}$  superlattice grown on GaAs(100) substrate misoriented 2° off axis towards (011̄) with an approximately 100 Å  $\text{Ga}_x\text{In}_{1-x}\text{P}$  ( $x \sim 0.51$ ) barrier and 90 Å GaAs well (Razeghi and Omnes 1991). A simple investigation of the raw data as measured for the (004), (002) and (000) reflections can provide lots of information for initial analysis. From the (004) data in figure 4.14(a) we can make a very good estimate of the superlattice period,  $151 \pm 9$  Å, as evaluated from

the measured separation of the superlattice satellites. The average superlattice mismatch of approximately  $-3116$  ppm is simply derived from the separation between the substrate and the zero-order superlattice peaks. A closer inspection of the data reveals weak pendellosung oscillations corresponding to a thickness of  $1511 \pm 90$  Å. This thickness may be associated with the total superlattice thickness, which indicates that 10 periods of superlattice are involved in this structure. On the contrary, the (002) reflection in figure 4.14(b) exhibits a very simple structure, which enables us to extract the average superlattice mismatch,  $-3323$  ppm, and superlattice period,  $145 \pm 9$  Å, to a higher degree of confidence than from the (004). What is immediately obvious from the data is that the even-order satellites  $\pm 2$  are missing, while the  $\pm 3$  satellites are clearly visible. These features indicate that the GaAs and GaInP layers within the superlattice must be of a very similar size (approximately 75 Å). The asymmetry between the  $\pm 1$  satellites further tells us that the superlattice unit cell is more complex than a simple GaAs/GaInP bilayer structure. According to the fine pendellosung fringes shown in figure 4.14(c) a thickness of  $1519 \pm 90$  Å also indicates that the number of periods is most likely to be 10. Furthermore, the reflectivity data in figure 4.14(d) exhibit features similar to the (004) and (002). What is most notable is the complete absence of any even-order satellites. This confirms the earlier observation that the GaAs and GaInP layers must be of a similar size, or to be more exact, that the superlattice unit cell is split into two areas of different electron density but very similar thickness of 75 Å. In addition, a strong broadening of the superlattice peaks, most likely resulting from thickness fluctuations, is in evidence as it moves away from the critical angle. The broadening is much more severe in this glancing angle measurement, and may indicate lateral inhomogeneity of the individual layer thicknesses averaged over the large illuminated surface area.

### *(b) Simulation results*

Based upon the initial results and the information concerning the growth process, random thickness fluctuations are expected and additional layers may be present in the superlattice to generate the observed asymmetries. One monolayer, 10 Å, of  $\text{Ga}_y\text{In}_{1-y}\text{P}$  is expected to appear between  $\text{Ga}_x\text{In}_{1-x}\text{P}$  and GaAs. This additional layer allows a large range of density and mismatch to be covered with small variations in the  $y$  component. In figures 4.15(a) to 4.15(c), the simulated data, using the dynamical x-ray diffraction theory and the x-ray reflectivity as simulation programs, for the (004), (002) and (000) reflections are compared with the measured data. The agreement between the simulated and measured (002) reflection is remarkably consistent, including the matched FWHM of the GaInP-layer Bragg peak. All of the observed features are reproduced. In direct contrast, the simulated (004) data near the substrate peak are not well reproduced. The simulated reflectivity (figure 4.15(c)) is in quite close agreement with the measured curve. All of the observed features in the x-ray reflectivity are reproduced including the negative dip where the second-order peak should be.

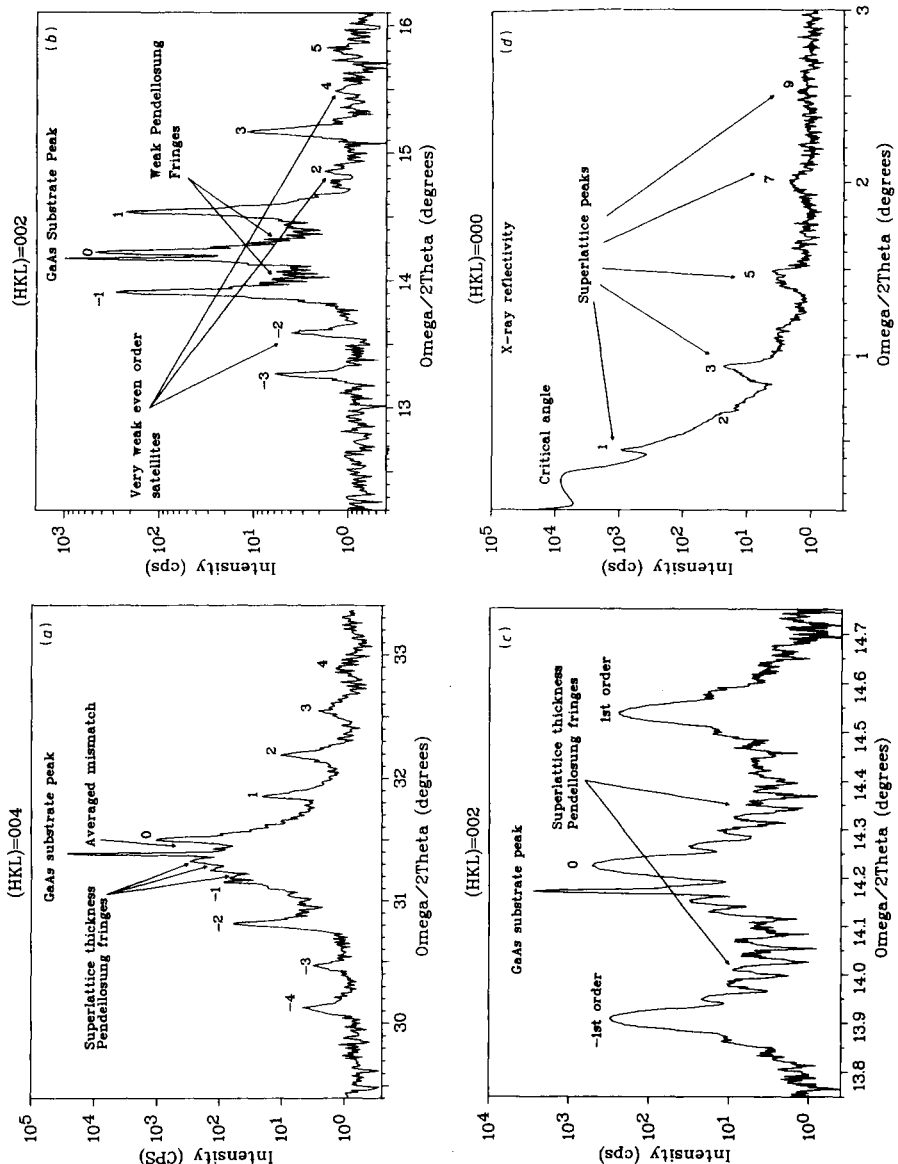


**Figure 4.14** Measured x-ray diffraction patterns of a 10-period  $\text{GaAs}/\text{Ga}_x\text{In}_{1-x}\text{P}$  superlattice for various  $(hkl)$  reflections: (a) (004), (b) (002), (c) expanded view of (002), and (d) (000). The (000) reflection is measured as x-ray reflectivity.

To reduce the satellite intensity in the simulation, the electron density difference between the GaAs and GaInP layer must be reduced. This is achieved by doping

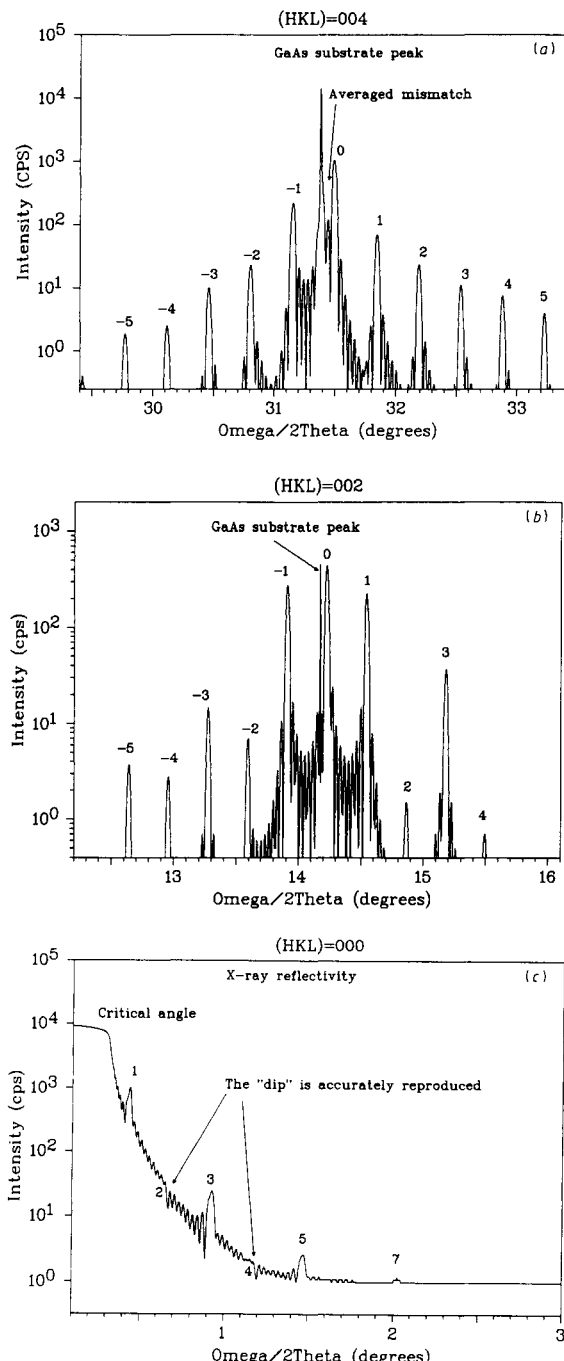


**Figure 4.15** Simulated satellite peak intensity profiles for various  $(hkl)$  reflections as a result of the parameter fitting. (a) (004), (b) (002), (c) (000). (a) and (b) are fitted by dynamical x-ray diffraction simulation and (c) is fitted by x-ray reflectivity simulation.

**Table 4.1** Information concerning the structure parameters of samples measured by x-ray diffraction and simulated by dynamical x-ray diffraction theory.

<i>hkl</i>	Measurement			Simulation		
	004	002	000	004	002	000
$\Delta a/a_0$ (Ga <sub>x</sub> In <sub>1-x</sub> P)	-6232 ppm	-6646 ppm	—	-322 ppm	-322 ppm	—
$\Delta a/a_0$ (Ga <sub>y</sub> In <sub>1-y</sub> P)	—	—	—	-0.043	-0.043	—
Period thickness	151 ± 9 Å	145 ± 9 Å	150 Å	152 Å	144 Å	157 ± 2 Å
GaAs thickness	—	—	—	76 Å	72 Å	78 ± 2 Å
Ga <sub>x</sub> In <sub>1-x</sub> P thickness	—	—	—	66 Å	62 Å	73 ± 2 Å
<i>x</i>	~ 0.56	~ 0.56	—	0.519	0.519	0.519
Ga <sub>y</sub> In <sub>1-y</sub> P thickness	—	—	—	10 Å	10 Å	5.1 ± 0.1 Å
<i>y</i>	—	—	—	0.82	0.82	0.82
Superlattice thickness	1511 ± 90 Å	1519 ± 90 Å	—	1520 Å	1440 Å	1570 ± 20 Å
Periods	10	10	—	10	10	10
Superlattice FWHM	109 s	92.3 s	—	117 s	99.9 s	—
Surface roughness (GaAs)	—	—	—	—	—	6.7 ± 0.1 Å
Surface roughness (Ga <sub>x</sub> In <sub>1-x</sub> P)	—	—	—	—	—	5 Å (7.1 Å for top layer)

the GaAs layer with 15% of P. This does not result in a true representation of reality but in an illustration of the degree of density modification required to model accurately the data. The main difference between the two data sets is in the higher-order peak broadening of the superlattice peaks. This provides the information on random thickness fluctuations of this sample.

As a consequence, due to the above detailed analysis, the fitting of the simulated data to the measured data gives the closest match to the third-order satellite asymmetry and the  $\text{GaAs}/\text{Ga}_{0.519}\text{In}_{0.481}\text{P}$  matched system with a mismatch of  $\Delta a/a_0 = -3.22 \times 10^{-4}$  is investigated. Without using the simulation programs, accurate structure parameters cannot be extracted. Information concerning the structure parameters of this sample is shown in table 4.1.

#### 4.4 PHOTOLUMINESCENCE

Luminescence is the term used to describe the non-equilibrium emission of radiation. Three processes are involved in the luminescence process: excitation, energy transfer and radiative transition of the electrons. When the light is absorbed as the excitation, the luminescence process is called photoluminescence (PL).

The study of photoluminescence spectroscopy, which is a technique to obtain the relation between the intensity and the wavelength of the emission of radiation, has become one of the most powerful techniques for the comprehensive and non-destructive assessment of materials since it yields a large amount of information about the electronic structure of the material (Bebb and Williams 1972).

Excess electron-hole pairs (EHPs) are generated when a semiconductor is illuminated by light with photon energy larger than the bandgap. The created EHPs will move or transfer their energy in the semiconductors, then recombine through various mechanisms, which can be radiative or non-radiative, such as the cascade phonon process and emission quench at defect centres etc.

The heart of the optical measurement is a spectrometer, which is used to discriminate between emission at different photon energies, resulting in a plot of light intensity as a function of energy. Multibeam interference is often the physical means used to achieve the spectrometer such as various grating monochromators. The dispersive prism is the oldest instrument to separate light into its component wavelengths. However, more and more, the Fourier transformation spectrometer is becoming the key spectrometer.

##### 4.4.1 Fourier transform spectroscopy

The foundations of modern Fourier transform spectroscopy (FTS) were laid in the latter part of the nineteenth century by Michelson. Soon after that, Raleigh

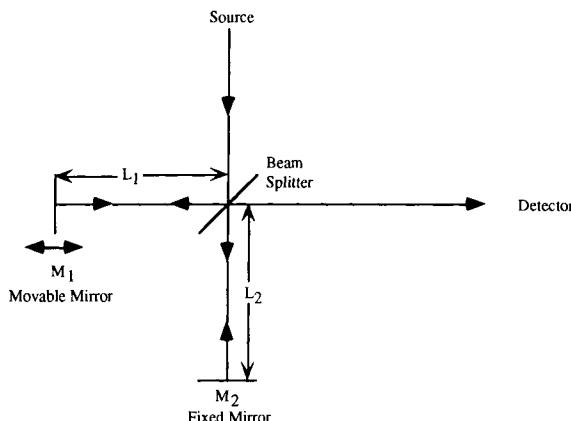


**Figure 4.16** Michelson interferometer.

recognized the relationship between an interferogram and its spectrum by a Fourier transform. It was not until the advent of reasonably priced computers and the fast Fourier algorithm that interferometry began to be applied to spectroscopic measurements in the 1970s.

The basic optical component of Fourier transform spectrometers is the Michelson interferometer shown in simplified form in figure 4.16. Light from an infrared source is collimated and incident on a beam splitter. An ideal beam splitter creates two separate optical paths by reflecting 50% of the incident light and transmitting the remaining 50%. In one path the beam is reflected by a fixed-position mirror back to the beam splitter where it is partially reflected to the source and partially transmitted to the detector. In the other arm of the interferometer, the beam is reflected by the movable mirror that is translated back and forth and maintained parallel to itself. The beam from the movable mirror is also returned to the beam splitter where it too is partially transmitted back to the source and partially reflected to the detector. When the two beams are combined, the interference phenomenon is produced. Typically the movable mirror rides on an air bearing for good stability. Detectors can be a cooled HgCdTe or germanium photodiode, depending on the wavelength of interest.

The light intensity reaching the detector is the sum of the two beams. The two beams are in phase and reinforce each other when  $L_1 = L_2$ . When  $M_1$  is moved, the optical path lengths are unequal, and an optical path difference  $d$  is introduced. If  $M_1$  is moved a distance  $x$ , the retardation is  $d = 2x$  since the light has to travel an additional distance  $x$  to reach the mirror and the same additional distance to reach the beam splitter.

Consider the output signal from the detector when the source emits a single frequency or wavelength. For  $L_1 = L_2$  the two beams reinforce each other because they are in phase,  $d = 0$ , and the detector output is a maximum. If  $M_1$  is moved by  $x = \lambda/4$ , the retardation becomes  $d = 2x = \lambda/2$ . The two wavefronts

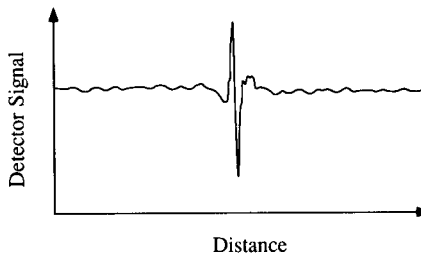


**Figure 4.17** A typical interferogram.

reach the detector  $180^\circ$  out of phase, resulting in destructive interference or zero output. For an additional  $\lambda/4$  movement by  $M_1$ ,  $d = 1$  and constructive interference results again. The detector output—the interferogram—consists of a series of maxima and minima. The interferometer always retains its maximum at  $x = 0$  where  $L_1 = L_2$  because all wavelengths interfere constructively for that and only that mirror position. For  $x \neq 0$ , waves interfere destructively, and the interferogram amplitude decreases from its maximum as shown in the interferogram for an Si wafer in figure 4.17. The strong maximum at  $x = 0$  is known as the centreburst.

The measured quantity in Fourier transform spectroscopy is the interferogram. The interferogram, however, is of little direct interest. It is the spectral response that is of interest, which is calculated from the interferogram using the Fourier transformation

$$B(f) = \int_{-\infty}^{\infty} I(x) \cos(2\pi xf) dx \quad (4.32)$$

where  $B(f)$  is the source intensity and  $I(x)$  is the intensity of the interferogram.

With the advent of computers of high calculation capacity and small size, all the calculations involved in a Fourier transform can be done in seconds. The data are stored in digital form and can be easily manipulated using different functions. In addition, many interferograms of a given sample can be collected and averaged for to give a higher signal-to-noise ratio.

FTS has two major advantages over prism or grating monochromators. One is the multiplex gain advantage. The entire spectrum is observed during the measurement of FTS while only a small portion of the entire spectrum is measured at a time in the normal monochromator. So FTS has a signal-to-noise advantage of  $N^{1/2}$  for a spectra with  $N$  spectral elements if only noise other than the photon noise is considered in the detector. FTS can also acquire data in a far shorter time. The second advantage is the Jacquinot advantage or optical throughput gain advantage. Slits are used in a monochromator to collect a fraction of the spectra. So the optical throughput is only a portion of the incident light. There are no slits in FTS, so nearly 100% light is collected to the detector. This gives FTS nearly 100% throughput gain.

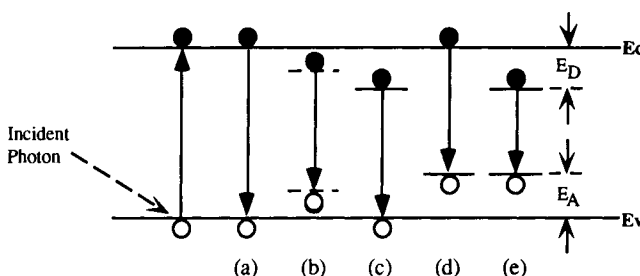


**Figure 4.18** Radiative transitions observed with photoluminescence (Smith 1981).

#### 4.4.2 Recombination processes

When a sample is excited with an optical source with  $h\nu > E_g$ , EHPs are created and subsequently recombine by one of several mechanisms. At low temperature, recombination is dominantly through the annihilation of the exciton. An exciton is formed when Coulombic attraction between an electron–hole pair leads to an excited state in which an electron and a hole remain bound to each other in a hydrogen-like state (Wolfe and Mysyrowicz 1984). When the exciton is formed by an electron in the conduction band and a hole in the valence band, the exciton is called a free exciton, since the exciton can move freely in the band with the electron and hole bound together. The energy of exciton recombination is slightly less than that of free EHP recombination due to the Coulombic attraction which results in a binding energy of the exciton  $E_x$ . With the exception of the free exciton, an exciton can be bound to some localized trap such as an ionized donor and acceptor and form a bound state at localized traps and impurity bands. This kind of exciton is called a bound exciton or Frank exciton. Typically,  $E_x$  is only about 30 meV which is comparable to the thermal energy at room temperature (26 meV), and in general no excitonic recombination is observable at room temperature. However, excitonic recombination dominates at low temperature. To obtain the maximum information, measurements at low temperature are required to decrease the thermal broadening of the emission peak and to eliminate the capture by thermally activated irradiation centres. For good PL output the majority of the recombination processes should be radiative. Figure 4.18 shows five of the most commonly observed PL transitions (Smith 1981).

Band-to-band recombination (figure 4.18(a)) is the process whereby a free electron in the conduction band recombines with a free hole in the valence band and gives out radiation equivalent to the bandgap energy. It dominates at room temperature but it is rarely observed at low temperatures where excitonic recombination dominates. In materials that are sufficiently pure and at low temperature, *free excitons* form and recombine by emitting photons. The emitted photon energy in a direct bandgap semiconductor is given by (Pankove 1975)

$$h\nu = E_g - E_x \quad (4.33)$$

where  $E_x$  is the free-exciton binding energy. In indirect bandgap semiconductors, momentum conservation requires the emission of a momentum conserving phonon, thus

$$h\nu = E_g - E_x - E_p \quad (4.34)$$

where  $E_p$  is the phonon energy.

Bound-exciton recombination dominates over free-exciton recombination for less pure materials. The free exciton moves through the crystal and combines with a donor (figure 4.18(c)) to form an excitonic ion or bound exciton. If the donor is ionized, a donor ion and exciton complex ( $D^+$ , X) is formed. The electron bound to the donor travels in a wide orbit about the donor. Similarly, the neutral donor and exciton form a donor-exciton complex ( $D^0$ , X). Likewise, electrons combining with acceptors also form bound excitons ( $A^-$ , X), ( $A^0$ , X) (figure 4.18(d)).

Lastly, an electron on a neutral donor can recombine with a hole on a neutral acceptor, the well known donor-acceptor ( $D^0$ , A) recombination, illustrated in figure 4.18(e). The emission line has an energy modified by the Coulombic interaction between donors and acceptors given by

$$h\nu = E_g - (E_A + E_D) + \frac{q^2}{\epsilon_r \epsilon_0 r} \quad (4.35)$$

where  $r$  is the distance between donor and acceptor.

Identification of the above recombinations depends on the careful consideration of the subtle competition between the above-mentioned mechanisms. For p-type semiconductors, ( $A^0$ , X) and ( $A^-$ , X) luminescence is stronger than the ( $D^0$ , X) and ( $D^+$ , X) luminescence. The opposite is true for n-type semiconductors. For the material of standard purity, the free-exciton luminescence is weaker than the bound-exciton luminescence. (D, A) recombination only exists at temperatures low enough so that dopants are not fully ionized. The energy position of the (D, A) peak is shifted to the lower-energy end when the semiconductor is heavily doped, due to the decrease of the average distance between the electrons in the donors and the holes in the acceptors. Another difference between (D, A) recombination and other recombination paths is that the full width at half maximum (FWHM) of the (D, A) recombination is typically  $< 3kT/2$  ( $k$  here is the Boltzman constant) and resemble slightly broadened delta functions. However, recombinations from other bound excitons are usually a few  $kT$  wide. The recombination between a band carrier and a deep centre can also appear in the spectra which potentially gives us a method for identifying deep impurity species. Sometimes, phonon replicas of the main transitions also appear in the spectra.

Quantum-size effects become appreciable when the layer thickness becomes less than  $\sim 50$  nm in III-V semiconductors, such as GaAs. This type of structure is called a quantum well, whereby quantum mechanics has to be employed to solve the equations yielding electronic states.

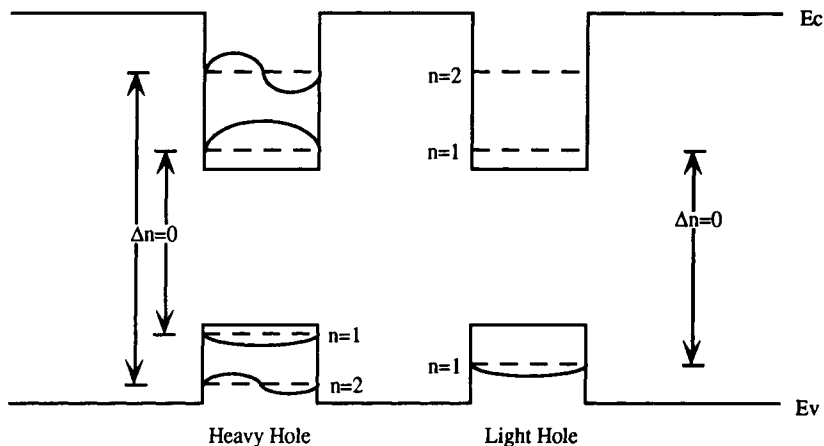


**Figure 4.19** Bound states and wavefunctions of quantized valence and conduction band states.

Since the pioneering work of Dingle (1975), a very large amount of literature has been published on the spectroscopic assessment of quantum-well structures. Photoluminescence spectroscopy is particularly important in the assessment of these structures.

The bound energy and hole states in the quantum well are shown in figure 4.19 and absorption spectra for 400, 21, and 14 nm GaAs layers are shown in figure 4.20. Dingle (1975) proposed that the transitions were between the bound-hole and bound-electron states with equal quantum number  $n$ , following the  $\Delta n = 0$  selection rule (see figure 4.19). It should be noted that this rule is generally valid but more recent work has shown that transitions can occur which violate the  $\Delta n = 0$  selection rule.

Low-temperature PL measurements primarily detect  $n = 1$  exciton recombination. PL provides a rapid assessment of well width, and the full width at half maximum (FWHM) of the luminescence peak is potentially a good measure of the quality of the interface since fluctuations in the well width produce considerable broadening, particularly in narrow wells. Bound exciton luminescence can also occur from donor and acceptors in the quantum wells. The binding energy depends both on the well width and the position of the impurity within the well.

Photoluminescence can be used for the following: the relative intensity and illumination energy provide knowledge of the relative concentration and type of the luminescence centre. The broadening of the peak is related to the quality of the sample. Generally, the higher the quality the narrower the peak. The shape of the peaks reflects the dominant luminescence mechanism. The shift and evolution of the peaks under different physical environments (e.g. pressure, temperature) gives information about the internal structure of the material. Time resolution photoluminescence and excitation photoluminescence

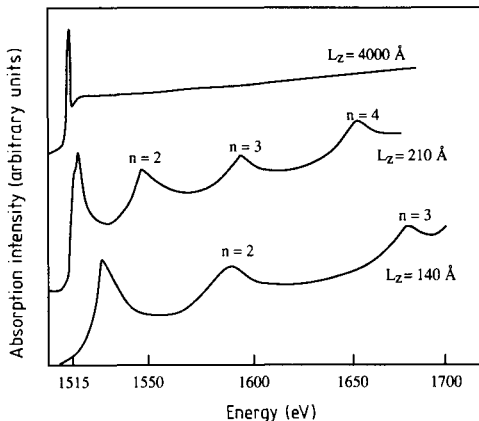


**Figure 4.20** Absorption spectra of 400, 21 and 14 nm thick GaAs quantum wells (Dingle 1975).

spectroscopy provide information about energy transfer inside the material. The above demonstrates that photoluminescence has become one of the main techniques in studying the properties of semiconductors.

## 4.5 ELECTROCHEMICAL CAPACITANCE–VOLTAGE AND PHOTOVOLTAGE SPECTROSCOPY

### 4.5.1 Electrochemical capacitance–voltage measurement

Capacitance–voltage ( $C$ – $V$ ) measurement is one of the major techniques used for determining the carrier concentration as a function of depth.

The capacitance of a junction is defined as:

$$C = dQ/dV \quad (4.36)$$

which gives rise to the explicit formula for the depletion width  $W_d$  and carrier concentration  $N$  at  $W_d$  under the depletion approximation for abrupt junctions.

$$W_d = \frac{\epsilon_r \epsilon_0 A}{C} \quad (4.37)$$

$$N = \frac{C}{q \epsilon_0 \epsilon_r A^2 (dC/dV)} \quad (4.38)$$

where  $\epsilon_r$  is the relative dielectric constant of the semiconductor,  $\epsilon_0$  the vacuum dielectric constant,  $A$  is the area of the Schottky junction and  $q$  is the charge on the electron.

The distribution of the carrier concentration is profiled by measuring the capacitance of a Schottky junction under different reverse-bias voltages, then the edge of the depletion region and the carrier concentration at that position are calculated using (4.37) and (4.38).

The minimum depth and maximum depth of the profile are restricted by the zero-bias voltage and the breakdown voltage, respectively. Outside this range, the depletion approximation fails due to the current flowing through the junction. The lower-range limit is a problem for low-doped semiconductors while the upper-range limit can be especially restrictive in highly doped materials where the depletion width is small. In GaAs, the breakdown field is about  $4 \times 10^5 \text{ V cm}^{-1}$  and so the maximum depletion depth for  $N_d \simeq 10^{18} \text{ cm}^{-3}$  is about 0.02  $\mu\text{m}$  (Sze 1981).

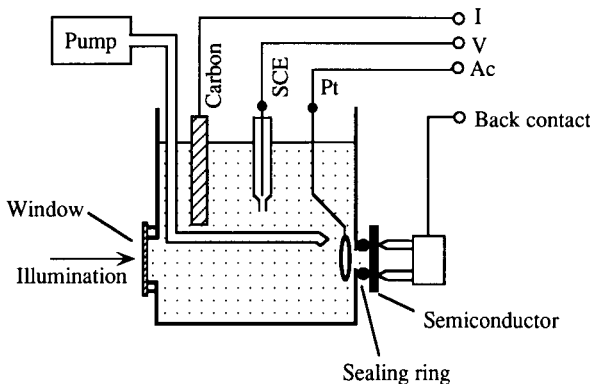
To overcome the disadvantages of the conventional  $C-V$  method, an alternate chemical etching and profiling with a temporary mercury barrier was originally introduced. However, this is a time consuming and tedious process. Ambridge *et al* (1973, 1974, 1975) used an electrolyte to form a electrolyte/semiconductor junction and to remove material electrolytically. Therefore, both etching and measuring processes can be carried out in the same electrochemical cell and controlled electronically to perform the repetitive etching/measuring cycles, generating a profile plot to the desired depth. This method is called electrochemical  $C-V$  (ECV).

Figure 4.21 shows a typical schematic diagram of the electrochemical cell used in ECV. The semiconductor sample is held against a sealing ring, which defines the contact area, by means of spring-loaded back contacts. In certain systems, such as a versatile system manufactured by Polaron Equipment Ltd (Blood 1986), a front contact is also available, which is very useful for samples with high-resistance substrates. The etching conditions are controlled by the potential across the cell by passing a DC current between the semiconductor sample and the carbon electrode to maintain the required over-potential measured potentiometrically with reference to the saturated calomel electrode (SCE). The AC signals are measured with respect to a platinum electrode located near the semiconductor surface to reduce the series resistance due to the electrolyte.

When a semiconductor is in contact with an electrolyte, charge exchange occurs. In an ECV system, charge transfer takes place from the semiconductor to the electrolyte (anodic current), supported by holes in the valence band of the semiconductor. The dissolution reaction of InP, a common III-V semiconductor, is shown below



The dissolution process results in the separation of electric charge. Equilibrium is achieved when the decrease in chemical free energy, as a result of dissolution, is balanced by the increase in the electrical energy associated with the separation of charge. The separation of charge forms a so-called Helmholtz electrical double layer and the potential drop across the layer is



**Figure 4.21** Schematic diagram of the electrochemical cell.

referred to as the equilibrium electrode potential. Provided the electrolyte is fairly concentrated, field penetration into the electrolyte is negligible and the semiconductor/electrolyte interface behaves as a Schottky junction. In this case, the potential drop across the Helmholtz layer is constant and the remaining applied potential is dropped across the depletion layer of width  $W_d$ .  $W_d$  is determined from (4.37) and the carrier concentration is determined from (4.38).

Etching or dissolution is accommodated by the hole transferred from the semiconductor to the electrolyte. With p-type material, the holes required for dissolution are obtained by applying a forward-bias voltage, or the anodic potential in electrochemical notation. The required holes in n-type semiconductors are generated by illuminating the sample with light under a proper anodic potential  $V_{\text{etch}}$ . Smooth removal of n-type material is achieved when the etching current depends upon the illumination intensity but not upon the anodic potential. So the proper anodic potential should be in the area that has constant and large light current in the  $I$ - $V$  curve as in figure 4.22. For the sake of consistency with the electrochemical convention, where the anodic potential corresponds to dissolution and the cathodic potential corresponds to deposition, the voltages in ECV are measured with reference to the electrolyte as the zero potential.

The carrier type of the semiconductor is identified by comparing the rest potential under dark and light conditions. For n-type material, the rest potential under dark conditions is lower than that at light conditions. p-type material is just the opposite. This measurement can be misleading if the structure has electrical junctions, very high doping levels or highly compensated material.

When the sample is etched, Faraday's law of electrolysis is used to calculate the etching depth  $W_{\text{etch}}$ ,

$$W_{\text{etch}} = \frac{M}{ZFDA} \int I dt \quad (4.40)$$

where  $M$  is the molecular weight and  $D$  is the density of the semiconductor,  $F$

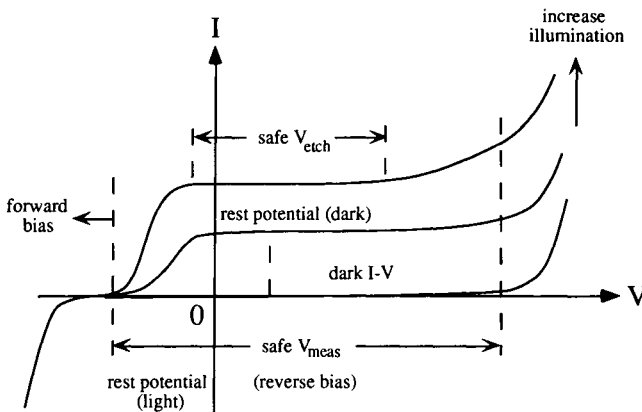


**Figure 4.22** Experimental parameters of the  $I$ - $V$  curve of an n-type sample.

is the Faraday constant ( $9.64 \times 10^4$  C),  $A$  is the dissolution area and  $Z$  is the charge transferred per molecule dissolved.

The carrier concentration is profiled by repetitive etching and then recording at a fixed measuring voltage. The etching current is integrated and processed to give the etch depth which is added to the depletion depth to give the total depth of the depletion edge with respect to the original surface. Two AC voltages are applied along with a DC bias voltage in the measurement. The AC voltage, called the modulation voltage, of about 3 kHz and 0.14 V peak-to-peak is used to measure the capacitance. Sometimes the modulation frequency has to be decreased to minimize the error from the large series resistance, but a modulation frequency lower than the emission rate of the deep level may ionize the deep centre and make the measured carrier concentration imprecise. The AC voltage of about 40 Hz and 0.28 V peak-to-peak, called the carrier voltage, is used to measure  $dC/dV$  which is used to calculate the carrier density  $N$  from (4.38). If the leakage current is too large, the carrier voltage has to be decreased to avoid the enclave of the carrier voltage to the large current area where the depletion application fails.

An ECV profiler has the following advantages:

- (i) it is a direct method of measuring the carrier concentrations,
- (ii) no sample preparation is needed except the conventional surface cleaning of the sample,
- (iii) ECV can be used in a wide range of structures and materials provided an adequate electrolyte is chosen,
- (iv) since the electrolyte used is transparent to light of wavelength shorter than  $1.2\ \mu\text{m}$ , the optical measurement can be performed in the same chemical cell.

The negative points of the ECV are:

- (i) difficult to measure at very high carrier concentrations ( $> 5 \times 10^{19}\ \text{cm}^{-3}$ )

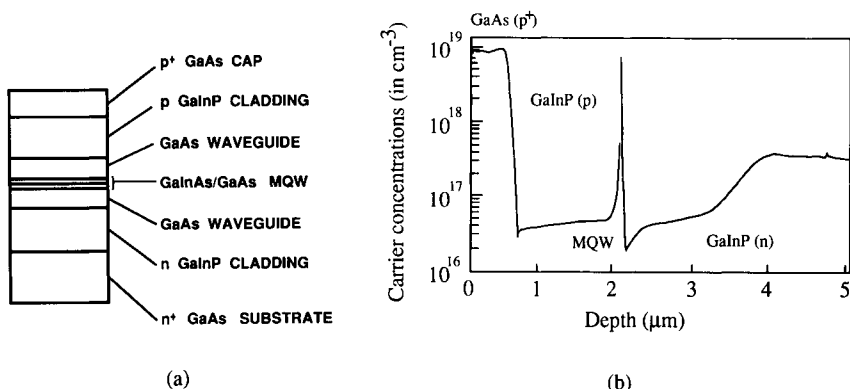


**Figure 4.23** ECV profile of a double-heterojunction laser.

where the capacitance is outside the measurement range of the system,

(ii) large surface depletion at very low carrier concentrations ( $< 1 \times 10^{19} \text{ cm}^{-3}$ ) makes the measurement of carrier concentrations in the top few microns impossible,

(iii) the use of chemicals destroys the sample and contaminates the unetched part of the sample,

(iv) the sealing-ring area needs careful calibration to assure reliable results.

Figure 4.23 shows an ECV profile for a double-heterojunction laser. From the ECV profile, the following information can be acquired:

(i) the carrier concentration and carrier type of each layer are clearly shown in the profile,

(ii) the thickness of each layer can be determined to the order of several Debye lengths if uniform etching is achieved.

Recently,  $C-V$  profiling has been widely used to determine the band discontinuity of the heterojunction since Kroemer and Chien (1981) showed that the Debye averaging process conserves both the charge increment and its total electric moment throughout the profile so the potential drop across the barrier is a precise variable, although the real carrier concentration distribution is different from the profiled one.

However, ECV is not supposed to be a preferred way to get the band offset. Unlike the CV technique where the carrier concentration and the depletion width are both obtained from a capacitance measurement and the potential drop of the junction is independent of the measurement of the area, in the ECV profile the depth scale is obtained predominantly from the integration of dissolution current which gives the potential drop of the junction inversely proportional to the fourth power of the etching area. Even if the etching area can be determined to sufficient accuracy, the measured carrier concentration includes averaging of the Debye tail as well as the etching toughness which makes the Kroemer and

Chien assumption invalid in the ECV case.

The precision of ECV is very sensitive to the appropriate choice of the various measuring conditions. The etching uniformity is the principal instrumental limit to the depth resolution. The area defined limits the absolute accuracy. The Helmholtz capacitance and the electrolyte resistance may limit operation of the instrument on highly doped material where the capacitance of the electrolyte/semiconductor junction is large and the Helmholtz capacitance is comparable to it. The choice of low operating frequencies to minimize the series-resistance effects results in increased sensitivity to deep states in the measurement of capacitance and depletion width.

#### 4.5.2 Photovoltage spectroscopy

An advantage of an electrolyte contact is that it is transparent to radiation at wavelengths shorter than  $1.2\ \mu\text{m}$ . With the addition of a variable monochromatic light source, photovoltage spectroscopy (PVS) can be measured in the same ECV system and also at different etching depth.

When light energy  $h\nu \geq E_g$  illuminates a junction (p–n, Schottky, n–n<sup>+</sup> or p–p<sup>+</sup>) or within a diffusion length from the junction, the photogenerated electrons and holes are separated by the junction field and create a photogenerated voltage drop across the junction. In ECV, when the electrolyte/semiconductor junction is illuminated from the front side with a continuous fixed wavelength, photovoltage spectroscopy (PVS) is measured. The open-circuit photovoltage  $V_{\text{oc}}$  is:

$$V_{\text{oc}} = \frac{qF\alpha(\lambda)(L + W_d)}{1/R_\ell + (qI_s)/kT}$$

where  $F$  is the photon flux density,  $\alpha(\lambda)$  is the absorption coefficient at wavelength  $\lambda$ ,  $W_d$  is the depletion width and  $L$  is the diffusion length.  $R_\ell$  is the leakage resistance,  $I_s$  is the reverse saturation current,  $k$  is the Boltzmann constant,  $T$  is the temperature in kelvin. The open-circuit voltage is measured in the ECV profile system to avoid electrochemical etching or deposition at the interface between the sample and electrolyte. PVS, in principle, gives the reflective absorption spectroscopy of the sample. The differences between PVS and absorption spectroscopy are: PVS is undetectable for a too leaky sample ( $R_\ell$  small) while absorption spectroscopy is still available; PVS signals are of opposite sign for n-type and p-type semiconductors while their absorption spectra are the same.

Although analysis of the PVS spectrum might be complicated due to the contribution from various junctions in a material, the combination of etching and PVS provides accurate information on the bandgap at each depth in the sample. The alloy composition of the sample is obtained by exploiting the relationship between bandgap  $E_g$  and alloy composition (Casey and Panish 1978) of the known alloy sample. Figure 4.24 shows a selection of photovoltage

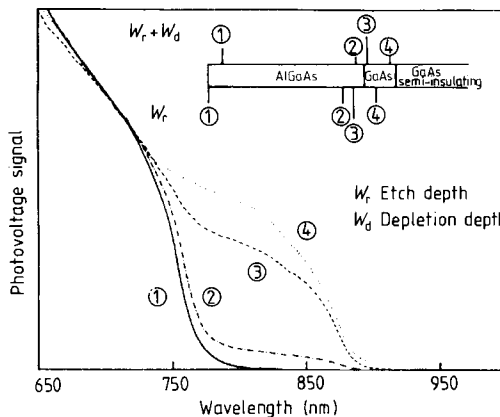


**Figure 4.24** Selection of photovoltage spectra recorded at different depths while performing an etching profile of a GaAs/GaAlAs double-heterojunction structure (Webster 1989).

spectra recorded at different depths while performing an etching profile of a GaAs/GaAlAs double-heterojunction structure (Webster 1989). In the case of materials with narrow bandgap ( $\lambda > 1.2 \mu\text{m}$ ), the electrolyte may have large absorption. To avoid this problem, back illumination is used, provided the substrate has a larger bandgap.

In summary, the ECV technique overcomes the restrictions on profiling depth compared to the case of conventional *C-V* measurement. Furthermore, due to the additional information that can be obtained from the method combining PVS and controlled etching, an ECV/PVS system is a very powerful characterization instrument in the field of semiconductor research.

## 4.6 RESISTIVITY AND HALL MEASUREMENT

### 4.6.1 Resistivity and resistivity measurement

The conductivity of a semiconductor with electron concentration  $n$ , hole concentration  $p$ , electron mobility  $\mu_n$  and hole mobility  $\mu_p$  is defined by:

$$\sigma = q(n\mu_n + p\mu_p). \quad (4.41)$$

The resistance of a rectangular semiconductor block is given by

$$R = \rho L / wt \quad (4.42)$$

where  $\rho$  is the resistivity defined as  $1/\sigma$ ,  $L$  is the length,  $w$  is the width and  $t$  is the thickness of the sample. The sheet resistance of a material is defined by

$$R_s = \rho / t \quad (4.43)$$

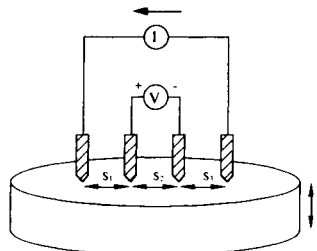


**Figure 4.25** Four-point probe method.

so that the resistance is given by

$$R = R_s L / w. \quad (4.44)$$

Therefore, if the sheet resistance is known, only the length and width of a sample need to be specified to determine the resistance.

*(a) The four-point probe method*

The resistivity of a material can be measured by placing two contacts on the sample, sending a fixed current through the probes and measuring the voltage across them, but this method is not accurate since the resistance measured includes the contact resistance and spreading resistance under the contacts. In order to avoid this problem the four-point probe method is commonly used to measure bulk or sheet resistivity of materials. In this case four contacts are placed on the sample, a fixed current is passed through the outer probes and the potential across the inner pair is measured. The arrangement is shown in figure 4.25. Since the current through the voltage probes is very small, the contact potential and spreading resistance at these probes is negligible leading to a more accurate measurement.

If the sample is large enough, it can be considered to be semi-infinite in which case resistivity is given by (Valdes 1954)

$$\rho = \frac{V}{I} \frac{2\pi}{(1/s_1 + 1/s_3 - 1/(s_1 + s_2) - 1/(s_2 + s_3))} \quad (4.45)$$

where  $V$  is the voltage across the inner probes,  $I$  is the current through the outer probes and  $s_1, s_2, s_3$  are indicated in figure 4.25. If the probe spacings are equal ( $s_1 = s_2 = s_3 = s$ ) equation (4.45) simplifies to

$$\rho = \frac{V}{I} 2\pi s. \quad (4.46)$$

A widely used probe spacing is 1.588 mm so that resistivity is given by  $\rho = V/I$ .

If the geometry of the sample is finite, which is more realistic than the assumption of a semi-infinite volume, the resistivity is defined by

$$\rho = \frac{V}{I} 2\pi s F \quad (4.47)$$

where  $F$  is the correction factor due to several factors including edge, thickness and misalignment in probe placement. For laterally large and thin ( $s \gg t$ ) samples with uniform probe spacing, the resistivity is given by

$$\rho = \frac{\pi t}{\ln 2} \frac{V}{I} = 4.532t \frac{V}{I}. \quad (4.48)$$

Very thin layers are usually characterized by their sheet resistance. Equation (4.48) gives the sheet resistance as

$$R_s = \frac{\rho}{t} = 4.532 \frac{V}{I} \quad (s \gg t). \quad (4.49)$$

Equations (4.48) and (4.49) are valid for a sample of very large lateral extent compared to its thickness. In order to have accurate results by using these expressions, the circular sample must have a diameter much larger than the probe spacing  $s$  ( $d \geq 40s$ ) (Schroder 1990).

#### (b) Van der Pauw's method

Van der Pauw (1958) showed that the sheet resistance of an arbitrarily shaped sample can be measured by placing four contacts on the periphery of the sample (see figure 4.26), injecting a fixed current  $I$  through one pair of contacts and measuring the voltage  $V$  across the other pair of contacts. The following conditions should be satisfied:

- (i) the contacts are at the edge of the sample,
- (ii) the contacts are small enough,
- (iii) the sample is flat and of uniform thickness,
- (iv) the surface of the sample is singly connected (no isolated holes).

Van der Pauw also showed that two of these measurements are related by

$$\exp\left(-\frac{\pi t R_{12,34}}{\rho}\right) + \exp\left(-\frac{\pi t R_{23,41}}{\rho}\right) = 1 \quad (4.50)$$

where  $t$  is the thickness of the sample,  $R_{12,34} = V_{34}/I_{12}$  and  $R_{23,41} = V_{41}/I_{23}$ .

In order to solve for  $\rho$  we can write equation (4.50) in the following form

$$\rho = \frac{\pi t}{2 \ln 2} (R_{12,34} + R_{23,41}) F\left(\frac{R_{12,34}}{R_{23,41}}\right) \quad (4.51)$$

where  $F$  is the correction factor for geometrical asymmetry. If the asymmetry is not too large ( $R_{12,34}/R_{23,41} < 10$ ), we can use the following approximation for  $F$ :

$$F = 1 - 0.3466 \left[ \frac{R_{12,34} - R_{23,41}}{R_{12,34} + R_{23,41}} \right] - 0.0924 \left[ \frac{R_{12,34} - R_{23,41}}{R_{12,34} + R_{23,41}} \right]^{-2}. \quad (4.52)$$

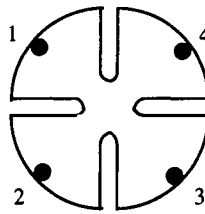


**Figure 4.26** Clover-shaped structure.

For a symmetrical structure  $R_{12,34} = R_{23,41}$  and

$$\rho = \frac{\pi t}{\ln 2} \frac{V_{34}}{I_{12}} = 4.352t \frac{V_{34}}{I_{12}} \quad (4.53)$$

which is similar to equation (4.48).

These equations are based on the assumption of infinitesimal ohmic contacts at the edge of the sample. The error introduced by real finite-size contacts which are not exactly on the periphery can be eliminated by the use of the clover-shaped structure shown in figure 4.26. This pattern is ideal and simple for making Hall measurements on epilayers in which the layer thickness is much smaller than the lateral dimension of the sample. This structure can be obtained by using Hall pattern makers designed for this purpose.

#### 4.6.2 Hall measurement

##### (a) Mobility

The electrical and optical properties of the material used for device fabrication are very important in determining the device performance. Mobility is one of these properties and determines device speed and current handling capabilities. Under low electric field strengths the carrier drift velocity is given by

$$v = \mu E. \quad (4.54)$$

Since device speed depends strongly on the velocity of the carriers, high mobility is required to obtain a high-frequency response. Due to the low resistivity of high-mobility materials, devices fabricated on these materials can handle high current levels without excessive heating. High current levels are desirable in high-speed applications where the capacitances in the circuits need to be charged rapidly.

The carrier mobility is determined by the combination of scattering processes in the material and depends on the temperature. We can define carrier mobility as the combination of mobilities due to different scattering mechanisms in the form (Jaeger 1990)

$$\frac{1}{\mu} = \sum_{i=1}^j \frac{1}{\mu_i} \quad (4.55)$$

**Table 4.2** The Hall mobilities of epitaxial InP layers grown on semi-insulating substrates.

Sample No	300 K		77 K	
	$N_D - N_A$ (cm $^{-3}$ )	$\mu_H$ (cm $^2$ V $^{-1}$ s $^{-1}$ )	$N_D - N_A$ (cm $^{-3}$ )	$\mu_H$ (cm $^2$ V $^{-1}$ s $^{-1}$ )
1	$2 \times 10^{15}$	5350	$1.5 \times 10^{15}$	59 800
2	$5 \times 10^{15}$	5240	$3.6 \times 10^{15}$	56 700
3	$5.7 \times 10^{15}$	4950	$3.6 \times 10^{15}$	53 320
4	$1 \times 10^{15}$	5500	$1 \times 10^{15}$	150 000

where  $j$  is the number of scattering mechanisms.

The mobility due to ionized impurity scattering can be expressed by (Sze 1981)

$$\mu_i = \frac{64\sqrt{\pi} \varepsilon_s^2 (2kT)^{3/2}}{N_I q^3 m^{*1/2}} \left\{ \ln \left[ 1 + \left( \frac{12\pi \varepsilon_s k T}{q^2 N_I^{1/3}} \right)^2 \right] \right\}^{-1} \quad (4.56)$$

where  $N_I$  is the ionized impurity density,  $\varepsilon_s$  is the permittivity,  $T$  is the temperature,  $k$  is the Boltzmann constant and  $m^*$  is the effective mass. From (4.56) we can see that mobility due to ionized impurity scattering is proportional to  $(m^*)^{-1/2} N_I^{-1} T^{3/2}$ . Therefore ionized impurity scattering is important in determining the mobility at low temperatures (low electron energy) and high ionized impurity densities.

The mobility due to acoustic phonon scattering is given by (Lundstrom 1990)

$$\mu_{AP} = \frac{\sqrt{2\pi} c_\ell q h^4}{D_A^2 m^{*5/2} (kT)^{3/2}} \quad (4.57)$$

where  $D_A$  is the acoustic deformation potential,  $h$  is Planck's constant and  $c_\ell$  is the elastic constant. This expression is proportional to  $(m^*)^{-5/2} T^{-3/2}$  which shows that this scattering mechanism is important at moderate or high temperatures. In addition to these scattering mechanisms, optical phonon scattering is one of the dominant scattering mechanisms in polar semiconductors such as GaAs and alloy scattering is observed in alloy materials due to the random arrangement of the constituent atoms. Table 4.2 shows the Hall mobilities of epitaxial InP layers grown on semi-insulating substrates.

### (b) Hall measurement

Hall measurements yield information about carrier concentration and mobility. Hall data also provide information on the electrically active impurities in a semiconductor. The measurement is based on the Hall effect discovered by Hall in 1879. He found that if a magnetic field is applied perpendicular to the direction of current flow in a conductor, an electric field perpendicular to the current and magnetic field is created.

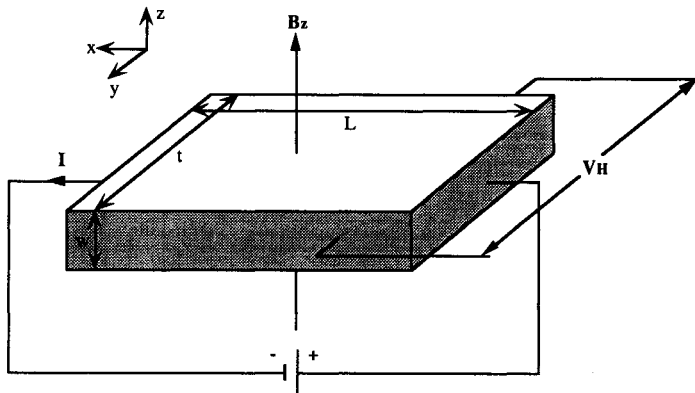


**Figure 4.27** Schematics of the Hall measurement.

Figure 4.27 shows an n-type semiconductor with an electric field,  $E_x$ , applied in the  $x$ -direction and a magnetic field,  $B_z$ , applied in the  $z$ -direction. Due to the electric field in the  $x$ -direction and the magnetic field in the  $z$ -direction the Lorentz force on an electron in the  $y$ -direction is given by

$$F = qB_zv_x \quad (4.58)$$

where  $q$  is the electronic charge and  $v_x$  is the electron velocity.

This force results in piling up electrons in the  $y$ -direction at one side of the sample and an electric field  $E_y$  is produced in this direction. Since there is no current in the  $y$ -direction,  $E_y$  should balance the Lorentz force, i.e.

$$qE_y = qB_zv_x. \quad (4.59)$$

The current in the  $x$ -direction due to the applied field is given by

$$I_x = qwt nv_x. \quad (4.60)$$

Using equations (4.60), (4.59) takes the form

$$qE_y = \frac{I_x B_z}{nwt}. \quad (4.61)$$

The Hall coefficient  $R_H$  is defined by

$$R_H = \frac{wV_H}{I_x B_z} \quad (4.62)$$

where  $V_H$  is the Hall voltage created in the  $y$ -direction due to  $E_y$ . Equations (4.61) and (4.62) give

$$R_H = -1/qn. \quad (4.63)$$

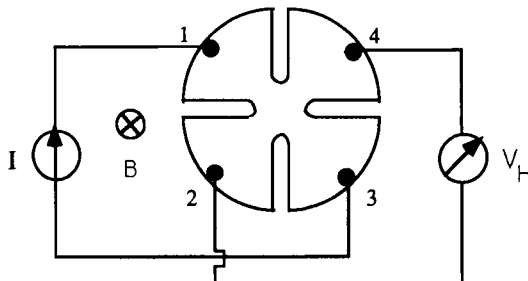


Figure 4.28 Hall effect set-up.

Similarly for p-type samples

$$R_H = 1/qp. \quad (4.64)$$

The sign of the Hall constant tells us the type of doping. In the case of mixed conduction when we have both holes and electrons,  $R_H$  is given by (Smith 1978)

$$R_H = \frac{[(p - b^2 n) + (\mu_n B)^2(p - n)]}{q[(p + bn)^2 + (\mu_n B)^2(p - n)^2]} \quad (4.65)$$

where  $b = \mu_n/\mu_p$ .

These expressions for the Hall coefficient are derived with the assumption that the relaxation time is energy independent. A numerical factor  $r$ , between one and two, called the Hall scattering factor, is usually included to account for the energy dependence of scattering mechanisms. The value of  $r$  depends on the dominant scattering mechanisms in the semiconductor ( $r = 1.18$  for acoustic scattering,  $r = 1.10$  for piezoelectric scattering and  $r = 1.93$  for ionized impurity scattering). In this case the Hall coefficient and mobility are expressed as

$$R_H = -r/qn \quad (4.66)$$

and

$$\mu = R_H \sigma / r. \quad (4.67)$$

We may define a quantity  $\mu_H$  called the Hall mobility which satisfies the relation:

$$\mu_H = R_H \sigma \quad (4.68)$$

so that  $\mu_H = r\mu$ . For thin layers, the sheet Hall coefficient is used which is defined as

$$R_{Hs} = R_H / t \quad (4.69)$$

which gives  $\mu_H = R_{Hs}/\rho_s$ .

An arrangement for measuring the Hall effect using a clover-shaped structure is shown in figure 4.28. A fixed current  $I$  is injected at two non-adjacent contacts

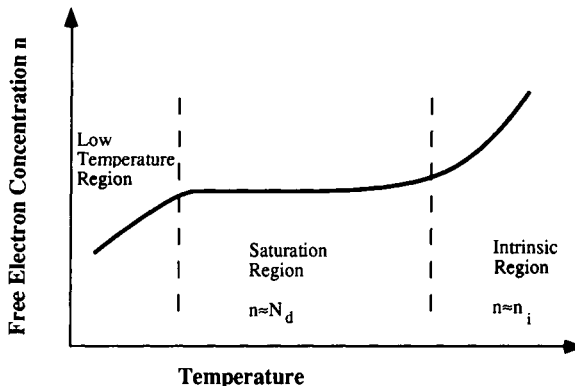


**Figure 4.29** Electron concentration against temperature in an n-type semiconductor.

and the potential across the other pair is measured under a constant magnetic field perpendicular to the sample surface. The Hall coefficient can be calculated using the measured Hall voltage  $V_H$ , the current  $I$  and the magnetic field  $B$  using equation (4.62). In order to increase the accuracy of the measurement the voltage across contacts 2 and 3 should be measured first without any magnetic field applied and the voltage drop due to misalignment of the contacts should be subtracted from the Hall voltage under magnetic field. Since the Hall voltage includes voltages generated by other effects, it is recommended to use an average value of  $V_H$  based on voltages measured for all permutations of contacts, current and magnetic field directions.

#### (c) Determination of the compensation ratio

Compensation reduces the free-carrier concentration and mobility in a semiconductor. The reduction in mobility is due to an increase in carrier scattering by ionized impurities. Therefore the compensation ratio is an important parameter to be determined in the characterization of materials.

Variable-temperature Hall measurements yield information about the donor and acceptor concentrations in a crystal. Figure 4.29 shows a schematic diagram of electron density as a function of temperature in an n-type doped semiconductor.

In the intermediate region, most of the donors are ionized and the free-carrier concentration does not change with temperature. In this region, electron concentration is approximately equal to the donor doping density  $N_d$  (assuming the acceptor doping density  $N_a = 0$ ). This region is also called the saturation region. In the low-temperature region, the free-carrier concentration decreases with temperature since the number of ionized donors depends on the temperature. In the intrinsic (high-temperature) region, the number of thermally agitated carriers is much larger than the electrons supplied by the donors and the electron concentration is approximately equal to the intrinsic carrier concentration  $n_i$ .

When impurities are added to the material, charge neutrality has to be preserved in the crystal. The equation that satisfies this condition is given by

$$n + N_a^- = p + N_d^+ \quad (4.70)$$

where  $N_d^+$  is the ionized donor density given by

$$N_d^+ = \frac{N_d}{1 + 2 \exp[(E_F - E_d)/kT]} \quad (4.71)$$

and  $N_a^-$  is the ionized acceptor density expressed as

$$N_a^- = \frac{N_a}{1 + 4 \exp[(E_a - E_F)/kT]}. \quad (4.72)$$

$E_d$  is the donor energy and  $E_a$  is the acceptor energy. Under non-degenerate conditions electron and hole concentrations are given by

$$n = N_c \exp[-(E_c - E_F)/kT] \quad (4.73)$$

and

$$p = N_v \exp[-(E_F - E_a)/kT] \quad (4.74)$$

respectively. In these expressions  $N_c$  is the density of conduction band states defined as:

$$N_c = 2 \left( \frac{2\pi m_{de} k T}{h^2} \right)^{3/2} \quad (4.75)$$

where  $m_{de}$  is the conduction band density of states effective mass.  $N_v$  is the density of valence band states given by

$$N_v = 2 \left( \frac{2\pi m_{dh} k T}{h^2} \right)^{3/2} \quad (4.76)$$

where  $m_{dh}$  is the valence band density of states effective mass. In the intermediate-temperature region almost all the donors and acceptors are ionized ( $N_a^- = N_a$ ,  $N_d^+ = N_d$ ). The charge neutrality condition gives

$$n - p = N_d - N_a. \quad (4.77)$$

Using the relation  $np = n_i^2$  with equation (4.77) we obtain:

$$n = \frac{N_d - N_a}{2} + \sqrt{\left( \frac{N_d - N_a}{2} \right)^2 + n_i^2} \quad (4.78)$$

and

$$p = -\frac{N_d - N_a}{2} + \sqrt{\left(\frac{N_a - N_d}{2}\right)^2 + n_i^2} \quad (4.79)$$

in the intermediate region. If  $N_d - N_a$  is much larger than  $n_i$  then

$$n \approx N_d - N_a \quad (4.80)$$

and

$$p = \frac{n_i^2}{N_d - N_a}. \quad (4.81)$$

Using equations (4.73) and (4.80) we can obtain the Fermi level in the intermediate region as

$$E_F = E_c - kT \ln \frac{N_c}{N_d - N_a} \quad (4.82)$$

which shows that the Fermi level rises towards the conduction band as the temperature is decreased. Therefore, in the low-temperature region, the Fermi level is close to the conduction band and the assumption  $N_d^+ = N_d$  loses its validity ( $N_a = N_a^-$  is still valid). In this region the hole density is negligible in an n-type semiconductor. If we write the charge neutrality equation under these conditions, we obtain:

$$N_c \exp\left(-\frac{E_c - E_F}{kT}\right) + N_a = \frac{N_d}{1 + 2 \exp(E_F - E_d)/kT} \quad (4.83)$$

or in terms of  $n$

$$\frac{2n(n + N_a)}{N_d - N_a - n} = N_c \exp\left(-\frac{E_c - E_d}{kT}\right). \quad (4.84)$$

To determine  $N_a$  and  $N_d$ , equation (4.84), which is the theoretical equation for the carrier concentration, must be fitted to the experimental Hall carrier concentration determined from variable-temperature Hall measurements. For semiconductors with deep donor ( $E_d$ ) levels it is also possible to determine  $E_d$  together with  $N_a$  and  $N_d$ .

Equation (4.71) is valid for a single donor level. If the impurity levels have excited states, the ionized donor density is given by

$$N_d^+ = N_d \left/ \left( 1 + \sum_{r=1}^j g_r \exp(E_F - E_r)/kT \right) \right. \quad (4.85)$$

where  $E_r$  is the energy and  $g_r$  is the degeneracy factor of the excited state  $r$ , and  $j$  is the total number of excited states.

In the high-temperature region, the carrier concentration is approximately equal to the intrinsic concentration which is given by

$$n_i = \sqrt{N_c N_v} \exp(-E_g/kT). \quad (4.86)$$

In this region,  $n$  varies theoretically as  $T^{3/2} \exp(-E_g/2kT)$  and  $E_g$  can be determined by using equation (4.86) and the experimental Hall concentration in the high-temperature region.

*(d) Depletion correction*

In lightly doped thin films it is possible for surface and interface depletion regions to deplete a significant portion or even all of the film. In this case the active film thickness is smaller than the physical film thickness and the bulk resistivity and carrier density must be corrected for surface and interface depletion. We can define the active film thickness by

$$t_{\text{act}} = t_m - t_i - t_s \quad (4.87)$$

where  $t_m$  is the metallurgical thickness,  $t_i$  is the thickness of the interface depletion layer and  $t_s$  is the surface depletion layer thickness. The thickness of the surface depletion layer is given within the abrupt depletion approximation by

$$t_s = \sqrt{\frac{2\varepsilon_0\varepsilon_r}{q(N_d - N_a)} \left( V_{BS} - \frac{kT}{q} \right)} \quad (4.88)$$

where  $V_{BS}$  is the built-in potential at the surface defined by

$$V_{BS} = \Phi_B - \frac{kT}{q} \ln \frac{N_c}{N_d - N_a}. \quad (4.89)$$

In this expression,  $\Phi_B = E_{cs} - E_{Fs}$  where  $E_{cs}$  and  $E_{Fs}$  are the conduction band energy and the Fermi level at the surface, respectively.

The depletion layer thickness at the interface is approximated as

$$l_i = \sqrt{\frac{2\varepsilon_0\varepsilon_r}{q(N_d - N_a)} \left( V_{Bi} - \frac{kT}{q} \right)} \quad (4.90)$$

where  $V_{Bi}$  is the built-in potential at the interface given by

$$V_{Bi} = \Phi_i - \frac{kT}{q} \ln \frac{N_c}{N_d - N_a} \quad (4.91)$$

$\Phi_i$  is the interface pinning potential.

Surface and interface depletion region thicknesses depend on the temperature, and unexpected carrier concentration shifts with temperature can be observed especially in thin layers if the necessary depletion corrections are not made (Lepkowski *et al* 1987).

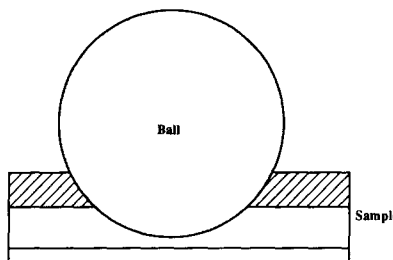


**Figure 4.30** Ball milling of the sample.

## 4.7 THICKNESS MEASUREMENT

Bevel stain measurement is a technique for measuring the thickness of a sample with an accuracy that can measure a few tens of ångströms thick layer with an error of  $\pm 10\text{ \AA}$ . It uses a rotating stainless steel ball to mill a hole on a sample and then the hole radius is measured by means of an optical microscope.

### 4.7.1 Ball polishing

This step mills a spherical hole in a sample by rotating a stainless steel ball as shown in figure 4.30. The first step is to choose the right ball for polishing because there are numerous balls of different radius ( $R$ ) which are used for different types of polishing. The second step is to put the sample on the sample holder before placing a drop of diamond paste on the sample. The diamond paste is added for the purpose of milling. Following this step, the system is turned on for a couple of seconds to let the ball mill the sample.

### 4.7.2 Revelation with RCA solution

Following ball polishing, a chemical etchant called RCA solution is used in an etching process to reveal the layer profile. The revelation of layers makes the observation and measurement of diameters easier.

RCA solution is a chemical etchant which consists of the following chemicals:

- (1) 250 g of  $\text{CrO}_3$  in  $300\text{ cm}^3$  of water
- (2) 2 g of  $\text{AgNO}_3$  in  $100\text{ cm}^3$  of water
- (3)  $250\text{ cm}^3$  of HF (48%) (at least 40%) in  $100\text{ cm}^3$  of water.

The solution is prepared by adding (2) to (1) followed by adding (3). For proper use, the reactant must be diluted in 10 volumes of water for one volume of reactant. Using this RCA solution, samples undergo revelation for a few seconds.

### 4.7.3 Rinsing procedure

Perfect cleaning of the sample and the ball prior to the ball milling procedure

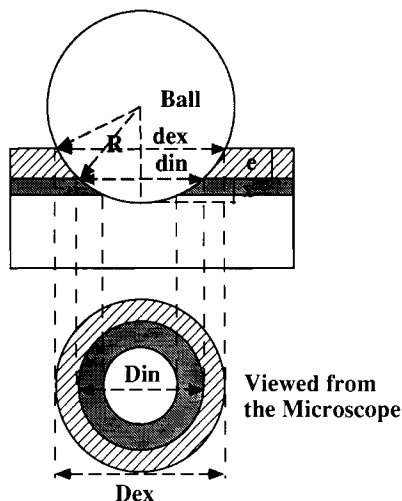


**Figure 4.31** Schematic diagram of the etched hole and diameters.

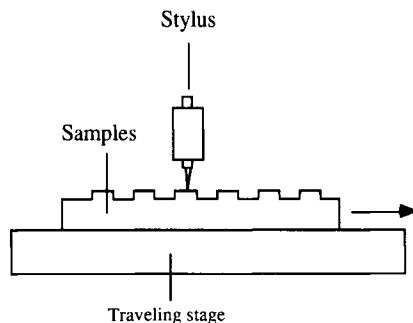


**Figure 4.32** Schematic diagram of a surface profiler.

is crucial since any dust or impurity on the sample or the ball can damage the sample. This would make the observation of the revealed layers difficult.

After the chemical revelation with RCA solution, the sample has to be rinsed once more to prevent any further attack by the RCA solution. This time it is first rinsed with water and then with methyl alcohol.

#### 4.7.4 Theory behind the thickness measurement

When a hole is etched on the sample, all the different epitaxial layers can be observed. Using an optical microscope of magnification rate  $G$ , the thickness of the observed layers can be determined by measuring the corresponding *magnified* diameters  $D_{\text{ex}}$  and  $D_{\text{in}}$  shown in figure 4.31. Note that the actual diameters (no magnification) are  $d_{\text{ex}}$  and  $d_{\text{in}}$ , respectively.

By simple mathematical relations and manipulation, using the condition  $d_{\text{ex}} < R$ , the formula of the thickness  $e$  can be derived as shown below

$$e = \frac{D_{\text{ex}}^2 - D_{\text{in}}^2}{8RG^2} \times 1000$$

where  $D_{\text{ex,in}}$  is in mm,  $G$  is the magnification of the microscope,  $R$  is the radius of the ball and  $e$  is in  $\mu\text{m}$ .

#### 4.7.5 Other thickness measurement techniques

Besides the bevel stain measurement mentioned above, the chemical bevel revelation discussed in section 4.1 can also be used for thickness measurement of epilayers as illustrated in figure 4.3 and figure 4.4. Other than chemical etching methods, surface profilers are available for measuring epilayer steps with a resolution as high as 1 Å. As shown in figure 4.32, a surface profiler profiles a sample electromechanically. A precision stage, travelling along an optically flat glass block, moves the sample beneath a diamond-tipped stylus. As the sample glides under the diamond-tipped stylus, variations in the sample surface cause vertical translation of the stylus. An LVDT core, mechanically coupled to the stylus, generates an analogue signal corresponding to the stylus movement. This signal is then amplified and digitized. Scan data are stored in computer memory for display, manipulation, measurement and readout.

## REFERENCES

- Abrahams M S and Buiocchi C J 1965 *J. Appl. Phys.* **36** 2855  
 Ambridge T, Elliot C R and Faktor M M 1973 *J. Appl. Electrochem.* **3** 1  
 Ambridge T and Faktor M M 1974 *J. Appl. Electrochem.* **4** 135  
 Ambridge T and Faktor M M 1975 *J. Appl. Electrochem.* **5** 319  
 Bebb H B and Williams E W 1972 *Semiconductors and Semimetals* vol 8, ed R K Willardson and A C Beer (New York: Academic) p 182  
 Blood P 1986 *Semicond. Sci. Technol.* **1** 7  
 Bond W L 1960 *Acta. Crystallogr.* **13** 814  
 Bragg W H and Bragg W L 1913a *Proc. R. Soc.* **88** 428  
 Bragg W H and Bragg W L 1913b *Proc. R. Soc.* **89** 246  
 Casey H C and Panish M B 1978 *Heterostructure Lasers (Part B)* (New York: Academic)  
 Cowley R A and Ryan T W 1987 *J. Phys. D: Appl. Phys.* **20** 61  
 Dean P J 1982 *Prog. Crystal Growth Charact.* **5** 89  
 Dingle R 1975 *Festkörperprobleme* **15** 21  
 Ewald P P 1916 *Ann. Phys.* **49** 117  
 Ewald P P 1917 *Ann. Phys.* **54** 519, 557  
 Ewald P P 1920 *Z. Phys.* **2** 323  
 Ewald P P 1921 *Phys. Z.* **21** 617  
 Ewald P P 1924 *Z. Phys.* **30** 1  
 Ewald P P 1925 *Phys. Z.* **26** 29

- Ewald P P 1958 *Acta Crystallogr.* **11** 888  
Fewster P F and Curling C J 1987 *J. Appl. Phys.* **62** 4154  
Hall E H 1879 *Am. J. Math.* **2** 287  
Huber A M, di Persio J, di Forte-Poisson M A, Brylinski C, Bisaro R and Grattepain C 1987 *Proc. SPIE* **796** 46  
Huber A M, Laurencin G and Razeghi M 1983 *J. Physique Coll.* **4** 409  
Huber A M, Razeghi M and Morillot G 1984 *Gallium Arsenide and Related Compounds 1984 (Inst. Phys. Conf. Ser. 74)* (Bristol: Institute of Physics) p 223  
Jaeger R C 1990 *Introduction to Microelectronic Fabrication (Volume V in the Modular Series on Solid State Devices)* (Reading, MA: Addison-Wesley)  
Kroemer H and Chien W Y 1981 *Solid State Electron.* **24** 655  
Lang D V 1974 *J. Appl. Phys.* **45** 3023  
Lang D V, Grimeiss H G, Meijer E and Jaros M 1980 *Phys. Rev. B* **22** 3917  
Lepkowski T R 1987 *J. Appl. Phys.* **61** 4808  
Lourenco J A 1984 *J. Electrochem. Soc.* **131** 1914  
Lundstrom M 1990 *Fundamentals of Carrier Transport* (Reading, MA: Addison-Wesley)  
Miller G L, Lang D V and Kimerling L C 1977 *Ann. Rev. Mater. Sci.* p 377  
Pankove J I 1975 *Optical Processes in Semiconductors* (New York: Dover)  
Razeghi M and Omnes F 1991 *Appl. Phys. Lett.* **59** 1034  
Schroder D K 1990 *Semiconductor Material and Device Characterization* (New York: Wiley)  
Smith K K 1981 *Thin Solid Films* **84** 171  
Smith R A 1978 *Semiconductors* (Cambridge: Cambridge University Press)  
Sze S M 1981 *Physics of Semiconductor Devices* (New York: Wiley)  
Takagi S 1962 *Acta Crystallogr.* **15** 1311  
Takagi S 1969 *J. Phys. Soc. Japan* **26** 1239  
Tapfer L and Ploog K 1986 *Phys. Rev. B* **33** 5565  
Taupin D 1964 *Bull. Soc. Fr. Mineral. Crystallogr.* **87** 469  
Thurmond C D 1975 *J. Electrochem. Soc.* **122** 1133  
Valdes L B 1954 *Proc. IRE* **42** 420  
Van der Pauw L J 1958 *Philips Res. Rep.* **13** 1  
Van Vechten J A and Thurmond C D 1976 *Phys. Rev. B* **14** 3539  
Webster G T W 1989 *PVS Instruction Manual* Bio-Rad Microscience Division  
Weyher J and Van de Ven J 1983 *J. Crystal Growth* **63** 285  
Weyher J and Van de Ven J 1986 *J. Electrochem. Soc.* **133** 799  
Weyher J and Van de Ven J 1988 *J. Crystal Growth* **88** 221  
Williams E W and Bebb H B 1972 *Semiconductors and Semimetals* vol 8, ed R K Willardson and A C Beer (New York: Academic) p 321  
Wolfe J P and Mysyrowicz A 1984 *Sci. Am.* **250** 98

## MOCVD Growth of GaAs Layers

### 5.1 INTRODUCTION

Over the past decade, metallorganic chemical vapour deposition (MOCVD) has developed into a versatile and reliable crystal growth technique. Very significant improvements have been made in understanding and controlling the purity, perfection and device properties of GaAs-based materials due mainly to the stimulus received from successful device applications in optoelectronics and microwave areas. GaAs has been considered as a possible alternative to silicon in the field of memories and microprocessors. However, technical improvements in silicon have raised requirements, challenging such possibilities. On the other hand, certain fields unexplored by silicon techniques, such as optoelectronics or TV satellite transmission, have turned out to be the major forces in propelling forward the future of GaAs and related compounds.

### 5.2 GaAs AND RELATED COMPOUNDS BAND STRUCTURE

As this volume is devoted to GaAs and related compounds, we will focus on GaAs,  $\text{Ga}_x\text{Al}_{1-x}\text{As}$  and  $\text{Ga}_{0.49}\text{In}_{0.51}\text{P}$  band structures, and their relevant physical properties (for an overview of InP and related compounds band structure, refer to volume 1 (Razeghi 1989).

GaAs has a zincblende structure and consists of two interpenetrating face-centred cubic lattices each of which contains Ga and As, respectively. Each Ga atom has four nearest neighbours of As and vice versa as shown in figure 5.1(a). The Ga and As atoms are tetrahedrally coordinated as shown in figure 5.1(b). The electronic configurations of a single Ga and As are  $3d^{10}4s^24p^1$  and  $3d^{10}4s^24p^3$ , respectively. The average number of valence electrons per atom is four. When Ga and As atoms form bonds in the crystal, the valence electrons are redistributed in  $sp^3$  hybridized orbitals which are oriented towards the nearest-neighbour atoms in  $\langle 111 \rangle$ ,  $\langle \bar{1}\bar{1}\bar{1} \rangle$ ,  $\langle 1\bar{1}\bar{1} \rangle$  and  $\langle \bar{1}1\bar{1} \rangle$  directions, respectively. The atomic orbitals that are used to form hybridized bonding orbitals are not the same as the ground states of the atoms. Even though this

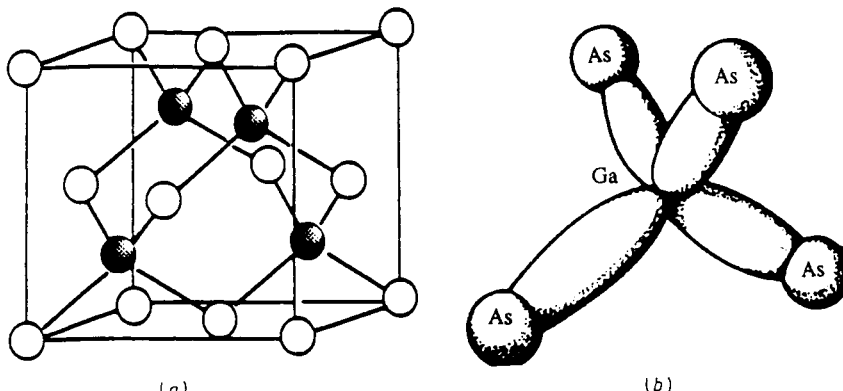


**Figure 5.1** (a) Zincblende lattice: the two interpenetrating cubic face-centred lattices are built by two different types of atom. (b)  $sp^3$  hybrid bond orbitals.

redistribution promotes electrons to a higher-energy state than the ground state, the total energy of the system is lowered by the formation of the bond. The bonding orbital consists of two directed orbitals associated with the two adjacent atoms, and is termed bonding or antibonding orbital depending on whether the two directed orbitals are in phase or out of phase. Such a bond is produced between two unlike atoms is called a heteropolar bond. In the case of GaAs, the valence electrons distribute more in the vicinity of As than Ga due to the larger value of electronegativity of As. Consider  $N$  primitive cells in a crystal: due to the hybridization between  $2N$  s states and  $6N$  p states there are two energy bands; each contains  $4N$  hybridized states and thus  $8N$  electrons. The  $8N$  valence electrons usually fill the lower band corresponding to the bonding orbitals and the upper band is empty.

Figure 5.2 shows the Brillouin zone (see e.g. Kittel (1971) for the theory of band structure in crystals) of the GaAs crystal (zincblende lattice), and indicates the most important symmetry points and symmetry lines, such as the centre of the zone ( $\Gamma = (2\pi/a)(0, 0, 0)$ ), the  $\langle 111 \rangle$  axes ( $\Lambda$ ) and their intersections with the zone edge ( $L = (2\pi/a)(\frac{1}{2}, \frac{1}{2}, \frac{1}{2})$ ), the  $\langle 100 \rangle$  axes ( $\Delta$ ) and their intersections ( $X = (2\pi/a)(0, 0, 1)$ ) and the  $\langle 110 \rangle$  axes ( $\Sigma$ ) and their intersections ( $K = (2\pi/a)(\frac{3}{4}, \frac{3}{4}, 0)$ ).

The currently used method for calculating the band structure around the  $\Gamma$  point is based on  $k \cdot p$  perturbation theory (Kane 1966). The crystal Hamiltonian, which has translation invariance properties through any lattice vector  $R$  and its eigenfunctions, can be written in Bloch's form:

$$\Phi_{n,k}(r) = \frac{1}{\sqrt{\Omega}} u_{n,k}(r) \exp(i\mathbf{k} \cdot \mathbf{r}) \quad (5.1)$$

where  $\Omega$  is the crystal volume,  $n$  is the index of the energy band and  $u_{n,k}$  is a Bloch function verifying:

$$u_{n,k}(\mathbf{r} + \mathbf{R}) = u_{n,k}(\mathbf{r}). \quad (5.2)$$

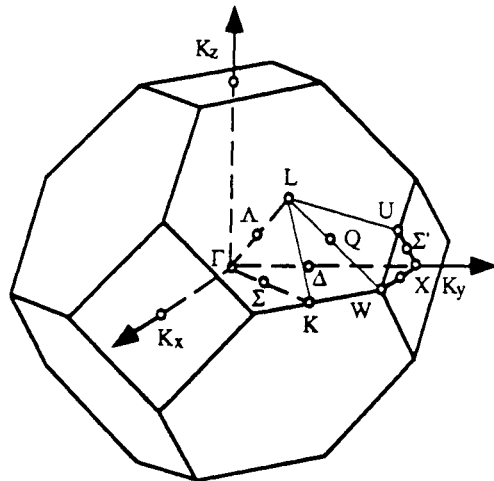


**Figure 5.2** First Brillouin zone for GaAs-based materials (zincblende lattice), including important symmetry points and lines.

$u_{n,k}$  can be deduced from the Schrödinger pseudoequation

$$H_k u_{n,k} = E_n(\mathbf{k}) u_{n,k} \quad (5.3)$$

with

$$H_k = \frac{\hbar}{2m_0} (-i\nabla + \mathbf{k})^2 + V(\mathbf{r}) + H_{\text{so}} \quad (5.4)$$

where  $m_0$  is the electron mass,  $V(\mathbf{r})$  is the crystal potential and  $H_{\text{so}}$  is the spin-orbit interaction Hamiltonian.

The  $\mathbf{k} \cdot \mathbf{p}$  perturbation method relies on the fact that the Hamiltonian  $H_k$  can be developed around  $\mathbf{k} = 0$ :

$$H_k = H_{k=0} + \left( \frac{\hbar}{m_0} \right) \mathbf{k} \cdot \mathbf{p} + \frac{\hbar^2 k^2}{2m_0} \quad (5.5)$$

$$H_k = H_{k=0} + H_1 + H_2. \quad (5.6)$$

By knowing the solutions of the Schrödinger equation around the  $\Gamma$  point ( $\mathbf{k} = 0$ ), the band structure can be determined for small  $\mathbf{k}$  by treating  $H_1 + H_2$  as perturbations.

Let  $L$  be the orbital kinetic momentum operator and  $S$  be the spin operator, with associated quantum numbers  $(l, m_l)$  and  $(s, m_s)$ . For a p-type band,  $l = 1$  and  $s = \frac{1}{2}$ . The total kinetic momentum operator  $J = L + S$  with quantum numbers  $(j, m_j)$  is introduced, so that due to the theorems relating to the composition of kinetics momentum, electrons verify  $j = \frac{1}{2}$  or  $j = \frac{3}{2}$ .

Spin-orbit coupling allows this degeneracy of a p bonding band to split, so that the valence band in  $\mathbf{k} = 0$  is separated into two points  $\Gamma_8$  ( $j = \frac{3}{2}$ ) and  $\Gamma_7$  ( $j = \frac{1}{2}$ ). The spin-orbit energy splitting is currently denoted  $\Delta = E_{\Gamma_8} - E_{\Gamma_7}$ .

**Table 5.1** Periodic part of Bloch's function.

$u_i  j, m_j\rangle$	$\Phi_j, m_j$	$E(\mathbf{k} = 0)$
$u_1  \frac{1}{2}, \frac{1}{2}\rangle$	$ s, +\rangle$	0
$u_3  \frac{3}{2}, \frac{1}{2}\rangle$	$-\sqrt{2}/3 z, +\rangle + 1/\sqrt{6} x + iy, -\rangle$	$-E_g$
$u_5  \frac{3}{2}, \frac{3}{2}\rangle$	$1/\sqrt{2} x + iy, +\rangle$	$-E_g$
$u_7  \frac{1}{2}, \frac{1}{2}\rangle$	$1/\sqrt{3} x + iy, -\rangle + 1/\sqrt{3} z, +\rangle$	$-E_g - \Delta$
$u_2  \frac{1}{2}, -\frac{1}{2}\rangle$	$ s, -\rangle$	0
$u_4  \frac{3}{2}, -\frac{1}{2}\rangle$	$-1/\sqrt{6} x - iy, +\rangle - \sqrt{2}/3 z, -\rangle$	$-E_g$
$u_6  \frac{3}{2}, -\frac{3}{2}\rangle$	$1/\sqrt{2} x - iy, -\rangle$	$-E_g$
$u_8  \frac{1}{2}, -\frac{1}{2}\rangle$	$-1/\sqrt{3} x - iy, +\rangle + 1/\sqrt{3} z, -\rangle$	$-E_g - \Delta$

When dealing with a direct bandgap material, the conduction-band minimum is at the  $\Gamma$  point at the zone centre (the conduction-band minimum is often called the conduction-band edge, and the valence-band maximum is called the valence-band edge). The minimum energy gap  $E_g$  is the energy difference between the conduction-band minimum ( $E_c$ ) and the valence-band maximum ( $E_v$ ), so the magnitude  $E_g$  of the energy gap in GaAs is given by

$$E_g = E_c - E_v. \quad (5.7)$$

The non-periodic part  $|j, m_j\rangle$  of Bloch's functions in the centre of the Brillouin zone is often expressed as a function of the orbitals  $p_x, p_y, p_z$ , which are denoted as  $|x\rangle, |y\rangle, |z\rangle$ . The results are shown in table 5.1, the energy origin being taken at the conduction band, in  $\mathbf{k} = 0$  ( $\Gamma_6$  point), and the spin sign being denoted + or -.

The problem being solved in  $\mathbf{k} = 0$ , a perturbation treatment can be applied to the Hamiltonian  $H_1 = \hbar(\mathbf{k} \cdot \mathbf{p})/m_0$  in the reduced basis  $(u_1, \dots, u_8)$ . The coupling terms  $\langle S | P_\alpha | \beta \rangle$  are null for  $\alpha \neq \beta$ , due to symmetry considerations.  $|S\rangle$  is the wavefunction of an s state electron;  $|\beta\rangle$  is the  $\beta$  component of the p state electron and  $P_\alpha$  is the  $\alpha$  component of the momentum operator. Furthermore,  $\langle S | P_\alpha | \alpha \rangle$  is independent of  $\alpha$ . Kane (1966) has noted that  $1/m_0 \langle S | P_\alpha | \alpha \rangle$  is a constant which is denoted as the constant  $P$ .

Once this coupling element is known, it is easy to write the matrix elements in the reduced base  $(u_1, \dots, u_8)$  for the first order in  $\mathbf{k} \cdot \mathbf{p}$  perturbation Hamiltonian (Kane 1966).

The eigenvalue equation  $\det(H - E_1) = 0$  leads to the dispersion relations:

$$E = -E_g \quad (5.8)$$

$$E(E + E_g)(E + E_g + \Delta) = p^2 \hbar^2 k^2 (E + E_g + 2\Delta/3). \quad (5.9)$$

By developing relation (5.9) around  $\mathbf{k} = 0$ , one can find the well known dispersion relation  $E(k) = \hbar^2 k^2 / 2m^*$  for the conduction band, thus leading

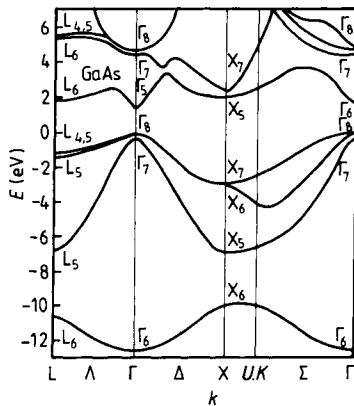


**Figure 5.3** The band structure of GaAs. It has a direct bandgap, with a minimum conduction band and a maximum valence band at the  $\Gamma$  point (after Sze 1981).

to an electronic effective mass

$$\frac{1}{m^*} = \frac{2P^2(E_g + 2\Delta/3)}{E_g(E_g + \Delta)}. \quad (5.10)$$

From (5.10), we can deduce that the electron effective mass increases with bandgap. This can be verified for  $\text{Ga}_{1-x}\text{Al}_x\text{As}$ , for which the effective mass increases with  $x$  from  $0.067m_0$  ( $x = 0$ ) to  $0.15m_0$  ( $x = 1$ ).

Note that the parabolic dispersion relation is only a first approximation. The exact equation deduced from relation (5.9) leads to an effective mass increasing with energy (non-parabolicity)

$$\frac{m^*(E)}{m^*} = \frac{(E + E_g)(E + E_g + \Delta)(E_g + 2\Delta/3)}{E_g(E_g + \Delta)(E + E_g + 2\Delta/3)}. \quad (5.11)$$

This effect varies with the bandgap approximately as  $1/E_g$  so that the non-parabolicity effect is more important for small gaps. Hence, the conduction band can be well defined around the  $\Gamma$  point with a first-order  $k \cdot p$  perturbation. This is not the case for the valence band, as seen from equation (5.8). This flat dispersion relation leads to an infinite heavy-hole mass. A second-order calculation is necessary to calculate the heavy- and light-hole masses (Dresselhaus *et al* 1955, Luttinger 1956). Figure 5.3 shows the band structure of GaAs. For an alloy like  $\text{Ga}_x\text{Al}_{1-x}\text{As}$ , there is a random location of Ga and Al on III sites, so that there is no more translation invariance. To find Bloch's solutions, it must be assumed that 'mean' atoms  $x\text{Ga} + (1 - x)\text{Al}$  are located on III sites.

The bandgap of GaAs at room temperature is around 1.42 eV. The main physical parameters of GaAs and of its related compounds are shown in table 5.2 (after Adachi 1985).

**Table 5.2** Physical parameters of GaAs and its related compounds (after Adachi 1985).

Parameter	GaAs	AlAs	$\text{Al}_x\text{Ga}_{1-x}\text{As}$
Bandgap energy $E_g^\alpha$ (eV)	$1.424 (E_g^\Gamma)^a$	$2.168 (E_g^X)^a$	$1.424 + 1.247x$ $(0 \leq x \leq 0.45)^a$ $1.900 + 0.125x + 0.143x^2$ $(0.45 < x \leq 1.0)^a$
Critical-point energy (eV)			
$E_0$	1.425 <sup>b</sup>	3.02 <sup>c</sup>	$1.425 + 1.155x + 0.37x^2$ <sup>w</sup>
$E_0 + \Delta_0$	1.765 <sup>b</sup>	3.32 <sup>c</sup>	$1.765 + 1.115x + 0.37x^2$
$E_1(1)$	2.89 <sup>b</sup>	3.82 <sup>c</sup>	$2.89 + 0.94x$
$E_1(2)$	2.96 <sup>b</sup>	3.96 <sup>c</sup>	$2.96 + 1.00x$
$E_1(1) + \Delta_1$	3.12 <sup>b</sup>	4.03 <sup>c</sup>	$3.12 + 0.91x$
$E_1(2) + \Delta_1$	3.19 <sup>b</sup>	4.16 <sup>c</sup>	$3.19 + 0.97x$
$E'_0$	4.44 <sup>b</sup>	4.54 <sup>c</sup>	$4.44 + 0.10x$
$E'_0 + \Delta'_0$	4.63 <sup>b</sup>	4.69 <sup>c</sup>	$4.63 + 0.06x$
$E_2$	4.99 <sup>b</sup>	4.89 <sup>c</sup>	$4.99 - 0.10x$
Electron affinity $\chi_c$ (eV)	4.07 <sup>d</sup>	3.5 <sup>d</sup>	$4.07 - 1.1x$ $(0 \leq x \leq 0.45)$ $3.64 - 0.14x$ $(0.45 < x \leq 1.0)$
Ionicity $f_i$	0.310 <sup>e</sup>	0.274 <sup>e</sup>	$0.310 - 0.036x$
Pressure coefficient of $E_g^\alpha$ ( $\times 10^{-6}$ eV bar <sup>-1</sup> )			
$dE_g^\Gamma/dP$	11.5 <sup>f</sup>	10.2 <sup>g</sup>	$11.5 - 13x$
$dE_g^X/dP$	-0.8 <sup>h</sup>	-0.8 <sup>i</sup>	-0.8
$dE_g^L/dP$	2.8 <sup>h</sup>	2.8 <sup>i</sup>	2.8
Temperature coefficient of $E_g^\alpha$ ( $\times 10^{-4}$ eV K <sup>-1</sup> )			
$dE_g^\Gamma/dT$	-3.95 <sup>j</sup>	-5.1 <sup>k</sup>	$-3.95 - 1.15x$
$dE_g^X/dT$	-3.6 <sup>j</sup>	-3.6 <sup>k</sup>	-3.6
Conduction-band effective mass			
$\Gamma$ valley $m_c^\Gamma$	0.067 <sup>a</sup>	0.150 <sup>a</sup>	...
X valley $m_{IX}$	0.23 <sup>m</sup>	0.19 <sup>n</sup>	...
$m_{IX}$	1.3 <sup>o</sup>	1.1 <sup>n</sup>	...
L valley $m_{IL}$	0.0754 <sup>p</sup>	0.0964 <sup>q</sup>	...
$m_{IL}$	1.9 <sup>r</sup>	1.9 <sup>s</sup>	...
Density-of-states electron mass $m_e^\alpha$			
$\Gamma$ valley $m_e^\Gamma$	0.067	0.150	$0.067 + 0.083x$
X valley $m_e^X$	0.85 <sup>t</sup>	0.71 <sup>t</sup>	$0.85 - 0.14x$
L valley $m_e^L$	0.56 <sup>t</sup>	0.66 <sup>t</sup>	$0.56 + 0.1x$

**Table 5.2** Continued.

Parameter	GaAs	AlAs	$\text{Al}_x\text{Ga}_{1-x}\text{As}$
Conductivity			
effective mass $m_e^\alpha$			
$\Gamma$ valley $m_e^\Gamma$	0.067	0.150	$0.067 + 0.083x$
X valley $m_e^X$	0.32 <sup>i</sup>	0.26 <sup>i</sup>	$0.32 - 0.06x$
L valley $m_e^L$	0.11 <sup>i</sup>	0.14 <sup>i</sup>	$0.11 + 0.03x$
Valence-band effective mass			
$m_{hh}$	0.087 <sup>u</sup>	0.150 <sup>v</sup>	$0.087 + 0.063x$
$m_{hh}$	0.62 <sup>v</sup>	0.76 <sup>v</sup>	$0.62 + 0.14x$
$m_{so}$	0.15 <sup>v</sup>	0.24 <sup>v</sup>	$0.15 + 0.09x$

<sup>a</sup> H C Casey Jr and M B Panish *Heterostructure Lasers* (Academic, New York, 1978)  
Part A.

<sup>b</sup> M Cardona, K L Shaklee and F H Pollak *Phys. Rev.* **154** 696 (1967).

<sup>c</sup> A Onton *Proceedings of the 10th International Conference on the Physics of Semiconductors* (Cambridge, Mass, 1970) p 107. Note that his symmetry assignment was corrected by W H Berninger and R H Rediker [*Bull. Am. Phys. Soc.* **16** 306 (1971)].

<sup>d</sup> These values are taken from a tabulation of A G Milnes and D L Feucht [*Heterojunctions and Metal-Semiconductor Junctions* (Academic, New York, 1972)].

<sup>e</sup> J C Phillips *Bonds and Bands in Semiconductors* (Academic, New York, 1973).

<sup>f</sup> R Zallen and W Paul *Phys. Rev.* **155** 703 (1967).

<sup>g</sup> Extrapolated from the data of  $\text{Al}_x\text{Ga}_{1-x}\text{As}$  by N Lifshitz, A Jayaraman, R A Logan and R G Maines [*Phys. Rev. B* **20** 2398 (1979)].

<sup>h</sup> Calculated by D L Camphausen, G A N Connell and W Paul [*Phys. Rev. Lett.* **26** 184 (1971)].

<sup>i</sup> Assumed similar to GaAs [see text].

<sup>j</sup> M Zvara *Phys. Status Solidi* **27** K157 (1968).

<sup>k</sup> B Monemar *Phys. Rev. B* **8** 5711 (1973).

<sup>l</sup> Assumed that  $dE_g^X/dT = dE_2/dT$  (see text). The data of  $dE_2/dT$  is taken from R R L Zucca and Y R Shen [*Phys. Rev. B* **1** 2668 (1970)].

<sup>m</sup> F H Pollak, C W Higginbotham, and M Cardona *J. Phys. Soc. Jpn. Suppl.* **21** 20 (1966).

<sup>n</sup> B. Rheinlander, H Neumann, P Fischer, and G Kuhn *Phys. Status Solidi b* **49** K167 (1972).

<sup>o</sup> E M Conwell and M O Vassell *Phys. Rev.* **166** 797 (1968).

<sup>p</sup> D E Aspnes and A A Studna *Phys. Rev. B* **7** 4605 (1973).

<sup>q</sup> Calculated from the usual  $k \cdot p$  theory.

<sup>r</sup> D E Aspnes *Phys. Rev. B* **14** 5331 (1976).

<sup>s</sup> Assumed similar to GaAs.

<sup>t</sup> Calculated from  $m_e^\alpha = N^{2/3} m_{ta}^{2/3} m_{la}^{2/3}$ , where  $N$  is the number of equivalent  $\alpha$  minima ( $\alpha = \Gamma, X$  or  $L$ ). Calculated also from  $m_e^\alpha = (2/m_{ta} + 1/m_{la})^{-1}$ .

<sup>u</sup> A L Mears and R A Stradling *J. Phys. C: Solid State Phys.* **4** L22 (1971).

<sup>v</sup> Taken from a tabulation of P Lawaetz [*Phys. Rev. B* **4** 3460 (1971)].

<sup>w</sup> Taken from H J Lee, L Y Juravel, J C Woolley and A J S Thorpe *Phys. Rev. B* **21** 659 (1980).

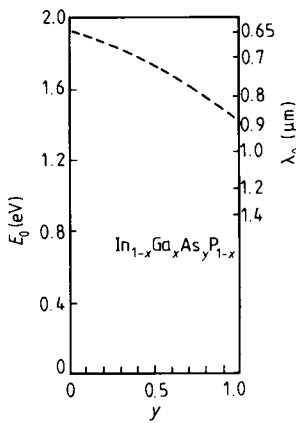


**Figure 5.4** The bandgap and wavelength of  $\text{Ga}_x\text{In}_{1-x}\text{As}_y\text{P}_{1-y}$  compounds lattice matched to GaAs (Adachi 1982).

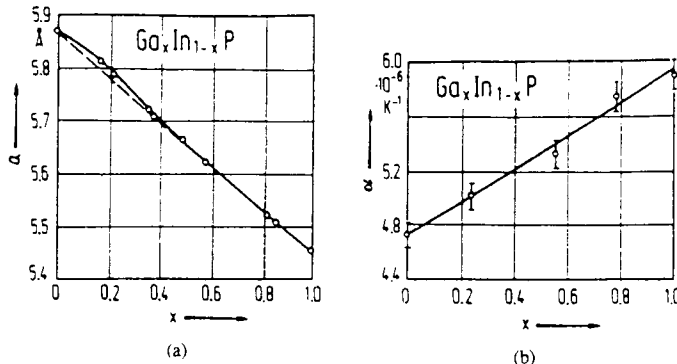
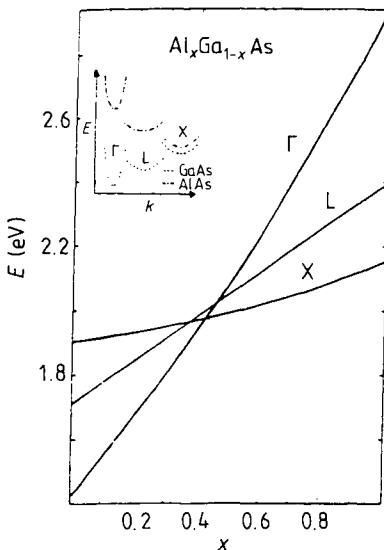


**Figure 5.5** (a)  $\text{Ga}_x\text{In}_{1-x}\text{P}$ . Composition dependence of the lattice parameter at 300 K. (b)  $\text{Ga}_x\text{In}_{1-x}\text{P}$ . Composition dependence of the coefficient of linear thermal expansion at 72 K (Landolt-Bornstein 1982).

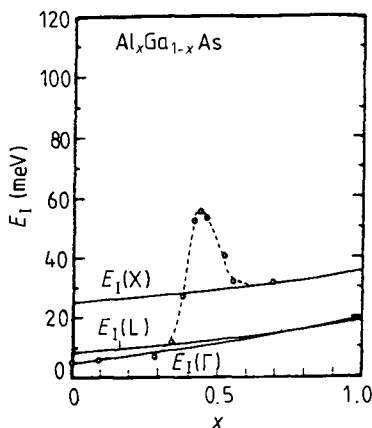
The bandgap and wavelength of  $\text{Ga}_x\text{In}_{1-x}\text{As}_y\text{P}_{1-y}$  compounds lattice matched to GaAs is illustrated in figure 5.4 (Adachi 1985). All of those materials have a direct bandgap. Note that the direct to indirect bandgap crossover for  $\text{Ga}_x\text{In}_{1-x}\text{P}$  compounds is for  $x = 0.74$ , far away from the lattice-matched GaAs composition ( $x = 0.49$ ).

Figure 5.5 shows some information about GaInP alloys lattice matched to GaAs substrate.  $\text{Ga}_x\text{Al}_{1-x}\text{As}$  compounds show a transition from direct to indirect bandgap, as illustrated in figure 5.6. The crossover of  $\Gamma$  and X bands occurs for  $x = 0.45$  at 300 K.

For  $x < 0.45$ : the minimum of the conduction band is at the  $\Gamma$  point, and the bandgap is direct. For  $x > 0.45$ : the minimum of the conduction band is at



**Figure 5.6** Energetic position of  $\Gamma$ , L and X bands in AlGaAs at  $T = 300$  K (Landolt-Bornstein 1982).



**Figure 5.7** Donor ionization energies,  $E_1(\Gamma)$ ,  $E_1(X)$  and  $E_1(L)$ , and acceptor ionization  $E_1(V)$  as a function of composition  $x$  for  $\text{Al}_x\text{Ga}_{1-x}\text{As}$  alloy. The theoretical curves (solid lines) are obtained from the hydrogen approximation using the band-mass parameters. The experimental data (open circles) are taken from Asai and Sugiura (1985).

the X point, and the bandgap is indirect ( $\Gamma \rightarrow X$  transition) (Hilsum 1962).

Figure 5.7 shows the evolution of the donor binding energy in  $\text{Ga}_x\text{Al}_{1-x}\text{As}$ , as a function of  $x$ , deduced from photoluminescence measurements.

The donor ionization energy switches from  $\Gamma$ -like ( $E_1(\Gamma)$ ) for  $x < 0.3$  to X-like ( $E_1(X)$ ) for  $x > 0.6$ , as expected from the crossover at  $x = 0.45$  (see figure 5.7). The energies  $E_1(\Gamma)$  and  $E_1(X)$  are deduced from the hydrogenoid binding energy, by taking into account the various electron masses in the  $\Gamma$  and X valleys, respectively (see table 5.2).

However, a sharp increase of this binding energy (nearly 50 meV) can be seen around  $x = 0.45$ , which cannot be explained by a simple  $\Gamma$ -like to X-like switch. From transport measurements, even higher binding energies reaching 150 meV near the  $x = 0.45$  crossover point were deduced. All these data agree in establishing that this singularity increases with the composition  $x$  of aluminum, reaching its maximum for  $x \approx 0.45$ , at the crossing of  $\Gamma$ , L and X bands. Hence, the defect centres are called DX centres. The presence of these centres is connected with persistent photoconductivity effects at low temperature: once the centres are optically emptied by irradiation at low temperature, a barrier is introduced to electron recapture (persistent photoconductivity). This barrier can be overcome by thermally heating the sample to higher temperatures where the persistent photoconductivity effect is reduced.

The detailed microscopic structure of DX centres remains unclear (Lang 1974, Bourgoin *et al* 1988) although it is clearly connected with the crossover of  $\Gamma$ , L and X bands around  $x = 0.45$ . Unfortunately, it leads to degradation in the performance of heterostructure lasers and modulation-doped field effect transistors (Stormer *et al* 1979). In this regard, it would be desirable to replace  $\text{Ga}_x\text{Al}_{1-x}\text{As}$  by  $\text{Ga}_{0.51}\text{In}_{0.49}\text{P}$ , composition lattice-matched to GaAs, since the crossover composition is  $\text{Ga}_{0.74}\text{In}_{0.26}\text{P}$ .

### 5.3 MOCVD GROWTH MECHANISM OF GaAs AND RELATED COMPOUNDS

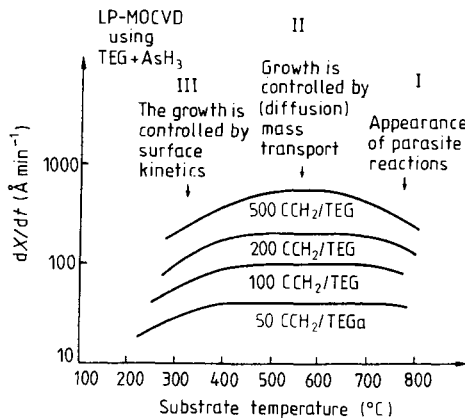
The general features of MOCVD growth mechanisms such as flow patterns and chemical reactions have been described in volume 1 of this work (Razeghi 1989).

Figure 5.8 shows the growth rate of GaAs layers, as a function of temperature. Three different zones are clearly evident in which:

- (i) growth is limited by the kinetics of cracking of growth species in the low-temperature range,
- (ii) growth is limited by the diffusion of group-III elements through the gas phase, and the growth rate is temperature independent,
- (iii) growth is limited by the desorption of species in the high-temperature range.

Van Sark *et al* (1990) have first derived the growth rate using an isothermal model by taking into account various flow profiles in a horizontal reactor tube.

Assuming that no diffusion occurs along the side walls ( $z$  direction) and along the flow direction ( $x$  direction), the diffusion equation can be written in



**Figure 5.8** Growth rate of GaAs, as a function of temperature for different TEGa flow rates (Razeghi *et al.* 1989).

the form (Van Sark *et al.* 1990)

$$v(y) \frac{\partial C(x, y)}{\partial x} = \frac{\partial}{\partial y} \left[ D(T(y)) \left( \frac{\partial C(x, y)}{\partial y} + (\alpha_T + 1) \frac{C(x, y)}{T(y)} \frac{\partial T(y)}{\partial y} \right) \right] \quad (5.12)$$

where  $v(y)$  is the flow velocity,  $C(x, y)$  is the concentration of growth species,  $D(T(y))$  is the binary diffusion coefficient of the group-III elements,  $\alpha_T$  is the thermal diffusion factor,  $\partial C / \partial y$  represents the diffusion due to the gradient concentration and

$$(\alpha_T + 1) \frac{C(x, y)}{T(y)} \frac{\partial T(y)}{\partial y}$$

represents the diffusion due to the thermal gradient.

Assuming no sidewall diffusion allows the problem to be essentially two dimensional ( $x, y$  plane). In an isothermal model, the temperature is assumed to be constant,  $T = T_0$ , so that there is no diffusion due to the thermal gradient.

The validity of each flow profile model is checked by defining the total deposition parameter which is equal to the ratio of the deposited growth species concentration over the input growth species concentration, and has to be close to unity.

By solving equation (5.12), the growth rate is derived:

$$R(x) = D(T_0) \frac{\partial C(x, y)}{\partial y} \Big|_{y=0}. \quad (5.13)$$

No essential difference is found between the ‘exact’ parabolic profile and the constant ‘plug’ flow  $v(y) = v_0$ , so that the plug flow is sufficient to calculate

the growth rate. The exact solution is found in the form

$$\frac{R(x)}{v_0 C_0} = \frac{D(T)}{v_0 h} \sum_{n=1}^{\infty} A_n \exp\left(-B_n \frac{D(T)}{v_0 h} \frac{x}{h}\right). \quad (5.14)$$

By retaining only the first-order term, the growth rate can be expressed in the simplified form

$$\frac{R(x)}{v_0 C_0} = A \frac{D(T)}{v_0 h} \exp\left(-B \frac{D(T)}{v_0 h} \frac{x}{h}\right). \quad (5.15)$$

The growth rate is found to decrease exponentially along a non-tilted susceptor. This fact has been experimentally evidenced by Van de Ven *et al* (1986) and Razeghi (1989).

The influence of surface kinetics is investigated by introducing a reaction rate constant  $k(T_0)$ , so that equation (5.13) is transformed into

$$D(T_0) \frac{\partial C(x, y)}{\partial y} \Big|_{y=0} = k(T_0) C(x, 0). \quad (5.16)$$

By defining the dimensionless CVD number:  $N_{\text{CVD}} = k(T_0)h/D(T_0)$ , Van Sark *et al* (1990) have found a limit for which

$N_{\text{CVD}} > \pi^2/4$  (fast surface reaction): growth is diffusion controlled,  
 $N_{\text{CVD}} < \pi^2/4$  (slow surface reaction): growth is kinetics controlled with slower growth rates.

The diffusion due to thermal gradients has been taken into account in equation (5.12). The influence of heating leads to thermal expansion, giving a mean flow velocity higher than in the previous case.

Considering the input temperature  $T_0 = 300$  K, and the substrate temperature  $T_s$ , the mean flow velocity can be approximated well by

$$v_T = \frac{T_s/T_0 - 1}{\log(T_s/T_0)} v_0. \quad (5.17)$$

Heating also has an influence on the diffusion coefficient, which increases with temperature, following the law

$$D(T) = D_0 \left(\frac{T}{T_0}\right)^{\gamma} \quad (5.18)$$

where  $\gamma$  is a coefficient close to 1.7 in the usual cases.

By solving equation (5.12) with thermal diffusion, Van Sark *et al* (1990) have expressed the growth rate under the general form (5.13), with an exponential decrease of the growth rate along the susceptor, thus leading to depletion effects. The thermal diffusion factor  $\alpha_T$  and the binary diffusion coefficient  $D(T)$  have

**Table 5.3** Optimum LP-MOCVD growth conditions for GaAs.

Growth pressure	76 Torr
Growth temperature	510 °C
Total H <sub>2</sub> flow rate	3 l min <sup>-1</sup>
AsH <sub>3</sub> flow rate	30 cm <sup>3</sup> min <sup>-1</sup>
H <sub>2</sub> through TEGa bubbler (at 0 °C)	120 cm <sup>3</sup> min <sup>-1</sup>
Growth rate	150 Å min <sup>-1</sup>

opposite effects on depletion: thermal diffusion toward the cold wall ( $\alpha_T$ ) weakens the depletion effect while an increase in  $D(T)$  increases the mass diffusion, thus leading to an increased depletion effect.

Taking into account the kinetics of a surface reaction with thermal effects leads to identical results without thermal effects. When the  $N_{\text{CVD}}$  constant is larger than unity, growth is essentially diffusion controlled. Note that depletion effects can be cancelled by tilting the susceptor a few degrees (Razeghi 1989).

Anyway, the modelling and interpretation of the growth mechanism of the MOCVD growth technique without accurate *in situ* diagnosis of the chemical reaction occurring in the gas phase and in the vicinity of the substrate during growth is very difficult.

#### 5.4 EXPERIMENTAL DETAILS

The growth apparatus has been described in detail in volume 1 (Razeghi 1989). GaAs layers can be grown either at atmospheric or low pressure in the temperature range between 500 and 550 °C. Triethylgallium (C<sub>2</sub>H<sub>5</sub>)<sub>3</sub>Ga (TEGa) or trimethylgallium (TMGa) (CH<sub>3</sub>)<sub>3</sub>Ga and pure arsine (AsH<sub>3</sub>) have been used as Ga and As sources. Pure H<sub>2</sub> can be used as a carrier gas. The growth rate depends linearly on the flow rate of group-III (Ga) elements and is independent of the AsH<sub>3</sub> flow rate, substrate temperature and substrate orientation, suggesting that the epitaxial growth is controlled by the mass transport of the group-III species.

Growth of GaAs layers has been carried out on (100) substrates misorientated up to 2° towards the (011) plane. The substrates were etched in a 5:1:1 (H<sub>2</sub>SO<sub>4</sub>:H<sub>2</sub>O<sub>2</sub>:H<sub>2</sub>O) solution for 20 s at 40 °C, rinsed with deionized water and dried under pure N<sub>2</sub>. The substrates were initially heated to the growth temperature under H<sub>2</sub> and AsH<sub>3</sub> for 5 min before growth began in order to remove any surface oxides. Table 5.3 lists the optimum growth conditions for the LP-MOCVD growth of GaAs, which were used for this study.

Epitaxial layers are n type for a wide range of V/III ratios and substrate temperatures. Suitable growth conditions such as growth temperature, growth rate, total flow rate, purity of starting materials and reactor design are responsible for the high quality of the epilayers.

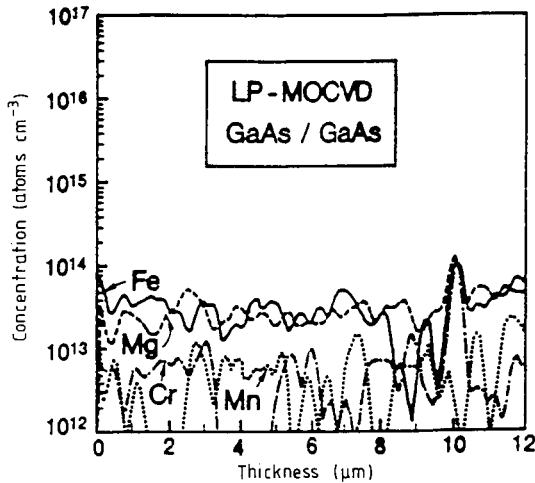


**Figure 5.9** SIMS profile for a  $10\text{ }\mu\text{m}$  thick undoped GaAs layer grown by LP- MOCVD (Razeghi *et al* 1989).

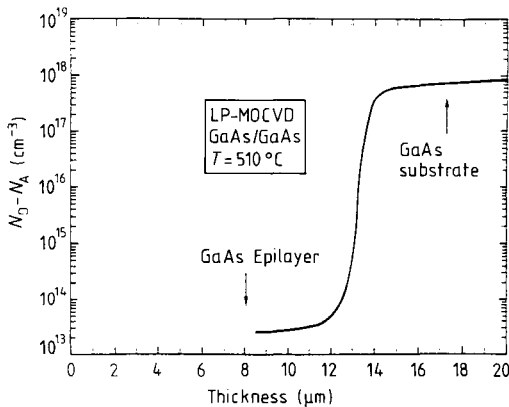


**Figure 5.10** Carrier concentration against depth profile of an ultrapure bulk GaAs grown by MOCVD (Razeghi *et al* 1989).

Figure 5.9 shows the SIMS profile for a  $10\text{ }\mu\text{m}$  thick GaAs layer grown by MOCVD at  $510^\circ\text{C}$ . The concentration of the impurities in the layer and at the interface is low and homogeneous. This result shows that the preparation of the substrate and the growth conditions were good.

Figure 5.10 shows the electrochemical  $C-V$  profile of a typical undoped GaAs layer. A high-purity epilayer with a residual carrier concentration as low as  $10^{13}\text{ cm}^{-3}$  for a  $12\text{ }\mu\text{m}$  thick layer has been obtained.

Electron Hall mobilities of epitaxial layers grown on semi-insulating

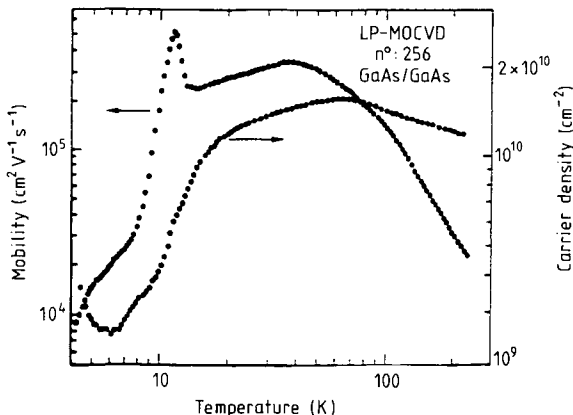
**Table 5.4** Measured values of the electron Hall mobility for three samples of undoped GaAs layers grown by LP-MOCVD.

	A	B	C
$N_d - N_a$ ( $\text{cm}^{-3}$ ) (polaron)	$2 \times 10^{13}$	$2 \times 10^{13}$	$3 \times 10^{13}$
Thickness ( $\mu\text{m}$ )	10	10	12
$N_d - N_a$ ( $\text{cm}^{-3}$ ) (Hall)	$1.6 \times 10^{13}$	$1.4 \times 10^{13}$	$10^{13}$
$\mu$ (300 K) ( $\text{cm}^2 \text{V}^{-1} \text{s}^{-1}$ )	8200	9000	9000
$\mu$ (77 K) ( $\text{cm}^2 \text{V}^{-1} \text{s}^{-1}$ )	190 000	200 000	210 000
$\mu_{\max}$ ( $\text{cm}^2 \text{V}^{-1} \text{s}^{-1}$ )	290 000 ( $T = 45$ K)	320 000 ( $T = 40$ K)	335 000 ( $T = 38$ K) 600 000 ( $T = 12$ K)

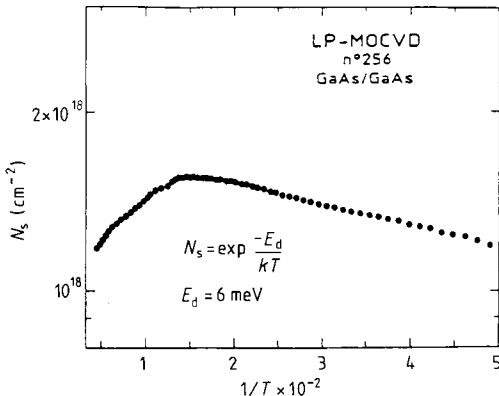
((Cr–O)-doped) GaAs substrates were measured in a magnetic field of 5 kG by a conventional Van der Pauw technique. Table 5.4 indicates the measured mobilities at 300 K, at 77 K and at low temperature (12 K) in the undoped GaAs epilayers.

Figure 5.11 shows the experimental mobility measured at 5 kG as a function of temperature. Electron Hall mobility as high as  $335\,000 \text{ cm}^2 \text{V}^{-1} \text{s}^{-1}$  at 38 K has been measured. The mobility curve contains an additional peak at 12 K with a mobility of  $600\,000 \text{ cm}^2 \text{V}^{-1} \text{s}^{-1}$ , which is the highest mobility reported for GaAs layers grown by any technique. This shoulder can result from changes in the ionized impurity concentration due to carrier freezeout (Colter *et al* 1983, Stillman and Wolfe 1976): a phenomenon which has been reported before for VPE GaAs samples (Wolfe and Stillman 1975). Two factors can contribute to a high low-temperature mobility: the relatively low scattering rate due to the ionized impurities and the relatively high screening effect due to neutral impurities (Colter *et al* 1983). For temperature less than 10 K the resistivity of the sample increases and measurements become very difficult. Figure 5.12 shows the variation of carrier concentration as a function of temperature for this epilayer. The activation energy measured from this curve is 6 meV, which corresponds to a shallow donor such as Si or S in the GaAs undoped epilayer (see figure 5.12).

Ehrenreich (1959) has examined the scattering mechanisms which determine the transport properties of GaAs layers and has shown that a combination of polar optical phonon and ionized impurity scattering yielded qualitative agreement with the temperature and impurity concentration dependence of the electron mobility for the pure bulk GaAs. Later, Stillman and Wolfe (1976) and Wolfe and Stillman (1975) have shown that the combination of polar optical phonons, piezoelectric acoustic phonon, deformation potential acoustic phonon, ionized impurity and neutral impurity scattering in the relaxation time approximation gave results which were in good agreement with the temperature



**Figure 5.11** Variation of electron Hall mobility and carrier density as a function of temperature for a high-purity GaAs layer grown by MOCVD (Razeghi *et al* 1989).



**Figure 5.12** Variation of  $N_s$  as a function of  $1/T$  (Razeghi *et al* 1989).

and concentration dependence of the electron mobility in high-purity GaAs grown by vapour phase epitaxy. In their analysis, they have assumed:

- (i) each scattering process is described by a relaxation time  $\tau(E)$  which may depend on the electron energy ( $E$ ),
- (ii) the scattering mechanisms are independent of each other,
- (iii) the electrons are scattered in a parabolic band. With the above approximation, an average relaxation time  $\langle \tau \rangle$  can be calculated from the equation

$$\langle \tau \rangle = \frac{4}{3\sqrt{\pi}} x \int_0^{\infty} \tau(E) \frac{E^{3/2} \exp(-E/k_B T)}{k_B T^{5/2}} dE \quad (5.19)$$

where  $E$  is the electron energy and  $k_B$  is the Boltzmann constant. The electron

mobility is then determined from  $\mu = e\langle\tau\rangle/m^*$ , where  $e$  is the electronic charge and  $m^*$  is the electron effective mass.

Satisfying agreement between the experimental results and calculations based on these simplifying assumptions has been obtained, assuming the residual doping level has been lowered down to less than the  $10^{14} \text{ cm}^{-3}$  range. This is confirmed by figure 5.10, which shows the typical electrochemical  $C-V$  profile of the undoped GaAs layers grown by MOCVD. Carrier concentrations as low as  $2 \times 10^{13} \text{ cm}^{-3}$  for a  $13 \mu\text{m}$  thick layer have been measured. All layers are n type.

Table 5.4 also shows the measured values of electron Hall mobility for undoped GaAs layers grown by MOCVD, under the growth conditions indicated in table 5.3.

Hall effect data indicated that the free electrons, of the order of  $10^{13} \text{ cm}^{-3}$ , are provided by donor impurities which are partially compensated by acceptor impurities. In order to provide additional information on the nature and concentration of the defects contained in these layers, deep-level transient spectroscopy (DLTS) has been used to evaluate the amount of electron compensation they induce and the influence they can have on the electron mobility.

For this experiment, identical layers under conditions described in tables 5.3 and 5.4 have been grown on  $n^+$ -substrates. Ohmic contact is made on the back of the substrate and Au Schottky barriers are evaporated on the top of the layers in order to perform capacitance–voltage ( $C-V$ ) and DLTS measurements.

The  $C^{-2}(V)$  characteristics indicate a uniform carrier profile and a free-electron concentration in the range of 1 to  $4 \times 10^{13} \text{ cm}^{-3}$  at 300 K, increasing noticeably at 400 K. This increase in electron concentration suggests the presence of a donor defect, which emits electrons between 300 and 400 K. Its concentration can be estimated from the difference between the electron concentrations at 300 and 400 K. This difference varies from 0.3 to  $7 \times 10^{13} \text{ cm}^{-3}$  depending on the sample studied. From DLTS results (see figure 5.13), this defect can be attributed to the so-called EL2 defect (Bourgoin *et al* 1988).

Capacitance transient measurements have been performed in the range 4–300 K. DLTS spectra show the existence of a large peak, labelled C, around 350 K and two small ones, labelled A and B, in the 250–300 K range (see figure 5.13). The signatures—the variation of emission rates with inverse temperature (figure 5.14)—give the following thermal ionization energies to the conduction band edge: 0.47 eV (A), 0.65 eV (B) and 0.75 eV (C). The signature of peak C is similar to the one expected for the EL2 defect; in some cases a difference is found which can be accounted for by the fact that the defect concentration is of the order of the free-carrier concentration (Stievenard *et al* 1985). Typically, in a layer containing  $1 \times 10^{13} \text{ cm}^{-3}$  free electrons at 300 K, the EL2 (C) concentration reaches  $4 \times 10^{12} \text{ cm}^{-3}$ . The concentrations of the 0.47 and 0.65 eV traps are similar, typically  $\sim 10^{12} \text{ cm}^{-3}$ .

Finally, a peak labelled D is also observed at 200 K; its concentration is

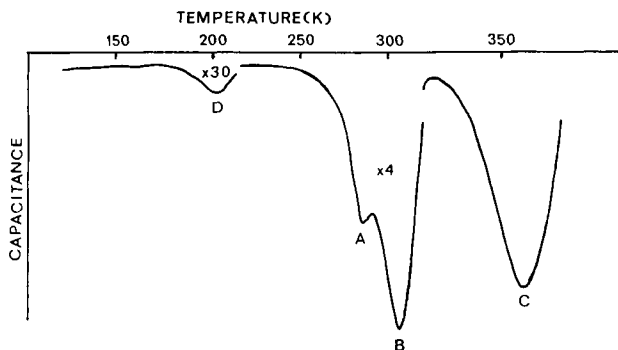


**Figure 5.13** Deep-level transient spectroscopy spectra of GaAs grown by MOCVD (Feng *et al* 1991).

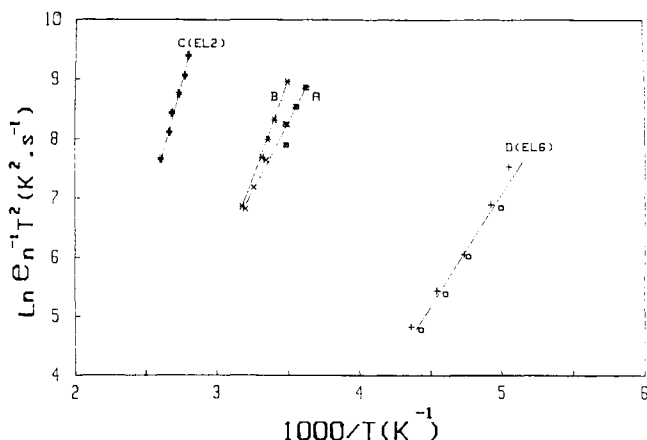


**Figure 5.14** Variation of the emission rates with the inverse of temperature (Feng *et al* 1991).

small ( $5 \times 10^{11} \text{ cm}^{-3}$ ) and it is associated with an ionization energy of 0.32 eV (see figure 5.14). Because it is located only near the surface, and its signature is very similar to the one associated with the so-called EL6 defect (Bourgoin *et al* 1988), one can attribute the existence of peak D to the EL6 defect.

Photoluminescence (PL) measurements were made at 4.2 K using a 633 nm He-Ne laser ( $P_{\text{exc}} = 1 \text{ W cm}^{-2}$ ) as an excitation source. The luminescence was detected using a 1 m double spectrometer equipped with a GaAs photomultiplier tube; the PL spectra are shown in figure 5.15. They are very similar to those of the purest VPE samples. The free-exciton (polariton) emission of sample C, which is  $12 \mu\text{m}$  thick, is particularly intense at 1.5149 and 1.5154 eV, with a shoulder at 1.5177 eV associated with the excited state ( $n = 2$ ) of the free exciton. This assignment has been confirmed by reflectivity measurements

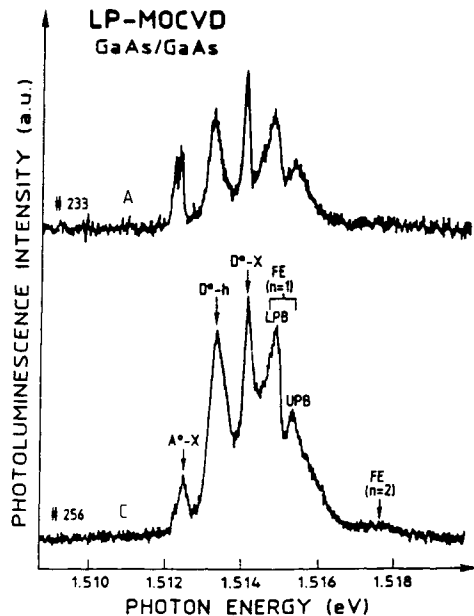


**Figure 5.15** Photoluminescence spectra at  $T = 4.2$  K of two ultrathick GaAs epilayers grown by MOCVD (Razeghi *et al* 1989).

showing a marked dip at the energy of the ( $n = 1$ ) free exciton between the two polariton branches. The sharp line at 1.5141 eV is due to the recombination of excitons bound to neutral donors ( $D^0-X$ ). The peaks at 1.5134 and 1.5125 eV originate from the recombination of free holes with neutral donors ( $D^0-h$ ) and from the recombination of excitons bound to neutral acceptors ( $A^0-X$ ). The weakness of this ( $A^0-X$ ) peak is an indication of the low degree of compensation of the samples. Further evidence of the low-acceptor background is given by the small ratio of the band to acceptor luminescence in the 1.49 eV range (not shown in figure 5.15) compared to the excitonic luminescence. This ratio amounts to 0.30, 0.23 and 0.16 for samples A, B and C, respectively, the lowest value being obtained for the highest-mobility sample, as expected. The better quality of sample C in comparison to sample A can also be seen in the PL spectra of figure 5.15. The relative intensity of the free-exciton emission is smaller for A, whereas the ( $A^0-X$ ) emission is stronger.

## 5.5 INCORPORATION OF IMPURITIES IN GaAs GROWN BY MOCVD

When an impurity atom is introduced in a GaAs lattice, if it occupies an As site, and it provides the crystal with one or more additional electrons than the atom it replaced, then the impurity is called a donor. Thus S, Se and Te on an

As site in GaAs are donors. If the impurity atom provides fewer electrons than the atom it replaces, it forms an acceptor, like Zn on a Ga site in GaAs.

Instead of replacing an atom of the GaAs crystal, the impurity may lodge itself in an interstitial position. Then its outer-shell electrons are available for conduction and the interstitial impurity becomes a donor.

A missing atom results in a vacancy and deprives the crystal of one electron per broken band. This makes the vacancy an acceptor. During the MOCVD growth of GaAs, a deviation from stoichiometry (due to the ratio of As/Ga) generates donors or acceptors depending on whether it is the Ga or As which is in excess. The extra electron of the donor is attracted most strongly to the positive charge of the impurity nucleus. Thus it acts as the electron of a hydrogen atom immersed in the high dielectric constant  $\epsilon$  of the GaAs crystal. This enables us to calculate the energy binding the electron to the impurity (its ionization energy):

$$E_i = \frac{m^* q^4}{2h^2 \epsilon^2 n^2} = \frac{m^*}{m \epsilon^2 n^2} 13.6 \text{ eV} \quad (5.20)$$

where  $q$  is the electron charge,  $m$  is the mass of an electron in vacuum,  $n$  is a quantum number  $\geq 1$ . The ionization energy from the ground state to the conduction band is obtained by making  $n = 1$ . Since  $\epsilon(\text{GaAs}) = 13.1$  and the effective mass ratio of an electron is 0.067 (and 0.48 for a hole), the ionization energy of a donor and acceptor in GaAs is then 6 meV and 40 meV, respectively.

Some impurities do not agree with the simple hydrogen model and form levels which may lie deep in the energy gap. All the transition elements seem to form deep levels in GaAs. The reasons for which certain impurities form a deep level are not yet completely understood.

Since the impurity is usually either larger or smaller than an atom of the GaAs lattice, a local mechanical strain can be obtained. An interstitial atom evidently induces a deformation potential corresponding to compressional strain, whereas a vacancy will have the opposite effect, since it produces dilatational strain. Usually in GaAs layers, both interstitials and vacancies should be present in addition to substitutional impurities. Dislocations are also usually present in GaAs epilayers. They occur at the edge of an extra plane of atoms. The misfit of such an extra plane results in compressional and dilatational strains, with the consequent onset of both lowering and raising of the potentials in the neighbourhood of the dislocation.

### 5.5.1 Residual impurities

The epitaxial layers of GaAs have been grown generally using triethylgallium (TEGa) or trimethylgallium (TMGa), and arsine ( $\text{AsH}_3$ ). The purity of source materials is one of the most important factors to be considered to improve the quality of products. For the MOCVD growth of GaAs, there have been many

publications dealing with residual impurities in the epitaxial layers. The quality of epitaxial GaAs layers is known to be affected by the impurities in TEGa or TMGa, for example silicon (Dapkus *et al* 1981, Hess *et al* 1982, Nakanishi *et al* 1981). Hence, great efforts have been made to improve the purity of TMGa and TEGa. On the other hand, Ge (germanium) as a dominant donor impurity was found in undoped MOCVD-grown GaAs layers and AsH<sub>3</sub> was found to be a possible source of germanium contamination.

### 5.5.2 Carbon incorporation in GaAs grown by MOCVD

Kuech *et al* (1988) studied the influence of hydrocarbons in MOCVD growth of GaAs. Quantitative measurements of carbon concentration in GaAs layers grown by MOCVD is required to elucidate both the growth reactions and the influence of reaction by-products. The influence of methane (CH<sub>4</sub>) in MOCVD on both the growth rate and the incorporation of carbon has been studied by several authors (Kuech *et al* 1988, El Jani *et al* 1982). In general, the introduction of CH<sub>4</sub> into the growth ambient does not substantially alter the growth rates or result in any additional electrically active carbon (Kuech *et al* 1988). The total additional carbon incorporation from methane, both electrically active and inactive, is also negligible. The low or negligible carbon incorporation has been attributed to both the high reaction efficiency between the hydrogen, which originates on the arsine, and the methyl radicals released on or near the growth surface. The other hydrocarbon sources, such as C<sub>2</sub>H<sub>2</sub>, C<sub>2</sub>H<sub>4</sub> and C<sub>2</sub>H<sub>6</sub>, should be more reactive due to the presence of the double carbon bond,  $\text{--C}=\text{C}\text{--}$ . These compounds lead to slight amounts of carbon incorporation when there are high concentrations in the gas phase. Similarly, these compounds may decompose in the gas phase. However, their reaction products must be either non-reactive with respect to the GaAs surface or react rapidly in the gas phase to form other, perhaps saturated, non-reactive hydrocarbons.

Mochizuki *et al* (1988) studied the mechanism by which carbon is incorporated into GaAs layers by atomic layer epitaxy using TEGa or TMGa and AsH<sub>3</sub>. They showed that the carbon density varied from  $1 \times 10^{13}$  to  $8 \times 10^{18} \text{ cm}^{-3}$  with TEGa or TMGa and AsH<sub>3</sub> pulse durations and mole fractions. They also observed that carbon incorporation drastically changed at the pulse duration and mole fraction where the growth rate per gas cycle started to saturate to one monolayer (0.283 nm/cycle for a (100) substrate). They explained the results by the selective adsorption of carbon on surface gallium, the reaction of methylgallium with arsine and the exchange interaction between arsenic and carbon atoms. They found that even when the TMGa source was used, the epitaxial layers grown under the optimized growth conditions exhibited an electron concentration of  $1 \times 10^{14} \text{ cm}^{-3}$  and a mobility of  $80\,000 \text{ cm}^2 \text{ V}^{-1} \text{ s}^{-1}$  at 77 K, with a photoluminescence spectrum with several sharp excitonic lines at the bandgap energy, and an extremely low level of carbon-related peaks.

In conclusion, the TMGa source is the origin of carbon impurities in the

GaAs layers grown by MOCVD. The probability of carbon incorporation in the epitaxial layers is increased by increasing the TMGa flow rate. When the ratio of  $\text{TMGa}/\text{AsH}_3 > 1$ , the epitaxial layers are p type, and when the ratio of  $\text{TMGa}/\text{AsH}_3 \ll 1$ , the epitaxial layers are n type. Arsine plays an important role in the incorporation of carbon in GaAs layers grown by MOCVD.

### 5.5.3 n-type GaAs

GaAs layers grown by MOCVD can be doped using Si, Se or S as explained in detail below.

#### (a) Silicon

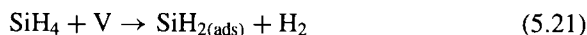
Silicon is one of the primary dopants in GaAs and related compounds. Controlled carrier concentrations from  $10^{15}$  up to  $10^{19} \text{ cm}^{-3}$  can be achieved using either silane ( $\text{SiH}_4$ ), or disilane ( $\text{Si}_2\text{H}_6$ ). The low diffusion coefficient of Si in GaAs and the availability of high-purity sources make the silanes attractive doping sources for device applications. Sharp doping profiles can be routinely achieved since neither silane nor disilane exhibits any ‘memory effect’ in the reactor.

Silane exhibits a strong temperature dependence as well as low efficiency for silicon incorporation. As a result, temperature variations across the susceptor lead to doping non-uniformities across the wafer. Kuech *et al* (1984) showed that doping from a disilane source has a much higher silicon incorporation efficiency and is relatively temperature independent under most typical growth temperatures and growth conditions. Shimazu *et al* (1987) found that for a particular reactor pressure, using  $\text{Si}_2\text{H}_6$ , and at low temperatures, the doping concentration has an Arrhenius dependence on temperature ( $K = A \exp(-k/RT)$ ), but becomes temperature independent at high temperatures. They showed, by increasing the total reactor pressure, that the overall doping efficiency increases, while the transition temperature at which the doping becomes temperature independent decreases. The reaction mechanism underlying the temperature dependence of Si doping using silane in MOCVD-grown GaAs is the same as in the case of InP (Razeghi 1989).

They proposed a simple model to describe the Si incorporation in GaAs from  $\text{SiH}_4$ . They assume the following.

(i) The thermal decomposition of  $\text{SiH}_4$  is heterogenous, and does not occur in the gas phase. (The Si–H bond strength in  $\text{SiH}_4$ , 3.2–3.4 eV, is comparable to the As–H bond strength of  $\text{AsH}_3$ , 2.9–3.2 eV (Saalfeld and Svec 1963)).

(ii) On (100) GaAs, each chemisorbed species forms two bonds to the surface so they expect  $\text{SiH}_{2(\text{ads})}$  doping as the initial adsorbed (ads) species leading to incorporation. They proposed that this adsorption reaction is the rate limiter:



where V is a vacant adsorption site.

- (iii) The adsorption rate equals the incorporation rate of Si on GaAs.
- (iv) The surface pressure of SiH<sub>4</sub> is approximately the same as the inlet pressure of SiH<sub>4</sub>. This is because the adsorption is limited by reaction (5.21) rather than by diffusion.

Shimazu *et al* (1987) explained the variation of Si doping with temperature and reactor pressure using this model, considering also the effects of vacancy coverage and variable adsorption energies. In addition, this model explains the variation of doping with arsine pressure.

Field and Ghandhi (1986) have grown GaAs at a range of temperatures, from 650 to 750 °C, by the MOCVD process at pressures from 0.046 to 1.0 atm, using SiH<sub>4</sub> as a dopant source. They found that the doping is proportional to SiH<sub>4</sub> pressure, inversely proportional to growth rate, and increases with temperature.

Veuhoff *et al* (1985) studied the incorporation of silicon in GaAs layers grown by MOCVD using SiH<sub>4</sub> and Si<sub>2</sub>H<sub>6</sub> doping sources. The layers were grown on ⟨100⟩, ⟨111⟩ A and ⟨111⟩ B surfaces over a wide range of growth temperatures and gas phase stoichiometries. They found an influence of the substrate orientation on silicon incorporation using SiH<sub>4</sub>. They described this behaviour by a qualitative model involving both surface-specific adsorption sites and possible surface chemical reactions. In the case of disilane, Si<sub>2</sub>H<sub>6</sub>, the incorporation process appears to be independent of substrate orientation and growth temperature. This temperature independence results in improved uniformity of the electron concentration over large areas of the substrate when disilane is used as the doping gas.

The incorporation of Si into GaAs epilayers grown by MOCVD using either an SiH<sub>4</sub> or Si<sub>2</sub>H<sub>6</sub> source is proportional to its mole fraction in the reactor, inversely proportional to the growth rate and growth temperature. Usually Si substitutes for Ga in the GaAs lattice and acts as a donor: as Si is amphoteric, the donor concentration depends on the III/V ratio.

Omnes *et al* (1991) studied silicon incorporation in LP-MOCVD GaAs layers grown at low temperature between 500 and 600 °C. They used 15 ppm silane diluted in pure H<sub>2</sub>. The electron concentration varies linearly with the silane flow rate and exponentially with the inverse of growth temperature in the following form:

$$N_D - N_A = B(P_{\text{SiH}_4}, P_{\text{AsH}_3}) \exp\left(-\frac{E_i}{k_B T}\right) \quad (5.22)$$

with  $E_i = 1.2$  eV, in good agreement with the results of Field and Ghandhi (1986). A weak dependence of electron-carrier concentration as a function of AsH<sub>3</sub> flow rate of the form  $(P_{\text{AsH}_3})^{-0.5}$  was observed previously by Field and Ghandhi (1986).

Bass and Oliver (1977) found a rise in doping level with increasing TMGa concentration, with a power law of about 0.6. The doping efficiency  $K$  is given by:

$$K \propto (\text{growth rate})^{-1.6}. \quad (5.23)$$

Luther and di Lorenzo (1975) found a similar law for the trichloride system and attributed it to kinetic effects. Another explanation is that the surface stoichiometry and hence the surface concentration of available arsenic sites is partly determined by the TMGa concentration. They found a considerable increase in doping level and doping efficiency as the growth temperature is decreased.

(b) *Selenium*

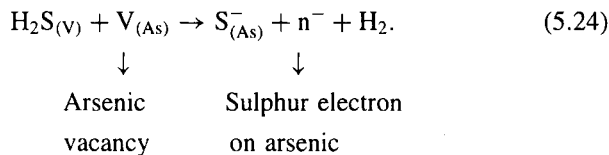
GaAs layers grown by MOCVD can be n-type doped using H<sub>2</sub>Se, DESe or DMSe as a source of Se. Sakaguchi *et al* (1988) showed that the carrier concentration of Se-doped GaAs increases when the V/III ratio decreases. As Se substitutes for As, the carrier concentration of GaAs doped with Se increases when the flow rate of AsH<sub>3</sub> decreases and is independent of group-III sources. In the case of using H<sub>2</sub>Se as a source of Se, the free-carrier concentration in the GaAs layers decreases when the growth temperature increases. The decomposition of the H<sub>2</sub>Se (primary species) is the rate limiting step: after decomposition, most of the secondary species (Se) is incorporated into the growing layer. Contrary to SiH<sub>4</sub>, H<sub>2</sub>Se shows a strong memory effect.

Asai and Sugiura (1985) proposed a model of the Se incorporation mechanism in MOCVD GaAs layers. Their model is based on the following assumptions.

- (i) Se and As species are competitively adsorbed on a growing surface.
- (ii) Subsequently, Se and As adsorbed at the surface react with gas phase Ga species and as a consequence the Se donor is incorporated into a GaAs epitaxial layer. According to this model, the doping concentration in the GaAs layer depends on the H<sub>2</sub>Se/AsH<sub>3</sub> ratio and is independent of the group-III Ga sources, which is confirmed experimentally.

(c) *Sulphur*

GaAs layers grown by MOCVD can be n-type doped using H<sub>2</sub>S. Bass and Oliver (1977) investigated the variation of the doping level with concentrations of H<sub>2</sub>S (hydrogen sulphide), AsH<sub>3</sub> and TEGa, as well as the growth temperature. They found a linear relationship between the H<sub>2</sub>S concentration and the doping level up to  $> 10^{18} \text{ cm}^{-3}$ . The incorporation of sulphur is given by:



Under equilibrium conditions, the mass action law gives:

$$K = \frac{[\text{S}_{\text{As}}^-][\text{n}^-]P_{\text{H}_2}}{P_{\text{H}_2\text{S}}} \quad (5.25)$$

If  $n < n_i$ , the intrinsic electron concentration, a linear law would be expected, while if  $n > n_i$ , a square root law would follow. The doping level is proportional

to the inverse of arsenic concentration. One would expect this from the above equation as  $V_{(As)}$  should be inversely proportional to the arsenic concentration.

We studied the behaviour of H<sub>2</sub>S doping in GaAs layers grown by LP-MOCVD. The doping level increases linearly when the growth temperature is increased with  $E_i = -1.46$  eV.

When the flow rate of H<sub>2</sub>S is kept constant, the free-carrier concentration varies exponentially with  $1/T$ , as in the case of H<sub>2</sub>Se. The free-carriers concentration in the epilayer decreases when the growth temperature increases. S substitutes for As and plays the role of donor in the GaAs lattice. The decomposition of the H<sub>2</sub>S (primary species) is the rate limiting step after decomposition. Most of the secondary species (S) are incorporated into the growing layers.

#### 5.5.4 p-type GaAs

##### (a) Zinc

GaAs layers grown by MOCVD can be p-type doped using pure or diluted DMZn ((CH<sub>3</sub>)<sub>2</sub>Zn) or DEZn ((C<sub>2</sub>H<sub>5</sub>)<sub>2</sub>Zn). Bass and Oliver (1977) studied incorporation of Zn in GaAs layers grown by MOCVD. Layers were p-type doped using two different concentrations of DMZn diluted in hydrogen as a doping gas. They found a near-linear relationship between the hole concentration and the DMZn concentration at higher levels. The doping level increases with arsenic concentration which one would expect from a stoichiometric effect on the vacancy concentration. Increasing the TMGa concentration showed an increase in doping level. This is not expected from vacancy theory and hence it must be a kinetic effect. They suggest that if the surface concentration of zinc is higher than the bulk concentration and is only slowly desorbed during growth, a higher doping level might be expected with higher growth rates. When the growth temperature increases, the hole concentration in the epilayer decreases.

Razeghi *et al* (1989) studied GaAs layers, doped with DEZn by LP-MOCVD, in the temperature range between 500 and 600 °C. The temperature of DEZn was kept at -15 °C during this study. The H<sub>2</sub> flow through the DEZn bubbler varied between 2.5 and 5 cm<sup>3</sup> min<sup>-1</sup>. Figure 5.16 shows that the hole concentration varies linearly with DEZn flow. The influence of growth temperature has been studied by keeping the DEZn, AsH<sub>3</sub> and TEGa flows constant. As shown in figure 5.17, the hole concentration in the layer decreases when the growth temperature increases. Figure 5.17 shows that the doping level varies exponentially with the inverse of temperature, with  $E_i = -2.6$  eV.

Keeping the growth temperature at 510 °C and a DEZn flow of 2.5 cm<sup>3</sup> min<sup>-1</sup>, the arsine flow has been varied between 60 and 90 cm<sup>3</sup> min<sup>-1</sup>. The arsine flow has no dependence on the doping level so that both parameters can be considered as independent.

The acceptor concentration depends on the flow rate of H<sub>2</sub> through the DEZn or DMZn bubbler. When the flow rate of DEZn or DMZn is kept constant, the

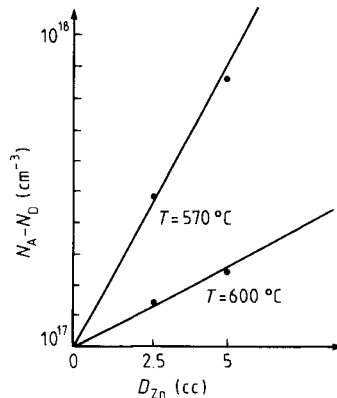


**Figure 5.16** Variation of hole concentration in GaAs as a function of flow rate of DEZn for different growth temperatures (Omnès *et al* 1991).

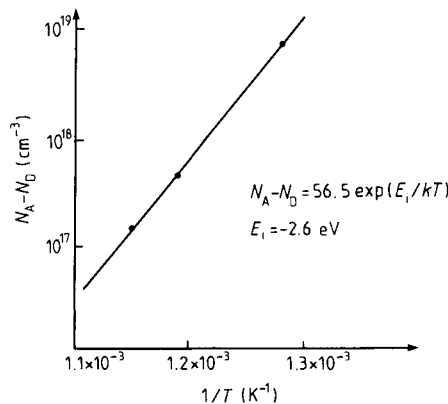


**Figure 5.17** Variation of hole concentration in GaAs as a function of  $1/T$  (Omnès *et al* 1991).

free-carrier concentration varies exponentially with  $1/T$ . The incorporation of dopants during MOCVD growth of GaAs using doping species such as DEZn or DMZn can be explained by using the model described in volume 1 (Razeghi 1989) as in the case of InP layers.

#### (b) Magnesium

The GaAs layer can be p-type doped using  $\text{Mg}(\text{C}_5\text{H}_5)_2$  or cyclopentadienyl magnesium ( $\text{CP}_2\text{Mg}$ ) as a source of Mg. Lewis *et al* (1983) showed that the Mg concentration in the MOCVD growth of GaAs exhibits a squared dependence on the  $\text{Mg}(\text{C}_5\text{H}_5)_2$  concentration,  $P(\text{Mg}) \approx (\text{CP}_2\text{Mg})^2$ , over the entire range of growth conditions. The doping efficiency is constant with growth temperatures

up to  $\sim 680^\circ\text{C}$  and drops exponentially at higher temperature with an Arrhenius-type behaviour ( $\exp(E/k_B T)$ , where  $E \approx 3 \text{ eV}$ ). The reproducibility of doping with  $\text{Mg}(\text{C}_5\text{H}_5)_2$  was found to be sensitive to water and oxygen in the reactor, particularly at low growth temperatures (Kuech *et al* 1987). Kuech *et al* (1988) observed the formation of a transient centre on the GaAs:Mg grown using  $\text{Mg}(\text{C}_5\text{H}_5)_2$ . The transients associated with the growth of GaAs:Mg layers using  $\text{Mg}(\text{C}_5\text{H}_5)_2$  can be influenced by a wide variety of system parameters.

The major cause of dopant transients comes from the interaction of the dopant precursor with the components of the gas panel and the internal surfaces of the reactor. The conditions for minimizing the formation of dopant transients depend largely on the incorporation kinetics of the precursor, as well as reactor design and growth conditions.

The growth of abrupt doping profiles in the case of Mg, Zn and Se is complicated by the interaction of the dopant precursor with the reactor internal surfaces. The adsorption and subsequent desorption of the dopant precursor from these surfaces leads to non-exponential transients in the carrier concentration profile.

These transients can be minimized for the dopant species (Zn, Mg, Se,...) which interact with the reactor components under conditions where the incorporation efficiency in the adjoining regions (reactor tube, lines, valves,...) of the dopant source is minimized.

Wang *et al* (1988) studied the deep-level characteristics in MOCVD-grown GaAs layers doped with Zn and Mg over a wide range of doping concentrations and growth temperatures. Four hole traps and a single electron trap were identified in GaAs:Mg while a single hole trap was noted in GaAs:Zn. The presence and characteristics of each deep level in these p-type MOCVD GaAs layers depend primarily on the doping concentration in the layer and are relatively insensitive to the growth temperature. Wang *et al* reported that the total trap concentration in GaAs:Mg was consistently higher than in GaAs:Zn.

### 5.5.5 Erbium-doped GaAs

Erbium-doped GaAs has attracted increasing interest, because of its sharp and temperature-independent emission peaks at  $1.54 \mu\text{m}$ . Uwai *et al* (1988) have reported uniform and high ( $10^{19} \text{ cm}^{-3}$ ) Er doping of GaAs grown by MOCVD using  $\text{Er}(\text{C}_5\text{H}_5)_3$ , cyclopentadienyl erbium. Er doping higher than  $10^{19} \text{ cm}^{-3}$  necessitates source temperatures of about  $200^\circ\text{C}$ , which results in high concentration of impurities and in addition the  $\text{Er}(\text{C}_5\text{H}_5)_3$  feedline must be heated to nearly  $250^\circ\text{C}$  to avoid deposition on the tube walls. This severely restricts the system design, making it highly desirable to reduce the source temperature.

Replacing cyclopentadienyl radicals in  $\text{Mg}(\text{C}_5\text{H}_5)_3$  ( $\text{M}$  = rare earth atom) by alkylcyclopentadienyl radicals usually increases the vapour pressure of rare earth metallorganic compounds. For example, tri-isopropylcyclopentadienyl

compounds of Nd, Pr and La show vapour pressures more than one order of magnitude higher than those of their cyclopentadienyl counterparts at 250°C.

GaAs can be doped with Er using  $\text{Er}(\text{C}_5\text{H}_5)_3$  or  $\text{Er}(\text{CH}_3\text{C}_5\text{H}_4)_3$ . Er concentrations as high as  $10^{20}\text{ cm}^{-3}$  can be obtained. The Er concentrations depend linearly on the flow rates through the sources, and do not depend on the growth temperature between 600 and 700°C. This suggests that  $\text{Er}(\text{C}_5\text{H}_5)_3$  and  $\text{Er}(\text{CH}_3\text{C}_5\text{H}_4)_3$  readily decompose in a simple monomolecular reaction without noticeable desorption from a growing surface at this temperature range. These characteristics guarantee reproducible doping controllability with  $\text{Er}(\text{CH}_3\text{C}_5\text{H}_4)_3$  or  $\text{Er}(\text{C}_5\text{H}_5)_3$  as source materials. The GaAs doped with Er shows a photoluminescence spectrum at  $1.54\text{ }\mu\text{m}$  at 77 K. The PL spectrum indicates the coexistence of various kinds of Er centre. The Er-related PL peak intensity increases almost linearly with Er concentration below  $10^{18}\text{ cm}^{-3}$ , above which it decreases abruptly with the highest PL intensity at  $5 \times 10^{18}\text{ cm}^{-3}$  (Uwai *et al* 1988).

## REFERENCES

- Adachi S 1982 *J. Appl. Phys.* **53** 8775  
Adachi S 1985 *J. Appl. Phys.* **58** R1  
Asai H and Sugiura H 1985 *Japan. J. Appl. Phys.* **24** L815  
Bass S J and Oliver P E 1977 *Gallium Arsenide and Related Compounds (Inst. Phys. Conf. Ser. 33b)* (Bristol: Institute of Physics) p 1  
Bourgoin J C, von Bardeleben H J and Stievenard D 1988 *J. Appl. Phys.* **64** R65  
Colter P C, Look D C and Reynolds D C 1983 *Appl. Phys. Lett.* **43** 282  
Dapkus P D, Manasevit H M, Hess K L, Low T S and Stillman G E 1981 *J. Crystal Growth* **55** 10  
Dresselhaus G, Kip A F and Kittel C 1955 *Phys. Rev.* **98** 368  
Ehrenreich H 1959 *J. Phys. Chem. Solids* **8** 130  
El Jani B, Leroux M, Grenet J C and Gibart P 1982 *J. Physique* **43** 303  
Feng S L, Bourgoin J C, Omnes F and Razeghi M 1991 *Appl. Phys. Lett.* **59** 941  
Field R J and Ghandi S K 1986 *J. Crystal Growth* **74** 543  
Hess K L, Dapkus P D, Manasevit H M, Low T S, Skromme B J and Stillman G E 1982 *J. Electron. Mater.* **11** 1115  
Hilsum C 1962 *Proc. IRE* **5** 185  
Kane E O 1966 *Semiconductors and Semimetals* vol 1, ed R K Willardson and A C Beer (New York: Academic)  
Kittel C 1971 *Introduction to Solid State Physics* (New York: Wiley)  
Kuech T F, Scilla G J and Cardon F 1988 *J. Crystal Growth* **93** 550  
Kuech T F, Veuhoff E and Meyerson B S 1984 *J. Crystal Growth* **68** 48  
Kuech T F, Wolford D L, Vauhoff E, Deline V, Mooney P M, Potemski R and Bradley J 1987 *J. Appl. Phys.* **62** 632  
Landolt-Bornstein 1982 *Numerical Data and Functional Relationships in Science and Technology* vol 17 (Berlin: Springer)  
Lang D V 1974 *J. Appl. Phys.* **45** 3023  
Lewis C R, Ludowise M J and Dietze F W T 1983 *Electronic Materials Conf. (Burlington, CA, 1983)*  
Luther L C and Di Lorenzo J V 1975 *J. Electrochem. Soc.* **122** 760

- Luttinger J M 1956 *Phys. Rev.* **102** 1030  
Mochizuki K, Ozeki M, Kodama K and Ohtsuka N 1988 *J. Crystal Growth* **93** 550  
Nakanishi T, Udagawa T, Tanaka A and Kamei K 1981 *J. Crystal Growth* **55** 255  
Nelson C R 1963 *RCA Rev.* **24** 603  
Omnes F, Defour M and Razeghi M 1991 *Rev. Tech. Thomson-CSF* **23** 3  
Razeghi M 1989 *The MOCVD Challenge: Volume 1: A Survey of GaInAsP-InP for Photonic and Electronic Applications* (Bristol: Hilger)  
Razeghi M, Omnes F, Nagle J, Defour M, Acher D and Bove P 1989 *Appl. Phys. Lett.* **55** 1677  
Saalfeld F E and Svec H J 1963 *Inorg. Chem.* **2** 46  
Sakaguchi H, Suzuki R and Meguro T 1988 *J. Crystal Growth* **93** 602  
Shimazu M, Kamon K, Kimura K, Mashita M, Mihara M and Ishii M 1987 *J. Crystal Growth* **83** 327  
Stievenard D, Lannoo M and Bourgoin J C 1985 *Solid State Electron.* **28** 485  
Stillman G E and Wolfe C M 1976 *Thin Solid Films* **31** 69  
Stormer H L, Dingle R, Gossard A C, Wiegman W and Sturge M D 1979 *Solid State Commun.* **29** 705  
Sze S M 1981 *Physics of Semiconductor Devices* (New York: Wiley)  
Uwai K, Nakagome H and Takahei K 1988 *J. Crystal Growth* **93** 583  
Van de Ven J, Rutten G M J, Raaijmakers M J and Giling L J 1986 *J. Crystal Growth* **76** 352  
Van Sark W G J H M, Janssen G, de Croon M H J M and Giling L J 1990 *Semicond. Sci. Technol.* **5** 16  
Veuhoff E, Kuech J F and Meyerson B S 1985 *J. Electrochem. Soc.* **132** 1958  
Wang P J, Kuech T F, Tischler M A, Mooney P M, Scilla G J and Cardone F 1988 *J. Crystal Growth* **93** 568  
Wolfe C M and Stillman G E 1975 *Appl. Phys. Lett.* **27** 564

---

## Growth and Characterization of the GaInP–GaAs System

### 6.1 INTRODUCTION

In the past few years, GaAs–GaAlAs heterostructures have emerged as a promising system for optoelectronic and microwave device applications. However, because of the strong reaction between Al and oxygen, even trace quantities of oxygen have a dramatic effect on the quality of GaAlAs layers due to the effective introduction of deep-level defects. Hence, photonic devices based on GaAs–GaAlAs suffer from the catastrophic dark line defect formation and rapid degradation. This is a major problem for monolithic integrated circuits and the technology of GaAs–GaAlAs heterostructures on Si substrates. One of the solutions to this problem is to replace GaAlAs by  $\text{Ga}_{0.51}\text{In}_{0.49}\text{P}$  lattice matched to GaAs which has a direct energy gap of 1.9 eV.

The electrical, optical and structural properties of GaAs–GaInP depend directly on how the system is lattice matched. Concerning  $\Delta E_c$ , there is a surprise: if we assume that the discontinuity in the conduction band is the difference in the electron affinities ( $\chi$ ) of  $\chi(\text{GaAs}) = 4.05$  eV,  $\chi(\text{InP}) = 4.4$  eV and  $\chi(\text{GaP}) = 4.0$  eV (the electron affinity of GaInP is taken as the average of  $\chi(\text{InP})$  and  $\chi(\text{GaP})$  and  $\chi(\text{Ga}_{0.51}\text{In}_{0.49}\text{P}) = 4.2$  eV), then  $\Delta E_c = \chi(\text{GaAs}) - \chi(\text{GaInP}) = -0.15$  eV. However, the experimental results show that  $\Delta E_c = 0.2$  eV and  $\Delta E_v = 0.28$  eV.

GaInP lattice matched to GaAs shows a number of unique and interesting features by comparison to GaAlAs. Its large valence band discontinuity makes it very suitable for n–p–n heterojunction bipolar transistors (HBTs) and p-channel FETs (Chen *et al* 1988).

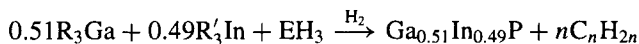
Another feature of the  $\text{Ga}_x\text{In}_{1-x}\text{P}$  heterostructure is that the crossover of its direct ( $\Gamma$ ) and indirect (X) conduction bands lies at  $x = 0.74$  (Casey and Panish 1978) and is therefore far from the lattice-matched composition ( $x = 0.51$ ). In the case of  $\text{Ga}_{1-x}\text{Al}_x\text{As}$ , the crossover of direct and indirect conduction bands is around  $x = 0.37$ . Donor-related deep traps, the so-called DX centres, are particularly important for  $x$  exceeding 0.3, i.e. close to the crossover point. Trap

activation energies in  $\text{Ga}_{1-x}\text{Al}_x\text{As}$  depend on the composition  $x$  in a similar way to the dependence of the indirect conduction band L (Chand *et al* 1984). Since the  $\text{Ga}_x\text{In}_{1-x}\text{P}$  lattice-matched composition corresponds to an  $x$  value which is well below the crossover point of the direct and indirect bands, it can be deduced that the presence of DX centres will be very small for this material as explained below.

The DX centre is a deep donor level and its activation energies follow one of the indirect conduction bands in III–V compounds. Once the composition of a ternary compound is near or over the crossover point of the bandgap transition, DX centres will start to affect the device electrical properties. For those compositions well below the crossover point, the trap energy lies above the minimum of the conduction band ( $\Gamma$ ) and deep-trap effects are negligible. Since this type of deep trap is quite common in all III–V semiconductors, a large separation between the lattice-matched composition and that of the crossover point helps to eliminate the DX centre problems. Therefore,  $\text{Ga}_{0.51}\text{In}_{0.49}\text{P}$  will allow operation without significant donor-related deep traps. Strong selective etching between GaAs and GaInP also make this system very promising for device fabrication.

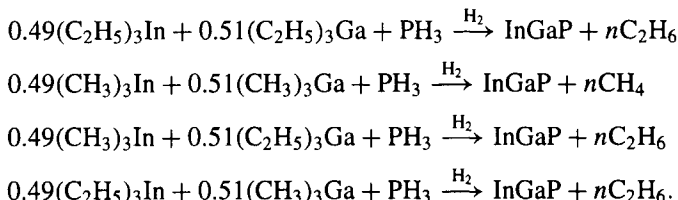
## 6.2 GROWTH DETAILS

GaInP layers can be grown by MOCVD, either at atmospheric pressure or low pressure and at low temperatures between 500 and 600 °C. One can use different group III alkyls for Ga and In sources, and hydrides or alkyls for group-V P sources. Chemical reactions occurring among these sources are as follows



where R, R' and E can be methyl, ethyl, alkyl or hydride.

One can also use any of the following as an example

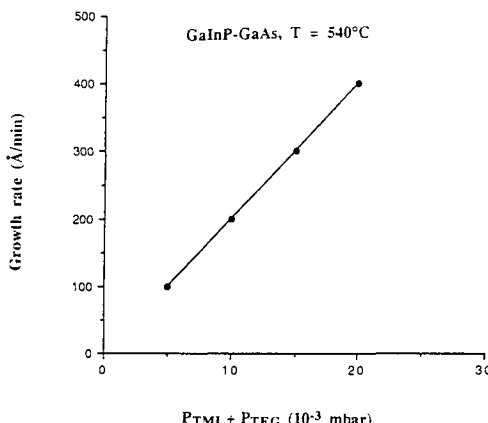


The GaInP layers can be grown at low temperature, between 500 and 550 °C, by using triethylgallium (TEGa), trimethylindium (TMIn) and pure phosphine ( $\text{PH}_3$ ) in a  $\text{H}_2$  carrier gas. The optimum growth conditions are given in table 6.1.

The growth rate ( $\text{dx}/\text{dt}$ ) of GaInP depends on the flow rates of TMIn and TEGa (group-III element) and is independent of  $\text{PH}_3$  flow rate (group-V element)

**Table 6.1** Optimum growth parameters for GaAs and GaInP by MOCVD.

	GaAs	GalnP
Growth pressure	76 Torr	76 Torr
Growth temperature	510°C	510°C
Total H <sub>2</sub> flow rate	31 min <sup>-1</sup>	31 min <sup>-1</sup>
AsH <sub>3</sub> flow rate	30 cc min <sup>-1</sup>	—
H <sub>2</sub> through TMIn bubbler at 18°C	—	200 cc min <sup>-1</sup>
H <sub>2</sub> through TEGa bubbler at 0°C	120 cc min <sup>-1</sup>	120 cc min <sup>-1</sup>
PH <sub>3</sub> flow rate	—	300 cc min <sup>-1</sup>
Growth rate (dx/dt)	150 Å min <sup>-1</sup>	200 Å min <sup>-1</sup>

**Figure 6.1** Variation of growth rate of GaInP layers grown by MOCVD at 540°C as a function of flow rate of group-III elements (Razeghi 1989a).

and growth temperature under the growth conditions listed in table 6.1. The distribution coefficients of indium and gallium are defined as

$$K = X_{\text{Ga}}^{\text{s}} / X_{\text{Ga}}^{\text{v}} \quad (6.1)$$

and

$$K' = X_{\text{In}}^{\text{s}} / X_{\text{In}}^{\text{v}} \quad (6.2)$$

are nearly equal to unity. Figure 6.1 shows the variation of growth rate  $dx/dt$  of GaInP lattice matched to GaAs with a growth temperature of  $T_G = 540^\circ\text{C}$  and growth pressure of 76 Torr. Similar results have been reported by Hsu *et al* (1985) at growth temperatures from 600 up to 650°C. They showed that there was no gas-phase reaction in their reactor leading to premature depletion of In or Ga.

An undoped GaInP layer grown under the conditions of table 6.1 has a free-electron carrier concentration of  $5 \times 10^{14} \text{ cm}^{-3}$  with a mobility of

$6000\text{ cm}^2\text{ V}^{-1}\text{ s}^{-1}$  at 300 K and  $40000\text{ cm}^2\text{ V}^{-1}\text{ s}^{-1}$  at 77 K. No GaAs buffer layer is grown in this case (Razeghi *et al* 1989b).

### 6.3 STRUCTURAL ORDER IN $\text{Ga}_x\text{In}_{1-x}\text{P}$ ALLOYS GROWN BY MOCVD

It was found that GaInP alloy has two phases, consisting of disordered and ordered structures. The disordered alloy has a bandgap of 1.92 eV at 300 K, while the ordered structure has a lower bandgap varying from 1.83 eV to 1.78 eV (Gomyo *et al* 1988, McDermott *et al* 1991). This type of combination of ordered and disordered structures has been found in various alloy systems such as GaInP (Ueda *et al* 1987, Bellon *et al* 1988, Kondow *et al* 1988a, Gomyo *et al* 1988), AlInP (Yasuami *et al* 1988), AlInAs (Ueda *et al* 1988a, b), GaInAs (Nakayama and Fujita 1986), GaAsSb (Jen *et al* 1987), GaAlAs (Kuan *et al* 1985), etc. Experimental results show that the kinetics of crystal growth plays an important role in the formation of an ordered structure (Kondow *et al* 1988a, b, c, Ueda *et al* 1988a, b). If growth kinetics generate ordered alloys, then the CuPt-type ordered structure that has been found in a  $\text{Ga}_{0.5}\text{In}_{0.5}\text{P}$  alloy may be also formed in a  $\text{Ga}_{0.7}\text{In}_{0.3}\text{P}$  alloy.

$\text{Ga}_3\text{InP}_4$  ordered structure exists in either of two variations, ‘famatinitite’ or ‘luzonite’ (Landau and Lifshitz 1969). The famatinite-type ordered structure is a  $(\text{GaP})_3(\text{InP})$  superlattice developing along the (2 1 0) direction. If a famatinite-type ordered structure exists, a diffraction pattern with an electron beam incident along the [1 0 0] crystal axis must show extra spots corresponding to the ordered structure (Bellon *et al* 1988). However, the presence of a luzonite-type ordered structure cannot be proved by a diffraction measurement because this ordered structure does not have an equivalent superlattice.

Several studies have been reported on the structural ordering of  $\text{Ga}_{0.5}\text{In}_{0.5}\text{P}$  (Kondow *et al* 1988a, b, c),  $\text{Ga}_{0.6}\text{In}_{0.4}\text{P}$  (Bellon *et al* 1988),  $\text{Ga}_{0.7}\text{In}_{0.3}\text{P}$  (Kondow *et al* 1989), and InGaAlP (Suzuki *et al* 1988a, b, c) grown by MOCVD. The structural order has been observed by transmission electron microscopy.

A correlation has been established between the degree of structural order in GaInP and energy-gap measurements by photoluminescence or electoreflectance which shows that the disorder-order transition is reflected in the energy-gap optical transition.

The most interesting structural ordering phenomena are observed in the  $\text{Ga}_{0.5}\text{In}_{0.5}\text{P}$  alloy. The structural order of  $\text{Ga}_{0.5}\text{In}_{0.5}\text{P}$  has been studied as a function of (i) growth temperature (Kondow *et al* 1988b, Gomyo *et al* 1987), and (ii) V/III vapour pressure ratio (Suzuki *et al* 1988b). In all the cases, the  $\text{Ga}_{0.5}\text{In}_{0.5}\text{P}$  samples were grown on (0 0 1)-oriented GaAs substrates. Transmission electron diffraction (TED) studies have been performed along the [1 1 0], [1  $\bar{1}$  0] or [0 0 1] directions (Kondow *et al* 1988c, Gomyo *et al* 1987). These studies have shown that the disordered phase consists of a cubic face-

centred, zincblende-type crystalline lattice with a random distribution of Ga and In atoms on the group-III sublattice. The transmission electron diffraction pattern of the disordered phase shows diffraction spots at  $(h k l)$  positions with  $h$ ,  $k$  and  $l$  all being even or odd integers. In this case, no superstructure was observed in the transmission electron diffraction pattern (Suzuki *et al* 1988a). The ordered phase is an ordered distribution of Ga and In atoms on the group-III element sublattice of the zincblende structure.

The most interesting TED studies were made using the [1 1 0] orientation for the incident beam. Using this orientation, the TED pattern of the ordered phase showed  $(h - \frac{1}{2}, k + \frac{1}{2}, l + \frac{1}{2})$  spots close to the  $(h, k, l)$  spots of the zincblende structure, corresponding to a double periodicity of the  $(\bar{1} 1 1)$  planes. Therefore, the ordered phase can be described as a regular alternation of GaP and InP monatomic planes in the  $[\bar{1} 1 1]$  direction, as in the CuPt structure (Kondow *et al* 1988a, b, c, Suzuki *et al* 1988a, b, c).

To confirm this assumption, transmission electron microscopic (TEM) studies have been performed by Suzuki *et al* on the ordered  $\text{Ga}_{0.5}\text{In}_{0.5}\text{P}$ , using a dark-field imaging technique with an aperture including  $(-\frac{1}{2}, \frac{1}{2}, \frac{1}{2})$ ,  $(-\frac{1}{2}, \frac{1}{2}, \frac{3}{2})$  and  $(\bar{1} 1 1)$  diffraction points. They observed at atomic resolution a double periodicity of  $6.5 \text{ \AA}$  of the  $(\bar{1} 1 1)$  planes, which can be related to TEM observations. It proves the ordering of GaP and InP monoatomic planes along the  $[\bar{1} 1 1]$  direction.

Suzuki *et al* also observed, by TEM imaging, an intermixing of disordered and ordered phases as well as antiphase boundaries on partially ordered phases, with a variation of the relative extensions of the disordered phase, antiphase boundaries, and ordered phases corresponding to a short- or long-range structural order.

The degree of structural order can also be estimated by the TED technique, looking at the intensity and the sharpness of the superstructure spots  $(h - \frac{1}{2}, k + \frac{1}{2}, l + \frac{1}{2})$  of the electron diffraction pattern.

The TED and TEM studies performed on  $\text{Ga}_{0.5}\text{In}_{0.5}\text{P}$  alloys grown at different growth temperatures in the range of  $550\text{--}750^\circ\text{C}$  showed that the degree of structural order increased with growth temperature, from a very short-range order at  $550^\circ\text{C}$  to a long-range order at  $700^\circ\text{C}$ . At low growth temperatures, the density of antiphase boundaries is high. Intermixing of disordered and ordered phases can also be observed at low growth temperatures (Suzuki *et al* 1988a, b, c). It is also observed that there is a negligible contribution of the V/III vapour pressure ratio on the structural ordering phenomena in  $\text{Ga}_{0.5}\text{In}_{0.5}\text{P}$ .

Photoluminescence measurements at  $300 \text{ K}$  have shown that there is a negligible difference in energy gaps for  $\text{Ga}_{0.5}\text{In}_{0.5}\text{P}$  alloys grown at the same growth temperature for different V/III ratios, from V/III = 60 to V/III = 440 (Gomyo *et al* 1987), although 4 K luminescence would yield more accurate  $E_g$  values.

A correlation has been established between energy-gap values and the degree of structural order in  $\text{Ga}_{0.5}\text{In}_{0.5}\text{P}$ . Photoluminescence and electroreflectance

studies have been performed on  $\text{Ga}_{0.5}\text{In}_{0.5}\text{P}$  alloys (Kondow *et al* 1989, Inoue *et al* 1988). Photoluminescence results showed a minimum energy gap for the  $\text{Ga}_{0.5}\text{In}_{0.5}\text{P}$  grown at 650 °C; for this growth temperature, the value of the energy gap of the  $\text{Ga}_{0.5}\text{In}_{0.5}\text{P}$  decreased to 1.85 eV at 300 K. As a comparison, the value observed for the energy gap of the disordered  $\text{Ga}_{0.5}\text{In}_{0.5}\text{P}$  is 1.90 eV at 300 K. Electroreflectance studies also showed similar results (Inoue *et al* 1988).

Gomyo *et al* (1987) reported that zinc diffusion through an ordered  $\text{Ga}_{0.5}\text{In}_{0.5}\text{P}$  alloy increases its bandgap by 50 meV, from 1.85 eV to 1.90 eV at 300 K; the effect of zinc diffusion is to produce an intermixing of the group-III elements, creating structural disorder by randomizing Ga and In positions. This clearly proved the relation between the energy gap of  $\text{Ga}_{0.5}\text{In}_{0.5}\text{P}$  and its structural order.

McDermott *et al* (1991) have grown  $\text{Ga}_{0.5}\text{In}_{0.5}\text{P}$ , at temperatures between 480 and 500 °C, using atomic layer epitaxy (ALE). They found that all the samples grown on 2°-misoriented substrates had CuPt structure, with typically two  $\frac{1}{2}\langle 1\ 1\ 1 \rangle$  variants. For samples grown on the (100) nominal substrates, no CuPt ordering was observed. However, the accurate origin of this anomaly in bandgap energies is not well understood.

#### 6.4 DEFECTS IN GaInP LAYERS GROWN BY MOCVD

Most of the studies performed on GaInP layers have been limited to the conditions of growth (Horng *et al* 1988, Hoshino *et al* 1986a, b, c, Kondow *et al* 1988a, b, c), in particular to investigate the influence of the growth temperature on structural ordering (Ueda *et al* 1989), and to the evaluation of a few optical devices (Hsieh *et al* 1984, Ishikawa *et al* 1986, Ikeda *et al* 1987).

Using deep-level transient spectroscopy (DLTS), the defects present in GaInP layers grown by MOCVD were characterized by Feng *et al* (1991). The layers were grown on n<sup>+</sup>-doped GaAs substrates in a horizontal cold-wall reactor using trimethylindium, triethylgallium and PH<sub>3</sub> as sources (Razeghi *et al* 1990). The layers, ~1 μm thick, have the following composition: Ga (0.51), In (0.49) for lattice matching on GaAs; they are not intentionally doped. After an ohmic contact has been deposited on the back of the wafer (Au–Ge alloy annealed at 450 °C for a few minutes), Au Schottky barriers (area: 0.07 mm<sup>2</sup>) are deposited by evaporation. Capacitance–voltage (C–V) measurements show that the layers are n type with a uniform concentration throughout the whole layer of 2.4–3.5 × 10<sup>15</sup> cm<sup>−3</sup>, depending on the location of the Schottky diode, at room temperature. This concentration increases slightly above room temperature from 2.8 × 10<sup>15</sup> cm<sup>−3</sup> at 300 K to 3 × 10<sup>15</sup> cm<sup>−3</sup> at 400 K. It also decreases with decreasing temperature from 2.4 × 10<sup>15</sup> cm<sup>−3</sup> at 300 K to 2.2 × 10<sup>15</sup> cm<sup>−3</sup> at 30 K, for another sample. This suggests that defects are present, which trap ~2 × 10<sup>14</sup> cm<sup>−3</sup> electrons in the 300–400 K range as well as below 300 K.

DLTS detects electron traps which account for the changes observed in the

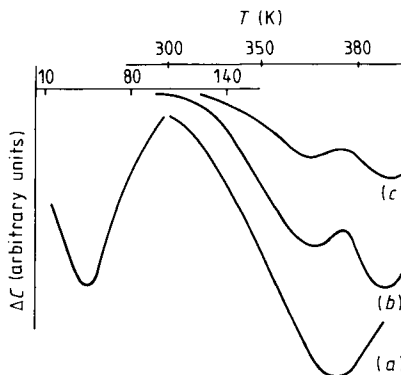


**Figure 6.2** DLTS spectra of GaInP grown on GaAs obtained in the temperature range 4–400 K. The low-temperature peak (60 K) was measured at bias –1 V, bias pulse 1 V, emission rate  $60 \text{ s}^{-1}$ , pulse duration 1 ms. High-temperature peaks were measured with an emission rate  $30 \text{ s}^{-1}$ , pulse duration 1 ms, bias pulse 1 V, and bias: (a) –3 V, (b) –2 V and (c) –1 V (Feng *et al* 1991).

electron concentration above room temperature, but not below. As shown in figure 6.2, a first peak is observed around 60 K corresponding to an ionization energy of 75 meV (figure 6.3) in a concentration of  $3 \times 10^{13} \text{ cm}^{-3}$ . This spectrum cannot be attributed to a possible emission over band discontinuities induced by the existence of ordered domains (having a larger bandgap). Indeed, in this case the emission rate should be strongly sensitive to the electric field and the width of the spectrum on the low-temperature side should increase then with this field, i.e. with the applied reverse bias. Thus, there should be no correlation between this spectrum and the large photoluminescence shift versus excitation intensity commonly observed in similar layers (Delong *et al* 1990). A second peak, rather wide and exhibiting a double structure, appears between 350 and 450 K. The shape of this structure varies with the duration of the filling pulse, suggesting that one of the traps is not completely filled (see figure 6.2). The activation energy associated with the first maximum of this peak is 0.92 eV (see figure 6.4). Only the order of magnitude of concentration of this trap, 15% of the free-carrier concentration (i.e.  $4.5 \times 10^{14} \text{ cm}^{-3}$ ), can be evaluated because it cannot be completely filled (see figure 6.5). The dependence of the high-temperature spectrum on the reverse bias, at constant pulse amplitude, indicates a non-uniform distribution of the associated defect: its concentration increases near the epi-substrate interface.

The GaInP layer, grown by MOCVD at optimum growth conditions, contains only one defect species emitting below room temperature (60 K) with a concentration of the order of 1% of the concentration of residual uncompensated donors. This defect cannot be attributed to a DX-like centre since its concentration is saturated with short filling times ( $\sim 50 \mu\text{s}$ ). If it

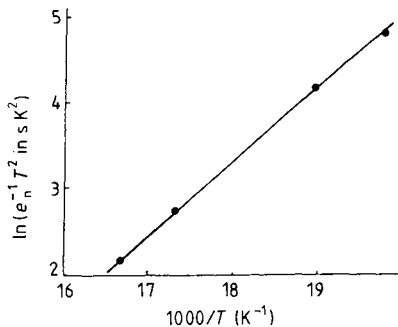


**Figure 6.3** Variation of the emission rate  $e_n$  versus temperature of the peak appearing around 60 K (Feng *et al* 1991).

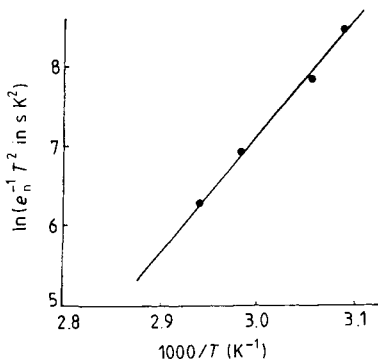


**Figure 6.4** Variation of the emission rate  $e_n$  versus temperature of the high-temperature peak under the bias conditions of figure 6.2(a) (Feng *et al* 1991).

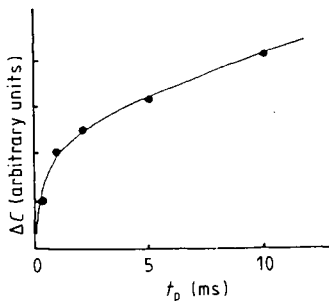


**Figure 6.5** Amplitude  $\Delta C$  of the high-temperature peak versus the filling pulse duration (Feng *et al* 1991).

existed, a DX centre should have an energy level resonant in the conduction band. According to Bourgoin (1991), donor impurities are expected to introduce a DX-like energy level in the forbidden gap when the X or L band lies at an

energy not larger than typically 0.2 eV from the bottom of the conduction band. In  $\text{Ga}_{1-x}\text{In}_x\text{P}$  the condition is fulfilled only when  $x \geq 0.7$ .

Consequently, the persistent photoconductivity which was observed by Ben Amor *et al* (1989) should be ascribed to electron emission from deep traps emitting above room temperature. These traps, because of their relatively high concentration ( $\sim 10^{14} \text{ cm}^{-3}$ ), should dominate the electrical properties of these layers for low doping densities.

Consequently, the unintentionally doped  $\text{Ga}_{1-x}\text{In}_x\text{P}$  ( $x = 0.51$ ) layers grown by MOCVD exhibit an uncompensated electron concentration of a few  $10^{15} \text{ cm}^{-3}$ . They contain one dominant defect, which is ionized just above room temperature, in a concentration of the order of  $10^{14}$ – $10^{15} \text{ cm}^{-3}$ . For the alloy composition considered, the DX centre, if present, is not localized in the gap.

## 6.5 DOPING BEHAVIOUR OF GaInP

### 6.5.1 n-type doping

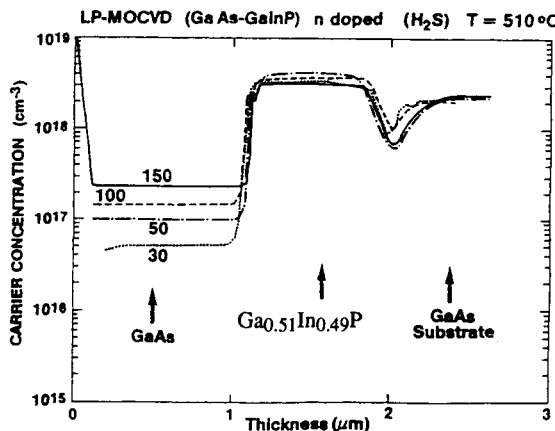
GaInP layers grown by MOCVD can be n-type doped using group-VI or group-IV elements such as: hydrogen sulphide,  $\text{H}_2\text{S}$ ; diethyl selenium,  $(\text{C}_2\text{H}_5)_2\text{Se}$ ; dimethyl selenium,  $(\text{CH}_3)_2\text{Se}$ ; hydrogen selenide,  $\text{H}_2\text{Se}$ ; diethyltellurium,  $(\text{C}_2\text{H}_5)_2\text{Te}$ ; dimethyltellurium,  $(\text{CH}_3)_2\text{Te}$ ; silane,  $\text{SiH}_4$ ; disilane,  $\text{Si}_2\text{H}_6$ ; germane,  $\text{GeH}_4$ .

#### $\text{H}_2\text{S}$

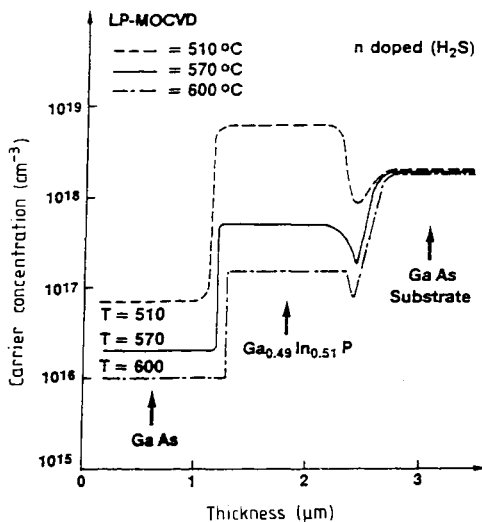
GaInP layers grown by MOCVD can be n-type doped using  $\text{H}_2\text{S}$ . The probability of incorporation of sulphur (S) in GaInP is very high. At the same growth temperature, growth conditions and  $\text{H}_2\text{S}$  flow rate, a GaInP layer is doped 100 times higher than a GaAs layer.

Figure 6.6 shows the electrochemical polaron profile of a GaInP–GaAs layer grown by MOCVD using the growth conditions of table 6.1. It is clear from this experimental result that for the same  $\text{H}_2\text{S}$  flow rate, the donor concentration in GaInP is much higher than in GaAs with the different curves corresponding to different  $\text{H}_2\text{S}$  flow rates. Figure 6.7 confirms this result. For different growth temperatures and constant  $\text{H}_2\text{S}$  flow rate, the donor concentration in the layer increases when the growth temperature decreases (Razeghi 1989c).

Figure 6.6 shows that the doping level in  $\text{Ga}_{0.51}\text{In}_{0.49}\text{P}$  saturates at  $4 \times 10^{18} \text{ cm}^{-3}$ . The  $\text{H}_2\text{S}$  flow has been first varied between 3 and  $15 \text{ cc min}^{-1}$ , keeping the growth temperature equal to  $510^\circ\text{C}$  and the  $\text{PH}_3$  flow equal to  $450 \text{ cc min}^{-1}$ . The  $\text{H}_2\text{S}$  flow was even lowered to  $1 \text{ cc min}^{-1}$  with no change. This means that much more diluted  $\text{H}_2\text{S}$  is necessary to reach the linear zone where the doping level is proportional to the  $\text{H}_2\text{S}$  flow. This saturation effect is in good agreement with work done on a chloride VPE system (Kitahara *et al* 1986).



**Figure 6.6** Electrochemical polaron profile of a GaInP layer grown by MOCVD using  $\text{H}_2\text{S}$  as doping source. Different curves are related to different  $\text{H}_2\text{S}$  flow rates into the reactor (Razeghi 1989a).



**Figure 6.7** Electrochemical polaron profile of a GaInP layer grown by MOCVD using  $\text{H}_2\text{S}$  as the doping source. Different curves are related to different growth temperatures, keeping other growth parameters constant (Razeghi 1989a).

The effect of growth temperature change is shown in figure 6.7. The concentration of donor decreases as growth temperature increases. It can be fitted using the relation

$$N_d - N_a = D_{\text{PH}_3} \exp(-E_i/k_B T) \quad (6.3)$$

assuming that by using 1000 ppm H<sub>2</sub>S and doping flows higher than 1 cc min<sup>-1</sup>, the doping level is independent of H<sub>2</sub>S flow.  $E_i = -2.16$  eV. The phosphine flow has been varied between 300 and 750 cc min<sup>-1</sup> by keeping the growth temperature at 510 °C. A relation between the doping level and the phosphine flow is found in the form:  $(D_{PH_3})^{-0.7}$ .

In conclusion, the doping level of H<sub>2</sub>S 1000 ppm in Ga<sub>0.51</sub>In<sub>0.49</sub>P grown with a fixed III element flow (i.e. a growth rate of 200 Å min<sup>-1</sup>) can be written in the form

$$N_d - N_a = 7 \times 10^5 \exp(2.16/k_B T) (D_{PH_3})^{-0.7} \quad (6.4)$$

where  $k_B T$  is in eV and  $D_{PH_3}$  is in cc min<sup>-1</sup>. In the flow range used for this study  $N_d - N_a$  saturates with  $D_{H_2S}$  so that it does not depend on that parameter (Razeghi and Omnes 1991a).

#### **SiH<sub>4</sub>**

GaInP layers grown by MOCVD can be n-type doped using SiH<sub>4</sub> or Si<sub>2</sub>H<sub>6</sub>. In the GaInP layer, Si substitutes Ga or In and plays the role of a donor. The concentration of Si in GaInP depends on different growth parameters such as growth temperature, growth pressure, growth rate, the ratio of III/V and the flow rate of SiH<sub>4</sub>.

In contrast to H<sub>2</sub>S doping of Ga<sub>0.51</sub>In<sub>0.49</sub>P, the doping level using SiH<sub>4</sub> varies linearly with silane flow (figure 6.8). The growth temperature is maintained at 540 °C while the phosphine flow is kept at 450 °C. By changing the growth temperature, an exponential dependence is found (figures 6.8 and 6.9). The doping level can be written in the form

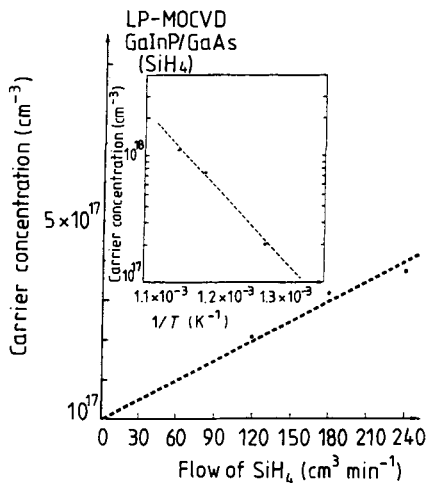
$$N_d - N_a \approx A \exp(-E_i/kT) \quad (6.5)$$

with  $E_i = 1.26$  eV.

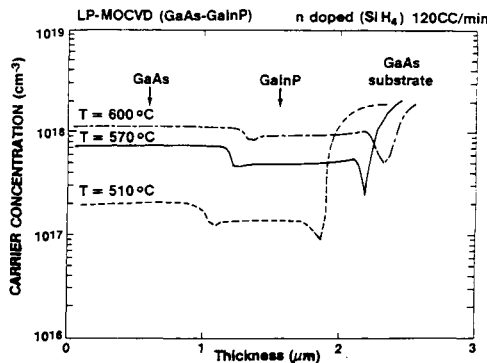
Omnes *et al* (1991) have studied the influence of PH<sub>3</sub> flow rate on doping concentration in GaInP layers grown by MOCVD using SiH<sub>4</sub> as n-type dopant. By keeping the growth temperature equal to 540 °C and the SiH<sub>4</sub> flow at 120 cc min<sup>-1</sup>, the PH<sub>3</sub> flow has been varied from 300 to 750 cc min<sup>-1</sup>.

Figure 6.10 shows that the doping level varies very slowly with PH<sub>3</sub> flow rate as  $(D_{PH_3})^{-0.2}$ . Similar results have been reported by Hsu *et al* (1985) and Kawamura and Asahi (1983). Due to the low diffusion coefficient and low vapour pressure, a sharp doping profile can be obtained with Si (Ladany 1971) reported that Si-doped GaAs has a very high electroluminescence quality.

Gomyo *et al* (1989) studied the effects of Si doping on the  $E_g$  behaviour and on the  $\langle \frac{1}{2}, \frac{1}{2}, \frac{1}{2} \rangle$  sublattice ordering in GaInP, grown at 700 °C by MOCVD under the conditions in which crystals show anomalously low  $E_g$  values unless dopants are introduced. An anomalously low  $E_g$  value, which was 1.836 eV for an undoped crystal, increased to a normal  $E_g$  value of 1.92 eV when the Si doping level increased at least up to  $n = 3.8 \times 10^{17}$  cm<sup>-3</sup>. At this doping condition, the TEM study revealed substantial disordering of the  $\langle \frac{1}{2}, \frac{1}{2}, \frac{1}{2} \rangle$



**Figure 6.8** Variation of electron carrier concentration in a GaInP layer grown by MOCVD at 540°C, using SiH<sub>4</sub> as a doping source, as a function of SiH<sub>4</sub> flow rate; the inset shows the variation of carrier concentration as a function of 1/T (Razeghi 1989b).



**Figure 6.9** Electrochemical polaron profile of GaInP layers grown by MOCVD using SiH<sub>4</sub> as a doping source for different growth temperatures (Razeghi 1989b).

superlattice (SL). In a range from  $3.8 \times 10^{17} \text{ cm}^{-3}$  to  $2 \times 10^{18} \text{ cm}^{-3}$ , the normal  $E_g$  value remained virtually unchanged. They observed a Burstein shift (i.e. the energy shifts towards a higher value due to a band-filling effect by free electrons) for  $n \geq 2 \times 10^{18} \text{ cm}^{-3}$ . Anomalous  $E_g$  values, which were around 1.87 eV for undoped crystals, started to increase at  $n = 1 \times 10^{18} \text{ cm}^{-3}$ . After the increase due to disordering of the  $(\frac{1}{2}, \frac{1}{2}, \frac{1}{2})$  SL, the Burstein shift occurred consecutively when  $n$  exceeded  $\approx 2 \times 10^{18} \text{ cm}^{-3}$  in contrast to the ‘two-stage’  $E_g$  behaviour for the Si doping due to the lower threshold doping concentration

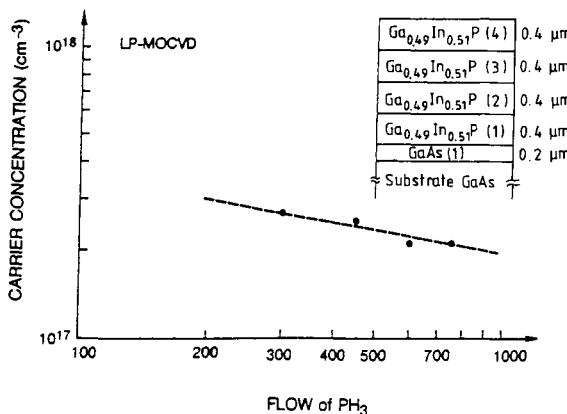


**Figure 6.10** Variation of electron carrier concentration in GaInP layers grown by MOCVD, using SiH<sub>4</sub> as a doping source, as a function of PH<sub>3</sub> flow rate. Inset is the structure of the epilayer (Razeghi 1989b).

$\lesssim 3.8 \times 10^{17} \text{ cm}^{-3}$  for the disordering (Gomyo *et al* 1989).

Anyway, such behaviour was not observed in GaInP layers doped with Si up to  $5 \times 10^{18} \text{ cm}^{-3}$  at low growth temperature between 510 and 550 °C (Razeghi *et al* 1989b). The  $E_g$  change appears to depend more on the alloy composition than on the doping level.

### Se

Gomyo *et al* (1989) studied GaInP layers doped with Se under the same conditions as Si. They found that the threshold for the SL disordering by Si doping ( $n = 3.8 \times 10^{17} \text{ cm}^{-3}$ ) is higher than that for Se doping ( $n \approx 2 \times 10^{18} \text{ cm}^{-3}$ ). They gave two reasons for this difference. The first one is the difference in the sublattice occupation between Si and Se. Si atoms substitute the group-III sublattice and Se atoms substitute the group-V sublattice. This difference in sublattice occupation affinity between Si and Se could be a cause for the  $n_{\text{th}}^{\text{disord}}$  difference. The second reason was the difference between the growth conditions. The V/III ratios of the growth for Si and Se doping were different. However, further studies will be needed to understand the reason behind ordering and disordering mechanisms in this system.

### Te

GaInP layers grown by MOCVD can be n-type doped using Te atoms as a doping element. In GaInP Te usually occupies the P site. Hsu *et al* (1985) used diethyltelluride (DETe) diluted to 5.45 ppm in H<sub>2</sub> as the source for the n-type dopant. They found a linear relation between the dopant mole fraction in the gas phase and carrier concentrations in the range  $10^{17} \text{ cm}^{-3}$  to  $10^{19} \text{ cm}^{-3}$  at a growth temperature of 625 °C. They reported a high distribution coefficient for Te with

$$K_{\text{Te}} = X_{\text{Te}}^{\text{s}} / X_{\text{Te}}^{\text{v}} = 54 \quad (6.6)$$

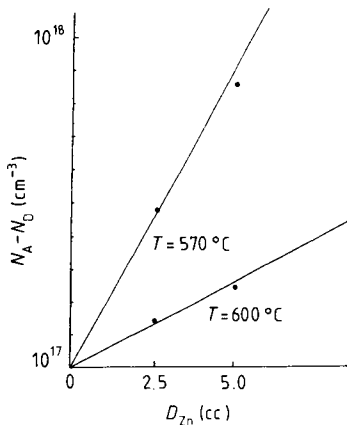


**Figure 6.11** Variation of hole concentration in GaInP as a function of flow rate of DEZn for different growth temperatures (Razeghi *et al.* 1990).

where

$$X_{\text{Te}}^s = \frac{\text{concentration of electron sites}}{\text{concentration of group-V sites}} \quad (6.7)$$

$$X_{\text{Te}}^v = \frac{\text{concentration of group-VI dopant in the vapour}}{\text{concentration of P in the vapour}}. \quad (6.8)$$

Since the concentration of group-VI dopant is much smaller than the concentration of P in both the solid and the vapour, they neglect the group-VI concentration in the denominator in calculating both  $X^s$  and  $X^v$ . Hsu *et al.* (1985) reported that the PL intensity of Te-doped GaInP increases with carrier concentration until  $n = 2 \times 10^{18} \text{ cm}^{-3}$  and the PL half-width increases with increasing carrier concentration. They found that the electron mobility decreases from 1020 to  $500 \text{ cm}^2 \text{ V}^{-1} \text{ s}^{-1}$  as carrier concentration increases from  $10^{16}$  to  $10^{19} \text{ cm}^{-3}$ .

### 6.5.2 p-type doping

GaInP layers grown by MOCVD can be p-type doped using Mg, Zn and Cd.

#### DEZn

The same type of study can be carried out on  $\text{Ga}_{0.51}\text{In}_{0.49}\text{P}$  for p-type doping. The growth temperature is kept at  $510^\circ\text{C}$  and the phosphine flow rate at  $450 \text{ cc min}^{-1}$ . The doping level is found to vary linearly with DEZn flow as for GaAs (figure 6.11).

The effect of growth temperature has been investigated between 500 and  $600^\circ\text{C}$  by keeping the DEZn flow constant and the phosphine flow equal to

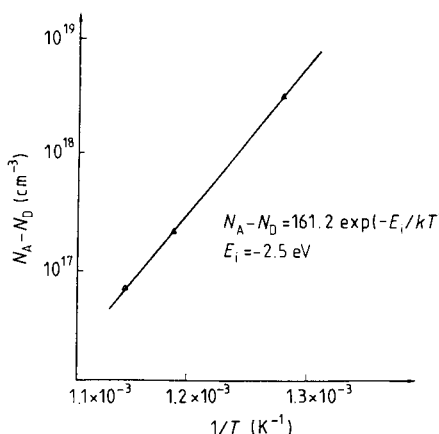


**Figure 6.12** Variation of the hole concentration in GaInP as function of  $1/T$  ( $T$  is the growth temperature) (Razeghi *et al.* 1990).

450 cc min<sup>-1</sup>. Figure 6.12 shows the evolution of the doping level as a function of  $1/T$ . It varies exponentially and decreases as the growth temperature increases

$$N_d - N_a = 1.6 \times 10^2 \text{ cm}^{-3} \exp(-E_i/kT) \quad (6.9)$$

with  $E_i = -2.5$  eV.

The influence of the phosphine flow has been investigated without significant results. No clear influence of group-V element flow has been found on p-type doping of GaInP with DEZn (Razeghi *et al.* 1989b). The acceptor doping level of DEZn in GaInP can be written in the general form

$$N_d - N_a = 10^2 D_{\text{DEZn}} \exp(2.5/k_B T) \quad (6.10)$$

with DEZn in cc min<sup>-1</sup> and  $k_B T$  in eV.

Hsu *et al.* (1985) used dimethylzinc (DMZn) as a p-type dopant source with a concentration of 474 ppm in H<sub>2</sub>. By varying the DMZn mole fraction in the gas phase, they obtained p-carrier concentrations in the range 10<sup>17</sup> cm<sup>-3</sup> to 10<sup>19</sup> cm<sup>-3</sup>. They calculated the Zn distribution coefficient as

$$K_{\text{Zn}} = X_{\text{Zn}}^s / X_{\text{Zn}}^v \quad (6.11)$$

with

$$X_{\text{Zn}} = [\text{DMZn}] / [\text{TMIn} + \text{TMGa}] = 0.0038 \quad (6.12)$$

at  $p = 10^{18}$  cm<sup>-3</sup> and a growth temperature of 625 °C. They attributed this low doping efficiency to the fact that Zn has a vapour pressure of 15 Torr at the growth temperature (Honig 1962) and most of the zinc is evaporated from the crystal surface before incorporation. They reported GaInP hole mobilities

in the range of  $20\text{--}40\text{ cm}^2\text{ V}^{-1}\text{ s}^{-1}$ . They did not observe any deep level in the PL spectrum of Zn-doped GaInP. They observed that at room temperature the PL intensity increases with carrier concentration, the maximum PL intensity for p-type GaInP being about the same as that of n-type samples, and the PL half-width increased at higher concentrations.

### Mg

Suzuki *et al* (1988a, b, c) have used bis-magnesium  $[(\text{C}_2\text{H}_5)_2\text{Mg}]$  as a p-type dopant for GaInP layers grown by MOCVD. They reported similar behaviour for Mg as Zn in GaInP layers. They studied the photoluminescence properties of Mg-doped GaInP layers as a function of hole concentration. The bandgap energy ( $E_g$ ) value for Mg-doped GaInP, grown under conditions in which undoped GaInP shows an anomalously low  $E_g$ , showed a steep increase for  $p \geq 1 \times 10^{18}\text{ cm}^{-3}$ . This anomalous behaviour was attributed to the Mg (or Zn) diffusion-enhanced randomization of the naturally formed monolayer  $(\frac{1}{2}, \frac{1}{2}, \frac{1}{2})$  superlattices on the column III sublattice.

### 6.5.3 Conclusions

n- and p-type doping of GaAs and  $\text{Ga}_{0.51}\text{In}_{0.49}\text{P}$  suggest an analytical expression giving the doping level as a function of dopant flow rate, growth temperature and the ratio of V/III. It can be written in the general form

$$n = \alpha D_{\text{dopant}}^\alpha D \exp(-E_i/k_B T). \quad (6.13)$$

With the exception of the case of  $\text{Ga}_{0.51}\text{In}_{0.49}\text{P}$  doping with  $\text{H}_2\text{S}$  where saturation occurs ( $\alpha = 0$ ), all the doping levels have been found to vary linearly with the amount of dopant introduced:  $\alpha = 1$ .

The doping level is always found to decrease slightly while increasing the V/III ratio with  $-1 < \alpha \leq 0$  (DEZn doping). The temperature dependence allows us to separate the dopants into two groups.

- For group-IV elements (Sn, Ge, Si), the energy  $E_i$  is positive so that the incorporation efficiency of the dopant increases while increasing the temperature.  $E_i$  is weakly dependent on the doping element and is close to 1 eV. Here, the main limiting step for incorporation of the dopant is thermal cracking.
- For group-II and -VI elements (Zn, S, Se), the energy  $E_i$  is negative so that the incorporation efficiency decreases while increasing the temperature. Its value is found to vary between  $-1$  and  $-2$  eV without being a characteristic of the dopant or of the host material. Here, the main limiting step for incorporation of the dopant is its desorption from the crystal surface (table 6.2).

## 6.6 GaAs–GaInP HETEROSTRUCTURES

Originally, it was assumed that the shortcomings of AlGaAs could be overcome by replacing the AlGaAs by  $\text{Ga}_{1-x}\text{In}_x\text{P}$ , which for  $x = 0.51$  is lattice matched

**Table 6.2** Summary of n- and p-type behaviour in III–V alloys.

Doping source	Materials	Doping flow rate	Group V flow rate	$E_i$ (eV)	Group III flow rate
DEZn	GaAs	$D_{DEZn}$	$D_{AsH_3}^{0.3}$	-2.6	
	GaInP	$D_{DEZn}$	$D_{PH_3}^{0.1}$	-2.5	
	GaInAs	$D_{DEZn}$		-2.2	
	InP	$D_{DEZn}$		-1.2	
H <sub>2</sub> S	GaAs	$D_{H_2S}$	$D_{AsH_3}^{-1}$	-1.4	
	GaInP	$D_{H_2S}$	$D_{PH_3}^{-0.7}$	-2.1	
	GaInAs	$D_{H_2S}$		-1	
	InP	$D_{H_2S}$		-2.1	
H <sub>2</sub> Se	GaAs	$D_{H_2Se}$	$D_{AsH_3}^{-1}$	-2.8	$D_{TEGa}$
SiH <sub>4</sub>	GaAs	$D_{SiH_4}$	$D_{AsH_3}^{-0.5}$	+1.2	$D_{TEGa}^{-1}$
	GaInP	$D_{SiH_4}$	$D_{PH_3}^{-0.2}$	+1.2	
	GaInAs	$D_{SiH_4}$			
	InP	$D_{SiH_4}$		+1.2	
TMSn	GaAs	$D_{TMSn}$	$D_{AsH_3}^{0.8}$	+1	
GeH <sub>4</sub>	GaAs	$D_{GeH_4}$		+1.5	$D_{TEGa}^{-1}$

to GaAs. GaInP is comparable to AlGaAs in that it acts as a barrier material for both electrons and holes. There are reports of the growth of corresponding heterostructures and the formation of two-dimensional electron gases (2DEGs) at the heterointerface. However, these heterostructures also reveal the persistent photoconductivity effect (PPC) upon illumination, which is probably due to a sort of DX centre in doped GaInP. Hence, besides the absence of Al, it is the general interest in an alternative to the GaAs–AlGaAs system that motivates the investigation of GaAs–GaInP. However, the study of two-dimensional electrons in GaAs–GaInP heterostructures suffers from extremely low mobilities compared to MBE-grown GaAs–AlGaAs heterostructures due to the interface quality of GaAs–GaInP–GaAs and the difficulty in growing high-quality multilayers.

### 6.6.1 Band offset measurements in the GaAs/Ga<sub>0.51</sub>In<sub>0.49</sub>P system

The band offsets of GaAs–GaInP were measured using different techniques as detailed below.

#### (a) Capacitance–voltage (*C*–*V*) profiling (Rao *et al* 1987)

$\delta E_V$  measurements:  $\delta E_V$  was determined from *C*–*V* profiling through the p-GaInP/p-GaAs heterojunction by reverse biasing the n<sup>+</sup>–p junction between the substrate and the p-GaAs epilayer. The measurement frequency was 1 MHz and the magnitude of the applied differential voltage was 30 mV. The apparent majority-carrier concentration profile  $p^*(x)$  was derived from the *C* – *V* profile

according to the standard relation:

$$p^*(x) = \frac{2}{q\varepsilon} \left( \frac{d}{dV} \frac{1}{C^2} \right)^{-1} \quad (6.14)$$

where

$$x = \varepsilon/C \quad (6.15)$$

is the width of the depletion layer (the distance of the depletion layer edge from the p–n junction),  $p^*(x)$  is the apparent majority-carrier (hole) concentration at position  $x$ ,  $V$  is the reverse bias voltage,  $C$  is the capacitance per unit area,  $\varepsilon$  is the dielectric permittivity of the semiconductor.

The value of  $\delta E_v$  is obtained from the electrostatic dipole moment associated with the charge imbalance between a presumably known doping distribution  $p(x)$  and the experimental  $p^*(x)$  curve, using the relation given by Kroemer *et al* (1980), adapted to the p–p case:

$$\delta E_v = \frac{q^2}{\varepsilon} \int_0^{+\infty} [p(x) - p^*(x)](x - x_i) dx - kT \ln \left( \frac{p_2 N_{v1}}{p_1 N_{v2}} \right) \quad (6.16)$$

where  $p(x)$  is the ionized acceptor distribution, assumed to be known and to level out far away from the heterojunction,  $p_{1,2}$  are the asymptotic values of the doping levels in the GaAs (1) and the GaInP (2),  $x_i$  is the distance of the GaAs–GaInP interface from the n<sup>+</sup>-GaAs substrate,  $N_{v1,2}$  are the valence band densities of states in GaAs and GaInP regions.

To evaluate  $\delta E_v$ , Kroemer *et al* (1980) assumed:

- (i) uniform doping on both sides of the interface at  $x = x_i$ ,
- (ii) an abrupt step in the doping at  $x = x_i$ ,
- (iii) the existence of a localized interface defect charge  $\sigma_i$  at  $x = x_i$ . For a given value of  $x_i$ , the value of  $\sigma_i$  is obtained from the requirement of overall charge neutrality:

$$\sigma_i = \int_0^{+\infty} [p(x) - p^*(x)] dx. \quad (6.17)$$

In such a model an accurate knowledge of the interface position  $x_i$ , the thickness of the epilayers and the doping level in epilayers are essential. They found  $\delta E_v = 0.238$  eV.

They also performed an additional check by performing a computer reconstruction of what the  $p^*(x)$  profile should have been for an abrupt interface, with given values of the band offset and interface charge, using a computer program that basically solves Poisson's equation for incremental voltage steps applied to the heterojunction. They obtained a satisfactory agreement between experimental and theoretical results.

$\delta E_c$  measurements: Rao *et al* (1981) used the following structure for  $\delta E_c$  measurements: first a 0.4 μm thick GaAs layer with an n-type doping level

of  $9 \times 10^{16} \text{ cm}^{-3}$  was grown on a (100)-oriented, n<sup>+</sup>-doped GaAs substrate; the next layer was a 0.5 μm thick GaInP layer with an n-type doping level of  $3 \times 10^{16} \text{ cm}^{-3}$ . An In ohmic contact was realized on the back side of the substrate. Finally, an Al Schottky contact was deposited on the GaInP epilayer (Rao *et al* 1987).

The Al Schottky barrier was reverse biased to obtain a C – V profile through the GaAs–GaInP heterojunction. The analysis of the data was analogous to that for the p–p structure. The value of  $\delta E_c = 0.22 \text{ eV}$  was obtained.

*Possible sources of errors:* The largest source of uncertainty in this measurement is the quality of the samples. Another source of error is the presence of deep levels near or at the interface, the ionization energy of which changes with changing bias. Errors in the capacitance measurements, such as errors in the diode area, can occur that may yield an incorrect apparent charge concentration.

(b) *Evaluation of the band offsets using DLTS (Biswas *et al* 1990)*

$\delta E_c$  and  $\delta E_v$  measurements: Deep-level transient spectroscopy (DLTS) measurements were carried out on GaInP/Au Schottky diodes having a GaAs single quantum well (SQW) in the depletion region. The emission energies of electrons and holes obtained from DLTS measurements are related to the band offsets  $\delta E_c$  and  $\delta E_v$ . The emission rate of electrons from a QW can be derived from the thermionic current due to electrons emitted from the well to the barrier region. This emission rate has been calculated by Martin *et al* (1983, 1988) and is given by:

$$e_n = \left( \frac{kT}{2\pi n_w^*} \right)^{1/2} \frac{1}{L_w} \exp \left( -\frac{\delta E_c}{kT} \right). \quad (6.18)$$

It is also possible, by drawing an analogy between an electron in a QW and a deep-level trap, to formulate a detailed balance between thermal capture and emission of electrons from the QW. From such a detailed balance, the emission rate of electrons is given by

$$e_n = \frac{16\pi^{3/2}}{3h^3} m_w^* X (kT)^{1/2} (\delta E_e)^{3/2} \exp \left( -\frac{\delta E_e}{kT} \right) \quad (6.19)$$

where  $\delta E_e$  is the electron emission energy from the conduction band well,  $m_w^*$  is the effective mass of electrons in the well material and  $X$  is a parameter related to the capture of carriers by the wells.

This is valid for hole emission from a valence band well from which  $\delta E_v$  can be measured. The thermal emission energy of carriers from a QW is related to the appropriate band offset.

Next, consider a SQW in the depletion region of a Schottky barrier. The existence of confined electrons in the well changes the depletion width  $W$ . Solution of Poisson's equation in the well and barrier regions with appropriate boundary conditions gives

$$W^2 = W_0^2 \left( 1 + \frac{2n_w L_w}{N_D W_0^2} \right) \quad (6.20)$$

where

$$W_0^2 = (2\varepsilon/qN_D)V \quad (6.21)$$

is the depletion region width in the absence of the well,  $N_D$  is the net donor density in the barrier and  $V = V_{\text{app}} + V_{\text{bi}}$ , where  $V_{\text{bi}}$  is the built-in potential of the junction. The transient capacitance  $\delta C$  is then given by

$$\frac{\delta C}{C(W)} = \frac{n_w L_w}{N_D W_0^2}. \quad (6.22)$$

The DLTS signal for rate windows  $t_1$  and  $t_2$  is then given by

$$S(t) = C(t_2) - C(t_1) = \frac{C_0 n_{w0} L_w}{N_D W_0^2} [\exp(-e_n t_1) - \exp(-e_n t_2)] \quad (6.23)$$

and

$$\delta E_c = \delta E_e + E_{e1} + L_w F \quad (6.24)$$

$$\delta E_v = \delta E_h + E_{h1} + L_w F \quad (6.25)$$

where  $E_{e1}$  and  $E_{h1}$  are the electron and hole ground-state subband energies,  $L_w$  is the well width and  $F$  is the electric field across the well region due to the applied reverse bias. The materials were grown by LP-MOCVD at 510°C. The structure for  $\delta E_c$  measurements was as follows. First, a 0.2 μm thick n<sup>+</sup>-doped GaAs buffer layer was grown on a n<sup>+</sup>-GaAs substrate, followed by a 0.5 μm n-doped GaInP layer with a doping level of  $2 \times 10^{16} \text{ cm}^{-3}$ . A 120 Å thick GaAs n-doped quantum well was grown, followed by a 0.5 μm thick n-doped GaInP layer with doping levels of  $2 \times 10^{16} \text{ cm}^{-3}$ . Finally, an Au Schottky contact was deposited on the GaInP cap layer.

The structure for  $\delta E_v$  measurements was obtained by growing p-type doped materials on a p<sup>+</sup>-doped GaAs substrate, with the same structure and doping levels used for  $\delta E_c$  measurements.

The values of  $\delta E_c$  and  $\delta E_v$  derived from this experiment are 0.198 eV and 0.285 eV, respectively. Also  $\delta E_c + \delta E_v = \delta E_g = 0.48$  eV which agrees with the measured value from photoluminescence. The values of  $\delta E_c$  and  $\delta E_v$  estimated in this study agree reasonably well with the measured values reported by Miyoko *et al* (1987), using MOCVD materials grown at 700°C. They also agree with the measured values reported by Rao *et al* (1987) using MBE materials.

*Possible sources of errors:* (i) the quality of the samples, the QW thickness, the carrier concentration in the QW and barrier, the interface quality, etc, (ii) the spread in the subband energies and the excess energy of carriers above the barrier during emission, (iii) reduced energy due to tunnelling, (iv) the values of  $E_{e1}$  and  $E_{h1}$  which are obtained from theoretical analysis.

(c)  $\delta E_c$  evaluation from the I–V curve of HEMTs (Chan *et al* 1990)

GaInP–GaAs HEMT structures have been grown by LP-MOCVD at 510°C.

Devices with a  $1\text{ }\mu\text{m} \times 150\text{ }\mu\text{m}$  gate had an extrinsic transconductance of  $163\text{ mS mm}^{-1}$  at  $300\text{ K}$  and  $213\text{ mS mm}^{-1}$  at  $77\text{ K}$  with  $V_{ds} = 3\text{ V}$ .

An extremely low gate inverse bias current ( $I_{rev} < 200\text{ nA}$  at  $V_g = -4\text{ V}$ ) was achieved, and a  $0.87\text{ eV}$  Schottky barrier height was evaluated from  $C - V$  measurements. The turn-on voltage was  $0.75\text{ V}$  and the value of the ideality factor was 1.18, indicating that thermionic emission and diffusion currents are present in the carrier transport. These results demonstrate the high quality of the sample.

According to the model proposed by Chen *et al* (1988), the  $I-V$  characteristics of HEMTs can be described by the combination of two diodes in series:  $D_1$  and  $D_2$  (see Chan *et al* 1990).  $D_1$  represents the metal-semiconductor Schottky diode and  $D_2$  is the heterojunction diode. Since the Schottky barrier ( $0.87\text{ eV}$  in this case) is much higher than the conduction band discontinuity, the gate current at low forward bias is determined by  $D_1$ . As the bias increases, especially when the potential drop across  $D_1$  is larger than the Schottky barrier height, the change of gate current is determined by  $D_2$ . Two slopes are observed in the gate current-voltage characteristics. By extrapolating the  $I-V$  curve under  $D_2$  operation it is possible to determine the value of the reverse saturation current of  $D_2$  ( $I_{ss}$ )

$$I_{ss} = AA^*T^2 \exp(-q\Phi(0)/kT) \quad (6.26)$$

where  $A$  is the diode area,  $A^*$  is the Richardson constant ( $A^* = 4\pi qk^2m_0/h^3$ ) and  $\Phi(0)$  is the potential difference between the channel and the top of the conduction band discontinuity at zero gate bias. In order to reduce the influence of the series resistance, a large-gate ( $200 \times 50\text{ }\mu\text{m}^2$ ) diode was measured. The value of  $\Phi(0)$  evaluated from  $I_{ss}$  is  $196\text{ meV}$ .

Using a self-consistent solution of the Schrödinger and Poisson equations, the potential difference between the Fermi level in the channel and the bottom of the conduction band discontinuity is found to be  $35\text{ meV}$ . Therefore the conduction band discontinuity of GaInP-GaAs is estimated to be  $\delta E_c = 0.231\text{ eV}$ , which is quite close to the previous results.

(d)  $\delta E_c$  measured by the temperature dependence of the collector current of HBTs (Kobayashi *et al* 1989)

The band offset in the emitter-base heterojunction can be evaluated from the temperature dependence of the collector current of HBTs.

Thermionic electrons from the emitter are injected into the base and diffuse towards the collector, recombining slightly with the majority holes. The collector current can be represented by

$$I_c = A^*T^2 \exp(-E_a/kT) \quad (6.27)$$

where  $A^*$  is the effective Richardson constant and  $E_a$  is the activation energy for injected electrons.  $E_a$  can be equated with the energy difference between the conduction band in the emitter edge adjacent to the base and the Fermi energy

$\delta_1$  in the neutral emitter, and is given by

$$E_a = (V_D - V_{be})\Gamma / (1 + \Gamma) + \delta_1. \quad (6.28)$$

$V_D$  is the diffusion potential at equilibrium

$$V_D = E_g(\text{GaAs}) + \delta E_c - \delta_1 - \delta_2 \quad (6.29)$$

where  $\delta_2$  is the Fermi level in the base,  $V_{be}$  is the emitter–base bias voltage. From these equations one gets:

$$\ln(I_c/A^*T^2) = -[E_g(\text{GaAs}) + \delta E_c - V_{be}] / nkT \quad (6.30)$$

where

$$n = (\Gamma + 1) / \Gamma \quad (6.31)$$

$\Gamma$  is the partition ratio of the diffusion potential under biasing

$$\Gamma = V_1 / V_2 = \varepsilon_2 N_A / \varepsilon_1 N_D \quad (6.32)$$

$\varepsilon_1$  and  $\varepsilon_2$  are the dielectric constant in the emitter and the base and  $N_D$  and  $N_A$  are the dopant densities in the emitter and the base.

Kobayashi *et al* (1989) used MOCVD to grow the npn HBT structure at 700 °C. They obtained a current gain as high as 200 in the current range of about 10 Å cm<sup>-2</sup>. The base doping was  $8 \times 10^{18} \text{ cm}^{-3}$  (using Zn as a p-type dopant), and the base thickness was 1500 Å.

They used equation (6.30) to determine the band offset in GaAs–GaInP and they deduced a value of  $\delta E_c = 30$  meV at 300 K.

*Possible sources of errors:* (i) An increase in  $n$  of 0.01 resulted in an increase in  $\delta E_c$  of 6 meV, (ii) temperature measurement resulted in an error in  $\delta E_c$  of 2.3 meV/°C, (iii) the quality of the sample, (iv) if zinc diffusion caused the p–n junction to be in the GaInP emitter, the evaluated  $E_a$  and hence  $\delta E_c$  in (6.30) are apparently larger than the true  $E_a$  and  $\delta E_c$ , (v) if the alloy composition of GaInP is not matched to GaAs, or if GaInP is contaminated with As at the heterointerface,  $\delta E_c$  decreases, (vi) in this sample, the bandgap energy of GaInP grown for HBT was 60 meV smaller than the energy gap of the intrinsic material grown by LPE. The band lineup must then be arranged so as to compensate for this 60 meV gap shrinkage, which can further reduce  $\delta E_c$ . (vii) In order to confirm the validity of these measurements, it is necessary to evaluate  $\delta E_v$  by using a pnp HBT structure, as was the case for other measurements.

#### (e) Conclusions

It was generally assumed that the energy bands on both sides of the junction in the GaInP–GaAs system were aligned so that approximately 40% of the total, direct bandgap difference ( $\delta E_g$ ) appeared as the conduction band discontinuity ( $\delta E_c$ ) and the remaining 60% made up the valence band discontinuity ( $\delta E_v$ ).

### 6.6.2 Observation of the two-dimensional properties of the electron gas in $\text{Ga}_{0.51}\text{In}_{0.49}\text{P}/\text{GaAs}$ heterojunctions grown by MOCVD (Razeghi *et al* 1986a)

The optimum conditions for the growth of GaAs and  $\text{Ga}_{0.51}\text{In}_{0.49}\text{P}$ , as determined during these investigations, are presented in table 6.1. The heterojunctions studied here were grown on a semi-insulating (100) GaAs substrate. A nominally undoped, 3000 Å thick GaAs layer with electron concentration of  $2 \times 10^{16} \text{ cm}^{-3}$  was covered by a sulphur- or silicon-doped, 1000 Å thick  $\text{Ga}_{0.51}\text{In}_{0.49}\text{P}$  layer with an electron concentration of  $2 \times 10^{17} \text{ cm}^{-3}$ .

From Auger profiling of phosphorus in a multiquantum well of  $\text{GaAs}/\text{Ga}_{0.51}\text{In}_{0.49}\text{P}$  grown under identical conditions, the interface was estimated to be abrupt within two atomic layers.

Magnetotransport measurements were performed on long bar-shaped samples with current and potential contacts. Standard Hall bridges were photolithographically defined. Shubnikov-de Haas (SDH) and quantum Hall effects (QHE) were measured in magnetic fields up to 18 T.

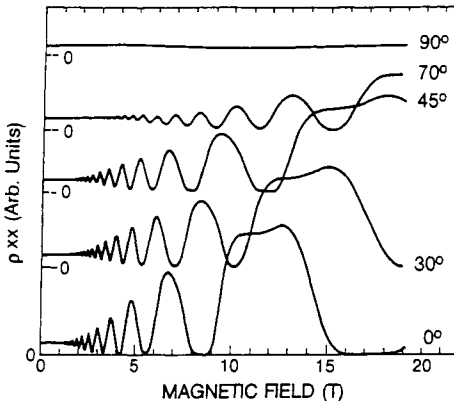
The low-field measurements performed on these heterojunctions gave electron mobilities of  $49\,000 \text{ cm}^2 \text{ V}^{-1} \text{ s}^{-1}$  at 4 K,  $38\,000 \text{ cm}^2 \text{ V}^{-1} \text{ s}^{-1}$  at 77 K and  $6000 \text{ cm}^2 \text{ V}^{-1} \text{ s}^{-1}$  at 300 K. SDH measurements were performed in normal and tilted-field configurations.

Figure 6.13 shows SDH oscillations for various angles between the field direction and the normal to the interface. Extrema of resistivity are observed at constant values of the perpendicular component of the magnetic field  $B_1 = B \cos \theta$  (figure 6.14), giving evidence of the two-dimensionality of electrons at the interface. Figure 6.15 shows the diagonal resistivity  $\rho_{xx}$  and the Hall resistivity  $\rho_{xy}$  as functions of magnetic field at 4.2 K. In the vicinity of 5.2, 7.8 and 16 T,  $\rho_{xx}$  approaches the zero-resistance state. At the same field positions  $\rho_{xy}$  develops plateaus at  $h/ie^2$  for  $i = 6, 4, 2$  characteristic of the QHE, hence giving further proof of the ideal 2D behaviour of this system.

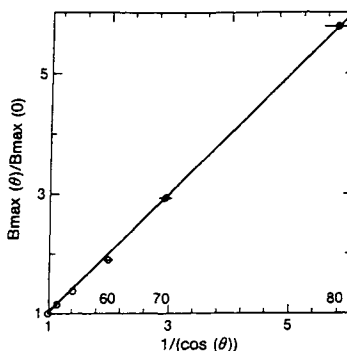
Another important feature of this system is the persistent increase of the 2D electron concentration which was observed after illuminating the sample at low temperature (persistent photoconductivity effect), similar to that observed in  $\text{GaAs}/\text{GaAlAs}$  heterostructures (Stormer *et al* 1981, Kastalsky and Hwang 1984).

Figure 6.16 shows the SDH oscillations before and after illuminating the sample. After illumination, a very clear shift towards higher fields is observed. The fundamental field  $N \times B_N$  increases from 31.6 to 39.0 T giving a change of the total concentration from  $7.64 \times 10^{11}$  to  $9.43 \times 10^{11} \text{ cm}^{-2}$ . The oscillations become more pronounced with increasing temperature because of the increased population of the first excited subband.

The population of the ground subband derived from the low-field SDH periodicity changes from  $7.51 \times 10^{11}$  to  $8.44 \times 10^{11} \text{ cm}^{-2}$ , leaving the difference  $n_1 = n_{\text{tot}} - n_0$  to be  $0.14 \times 10^{11}$  and  $0.98 \times 10^{11} \text{ cm}^{-2}$ , respectively, for the first



**Figure 6.13** Shubnikov–de Haas oscillations in a GaInP–GaAs heterostructure as a function of magnetic field for various tilt angles measured at 4.2 K (Razeghi *et al* 1986a).



**Figure 6.14** Field value  $B_{\max}(\theta)$  of magnetoresistance extrema at angle  $\theta$  divided by  $B_{\max}(\theta = 0)$  of corresponding extrema at  $\theta = 0$  as a function of  $[\cos(\theta)]^{-1}$  (Razeghi *et al* 1986a).

excited subband's population.

Using the persistent photoconductivity effect to tune the 2D electron concentration, one can measure the population of each subband as a function of the total population (figure 6.17). The results are fitted well by linear dependences and are very similar to the predictions of numerical calculations (Ando 1982) for GaAs/GaAlAs heterojunctions. Extrapolation of this plot indicates that the second subband starts to be populated at about  $7.3 \times 10^{11} \text{ cm}^{-2}$ .

It is worth adding that the low-field Hall concentration underestimated the total 2D electron concentration  $n_{\text{tot}}$ . The difference  $\Delta n_H = n_{\text{tot}} - n_H$  clearly exceeded the experimental error and was obviously connected with a two-subband conduction, each subband having a different scattering rate. The Hall

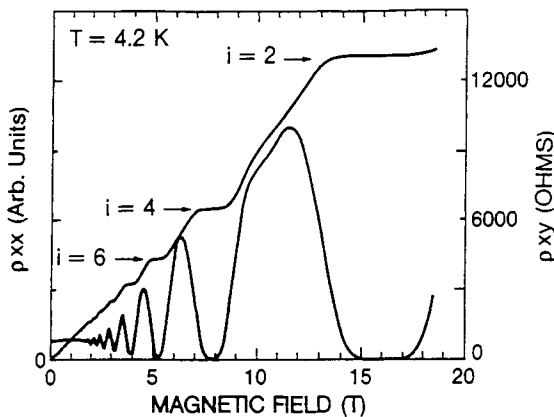


**Figure 6.15** Shubnikov–de Haas and quantum Hall effect as a function of magnetic field (Razeghi *et al* 1986a).

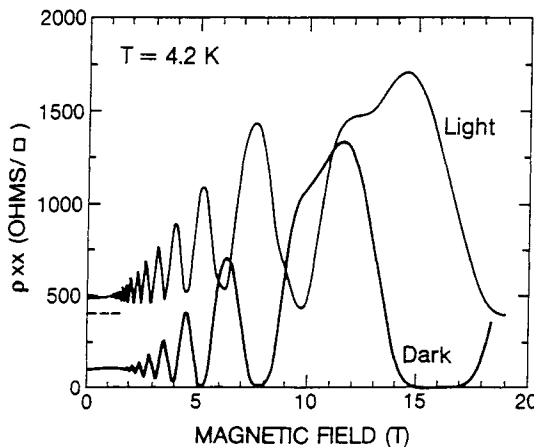


**Figure 6.16** Shubnikov–de Haas oscillations before and after illuminating the samples as a function of magnetic field (Razeghi *et al* 1986a).

mobility decreased slightly as the second subband was populated probably due to intersubband scattering.

### 6.6.3 High-mobility GaInP–GaAs heterostructures

Electron mobilities as high as  $780\,000\,\text{cm}^2\,\text{V}^{-1}\,\text{s}^{-1}$  at a two-dimensional electron concentration  $N_s = 4.1 \times 10^{11}\,\text{cm}^{-2}$  have been measured in GaAs–GaInP heterostructures grown by low-pressure metallorganic chemical vapour deposition (LP-MOCVD) (Razeghi *et al* 1989b).

The sample reported was grown on a semi-insulating GaAs substrate, oriented  $2^\circ$  off the (0 0 1) plane towards the (1 1 0) plane. On top of the substrate,

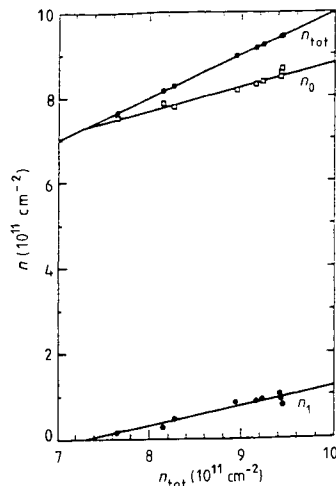


**Figure 6.17** Plot of electron populations in the first two electric subbands  $n_0$  and  $n_1$  as a function of the total electron concentration,  $n_{tot}$  (Razeghi *et al.* 1986a).

a  $1\ \mu\text{m}$  thick unintentionally doped GaAs layer followed by a  $2000\text{\AA}$  thick unintentionally doped layer of GaInP lattice matched to GaAs were grown. The GaInP layer was grown at a low pressure ( $p = 76$  Torr) at a substrate temperature in the range  $500$ – $550^\circ\text{C}$  using triethylgallium, trimethylindium and pure phosphine with hydrogen as the carrier gas. The optimum growth conditions are summarized in table 6.1. For the growth conditions of the GaAs layer, refer to Razeghi *et al.* (1989b). Corresponding layers of GaAs and GaInP with thicknesses of  $2$ – $3\ \mu\text{m}$ , grown under identical conditions as the much thinner layers in the heterostructure, revealed  $N_D - N_A \leqslant 5 \times 10^{14}\ \text{cm}^{-3}$  for GaAs and  $N_D - N_A \leqslant 10^{15}\ \text{cm}^{-3}$  for GaInP ( $N_D - N_A$ : donor and acceptor density), respectively, determined by Hall measurements. The sample was structured into a standard Hall bar geometry, Au–Ge and Ni metallizations were evaporated and then alloyed for 2 min at  $420^\circ\text{C}$  in a hydrogen atmosphere to act as ohmic contacts.

Surprisingly, this nominally undoped heterostructure contains, depending slightly on the cooling procedure, about  $1.7 \times 10^{11}\ \text{cm}^{-2}$  electrons, determined from the periodicity of the Shubnikov–de Haas oscillations. The fact that there are electrons and that they are on the GaAs side of the interface is clear from cyclotron resonance experiments (figure 6.18), as the dependence of the cyclotron energy  $\hbar\omega_c = \hbar eB/m^*$  (see inset in figure 6.18) yields the effective mass expected for GaAs heterostructures  $m^*/m_0 = 0.069$ – $0.070$ . (Here,  $\hbar$  is Planck's constant,  $\omega_c$  the cyclotron frequency,  $e$  the elementary charge,  $B$  the magnetic field and  $m^*$  and  $m_0$  the effective mass and the free-electron mass, respectively.) This  $m^*$  is clearly distinguishable from the estimated value  $m^*/m_0 \approx 0.1$  in GaInP (Watanabe and Ohba 1987). The question of where the

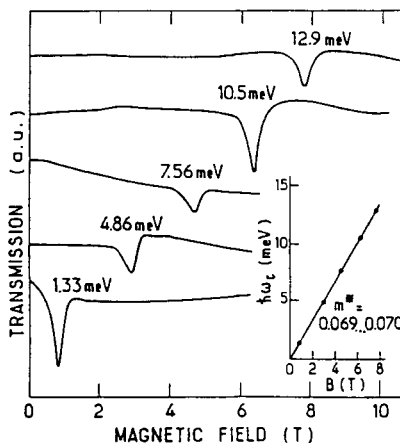


**Figure 6.18** Cyclotron resonance absorption in GaInP–GaAs for different photon energies (at  $T = 1.6$  K). The far-infrared radiation originated from a CO<sub>2</sub>-pumped molecular laser and a carcinotron. The inset shows the cyclotron energy, derived from the absorption peak position, as a function of magnetic field (Razeghi 1989a).

electrons come from remains open. If they originate from donors in the barrier material, their concentration has to be at least of the order of  $N_D \approx 2 \times 10^{16} \text{ cm}^{-3}$ , as a simple calculation (disregarding surface depletion) shows. It is possible that the 2000 Å thick GaInP layer in the heterostructure has properties different from the 3 μm thick reference layer ( $N_D - N_A \leq 10^{15} \text{ cm}^{-3}$ ) although these were grown under identical conditions. Such a big difference is rather surprising.

Successive illumination of the sample with light pulses from a red light emitting diode (LED) at liquid-helium temperatures persistently increases the electron concentration. The photon energy of the LED is centred around  $E = 1.87$  eV, comparable to the bandgap of Ga<sub>0.51</sub>In<sub>0.49</sub>P (1.9 eV) (Madelung 1991) and above that of GaAs. The PPC is well known for GaAs–AlGaAs heterostructures (Stormer *et al* 1979) and was also recently reported for GaAs–GaInP heterostructures with intentionally n-doped barrier material. The mechanism for the PPC in the latter material combination, however, is not yet understood in detail, but it involves the ionization of a DX-centre-like deep trap (Ben Amor *et al* 1989). Using the PPC, the electron concentration could be increased up to  $N_s = 3.9 \times 10^{11} \text{ cm}^{-2}$  ( $N_s$  was determined from the periodicity of the Shubnikov–de Haas oscillations; a typical trace is shown in figure 6.19). Steady illumination increased  $N_s$  further on up to  $4.1 \times 10^{11} \text{ cm}^{-2}$  (transient photoconductivity (Schubert *et al* 1985a, b)). One cannot exclude that a stronger illumination might increase  $N_s$  even more since, in the intensity range explored, there were no signs of saturation.

Razeghi *et al* (1986b) do not see any evidence for parallel conduction through the barrier material after strong illumination. A current bypass would manifest

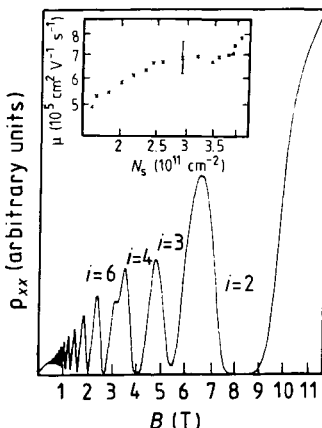


**Figure 6.19** Magnetoresistivity  $\rho_{xx}$  of a GaAs–GaInP heterostructure for an electron density of  $N_s = 3.9 \times 10^{11} \text{ cm}^{-2}$  at a temperature  $T = 1.4 \text{ K}$ . This  $N_s$  has been reached by illumination with red light using the persistent photoconductivity effect. Some filling factors  $i = N_s h / (eB)$  are indicated. The inset shows the mobility as a function of the electron density varied by light pulses of a red light emitting diode using the persistent photoconductivity effect. For clarity, the error bar is only shown on one of the points. (Razeghi 1989a.)

itself in a non-zero magnetoresistivity  $\rho_{xx}$  in the plateau regions of the quantum Hall effect (von Klitzing and Ebert 1984), especially also at filling factor  $i = 2$  (see figure 6.19). The lack of parallel conduction might find its explanation in the low doping level in the GaInP which is not intentionally doped.

After each successive illumination, the mobility  $\mu$  was determined from the electron concentration  $N_s$  and the resistivity  $\rho$  at  $B = 0$ , according to the classical relation  $\mu = (epN_s)^{-1}$ , as shown in the inset of figure 6.19. The sheet resistivity  $\rho$  deduced from the resistance  $R$  by using  $\rho = (w/l)R$  (where  $w$  is the width of the current carrying channel,  $l$  is the distance of the potential probes) involves an uncertainty of  $\pm 10\%$  due to the finite extent of the potential probes. The mobility increases with  $N_s$  up to a concentration of about  $2.5 \times 10^{11} \text{ cm}^{-2}$  and then remains constant upon further increasing  $N_s$  until  $\simeq 3.8 \times 10^{11} \text{ cm}^{-2}$  when  $\mu$  again increases with  $N_s$ , leading in this sample to a final value of  $\mu = 780000 \text{ cm}^2 \text{ V}^{-1} \text{ s}^{-1}$  at  $N_s = 4.1 \times 10^{11} \text{ cm}^{-2}$ . The half width at half amplitude  $\Delta B_{1/2}$  of the cyclotron resonance line confirmed the high mobility if one used the semiempirical expression  $\Delta B_{1/2} = 0.63\mu^{-1/2}B^{1/2}$  established in the case of GaAs–AlGaAs heterojunctions (Voisin *et al* 1981). The value  $\Delta B_{1/2} = 0.18 \text{ T}$  measured for a resonance magnetic field  $B = 6.5 \text{ T}$  (a photon energy of 10.5 meV in figure 6.18 would lead to  $\mu = 800000 \text{ cm}^2 \text{ V}^{-1} \text{ s}^{-1}$ ) is in good agreement with the value deduced from transport experiments. This extremely high mobility proves the very high purity of the GaAs. For GaAs–

AlGaAs heterostructures, such high mobilities are only reached by the growth of an undoped spacer layer, which separates the two-dimensional electrons from the ionized impurities in the barrier material. If we assume that the electrons are coming from the barrier material (residual donors in GaInP), there is nothing equivalent to a spacer layer, provided the growth of the barrier layer is uniform. The reduction of ionized impurity scattering in this heterostructure may be due to the fact that MOCVD-grown GaAs samples are slightly n type, yielding an accumulation layer, contrary to the usual case for MBE-grown GaAs heterostructures having quasi-two-dimensional electron inversion layers. For accumulation layers, the penetration of the electronic wavefunction into the barrier is weaker, thus reducing ionized impurity scattering in the barrier material. In addition, the density of ionized impurities is small, as the barrier is not intentionally doped. Therefore, the whole barrier might be assumed to act as a spacer layer.

The plateau-like behaviour of the mobility beginning at  $N_s \approx 2.5 \times 10^{11} \text{ cm}^{-2}$  (cf. inset in figure 6.19) is due to the onset of intersubband scattering, and indicates that the first excited electric subband is starting to be populated. A comparison of this critical  $N_s$  with corresponding calculations of the confining interface potential and the electronic wavefunctions leads to a depletion charge of the order of  $10^9 \text{ cm}^{-2}$  (Bastard 1988). These calculations have been carried out for the GaAs–AlGaAs system. The results may be slightly different for GaAs–GaInP (e.g., due to a different conduction band offset), but in any case, the order of magnitude of the depletion charge would be far too small for an inversion layer. This confirms again the well known fact that unintentionally doped MOCVD-grown GaAs is usually slightly n type. In  $\rho_{xx}$  (see figure 6.19), a slight occupation of the second subband can be inferred from the positive magnetoresistance. For some electron concentrations, additional structure in the Shubnikov–de Haas oscillations is observed, which is typical of second-subband occupation.

Magnetotransport measurements showed that LP-MOCVD-grown GaAs–GaInP heterostructures can reach extremely high electron mobilities, which up to now have been exclusively attained by MBE-grown GaAs–GaAlAs heterostructures. One can interpret this very high mobility as an indication of reduced ionized impurity scattering due to the high purity of the materials in the nominally undoped heterostructures.

#### 6.6.4 Electron spin resonance in the two-dimensional electron gas of a GaAs–Ga<sub>0.51</sub>In<sub>0.49</sub>P heterostructure (Dobers *et al* 1989a, b)

One possibility for the magneto-optic investigation of two-dimensional electron gases (2DEGs) is electron spin resonance (ESR). The most frequently used method, cyclotron resonance (Merkt 1987), yields the effective mass  $m^*$ , but ESR yields the  $g$  factor. Both of these band structure parameters enter into the energy spectrum of a 2DEG in a perpendicular magnetic field (Ando *et al* 1982)

$$E_{Nm_s} = E_0 + (N + \frac{1}{2})(e\hbar/m^*)B + m_s g \mu_B B \quad (6.33)$$

where  $E_0$  is the energy of the lowest electric subband (higher ones are not considered),  $e$  is the elementary charge,  $\hbar$  Planck's constant,  $\mu_B$  Bohr's magneton and  $B$  the magnetic field.  $N = 0, 1, 2, \dots$  is the Landau level index and  $m_s$  is the magnetic spin quantum number, which takes the values  $m_s = \frac{1}{2}$  ('spin up') and  $m_s = -\frac{1}{2}$  ('spin down'). Strictly speaking, this energy spectrum is only valid in the case of parabolic bands, where  $m^*$  and  $g$  are really constants, independent of the magnetic field and the Landau level. In reality, however, the non-parabolicity of the conduction bands of the semiconductors involved makes both of them vary with the magnetic field and the Landau quantum number (Rossler *et al* 1989).

The dependence of the  $g$  factor on  $B$  and  $N$  has been studied systematically in the 2DEG of GaAs–AlGaAs heterostructures (Dobers *et al* 1988a, b). These experiments were done by looking at the change of the magnetoresistivity  $\rho_{xx}$ . Using the samples themselves as a detector for ESR, the sensitivity was high enough to see ESR. A basic requirement for this, however, turned out to be the following: the spin splitting must be resolved in  $\rho_{xx}$ , i.e. minima in the Shubnikov–de Haas oscillations corresponding to odd filling factors  $i = N_s h/(eB)$  have to be visible ( $N_s$ : concentration of 2D electrons). This limits the measurability of ESR to high-mobility heterostructures.

The availability of very high-mobility GaAs–GaInP heterostructures grown by low-pressure metallorganic vapour deposition (LP-MOCVD) (Razeghi *et al* 1989b) also permits the study of the spin splitting of the Landau levels in the 2DEG of GaAs–GaInP heterostructures.

Consider a GaAs–GaInP heterostructure, grown by LP-MOCVD, which consists of a 1  $\mu\text{m}$  thick undoped GaAs layer on top of a semi-insulating GaAs substrate followed by a 200 nm thick, unintentionally doped layer of  $\text{Ga}_x\text{In}_{1-x}\text{P}$  lattice matched to GaAs ( $x = 0.51$ ). The concentration of 2D electrons was about  $N_s = 1.7 \times 10^{11} \text{ cm}^{-2}$ , depending slightly on the cooling procedure. By illumination with short light pulses of a red LED,  $N_s$  could be increased using the persistent photoconductivity effect (Razeghi *et al* 1989a). In order to see two resolved spin minima in the SDH oscillations within the available magnetic field range ( $B \leq 12 \text{ T}$ ),  $N_s$  was increased to  $N_s = 2.7 \times 10^{11} \text{ cm}^{-2}$ . The mobility at this concentration was  $\mu = 650\,000 \text{ cm}^2 \text{ V}^{-1} \text{ s}^{-1}$ . At this concentration, which remained constant for all the ESR experiments to be discussed, not only the  $i = 1$  minimum but also the  $i = 3$  minimum of the SDH oscillations became resolved (at  $T = 1.3 \text{ K}$ ), thus permitting the study of ESR in the two lowest Landau levels. At about  $N_s = 2.5 \times 10^{11} \text{ cm}^{-2}$  the second subband may begin to be populated (Razeghi *et al* 1989a). This might also be the case during the ESR study ( $N_s = 2.7 \times 10^{11} \text{ cm}^{-2}$ ). However, there is neither an additional oscillation in  $\rho_{xx}$  typical for second subband occupation nor a positive magnetoresistance at small magnetic fields (see figure 6.20). Therefore, the possibility of second-subband occupation must be extremely small, and it will not be considered

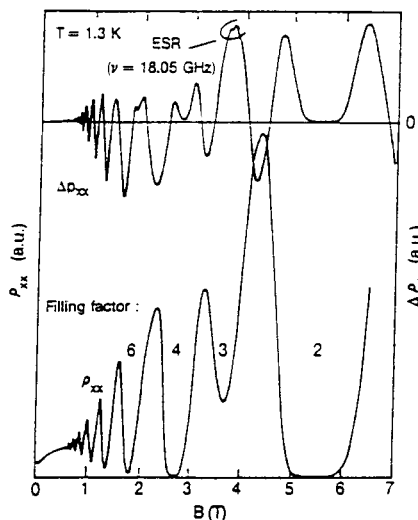


**Figure 6.20** Magnetoresistivity  $\rho_{xx}$  of a GaAs–GaInP heterostructure (lower trace) and its change due to microwave radiation  $\Delta\rho_{xx}$  (upper trace) as a function of the magnetic field. ESR occurs at  $B \approx 3.7$  T. Note that the scale for  $\Delta\rho_{xx}$  is greatly magnified compared with that of  $\rho_{xx}$  (Dobers *et al* 1989b).

further.

The sample had a standard Hall bar geometry, and was located inside an oversized waveguide, immersed in liquid helium. In magnetic fields perpendicular to the plane of the 2DEG,  $\rho_{xx}$ , was measured by a standard lock-in detection utilizing frequencies of the order of 10 Hz. Changes of the sample resistivity due to the chopped microwave radiation (of the order of 1 kHz) were detected using a second lock-in amplifier. Different klystrons and backward-wave oscillators were used to cover the frequency range up to 60 GHz, with magnetic fields up to 12 T. The output power of these microwave sources lay between a few mW and several hundred mW.

In figure 6.20, both  $\rho_{xx}$  and its change due to microwave radiation  $\Delta\rho_{xx}$  are shown. The lower trace,  $\rho_{xx}$ , reveals pronounced SDH oscillations already beginning at  $B \approx 0.5$  T. There are broad regions of vanishing  $\rho_{xx}$ , typical for the quantum Hall effect. At  $B \approx 3.7$  T, the spin minimum corresponding to  $i = 3$  is visible, whereas the next higher one ( $i = 5$ ) is not resolved, because the magnetic field is too low. The upper trace shows  $\Delta\rho_{xx}$ . The broad spectrum reflects the periodicity of the SDH oscillation. It is due to a non-resonant heating of the sample (Stein *et al* 1984, Guldner *et al* 1987), and is related to the derivative of  $\rho_{xx}$  with respect to the temperature. On top of this broad spectrum, there is a sharp resonance structure, in this case ( $\nu = 18.05$  GHz) at  $B \approx 3.7$  T. Whereas the broad non-resonant spectrum does not depend on the microwave frequency, the position of the ESR structure shifts with the applied microwave frequency

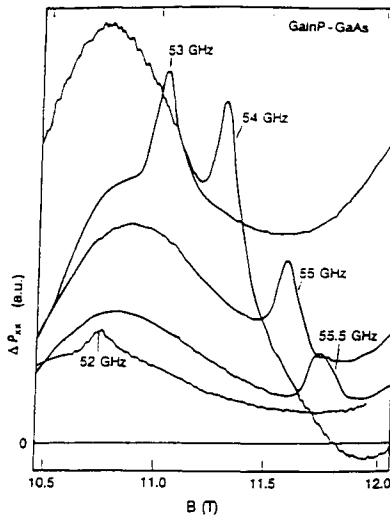


**Figure 6.21** Typical ESR structures in the change of magnetoresistivity due to microwave radiation  $\Delta\rho_{xx}$  for different microwave frequencies. These ESR structures occur around filling factor  $i = 1$  (Dobers *et al* 1989b).

on top of the non-resonant background. This can be seen in figure 6.21 which shows  $\Delta\rho_{xx}$  for several microwave frequencies yielding ESR in the vicinity of the filling factor  $i = 1$ . Here, the background changes because of a continuous variation of the bath temperature between  $T \approx 2$  K and  $T \approx 3$  K, and also due to different microwave powers at different frequencies; the width of the ESR structures is of the order of  $\Delta B = 100$  mT. This is a factor of two to three larger than has, up to now, been seen in the case of GaAs-AlGaAs (Dobers *et al* 1988a, b).

The ESR structures shown in figure 6.21 consist of an increase of  $\rho_{xx}$  due to ESR. Approaching the even filling factor  $i = 2$ , the effect of ESR on  $\rho_{xx}$  (and  $\Delta\rho_{xx}$ ) turns into a decrease. The same observation has been made in the  $N = 1$  Landau level: around  $i = 3$ , ESR results in an increase; approaching the neighbouring even filling factors, say around  $i = 2.5$  and  $i = 3.5$ , ESR decreases  $\rho_{xx}$ . This is the same finding as in GaAs-AlGaAs heterostructures (Dobers *et al* 1989a, b), which might give some evidence to the assumption that this is an intrinsic property of a 2DEG.

A very weak hysteresis of the ESR structure, found during a decrease of the magnetic field, is an indication of an Overhauser shift of the ESR (Dobers *et al* 1988a, b) which is due to a dynamic nuclear spin polarization of the lattice nuclei via hyperfine interaction. This effect is only visible during very slow magnetic field sweeps ( $\approx 0.1$  T min $^{-1}$ ), and even then it is very weak. Thus in practice, there was no complication for a determination of the electronic  $g$  factors. Although one is not able to quantify properly the 'strength' of a

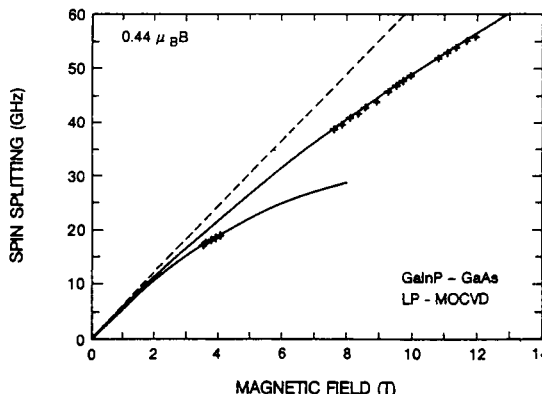


**Figure 6.22** Measured spin splittings of the two lowest Landau levels. The full curves are least-squares fits to the experimental data leading to the two coefficients in equation (6.34). For comparison, the spin splitting due to the bulk GaAs conduction band edge  $g$  factor,  $g = 0.44$ , is indicated as a broken line (Dobers *et al.* 1989b).

dynamic nuclear spin polarization, it became obvious that it is much weaker in the present case of a GaAs–GaInP heterostructure compared with the GaAs–AlGaAs heterostructures (Dobers *et al.* 1988a, b), as all experiments were done with the same experimental set-up. Basically, there are two possibilities for the weakness of the Overhauser shift: either the nuclear spin relaxation times are very short, so that a nuclear spin polarization, once created, immediately relaxes, or more likely the electrons relax directly, without polarizing the nuclei, thus leaving the nuclear spin polarization unchanged from the beginning. The broader ESR structures in GaAs–GaInP indicate smaller electronic spin relaxation times. Thus, the electrons feel more spin-flip scattering and the second interpretation seems to be preferable: among the different electronic spin relaxation channels, the dynamic nuclear spin polarization is less important, because all the others are more effective here.

From a series of experiments with different microwave frequencies, as shown in figure 6.21, the magnetic field dependence of the spin splitting can be deduced. This is shown in figure 6.22. The experimental results for a certain Landau level cover only a limited magnetic field range, as does the Fermi level. The spin splittings are smaller than the spin splitting in bulk GaAs (broken line). Both of the two sets of data ( $N = 0$  and  $N = 1$ ) follow the quadratic magnetic field dependence

$$\Delta E = 0.418\mu_B B - 0.0133(1/T)(N + \frac{1}{2})\mu_B B^2 \quad (6.34)$$

the two coefficients being determined by a common least-squares fit of all the data. From equation (6.34), a magnetic-field- and Landau-level-dependent  $g$  factor can be deduced

$$g(B, N) = 0.418 - 0.0133(1/T)(N + \frac{1}{2})B. \quad (6.35)$$

This qualitative magnetic field dependence is predicted by theory (Lommer *et al* 1985), and confirmed by experiments (Dobers *et al* 1988a, b, 1989a, b), in the case of GaAs–AlGaAs. It turns out to be valid also in GaAs–GaInP heterostructures. Furthermore, the two coefficients are also found to be in the same range (Dobers *et al* 1989a, b). The similarity of the spin splitting in GaAs–GaInP heterostructures and those consisting of GaAs–AlGaAs is because the 2DEG is in both cases on the GaAs side of the interfaces. The extent of the electronic wavefunctions into the barrier material is only very small, in either case. Therefore, an exchange of the barrier material does not alter the properties of the 2DEG very much.

MOCVD-grown GaAs is known to be slightly *n* type. Thus, the 2DEG in MOCVD-grown GaAs heterostructures forms an accumulation layer, in contrast with MBE-grown heterostructures. The 2DEG, therefore, is confined at a slightly larger distance to the interface and enters to a lesser extent into the barrier material, an effect that is still supported by the high conduction band offset in GaAs–GaInP. The spin splitting, therefore, should be more ‘GaAs-like’. There is slight evidence for this: according to Lommer *et al* (1985), the magnetic field dependence of the *g* factor

$$g(B, N) = g_0 - c(N + \frac{1}{2})B \quad (6.36)$$

is simply an average of two corresponding quantities, one for each of the two materials, weighted with the probability of finding the electrons on either of the two sides of the interface. The coefficient *c* is equal to  $0.0133\text{T}^{-1}$ . If the electrons are more on the GaAs side, the coefficient *c* is bigger (Lommer *et al* 1985). In fact, for the actual GaAs–GaInP heterostructure, the magnetic field dependence of the *g* factor is slightly stronger than found in GaAs–AlGaAs heterostructures (Dobers *et al* 1989a, b), but, unfortunately, not strong enough to verify the significance of this difference. Anyway, the experimental findings are consistent with the 2DEG being an accumulation layer at a higher conduction band offset, compared with that in GaAs–AlGaAs.

From these investigations, one can obtain the dependence of the *g* factor on the magnetic field and the Landau level which turned out to be quantitatively comparable to its dependence in GaAs–AlGaAs heterostructures.

### 6.6.5 Magnetotransport measurements in GaInP/GaAs heterostructures using $\delta$ -doping

The electrical properties of the two-dimensional electron gas in selectively S- and Si-doped GaInP/GaAs heterostructures grown by low-pressure MOCVD have been studied by Ranz *et al* (1990). The influence of the spacer thickness on the sheet carrier density derived from Shubnikov–de Haas oscillations is analysed.

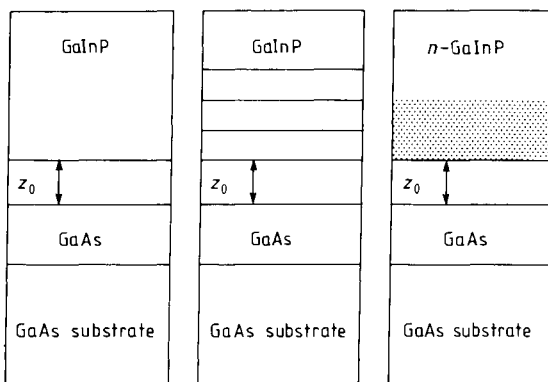


**Figure 6.23** Schematic diagram of GaInP/GaAs heterostructures with single  $\delta$ -doping, multi- $\delta$ -doping and uniform doping (Ranz *et al* 1990).

Persistent photoconductivity is studied through the temperature dependence of the Hall effect and is used to increase the electronic density. At each step of illumination the classical to quantum lifetimes ratio is derived and an increase of this ratio is observed. Comparison with AlGaAs/GaAs heterostructures shows that DX-like centres are not necessarily responsible for the observed persistent photoconductivity effect (Ranz *et al* 1990).

The samples were single-interface GaInP/GaAs heterostructures grown by low-pressure MOCVD (Razeghi *et al* 1986b) schematically represented in figure 6.23. Several types of doping process were made use of in the GaInP layer: using  $\delta$ -doping with variable spacers, multi- $\delta$ -doping and uniform doping. Both the transverse magnetoresistance and the Hall effect were measured under magnetic fields up to 20 T. Shubnikov-de Haas (SDH) oscillations and Hall plateaus (with  $i = 2, 4, 6$ ) were observed at 4.2 K indicating the formation of a two-dimensional electron gas (2DEG) at the interface. The temperature dependence of the Hall effect at low magnetic field was also used before and after optical excitation at 77 K using a LED emitting at 1.8 eV.

For the uniform and multi- $\delta$ -doped samples, the shape of the transverse magnetoresistance curves are very similar and indicate that parallel conduction is present in the doped GaInP layer. Strong oscillations of the Hall effect traces were also detected and can be explained by assuming the existence of a Hall current in the interface region opposite to the one for the parallel conduction region.

Parallel conduction was completely eliminated by using  $\delta$ -doped GaInP layers with spacer thickness less than 500 Å. Mobilities of the order of  $10^5 \text{ cm}^2 \text{ V}^{-1} \text{ s}^{-1}$  and evidence of only one occupied electrical subband were then obtained. The carrier density of this subband ( $N_s$ ) was derived from the period of the SDH oscillations. The carrier density decrease observed with increasing spacer thickness ( $z_0$ ), as shown in figure 6.24, can be explained by the increase of

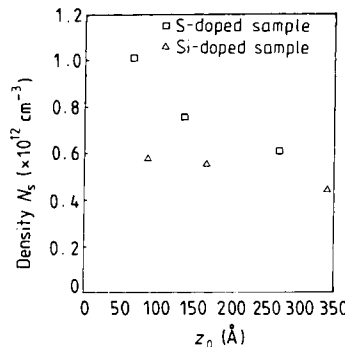


**Figure 6.24** Electron density  $N_s$  as a function of the spacer thickness ( $z_0$ ) in  $\delta$ -doped GaInP/GaAs heterostructures with S and Si (Ranz *et al.* 1990).

the electrostatic potential in the spacer layer, the Fermi level being fixed at the donor-level positions.

Temperature-dependent Hall measurements have been performed on the highest-mobility S- and Si-doped samples. The data before and after illumination shown in figure 6.25 indicate a small persistent photoconductivity (PPC) effect already described for similar heterostructures (Razeghi *et al.* 1986b). However, the behaviour of the photoexcited Hall density is very different from the one reported by Ben Amor *et al.* (1989), where a continuous decrease of the Hall density after illumination is observed with increasing temperature. This decrease, which was attributed to a capture process through a lattice-relaxation energy barrier, is not observed in this sample (figure 6.25). The small enhancement of the Hall mobility obtained after illumination can be attributed to an increased screening of the impurity potential by the 2DEG, involving an increase of the small-angle scattering process. Such a conclusion is also supported by the following analysis of the classical to quantum lifetimes ratio.

In order to study the change of the scattering processes when the PPC effect is used to increase the Fermi wavevector, low-field SDH oscillations and Hall effect data have been analysed to obtain the quantum and classical lifetimes. The scattering (or classical) lifetime  $\tau_s$  is related to the mobility through the relation  $\mu = e\tau_s/m^*$  where  $m^*$  is the effective mass. The single-particle (or quantum) lifetime  $\tau_q$  is related to the lifetime of the unperturbed one-electron Hamiltonian eigenstate in the presence of scatterers. This characteristic time is partly responsible for the damping of the SDH oscillations at low magnetic field. Using the Ando formula, the amplitude  $A$  of the SDH oscillations can be expressed as (Ando *et al.* 1982)

$$A \propto T \omega_c^{-3} \exp\left(-\frac{\pi}{\omega_c \tau_{\text{eff}}}\right) \quad (6.37)$$

where  $\omega_c$  is the cyclotron frequency and  $\tau_{\text{eff}}$  is defined by  $\tau_{\text{eff}}^{-1} = \tau_T^{-1} + \tau_q^{-1}$

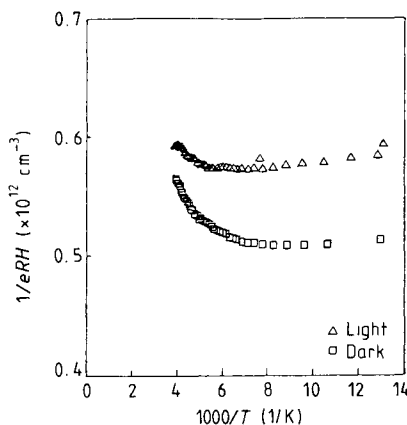


**Figure 6.25** Hall concentration versus  $1/T$  in the dark and after illuminations (Ranz *et al* 1990).

with  $\tau_T = h/2\pi kT$ . It is worth noting that this formula is valid for  $\omega_c \tau_q \gg 1$  and for the sinusoidal oscillation regime.

The magnetic field limit for the analysis was chosen to be below the field at which quantization of the Hall plateaus becomes observable (for  $B \leq 2$  T). The determination of  $\tau_q$  is illustrated in figure 6.26. At each step of illumination, the Hall mobility and  $\tau_q$  were derived in order to obtain the classical to quantum lifetimes ratio ( $R = \tau_s/\tau_q$ ). At the same time the Fermi wavevector  $k_F$  was derived from the SDH carrier density ( $k_F = \sqrt{2\pi} N_s$ ). The plot of  $R$  as a function of the normalized Fermi wavevector  $k_F/q_{TF}$  (where  $q_{TF} = 2 \times 10^6 \text{ cm}^{-1}$  is the Thomas–Fermi screening parameter in GaAs) is shown in figure 6.27. This ratio is always greater than one, indicating that small-angle scattering is the predominant scattering process. This ratio increases after each illumination dose.

It is interesting to compare these results with those reported in AlGaAs/GaAs heterostructures. In AlGaAs/GaAs a decrease of  $R$  with increasing  $k_F$  was found after illumination. This decrease was attributed to the effect of DX centres by assuming a negative- $U$  character of the defect.

In this case, such a conclusion is no longer valid and the predominance of remote impurity scattering is sufficient to explain the behaviour of  $R$  with a light-induced increase of  $k_F$ . Hence, the PPC effect observed here does not have the same origin as in AlGaAs/GaAs heterostructures.

### 6.6.6 Persistent photoconductivity in $\text{Ga}_{0.51}\text{In}_{0.49}\text{P}/\text{GaAs}$ heterojunctions (Ben Amor *et al* 1989)

It was originally predicted that several problems associated with the use of AlGaAs (oxidation, presence of DX centre) could be avoided by using GaInP. Razeghi *et al* (1986b) reported the observation of a strong persistent

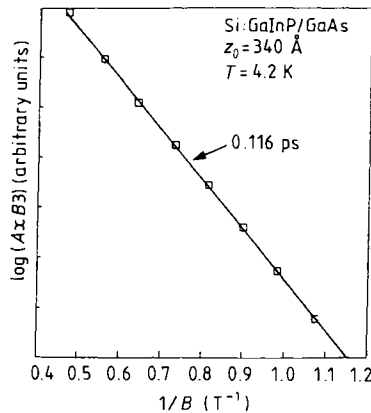


**Figure 6.26** Analysis of the SDH amplitude; the effective lifetime  $\tau_{\text{eff}}$  derived from the slope is indicated (Ranz *et al* 1990).

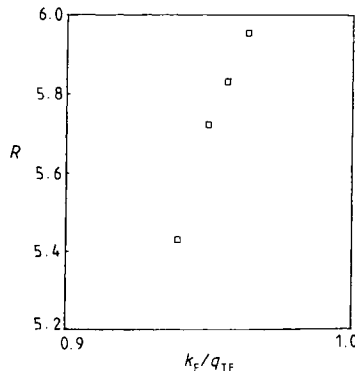


**Figure 6.27** Classical to quantum lifetimes ratio  $R = \tau_s/\tau_q$  versus normalized Fermi wavevector in GaInP/GaAs. Saturation corresponds to an increase of 6% of the initial density (Ranz *et al* 1990).

photoconductivity effect (PPC) in these structures and PPC was recently reported to occur in S-doped bulk GaInP layers. Ben Amor *et al* (1989) focus on the study of PPC in single-heterojunction systems. They observe an important and persistent increase of the electron concentration which remains at surprisingly high temperatures, as high as 330 K for one sample. Temperature-, as well as time-dependent Hall measurements were also performed. They have investigated the effect of hydrostatic pressure ( $P < 12$  kbar) on quantum transport (quantum Hall effect and Shubnikov-de Haas (SDH) oscillations) at 4.2 K, as well as on the number of photoexcited carriers and their recombination rate at higher temperature. Thermal cycling of the samples decreased the number of free 2D electrons (in the dark) until the sample became semi-insulating. However,

**Table 6.3** Characteristics of the studied samples.

	A	B
GaInP layer	1000 Å	3000 Å
GaInP doping	$3 \times 10^{17} \text{ cm}^{-3}$	$1 \times 10^{17} \text{ cm}^{-3}$
Carrier density (dark)	$6 \times 10^{11} \text{ cm}^{-2}$	$1 \times 10^{11} \text{ cm}^{-2}$
Mobility (4.2 K)	$42\ 000 \text{ cm}^2 \text{ V}^{-1} \text{ s}^{-1}$	$27\ 000 \text{ cm}^2 \text{ V}^{-1} \text{ s}^{-1}$
Quenching temperature	330 K	210 K
Growth temperature	550 °C	650 °C

illumination restored the samples to their original precycling state. The critical temperature at which the PPC is suppressed is also strongly affected by the thermal cycles. Finally, optical experiments were performed which reveal an optical threshold energy of 1.15 eV for the PPC and a partial infrared quenching after saturation of the PPC (Ben Amor *et al.* 1989).

The samples studied were grown by low-pressure MOCVD (Omnès and Razeghi 1991). They consist of a semi-insulating (100) GaAs substrate followed by an undoped GaAs layer and finally by a S- and Si-doped  $\text{Ga}_{0.51}\text{In}_{0.49}\text{P}$  layer. The parameters of the samples studied are summarized in table 6.3. The temperature- and time-dependent Hall measurements were performed in a small 0.25 T electromagnet. The excitation wavelength dependence of the PPC was studied by illuminating the sample, cooled down in the dark, with monochromatic light and waiting for any change in the conductivity to saturate. However, the transport measurements were performed using a pulsed red electroluminescent diode (LED) to control the PPC. For the temperature-dependent Hall effect the sample was illuminated at low temperature and then slowly heated (about  $1 \text{ K min}^{-1}$ ). The time-dependent conductivity and Hall measurements were performed at a stabilized temperature ( $\pm 0.3 \text{ K}$ ) using the internal clock of the monitoring computer. The pressure apparatus was a liquid helium cell allowing us to reach 12 kbar at 4.2 K. A small LED was inserted in the cell and allowed us to illuminate the sample under pressure. The light-induced concentration increase is in the 2D layer over the whole range of temperatures (4.2–330 K). This was demonstrated by angle-dependent SDH oscillations at 4.2 K (Razeghi *et al.* 1986b). At higher temperatures, the Hall coefficient is found to be unaffected by a strong magnetic field (19 T), thus proving that only one type of carrier is present (i.e. only 2D carriers).

(a) *Temperature- and pressure-dependent transport in GaInP–GaAs grown by MOCVD*

Typical temperature-dependent Hall measurements are shown in figure 6.28 before and after illumination. Several traces were observed in the dark, of which only two are represented here. The Hall density slightly decreases with increasing temperature. After illumination, the photoexcited Hall concentration drops smoothly with increasing temperature and finally joins the ‘dark’ trace

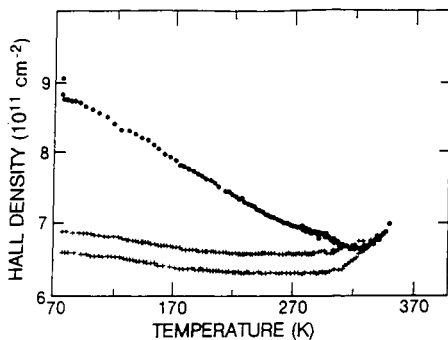


**Figure 6.28** Hall density as a function of temperature. Circles stand for the density after illumination. Two dependences in the dark are shown (crosses), as the sample did not reach thermal equilibrium during the temperature cycle (Ben Amor *et al* 1989).

at a critical temperature  $T_c$ . The most striking point is the very high critical temperature at which the PPC is suppressed. Due to this high quenching temperature, cycling the sample to room temperature is not sufficient to bring the sample to an equilibrium state, hence the different temperature dependences in the dark. The temperature-independent Hall density is characteristic of a predominantly shallow-donor behaviour in the barrier (as is also reported in Kitahara *et al* 1988). The slight decrease of the 2D density for increasing temperatures is due to a less efficient electron transfer from GaInP to GaAs as the temperature is raised. The smooth temperature decrease of the photoexcited Hall density is in sharp contrast to the behaviour of photoexcited DX centres in  $\text{Al}_x\text{Ga}_{1-x}\text{As}$  ( $x = 0.2\text{--}0.4$ ) which usually exhibits an abrupt drop in density at around 150 K, but is consistent with the smooth decay of PPC observed in bulk S-doped GaInP of comparable compositions by Kitahara *et al*. At a given temperature, the photoexcited Hall concentration measured immediately after the end of the illumination is always the same regardless of the history of the sample. The metastability is, therefore, confirmed to be associated with the PPC donor centres.

The number of photoexcited carriers (immediately after saturation of the PPC) diminishes strongly with increasing pressure at high temperatures, close to  $T_c$ , as can be seen in figure 6.29. It has been shown by Chand (1984) that if a DX-like centre is associated with a non-gamma minimum of the conduction band, then applying pressure to the sample will increase the recombination barrier energy in the case of a small relaxation centre and decrease it in the case of a large lattice relaxation centre (LLR). Kitahara *et al* (1988) have reported that the centre responsible for PPC in S-doped GaInP is associated with a non-gamma minimum. Therefore, the observations of this work are compatible with a LLR centre in which the recombination barrier is smaller at higher pressure and more easily overcome at higher temperatures (the large optical activation energy (1.15 eV)

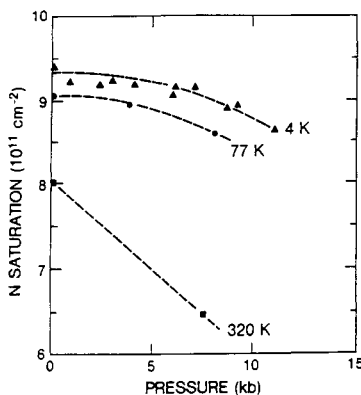


**Figure 6.29** Hall density after saturation of the PPC as a function of pressure for three temperatures. The dashed lines are guides for the eye (Ben Amor *et al* 1989).

and the infrared quenching of the PPC (as shown below) are further indications of the LLR character of the centre).

Pressure measurements at 4 K (after saturation of the PPC to keep the system in a quasistable state) are also shown in figure 6.29. One can observe a weak dependence of the density on applied pressure. Possible reasons for such a pressure dependence are a change of the band offset (as the bandgaps on each side of the interface have rather different pressure dependences) or some other non-gamma character impurity in the barrier, as found in GaAlAs/GaAs (Mercy *et al* 1984). In this case, however, the latter effect should be small because the donor level is emptied by the PPC and the electrons cannot easily recombine with their parent centre.

As can be seen in table 6.3, the second sample studied (B) showed a very different temperature dependence of the PPC quenching. The higher growth temperature resulted in a much lower quenching temperature of 210 K (still much higher than the quenching temperature of a DX centre in AlGaAs). This behaviour was simulated in the first sample by a short (2 min) annealing at 700 K. This produced the striking result that the sample became semi-insulating in the dark, while PPC was no longer observed at room temperature.

These observations show that the PPC is correlated with extrinsic defects. In this system, the interface stress is very sensitive to the composition and the growth temperature. If defects were due to interface stress, annealing would then change the defect density at the interface, and, as for InAs/GaSb structures (Beerens *et al* 1987), the interface defects would influence the number of electrons in the well.

Quantum transport was performed at 4.2 K, and from SDH oscillations and the quantum Hall effect, one can obtain the illumination-dependent concentration in each populated electric subband, as well as the classical and quantum mobility

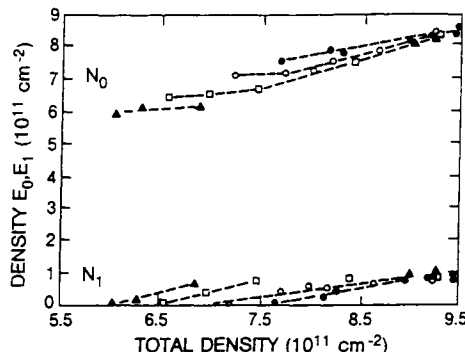


**Figure 6.30** Division of the electrons (as obtained from SDH measurements at 4.2 K) between the different subbands as a function of the total two-dimensional density for several temperature cycles. The longer the sample is annealed at 350 K, the lower the electron density before illumination. After saturation, the electron densities are always the same whatever the history of the sample. The dashed lines have no physical meaning (Ben Amor *et al* 1989).

of the electrons. After each temperature cycle (a few minutes annealing at 350 K), i.e. after a change in both the 2D concentration and the ionized defect density, a different electronic density prior to illumination is observed (figure 6.30) but all the carriers appear to be in the lowest electric subband. After each cycle, illumination of the sample will populate the second electric subband with a different density threshold (figure 6.30), suggesting that the depletion charge in the GaAs has somewhat changed. After saturation of the PPC, the total 2D density is always the same as is the mobility (figure 6.31). The density of photoexcited donors thus appears to control simultaneously the electron density, the electron mobility and the population of electrons between subbands. The classical mobility is proportional to the density in the dark, as measured after each annealing cycle, as expected for a sample with no spacer layer where the dominant scattering centres are ionized impurities (Ando 1982). On illumination, the drop in mobility corresponds to the population of the second electric subband which causes increased scattering (Stormer *et al* 1983, Harris *et al* 1987). Analysis of the amplitude of the SDH oscillations shows that the single-particle lifetime is of the order of 0.1 of the classical lifetime for the fundamental subband (prior to illumination), which is further proof that the dominant scattering centre is by remote ionized impurity scattering (small angle) (Harrang *et al* 1985).

#### (b) Time-dependent transport in GaInP-GaAs grown by MOCVD

In order to investigate further the recombination of the photoexcited donors in GaInP-GaAs Ben Amor *et al* (1989) performed time-dependent Hall effect and conductivity measurements. The Hall mobility was almost independent of the

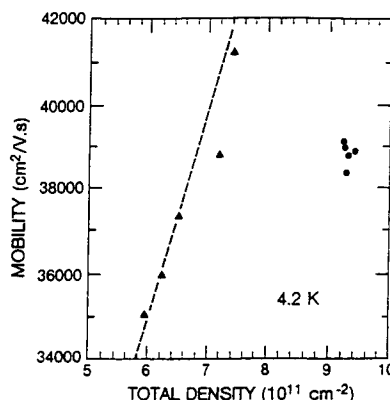


**Figure 6.31** Classical mobility as a function of the total density. After each annealing cycle, a new density (mobility) is obtained in the dark (triangles); after saturation of the PPC, the electron density and mobility always return to the same values. The dashed line represents the calculated ionized-impurity-limited mobility in a sample with no spacer (Ando 1982).

illumination at temperatures over 77 K. Typical normalized conductivity results are displayed in figure 6.32. They observe a very slow relaxation tail at room temperature. At room temperature and ambient pressure, the relaxation of all the photoexcited carriers takes several days. However, a much quicker relaxation process is also present in these samples, as can be observed in the first seconds of the measurement, by focusing on the slower recombination process. The decay of the photoexcited concentration is strongly non-exponential. The relaxation rate increases only slightly with increasing temperature, in contrast with DX centres in AlGaAs. Both the non-exponential behaviour and the weak thermal sensitivity made the determination of a recombination barrier meaningless; however, the observation of a room-temperature PPC several thousands of seconds after the end of illumination suggests the presence of a high barrier. Moreover, the application of a hydrostatic pressure strongly increases the relaxation rate as expected in the LLR description. Such a non-exponential decay was observed in AlGaAs/GaAs structures and was attributed to the spread in the DX centre's energies (Mooney *et al.* 1985) or to tunnelling through the barrier to the impurity site (Schubert 1985a, b).

The latter process can be excluded as it depends strongly on temperature (through the temperature increase of the capture cross-section of the impurity). Queisser and Theodorou (1986) observed a logarithmic decay with time which they associated with the recombination of spatially separated electron-hole pairs. In the present case, the decay is not logarithmic and one can exclude this mechanism for the observed PPC. The observed non-exponential behaviour is therefore due to the spread of the recombination barrier energies of the centres. This is confirmed by the broad (300 meV) spread of the optical activation

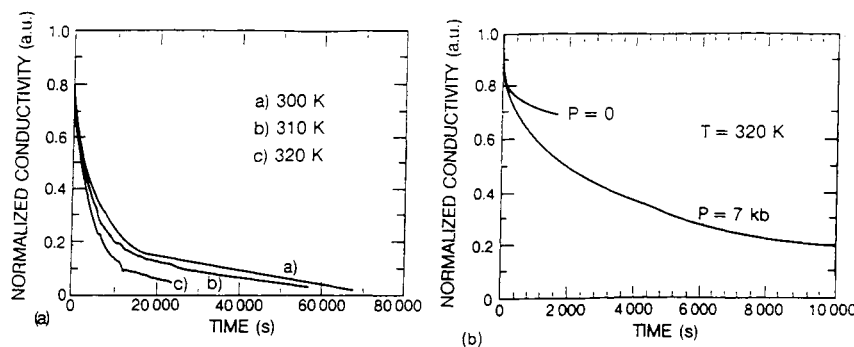


**Figure 6.32** Normalized conductivity as a function of time spent since the end of illumination. (a) Temperature effect at constant pressure ( $7 \pm 0.3$  kbar) and (b) pressure effect at constant temperature (320 K) (Ben Amor *et al.* 1989).

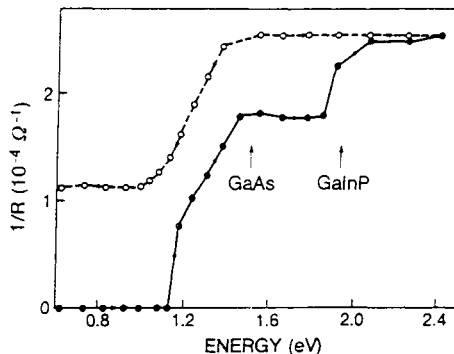


**Figure 6.33** Effect of illumination on a semi-insulating sample as a function of photon energy. The dark circles (and continuous line) represent the absolute changes in the conductivity. The open circles (and dashed line) represent the relative recovery when the photon energy is decreased after PPC saturation (Ben Amor *et al.* 1989).

energies shown in figure 6.33.

Ben Amor *et al.* (1989) performed photoconductivity experiments at 77 K in GaAs–GaInP layers grown by MOCVD. Figure 6.33 shows the variation of photoconductivity as a function of the excitation wavelength for sample A after a high-temperature anneal (semi-insulating sample). The sample was cooled in the dark and monochromatic light was applied of progressively increasing energy, having waited for the response to saturate. A large PPC occurred (four orders of magnitude) above a threshold of 1.15 eV, rather similar to that found in AlGaAs (Nathan *et al.* 1983). The response saturated just below the GaAs bandgap, confirming that the electron–hole spatial separation process is not of major importance. There is a further significant doubling of the PPC at energies

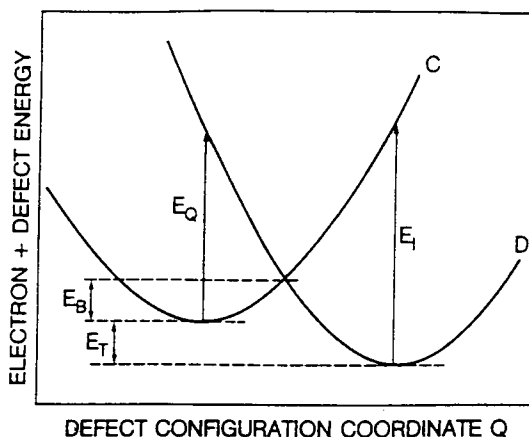


**Figure 6.34** A configuration coordinate model for a donor defect centre in GaInP–GaAs heterostructures (Ben Amor *et al.* 1989).

corresponding to the GaInP bandgap. This may be due to interband excitation and subsequent capture of free holes at impurities in the GaInP or at the interface.

Following illumination at high energies, the photon energy was then reduced, and it was found that below 1.4 eV a partial quenching of the PPC occurs. This effect peaks at around 1 eV with the removal of over 50% of the PPC at an energy below that where any photoresponse was seen before the PPC. This is again reminiscent of infrared quenching (IRQ) measurements in AlGaAs (Nathan *et al.* 1983, Kastalsky and Hwang 1984). Both activation and quenching energies are spread over 300 meV. This shows that the defects are broadly distributed in energy and explains the non-exponential decays.

The optical measurements on the annealed sample support the idea of a LLR DX-like centre, where the optical ionization energy  $E_I$  (see figure 6.34) is much greater than the trap energy ( $E_T$ ) or thermal barrier energy ( $E_B$ ). Similarly, the optical capture energy  $E_Q$  is large but significantly lower than  $E_I$  to favour quenching at low energies.

Most of these observations are very similar to the effect of DX centres in the barrier of AlGaAs/GaAs heterostructures. A donor and defect-related DX-like centre accounts for the PPC and the IRQ, as well as for the low-temperature behaviour of the electron density and mobility. The strong pressure dependence of the PPC and the optical measurements suggest a large lattice relaxation centre. The non-exponential decays are presumably related to the dispersion of the centre's energies due to inhomogeneities or alloy disorder. However, the high quenching temperature corresponds to recombination barriers in the eV range which are much larger than typical recombination barriers in DX centres (0.2 eV).

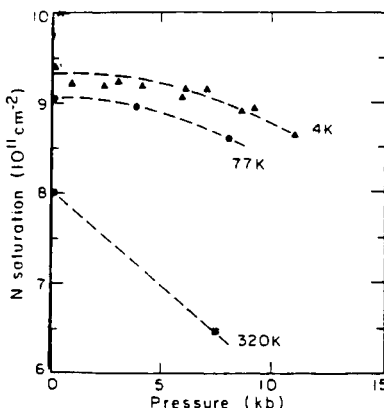


**Figure 6.35** Hall density after saturation of the PPC as a function of pressure for three temperatures. The broken curves are guides for the eye (Ben Amor *et al* 1989).

### 6.6.7 Quantum and classical lifetimes in a $\text{Ga}_{0.51}\text{In}_{0.49}\text{P}/\text{GaAs}$ heterojunction

The subband structure of  $\text{Ga}_{0.51}\text{In}_{0.49}\text{P}/\text{GaAs}$  heterostructures has been studied by magnetotransport under hydrostatic pressure (Ben Amor *et al* 1990). The samples were single-interface  $\text{Ga}_{0.51}\text{In}_{0.49}\text{P}/\text{GaAs}$  heterojunctions grown by low-pressure metallorganic chemical vapour deposition (MOCVD) (Razeghi *et al* 1990). The 1000 Å wide  $\text{Ga}_{0.51}\text{In}_{0.49}\text{P}$  layer was S and Si doped ( $3 \times 10^{17} \text{ cm}^{-3}$ ) and no undoped spacer separated the doped layer from the two-dimensional electron gas (2DEG). The GaAs layer was n-type residual in contrast with molecular-beam-epitaxy-grown GaAs. Hydrostatic pressure was applied at room temperature and the samples were cooled in the dark using a liquid-pressure cell that permitted up to 12 kbar at 4.2 K to be applied (Ben Amor *et al* 1989). A small light-emitting diode (LED) was inserted in the cell allowing variation of  $N_{2D}$  under pressure by controlled light exposure.

The effect of pressure on  $N_{2D}$  is shown in figure 6.35. In  $\text{AlGaAs}/\text{GaAs}$  heterostructures (Mercy *et al* 1984), the pressure deepening of the DX centre energy level drives the Fermi level deeper in the gap, thus decreasing  $N_{2D}$  and the ionized donor density. However, illumination damps the pressure effects (Maude *et al* 1987) on DX centres and reionizes the donors. These results were obtained after saturation of PPC at each pressure so  $N_{2D}$  is expected to have a weak pressure dependence. The striking point of the observations is that there is a slight increase of the 2DEG density at low pressures, while  $N_{2D}$  decreases for  $P > 3$  kbar.

The only mechanism to give an overall increase in  $N_{2D}$  is the pressure-related increase of the effective mass ( $m^*$ ) (around 1% kbar), which increases the density of states and in turn  $N_{2D}$ . Since there is a turnover and decrease in  $N_{2D}$  for

$P > 3$  kbar, it is also necessary to account for a mechanism that decreases  $N_{2D}$  as pressure is applied. The bandgaps on both sides of the interface have different pressure dependences, so the decrease in  $N_{2D}$  for  $P > 3$  kbar could arise from a pressure-induced decrease in the band discontinuity. At ambient pressure it was shown (Rao *et al* 1987) that the bandgap discontinuity ( $\Delta E_g$ ) was equally divided between conduction and valence bands. Assuming this partition of band discontinuities to be pressure independent (a reasonable assumption in the present case of hydrostatic pressure), the conduction band discontinuity should decrease at a rate of  $2 \pm 1$  meV kbar $^{-1}$ . Using a simple model of the band structure (Gregoris *et al* 1987) that accounts for the pressure decrease of  $\Delta E_g$  and the pressure increase of  $m^*$ , good agreement was obtained with the observed behaviour in  $N_{2D}$  (including a predicted turnover at  $\approx 5$  kbar).

One can obtain the classical scattering time  $\tau_0$  from the DC conductivity and the low-field Hall effect (the classical mobility is about  $40\,000\,\text{cm}^2\,\text{V}^{-1}\,\text{s}^{-1}$ ). The broadening of the Landau levels is reflected through the single-particle (i.e. quantum) lifetime  $\tau_q$ . The quantum lifetime was obtained from the magnetic field dependence of the SDH oscillations by fitting Ando's expression for the conductivity (Ando 1982)

$$\delta\sigma \propto (\omega_c \tau_q)^2 \frac{\exp[-\pi/(\omega_c \tau_q)] \Phi \cosh(\Phi)}{[1 + (\omega_c \tau_q)^2]^2} \quad (6.38)$$

where

$$\Phi = 2\pi^2 kT/\hbar\omega_c \quad (6.39)$$

$$\omega_c = eB/m^* \quad (6.40)$$

and  $T$  is the temperature. The amplitude  $A$  of the SDH oscillations can be expressed as (Fang *et al* 1988)

$$A = T\omega_c^{-3} \exp\left(-\frac{\pi}{\omega_c \tau_q}\right) \exp(-\Phi). \quad (6.41)$$

A typical fit is displayed in figure 6.36. It is important to note that in this approximation,  $\tau_q$  is determined at a given temperature without any fitting parameters. Spatial fluctuations of  $N_{2D}$  along the sample can alter the shape of the SDH oscillations (i.e.  $\tau_q$ ). In the present case, however, no evidence of amplitude anomalies or beating structures was seen in the SDH envelopes.

Figure 6.37 displays the dependence of the ratio  $R_a = \tau_c/\tau_q$  on the PPC-induced increase in  $N_{2D}$ . The quantum lifetime is almost an order of magnitude smaller than the scattering time. This confirms the dominance of small-angle scattering mechanisms in heterostructures (Harrang *et al* 1985, Stern and Sarma 1985) (i.e. scattering by remote ionized impurities). The surprising point is the 2DEG density dependence of  $R_a$ , which decreases with increasing  $N_{2D}$ ,

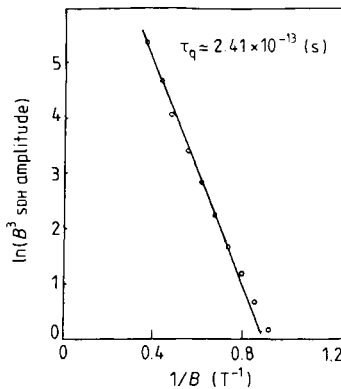


**Figure 6.36** Typical fit of the SDH amplitudes at 4.2 K. The quantum lifetime is directly deduced from the slope (Ben Amor *et al* 1990).

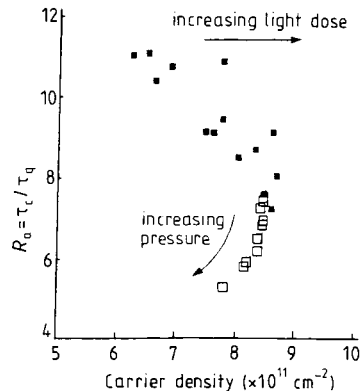


**Figure 6.37** Ratio of the classical to quantum lifetimes,  $R_a$ , as a function of PPC-induced increases in  $N_{2D}$  (■), and the pressure-induced changes in  $R_a$  plotted against the corresponding pressure-induced values of  $N_{2D}$  (□) (Ben Amor *et al* 1990).

although theory predicts the opposite even if the scattering centres are at the interface (Stern and Sarma 1985). A similar discrepancy was reported by Mani and Anderson (1988) in an AlGaAs/GaAs heterostructure and was attributed to the dominant effect of DX centres rather than shallow impurities. In the sample studied here,  $N_{2D}$  has been shown to be high enough so that the first two subbands are occupied; hence it is likely that intersubband scattering causes the PPC-induced decrease in  $R_a$ .

It is obvious that the misfit strain at the interface of heterostructures of GaAs and III-V alloys increases with increasing difference in the lattice constants of the binary members. From this point of view the  $\text{GaAs}/\text{Ga}_x\text{Al}_{1-x}\text{As}$  system, where the lattice constants,  $a_0$ , of GaAs and AlAs are 5.6533 and 5.661 Å

(Pierron *et al* 1967), presents fewer problems than that of GaAs and  $\text{Ga}_x\text{In}_{1-x}\text{P}$ , where  $a_{\text{GaP}} = 5.451 \text{ \AA}$  and  $a_{\text{InP}} = 5.8694 \text{ \AA}$  (Alferov *et al* 1974). It was shown that the quality of  $\text{Ga}_x\text{In}_{1-x}\text{P}$  layers grown on GaAs substrates, and consequently the quality of the  $\text{Ga}_x\text{In}_{1-x}\text{P}$  interface itself, are strongly affected by small deviations of the composition from  $x \approx 0.5$ , at which the lattice constant of  $\text{Ga}_x\text{In}_{1-x}\text{P}$  is equal to the lattice constant of the GaAs substrate. Because of the large difference in compressibility of GaAs and GaInP, application of hydrostatic pressure (similar to a change in alloy composition) creates a misfit strain at the interface, even in a perfectly lattice-matched system at ambient pressure. It was shown in photoluminescence studies of GaAs/GaInP heterostructure grown by vapour phase epitaxy that outside some range of misfit strain, arrays of misfit dislocations are generated and the interface recombination velocity between GaAs and GaInP increases approximately linearly with misfit strain (Ettenberg and Olsen 1977). The strong decrease of  $R_a$  with pressure is due to the increasing role of interface-related scattering mechanisms (i.e. some interface states induced by increasing misfit strain or interface dislocations that relaxed the pressure-induced misfit strain).

### **6.6.8 FIR magnetoemission study of the quantum Hall state and the breakdown of the quantum Hall effect in GaAs–GaInP (Raymond *et al* 1990)**

The Landau emission has been suggested as a very useful tool to investigate two-dimensional systems. An analysis of the emission spectra allows us to determine, for example, the cyclotron mass of the 2D electrons (Chabot *et al* 1991), the amount and the position of impurities in the quantum well (Gornik *et al* 1987, Robert *et al* 1988, Knap *et al* 1990), and to study the polaron effects (Seidenbush 1987). The Landau emission experiments are performed in a quantizing magnetic field and coincide, for a degenerated 2D electron gas, with the quantum Hall effect (QHE) regime. In the emission technique, Raymond *et al* (1990) studied both the FIR emission spectra and the components  $\rho_{xx}$  and  $\rho_{xy}$  of the resistivity tensor in the QHE regime of GaAs–GaInP heterojunctions. By varying the heating electric field, Raymond *et al* (1990) analysed the evolution of the emission spectra and the breakdown of the QHE when the electric field increases.

Using cyclotron emission, they performed simultaneously optical far-infrared (FIR) and transport measurements on quasi-2DEGs in GaInP/GaAs heterojunctions. In low-electric-field conditions, the FIR spectrum showed, beside the cyclotron resonance line, supplementary lines in coincidence with minima of  $\rho_{xx}$  (Hall plateaus). These supplementary lines were interpreted in terms of a non-homogeneous distribution of potential in the quantum Hall state.

As a result of a non-equilibrium carrier distribution, in high-electric-field conditions ( $E > 3 \text{ V cm}^{-1}$ ), the width of the Hall plateaus is reduced and the ‘zeros’ of  $\rho_{xx}$  are less pronounced. This phenomenon is due to the breakdown

**Table 6.4** Structural details of a GaInP/GaAs superlattice grown by LP-MOCVD.

Sample No II.31	Growth time (s)	Thickness (Å)
GaAs buffer layer	600	1000
GaAs wells	120	$d_1 = 200$
10×		
GaInP barriers	40	$d_2 = 135$
GaInP cap layer	210	700

of the equation  $N_s = i(eB/h)$  and leads to the breakdown of the QHE when the electric field increases further.

For Landau emission experiments, the electric field is used to heat the electrons. To spectroscopically investigate impurities in quantum wells by Landau emission, the heating electric field must be very low ( $\approx 1 \text{ V cm}^{-1}$ ).

## 6.7 GROWTH AND CHARACTERIZATION OF GaInP–GaAs MULTILAYERS BY MOCVD

Extensive experimental studies of low-dimensional structures of GaInP–GaAs have been performed (Razeghi *et al* 1990, 1991a, b). The quantum size effect and excitonic absorption in GaAs–GaInP multiquantum wells (MQWs) and superlattices have attracted a great deal of interest because of their novel physical properties and their potential use in optoelectronic (Guanapala *et al* 1990) and electronic devices (Chan *et al* 1988).

Sample No II.31 is a typical ten-period GaAs/Ga<sub>0.51</sub>In<sub>0.49</sub>P superlattice. Its structure, deduced from growth rates of GaAs and Ga<sub>0.51</sub>In<sub>0.49</sub>P, is briefly described in table 6.4.

Figure 6.38 shows the simple diffraction pattern of the sample, performed using K $\alpha$  of Cu as x-ray source, in a classical ( $\theta$ ,  $2\theta$ ) configuration. K $\alpha_1$  and K $\alpha_2$  components of the satellites, due to the superperiod  $D = d_1 + d_2$  artificially introduced by the growth, can be seen up to order  $n = \pm 3$ . This fact is remarkable, especially using simple diffraction, and suggests that the thicknesses of the wells and barriers are perfectly controlled. The corresponding data are summarized in table 6.5.

A mean value of  $2\delta\theta = 0.31^\circ$ , corresponding to the spacing between two satellites, is found. The superperiodicity  $D = d_1 + d_2$  can then be deduced by the well known relation

$$D = \frac{\lambda}{2\delta\theta \cos \theta_0} \quad (6.42)$$

where  $\theta_0$  represents the Bragg angle at which the (400) reflection of the GaAs

**Table 6.5** X-ray data of GaInP/GaAs superlattices grown by LP-MOCVD.

Order $n$ of the $K\alpha_1$ component of the satellite	$2\theta$ (deg)
-3	66.97
-2	66.66
-1	66.35
0	66.02
+1	65.73
+2	65.43
+3	65.12

LP-MOCVD  
No II-31  
GaAs/Ga<sub>0.49</sub>In<sub>0.51</sub>P Superlattice

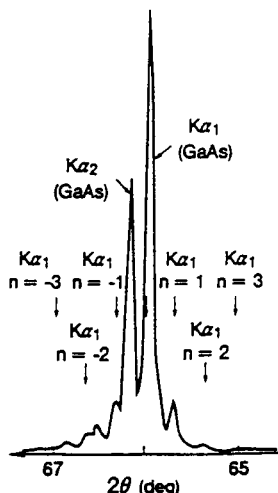


**Figure 6.38** Simple x-ray diffraction pattern of a typical GaAs/Ga<sub>0.51</sub>In<sub>0.49</sub>P superlattice (Razeghi 1989a).

occurs ( $\theta_0 = 33.01^\circ$ ).  $\lambda$  is the x-ray wavelength, which is about  $1.54 \text{ \AA}$  for the Cu  $K\alpha_1$  ray.

One finds  $D = 340 \text{ \AA}$ , which is in good agreement with the value obtained from the growth times and deposition rates (see table 6.4).

The morphology of this GaInP/GaAs superlattice sample was examined by cross-sectional transmission electron microscopy (TEM). A dark-field image of the complete superlattice is shown in figure 6.39(a). This image was taken using the (200) reflection, with GaInP appearing brighter than GaAs. The ten periods of GaInP/GaAs are clearly visible with each GaInP layer measuring  $140 \text{ \AA}$  and

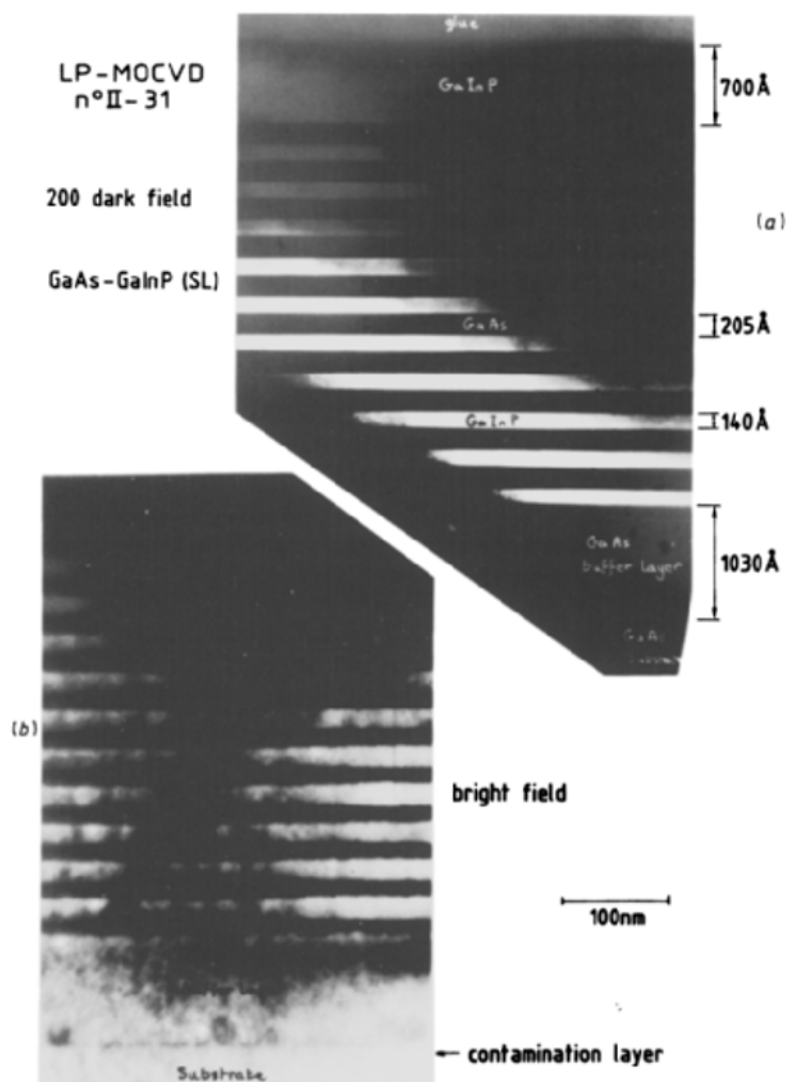


**Figure 6.39** Transmission electron micrograph of a typical GaAs/Ga<sub>0.51</sub>In<sub>0.49</sub>P superlattice (Razeghi 1989a).

each GaAs layer 205 Å in thickness. The layers are extremely regular and no local layer thickness variations were seen in the area examined. The GaAs buffer layer can be distinguished from the GaAs substrate by a dark contamination line, most clearly visible in figure 6.39(b), whose presence has not affected the quality of the buffer layer. One defect in the superlattice was found and is shown in figure 6.39(b). It originates at the boundary between the buffer layer and the

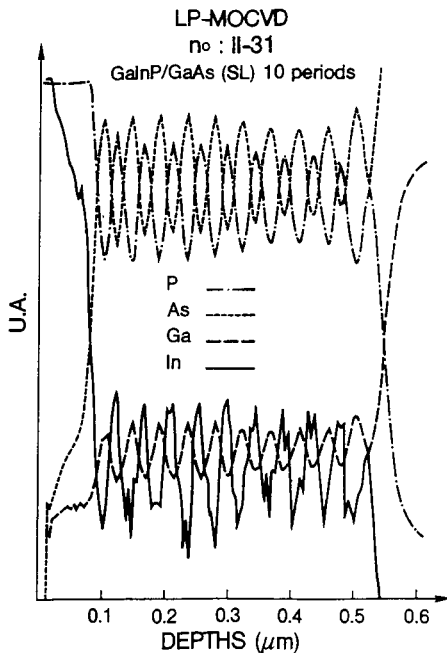


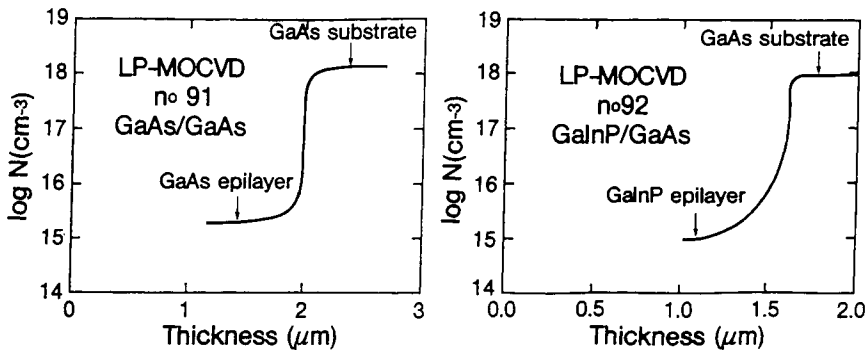
**Figure 6.40** SIMS profile relative to the majority species (In, Ga, As and P) of a typical GaAs/Ga<sub>0.51</sub>In<sub>0.49</sub>P superlattice (Razeghi 1989a).

first GaInP layer.

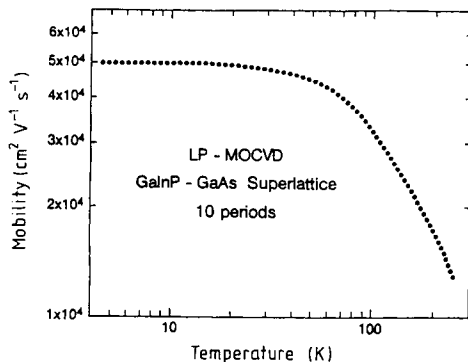
The SIMS profile of the sample is shown in figure 6.40. The signals relative to the majority species (Ga, In, As and P) have been plotted. The ten periods of the superlattice are clearly evidenced by following the oscillations of the different signals. The Ga<sub>0.51</sub>In<sub>0.49</sub>P top layer and GaAs substrate appear on each side.

Figure 6.41 shows the electrochemical (polaron) profiles of Ga<sub>0.51</sub>In<sub>0.49</sub>P layers. The residual doping level is  $8 \times 10^{14} \text{ cm}^{-3}$ . This explains why a concentration of carriers of  $n = 2.9 \times 10^{11} \text{ cm}^{-2}$  is measured at  $T = 4 \text{ K}$  by the classical Hall method, in the unintentionally doped multiquantum well structure.

Carriers arising from the donor impurities are confined in the GaAs quantum wells, where they form a two-dimensional electron gas. This fact is evidenced by the mobility curve plotted against temperature (figure 6.42). The mobility reaches a constant value of  $50000 \text{ cm}^2 \text{ V}^{-1} \text{ s}^{-1}$  at temperatures below 50 K. This is clearly characteristic of the transport properties of a two-dimensional electron gas. Because of the spatial separation between carriers and donors, the ionized impurity scattering becomes much less efficient than in three-dimensional systems, so the mobility does not decrease at low temperatures under this effect.



**Figure 6.41** Polaron profile of bulk GaAs and GaAs/Ga<sub>0.51</sub>In<sub>0.49</sub>P (Razeghi 1989a).



**Figure 6.42** Mobility curve versus temperature of a typical GaAs/Ga<sub>0.51</sub>In<sub>0.49</sub>P superlattice (Razeghi 1989a).

An Auger spectrum has been taken from a GaAs/Ga<sub>0.51</sub>In<sub>0.49</sub>P multiquantum well structure, with GaAs wells of 15, 50 and 100 Å thickness and GaInP barriers of 1000 Å (figure 6.43). Resolution good enough to identify wells of thickness down to 15 Å was obtained by scanning the surface of a chemical bevel and correcting the arsenic signal.

## 6.8 OPTICAL AND STRUCTURAL INVESTIGATIONS OF GaAs-GaInP QUANTUM WELLS AND SUPERLATTICES GROWN BY MOCVD

High-quality GaInP-GaAs multiquantum wells and superlattices were grown by LP-MOCVD (Omnès and Razeghi 1991). Growth was carried out at 76 Torr and at a substrate temperature of 510 °C. Trimethylindium (TMIn) and triethylgallium (TEGa) were used as sources of In and Ga, while pure arsenic (AsH<sub>3</sub>) and

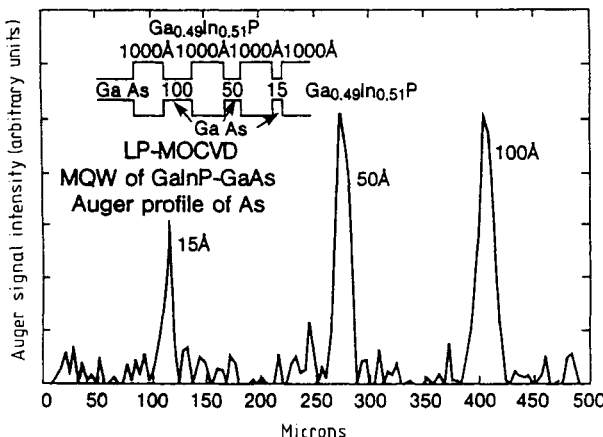


**Figure 6.43** Auger spectrum of As species of a typical GaAs/Ga<sub>0.49</sub>In<sub>0.51</sub>P multiquantum well (Razeghi 1989a).

(AsH<sub>3</sub>) and phosphine (PH<sub>3</sub>) provided As and P, respectively. Hydrogen (H<sub>2</sub>) was used as a carrier gas.

The GaAs–GaInP interfaces were realized by turning off the AsH<sub>3</sub> flow and turning on both the TMIn and PH<sub>3</sub> flows. The reverse procedure was used to obtain GaInP–GaAs interfaces. The GaInP–GaAs interfaces are more critical due to the memory effect of In, so purging of In at the GaInP–GaAs interface improves the optical confinement in the GaAs quantum well.

The growth rate was small and the gas flow stabilized to its new steady-state value in less than a few seconds after switching. The optimum growth conditions of GaAs–GaInP as determined during these investigations are given in table 6.6.

**Table 6.6** Optimum growth parameters.

	GaAs	GaInP
Growth temperature	510 °C	510 °C
Growth pressure	76 Torr	76 Torr
Total H <sub>2</sub> flow rate	3 l min <sup>-1</sup>	3 l min <sup>-1</sup>
AsH <sub>3</sub> flow rate	20 cm <sup>3</sup> min <sup>-1</sup>	—
PH <sub>3</sub> flow rate	—	200 cm <sup>3</sup> min <sup>-1</sup>
H <sub>2</sub> through TMIn	—	220 cm <sup>3</sup> min <sup>-1</sup>
H <sub>2</sub> through TEGa	180 cm <sup>3</sup> min <sup>-1</sup>	—
Growth rate	180 Å min <sup>-1</sup>	360 Å min <sup>-1</sup>

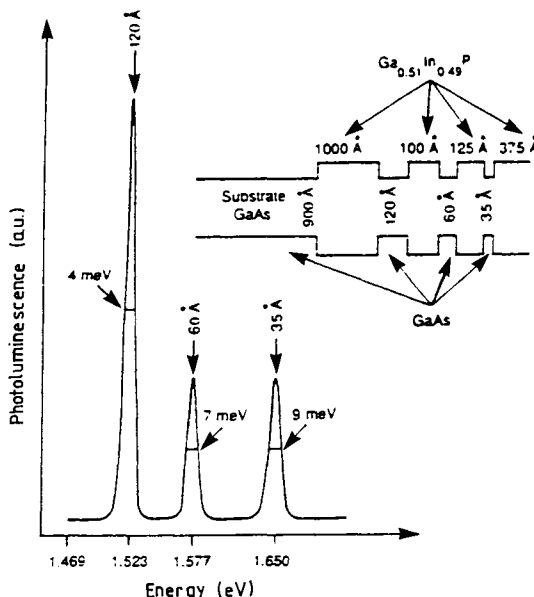


**Figure 6.44** Photoluminescence spectrum of GaAs–Ga<sub>0.51</sub>In<sub>0.49</sub>P sample (No 1219) measured at 4 K using a 5435 Å argon laser operating at 2 mW. Inset: schematic representation of sample No 1219 grown by LP-MOCVD (Omnes and Razeghi 1991).

The quantum well and superlattice samples grown for this study were unintentionally doped. Residual impurity concentrations are assumed to be of the order of those determined for bulk layers. Corresponding layers of GaAs and GaInP with thicknesses of 3 μm, grown under identical conditions, revealed  $N_D - N_A \leq 10^{14} \text{ cm}^{-3}$  for GaAs (Razeghi *et al.* 1989a) and  $N_D - N_A \leq 5 \times 10^{14} \text{ cm}^{-3}$  for GaInP (Razeghi *et al.* 1989b), and a uniform distribution of impurities in the direction perpendicular to the layers.

Figure 6.44 shows a typical PL spectrum of a three-well structure of GaAs–GaInP. The GaAs (well) and GaInP (barrier) indicated ‘nominal’ thicknesses are those deduced from the measured growth rate of thick layers. The substrates were GaAs (100) misoriented 2° off axis towards  $\langle 0\bar{1}\bar{1} \rangle$ .

The PL measurements were done at 4 K using a 5435 Å argon laser operating at 2 mW, and dispersed on a HRS Jobin–Yvon monochromator equipped with a photomultiplier tube. The full widths at half maximum of the PL spectra are 4, 7 and 9 meV for the nominal QW thicknesses of 120, 60 and 35 Å.

The quality of PL peaks of GaAs wells is proved by PLE spectroscopy, using a tunable pyridine dye laser pumped with an argon laser. The dye laser power is locked at 2 mW in the whole wavelength range. Figure 6.45 shows the PLE spectrum of a GaAs–GaInP quantum well of 120 Å thickness at 4 K. The PLE spectrum exhibits a series of peaks, which can be attributed to the heavy-hole

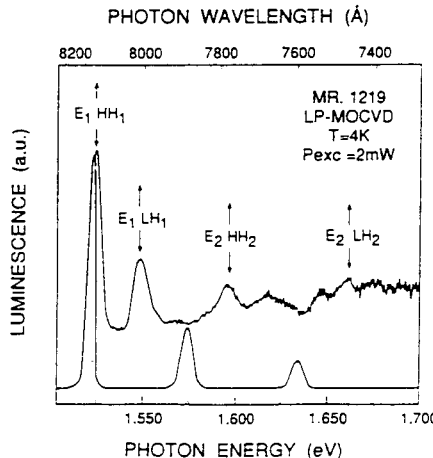


**Figure 6.45** Photoluminescence and photoluminescence excitation spectrum of the quantum well of 120 Å thickness at 4 K (sample No 1219) (Ornnes and Razeghi 1991).

exciton and light-hole exciton as shown in figure 6.45. These results show that high-quality GaAs–GaInP MQWs have been achieved. The intensity of the PLE peaks indicates that the GaAs–GaInP system is of type 1, i.e. the GaAs layers are simultaneously QWs for both the conduction and valence band states.

By comparing the PL and PLE spectra taken at 4 K in figure 6.45, we find that the energy of the  $E_1 \rightarrow HH_1$  subband transition, as determined by PLE, is 1524 meV and the peak energy of the (e, h) emission in the PL spectrum is at 1522 meV, indicating the high quality of the interfaces of GaInP–GaAs MQWs grown by LP-MOCVD. The variation of the PL intensity as a function of excitation power at low temperature is linear. X-ray diffraction measurements carried out on this sample showed a  $\Delta a/a$  of about  $10^{-4}$ .

Figure 6.46 shows the x-ray (400) diffraction pattern of a three-well structure of  $\text{GaAs}/\text{Ga}_{0.51}\text{In}_{0.49}\text{P}$  (shown inset), with GaInP barriers of about  $L_{B1} = 1000 \text{ \AA}$ ,  $L_{B2} = 100 \text{ \AA}$ ,  $L_{B3} = 125 \text{ \AA}$  and  $L_{B4} = 375 \text{ \AA}$  and GaAs wells of about  $L_{Z1} = 900 \text{ \AA}$ ,  $L_{Z2} = 120 \text{ \AA}$ ,  $L_{Z3} = 60 \text{ \AA}$  and  $L_{Z4} = 35 \text{ \AA}$ . A synchrotron beam ( $\lambda = 1.47596 \text{ \AA}$ ) is used as the x-ray source. The GaAs (well) and GaInP (barrier) indicated ‘nominal’ thicknesses are those deduced from the measured growth rate of thick layers. This multiquantum well structure is shown in figure 6.46 (inset); the substrate was  $\text{GaAs}(1\ 0\ 0)$  misoriented  $2^\circ$  off axis towards  $\langle 0\ 1\ \bar{1} \rangle$  (Razeghi and Ornnes 1991).

The fringe spacing is inversely related to layer thickness. This means that the larger the fringe spacing, the thinner the epilayer. Thus, due to the different fringe spacings seen in figure 6.46, different layer thicknesses can be determined. From the angular separations  $\Delta\theta_1 = 120''$ ,  $\Delta\theta_2 = 720''$ ,  $\Delta\theta_3 = 1080''$  and  $\Delta\theta_4 = 540''$ , we deduce, using the classical expression

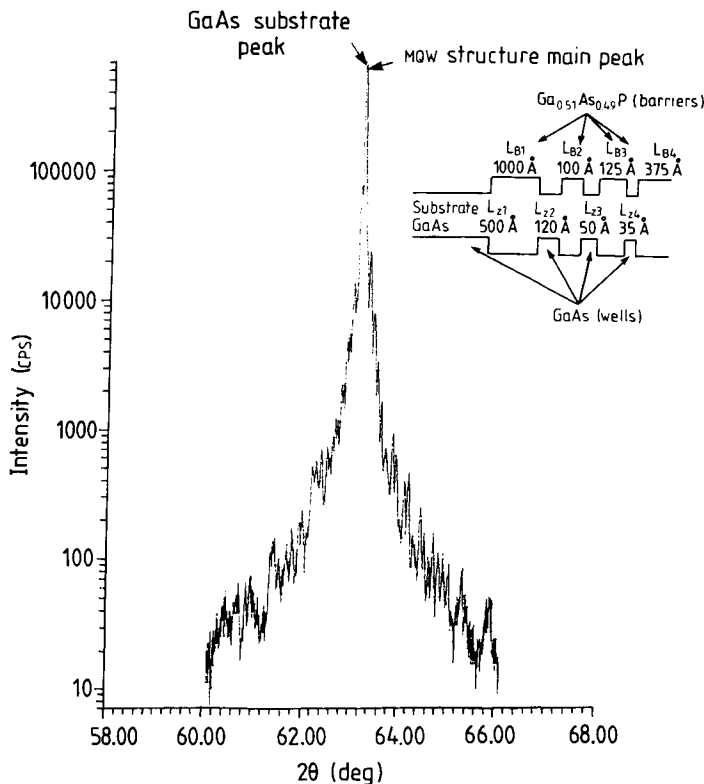


**Figure 6.46** X-ray diffraction pattern of a three-well GaAs/Ga<sub>0.51</sub>In<sub>0.49</sub>P MQW structure. Inset: schematic representation of this MQW sample grown by LP-MOCVD (Papalus *et al.* 1991).

$$L'_B + L'_Z = \frac{\lambda}{2\Delta\theta \cos\theta} \quad (6.43)$$

that the thicknesses of the quantum well and barrier layer are  $L_1 (L'_B + L'_Z) = 1490 \text{ \AA}$ ,  $L_2 = 248 \text{ \AA}$ ,  $L_3 = 166 \text{ \AA}$  and  $L_4 = 331 \text{ \AA}$ ; these values are consistent with those expected from growth parameters.

Although there is no hyperfine structure observed near the substrate Bragg peak in figure 6.46, the angular separation arising from pendellosung oscillations can also be determined by means of the classical equation

$$\Delta\theta = \frac{\lambda}{2L \cos\theta} \quad (6.44)$$

with  $L = 2750 \text{ \AA}$ ; we find  $\Delta\theta = 65''$ . Comparing this value to the  $x$ -axis scale shown in figure 6.46, it is obvious that this kind of angular separation is too small to be observed.

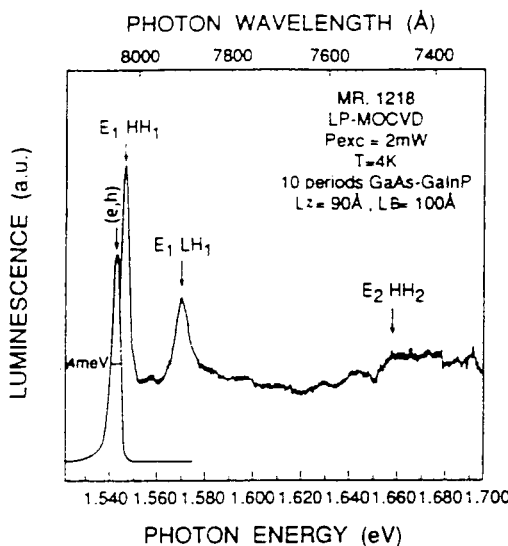


**Figure 6.47** Photoluminescence and photoluminescence excitation spectrum of a GaAs–GaInP superlattice consisting of ten periods of 90 Å thick GaAs quantum wells and 100 Å thick  $\text{Ga}_{0.51}\text{In}_{0.49}\text{P}$  barriers (Omnès and Razeghi 1991).

Because of the cubic structure of this sample and the differential equation of the Bragg law with respect to  $\theta$ , we obtain

$$\frac{\Delta a}{a} = -\frac{\Delta \theta}{\tan \theta} \quad (6.45)$$

where  $a$  is the lattice parameter,  $\theta$  the average diffraction angle and  $\Delta\theta$  is half the angular separation of layer and substrate Bragg peaks. From the angle  $\Delta\theta = 90''$  between the quantum well diffraction peak and the GaAs substrate Bragg peak, Papalus *et al* (1991) concluded, using (6.45), that x-ray diffraction measurements exhibited a  $\Delta a/a$  up to  $7.1 \times 10^{-4}$ . This result shows the high quality of GaAs–GaInP MQWs grown by LP-MOCVD (Omnès and Razeghi 1991).

Figure 6.47 shows the low-temperature PL and PLE spectra of a GaAs–GaInP superlattice grown by LP-MOCVD under the conditions indicated in table 6.6. The superlattice consists of ten periods of approximately 100 Å thick GaInP barriers and 90 Å thick GaAs wells. The 4 K PL spectrum has a full width at half maximum of 4 meV evidencing a good layer to layer reproducibility. The PLE spectrum of the 90 Å QWs exhibits a series of sharp peaks, which can be attributed to the electron to light hole and electron to heavy hole transitions as indicated in figure 6.47. The energy of the  $E_1 \rightarrow HH_1$  subband transition, as determined by PLE, is 1545 meV and the peak energy of the (e, h) emission in the PL spectrum is at 1542 meV, providing evidence of the high quality of interfaces and layer to layer homogeneity.

**Table 6.7** Experimental and theoretical values of energy levels for GaAs/GaInP MQWs.

Samples	$L_z$ (Å)	Energy level	Calculation (meV)	Exp. (meV)	PL (e, h) (meV)
<b>Superlattice</b>					
No 1218	90	$E_1 \rightarrow HH_1$	1555	1546	1544
		$E_1 \rightarrow LH_1$	1576	1575	
		$E_2 \rightarrow HH_2$	1661	1664	
<b>MQW</b>					
No 1219	120	$E_1 \rightarrow HH_1$	1541	1524	1522
		$E_1 \rightarrow LH_1$	1554	1550	
		$E_2 \rightarrow HH_2$	1608	1597	
		$E_2 \rightarrow LH_2$	1659	1661	
	60	$E_1 \rightarrow HH_1$	1582	1580	1574
		$E_1 \rightarrow LH_1$	1617	1618	
	35	$E_1 \rightarrow HH_1$	1637	1635	1634

Using a standard quantum well calculation of energy levels, where we introduce, in a simple iterative form, the non-parabolicity of the energy bands, Omnes and Razeghi (1991) have calculated the transition energies for the nominal QW thicknesses reported here. The parameters used for this study are the following where all values are taken at a temperature of 4 K (Landolt-Börnstein 1982)

$$\text{GaAs: } E_g = 1518 \text{ meV}, m_0^* = 0.0665m_0$$

$$m_{hh} = 0.475m_0, m_{lh} = 0.087m_0$$

$$\text{GaInP: } E_g = 1984 \text{ meV}, m_0^* = 0.1175m_0$$

$$m_{hh} = 0.660m_0, m_{lh} = 0.145m_0$$

$$\text{GaAs/GaInP: } \Delta E_c / \Delta E_v = 0.4.$$

Table 6.7 indicates the experimental and theoretical values of the energy levels of GaAs–GaInP quantum wells of 90, 120, 60 and 35 Å thickness. A satisfying agreement between theoretical and experimental values is observed for quantum wells of 90, 60 and 35 Å thickness. There is a noticeable discrepancy between the measured and calculated heavy-hole–light-hole splitting for the widest quantum well which could be attributed to compressive strain within this quantum well. However, the fundamental transition should increase in this case, which is contrary to the observed trend. Such behaviour is not clear at present but could be related to In segregation and subsequent localized strain. This could also be a source of uncertainty on the quantum well thickness. One could expect the widest quantum well to be the least sensitive to interface effects, but one should note that this widest well is the first of the whole structure: we carried out a mechanochemical bevel on this structure which showed that the first quantum well interface was not as good as the following ones.

Figure 6.48 shows the x-ray (400) diffraction pattern of a 10-period GaAs/Ga<sub>0.51</sub>In<sub>0.49</sub>P superlattice, with approximately 100 Å thick ( $L_B$ ) GaInP

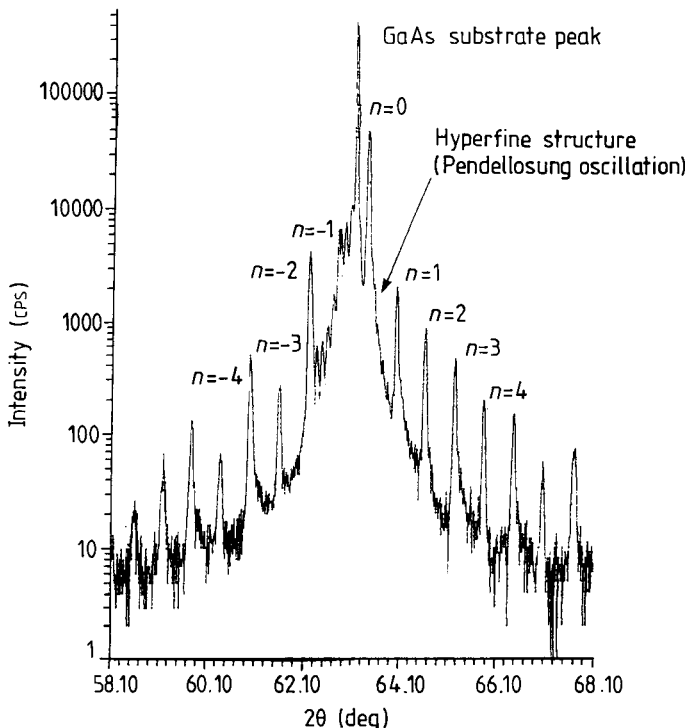


**Figure 6.48** X-ray diffraction pattern of a 10-period GaAs/Ga<sub>0.51</sub>In<sub>0.49</sub>P superlattice grown by LP-MOCVD.  $L_B(\text{GaInP}) = 100 \text{ \AA}$  and  $L_Z(\text{GaAs}) = 90 \text{ \AA}$  (Papalus *et al* 1991).

barriers and 90 Å thick ( $L_Z$ ) GaAs wells (Razeghi *et al* 1991b). A synchrotron beam of wavelength  $\lambda = 1.47596 \text{ \AA}$  is used as the x-ray source. Satellites corresponding to the artificial crystalline period  $L_B + L_Z$  introduced during growth have been resolved up to  $n = \pm 7$ . This rarely observed result demonstrates the excellent structural quality of the sample under study. The  $n = 0$  satellite, attributed to the (400) Bragg diffraction of the mean parameter of the superlattice, appears close to the position of the GaAs substrate Bragg peak. The x-ray measurements carried out on this sample showed a  $\Delta a/a$  of about  $2.8 \times 10^{-3}$  using (6.45).

From the angular separation  $\Delta\theta = 1080''$  between two adjacent satellites, one can deduce, using equation (6.43), that the superlattice period is  $L'_B + L'_Z = 166 \text{ \AA}$ ; this corresponds well to the value expected from the growth parameters.

The hyperfine structure observed in figure 6.48 near the substrate Bragg peak may be attributed to the interaction between incident and reflected waves through the whole epitaxial layer (pendellosung oscillations). According to the angle difference value  $\Delta\theta = 90''$  between two peaks in the hyperfine structure,

if we use (6.43), one can find  $L = 1985 \text{ \AA}$ , in good agreement with the growth parameters. The behaviour observed in figure 6.48 has rarely been observed in III-V superlattices.

## 6.9 CHARACTERIZATION OF GaAs–GaInP QUANTUM WELLS BY AUGER ANALYSIS ON CHEMICAL BEVELS

Understanding the initial stage of epitaxial growth is essential for multilayer semiconductor materials, where interfaces between layers play a prominent part in their optical and electrical properties. The physical study of the chemical species concentrations at the interfaces can give valuable information on the initial steps of epitaxial growth.

The theoretical calculations of Auger currents given by Auger line scan measurements on chemically beveled heterostructures were performed by Olivier *et al* (1987), assuming exponentially varying concentrations at the interface and compared with experimental results.

Combined with ion etching, Auger electron spectroscopy (AES) can be used to get elemental concentration profiles within overlayers. However, several factors affect the resolution depth as described below. There are different mechanisms which broaden the concentration profiles:

- (i) Auger electron escape depth and ion bombardment effects (ion knock-on mixing, preferential sputtering and ion-induced roughness).
- (ii) In order to avoid the disadvantages of ion milling, Bisaro *et al* (1982) developed a method of chemical beveling coupled with line scan Auger measurements to check interfaces of epitaxial III-V compounds.

The chemical bevels are produced by a technique in which the liquid–liquid interface between pure methanol and a bromine–methanol solution is raised progressively over the sample. The bevel angle  $\alpha$  can be controlled by the speed of the etching solution flowing up the sample, and can be as small as 0.05 or less giving a magnification coefficient of  $M = (\sin \alpha)^{-1} > 10^3$ . In contrast to sputtering, the absolute depth resolution  $R$  of the bevel Auger profiling method is independent of the film thickness to be examined and is of the order of the electron beam size  $s$  plus the beam deflection resolution  $d$  divided by the lateral magnification of the bevel angle (Tarn and Fisher 1978)

$$R = (s + d)/M. \quad (6.46)$$

A schematic diagram of the bevel is shown in figure 6.49.

In the present experiment, the beam diameter was 2000 to 7500  $\text{\AA}$  (primary energy and current: 10 keV, 1 nA and 5 keV, 20 nA respectively) and the deflection resolution  $\leq 500 \text{ \AA}$ . With a magnification coefficient  $M = 1000$ , the absolute resolution  $R$  is 8  $\text{\AA}$  in the worst case.

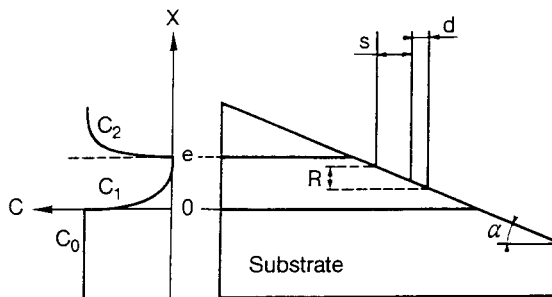


**Figure 6.49** Schematic diagram of the bevel. The mean parameters are the bevel angle  $\alpha$ , the electron beam size  $s$ , the beam deflection resolution  $d$  and the depth resolution  $R$ . The phosphorus exponential composition profiles taken into account are  $C_1(x) = C_0 \exp(-x/\Lambda_1)$  and  $C_2(x) = C_0[1 - \exp(-(x - e)/\Lambda_2)]$  (Olivier *et al* 1987).

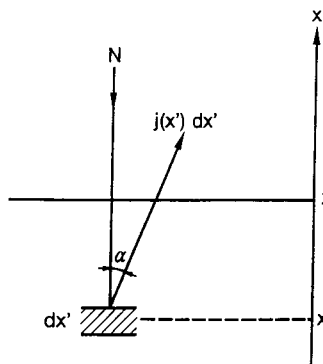


**Figure 6.50** Schematic diagram of the Auger current produced at  $x'$  by  $dx'$ , which is partially absorbed by the thickness  $(x - x')$  before leaving the sample and entering the analyser an angle  $\alpha$  (Olivier *et al* 1987).

The Auger current produced at  $x'$  by  $dx'$  is partially absorbed by the thickness  $(x - x')$  before leaving the sample and entering the analyser with an angle  $\alpha$

$$J(x') dx' = kn(x') \exp\left(-\frac{x - x'}{L_A \cos \alpha}\right) dx' \quad (6.47)$$

where  $k$  is proportional to the product of the cross-section for ionization of a level, of the Auger transition probability and of the secondary-electron coefficient  $(1 + r)$  (figure 6.50).

$$n(x') dx' = N \exp\left(-\frac{x - x'}{L_p}\right) dx' \quad (6.48)$$

is the attenuated primary electron beam.  $C(x') = C_B f(x')$  is the material atomic concentration.  $L_A$  is the mean free path of the Auger electron. Thus the Auger

bulk current of a substrate of concentration  $C_0$  is

$$I_B = kNC_B L \quad (6.49)$$

with

$$(L)^{-1} = (L_p)^{-1} + (L_A \cos \alpha)^{-1}. \quad (6.50)$$

The elementary Auger signal emerging from the surface  $x$ , normalized by the bulk value, is expressed as:

$$J(x') dx' = \frac{f(x')}{L} \exp\left(-\frac{x - x'}{L}\right) dx'. \quad (6.51)$$

In the case of a QW with exponentially varying concentrations at the interfaces, the normalized Auger currents are expressed by

$x < 0$

$$I(x) = 1$$

$0 < x < e$

$$I(x) = \frac{\Lambda_1}{\Lambda_1 - L} \exp\left[-\frac{x}{\Lambda_1}\right] - \frac{L}{\Lambda_1 - L} \exp\left[-\frac{x}{L}\right] \quad (6.52)$$

$x > e$

$$\begin{aligned} I(x) = 1 + & \left\{ \frac{L}{\Lambda_2 - L} - \frac{L}{\Lambda_1 - L} \exp(e - L) \right. \\ & - \left[ \frac{L(\Lambda_1 - \Lambda_2)}{(\Lambda_2 - L)(\Lambda_1 - L)} \right] \exp\left(-\frac{e}{\Lambda_1}\right) \Big\} \exp\left[-\frac{x - e}{L}\right] \\ & - \frac{\Lambda}{(\Lambda_2 - L)} \left[ 1 - \exp\left(-\frac{e}{\Lambda_1}\right) \right] \exp\left[-\frac{x - e}{\Lambda_2}\right] \end{aligned} \quad (6.53)$$

where  $e$  is the escape depth.

For abrupt interfaces:  $\Lambda_1 = \Lambda_2 \approx 0$

$$0 < x < e \quad I(x) = \exp(-x/L) \quad (6.54)$$

$$x > e \quad I(x) = 1 - \exp[-(x - e)/L] \quad (e \gg L). \quad (6.55)$$

A log scale for  $I(x)$  or  $1 - I(x)$  gives straight lines, the slope of which allows the escape depth of the Auger electron to be deduced.

The exact interface position does not correspond to a relative intensity of about 50% as usually assumed: it corresponds either to the beginning of the decrease from unity ( $0 < x < e$ ) or the beginning of the increase from zero ( $x > e$ ). The QW profiles are asymmetric.

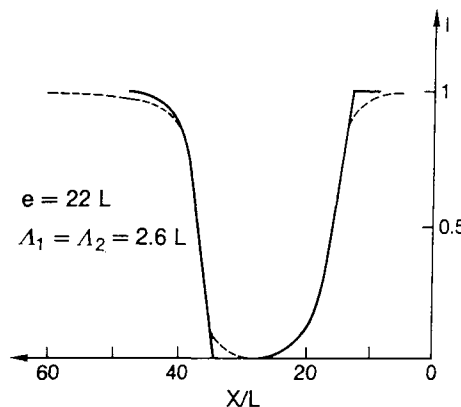


**Figure 6.51** Theoretical phosphorus Auger line scan of a GaInP/GaAs/GaInP QW. The dashed lines are the experimental curves (Olivier *et al* 1987).

For gradual interfaces:  $\Lambda_1$  and  $\Lambda_2 \gg L$

$$0 < x < e \quad I(x) = \exp(-x/\Lambda_1) \quad (6.56)$$

$$x > e \quad I(x) = 1 - \exp[-(x - e)/\Lambda_2] \quad (e \gg \Lambda_1). \quad (6.57)$$

Thus in a log scale, the characteristic widths  $\Lambda_1$  and  $\Lambda_2$  govern the slope of the straight lines, when  $\Lambda_1$  and  $\Lambda_2 \gg L$ .

Although one now has two interfaces of finite thickness, here one can also precisely determine the point that corresponds to the start or interruption of the gas flow in the growth reactor. The distance between these two points corresponds to the same thickness as deduced from the steady-state growth speed determined by measurements on thicker layers.

Figure 6.51 shows the experimental phosphorus Auger line scan of the MOCVD growth of a QW of GaInP/GaAs/GaInP. The good agreement between experimental and theoretical curves *a posteriori* justifies the reasonable hypothesis of exponentially varying concentrations at the interfaces.

The experimental increase of the Auger signal that is less steep than the theoretical one at the two extremities of the well can be explained by a slight atomic mixing resulting from a short ion cleaning before the Auger line scan was taken. The two characteristic lengths are very different. The explanation is likely to come from the dynamics of low-pressure MOCVD growth: in the neighbourhood of the growth surface, there is a gas layer whose characteristics change gradually from those of the convective gas phase, to those of the growth-surface-gas-phase interface (Razeghi 1985). The evolution of that boundary layer by stopping or setting up again the phosphine flux in the reactor is the key to the problem.

A GaAs QW of intended width  $e = 100 \text{ \AA}$  is fitted with a theoretical curve calculated using the following parameters:  $L = 4.75 \text{ \AA}$ ,  $e = 105 \text{ \AA}$ ,

**Table 6.8** Previously measured values for the band offsets of GaAs/GaInP.

Technique	$\Delta E_c$ (eV)	$\Delta E_v$ (eV)	Reference
Capacitance–voltage profiling	0.238		Rao <i>et al</i> (1987)
DLTS	0.198	0.285	Biswas <i>et al</i> (1990)
<i>I</i> – <i>V</i> curves of HEMTs	0.231		Chan <i>et al</i> (1990)
Temperature dependence of the collector current of HBTs	0.03		Kobayashi <i>et al</i> (1989)

$\Lambda_1 = \Lambda_2 = 12.5$  Å. The characteristic lengths  $\Lambda$  are equal, showing sharp interfaces and that both interfaces are equivalent.

### 6.10 EVALUATION OF THE BAND OFFSETS OF GaAs/GaInP MULTILAYERS BY ELECTROREFLECTANCE (RAZEGHI *et al* 1992)

The band offsets of GaAs/GaInP have already previously been measured by different techniques. The results are summarized in table 6.8.

Electroreflectance (ER) is the best and most direct technique for the determination of band profiles (Kassel *et al* 1990, 1991a, b) in general and band offsets in particular. This is because ER produces especially sharp optical spectra and yields enhanced signals from interfacial surfaces. Thus, ER allows the determination of many more transition energies than does photoluminescence. In particular, ER allows one to observe and measure the energies of transitions between states allowed only on one side of an interface and the tails of states allowed only on the other side; such transitions are called crossover transitions. For a type-I quantum well or superlattice, these crossover transitions are between well states and the barrier band edges. Because of the ability to obtain a better signal to noise ratio, to control better the modulating electric field and to apply bias voltages, electrolyte electroreflectance (EER) also gives many more transition energies than does photoreflectance. In particular, the ability to apply a bias voltage allows one to observe and identify many transitions forbidden by symmetry in the absence of an electric field, as well as crossover transitions. This allows one to measure directly intersubband, intraband transition energies without the use of band calculations. It also allows one to measure almost directly the band offset in both samples, with the only theoretical input being the energy of the first heavy-hole level relative to the valence band edge in the well.

Razeghi *et al* (1992) obtained approximately 20 EER spectra, at different bias voltages. This result is the first reported direct optical measurement of either of these types of quantity for type-I superlattices or quantum wells. Two GaAs/Ga<sub>0.51</sub>In<sub>0.49</sub>P-based samples (a superlattice and a multiple quantum well) have been used for this study. The EER spectra were fitted using the generalized ER lineshape (Garland and Raccah 1986) to obtain the transition energies and linewidths, as well as the coefficients of the first-, second- and third-derivative terms in the generalized lineshape. Well state to well state transitions were assumed to have only a first-derivative term and crossover transitions were assumed to be primarily first derivative in nature. This study of the spectra as a function of the bias voltage helped to confirm the identification of the types of transition observed. For example, for quantum wells and superlattices, the linewidth of the crossover transitions increases much more rapidly with internal electric field than does that of any other type of transition.

For the superlattice, 35 transitions were identified. This large number of observed transitions gives a multiplicity of self-consistency conditions and thus gives many checks both on the accuracy of our values for the transition energies and the identification of the transitions. All of the self-consistency conditions were well satisfied. For the multiple quantum well, which contained wells of three different widths, 30 transitions were identified. For both samples, the observed transition energies were fitted with a parametrized envelope function band calculation in which the energy dependence of the effective masses was taken into account. The well widths obtained from these fittings were in excellent agreement with those obtained by calibration of the growth rate.

The GaAs–GaInP multiquantum wells and superlattices used for this study were grown by low-pressure metallorganic chemical vapour deposition. The growth temperature was 510°C and the growth pressure was 76 Torr. Triethylgallium (TEG), trimethylindium (TMI), pure arsine (AsH<sub>3</sub>) and pure phosphine (PH<sub>3</sub>) were used as Ga, In, As and P sources, respectively. Pure H<sub>2</sub> was used as the carrier gas. The quantum well and superlattice samples grown for this study were unintentionally doped. Residual impurity concentrations are assumed to be of the order of those determined for bulk layers.  $N_d - N_a \approx 10^{14} \text{ cm}^{-3}$  for GaAs (Razeghi *et al* 1989a) and  $5 \times 10^{14} \text{ cm}^{-3}$  for GaInP layers (Omnes and Razeghi 1991).

For both samples studied (a superlattice (SL) and a three-quantum-well (3QW) structure) the linewidths of the well-state to well-state transitions were very narrow, from 3 meV for the lowest-energy transitions up to 8 meV for the highest-energy well-state to well-state transitions. These linewidths are narrower than we have seen before at room temperature, even on other quantum-well systems. These narrow linewidths are evidence of the unusually high quality of these samples. More evidence of their exceptional quality was our ability to see many more transitions than is usual for such samples.

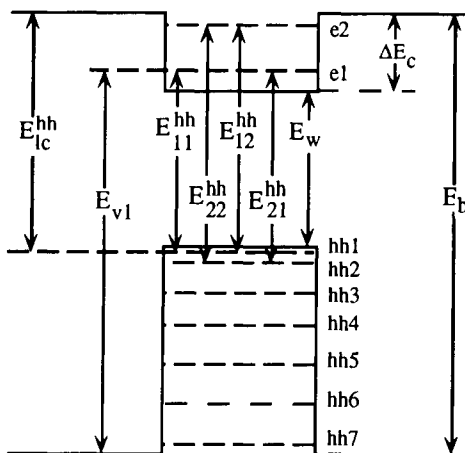


**Figure 6.52** Schematic diagram of a single GaAs/Ga<sub>0.51</sub>In<sub>0.49</sub>P quantum well (Razeghi *et al.* 1992).

### 6.10.1 The study of the GaAs/GaInP superlattice

The GaAs/GaInP SL consists of 10 periods of 90 Å thick GaAs wells between Ga<sub>0.51</sub>In<sub>0.49</sub>P barriers approximately 100 Å thick. Because of the thickness of the barriers, the well subbands are very narrow, of the order of 1 meV or less in width. For this reason, one could not clearly distinguish transitions associated with the bottom of a given subband from those associated with the top. Thus, the observed spectrum is equivalent in form to that which would be observed for a single quantum well.

Figure 6.52 shows the conduction band offset and the heavy-hole and conduction band levels for a single well, along with examples of the different types of transition observed. For simplicity, the light-hole and split-off states and the transitions to and from these states are not shown. The energies of the well states are determined by the following quantities:

- $E(em)$  the energy from the bottom of the conduction band well to the  $m$ th conduction band well level
- $E(hhm)$  the energy from the  $m$ th heavy-hole level up to the top of the valence band well
- $E(lhm)$  the energy from the  $m$ th light-hole level up to the top of the valence band well
- $E(som)$  the energy from the  $m$ th split-off well level up to the top of the split-off well
- $\Delta_w$  the energy from the split-off well edge to the valence band well edge
- $\Delta_b$  the energy from the split-off barrier edge to the valence band barrier edge
- $E_w$  the well material bandgap

- $E_b$  the barrier bandgap  
 $\Delta E_c$  the conduction band discontinuity.

The EER spectrum determines the optical transition energies from which all of these quantities can be directly calculated, given only  $E(\text{hh}1)$  and either  $E_w$  or  $E(e1)$ . The quantity  $E(\text{hh}1)$  can be calculated easily to an accuracy of better than 1 meV;  $E(e1)$  can be calculated to an accuracy of 1–2 meV. Thus, the energies of all the well states are accurately determined from the EER data, as are the band discontinuities  $\Delta E_c$  and  $\Delta E_v = E_b - E_w - \Delta E_c$ . The observed optical transition energies are of the following types:

- $E_b$  the barrier bandgap  
 $E_{mn}^{\text{hh}}, (E_{mn}^{\text{lh}}, E_{mn}^{\text{so}})$  the transition energy from the  $m$ th heavy-hole (light-hole, split-off) level to the  $n$ th conduction band level in the well  
 $E_{mc}^{\text{hh}}, (E_{mc}^{\text{lh}}, E_{mc}^{\text{so}})$  the transition energy from the  $m$ th heavy-hole (light-hole, split-off) level to the conduction band edge in the barriers  
 $E_{vm}(E_{sm})$  the transition energy from the valence band (split-off) edge in the barriers to the  $m$ th conduction band level in the well.

Twenty-two experimental EER spectra were obtained and analysed, at different bias voltages and modulating voltages. Figure 6.53(a) shows a typical EER spectrum at room temperature (RT) and the fit to that spectrum. The details of the spectrum and its fit from 1.48 eV to 1.88 eV are shown in figure 6.53(b). The spectrum has a rich structure due to the large number of transitions observed. Table 6.9 lists the transitions observed and gives the transition energies measured by EER at RT and by photoluminescence (PL) at low-temperature (LT). Only transitions observed in all of the spectra are listed. The uncertainties listed for the energies represent maximum deviations from the values listed, considering all 22 spectra and different fitting methods; the root-mean-square deviations are smaller by factors of two to five.

From the measured optical transition energies, the conduction band discontinuity can be deduced from any of the following relations

$$\begin{aligned}\Delta E_c &= E_{nc}^{\text{hh}} - E_{nm}^{\text{hh}} + E(em) \\ &= E_{nc}^{\text{lh}} - E_{nm}^{\text{lh}} + E(em) \\ &= E_b - E_{vm} + E(em) \\ &= E_{nc}^{\text{hh}} - E_w + E(hhm) \\ &= E_{nc}^{\text{lh}} - E_w + E(lhm).\end{aligned}\quad (6.58)$$

The first of these relations is the most precise: with  $n = m = 1$  it yields a value of  $\Delta E_c$  correct to within 4 meV; using other values of  $n$  and  $m$  and the other relations yields 15 other determinations of  $\Delta E_c$ , all of which are consistent with the first, most precise, determination. The conduction band offset was found to be  $159 \pm 4$  meV and the valence band offset was found to be  $388 \pm 6$  meV.

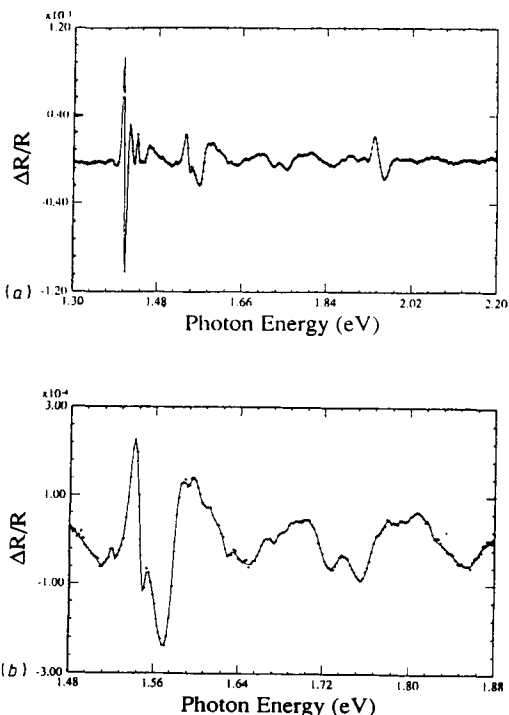


**Figure 6.53** (a) EER spectrum of the GaAs/GaInP superlattice and its fit. (b) Detailed structure of the EER spectrum and its fit. The dots show the experimental data points and the solid lines show the fit (Razeghi *et al* 1992).

The energy difference between any two valence band levels is given directly in terms of the measured optical transition energies by the equations

$$E(\alpha m) - E(\beta n) = E_{mr}^\alpha - E_{nr}^\beta \quad (6.59)$$

or

$$E(\alpha m) - E(\beta n) = E_{mc}^\alpha E_{nc}^\beta \quad (6.60)$$

where  $\alpha$  and  $\beta$  can be hh, lh or so, and  $r$  can be 1 or 2. These energy differences are important to know for the conception of III-V IR detectors and for other applications. Equations (6.59) and (6.60) provide two direct self-consistency conditions for each pair  $(\alpha m, \beta n)$ ; each of these conditions is well satisfied. For the low-lying subbands, the energy differences  $E(\alpha m) - E(\beta n)$  are determined within  $\pm 2$  meV.

Knowing  $E(\text{hh1})$  from theory or from a theoretical fit to the measured transition energies, one can find  $E(\text{hhm})$ ,  $E(\text{lhm})$  and  $E(\text{som})$  from the relations

$$E(\text{hhm}) = E(\text{hh1}) + E_{mn}^{\text{hh}} - E_{1n}^{\text{hh}} \quad (6.61)$$

**Table 6.9** Observed optical transition energies for the GaAs/GaInP superlattice from 1.4 eV to 2.0 eV.

Transition	RT EER	LT PL
Band to band transitions		
$E_0$ (bulk GaAs)	$1412 \pm 3$	1518
$E_0 + \Delta_0$ (bulk GaAs)	$1757 \pm 3$	
$E_b$	$1952 \pm 8$	1984
Well state to well state transitions		
$E_{11}^{hh}$	$1437 \pm 1$	1546
$E_{21}^{hh}$ and $E_{11}^{lh}$	$1455 \pm 2$	1575
$E_{31}^{hh}$	$1512 \pm 2$	
$E_{12}^{hh}$	$1520 \pm 4$	
$E_{22}^{hh}$ and $E_{12}^{lh}$	$1540 \pm 2$	1661
$E_{41}^{hh}$ and $E_{21}^{lh}$	$1550 \pm 2$	
$E_{32}^{hh}$	$1576 \pm 3$	
$E_{51}^{hh}$	$1614 \pm 4$	
$E_{42}^{hh}$ and $E_{22}^{lh}$	$1628 \pm 2$	
$E_{52}^{hh}$ , $E_{61}^{hh}$ and $E_{31}^{lh}$	$1704 \pm 6$	
$E_{11}^{so}$	$1773 \pm 3$	
$E_{62}^{hh}$	$1785 \pm 3$	
$E_{32}^{lh}$	$1796 \pm 3$	
$E_{12}^{so}$	$1865 \pm 3$	
$E_{22}^{so}$	$1908 \pm 3$	
Transitions between well states and band edges		
$E_{1c}^{hh}$	$1572 \pm 2$	
$E_{2c}^{hh}$ and $E_{1c}^{lh}$	$1598 \pm 2$	
$E_{3c}^{hh}$	$1643 \pm 2$	
$E_{4c}^{hh}$ and $E_{2c}^{lh}$	$1683 \pm 2$	
$E_{5c}^{hh}$	$1760 \pm 2$	
$E_{v1}$	$1817 \pm 2$	
$E_{6c}^{hh}$ and $E_{3c}^{lh}$	$1828 \pm 2$	
$E_{v2}$	$1888 \pm 2$	
$E_{1c}^{so}$ and $E_{s1}$	$1917 \pm 2$	
$E_{1c}^{hh}$	$1937 \pm 2$	
$E_{2c}^{so}$	$1989 \pm 2$	

$$E(lhm) = E(hh1) + E_{mn}^{lh} - E_{1n}^{hh} \quad (6.62)$$

$$E(som) = E(hh1) + E_{mn}^{so} - E_{1n}^{hh} - \Delta_w \quad (6.63)$$

or from the relations

$$E(hhm) = E(hh1) + E_{mc}^{hh} - E_{1c}^{hh} \quad (6.64)$$

$$E(lhm) = E(hh1) + E_{mc}^{lh} - E_{1c}^{hh} \quad (6.65)$$

$$E(som) = E(hh1) + E_{mn}^{so} - E_{1c}^{hh} - \Delta_w. \quad (6.66)$$

These relations provide further, more direct, self-consistency checks on the data and on the interpretation of the spectra. All of these self-consistency checks are well satisfied. Similarly, knowing  $E(e1)$ , one can find  $E(e2)$  from any of six equations analogous to (6.61)–(6.66), each valid for different values of  $m$ . The resultant self-consistency conditions are also well satisfied.

The bandgap,  $E_w$ , and spin splitting energy,  $\Delta_w$ , for the wells is not exactly the same as for bulk GaAs, presumably because of strain. From the relations

$$E_w = E_{11}^{hh} - E(hh1) - E(e1) \quad (6.67)$$

and

$$\Delta_w = E_{11}^{so} + E(hh1) - E_{11}^{hh} - E(so1) \quad (6.68)$$

or from a fitting of all the observed transition energies to a parametrized band calculation, one can find  $E_w = 1.405$  eV and  $\Delta_w = 0.33$  eV (0.009 and 0.01 eV less than the values for bulk GaAs). The fitting yields a 91 Å well width, in excellent agreement with the value of 90 Å found by calibration of the rate of epitaxial growth. The values found for the conduction band, heavy-hole and light-hole masses in the barriers and the wells and for the split-off well mass are in excellent agreement with the literature.

### 6.10.2 The study of the GaAs/GaInP three-quantum-well structure

A 3QW structure was grown by LP-MOCVD under the same conditions as the superlattice (SL). The quantum wells were 120, 60 and 35 Å in width, as shown in figure 6.54. The barriers separating the wells were sufficient to decouple the wells. All of the analysis discussed for the SL is equally applicable to the 3QW structure, but with each of the three wells contributing its own spectrum. However, the weaker transitions seen for the SL are not seen for the 3QW structure because in the 3QW structure each transition occurs in only one well.

Nineteen experimental EER spectra were obtained and analysed for the 3QW structure. Figure 6.54 also shows a typical EER spectrum at RT and our fit to that spectrum. Table 6.10 lists some of the transitions observed and gives the transition energies measured by EER at room temperature (RT) and by PL at low temperature (LT). The conduction and valence band offsets found for the 3QW

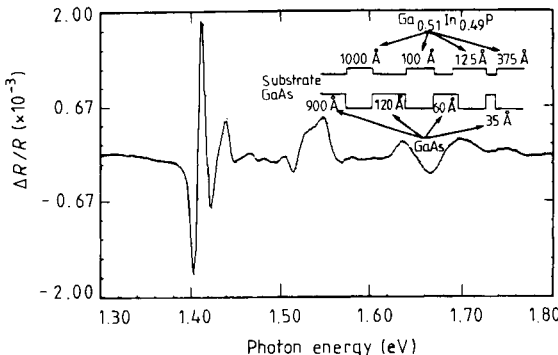


**Figure 6.54** EER spectrum of a GaAs/GaInP multiple QW along with a schematic diagram of the band structure (Razeghi *et al* 1992).

structure were the same as those found for the SL within experimental error, as were the band masses.

### 6.10.3 III-V intersubband infrared detectors

There has been considerable research in the area of III-V intersubband quantum well infrared photodetectors (QWIP) for the  $8\text{--}12 \mu\text{m}$  wavelength region as an alternative to HgCdTe (MCT) detectors (Levine *et al* 1991, 1992, Rosencher *et al* 1992). Of all the III-V quantum well intersubband detectors, AlGaAs-GaAs quantum wells and superlattices have been extensively studied and they show great promise for focal plane array applications. However, the performance of these detectors remains inferior, with a lower detectivity and quantum efficiency, higher dark current and lower operating temperature, compared to MCT detectors. The major disadvantages of MCT technology are non-uniform composition, lack of high-quality lattice-matched substrates, mechanical softness, small wafer size, high cost and low yield. On the other hand, the advantages of III-V QWIPs are uniform composition, large excellent-quality substrates, mature processing technology, higher possibility of monolithic integration, multispectral detectors, ultrahigh speed and radiation hardness. At present there are many factors which are limiting the performance of AlGaAs-GaAs QWIPs and most of the problems arise from the AlGaAs barrier, the poor AlGaAs/GaAs interface due to higher growth temperature, oxygen-induced defects in the AlGaAs layer and low barrier height due to the limitation of AlGaAs composition. Hence, an improvement in the quality of the barrier material or an alternative barrier material is necessary for further improvement in device performance. GaInP has been considered as the best alternative for AlGaAs because of its superior material properties such as its insensitivity to oxygen, higher carrier mobility and carrier mobility insensitivity

**Table 6.10** Transition energies identified for the GaAs/GaAs/Ga<sub>0.51</sub>In<sub>0.49</sub>P multiple quantum well.

Transition	RT EER	LT PL
Band to band transitions		
$E_0$ (bulk GaAs)	$1419 \pm 1$	1522
$E_0 + \Delta_0$ (bulk GaAs)	$1760 \pm 2$	
$E_b$	$1912 \pm 1$	1984
Well state to well state transitions (120 Å QW)		
$E_{11}^{hh}$	$1424 \pm 1$	1524
$E_{11}^{lh}$ and $E_{21}^{hh}$	$1439 \pm 2$	1550
$E_{31}^{hh}$	$1460 \pm 2$	
$E_{22}^{hh}$	$1487 \pm 2$	1597
$E_{51}^{hh}$	$1532 \pm 1$	
$E_{22}^{lh}$ and $E_{42}^{hh}$	$1555 \pm 1$	1661
$E_{31}^{lh}$	$1600 \pm 2$	
$E_{71}^{hh}$	$1641 \pm 2$	
$E_{62}^{hh}$ and $E_{71}^{hh}$	$1641 \pm 2$	
$E_{82}^{hh}$	$1769 \pm 2$	
$E_{11}^{so}$	$1772 \pm 1$	
$E_{42}^{lh}$	$1792 \pm 1$	
$E_{22}^{so}$	$1866 \pm 1$	
Well state to well state transitions (60 Å QW)		
$E_{11}^{hh}$	$1464 \pm 2$	1580
$E_{11}^{lh}$ and $E_{21}^{hh}$	$1504 \pm 2$	1618
$E_{22}^{hh}$	$1515 \pm 1$	
$E_{31}^{hh}$	$1585 \pm 4$	
$E_{22}^{lh}$	$1677 \pm 4$	
Well state to well state transitions (35 Å QW)		
$E_{11}^{hh}$	$1515 \pm 1$	1635
$E_{11}^{lh}$ and $E_{21}^{hh}$	$1585 \pm 4$	

to DX centres. Also, it was recently found that the GaInP/GaAs interface is better due to its lower growth temperature (Razeghi 1985), and the interface recombination velocity is 10 times lower than AlGaAs/GaAs (Olsen *et al* 1989). All these properties clearly suggest that by replacing AlGaAs with GaInP, it is possible to improve the performance of III-V QWIPs.

The first step is to obtain high-quality GaInP/GaAs multiquantum wells (MQWs) and superlattices by LP-MOCVD on GaAs, InP and Si substrates. In order to achieve the above objective, growth conditions were varied for GaInP/GaAs heterostructures. Both multiquantum well

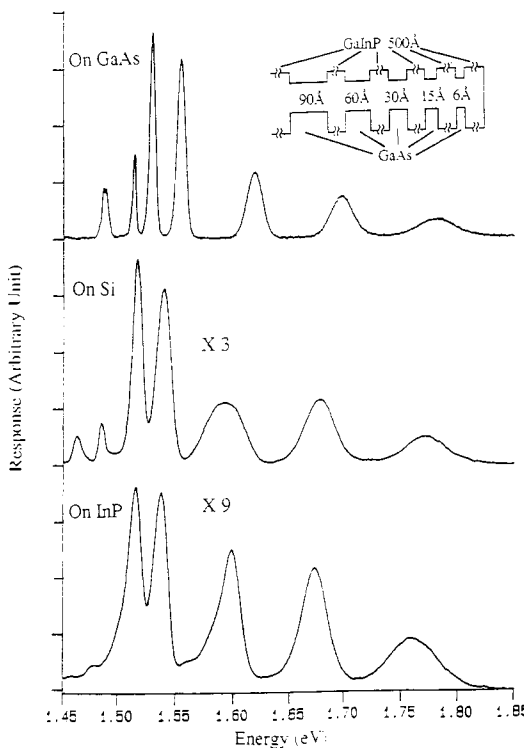


**Figure 6.55** 4 K PL spectra of the GaAs–GaInP MQWs grown on GaAs, Si and InP substrates. The inset shows the schematic of the multiquantum well structures (He and Razeghi 1992).

structures and superlattices were grown by LP-MOCVD (Razeghi *et al* 1989a). Heterostructures were characterized by several techniques such as x-ray diffraction, photoluminescence and photovoltage spectroscopy for interface quality and subband energies.

Several high-quality GaInP–GaAs quantum wells and superlattices were grown by LP-MOCVD. In order to demonstrate the quality of GaInP–GaAs quantum well structures grown by LP-MOCVD, five quantum wells with different well thicknesses were grown simultaneously on GaAs, Si and InP substrates and the structure is shown in figure 6.55. First photoluminescence measurements were performed to assess the quality of the samples (He and Razeghi 1992). Sharp photoluminescence peaks ( $\text{FWHM} = 5 \text{ meV}$  at 4 K) are observed on all three samples, indicating good interfaces and uniform layer thicknesses. Also, another important result observed was that the optical quality of the MQW grown on the Si substrate is better than that grown on the InP substrate. Theoretical calculations were performed to determine the subband energies and it was found that we were able to observe the subband due to the thinnest well (6 Å), which

## Photovoltage Spectra of Multiquantum Wells 1219

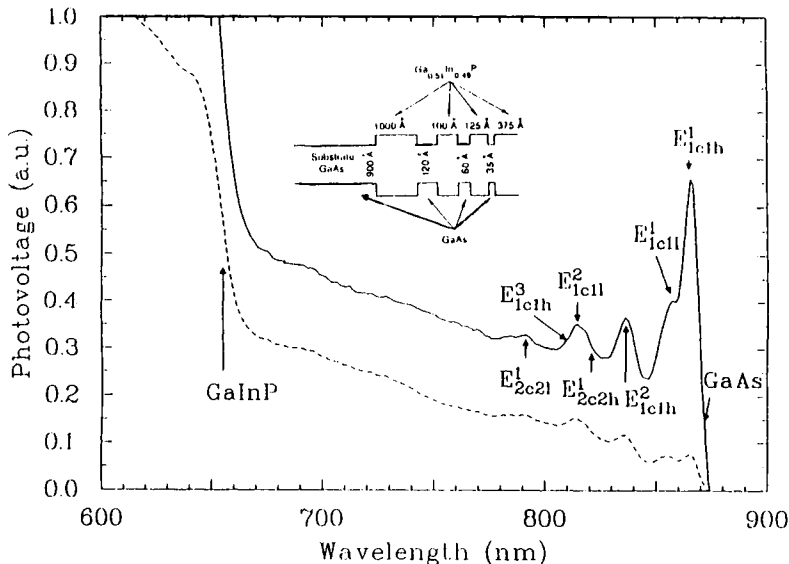


**Figure 6.56** The structure of a three-well MQW sample and its PVS. The marked positions are the calculated peak positions. The broken line displays the raw PVS. The solid line displays the calibrated PVS (He and Razeghi 1993a).

further confirms the high quality of the interface. The photoluminescence spectra of the samples grown on Si and InP substrates showed a shift of 15 meV from the corresponding peaks of the sample grown on the GaAs substrate. There are two possible explanations for this behaviour: diffusion of In along the dislocation threads from GaInP to GaAs or localized strain induced by defects and In segregation (He and Razeghi 1992).

Room-temperature photovoltage measurements were performed on a 10-period GaInP-GaAs superlattice with a nominal well width of 90 Å and barrier width of 100 Å. Figure 6.56 shows the room-temperature photovoltage spectroscopy (PVS) of a GaInP-GaAs superlattice. The well resolved peaks correspond to transitions from several sublevels. Also, the sharp peak, rather than a steplike profile, of the photovoltage spectrum indicates a pronounced exciton absorption behaviour at room temperature. These results clearly demonstrate that photovoltage spectroscopy is a simple and powerful tool to study quantum confinement structures which will be of use in the mass production of these devices (He and Razeghi 1993a).

High-resolution x-ray diffraction measurements were performed to investigate the interface properties of GaInP/GaAs structures. Figure 6.57 shows the x-ray diffraction pattern obtained in one of the samples. The superlattice satellites were observed over a 4 degree angle indicating that the interface roughness and

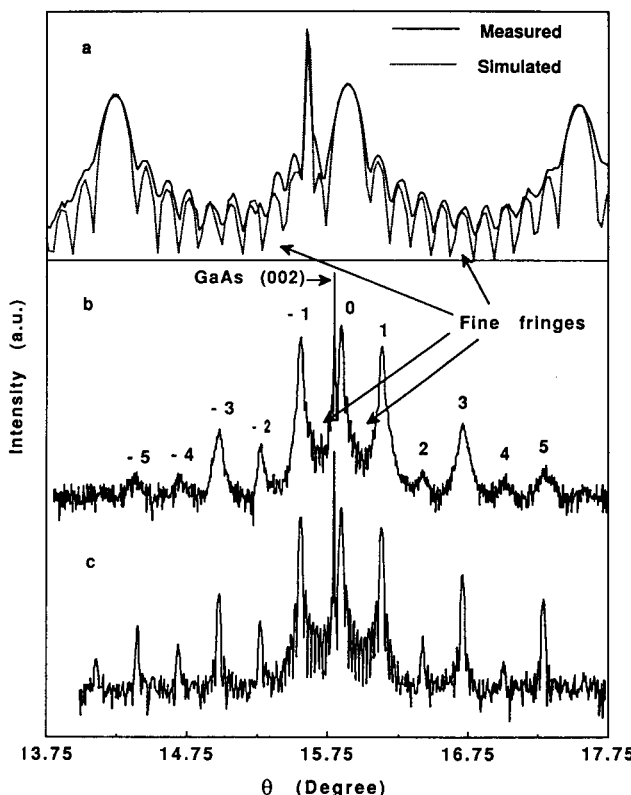


**Figure 6.57** (002) x-ray diffraction pattern of GaInP/GaAs superlattice. (a) Magnified view of both the measured and simulated patterns for  $\theta$  between 15.75 and 16.2°. (b) Measured pattern, and (c) simulated pattern for the layer model (He and Razeghi 1993b).

disorder in the sample are low. In summary, we have shown that good-quality GaInP-GaAs multiple quantum wells and superlattices can be obtained by LP-MOCVD (He and Razeghi 1993b). The fabrication of QWIPs using GaInP/GaAs will be the next step towards the realization of focal plane arrays.

### 6.11 INTERSUBBAND HOLE ABSORPTION IN GaAs–GaInP QUANTUM WELLS

In some semiconductor systems (GaAs/GaInP, GaAs/AlGaAs, GaInAs/AlGaAs), band offsets are such that they induce potential wells for electrons and/or holes in the different bands. Progress in growth technology such as molecular beam epitaxy and metallorganic chemical vapour deposition allow us to obtain extremely thin films of semiconductors with a precision of one atomic layer. These wells are so thin that the electron and hole motion is quantized in the

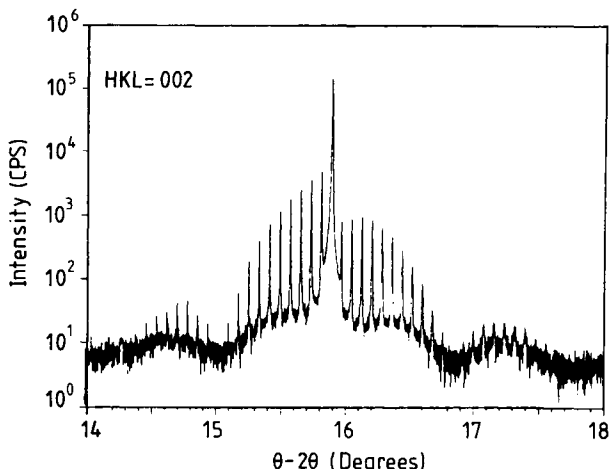


**Figure 6.58** (002) x-ray diffraction pattern of a GaAs–GaInP quantum well.

direction normal to the layers. The carrier energy is then distributed in different subbands, the bottoms of which are the one-dimensional quantized states  $E_i$  in the wells. Light can then induce transitions between these subbands. The resulting absorption is resonant between these quantized states (or bound states), with values as high as several  $10^3 \text{ cm}^{-1}$ . This resonant absorption between quantized states is termed intersubband absorption.

Intersubband hole absorption has been observed in p-type GaAs–GaInP multiquantum wells. The multiquantum well consists of 50 zinc-doped GaAs quantum wells, nominally  $45 \text{ \AA}$  thick, separated by undoped lattice-matched GaInP barriers nominally  $500 \text{ \AA}$  thick. This multiple quantum well is grown between zinc-doped GaAs contact layers of thickness  $1 \mu\text{m}$  (bottom) and  $0.5 \mu\text{m}$  (top). All p-type layers have been doped with  $N_a - N_d = 1 \times 10^{18} \text{ cm}^{-3}$ . Only the middle  $35 \text{ \AA}$  of each well has been doped in order to prevent dopant migration into the barrier region.

Figure 6.58 shows the (002) x-ray diffraction pattern for a GaAs–GaInP quantum well. Satellites are clearly observed up to 20th order, evidencing the high structural quality of the superlattice. A superlattice period of  $560 \text{ \AA}$  is deduced from the satellite spacing. A modulation of the superlattice satellite peaks is clearly observed every other 11 satellites. This modulation period is consistent with the nominal barrier to well width ratio. The slight asymmetry of the diffraction pattern indicates a difference between the two quantum well interfaces (He and Razeghi 1993a, b). The angular separation between the GaAs peak and the zero-order superlattice satellite yields a lattice mismatch of 0.024% for the barrier, indicating good composition control.

Figure 6.59 shows a low-temperature (4 K) photoluminescence spectrum of the sample obtained using a pump Ar laser, after selectively etching away the top contact layer. We attribute the sharp peak at 1.57 eV to the  $e_1\text{-}hh_1$  transition,

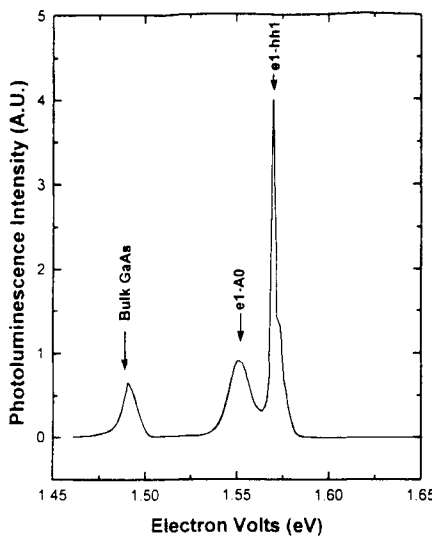
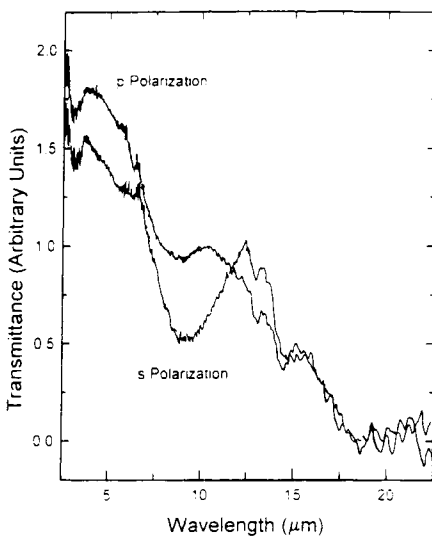


Figure 6.59 Low-temperature PL spectrum.

which is consistent with the nominal superlattice parameters. The full width at half maximum (FWHM) is 11 meV, which is quite small for doped quantum wells. The doping level in the contact layers was ascertained to be close to the nominal value by electrochemical C-V profiling. Since the wells were doped under the same conditions, we expect the doping level of the wells to lie in the  $10^{18} \text{ cm}^{-3}$  range as well. We attribute this narrow FWHM to the good superlattice quality. The broader peak at 1.55 eV originates from an acceptor-related transition (e1-A0) because its relative magnitude decreases with increasing pump intensity (Bastard 1988). The weak peak at 1.49 eV corresponds to bulk GaAs. At room temperature, an additional peak is found at 1.87 eV corresponding to the GaInP barriers.

After selectively etching away the top contact layer, the sample was processed into an optical waveguide with polished 45° facets. The waveguide transmission was measured in a Fourier transform infrared (FTIR) spectrometer. The infrared beam was focused onto the polished facets using KBr lenses, and its polarization was controlled with a grid wire polarizer. Figure 6.60 shows the transmission spectra for two perpendicular polarizations labelled s and p (where for s polarization, the infrared light electric field lies in the plane of the quantum wells, and p polarization is perpendicular to the s polarization). A broad minimum in the transmission is observed around 9  $\mu\text{m}$  for the two polarizations, which is attributed to intersubband transitions. The doublet around 13–14  $\mu\text{m}$  and the complete fallout of the transmission beyond 15  $\mu\text{m}$  are due to multiphonon absorption processes in the GaAs substrate. These same features are observed in a simple GaAs substrate waveguide as well. The slowly decreasing transmission



**Figure 6.60** Transmission spectra for two perpendicular polarizations.

background with increasing wavelength originates from free-carrier absorption in the bottom GaAs doped layer, as was checked by selectively etching away all the quantum wells. The intersubband absorption of s-polarized light is roughly twice as strong as that of p-polarized light. Since the p-polarization can be decomposed into equal TE and TM polarizations,  $p = \frac{1}{2}(TE + TM)$ , and since the s-polarization is purely TE,  $s = TE$ , this means that the TM absorption is almost negligible compared to the TE absorption. Here, TE polarization (TM polarization, respectively) corresponds to the light electric field in the plane (perpendicular to the plane, respectively) of the quantum wells. This polarization dependence corresponds to an enhanced normal incidence absorption, which is in qualitative agreement with results on p-doped GaAs-GaAlAs QWIPs (Levine 1991), as well as with theoretical calculations (Chang and James 1989, Teng *et al* 1992). Because of the large valence band discontinuity in excess of 200 meV (Omnes and Razeghi 1991), the observed absorption around  $9\text{ }\mu\text{m}$  originates from transitions between bound states. The broad character of the absorption peak suggests that several of such bound to bound transitions contribute to it. A Kronig-Penney calculation yields a 180 meV energy difference between the heavy-hole ground state and heavy-hole second excited state corresponding to an expected transition at  $7\text{ }\mu\text{m}$  wavelength. Calculated energy differences between the heavy-hole ground state and light-hole states do not fall within the wavelength range of interest, but it should be pointed out that these calculated transitions are sensitive to slight discrepancies between the nominal and actual band diagram. Taking into account the waveguide dimensions (length 6 mm  $\times$  thickness 0.4 mm), the observed intersubband absorption is estimated

to peak at  $10^{-3}$  per well (i.e.  $2.2 \times 10^3 \text{ cm}^{-1}$  normalized to the 45 Å well width), in reasonable agreement with values calculated for GaAs–GaAlAs by Man and Pan (1992).

## REFERENCES

- Alferov Zh I, Garbusov D Z, Mishurnyi V A, Rumyantsev V D and Tret'yakov D N 1974 *Sov. Phys.–Semicond.* **7** 1534
- Ando T 1982 *J. Phys. Soc. Japan* **51** 3900
- Ando T, Fowler A B and Stern F 1982 *Rev. Mod. Phys.* **54** 437
- Bastard G 1988 *Wave Mechanics Applied to Semiconductor Heterostructures* (Les Ulis: Les Editions de Physique) p 175
- Beeren J, Gregoris G, Portal J C, Mendez E E, Chang L L and Esaki L 1987 *Phys. Rev. B* **36** 4742
- Bellon P, Chevalier J P, Martin G P, Dupont-Nivel E, Theibant C and Andre J A 1988 *Appl. Phys. Lett.* **52** 567
- Ben Amor S, Dmowski L, Portal J C, Martin K P, Higgins R J and Razeghi M 1990 *Appl. Phys. Lett.* **57** 2925
- Ben Amor S, Dmowski L, Portal J C, Pulsford N J, Singleton J, Nicholas R J and Razeghi M 1989 *J. Appl. Phys.* **65** 2756
- Bisaro R, Laurincin G, Friederich A and Razeghi M 1982 *Appl. Phys. Lett.* **40** 978
- Biswas D, Debbar N, Bhattacharya P, Razeghi M and Omnes F 1990 *Appl. Phys. Lett.* **56** 833
- Bourgoin J C 1991 *Appl. Phys. Lett.* **59** 941
- Casey H C Jr and Panish M B 1978 *Heterostructure Lasers Part B* (New York: Academic) p 20
- Chan Y J, Pavlidis D, Razeghi M, Jaffe M and Singh J 1988 *Gallium Arsenide and Related Compounds (Inst. Phys. Conf. Ser. 96)* ed J S Harris (Bristol: Institute of Physics) p 459
- Chan Y J, Pavlidis D, Razeghi M and Omnes F 1990 *IEEE Trans. Electron. Dev.* **ED-37** 2141
- Chand N, Henderson T, Klem J, Masselink W T, Fischer R, Chang Y C and Morkoc H 1984 *Phys. Rev. B* **30** 4481
- Chaubet C, Raymond A, Knap W, Mulot J Y, Baj M and Andre J P 1991 *Semicond. Sci. Technol.* **6** 160
- Chen C H, Baier S M, Arch D K and Shur M 1988 *IEEE Trans. Electron. Dev.* **ED-35** 570
- Chang Y C and James R B 1989 *Phys. Rev. B* **39** 12 672
- Delong M C, Taylor P C and Olson J M 1990 *Appl. Phys. Lett.* **57** 620
- Dobers M, Malcher F, von Klitzing K, Rossler U, Ploog K and Weimann G 1989a *Semiconductors in High Magnetic Fields (Springer Series in Solid State Sciences)* ed G Landwehr (Berlin: Springer)
- Dobers M, Vieren J P, Razeghi M, Defour M and Omnes F 1989b *Semicond. Sci. Technol.* **4** 687
- Dobers M, von Klitzing K, Schneider J, Weimann G and Ploog K 1988a *Phys. Rev. Lett.* **31** 1650
- Dobers M, von Klitzing K and Weimann G 1988b *Phys. Rev. B* **38** 5453
- Ettenberg M and Olsen G H 1977 *J. Appl. Phys.* **48** 4275
- Fang F, Smith T P III and Wright S L 1988 *Surf. Sci.* **196** 310
- Feng S L, Bourgoin J C, Omnes F and Razeghi M 1991 *Appl. Phys. Lett.* **59** 941
- Garland J W and Raccah P M 1986 *SPIE* **659** 32

- Gomyo A, Hotto H and Hino I 1989 *Japan. J. Appl. Phys.* **28** L1330  
 Gomyo A, Suzuki T and Iijima S 1988 *Phys. Rev. Lett.* **60** 2645  
 Gomyo A, Suzuki T, Kohayashi K, Kawata S, Hino I and Yuara T 1987 *Appl. Phys. Lett.* **50** 673  
 Gornik E, Seidenbush W, Christianell R, Lasnig R and Pidgeon C R 1987 *Surf. Sci.* **196** 339  
 Gregoris G, Beerens J, Ben Amor S, Dmowski L, Portal J C, Sivco D L and Cho A Y 1987 *J. Phys. C: Solid State Phys.* **20** 425  
 Guldner Y, Voos M, Vieren J P, Hirtz J P and Heiblum M 1987 *Phys. Rev. B* **36** 1266  
 Gunapala S D, Levine B F, Logan R A, Tanbun-Ek T and Humphrey D A 1990 *Appl. Phys. Lett.* **57** 1802  
 Harrang J P, Higgins R J, Goodall R K, Jay P R, Laviron M and Deslecluse P 1985 *Phys. Rev. B* **32** 8126  
 Harris J J, Lacklison D E, Foxon C T, Selten F M, Suckling A M, Nicholas R J and Barnham K W J 1987 *Semicond. Sci. Technol.* **2** 783  
 He X and Razeghi M 1992 *Appl. Phys. Lett.* **61** 1703  
 He X and Razeghi M 1993a *Appl. Phys. Lett.* **62** 618  
 He X and Razeghi M 1993b *J. Appl. Phys.* **73** 3284  
 Honig R E 1962 *RCA Rev.* **23** 657  
 Horng R H, Wuu D S and Lee M K 1988 *Appl. Phys. Lett.* **53** 2614  
 Hoshino M, Kodama K, Kitahara K, Komono J and Ozeki M 1986a *Appl. Phys. Lett.* **48** 983  
 Hoshino M, Kodama K, Kitahara K, Komono J and Ozeki M 1986b *Japan. J. Appl. Phys.* **25** L534  
 Hoshino M, Kodama K, Kitahara K and Oseki M 1986c *Appl. Phys. Lett.* **48** 770  
 Hsieh S J, Patten E A and Wolfe C M 1984 *Appl. Phys. Lett.* **45** 1125  
 Hsu C C, Yuan J S, Cohen R M and Stringfellow G B 1985 *J. Appl. Phys.* **59** 395  
 Ikeda M, Toda A, Nakano K, Mori Y and Watanabe N 1987 *Appl. Phys. Lett.* **50** 1033  
 Inoue Y, Nishino T, Hamakawa Y, Kondow M and Minagawa S 1988 *Optoelectron. Dev. Technol.* **3** 61  
 Ishikawa M, Ohla Y, Sugawara H, Yamamoto M and Nakanisi T 1986 *Appl. Phys. Lett.* **48** 207  
 Jen H R, Jou M J, Cerng Y T and Stringfellow G B 1987 *J. Crystal Growth* **85** 175  
 Kassel L, Garland J W, Abad H, Raccah P M, Potts J E, Haase M A and Cheng H 1990 *Appl. Phys. Lett.* **56** 42  
 Kassel L, Garland J W, Raccah P M, Haase M A and Chang H 1991a *Semicond. Sci. Technol.* **6** A146  
 Kassel L, Garland J W, Raccah P M, Tamargo M C and Farrell H 1991b *Semicond. Sci. Technol.* **6** A152  
 Kastalsky A and Hwang J C M 1984 *Solid State Commun.* **51** 317  
 Kawamura Y and Asahi H 1983 *Appl. Phys. Lett.* **43** 780  
 Kitahara K, Hoshino M, Kodama K and Ozeki M 1986 *Japan. J. Appl. Phys.* **25** L534  
 Kitahara K, Hoshino M and Ozeki M 1988 *Japan. J. Appl. Phys.* **27** L110  
 Knap W, Huant S, Chaubet C and Etienne B 1990 *Proc. 5th Int. Conf. on the Physics of Electro-optic Microstructures and Microdevices (Heraklion, 1990)*  
 Kobayashi T, Taira K, Nakamura F and Kawai H 1989 *J. Appl. Phys.* **65** 4898  
 Kondow M, Kakabayashi H and Minagawa S 1988a *J. Crystal Growth* **88** 291  
 Kondow M, Kakabayashi H, Minagawa S, Inoue Y, Nishino T and Hamakawa Y 1988b *Appl. Phys. Lett.* **53** 2053  
 Kondow M, Kakabayashi H, Minagawa S, Inoue Y, Nishino T and Hamakawa Y 1988c *J. Crystal Growth* **93** 412  
 Kondow M, Kakabayashi H, Tanaka T and Minagawa S 1989 *Phys. Rev. Lett.* **63** 884

- Kroemer H, Chien W Y, Harris J S and Edwall D D 1980 *Appl. Phys. Lett.* **36** 295  
 Kuan T S, Kuech T F, Wang W I and Wilkie E L 1985 *Phys. Rev. Lett.* **54** 201  
 Kudman I and Poff R J 1972 *J. Appl. Phys.* **43** 3760  
 Ladany I 1971 *J. Appl. Phys.* **42** 654  
 Landau L D and Lifshitz E M 1969 *Statistical Physics* (Oxford: Pergamon) ch 14  
 Landolt-Börnstein New Series 1982 Group III, vol 17a (Berlin: Springer)  
 Levine B F, Gunapala S D, Kuo J M, Pei S S and Hui S 1991 *Appl. Phys. Lett.* **59** 1864  
 Levine B F, Zussman A, Gunapala S D, Asom M T, Kuo J M and Hobson W S 1992 *J. Appl. Phys.* **72** 4429  
 Lommer G, Malcher F F and Rossler U 1985 *Phys. Rev. B* **32** 6995  
 Madelung O 1991 *Semiconductors (Data in Science and Technology)* (Berlin: Springer)  
 Man P and Pan D S 1992 *Appl. Phys. Lett.* **61** 2799  
 Mani R G and Anderson J R 1988 *Phys. Rev. B* **37** 4299  
 Martin K P, Higgins R J, Rascol J J L, Yoo H M and Arthur J R 1988 *Surf. Sci.* **196** 323  
 Martin P A, Meehan K, Gavrilovic P, Hess K, Holonyak N and Coleman J J 1983 *J. Appl. Phys.* **54** 4689  
 Maude D K, Portal J C, Dmowski L, Foster T, Eaves L, Nathan M, Heiblum M, Harris J and Beall R B 1987 *Phys. Rev. Lett.* **59** 815  
 McDermott B T, El-Marry N A, Jiang B L, Hyuga F and Bedair S M 1991 *J. Crystal Growth* **107** 96  
 Mercy J M, Bousquet C, Robert J L, Raymond A, Gregoris G, Beerens J, Portal J C, Frijlink P M, Delescluses P, Chevrier J and Linh N T 1984 *Surf. Sci.* **142** 298  
 Merkt U 1987 *Festkorperproblem* **27** 109  
 Miyoko O, Watanabe N and Ohba Y 1987 *Appl. Phys. Lett.* **50** 906  
 Mooney P, Fisher R and Morkoc H 1985 *J. Appl. Phys.* **57** 1928  
 Nakayama H and Fujita H 1986 *GaAs and Related Compounds 1985 (Inst. Phys. Conf. Ser. 79)* ed M Fujimoto (Bristol: Institute of Physics) p 289  
 Nathan M I, Jackson T N, Kiirchner P D, Mendez E E, Petit G D and Worlock J W 1983 *J. Electron. Mater.* **12** 719  
 Olivier J, Etienne P, Razeghi M and Alnot P 1987 *Nat. Res. Soc. Symp. Proc.* **91** 497  
 Olsen J M, Ahrenkiel R K, Dunlavy D J, Keys B and Kibbler A E 1989 *Appl. Phys. Lett.* **55** 1208  
 Omnes F, Defour M and Razeghi M 1991 *Rev. Tech. Thomson-CSF* **23** No 3 September  
 Omnes F and Razeghi M 1991 *Appl. Phys. Lett.* **59** 1034  
 Papalus G, Lin S Z and Razeghi M 1991 unpublished results  
 Pierron E D, Parker D L and McNeely J B 1967 *J. Appl. Phys.* **38** 4669  
 Queisser H J and Theodorou D E 1986 *Phys. Rev. B* **33** 4027  
 Ranz E, Lavielle D, Cury L A, Portal J C, Razeghi M and Omnes F 1990 *Superlatt. Microstruct.* **8** 245  
 Rao M A, Caine E J, Kroemer H, Long S J and Babic D 1987 *J. Appl. Phys.* **61** 643  
 Raymond A, Chaulet C and Razeghi M 1990 *Proc. SPIE* **1362** 275  
 Razeghi M 1985 *Semiconductors and Semimetals* vol 22 Part A, ed R K Willardson and A C Beer (New York: Academic) chapter 5 p 305  
 Razeghi M 1989a *EIT Workshop on Photonics (Vienna, 6–8 November 1989)* (Banca Popolare di Verona) p 49  
 Razeghi M 1989b unpublished  
 Razeghi M 1989c *The MOCVD Challenge Volume 1: A Survey of GaInAsP-InP for Photonic and Electronic Applications* (Bristol: Hilger)  
 Razeghi M, Defour M, Omnes F, Dobers M, Vieren J P and Guldner Y 1989a *Appl. Phys. Lett.* **55** 457  
 Razeghi M, Duchemin J P, Portal J C, Dmowski L, Remeni G, Nicholas R J and Briggs A 1986a *Appl. Phys. Lett.* **48** 712

- Razeghi M, Machado A, Koch S M, Acher O, Omnes F and Defour M 1990 *SPIE* **1283** 64
- Razeghi M, Maurel P, Omnes F, Ben Amor S, Dmowski L and Portal J C 1986b *Appl. Phys. Lett.* **48** 1267
- Razeghi M and Omnes F 1991a *Appl. Phys. Lett.* **59** 1034
- Razeghi M, Omnes F, Maurel P, Chan J and Pavlidis D 1991b *Semicond. Sci. Technol.* **6** 103
- Razeghi M, Omnes F, Nagle J, Defour M, Acher O and Bove P 1989b *Appl. Phys. Lett.* **55** 1677
- Razeghi M, Yang D, Garland J W, Zhang Z and Xue D 1992 *Proc. SPIE* **1676** 130
- Robert J L, Raymond A, Mulot J Y, Bousquet C, Andre J P, Knap W, Kubiza M, Zawadski W, Gornik E, Seidenbush W and Vitzani M 1988 *Proc. 19th ICPS* ed W Zawadski (Warsaw: Institute of the Polish Academy of Science)
- Rosencher E, Vinter B and Levine B 1992 *Intersubband Transitions in Quantum Wells* (New York: Plenum)
- Rossler U, Malcher F and Lommer G 1989 *Semiconductors in High Magnetic Fields* (*Springer Series in Solid State Sciences*) ed G Landwehr (Berlin: Springer)
- Schubert E, Fisher A and Ploog K 1985a *Phys. Rev. B* **31** 7937
- Schubert E, Knecht J and Ploog K 1985b *J. Phys. C: Solid State Phys.* **18** L215
- Seidenbush W 1987 *Phys. Rev. B* **36** 1877
- Smith J S, Chiu L C, Margalit S and Yariv A 1983 *J. Vac. Sci. Technol. B* **1** 376
- Stein D, Ebert G, von Klitzing K and Weimann G 1984 *Surf. Sci.* **142** 406
- Stern F and Sarma S D 1985 *Phys. Rev. B* **32** 8442
- Stormer H L, Dingle R, Gossard A C, Wiegman W and Sturge M D 1979 *Solid State Commun.* **29** 705
- Stormer H L, Gossard A C and Wiegmann W 1983 *Solid State Commun.* **41** 707
- Stormer H L, Gossard A C, Wiegmann W and Baldwin K 1981 *Appl. Phys. Lett.* **39** 912
- Suzuki T, Gomyo A, Hino I, Kobayashi K, Kawata S and Iijima S 1988a *Japan. J. Appl. Phys.* **27** L1549
- Suzuki T, Gomyo A and Iijima S 1988b *J. Crystal Growth* **93** 389
- Suzuki T, Gomyo A, Iijima S, Kobayashi K, Kawata S, Hino I and Yuasa T 1988c *Japan. J. Appl. Phys.* **27** 2098
- Tarng M L and Fisher D G 1978 *J. Vac. Sci. Technol.* **15** 50
- Teng D, Lee C and Eastman L F 1992 *J. Appl. Phys.* **72** 1539
- Ueda O, Fujii T, Nakada Y, Yamada H and Umebu I 1988a *Workbook 5th Int. Conf. on Molecular Beam Epitaxy (Sapporo, 1988)* unpublished p 45
- Ueda O, Takechi M and Komeno J 1989 *Appl. Phys. Lett.* **54** 2312
- Ueda O, Takikawa M, Komeno J and Umebu I 1987 *Japan. J. Appl. Phys. (Part 2)* **26** L1824
- Ueda O, Takikawa M, Takechi M, Komeno J and Umebu I 1988b *J. Crystal Growth* **93** 418
- Voisin P, Guldner Y, Vieren J P, Voos M, Deslecluse P and Linh N T 1981 *Appl. Phys. Lett.* **39** 982
- von Klitzing K V and Ebert G 1984 *Two-Dimensional Systems, Heterostructures and Superlattices* (*Springer Series in Solid State Sciences* 53) ed G Bauer, F Kuchar and H Heinrich (Berlin: Springer) p 242
- Watanabe M O and Ohba Y 1987 *Appl. Phys. Lett.* **50** 906
- Yasuami S, Nozaki C and Ohba Y 1988 *Appl. Phys. Lett.* **52** 2031

## Optical Devices

### 7.1 ELECTRO-OPTICAL MODULATORS

#### 7.1.1 Introduction

Electro-optical modulators are key components that enable electrical control of light. This can refer to both phase modulation and intensity modulation. Phase modulation is obtained directly through refractive index modulation. Historically, the variation of the refractive index under application of an electric field is known as the Pockels linear electro-optic effect. It finds its origin in the displacement of the bond charges and in a possible slight deformation of the ion lattice (Yariv and Yeh 1984). The Pockels effect displays negligible dispersion which eases device design and operation specifications. The counterpart of this negligible dispersion is that this effect is weak. This is the reason why guided-wave devices have to be used in order to increase the interaction length between light and the electro-optic material. Phase modulators as well as directional couplers have thus been realized in GaAs- and InP-based materials (Carencio 1987). Intensity modulation has also been made possible using the Pockels effect through the use of Mach-Zehnder interferometers.

By the end of the 1950s, the effect of an electric field on the absorption spectrum of a semiconductor had been investigated by Franz (1958) and Keldysh (1958). The net result is a red-shift of the absorption edge. Because of this shift, absorption can become significant under the application of an electric field at a wavelength where the semiconductor is normally transparent. These absorption variations (electroabsorption) have been exploited to realize intensity modulators. However, these absorption variations are only moderate and relatively long waveguide devices have to be used in order to obtain a significant contrast ratio.

Semiconductor microstructures, such as multiquantum wells and superlattices, whose dimensions are comparable to atomic dimensions and whose interfaces are atomically smooth, exhibit novel optical properties not encountered in the parent compounds. Advances in material growth and processing have made

it possible to fabricate these thin semiconductor layers with unprecedented precision, making it possible to fabricate practical devices based on novel quantum mechanical effects. Most of these new phenomena rely on the original electroabsorption properties of these new structures. They have led to the improvement of previously existing devices as well as to the development of new functionalities.

When compared to previous devices made out of bulk III–V semiconductor or dielectric materials such as  $\text{LiNbO}_3$ , electro-optic devices made out of quantum structures offer the advantages of improved performance, reduced dimensions and possible integration with other semiconductor devices such as semiconductor lasers. In the following, we present the two major electroabsorption phenomena that have led to considerable research activity over the past few years: the quantum-confined Stark effect in multiple quantum wells and Wannier–Stark localization in superlattices, along with the corresponding device applications. This chapter will conclude with a discussion of new trends in this research area.

### 7.1.2 Multiple-quantum-well modulators based on the quantum-confined Stark effect

#### *(a) The absorption spectrum of a multiple quantum well*

The absorption edge (absorption spectrum near the bandgap) of a quantum well structure displays several interesting features that originate from the carrier quantum confinement (Bastard 1988).

First of all, the carrier motion in the direction perpendicular to the layers is quantized which results in a two-dimensional density of states. Therefore, the absorption edge displays a steplike behaviour which reflects the steplike two-dimensional density of states. This is in contrast with the typical parabolic three-dimensional density of states of a bulk semiconductor.

The second interesting feature originates from the Coulombic interaction between confined electrons and holes, also called excitonic interaction. Excitons are electron–hole ( $e\text{-}h$ ) pairs forming a bound state analogous to the hydrogen atom. They produce very sharp resonance peaks just below the bandgap where a large oscillator strength is concentrated in a narrow spectral domain. This excitonic interaction is also present in bulk semiconductors, but here the excitonic orbital dimension is large and the interaction is weak. Consequently, excitonic transitions are usually observed in bulk semiconductors only at low temperature: as the temperature is increased, the resonances broaden due to phonon collisions and by room temperature they are usually only marginally resolvable from the interband absorption. By reducing the well width below the typical excitonic orbital dimensions, the excitonic orbit is squeezed in the growth direction as illustrated in figure 7.1. As a result, the interaction is strengthened and sharp exciton absorption peaks have been observed in quantum wells at room temperature (Miller *et al* 1982).

Another distinction between bulk and quantum well semiconductors is the change in symmetry because of the layered structure. The degeneracy between

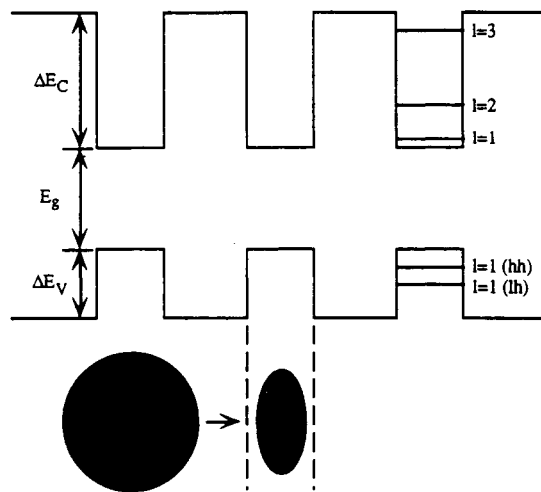


**Figure 7.1** Schematic of the band structure of a multiple-quantum-well structure. The shaded circle and ellipse illustrate how the exciton is compressed by the confinement.

light and heavy holes at the zone centre is removed by introducing splitting between the heavy and light holes. The quantum confinement energies of the two holes are different and the exciton resonances associated with the two holes are now distinct, giving two clear peaks in the spectrum near the band edge as seen in figure 7.2(a).

(b) *Quantum-confined Stark effect (Miller et al 1985)*

The application of an electric field perpendicular to the layers of a quantum well structure modifies the potential well profile as schematized in figure 7.3. Wavefunctions and energy levels are modified, and an easy way to guess the final result is to consider the classical counterpart: if classical particles were located in such distorted potential wells, they would be pulled against the potential barriers, and their potential energies would be reduced by half the potential drop over the quantum well (figure 7.4). The trends are the same for the present case: electrons and holes are pulled towards opposite sides of the well and their confinement energies are reduced. Therefore the fundamental transition energy of the quantum well is reduced which leads to a red-shift of the absorption edge. In contrast to bulk semiconductors where excitons are ionized very rapidly by the electric field, strong excitonic transitions are maintained in that case. The reasons for this behaviour are the following: firstly the well is narrow compared to the bulk exciton diameter so that the Coulomb interaction is still strong even though electrons and holes are pulled towards opposite sides of the well, and secondly potential barriers inhibit the field ionization of the exciton.

This red-shift of the absorption edge together with the persistence of strong excitonic interaction is called the quantum-confined Stark effect. One should

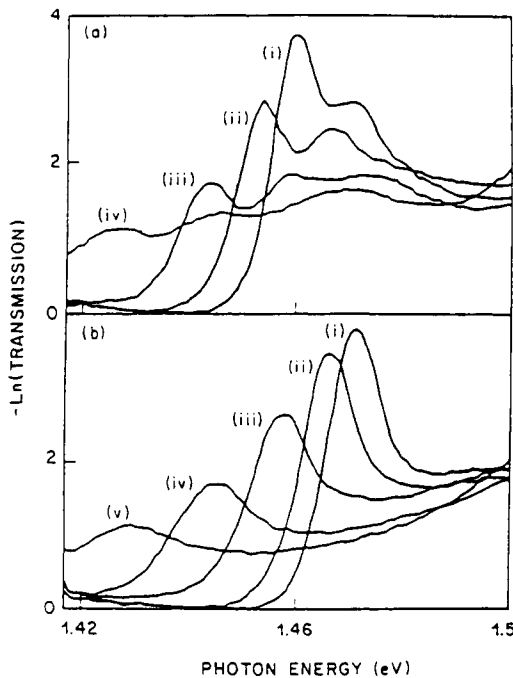


**Figure 7.2** Absorption spectra of a quantum well waveguide as a function of electric field applied perpendicular to the layers (Weiner *et al* 1985). (a) Incident optical polarization parallel to the plane of the layers for fields of (i)  $1.6 \times 10^4 \text{ V cm}^{-1}$ , (ii)  $10^5 \text{ V cm}^{-1}$ , (iii)  $1.3 \times 10^5 \text{ V cm}^{-1}$  and (iv)  $1.8 \times 10^5 \text{ V cm}^{-1}$ . (b) Incident optical polarization perpendicular to the layers for fields of (i)  $1.6 \times 10^4 \text{ V cm}^{-1}$ , (ii)  $10^5 \text{ V cm}^{-1}$ , (iii)  $1.3 \times 10^5 \text{ V cm}^{-1}$ , (iv)  $1.8 \times 10^5 \text{ V cm}^{-1}$  and (v)  $2.2 \times 10^5 \text{ V cm}^{-1}$  (Weiner *et al* 1985).

be aware that the excitonic oscillator strength undergoes a decrease under the application of the electric field because of the reduction in the overlap between the electron and hole wavefunctions which reduces the probability of finding the electron and the hole in the same unit cell.

A typical set of absorption spectra with increasing field is shown in figure 7.2(b). The exciton peaks remain resolved up to very high fields of  $2 \times 10^5 \text{ V cm}^{-1}$  and show very large shifts of 40 meV. This corresponds to a shift of about four times the zero-field binding energy at a field of about 100 times the classical ionization field of an unconfined exciton of comparable binding energy.

### (c) Device application

Large absorption variations are obtained for wavelengths corresponding to the normally transparent region. These absorption variations enable light intensity modulation as was first demonstrated by Wood *et al* (1984). In

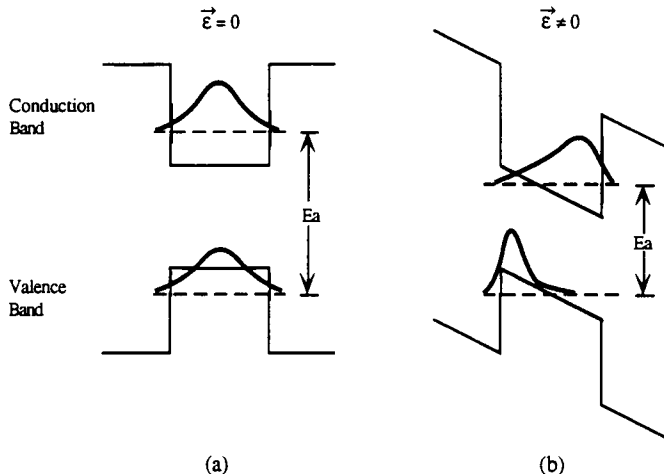


**Figure 7.3** Schematic view of the electroabsorption effect in MQWs. The conduction band minimum and valence band maximum and the energy levels of the ground states for electrons and holes along with the wavefunction envelopes are shown. These items are shown in the absence of an electric field in (a) and with an electric field perpendicular to the quantum well layers in (b).

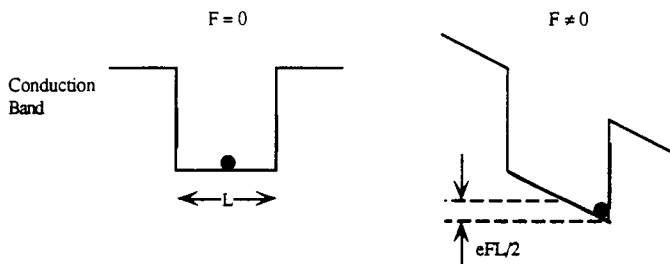


**Figure 7.4** Effect of a distorted potential well on a classical particle.

the initial demonstrations light was propagating perpendicularly to the layers. Such modulators are particularly well suited for optical signal processing and computing because they can be integrated in two-dimensional arrays.

Starting from this elementary modulator, a new bistable device was invented by Miller *et al* (1984): this device, called the self-electro-optical device (SEED), consists of a reverse-biased modulator connected with a series resistance as shown in figure 7.5. The modulator is illuminated with a wavelength corresponding to the zero-field exciton position. This is a normally absorbing wavelength region as indicated by the dashed line in figure 7.6. When weak light is shining, there is a negligible current flow and all of the supply voltage appears across the diode, resulting in a relatively small absorption. As the

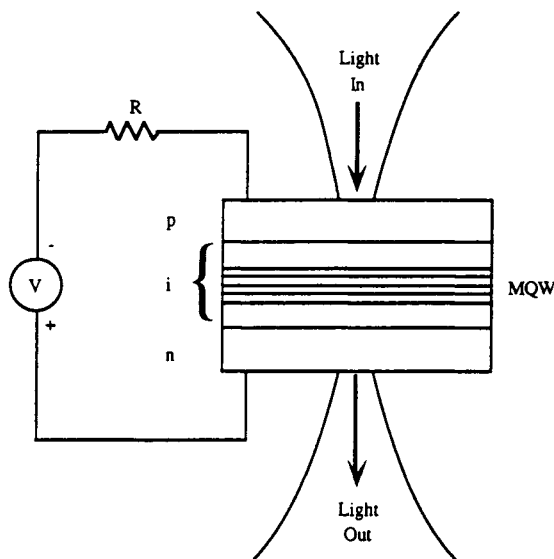


**Figure 7.5** Schematic of the quantum well SEED.

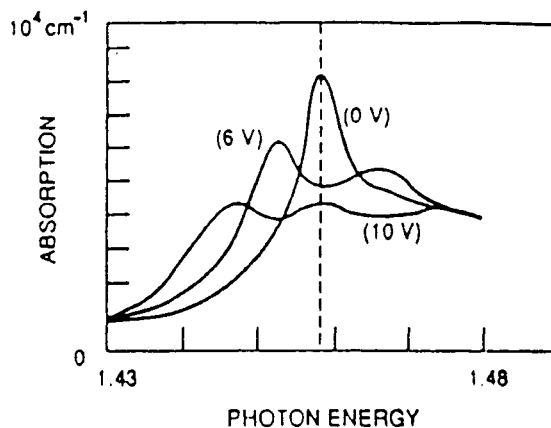


**Figure 7.6** Schematic of SEED operation.

illumination power increases, a voltage drop occurs across the resistor due to the photocurrent thus reducing the voltage across the diode. Consequently, the absorption of the diode increases as the exciton recovers its original position. This demonstrates the feedback mechanism that is necessary to reach bistability. The basic operation of a SEED is represented in figure 7.6.

Other types of modulator with light propagating perpendicularly to the layers have been developed based on the quantum-confined Stark effect. For example,

devices consisting of Fabry-Pérot interferometers made out of epitaxially grown Bragg reflectors, that include quantum wells in between, have been realized. Such devices usually operate in a reflection mode and are based on the vanishing of a Fabry-Pérot resonance because of increased absorption.

Most of these vertical cavity devices have been realized out of GaAs-based materials because higher-quality quantum wells are more readily obtained in this material system. Guided-wave devices have been proposed as well. Although the first demonstrations were realized in the same material system (Wood *et al* 1985), a lot of recent work has concentrated on InP-based materials because the use of external intensity modulators is an attractive way to reduce wavelength chirping occurring in directly modulated semiconductor lasers (Koch and Bowers 1984). This chirping is detrimental to high-bit-rate and long-distance optical fibre transmission systems operating in the long-wavelength range (Koyama and Iga 1988). Modulation bandwidths of over 20 GHz have been achieved in both MBE-grown InGaAlAs quantum wells (Wakita *et al* 1990, 1992) and MOCVD-grown InGaAsP quantum wells (Devaux *et al* 1992, Razeghi *et al* 1986, 1989). Several groups are now concentrating their efforts towards the monolithic integration of such modulators with DFB lasers (Wakita *et al* 1992, Kato *et al* 1992, Aoki *et al* 1992).

Although large absorption variations can be obtained using the quantum-confined Stark effect, the required electric fields are large because of its quadratic relationship (Bastard *et al* 1983). Large electric fields usually imply large drive voltages which is a major drawback for any application. The need for smaller drive voltages has been one of the stimuli for research in new electroabsorption phenomena (Rao *et al* 1987).

### 7.1.3 Superlattice modulators based on Wannier-Stark localization

#### (a) Wannier-Stark localization (Bleuse *et al* 1988a, Mendez *et al* 1988)

When quantum wells are separated by very thin barriers in a periodic structure called a superlattice, wells are coupled to each other through the resonant tunnelling process. Due to this resonant coupling, carriers are delocalized and the original QW discrete energy levels broaden into minibands of widths  $\Delta_c$  and  $\Delta_v$  (Esaki and Tsu 1970). This carrier delocalization and miniband formation is quite similar to the band formation in a crystal lattice, and the superlattice exhibits, to some extent, a three-dimensional behaviour. Because of the miniband broadening, the bandgap of the superlattice  $E_g^{\text{SL}}$  is smaller than that of an isolated quantum well  $E_g^{\text{QW}}$  by about  $\frac{1}{2}(\Delta_c + \Delta_v)$ . The absorption edge of a superlattice reflects the miniband density of states that is given by an arccosine function, in the tight-binding approach (Bastard 1988). This broadened absorption edge is represented schematically in figure 7.7 (solid line) in the case of an ideal superlattice without any source of broadening and without taking any excitonic contribution into account.

The application of an electric field parallel to the growth axis of the SL

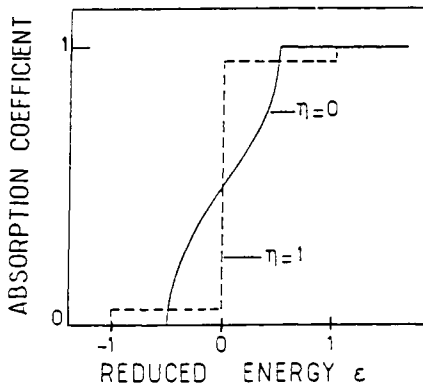


**Figure 7.7** Absorption spectra of an ideal superlattice without applied electric field (solid line) and in the high-field limit:  $eFd/(\Delta_c + \Delta_v) = 1$  (dashed line).

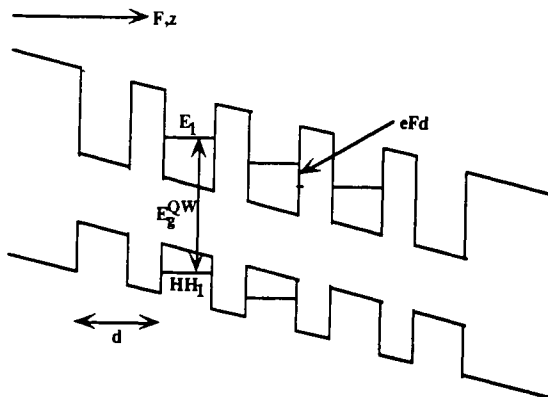


**Figure 7.8** Band structure in real space of a superlattice when an electric field  $F$  is applied in the  $z$ -direction.  $E_1$  and  $HH_1$  are the ground conduction and valence subbands.

shows interesting behaviour (Bleuse *et al* 1988a). As schematized in figure 7.8, with the application of an electric field  $F$ , the genuine energy levels in adjacent quantum wells become misaligned by  $eFd$ , where  $d$  is the SL period and  $e$  the electron charge. Due to this potential drop, the tunnelling probability decreases drastically and the resonant tunnelling process is turned off. Carriers localize into the wells and the superlattice tends to recover its original isolated quantum-well behaviour. This phenomenon is called Wannier–Stark localization. The scaling factor is the ratio of the energy misalignment to the total miniband width.

The SL broadened absorption spectrum tends to recover its QW steplike absorption spectrum. This should result in a blue-shift of the absorption edge of

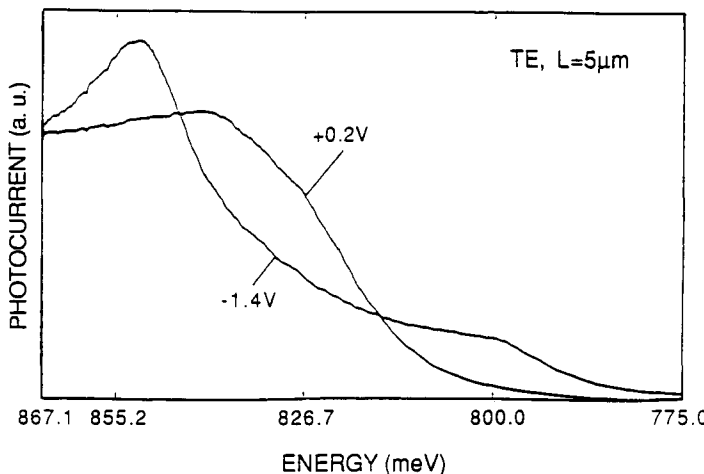


**Figure 7.9** Electroabsorption spectra of an InGaAs-InAlAs superlattice (Bigan *et al* 1990).

the order of  $\frac{1}{2}(\Delta_c + \Delta_v)$ . However, a blue-shift of the absorption edge is only effective because carrier localization is incomplete as the wavefunctions exhibit additional lobes in adjacent quantum wells. As a consequence the main step at  $E_g^{QW}$  is accompanied by smaller ones at

$$E_g^{QW} + peFd \quad (p = \pm 1, \pm 2, \dots) \quad (7.1)$$

corresponding to ‘oblique’ transitions in real space, connecting an electron localized near the  $n$ th quantum well with a hole in the  $(n+p)$ th quantum well. In the ‘high-field’ limit,  $eFd/(\Delta_c + \Delta_v) = 1$ , the SL behaves more as a series of uncoupled quantum wells with the wavefunction localized over each quantum well and only the ‘oblique’ transitions connecting adjacent wells ( $p = \pm 1$ ) are significant. The corresponding absorption spectra for an ideal SL at zero field and in the high-field limit are shown in figure 7.7.

These theoretical predictions have been confirmed experimentally. However excitonic features play an important role in determining the actual electroabsorption spectra. Since the structure evolves from a three-dimensional behaviour to a two-dimensional behaviour, an enhancement of the excitonic oscillator strength is expected. This is observed experimentally and is in contrast with the usual electric-field-induced exciton ionization in bulk materials or multiple quantum wells. Figure 7.9 shows experimental electroabsorption spectra for an InGaAs-InAlAs superlattice and it can be seen that the excitonic enhancement as well as the low-energy oblique transition tend to hide the effective blue-shift of the absorption edge. Nevertheless, large absorption variations can be obtained both below and above the superlattice bandgap using the effective blue-shift of the absorption edge and the low-energy oblique transitions, respectively.

SLs are unique systems where the conduction and valence miniband widths can be tailored with a judicious choice of the host materials and layer thicknesses, in the range of a few tens of meV while the corresponding periods fall in the range of a few tens of Å. This means that the high-field limit can be attained with moderate electric fields in the range of a few tens of kV cm<sup>-1</sup>. These electric fields are significantly smaller than those required for observation of the quantum-confined Stark effect.

*(b) Device application (Bleuse *et al* 1988b)*

Most of the various modulators first introduced using the quantum-confined Stark effect have been reproduced using Wannier–Stark localization, taking advantage of both the effective blue-shift of the absorption edge and the low electric fields required. Vertical cavity devices such as Fabry–Pérot reflection modulators and SEEDs (Bar-Joseph *et al* 1989) have been implemented using GaAs–GaAlAs superlattices. SEEDs based on Wannier–Stark localization strongly benefit from the large negative differential photoconductivity occurring in the blue-shifted spectral region. Such negative differential photoconductivity is necessary in order to achieve bistability in a SEED device.

There have been fewer reports of waveguided modulators based on Wannier–Stark localization. These devices operate in the normally transparent spectral region and use the low-energy oblique transitions to circumvent the problems of large on-state attenuation encountered in the blue-shifted spectral region (Bigan *et al* 1990). They benefit from the low electric fields required and subvolt drive voltage intensity modulators operating in the 1.5 μm wavelength range have been demonstrated and optimized (Bigan *et al* 1992a). The advantage of superlattice waveguide modulators has been demonstrated using a figure of merit that allows comparison of different electroabsorptive waveguide modulators. As this subject closely follows the work on multiple quantum wells, work towards monolithic integration of these modulators with DFB lasers is under progress (Bigan *et al* 1992b).

### 7.1.4 Perspectives

One of the main problems encountered in absorptive devices is saturation at high optical powers. These saturation effects originate from electric-field screening through carrier accumulation (Wood *et al* 1990). These problems stimulate the use of refractive index changes associated with electroabsorption effects; here only virtual transitions are involved and there is no carrier generation. As a result, saturation effects are expected to be eliminated. This stimulates the development of intensity modulators based on Mach–Zehnder interferometers (Zucker *et al* 1989). Such interferometers operating in the 1.5 μm wavelength range have thus been realized.

New structures based on carrier transfer from a delta-doped layer into a quantum well located nearby have also been proposed to increase refractive index variations. These structures named BRAQWETs (barrier reservoir and

asymmetric quantum well electron transfer), might prove to be interesting alternatives to conventional modulators (Zucker *et al* 1990, 1991) although their integration with DFB lasers might be more difficult.

## 7.2 GaAs-BASED INFRARED PHOTODETECTORS GROWN BY MOCVD

### 7.2.1 Basic physics of photodetectors

Photodetectors are semiconductor devices that can convert optical signals into electrical signals. A general photodetector has basically three processes: (i) carrier generation by incident light, (ii) carrier transport and/or multiplication by whatever current-gain mechanism may be present and (iii) interaction of current with the external circuit to provide the output signal. Also, photodetectors must satisfy stringent requirements such as high sensitivity at operating wavelengths, high response speed and minimum noise.

The performance of a photodetector in general and a photoconductor in particular is measured in terms of three parameters: the quantum efficiency or gain, the response time and the sensitivity (detectivity).

#### (a) Quantum efficiency ( $\eta$ ) and gain

The quantum efficiency  $\eta$  is the number of electron–hole pairs generated for each incident photon. For a photoconductor with an illuminated area  $A = WL$  and thickness  $T$ , the photocurrent flowing between the electrodes is

$$I_p = (\Delta\sigma E)WT = (q\mu_n\Delta n E)WT = (q\Delta n v_d)WT = q(\eta P_{out}/h\nu)(\mu_n\tau E/L) \quad (7.2)$$

where  $n$  is the number of carriers per unit volume (carrier density),  $\Delta n$  is the excess carrier density,  $E$  is the electric field inside the photoconductor,  $\mu_n$  is the mobility,  $v_d$  is the drift velocity,  $\tau$  is the carrier lifetime,  $P_{out}$  is the incident optical power and  $h\nu$  is the photon energy. If the primary photocurrent is defined as

$$I_{ph} = q(\eta P_{out}/h\nu) \quad (7.3)$$

then the photocurrent gain can be expressed as

$$\text{gain} = I_p/I_{ph} = \mu_n\tau E/L = \tau/t_r \quad (7.4)$$

where  $t_r = L/v_d$  is the carrier transit time. The gain which depends on the ratio of carrier lifetime to the transit time is a critical parameter in photoconductors.

#### (b) Figures of merit

The infrared system is often designed around the characteristics of the infrared detector. They are defined by certain figures of merit describing the performance of the detector under specified operating conditions.

Many infrared detectors exhibit a signal which is a function of the wavelength of the radiation, being sensitive only to radiation in a given spectral interval and exhibiting a response which is dependent on wavelength within that interval. Also, like all other types of electromagnetic radiation detector, the ultimate performance of infrared detectors is limited by noise. Because most detectors are based upon photoeffects in semiconductors, the mechanisms encountered most frequently are those which pertain to semiconductors: current noise, thermal noise, generation-recombination noise and photon noise. The measured noise voltages for all noise mechanisms is proportional to the square root of the electrical bandwidth, and for some mechanisms is a function of frequency.

The most important figures of merit which relate to the problem of characterizing the signal-to-noise ratio to be expected from a detector for a given intensity of radiant power can be described as follows.

(i) One of the most commonly used figures of merit relating the radiation power capable of producing a signal voltage equal to the noise voltage, that is, a signal-to-noise ratio of unity, is the noise-equivalent power, NEP. The NEP is defined as the RMS value of the sinusoidally modulated radiant power falling upon a detector which will give rise to an RMS signal voltage equal to the RMS noise voltage from the detector. The NEP is determined experimentally by measuring the signal-to-noise ratio in a specified narrow electrical bandwidth, called the measurement bandwidth. The value obtained for a known amount of radiant power is extrapolated linearly to the power required to give a signal-to-noise ratio of unity. Thus the noise-equivalent power is given by

$$\text{NEP} = H A_D (V_n/V_s)[1/(\Delta f)]^{1/2} \quad (7.5)$$

where  $H$  is the RMS value of the irradiance falling on the detector of area  $A_D$ , and  $V_n/V_s$  is the ratio of the RMS noise voltage in the bandwidth  $\Delta f$  to the RMS signal voltage. Here it is assumed that  $\Delta f$  is sufficiently small so that the noise voltage per cycle within  $\Delta f$  is independent of frequency. The units of NEP are  $\text{W Hz}^{-1/2}$ . The noise-equivalent power for a 500 K black-body source, 900 Hz chopping frequency and 1 Hz bandwidth is written as NEP(500 K, 900, 1). Also, the detecting capability of the detector improves as the NEP decreases.

(ii) Another common figure of merit is the noise-equivalent incidence NEI. This is the radiant power per unit area of detector required to give rise to a signal-to-noise ratio of unity. The conditions of measurement are the same as those for the NEP. Thus the NEI is simply the NEP divided by the detector area. The NEI can be expressed as follows

$$\text{NEI} = \text{NEP}/A_D. \quad (7.6)$$

The units of NEI are  $\text{W Hz}^{-1/2} \text{ cm}^{-2}$ .

(iii) Most detectors exhibit a noise-equivalent power which is directly proportional to the square root of the area of the detector. An area-independent

figure of merit can be obtained by dividing the NEP by the square root of the area. The reciprocal of this quantity is known as  $D^*$ . Thus  $D^*$  is defined as

$$D^* = \frac{A_D^{1/2}}{\text{NEP}} = \frac{1}{A_D^{1/2}(\text{NEI})}. \quad (7.7)$$

The units of  $D^*$  are  $\text{cm Hz}^{1/2} \text{W}^{-1}$ . The reference bandwidth is always 1 Hz and the measured value of  $D^*$  is written in a manner analogous to that of the NEP, such as  $D^*(500 \text{ K}, 900, 1)$ . Therefore,  $D^*$  is a widely used figure of merit to be referred to as detectivity. Wherever the term detectivity occurs herein, it refers to  $D^*$ .

The figures of merit with which we have been concerned refer to the response of the detector to radiation from a black-body source of a specified temperature. Since the responses of many types of detector are dependent upon the wavelength of the incident radiation, the values of NEP, NEI and  $D^*$  can be expressed in terms of their responses to monochromatic radiation. In this case, the wavelength  $\lambda$  is specified and the figures of merit are written as  $\text{NEP}_\lambda$ ,  $\text{NEI}_\lambda$  and  $D_\lambda^*$ . If the performance at only a single wavelength is given, it is usually that at which the detector performs best.

The other thing we have to consider is the problem of characterizing the signal voltage per unit radiant power. Because we are only interested in the amplitude of the signal, the noise can be neglected. However, knowledge is still required of the black-body temperature, the temperature of the detector and the area of the detector. Knowing these, the responsivity  $R$  can be defined to be the RMS signal voltage  $V_s$  per unit RMS radiant power  $P$  incident upon the detector. Thus

$$R = V_s/P = V_s/H A_D. \quad (7.8)$$

Also, we can see that the responsivity is related to the NEP and  $D^*$  by

$$R = V_n/\text{NEP}(\Delta f)^{1/2} = D^* V_n/(A_D \Delta f)^{1/2}. \quad (7.9)$$

We also specify a spectral responsivity  $R_\lambda$ , the responsivity to monochromatic radiation of wavelength  $\lambda$ .

### 7.2.2 II-VI-material-based photodetectors

The most important II-VI semiconductors used for thermal imaging are mercury cadmium telluride ( $\text{Hg}_{1-x}\text{Cd}_x\text{Te}$ ) bulk material and HgTe-CdTe superlattices.

#### (a) $\text{Hg}_{1-x}\text{Cd}_x\text{Te}$ -based photodetectors

In  $\text{Hg}_{1-x}\text{Cd}_x\text{Te}$ , the electronic structure is dramatically changed by varying the Hg composition  $x$  while the crystalline structure is only slightly perturbed (figure 7.10).

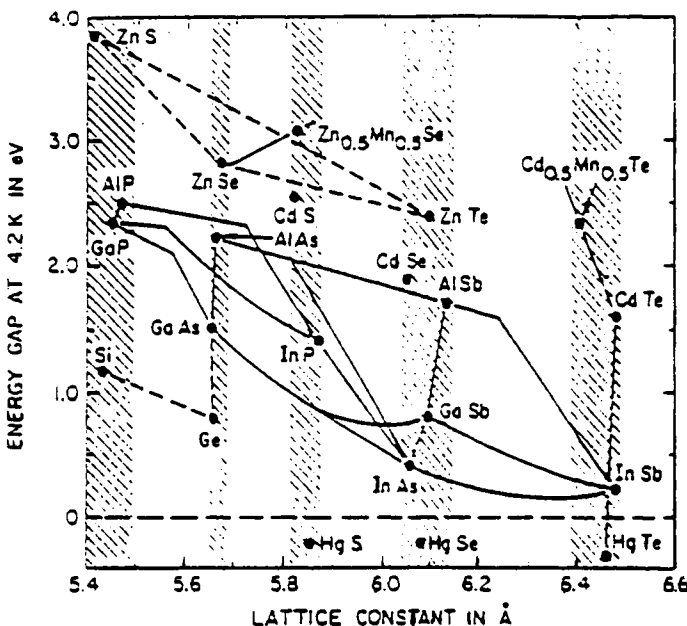


**Figure 7.10** Bandgap energy of the main semiconductors and compounds as a function of lattice parameter (Esaki 1986).

For  $x = 0$ , the compound is a semimetal and for  $x = 1$ , it is a wide-gap (1.5 eV) semiconductor. It is therefore possible to tune the bandgap of the semiconductor to a desired photon energy by adapting the Hg content. The optical detection is obtained by interband transitions (from valence to conduction band). Absorption coefficients of  $10^4 \text{ cm}^{-1}$  are obtained in the  $8\text{--}12 \mu\text{m}$  window which leads to quantum yields higher than 90% in the p–n junctions. However, this technology has a certain number of disadvantages:

- Small uncertainties in the Hg composition lead to large variations in bandgap energy. For example, a relative non-uniformity of 3% in Hg content yields a variation of cut-off wavelength from  $12 \mu\text{m}$  to  $14 \mu\text{m}$ . Very good uniformity is extremely difficult to obtain in the growth of HgCdTe compounds.
- The Hg diffusion coefficient is so high that the detectors must not be exposed even to moderate temperatures.
- Large numbers of Shockley–Read–Hall trap centres throughout the bandgap produce substantial and detrimental tunnelling currents.
- For large arrays, high yields are difficult to obtain.

Furthermore, high dislocation density, lack of low-cost and high-quality lattice-matched substrate, fabrication difficulties,  $1/f$  noise and sensitivity to elevated temperatures are also problems associated with this technology.

Some of these difficulties have been overcome by the use of MOCVD to grow

HgCdTe layers. This technique has been used for the fabrication of high-quality HgCdTe photoconductors (Specht *et al* 1986, Bethea *et al* 1988, Doll *et al* 1990, Druilhe *et al* 1990), and photovoltaic detectors (Bubulac *et al* 1990, Irvine 1992, Summers *et al* 1994), operated in the near-, middle- and long-wavelength ranges of the infrared spectrum. Direct alloy growth or the interdiffused multilayer process, in which thin layers of HgTe and CdTe are alternatively grown and subsequently interdiffused during a post-grown annealing are used by various groups. Near room temperature double-heterojunction long-wavelength devices have also been reported by Elliott *et al* (1994). MOCVD seems to be the most promising for future large-scale and low-cost production of HgCdTe epilayers. The flexibility of MOCVD largely enables us to integrate the growth and device processing in one run. Arsenic is the preferred dopant for p-type layers, while indium and iodine are preferable for n-type layers. Close to 100% doping efficiency with control of dopants over a wide range of concentrations was obtained. The devices are usually passivated with CdTe or ZnS. Lattice and thermal mismatch, spurious growth and impurity doping from the substrates are the most serious remaining problems which would require considerable development to meet the stringent requirements of high-performance devices.

Despite the direct fabrication of sensitive elements, MOCVD is also frequently used for preparation of the hybrid substrates GaAs- and CdZnTe-coated silicon or sapphire, which are then used for deposition of HgCdTe by other methods. High-quality focal plane arrays (FPAs) have been fabricated with this approach with a number of elements exceeding  $640 \times 480$  (Tung *et al* 1992, Johnson *et al* 1993).

#### *(b) HgTe–CdTe-superlattice-based photodetectors*

The HgTe–CdTe superlattice was originally proposed as an infrared (IR) material by Schulman and McGill (1979). Smith *et al* (1983) proposed that this superlattice should exhibit properties superior to those of the HgCdTe alloy as an infrared detector material. Their calculations showed that the superlattice tunnelling length is shorter than that of the alloy with the same gap. For a given cut-off wavelength tolerance, it has been found that less fractional precision is needed in the superlattice control parameter (layer thickness) than in the alloy control parameter (composition). They have also stated that p-side diffusion currents should be reduced due to the larger superlattice electron effective mass. Later, Arch *et al* (1986) proposed that interdiffusion of the layers of HgTe–CdTe superlattices at temperatures near the growth temperature ( $< 200^\circ\text{C}$ ) would be large due to the large equilibrium vacancy concentration normally present in the HgCdTe system. They have investigated the extent of intermixing of the HgTe and CdTe layers by making high-temperature x-ray diffraction measurements on HgTe–CdTe superlattices. The interdiffusion coefficients they obtain ( $4.23 \times 10^{-18} \text{ cm}^2 \text{ s}^{-1}$  at  $185^\circ\text{C}$ ) show that the interface intermixes rapidly at this temperature, and abrupt interfaces are difficult to achieve with this system. They have stated that the interface would intermix about  $12 \text{ \AA}$  for a 1 h growth

run and they have concluded that an unstable HgTe–CdTe interface might pose serious problems in using this material for optoelectronic devices.

### 7.2.3 InAs<sub>1-x</sub>Sb<sub>x</sub> materials

#### (a) InAs<sub>1-x</sub>Sb<sub>x</sub>-based photodetectors

InAs<sub>1-x</sub>Sb<sub>x</sub> has received increasing attention over the past few years for applications as infrared sources and detectors. The theoretical results indicate that the bandgaps of these InAsSb strained-layer superlattices (SLS) vary relatively slowly with composition. Thus, InAsSb SLS detectors can possess a broad spectral response. As a result, small, lateral compositional variations across the superlattice wafer will not result in larger variations in wavelength response. Furthermore, it has recently been proposed that, in low-bandgap cases, band-to-band tunnelling in superlattice p–n junctions may be reduced compared to such tunnelling in bulk materials (Smith *et al* 1983). Junctions in InAsSb strained-layer superlattices would also benefit from this effect. All these results indicate that InAsSb strained-layer superlattice materials offer potential advantages for 8–12 μm applications and are a better alternative to HgCdTe-based detectors.

Another important advantage of InAsSb-based detectors is the monolithic integration of devices. Silicon is currently the best semiconductor adapted to logical circuitry. InAsSb can be epitaxially grown on Si substrate and therefore high-speed optoelectronic integrated circuits are possible. Hence, InAsSb is a natural choice of material for infrared imaging, both for 3–5 μm and the 8–12 μm applications. Kurtz *et al* demonstrated a photodiode consisting of a p–n junction embedded in an InAs<sub>0.09</sub>Sb<sub>0.91</sub>/InSb strained-layer superlattice. The non-optimized device exhibited a photoresponse out to a wavelength of 8.7 μm at 77 K (Kurtz *et al* 1988). Later, Kurtz *et al* fabricated long-wavelength infrared photodiodes using InAs<sub>0.15</sub>Sb<sub>0.85</sub>/InSb strained-layer superlattices. The detectors displayed broad spectral responses with a detectivity  $\geq 10^{10} \text{ cm Hz}^{1/2} \text{ W}^{-1}$  at wavelengths of  $\leq 10 \mu\text{m}$  (Kurtz *et al* 1990).

However, for InAsSb materials, the valence-to-conduction-band transition is the most efficient way to detect light. We can obtain small energy gaps by extending the energy gap of small-gap semiconductors towards smaller values using strained-layer structures such as InSb/InAsSb or InAs/GaSb. However, in these structures, type-II superlattices are obtained. In type-II superlattices optical transitions between the valence and conduction bands are indirect in space and this results in less absorption and a small quantum yield. Other disadvantages of this structure are: firstly, InAsSb materials can only be lattice matched to some suitable substrate, secondly, due to strain, a high density of Shockley–Read generation centres is created and this leads to a high leakage current density.

#### (b) Strained-layer superlattices (SLSs) and multiple quantum wells

An attractive way to tailor semiconductor bandgaps by alloying is the use of

multiquantum wells (MQW) and superlattices (SL), which are usually periodic structures made from two compounds with different bandgaps. The use of multiquantum wells also opens up the possibilities of using quantum size effects and special exciton-related properties in these materials for switching and coupling applications. The exciton binding energies are greatly enhanced, giving rise to a large non-linearity in the refractive index and absorption (Frank and van der Merwe 1949). The use of strained-layer superlattices (SLS) and strained MQW eliminates the need for lattice matching and, in principle, high-quality defect-free samples can be grown by MBE or MOCVD (Matthews 1975). The dominant effect of strain is to lift certain degeneracies in the Brillouin zone and alter the density of states at band edges and to affect bandgaps. These effects can have a significant influence on transport and optical properties of devices.

The strain-induced band structure changes may lead to increased charged-carrier mobility within the pseudomorphic layers. Pseudomorphic layers are layers that have a slight lattice mismatch between them so that it is possible to accommodate this lattice mismatch through elastic strain rather than dislocation formation. Strain induces modifications of the energy band structure which result in significant modifications of the bulk optical and electronic properties of pseudomorphic layers.

The strain-induced bandgap shift is given by

$$\Delta E = -\alpha \varepsilon \quad (7.10)$$

where  $\alpha$  is the constant including all elastic hydrostatic and shear deformation potentials of the material and  $\varepsilon$  is the strain parameter. Its value is negative for compressive strain and positive for tensile strain. As a result,  $\Delta E$  is positive for negative strains which results in a net bandgap increase with biaxial compression (figure 7.11) (Kato *et al.* 1986).

Figure 7.11 shows the bandgap shifts due to strain. These bandgap shifts ( $\Delta E$ ) are experimentally determined by directly comparing the photoluminescence peak energies of strained layers with those of unstrained bulklike films.

From photoluminescence experiments it has been established that quantum wells of different thicknesses give rise to peaks at different wavelengths. Each wavelength corresponds to a certain bandgap energy which is different from the bandgap of the bulk layer by an amount  $\Delta E$ . If we reduce the thickness of the quantum well, the strain associated with it becomes higher and  $\Delta E$  becomes larger. This is a useful mechanism to tailor the wavelength of absorbed light without a change in the material composition.

Bandgaps of strained-layer superlattices vary relatively slowly with composition, so that small compositional variations across the wafer will not result in large variations in wavelength response.

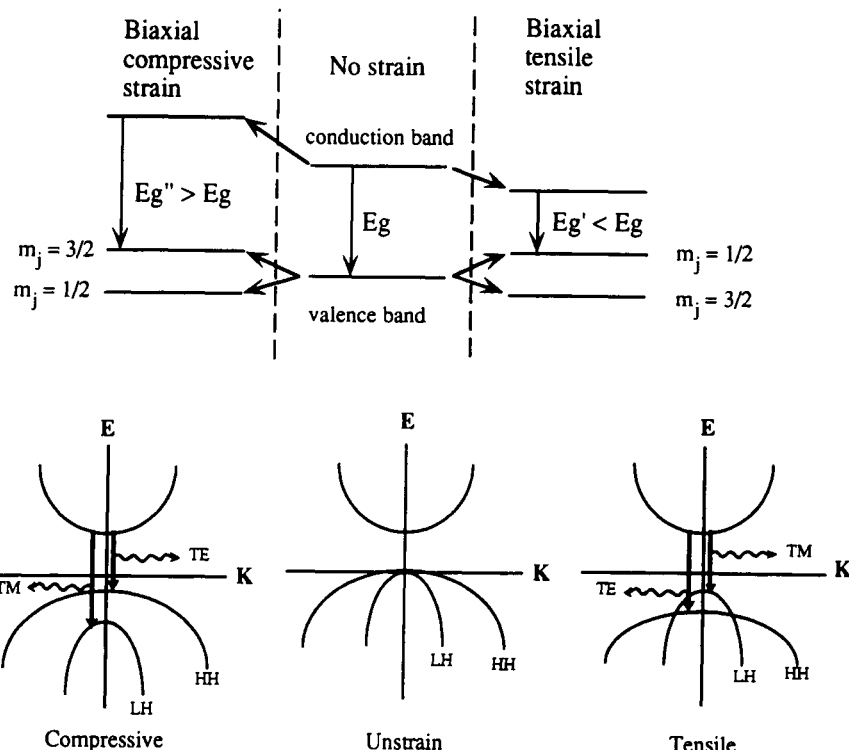
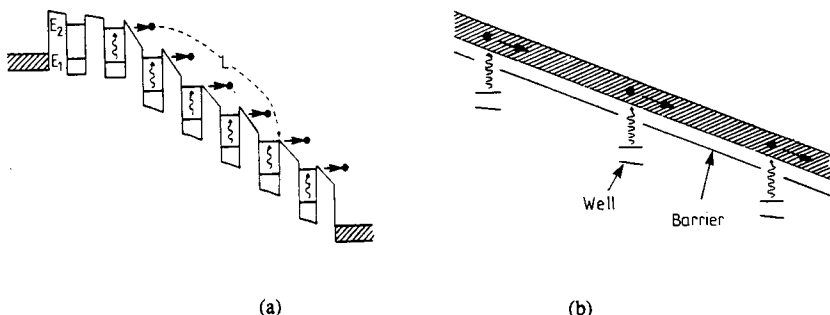


Figure 7.11 Changes in the energy diagram due to strain.

#### 7.2.4 Intersubband GaAs quantum well photodetectors

Another important technology of thermal infrared detection is the intersubband GaAs quantum well (QW) detectors. They have a number of potential advantages with respect to HgCdTe and InAsSb devices. For example, growth, processing, and passivation technologies of GaAs are more mature than those of HgCdTe. With monolithic integration of these detectors with GaAs field-effect transistors (FETs), charge-coupled devices and high-speed signal processing electronics are possible. In addition, GaAs substrates are larger, cheaper and of higher quality than CdTe substrates. Also, GaAs is more thermally stable than HgCdTe. Furthermore, compared to InAsSb-based detectors, GaAs QW devices can achieve higher quantum yields and reduce the tunnelling dark current. Finally, for GaAs QW technology, we also can vary the peak absorption wavelength over the atmospheric window region ( $8\text{--}14 \mu\text{m}$ ) by varying the GaAs well dimensions and composition, and the thickness of the wider-gap materials.

In some semiconductor systems (such as GaAs/GaInP, GaAs/AlGaAs, GaInAs/AlGaAs), band offsets are such that they induce potential wells for electrons and/or holes in the different bands. Progress in growth technology



**Figure 7.12** Energy band diagrams of quantum well photodetectors. Bound-to-bound transitions (*a*) and bound-to-extended transitions (*b*).

such as molecular beam epitaxy and metallorganic chemical vapour deposition allow us to obtain extremely thin films of semiconductors with a precision of one atomic layer. These wells are so thin that the electron and hole motion is quantized in the direction normal to the layers. The carrier energy is then distributed in different subbands, the bottoms of which are the one-dimensional quantized states  $E_i$  in the wells. Light can then induce transitions between these subbands. The resulting absorption is resonant between those quantized states (or bound states), with values as high as several  $10^3 \text{ cm}^{-1}$  (West and Egash 1985). In the GaAs/AlGaAs system, perfect lattice matching allows us to vary independently the thickness of the GaAs well and the potential height of the AlGaAs barrier in order to tune the transition towards the desired wavelength.

### (a) Photoconductive detectors

Levine *et al* at Bell Laboratories have constructed infrared detectors using intersubband transitions. In the first version, optical transitions occurred between the bound states in the well ( $E_1$  and  $E_2$ ) (Levine *et al* 1987). The structure is biased so that the electron on  $E_2$  has a much higher probability to tunnel out of the well than on  $E_1$  (figure 7.12(a)). However, because of the high electric field necessary to obtain this tunnelling mechanism, the dark current is very important in these photoconductors. In a more recent version, Levine and his coworkers have optimized their structure so that the level  $E_2$  is in the conduction band continuum of the AlGaAs barrier (extended state) and the transition is thus bound to extended (Levine *et al* 1988) (figure 7.12(b)). The dark current has sharply decreased. They have demonstrated a high-detectivity ( $1 \times 10^{10} \text{ cm Hz}^{1/2} \text{ W}^{-1}$  at 77 K) GaAs/GaAlAs quantum well infrared photodetector with a sensitivity peak at  $8 \mu\text{m}$ . Later, by lowering the quantum well barriers, they extended the responsivity peak out to  $10 \mu\text{m}$  with a sensitivity covering the spectral region from  $8\text{--}19 \mu\text{m}$  (Levine *et al* 1989, 1992, Levine 1993). The detectivity for  $\lambda = 19 \mu\text{m}$  increased from  $10^9 \text{ cm Hz}^{1/2} \text{ W}^{-1}$  at 50 K up to  $2 \times 10^{12} \text{ cm Hz}^{1/2} \text{ W}^{-1}$  at 20 K.

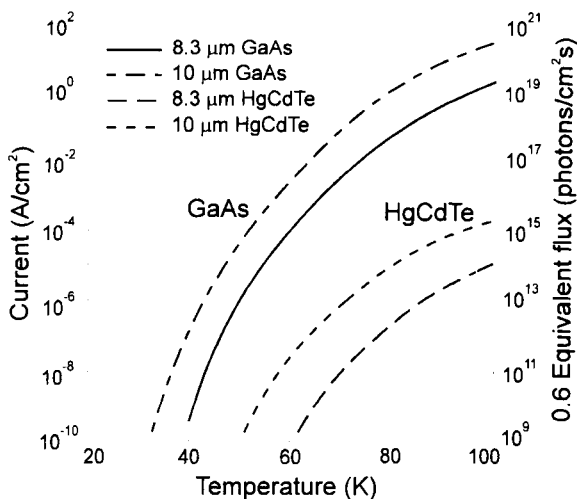


**Figure 7.13** Thermal generation current versus temperature for GaAs/AlGaAs multiple quantum wells and HgCdTe alloys at  $\lambda_c = 8.3 \mu\text{m}$  and  $10 \mu\text{m}$ . The assumed effective quantum efficiencies are  $\eta = 12.5\%$  and  $70\%$  for AlGaAs/GaAs and HgCdTe, respectively (Kinch and Yariv 1989).

Levine *et al* have also showed that thermionic-assisted tunnelling is a major source of dark current (Levine *et al* 1990) and, by increasing the quantum well barrier width from  $300 \text{\AA}$  to  $500 \text{\AA}$ , they have reduced the tunnelling dark current by an order of magnitude and increased the black-body detectivity. For a GaAs quantum well infrared detector having a cut-off wavelength of  $10.7 \mu\text{m}$ , they have achieved a black-body detectivity of  $1 \times 10^{10} \text{ cm Hz}^{1/2} \text{ W}^{-1}$  at 68 K. Hasnain *et al* demonstrated a GaAs/AlGaAs quantum well infrared photodetector with an optical gain of 8.1, showing that bound-to-continuum-state intersubband transitions can have a photoconductive gain much greater than unity similar to extrinsic photoconductors (Hasnain *et al* 1990). Hasnain's work also shows that the photocarrier lifetime is not limited by the transit time (i.e. photocurrent gain is not limited to  $\frac{1}{2}$ ). Thus, in general, carrier lifetimes or optical coupling can be increased with proper device optimization and design. In other words, quantum well infrared photodetectors (QWIPs) simultaneously having large quantum efficiencies and large gains can be expected and therefore lead to significantly improved detectivity.

In spite of achievements in GaAs/AlGaAs QWIPs technology, direct bandgap intrinsic semiconductors, as typified by HgCdTe, exhibit superior performance to the GaAs/AlGaAs superlattice at the same cut-off wavelength and temperature. Kinch and Yariv (1989) have presented an investigation of the fundamental physical limitations of individual GaAs/AlGaAs multiple quantum well IR detectors as compared to ideal HgCdTe photoconductors with cut-off

wavelengths  $\lambda_c = 8.3$  and  $10 \mu\text{m}$ . It appears that in the range 40 to 100 K the thermal generation rate is approximately five orders of magnitude smaller than the corresponding GaAs/AlGaAs superlattice (see figure 7.13). The dominant factor favouring HgCdTe in this comparison is the excess carrier lifetime, which for n-type HgCdTe is greater than  $10^{-6} \text{ s}$  at 80 K, compared to about  $10^{-11} \text{ s}$  for the GaAs/AlGaAs superlattice. In the superlattice the confined carriers are free to move within the plane (there is no energy gap separating confined from unconfined states), so the net carrier recombination rate is very high.

### (b) Focal plane arrays

It is well known that the detectivity  $D^*$  is not the relevant figure of merit for large arrays. One measure of performance of a thermal image system is the noise-equivalent temperature difference ( $\text{NE}\Delta T$ ), the temperature change of a scene required to produce a signal equal to the root mean square (RMS) noise. An array having  $D^* = 10^{10} \text{ cm Hz}^{1/2} \text{ W}^{-1}$  would achieve a very sensitive  $\text{NE}\Delta T = 0.01 \text{ K}$ . This would produce an excellent image, comparable to that of present arrays which are uniformly limited. Despite large research and development efforts, large photovoltaic HgCdTe focal plane arrays (FPAs) remain expensive, primarily because of the low yield of operable arrays. The low yield is due to the high incidence of electrically active defects and to the sensitivity of long-wavelength infrared (LWIR) HgCdTe devices to defects and surface leakage, which is a consequence of basic material properties. With respect to HgCdTe detectors, GaAs/AlGaAs quantum well devices have a number of potential advantages, including the use of standard manufacturing techniques based on mature GaAs growth and processing technologies (monolithic integration of these detectors with GaAs field effect transistors, CCDs and high-speed signal processing electronics is possible), highly uniform and well-controlled MBE and MOCVD growth on greater than 4 inch GaAs wafers, high yield and thus low cost, more thermal stability, and intrinsic radiation hardness.

At present, large  $128 \times 128$  and  $256 \times 256$  focal plane arrays (FPAs) with long-wavelength infrared imaging performance comparable to state of the art HgCdTe have been fabricated. Levine *et al* (1991) have presented thermal imaging data of hybrid  $128 \times 128$  GaAs/AlGaAs FPAs consisting of  $50 \times 50 \mu\text{m}^2$  photoconductors having peak response at  $\lambda_p = 9 \mu\text{m}$ . To improve the optical coupling, different types of grating are used (Levine 1993). The 99% yield of this array technology is a result of the excellent MBE growth uniformity (1%) in thickness and the mature processing technology. After correction, the measured non-uniformity of the array was better than 0.1%, and a  $\text{NE}\Delta T$  of 0.01 K was observed at 60 K. Recently, Kozlowski *et al* (1994) have reported a background limited  $128 \times 128$  GaAs/AlGaAs QWIP FPA with  $\lambda_p = 8.8 \mu\text{m}$  and  $> 99.4\%$  pixel operability at 35–40 K operating temperature. Typical  $\text{NE}\Delta T$ s of  $\approx 0.008 \text{ K}$  and detectivity  $> 4.0 \times 10^{10} \text{ cm Hz}^{1/2} \text{ W}^{-1}$  were measured at conventional imaging backgrounds at operating temperatures up to 65 K. For comparison, at 77 K, the operability of HgCdTe photodiodes is  $\geq 95\%$ , but at 40 K the sport population

limits the operability from 70 to 80%. The uniformity of QWIPs is higher and this characteristic is superior to HgCdTe photodiode arrays operated at 40 K.

GaAs QWIPs combine the advantages of PtSi Schottky barrier arrays (high uniformity, high yield, radiation hardness, large arrays with monolithically integrated electronics, low cost) with the advantages of HgCdTe (high quantum efficiency and long-wavelength response).

*(c) Advantages of intersubband GaAs quantum well detectors*

(i) *Wavelength range*: The intersubband spacing and thus the cut-off wavelength of the detectors can be tuned. Moreover, multicolour detectors may be realized in the same structure by growing multiquantum wells with different growth parameters.

(ii) *Spectral bandwidth*: The spectral bandwidth may also be tuned by choosing a bound-to-bound or a bound-to-extended transition. The spectral width of the bound-to-bound absorption peak is determined by the electron dephasing time in the subbands. This bandwidth is extended to larger values by choosing a bound-to-extended transition.

(iii) *Temporal bandwidth*: The intrinsic transient behaviour of the intersubband QW detectors is determined by the electron lifetime in the excited state ( $E_2$  for bound to bound, the conduction band of the wider-gap material for bound to extended). This lifetime, though not accurately known, is considerably faster than in HgCdTe detectors. The spectral bandwidth is thus controlled by the reading electronics and a time response smaller than 5 ns has been measured in a QW photoconductor.

(iv) *Integration capabilities*: The industrial skills developed in GaAs integrated circuits could allow the complete integration of detectors with the reading electronics. This would also enhance the reliability of the arrays. Finally, localized GaAs epitaxy on patterned silicon is developing very fast. GaAs materials on Si could allow the use of Si circuitry for reading electronics.

*(d) GaAs/GaInP p-type quantum well infrared photodetectors*

The presence of aluminium in the GaAlAs barrier layers suggests reliability and fabrication limitations due to oxidation. Therefore, in an effort to further the development of QWIPs, researchers have turned to other material systems such as GaAs/InGaAs, GaInAs/InP and GaAs/GaInP (Levine 1993). Compared to AlGaAs, GaInP presents several advantages which are expected to lead ultimately to better device performance (Omnès and Razeghi 1991). Dislocation and impurity motion is much lower than in AlGaAs because of the large difference in atomic size between indium and gallium. GaAs/GaInP should ultimately lead to better performance because of the better transport properties in direct bandgap semiconductors. Finally, surface and recombination velocities are lower than for AlGaAs, and selective etchants are available.

The first n-type GaAs/GaInP QWIPs have been fabricated by Gunapala *et al* (1990). They have determined the conduction band and valence band offsets to

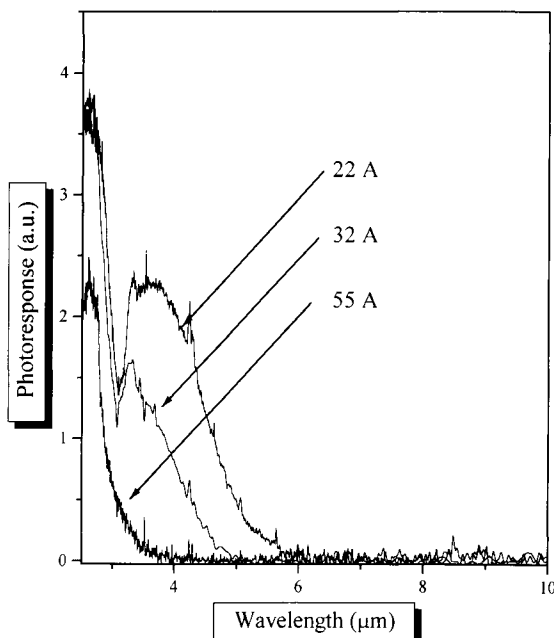


**Figure 7.14** Normalized photoresponse spectra for the three samples, measured under normal incidence illumination at 77 K (Hoff *et al* 1995).

be 221 meV and 262 meV respectively by comparing the theoretical absorption spectrum and the measured responsivity spectrum. An absorption coefficient of  $1900\text{ cm}^{-1}$  and quantum efficiency of 6.1% at  $8\text{ }\mu\text{m}$  have been obtained.

However, for n-type QWIPs, intersubband transitions are limited by dipole selection rules to couple only to radiation with a polarization component perpendicular to the quantum wells (i.e. normal incidence is forbidden). Since the pioneering work of Chang and James (1989), it has been known that, unlike n-type QWIPs, p-type QWIPs allow absorption of infrared radiation at normal incidence.

Hoff *et al* (1995) have fabricated p-type QWIPs from the GaAs/GaInP material system. The structures consist of 50 GaAs quantum wells doped with zinc with nominal thicknesses of 55, 32 and 22 Å, respectively. The barrier is an undoped lattice-matched  $\text{Ga}_{0.51}\text{In}_{0.49}\text{P}$  nominally 280 Å thick. This MQW structure is cladded between zinc-doped GaAs contact layers with thicknesses of 1  $\mu\text{m}$  (bottom) and 0.5  $\mu\text{m}$  (top). All the GaAs layers were doped with zinc to a net acceptor concentration of  $3.0 \times 10^{18}\text{ cm}^{-3}$ .

400  $\mu\text{m} \times 400\text{ }\mu\text{m}$  mesa detectors were fabricated using photolithography and wet chemical etching, and 100  $\mu\text{m} \times 100\text{ }\mu\text{m}$  square Au/AuZn electrodes were evaporated and alloyed. Figure 7.14 shows the normalized photoconductive response spectra for the three samples measured using a Fourier transform

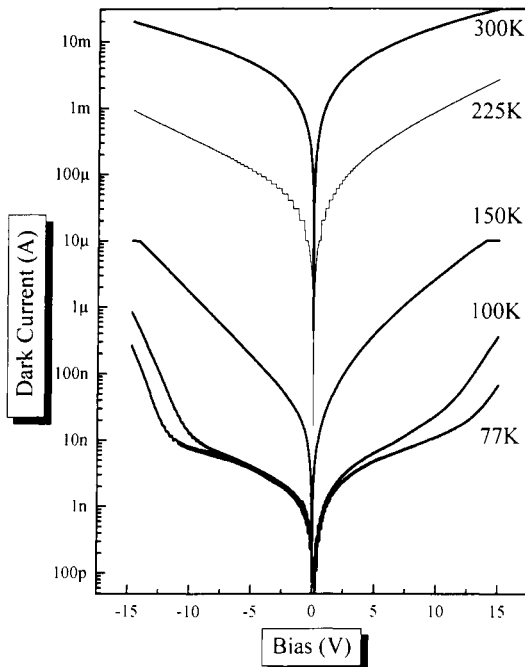


**Figure 7.15** Dark current versus bias for different temperatures between 77 K and 300 K for the 22 Å wide well sample (Hoff *et al.* 1995).

infrared spectrometer. The spectral response shifts towards longer wavelength as the well width is reduced, which is expected as the hole ground state is pushed up towards the top of the barrier. At 77 K, the current responsivity of the 22 Å wide well QWIP at 2.5  $\mu\text{m}$  wavelength was 0.5 mA W $^{-1}$  at 5 V bias and increased linearly to 2 mA W $^{-1}$  at 20 V bias. The current responsivity spectral shape and magnitude were found to be independent of temperature from 77 K up to 200 K. The photoconductive gain was rather small, about 0.18, which combined with the current responsivity of 0.5 mA W $^{-1}$  at 2.5  $\mu\text{m}$  yields an absorption quantum efficient of  $1.4 \times 10^{-3}$ . The estimated detectivities for this preliminary device at 2.5  $\mu\text{m}$  were  $9 \times 10^6$  cm Hz $^{1/2}$  W $^{-1}$  and  $8 \times 10^8$  cm Hz $^{1/2}$  W $^{-1}$  at 200 K and 77 K, respectively.

The dark current was measured versus bias voltage at temperatures between 77 K and 300 K. Figure 7.15 shows a set of measurements for the 22 Å wide well sample. At low bias, tunnelling is negligible and the dark current originates from thermionic emission above the top of the barrier. Arrhenius plots of the dark current measured at a fixed low bias of 0.1 V are shown in figure 7.16 for each of the three samples, which reveal respective activation energies of 235 meV, 300 meV, and 330 meV for the 22 Å, 32 Å and 55 Å wide well QWIPs. These activation energies correspond to wavelengths of 5.28  $\mu\text{m}$ , 4.13  $\mu\text{m}$ , and

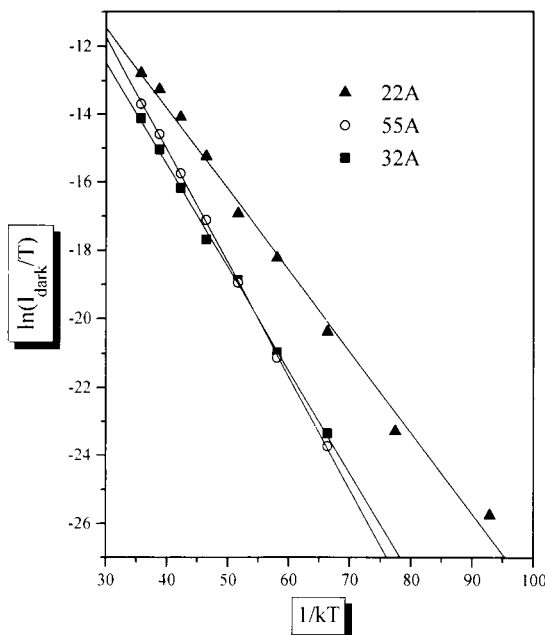


**Figure 7.16** Arrhenius plot of the normalized dark current versus inverse thermal energy for the three samples. The dark current values have been taken at a fixed bias value of 0.09 V (Hoff *et al* 1995).

3.75  $\mu\text{m}$ , respectively. These values closely correspond to the observed cut-off wavelengths in figure 7.14, which is expected because the Fermi level lies within a few meV of the heavy hole ground state.

Hoff *et al* (1995) have also performed theoretical calculations of the cut-off wavelength of GaAs/Ga<sub>0.51</sub>In<sub>0.49</sub>P and GaAs/Ga<sub>x</sub>In<sub>1-x</sub>P<sub>1-y</sub> QWIPs using a modified Kronig–Penney model and taking into account the effective mass discontinuity and the well/barrier interface, and reported parameters for GaAs and Ga<sub>0.51</sub>In<sub>0.49</sub>P (see Omnes and Razeghi 1991). The cut-off wavelength corresponds to the energy difference between the top of the barrier and the ground-state heavy-hole energy level. Figure 7.17 shows measured and calculated cut-off wavelengths as a function of well width for a 280 Å barrier. Theoretical predictions closely match experimental observations, and further show that extremely narrow GaAs quantum wells must be used in order to reach the 8–12  $\mu\text{m}$  atmospheric window. Such narrow wells can be difficult to manufacture with high yield. It can be seen that GaInAsP alloys should be used in order to reduce the valence band discontinuity thereby permitting operation at longer wavelength.

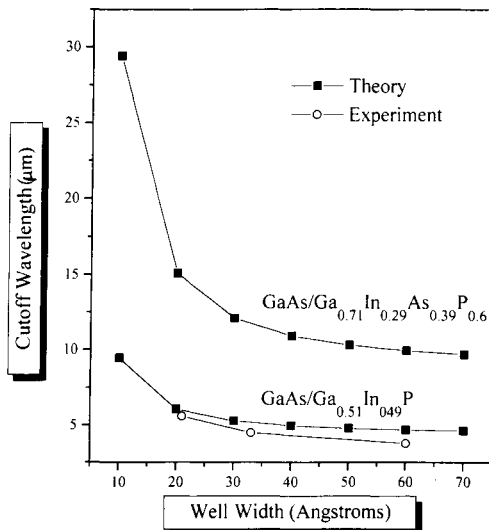


**Figure 7.17** Calculated cut-off wavelength of GaAs/Ga<sub>0.51</sub>In<sub>0.49</sub>P and GaAs/Ga<sub>x</sub>In<sub>1-x</sub>As<sub>y</sub>P<sub>1-y</sub> QWIPs versus quantum well width. Circles represent experimental data for the three GaAs/Ga<sub>0.51</sub>In<sub>0.49</sub>P QWIPs (Hoff *et al* 1995).

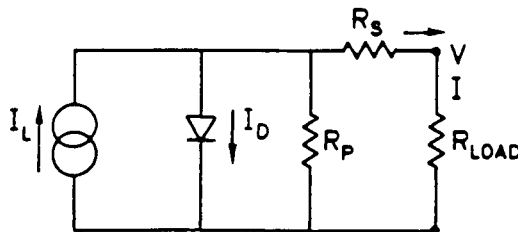


**Figure 7.18** Equivalent circuit of the solar cell.

### 7.3 SOLAR CELLS AND GaAs SOLAR CELLS

The invention of the p–n junction in 1949 formed the basis of the discovery of the crystalline Si solar cell. Since then, solar cells have been developed and produced with polysilicon, CdTe, and GaAs. Over 95% of solar cells in production are silicon based. Solar cells continue to be a critical technology for overcoming global environmental and energy problems.

The radiation reaching Earth is scattered and absorbed in the atmosphere and the intensity is dependent on the angle of incidence. Depending on this angle, the intensity can vary between 500 and 1000 W m<sup>-2</sup>. The power level of the solar spectrum in outer space, where there is no absorption of the radiation, is about 140 mW cm<sup>-2</sup>. This is commonly termed the air-mass-zero (AM0)

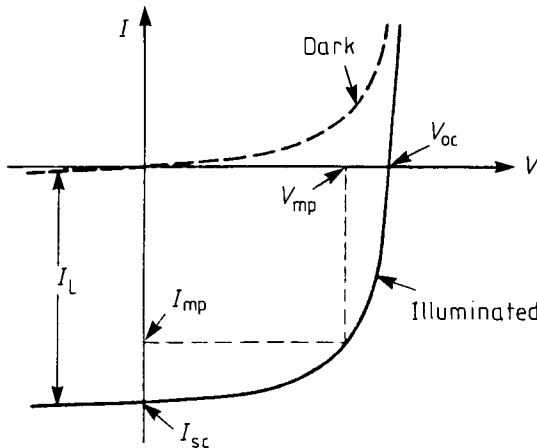


**Figure 7.19**  $I$ - $V$  characteristics of the circuit shown in figure 7.18 equivalent to a solar cell.

spectrum. On Earth at sea level, with the sun at zenith, the power level is reduced to nearly  $100 \text{ mW cm}^{-2}$ . This is the AM1 spectrum. At an angle of incidence that results in twice the path length through the atmosphere, the power level drops to approximately  $80 \text{ mW cm}^{-2}$  and the corresponding spectrum is termed AM2.

A solar cell is normally a p-n diode. When sunlight falls on the surface of a semiconductor, electron-hole pairs are generated which are then separated by the potential barrier across the p-n junction. Since the solar cell is a diode, the  $I$ - $V$  characteristics of a solar cell are given by

$$I_d = I_s(\exp(qV/kT) - 1) \quad (7.11)$$

where  $I_d$  is the diode current,  $I_s$  is the reverse saturation current and  $V$  is the applied voltage. Upon illumination, the diode equation is modified as

$$I = I_s(\exp(qV/kT) - 1) - I_L \quad (7.12)$$

where  $I_L$  is the photocurrent which opposes the dark current of the diode and  $I$  is the current through the diode. The equivalent circuit of a solar cell is shown in figure 7.18 and the corresponding  $I$ - $V$  characteristic is shown in figure 7.19. Upon illumination, the  $I$ - $V$  curve shifts down to the fourth quadrant and, hence, power can be extracted from the device. The most important parameter of a solar cell is the efficiency. The efficiency is defined as the ratio of the power output ( $P_m$ ) to the power input ( $P_{in}$ )

$$\text{efficiency} = P_m/P_{in}. \quad (7.13)$$

The output power of the solar cell can be written as  $P_m = I_{mp}V_{mp}$  where  $I_{mp}$  and  $V_{mp}$  are the current and voltage corresponding to the maximum power point.

$P_m$  can also be defined as  $P_m = I_{sc}V_{oc}\text{FF}$  where  $I_{sc}$  is the short-( $V = 0$ ), and  $V_{oc}$  is the open-circuit voltage ( $I = 0$ ), and FF is the fill factor which is defined as the measure of squareness. Then, the efficiency can be written as

$$\text{efficiency} = V_{oc}I_{sc}\text{FF}/P_{in}. \quad (7.14)$$

The solar cell parameters such as open-circuit voltage ( $V_{oc}$ ), short-circuit current ( $I_{sc}$ ), fill factor (FF) and efficiency can be calculated from figure 7.19. The open-circuit voltage ( $V_{oc}$ ) can be calculated by substituting  $I = 0$  and  $V = V_{oc}$  in equation (7.12) and rearranging terms

$$V_{oc} = (kT/q) \ln\{(I_{sc}/I_s) + 1\}. \quad (7.15)$$

The fill factor (FF) is defined as the measure of squareness, which is defined as

$$\text{FF} = (V_{mp}I_{mp})/(V_{oc}I_{sc}). \quad (7.16)$$

In solar cell conversion efficiency, it is important to note that photons which have an energy  $h\nu$  smaller than the semiconductor bandgap will not produce any electron–hole pairs. Also, photons with energy greater than the bandgap will produce electrons and holes with the same energy ( $E_g$ ) regardless of how large ( $h\nu - E_g$ ) is. The excess energy  $h\nu - E_g$  is simply dissipated as heat. Thus the solar cell efficiency depends quite critically on how the semiconductor bandgap matches with the solar energy spectra.

Two major paths have been identified from the past two decades of photovoltaic research and development to bring the cost of photovoltaic modules down to target values. The first is to achieve very high efficiencies using a variety of materials, such as Si, GaAs and related alloys. However, due to the high cost of material growth and fabrication, an alternative approach was developed. The alternative approach is to develop low-cost thin-film polycrystalline solar cells grown on an inexpensive substrate such as glass with moderate efficiencies. For the first approach, the metallorganic chemical vapour deposition technique has been widely used because of its advantages such as compositional control over a large area, suitability for large-scale production, reproducibility and versatility.

The properties of GaAs are well suited for photovoltaic applications. As a single-junction cell, its bandgap is almost ideally suited for the solar spectrum. GaAs is also more radiation resistant than Si, making it more attractive for space applications. The largest component of the production cost of high-efficiency compound semiconductor solar cells today is the cost of epitaxy. Almost all the III–V solar cells with record efficiencies to date have been produced by MOCVD as shown in table 7.1. The first GaAs cell with an efficiency of 22% was grown by LPE (Woodall and Hovel 1977), while early MOCVD-grown GaAs single-junction cell efficiencies were only in the range of 18–20% (Tobin *et al* 1988).

Cr/Au	
p <sup>+</sup> GaAs	AR coating
0.03 μm	p Al <sub>0.8</sub> Ga <sub>0.2</sub> As
0.50 μm	p GaAs 4×10 <sup>18</sup> cm <sup>-3</sup>
3-4 μm	n GaAs 2×10 <sup>17</sup> cm <sup>-3</sup>
1.0 μm	n <sup>+</sup> Al <sub>0.3</sub> Ga <sub>0.7</sub> 1×10 <sup>18</sup> cm <sup>-3</sup>
1.0 μm	n <sup>+</sup> GaAs 1×10 <sup>18</sup> cm <sup>-3</sup> Buffer layer
	n <sup>+</sup> GaAs substrate
	Au:Ge/Au back contact

**Figure 7.20** Structure of a high-efficiency (24.8%) GaAs solar cell (Tobin and Vernon 1989).

More recently, MOCVD has surpassed other techniques and a record efficiency of 24.8% (AM1.5) was achieved for a single-junction GaAs cell with the structure shown in figure 7.20 (Tobin and Vernon 1989). This enhanced performance was primarily attributed to an improved MOCVD process where an increased growth temperature from 720°C to 790°C resulted in reduced recombination in the Si-doped GaAs base layer as well as at the GaAs/AlGaAs interface. Even though the active epitaxial region is thin in the above cell design, the use of crystalline GaAs wafer makes it expensive for terrestrial applications. The challenge of growing high-quality crystalline GaAs films without consuming a GaAs wafer is being addressed by the cleavage of lateral epitaxial films for transfer (CLEFT) technique (McClelland *et al* 1980) and by heteroepitaxy of GaAs on Si and Ge substrates. In the CLEFT process, the MOCVD-grown single-junction epitaxial cell is cleaved from the substrate which is reused for epitaxial growth (Okamoto *et al* 1988, Yeh *et al* 1990). Efficiencies over 23% (AM1.5) for a 4 cm<sup>2</sup> total area have been obtained using the CLEFT process (McClelland *et al* 1990). An MOCVD-grown single-junction GaAs/Ge cell with an AlGaAs window has resulted in a 4 cm<sup>2</sup> cell efficiency of 24.3% (AM1.5) (Benner 1991) and a 16–36 cm<sup>2</sup> GaAs/Ge cell efficiency of 18% (AM0) (Chu *et al* 1991).

One of the first terrestrial products using III–V MOCVD is likely to be high-efficiency (> 30%) concentrator cells. In order to improve the efficiency beyond 25%, two- or four-terminal multijunction or tandem cells are being fabricated using MOCVD. Figure 7.21 illustrates the different configurations and concepts of tandem cells (Kazmerski 1989). MOCVD is best suited for these structures because of its controlled multilayer growth.

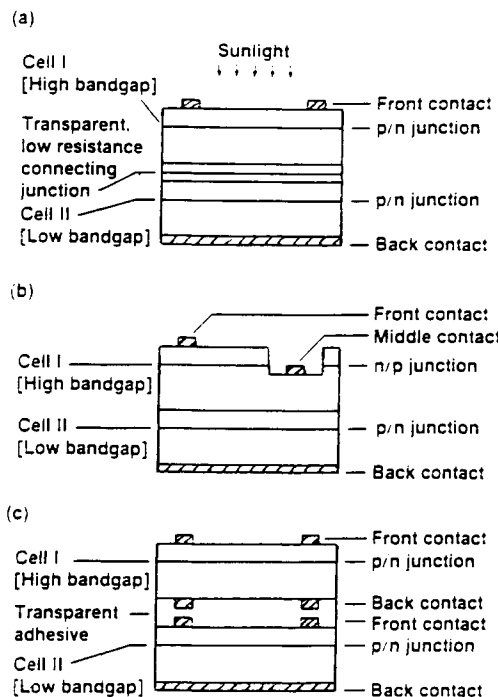


**Figure 7.21** Structure of the tandem cell. (a) Two-terminal, monolithic; (b) three-terminal, monolithic and (c) four-terminal, mechanically stacked (Kazmerski 1989).

It has been shown that for  $\alpha > 30\%$  efficient multijunction cell, the top cell should have a bandgap of  $\sim 1.75$  eV and the bottom cell bandgap should be  $\sim 1.1$  eV (Fan and Palm 1984). The first cell with efficiency greater than 30% was reported for a mechanically stacked MOCVD-grown GaAs cell on top of an Si cell. This four-terminal multijunction cell gave an efficiency of 31% at AM1.5 under a concentration of 347 suns (Gee and Virshup 1988). This record efficiency was surpassed recently by another multijunction structure with an efficiency of 34% at 100 suns concentration. This cell consists of an MOCVD-grown GaAs cell on a GaSb cell (Frass *et al.* 1990).

The best two monolithic multijunction solar cells to date were also grown by MOCVD. A two-terminal AlGaAs cell on a GaAs cell was the first monolithic tandem cell to produce one-sun efficiency of 27.6% under AM1.5 conditions (Macmillan *et al.* 1988). A GaInP/GaAs monolithic tandem cell was suggested as an alternative for AlGaAs/GaAs, and it produced a one-sun efficiency of 27.3% under AM1.5 conditions (Olson *et al.* 1988). This structure is very attractive because the GaInP cell efficiency can be improved further by optimizing the growth conditions. More recently, three-terminal monolithic multijunction cells, based on InP and GaInAs materials, gave an efficiency of 31.8% at a

**Table 7.1** High-efficiency, compound semiconductor solar cells.

Cell type	$V_{oc}$ (mV)	$J_{sc}$ (mA cm $^{-2}$ )	FF (%)	Efficiency (%)
<i>Single junction</i>				
GaAs/AlGaAs	1022	28.2	87.1	25.1
GaAs/Ge	1035	27.6	85.3	24.3
GaAs/Si	891	25.5	77.7	17.6
GaAs/GaInP	1038	28.7	86.4	25.7
<i>Multijunction</i> <i>/Concentrator</i>				
GaAs concentrator			28.7	
GaInAsP concentrator			27.5	
Monolithic InP/GaInAs (3 terminal)			31.8	
Monolithic GaInP/GaAs			27.5	
Monolithic AlGaAs/GaAs			27.6	
Stacked GaAs on GaSb			34.2	
Stacked GaAs on Si			31.0	
Stacked GaAs on GaInAsP			30.2	

concentration of 50 suns (Wanlass *et al* 1991). To reduce the cost of concentrator cells further, GaAs/Ge tandem cells are being investigated because of the low cost of lattice-matched Ge substrate (Wojtczuk *et al* 1990).

## REFERENCES

- Aoki T, Takahashi M, Suzuki M, Suno H, Uomi K, Kawano T and Takai A 1992 *IEEE Photon. Technol. Lett.* **4** 580
- Arch D K, Staudenmann J L and Faurie J P 1986 *Appl. Phys. Lett.* **48** 1588
- Bar-Joseph I, Goossen K W, Kuo J M, Kopf R F, Miller D A B and Chemla D S 1989 *Appl. Phys. Lett.* **55** 340
- Bastard G 1988 *Wave Mechanics Applied to Semiconductor Heterostructures* (Paris: Editions de Physique)
- Bastard G, Mendez E E, Chang L L and Esaki L 1983 *Phys. Rev. B* **28** 3241
- Benner J P 1991 *Proc. 22nd IEEE Photovoltaic Specialists Conf. (Las Vegas, 7-11 October)*
- Bethea C G, Levine B F, Lu P Y, Williams L M and Ross M H 1988 *Appl. Phys. Lett.* **53** 1629
- Bigan E, Allovon M, Carré M, Carencio A and Voisin P 1992a *IEEE J. Quantum Electron. QE-28* 214
- Bigan E, Allovon M, Carré M and Voisin P 1990 *Appl. Phys. Lett.* **57** 327

- Bigan E, Harmand J C, Allovon M, Carré M, Carenco A and Voisin P 1992b *Appl. Phys. Lett.* **60** 1936
- Bleuse J, Bastard G and Voisin P 1988a *Phys. Rev. Lett.* **60** 220
- Bleuse J, Voisin P, Allovon M and Quillec M 1988b *Appl. Phys. Lett.* **53** 2632
- Bubulac L O, Edwall D D, McConnel D, DeWames R E, Blazejewski E R and Gertner E R 1990 *Semicond. Sci. Technol.* **5** S45
- Carenco A 1987 Semiconductor waveguides in III-V materials for integrated optics *Proc. 4th Eur. Conf. on Integrated Optics (ECIO 87) (Glengow, 1987)* and references therein
- Chang Y C and James R B 1989 *Phys. Rev. B* **39** 12672
- Chu C, Iles P, Yoo H, Reed B and Krogen J 1991 *Proc. 22nd IEEE Photovoltaic Specialists Conf. (Las Vegas, 7-11 October)*
- Devaux F, Bigan E, Ovgazzaden A, Pierre B, Hvet F, Carré M and Carenco A 1992 *IEEE Photon. Technol. Lett.* **4** 720
- Doll B, Bruder M, Wendler J, Ziegler J and Maier H 1990 *4th Int. Conf. Advanced Infrared Detectors and Systems* (London: IEE) p 120
- Druilhe R, Katty A and Triboulet R 1990 *4th Int. Conf. Advanced Infrared Detectors and Systems* (London: IEE) p 20
- Elliott T, Gordon N T, Hall R S, Philips T J, Jones C L, Matthews B E, Maxey C D and Metcalfe N E 1994 *Proc. SPIE* **2269** 618
- Esaki L 1986 *IEEE J. Quantum Electron.* **QE-22** 1611
- Esaki L and Tsu R 1970 *IBM J. Res. Dev.* **14** 61
- Fan J C C and Palm B J 1984 *Solar Cells* **12** 401
- Frank F C and van der Merwe J H 1949 *Proc. R. Soc. A* **198** 205
- Franz W 1958 *Naturf. Z.* **13** 484
- Frass L M, Avery J E, Martin J, Sundaram V S, Givard G, Dinh V T, Davenport T M, Yerkes J W and O'Neill J 1990 *IEEE Trans. Electron Devices* **ED-37** 443
- Gee J M and Virshup G F 1988 *Proc. 20th IEEE Photovoltaic Specialists Conf.* p 754
- Gunapala S D, Levine B F, Logan R A, Tanbun-Ek T and Humphrey D A 1990 *Appl. Phys. Lett.* **57** 1802
- Hasnain G, Levine B F, Gunapala S and Chand N 1990 *Appl. Phys. Lett.* **57** 608
- Hecht E 1987 *Optics* (New York: Addison-Wesley)
- Hoff J, Bigan E, Brown G J and Razeghi M 1995 *Proc. SPIE* **2397** 445
- Irvine J C 1992 *Proc. SPIE* **1735** 92
- Irvine S J C, Gertner E R, Bubulac L O, Gill R V and Edwall D D 1991 *Semicond. Sci. Technol.* **6** C15
- Johnson S M, Vigil J A, James J B, Cockrum C A, Konkel W H, Kalisher M H, Risser R F, Tung T, Hamilton W J, Ahlgren W L and Myrosnyk J M 1993 *J. Electron. Mater.* **22** 835
- Kato H, Iguchi N, Chika S, Nakayama M and Sano N 1986 *J. Appl. Phys.* **59** 588
- Kato T, Sasoki T, Komatsu K and Mito I 1992 *Electron. Lett.* **28** 253
- Kazmerski L L 1989 *Int. Mater. Rev.* **34** 185
- Keldysh L V 1958 *Sov. Phys.-JETP* **7** 788
- Kinch M A and Yariv A 1989 *Appl. Phys. Lett.* **55** 2093
- Koch T L and Bowers J E 1984 *Electron. Lett.* **20** 1038
- Koyama F and Iga K 1988 *IEEE J. Lightwave Technol.* **6** 87
- Kozlowski L J, Arias J M, Williams G M, Vural K, Cooper D E, Cabelli S A and Bruce C 1994 *Proc. SPIE* **2274** 93
- Kurtz S R, Dawson L R, Zipperian T E and Lee S R 1988 *Appl. Phys. Lett.* **52** 1581
- Kurtz S R, Dawson L R, Zipperian T E and Whaley R D 1990 *IEEE Electron Devices Lett.* **11** 54
- Levine B F 1993 *J. Appl. Phys.* **74** R1
- Levine B F, Bethea C G, Glogovsky K G, Stay J W and Leibenguth R E 1991 *Semicond.*

- Sci. Technol.* **6** C114
- Levine B F, Bethea C G, Hasnai G, Shen V O, Pelve E, Abbot R R and Hsieh S J 1990 *Appl. Phys. Lett.* **56** 851
- Levine B F, Bethea C G, Hasnai G, Walker J and Malik R J 1988 *Electron Lett.* **24** 747
- Levine B F, Choi K K, Bethea C G, Walker J and Malik R J 1987 *Appl. Phys. Lett.* **50** 1092
- Levine B F, Hasnain G, Bethea C G and Chand N 1989 *Appl. Phys. Lett.* **54** 2704
- Levine B F, Zussman A, Kuo J M and de Jong J 1992 *J. Appl. Phys.* **71** 5130
- Macmillan H F, Hamaker H C, Virshup G F and Werthen J E 1988 *Proc. 20th IEEE Photovoltaic Specialists Conf.* p 48
- Matthews J W 1975 *Epitaxial Growth* (New York: Academic) ch 8 p 559
- McClelland R W, Bozler C O and Fan J C C 1980 *Appl. Phys. Lett.* **37** 560
- McClelland R W, Dingle B D, Gale R P and Fan J C C 1990 *Proc. 21st IEEE Photovoltaic Specialists Conf.* p 168
- Mendez E E, Agullo-Rueda F and Hong J M 1988 *Phys. Rev. Lett.* **60** 2426
- Miller D A B, Chemla D S, Damen T C, Gossard A C, Wiegmann T H, Wood C A and Burrus C A 1984 *Appl. Phys. Lett.* **45** 13
- Miller D A B, Chemla D S, Damen T C, Gossard A C, Wiegmann T H, Wood C A and Burrus C A 1985 *Phys. Rev. B* **32** 1043
- Miller D A B, Chemla D S, Eilenberger D J, Smith P W, Gossard A C and Tsang W T 1982 *Appl. Phys. Lett.* **41** 679
- Mullin J B, Irvine S J C, Gies J and Ryple A 1988 *J. Crystal Growth* **88** 161
- Okamoto H, Kadota Y, Watanabe Y, Fukuda Y, Oh'Hara T and Ohmachi Y 1988 *Proc. 20th IEEE Photovoltaic Specialists Conf.* p 475
- Olson J M, Kurtz S R and Kibber A E 1988 *Proc. 20th IEEE Photovoltaic Specialists Conf.* p 777
- Olson J M, Kurtz S R, Kibber A E and Faine P 1989 *Appl. Phys. Lett.* **55** 1208
- Omnes F and Razeghi M 1991 *Appl. Phys. Lett.* **59** 1034
- Rao M, Caine E, Kroemer H, Long S and Babic D 1987 *J. Appl. Phys.* **61** 643
- Razeghi M, Defour M, Omnes F, Dobers M, Vieren J P and Guldner Y 1989 *Appl. Phys. Lett.* **55** 457
- Razeghi M, Maurel P, Omnes F, Amor S B, Dmowski L and Portal J C 1986 *Appl. Phys. Lett.* **48** 1267
- Schulman J N and McGill T C 1979 *Appl. Phys. Lett.* **34** 663
- Smith D L, McGill T C and Schulman J N 1983 *Appl. Phys. Lett.* **43** 180
- Specht L T, Hoke W E, Oguz S, Lemonias P J, Kreismanis V G and Korenstein R 1986 *Appl. Phys. Lett.* **48** 417
- Summers C J, Wagner B K, Benz R G and Conte Matos A 1994 *Proc. SPIE* **2021** 56
- Tobin S P and Vernon S M 1989 *4th Int. Photovoltaic Science Eng. Conf. (Sydney, Australia)* p 47
- Tobin S P, Vernon S M, Bajgar C, Geffory L M, Keavney C J, Sanfacon M M and Haven V E 1988 *Solar Cells* **24** 103
- Tung T, DeArmond L V, Herald R F, Herning P E, Kalisher M H, Olson D A, Risser R F, Stevens A P and Tighe S J 1992 *Proc. SPIE* **1735** 109
- Wakita K, Kotaka I, Asai H, Okamoto M, Kondo Y and Naganuma M 1992 *IEEE Photon. Technol. Lett.* **4** 16
- Wakita K, Kotaka I, Mitomi O, Asai H, Kawamura Y and Naganuma M 1990 *IEEE J. Lightwave Technol.* **LT-8** 1027
- Wanlass M W, Coutts T J, Ward J S, Emery K A, Gessert T A and Osterwald C R 1991 *Proc. 22nd IEEE Photovoltaic Specialists Conf. (Las Vegas, 7–11 October)*
- Watanabe M O and Ohba Y 1986 *J. Appl. Phys.* **60** 1032
- Weiner J S, Miller D A B, Chemla D S, Damen T C, Burrus C A, Wood T H, Gossard

- A C and Wiegmann W 1985 *Appl. Phys. Lett.* **47** 1148  
West L C and Egash S J 1985 *Appl. Phys. Lett.* **46** 1156  
Wojtczuk S J, Tobin S P, Keavney C J, Bajgar C J, Sanfancon M M, Geoffroy L M,  
Dixon T M, Vernon S M, Scofield J D and Ruby D S 1990 *IEEE Trans. Electron  
Devices* **ED-37** 455  
Wood T H, Burrus C A, Miller D A B, Chemla D S, Damen T C, Gossard A C and  
Wiegmann W 1984 *Appl. Phys. Lett.* **44** 16  
Wood T H, Burrus C A, Tucker R S, Weiner J S, Miller D A B, Chemla D S, Damen T  
C, Gossard A C and Wiegmann W 1985 *Electron. Lett.* **21** 693  
Wood T H, Pastalan J Z, Burrus C A Jr, Johnson B C, Miller B I, de Miguel J L, Koren  
U and Young M G 1990 *Appl. Phys. Lett.* **57** 1081  
Woodall J M and Hovel H J 1977 *Appl. Phys. Lett.* **30** 492  
Yariv A and Yeh P 1984 *Optical Waves in Crystals* (New York: Wiley)  
Yeh Y C M, Cheng C, Ho F and Yoo H 1990 *Proc. 21st IEEE Photovoltaic Specialists  
Conf.* p 79  
Zucker J E, Jones K L, Toung M G, Miller B I and Koren V 1989 *Appl. Phys. Lett.* **55**  
2280  
Zucker J E, Jones K L, Wegener M, Chang T Y, Sauer N J, Divino M D and Chemla D  
S 1991 *Appl. Phys. Lett.* **59** 201  
Zucker J E, Wegener M, Jones K L, Chang T Y, Sauer N and Chemla D S 1990 *Appl.  
Phys. Lett.* **56** 1951

---

## GaAs-based Lasers

### 8.1 INTRODUCTION

Semiconductor lasers based on GaAs and related materials are the subject of a vast part of the research in this field. The first suggestion to use semiconductors as laser materials was expressed by Aigrain as early as 1958. Electroluminescence spectrum narrowing in GaAs at 77 K observed by Nasledov *et al* in 1962 as experimental evidence of high-efficiency radiative recombination gave a strong impulse to the laser-oriented activity. The first homojunction semiconductor lasers were created using GaAs in 1962 almost simultaneously by three groups of American scientists (Hall *et al* 1962, Nathan *et al* 1962 and Quist *et al* 1962). In the same period, Holonyak and Bevacqua (1962) reported lasing in GaAsP. Those early devices were only able to operate at low temperatures due to the very high threshold current density. The solution to this problem was proposed in 1963 by Alferov and Kazarinov (1963) and soon after that by Kroemer (1963). The idea was to use double heterostructures to ensure electrical and optical confinement and reduce the threshold current. At that time the possibility of efficient carrier injection through a heterojunction still seemed to be very vague because of the extremely high carrier recombination rate on the interface of polycrystalline heterojunctions. However, by 1969 Kressel and Nelson (1969), Panish *et al* (1969) and Hayashi *et al* (1969) successfully applied liquid phase epitaxy to obtain laser-quality heterojunctions in GaAs-AlGaAs with a decreased threshold current density. A breakthrough was made in 1970 when Alferov's group achieved continuous wave operation of a GaAs-AlGaAs double-heterostructure laser at room temperature (Alferov *et al* 1971), again in GaAs-based material. A breathtaking competition took place at that time as witnessed by Casey and Panish (1978), impressive by its scientific significance as well as by emotional strength.

Studies of heterostructure lasers in the very attractive GaAs-AlGaAs system of solid solutions and other related materials stimulated the development of new growth techniques for producing ultrathin layers and multilayer structures: molecular beam epitaxy (MBE) and metallorganic chemical vapour deposition (MOCVD). Extensive research resulted in obtaining a miscellany of new laser

materials and in designing even more efficient types of laser structure. Major advances have been made in achieving such parameters as low threshold current density and absolute threshold current, high output power, stable single longitudinal and transverse mode operation and a broad-bandwidth frequency response. A wide range of applications arose for these new devices: high-power lasers for optical pumping of solid-state laser crystals, fast-switching and high-coherence single-mode lasers for high-data-rate optical communications, surface-emitting and ultralow-threshold lasers for optical interconnects in integrated circuits and many others.

Since the first attempts to use MOCVD for the growth of laser heterostructures this technique has demonstrated an unimpaired ability to produce high-quality materials for all kinds of application. MOCVD-grown GaAs-based lasers cover wavelengths ranging from mid-infrared in Sb-containing solid solutions to visible AlGaInP devices. Its flexibility and potential to yield a broad range of growth rates resulted in layers featuring thicknesses from tens of microns down to several nanometres. Planar structures containing quantum wells with atomically flat interfaces, superlattices, strained or graded-index layers were successfully grown by MOCVD. Furthermore, MOCVD proved its efficiency in producing a variety of laser devices by overgrowth and epitaxy on patterned substrates. One aspect of the importance of MOCVD is strongly enhanced by the possibility of large-scale production by simultaneous growth on several substrates in one process. Parameter variation as low as 2% has been observed across wafers 3 inches in diameter.

## 8.2 BASIC PHYSICAL CONCEPTS

The fundamental principles of semiconductor laser operation are briefly discussed in this chapter. Some useful references are given where a more detailed discussion of the subject may be of interest. We also indicate the most important problems arising when specific applications impose requirements on the basic characteristics of laser devices.

### 8.2.1 Optical gain and feedback

A semiconductor laser is a source of highly coherent radiation generated by recombining carriers, excited electrons and holes, in the semiconductor medium with optical gain and feedback.

Free electrons pumped from valence to conduction bands by either electric current or external irradiation may recombine with a hole spontaneously, emitting a random photon (figure 8.1(a)) or undergo stimulated emission. In this latter process an electron interacts with a stimulating photon and recombines giving birth to another photon of identical energy and phase (figure 8.1(b)). If pumping makes the electron concentration in the conduction band high enough to

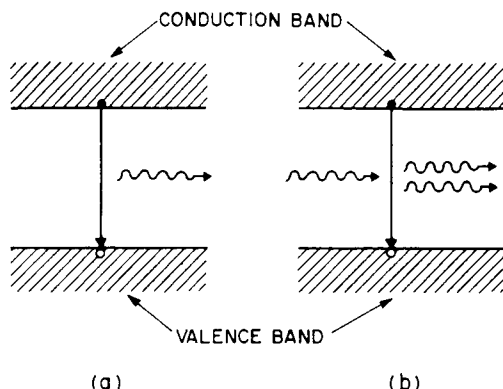


**Figure 8.1** Schematic illustration of (a) spontaneous emission, and (b) stimulated emission processes wherein an electron-hole pair recombines to generate a photon. In the case of stimulated emission the two outgoing photons match in their frequency and direction of propagation.

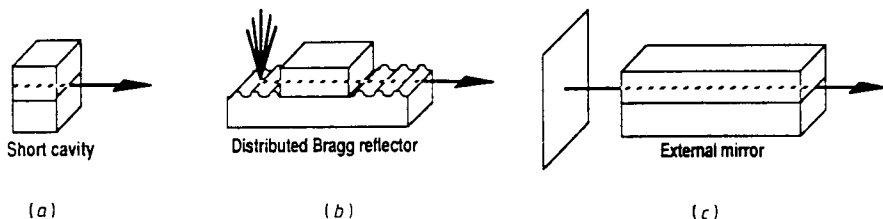


**Figure 8.2** Examples of single-mode lasers.

equalize the probabilities of valence band absorption and stimulated emission, the medium becomes transparent. In this situation light amplification due to stimulated emission neutralizes absorption loss. The transparency condition corresponds to zero optical gain. Under stronger pumping more and more electrons are excited to the conduction band, resulting in a population inversion, when photons stimulate recombination from the conduction band rather than become absorbed by valence-band electrons. A positive optical gain is thus achieved (Sze 1981).

In order for the gain medium to lase it should be confined in a resonator cavity providing optical feedback, that is restricting the range of amplified wavelengths to a limited number of resonant modes. A semiconductor crystal with mirror-like facets perpendicular to propagating beam is a Fabry-Pérot resonator by itself (figure 8.2(a)). Otherwise it may be integrated with Bragg mirror gratings (figure 8.2(b)) or equipped with an external mirror (figure 8.2(c)) (Buus 1991).

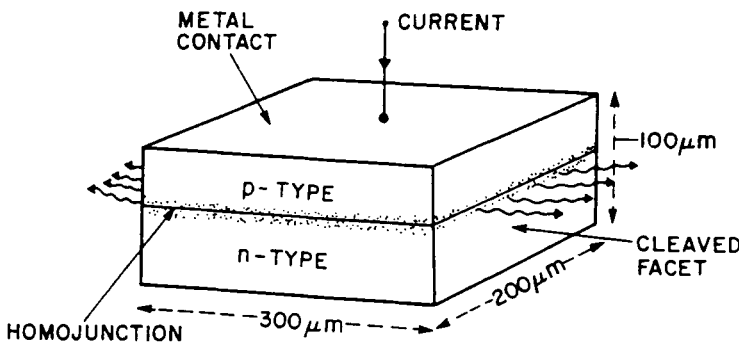


**Figure 8.3** Schematic illustration of a homostructure semiconductor laser with its typical physical dimensions.

### 8.2.2 Threshold current

Let us consider a semiconductor crystal with a p–n junction plane and cleaved mirror facets (figure 8.3). Under forward bias voltage, electrons are injected into the p-region and holes into the n-region thus providing the population inversion necessary for achieving optical gain. However, lightwaves resonating in the Fabry–Pérot cavity are absorbed by free carriers and scattered on defects and optical inhomogeneities. Due to the limited reflectivity of the mirrors some part of the radiation comes out of the resonator or becomes absorbed. All this results in internal and mirror losses. The optical field is just partly confined within the excited region, while some fraction of the light propagates outside the gain layer adjacent to the p–n junction plane. The threshold condition for laser light emission to occur is that the gain should be high enough to compensate for all losses through the length of the cavity during one period of oscillation. A fundamental equation for the threshold gain can be derived from this consideration:

$$g_{\text{th}} = 1/G(\alpha_i + (1/L) \ln(1/R)) \quad (8.1)$$

where  $G$  is the optical confinement factor,  $\alpha_i$  is the internal loss,  $L$  is the cavity length and  $R$  is the reflectivity of the end mirrors (Casey and Panish 1978).

The pumping electric current providing the threshold gain is a threshold current, characterizing the efficiency of the entire laser device. Minimization of the threshold current is one of the key issues to achieve high-speed modulation of laser output as long as this value limits the current rise and drop necessary to switch the device on and off.

It is convenient to describe the quality of a planar laser structure in terms of its threshold current density rather than its absolute threshold current. Since a laser bar is long and broad enough to neglect all mirror and lateral effects, the threshold current per unit area depends exclusively on the specific quality of the wafer. A minimal threshold current density is highly desirable in most

cases. It results in low Joule heating of the laser device and therefore is crucial for high-power applications.

A useful expression for the threshold current density for a uniformly excited GaAs layer at room temperature is given by Casey and Panish (1978)

$$J_{\text{th}}(\text{A cm}^{-2}) = d/\eta(4.5 \times 10^3 + 20g_{\text{th}}). \quad (8.2)$$

Here  $d$  is the layer thickness in microns and  $\eta$  is the internal quantum efficiency given by the ratio of the radiative recombination rate to the total recombination rate. This important parameter is the number of photons emitted in the medium per electron injected. It summarizes the influence of intrinsic features of the material (Auger recombination and spontaneous emission probabilities), extrinsic characteristics (concentration of defect centres where non-radiative recombination occurs) and pumping level (carrier concentration) (Agrawal and Dutta 1986). An internal quantum efficiency close to 100% may be achieved in laser-quality GaAs.

Another useful quantity describing laser operation is the differential (or external) quantum efficiency taking into account all the losses in the laser structure. It is given by the ratio of the surplus in coherently emitted power to the rise of pumping power required to give this surplus. In other words, it is a fraction of the number of electrons that may be converted into stimulated emission if injected by increasing the driving current

$$\eta_d = e \Delta P_{\text{out}} / h\nu \Delta I. \quad (8.3)$$

At threshold  $\eta_d$  is related to the internal quantum efficiency by

$$1/\eta_d = (1/\eta)(1 + \alpha_i L / \ln(1/R)). \quad (8.4)$$

MOCVD-grown semiconductor lasers may exhibit an external quantum efficiency above 80% (Wagner *et al* 1988).

### 8.2.3 Spectrum of longitudinal modes

A sequence of equidistant wavelengths (longitudinal modes) satisfies a resonant condition in the laser structure shown in figure 8.4. For a typical resonator cavity length of several hundred microns the wavelength separation is small enough with respect to the range of photon energies where gain is higher than loss. This permits a number of modes to be amplified and results in a multimode lasing spectrum. At the same time, single-longitudinal-mode operation is required for many important applications, primarily for optical fibre communication. Different modes travel with different velocities through the fibre and the optical pulse broadens thus limiting the data transmission rate (Buus 1991).

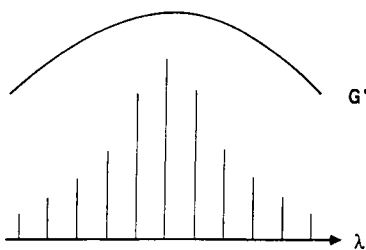


**Figure 8.4** Schematic of a laser spectrum.

#### 8.2.4 Carrier and light confinement

In order to achieve the high gain necessary for lasing, both excited carriers and resonant lightwaves should be spatially confined in some limited volume (active region). Poor optical confinement results in a low value of  $G$  and high loss, while excited carriers leaking from the gain area can prevent the build-up of a population inversion. These effects are the reason for the high threshold current densities observed in homostructure lasers like the one shown in figure 8.3. Efficient optical and electrical confinement may be ensured by placing the narrow-bandgap active region between wider-bandgap cladding regions having lower refractive index. In this case the bandgap difference provides a potential barrier to confine injected carriers as illustrated in figure 8.5. At the same time, light traveling through the high-refractive-index active layer is guided by the cladding layers due to total internal reflection. Figure 8.6 presents this kind of sandwich structure, called a dielectric waveguide. The optical confinement factor  $G$  in equation (8.1) refers to transverse waveguiding in the plane normal to the p-n junction. Carrier confinement between p- and n-cladding layers in figure 8.5 also prevents them from leakage in the direction normal to the junction plane. In this way a low threshold current density may be achieved. For a low total threshold current to be obtained, carriers and light should also be confined in the lateral direction parallel to the junction plane. This requires formation of a stripe contact locating the current flow to the finite recombination (active) region (see figure 8.7). A well defined gain region may provide a refractive index step sufficient for optical confinement (gain guiding). Otherwise a stripe geometry active region may be surrounded by higher-index cladding layers to form a dielectric waveguide similar to that in figure 8.6 (index guiding). Near-and far-field patterns of the laser beam may be tailored by varying the stripe width and waveguiding refractive index step as shown in figure 8.8(a) and (b) (Yonezu *et al* 1973). A variety of laser device structures were designed on the way to obtaining the most efficient transverse and lateral confinement. A profound discussion of the physical aspects of this problem and basic device concepts can be found in Casey and Panish (1978).

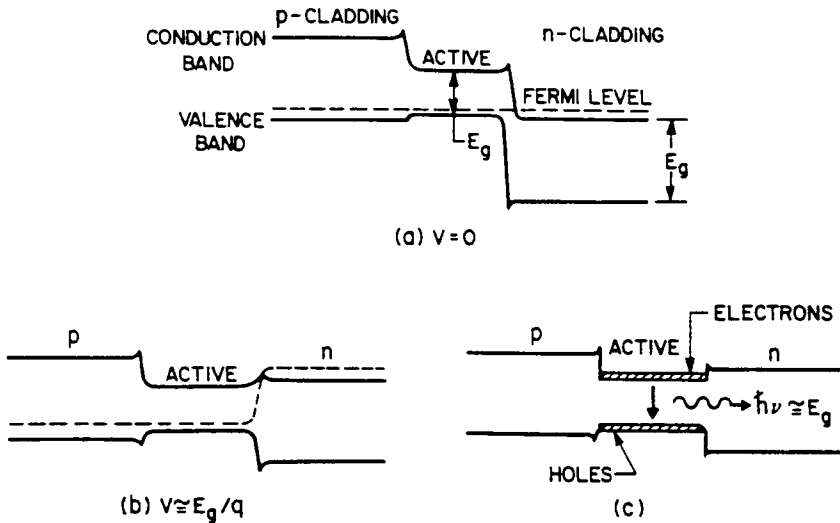


**Figure 8.5** Energy band diagram of a double-heterostructure semiconductor laser at (a) zero bias and (b) forward bias. (c) The bandgap discontinuities at the two heterojunctions help to confine electrons and holes inside the active region, where they recombine to produce light.

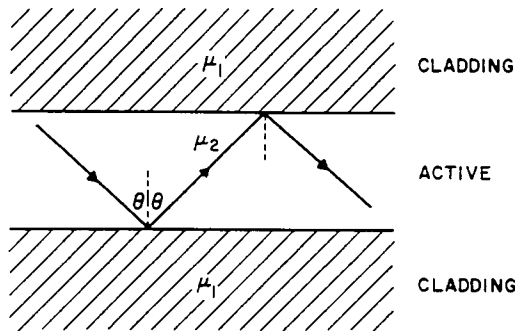


**Figure 8.6** Dielectric waveguiding in a heterostructure semiconductor laser. The relatively higher refractive index  $\mu_2 > \mu_1$  of the active layer allows total internal reflection to occur at the two interfaces for angles such that  $\sin \theta > \mu_1/\mu_2$ .

### 8.2.5 High-speed modulation

Since high-data-rate transmission is one of the fields where semiconductor lasers are most extensively applied, modulation of laser output is of great interest. A semiconductor laser can be directly modulated by applying a periodical

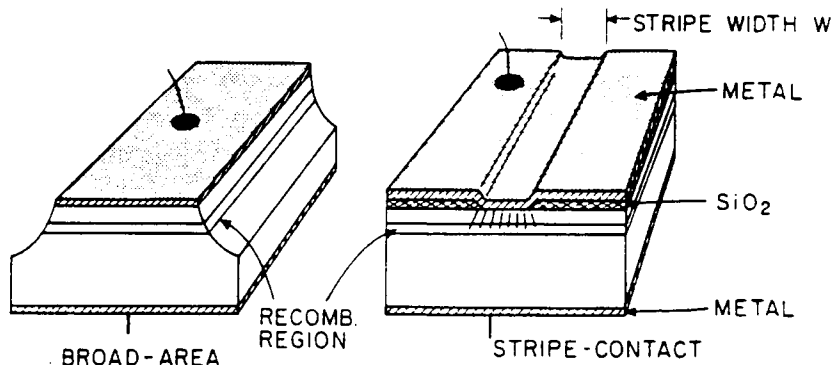


**Figure 8.7** Stripe contact: a simple way to confine the recombination region in the lateral direction (Kressel 1980).

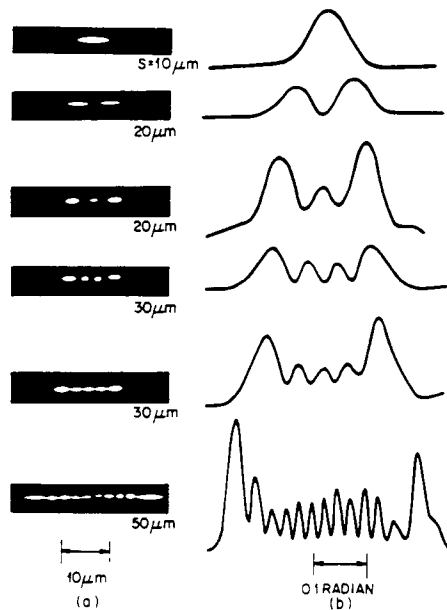


**Figure 8.8** Modes along the junction planes as a function of stripe width  $S$  for planar stripe DH lasers. (a) Near-field patterns. (b) Far-field patterns (Yonezu *et al* 1973).

or pulsing driving current. The modulation efficiency is characterized by the frequency-dependent transfer function  $H(\omega)$ , representing a change in external quantum efficiency due to impaired device response

$$\eta_d(\omega) = H(\omega)\eta_d(0). \quad (8.5)$$

A typical transfer function is shown in figure 8.9 in units of dB, that is  $10 \log H(\omega)$ . The range of frequencies where the response function is higher

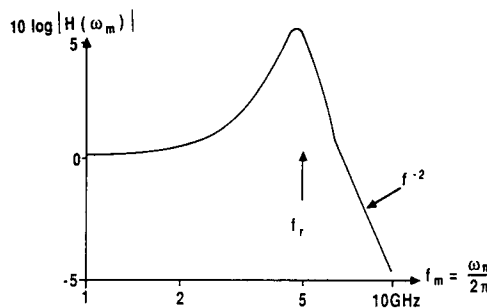


**Figure 8.9** Amplitude modulation transfer function as a function of the modulation frequency (Agrawal and Dutta 1986).

than  $-3$  dB is usually referred to as the modulation bandwidth. It is limited by the delay time between the pumping current rise and light pulse onset and by a transitional period when relaxation oscillations occur. Parasitic electrical effects of the device structure as well as of the driving circuit also decrease the modulation bandwidth. For further details see Buus (1991) and also a review by Arnold *et al* (1982).

### 8.2.6 Quantum size effect

As soon as the active layer of a semiconductor laser is made very thin (of the order of the de Broglie wavelength for the carrier), it acts like a two-dimensional potential well for carriers and quantum size effects are manifested in carrier motion in the  $z$ -direction perpendicular to the layer plane. That is, instead of a continuum of conduction band states available for electrons in bulk material, these are confined to a series of discrete levels separated from the band edge by the energies  $E_n = n^2 h^2 / 8m^* L_z^2$  for the ideal case of an infinitely deep well. Bound-state energies depend on the well depth (width) (see figure 8.10). Quantization effects resulted in a number of consequences which proved to be very advantageous for laser applications. First of all, with the volume of the active layer being small in comparison with the DH laser, the transparency current necessary to reach population inversion is proportionally lower. Free-carrier absorption contributes less to the internal losses for exactly the same reason. Therefore, quantum well lasers operate at low threshold current densities, high differential quantum efficiencies and narrow spectral linewidth. The density of states in a quantum well demonstrates a steplike energy dependence as shown in figure 8.11. It rises rapidly when reaching the first energy level and so does the concentration of injected carriers taking part in stimulated emission. This consideration implies a high differential optical gain which yields a more abrupt optical pulse front and permits improved modulation properties. The last, but not least, advantage is a possibility to tailor the lasing wavelength precisely by changing the quantum well width and shifting

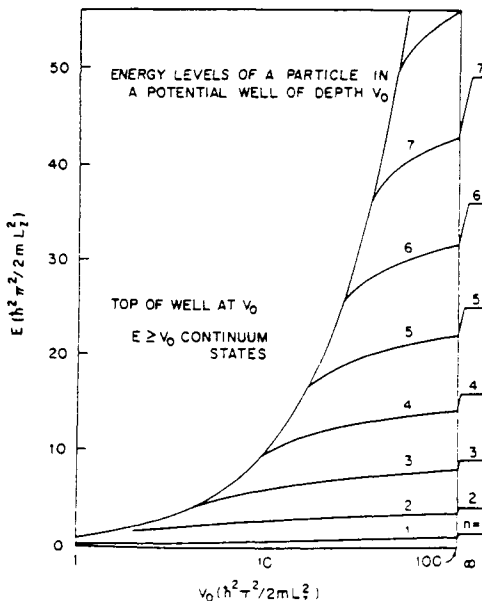


**Figure 8.10** Dependence of bound-state energies (reduced energy units  $\hbar^2\pi^2/2mL_z^2$ ) on the well depth of a rectangular potential well (Adams 1973).

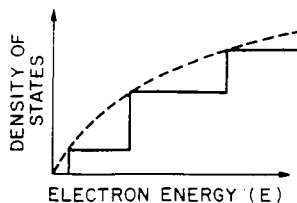


**Figure 8.11** Schematic representation of the density of states in a quantum well.

energy levels in the well. In Yariv's book (1989b), an excellent introduction to the physics of quantum well lasers is provided.

### 8.3 LASER STRUCTURES

Since 1962 when the first semiconductor laser appeared, scientific interest and application requirements have brought to life miscellaneous structures and designs elaborated as a result of extensive research efforts. Whole new fields of application have arisen with the continuous improvement of basic device parameters: threshold current density and total threshold current, output power, frequency stability and tuning, modal pattern and modulation bandwidth. In

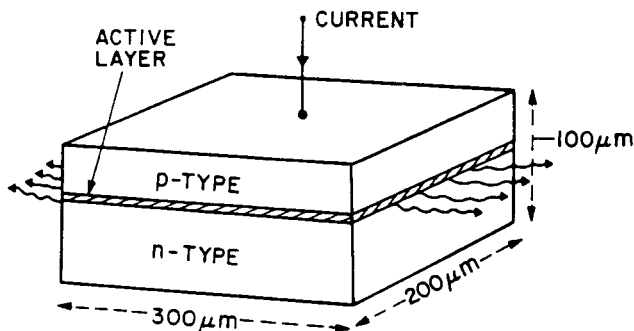


**Figure 8.12** Schematic illustration of a double-heterostructure laser with its typical physical dimensions.

in this section we shall present laser structures which provided major steps and breakthroughs for this progress in semiconductor laser design.

### 8.3.1 Threshold current density and transverse waveguiding

#### (a) Double-heterostructure lasers

The transition from early homostructure lasers to heterostructures was probably the most impressive innovation affecting the very attitude of the scientific community and related industries to the future of this new class of semiconductor devices. Continuous wave operation at room temperature has become possible due to the two orders of magnitude decrease in the threshold current density from  $\sim 50\,000 \text{ A cm}^{-2}$  for homostructure lasers to less than  $500 \text{ A cm}^{-2}$  for heterostructure devices.

Figure 8.12 shows a common broad-area double-heterostructure (DH) laser with thin GaAs active layer confined between n-type and p-type layers of  $\text{Al}_x\text{Ga}_{1-x}\text{As}$  solid solution. A typical active layer thickness is 0.1–0.5 micron while values of  $x$  are usually chosen to be 0.3–0.4. Under forward electric bias, majority carriers are injected from  $\text{Al}_x\text{Ga}_{1-x}\text{As}$  cladding layers to the active region giving rise to population inversion and thus providing conditions for light amplification. Since the solid solution has a broader bandgap than GaAs, the gap discontinuity leads to the formation of a potential barrier confining injected carriers within the active layer. Refractive index dependence on  $x$  is given by  $n = 3.6 - 0.7x$  and the structure described behaves as a dielectric waveguide concentrating lightwaves in the active region.

The operating properties of the GaAs– $\text{Al}_x\text{Ga}_{1-x}\text{As}$  DH laser are dependent primarily upon the structure geometry and cladding-layer composition which is critical for the optical and electrical confinement. Figure 8.13 presents a plot of the room-temperature threshold current density dependence on active layer thickness. The minimal threshold current density is limited by the rise at small thickness due to the low optical confinement factor  $G$ , as can be seen from

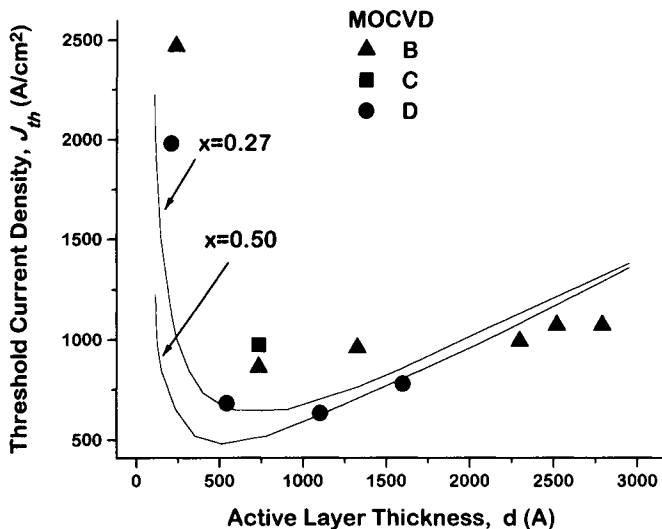


Figure 8.13 Experimental dependence of  $J_{th}$  on  $d$  and  $x$  for MOCVD broad-area DH lasers (closed data points). For comparison, the results of theoretical calculations (curves) are also shown (Dupuis *et al* 1978).

equations (8.1) and (8.2) of the previous section. The lowest threshold current densities obtained for double heterostructure lasers with  $d = 0.06$  micron are about  $390 \text{ } \text{\AA} \text{ cm}^{-2}$  which is close to the theoretical limit (Tsang 1984). Low threshold current densities for DH lasers grown by MOCVD were observed by Dupuis *et al* (1978).

Transverse mode behaviour is governed by the ability of the laser waveguide to support specific modes. Strong optical confinement resulting from large refractive index steps at the heterojunction permits higher-order transverse modes to propagate in a thick waveguide. However, a sufficiently small active layer thickness leads these modes to a cut-off and stable fundamental transverse mode operation is observed for lasers with an active layer thickness of less than 0.2 micron. At the same time a thin active layer in a DH laser increases the optical power density on the laser mirror and, subsequently, the risk of mirror damage. Laser beam divergence as high as  $47.5^\circ$  is observed for 0.1 micron thick active layers (Casey *et al* 1973) which may prevent the efficient coupling of emission into an optical fibre.

The above-mentioned limitations imposed on the performance of double-heterostructure lasers by their very nature stimulated a search for a more efficient laser structure design. An important step on the way was provided by the introduction of multilayer structures of which separate confinement heterostructures proved to be the most promising.

#### (b) Separate confinement heterostructure lasers

A separate confinement heterostructure (SCH) laser, as proposed in 1973 by

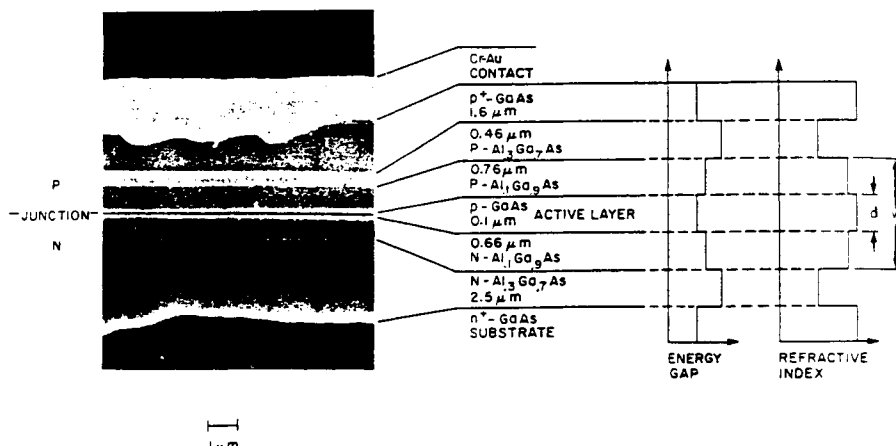


**Figure 8.14** Scanning electron photomicrograph of the selectively etched surface of the SCH laser. The layer thickness, Al composition and the conductivity type are indicated for each layer. A representative variation in the energy gap and refractive index is also shown. The active layer thickness is  $d$  and the optical waveguide thickness is  $w$  (Casey *et al* 1974).

Thompson and Kirkby (1973) and as shown in figure 8.14, is basically a four- or five-layer dielectric waveguide where, first, a smaller composition step gives an energy-band discontinuity necessary to confine injected carriers within the active layer, while a larger step in the refractive index between the waveguide and cladding layers provides light confinement within the optical cavity. Separate optical and electrical confinement ensures moderate beam divergence and low optical power density on the laser mirror while preserving fundamental transverse mode operation and low threshold current density for the lasers with thin active layers. Though SCH lasers did not immediately demonstrate threshold current densities lower than that of contemporary double heterostructures, they readily helped to reduce the beam half width to  $10^\circ$  and improve the uniformity of near-field emission and external quantum efficiency (Thompson *et al* 1976).

Figure 8.14 illustrates the sequence of epitaxial layers grown on a GaAs substrate by liquid phase epitaxy to form a SCH laser with thick waveguide. Bandgap and refractive index profiles are also shown. Structure geometry can be optimized easily to minimal threshold current density by selecting the waveguide and active layer thickness and composition corresponding to the maximal optical confinement factor  $G$  for the active region (Casey *et al* 1974). With a thin active layer ( $d < 0.2 \mu\text{m}$ ), fundamental transverse mode emission is retained for thick optical cavities which would give rise to higher-order modes in DH lasers. A typical waveguide thickness for SCH lasers is  $0.2\text{--}1.0$  micron depending on the application supposed, while an active layer thickness is usually  $0.1$  micron or

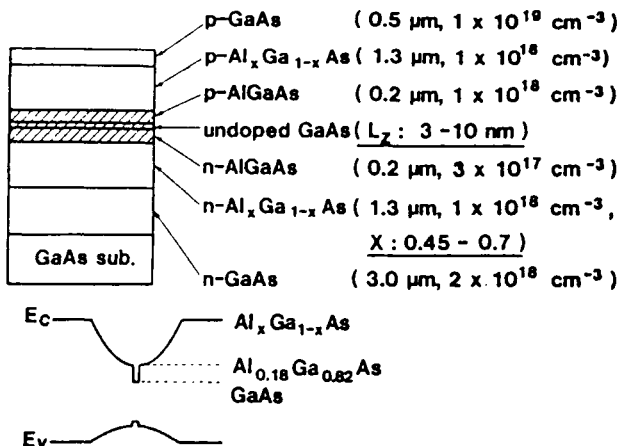


**Figure 8.15** Schematic diagram of a GaAs-AlGaAs GRIN-SCH laser grown by MBE and the corresponding energy band diagram of the laser (Fujii *et al.* 1984).

less. Four-layer heterostructures and asymmetric composition profiling were used for different purposes some of which will be discussed later.

Versatile and efficient by itself, the SCH laser has unavoidably become dominant after progress in crystal growth technology resulted in the introduction of laser structures with quantum well size active layers and graded-index heterostructure materials.

#### (c) Graded-index separate confinement heterostructure lasers (GRIN-SCH)

In 1976, Kazarinov and Tsarenkov (1976) theoretically predicted that a graded composition region surrounding a DH laser active region would efficiently guide the lightwave and collect electrons in the active layer, thus helping to achieve a lower threshold current density. As soon as molecular beam epitaxy developed into an efficient tool to control the growing layer composition, Tsang (1981a) modified a separate confinement heterostructure by gradually changing the waveguide layer composition rather than by making an abrupt step to the active layer. This enabled the matching of a far-field profile to a particular type of optical fibre, further improving higher-order mode discrimination and increasing the cut-off thickness for the first-order mode in asymmetrical waveguide structures. The threshold current density, however, remained within the range of that for DH lasers. The sequence of layers shown in figure 8.15 is referred to as a GRIN-SCH, standing for graded-index separate confinement heterostructure.

GRIN-SCH demonstrated its full potential after extremely thin ( $d < 0.05$  micron) active layers had become possible to grow by modern epitaxial methods, MBE and MOCVD. Conventional double-heterostructure thin active layers resulted in a negligible optical confinement factor and the threshold current densities observed in these early experiments varied from 2 to 3  $\text{kA cm}^{-2}$

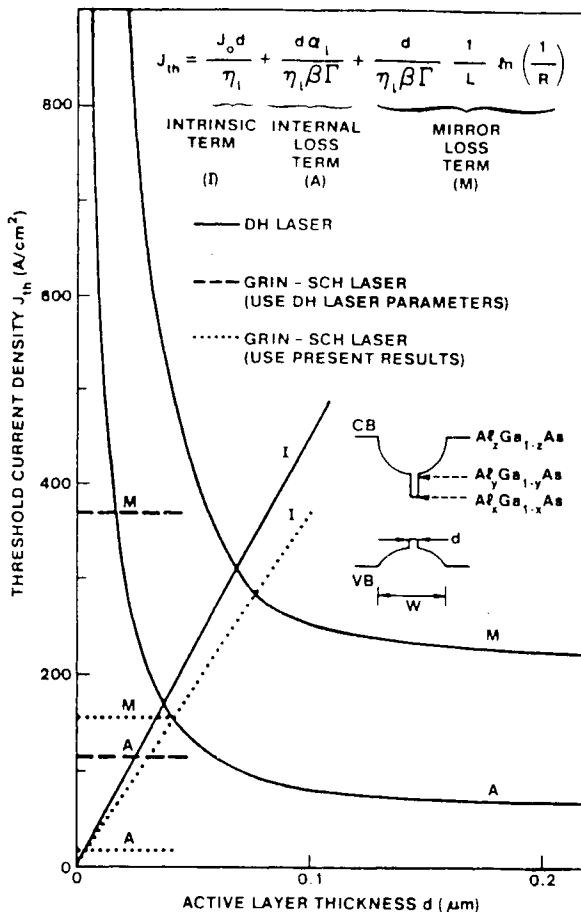


**Figure 8.16** Relative importance of the contributions to  $J_{th}$  of intrinsic, internal loss and mirror loss terms. The solid curves were calculated for regular DH lasers, while the dashed curves were calculated for GRIN-SCH lasers (Tsang 1982).

(Dupuis *et al.* 1978, Tsang *et al.* 1979). The new-born GRIN-SCH technology helped to change the situation dramatically, immediately yielding  $250 \text{ A cm}^{-2}$  for the same device area and as low as  $160 \text{ A cm}^{-2}$  for a longer optical cavity (Tsang 1982). The latest world records for low threshold current density have been made by employing basically the same generic GRIN-SCH structure (Chen *et al.* 1987, Chand *et al.* 1991). Its efficiency is rooted in its different  $G(d)$  dependence when compared with double heterostructures, as well as in a better carrier confinement due to the ‘funnelling’ effect (Kazarinov and Tsarenkov 1976, Hersee *et al.* 1984). Some contradictory evidence for this latter suggestion shows that a convincing analysis has not yet been performed. The former can be easily seen from figure 8.16 where the relative contributions of three terms

to the value of  $J_{\text{th}}$  are shown (compare this to equations (8.1) and (8.2) of the previous section). For a three-layer waveguide,  $G$  is approximately proportional to  $d^2$  and losses increase with decreasing  $d$ , while for a separate confinement case the optical intensity distribution within the waveguide is independent of the thin active layer size making  $G$  directly proportional to  $d$ . This, in turn, results in  $d$ -independent losses and the threshold current density drops together with the transparency current densities for thin layers. Further progress in achieving low threshold current densities was associated with ultrathin (quantum well) active layers.

#### *(d) Quantum well lasers*

The concept of quantized carrier behaviour in extremely thin layers of semiconductor material originated as early as 1970 (Esaki and Tsu 1970) and was later recognized by the Nobel Prize. Experimental realization required a growth technique to produce high-quality heterostructures consisting of layers of alternating composition of thickness less than 50 nm. Laser oscillation from MBE-grown multiquantum well (MQW) GaAs-AlGaAs heterostructures under optical pumping was first reported in 1975 (van der Ziel *et al* 1975). Soon after that, progress made in MOCVD crystal growth resulted in the first room-temperature GaAs-AlGaAs single-quantum-well (SQW) injection laser (Dupuis *et al* 1978) and initiated the overwhelming domination of this type of semiconductor laser as predicted in a paper by Yariv (1989a). A combination of high gain, typical for QW lasers, and tight optical confinement in a GRIN-SCH structure made it possible to fabricate a laser with a threshold current density of  $232 \text{ A cm}^{-2}$  for a reasonable cavity length of  $413 \mu\text{m}$ , while low intrinsic losses in the quantum well and excellent heterointerface abruptness within two monolayers performed by MOCVD helped to achieve the value of  $121 \text{ A cm}^{-2}$  for an extremely long  $1788 \mu\text{m}$  cavity (Hersee *et al* 1982). Quantum well lasers demonstrate high-temperature stability of the threshold current density thanks to the relative independence of carrier temperature in the well on the lattice temperature (Chin *et al* 1980). SQW-GRIN-SCH structures, and separately confined modified multiquantum well (MMQW) structures (Tsang 1981b) were employed in numerous device designs for low-threshold, single-frequency and high-power applications. Figure 8.17 gives a schematic view of the structures discussed above.

### 8.3.2 Threshold current and lateral mode control

While the threshold current density is a representative characteristic of laser-structure quality, it is the absolute threshold current which has to be as low as possible in an actual device. That is why the search operates in parallel to find an optimal way to define a stripe or array of stripes thus limiting device area to the extent dictated by a specific application. Issues of concern here are the minimal current spreading outside the stripe, preventing lateral carrier diffusion, optical confinement providing single-lobe, i.e. fundamental-mode, operation,

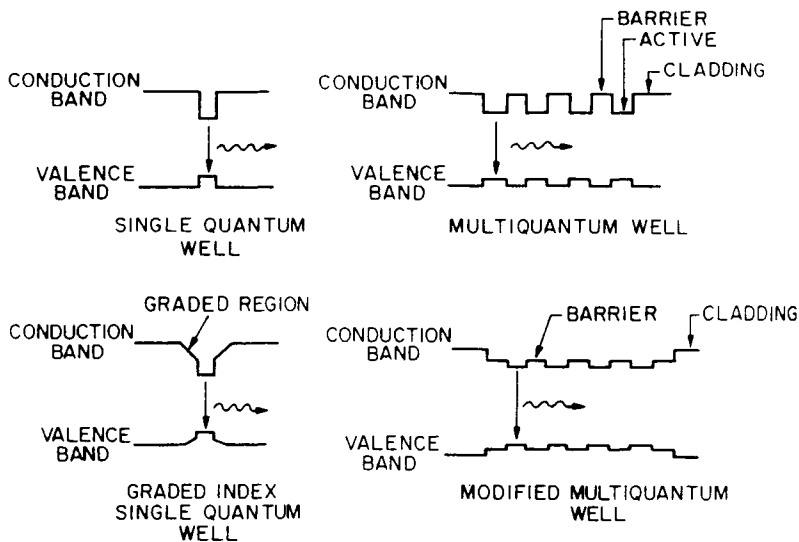


**Figure 8.17** Different single-quantum-well and multiquantum-well laser structures shown schematically.

and the absence of fabrication-induced defects leading to a high irradiative recombination rate and shorter device lifetime. Simplicity of the fabrication process is always a plus, albeit often sacrificed to the efficiency of the eventual laser.

#### (a) Broad-area lasers

Although broad-area lasers are of small practical importance because of their high threshold currents, the data obtained for them are often used as reference values or for comparison purposes and therefore some discussion of these could be useful. Early semiconductor lasers were just bars sawn or cleaved from an initial wafer and had a large area due to the easy process of their fabrication. Later on, broad-area lasers were prepared by depositing metal contact through the mask leaving a wide window open. These devices show a non-uniform optical intensity distribution along the junction plane in the form of separate filaments. Current spreading to as far as  $50\text{ }\mu\text{m}$  from the stripe may occur, strongly affecting the actual width of the pumped region. Finally, internally circulating modes may be excited in the chips with four cleaved facets. All these effects should be taken into account when fabricating and characterizing broad-area or wide-stripe samples.

#### (b) Stripe geometry lasers

A miscellany of techniques has been applied to the fabrication of lasers with stripe geometry active regions in order to ensure low threshold current, single lateral mode and high output power. Most of them are discussed in detail

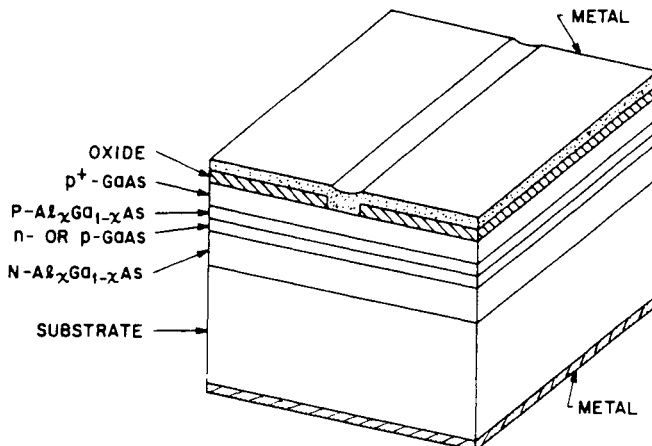


**Figure 8.18** Stripe geometry DH laser with four heteroepitaxial layers on the  $n^+$  GaAs substrate. The oxide layer isolates all but the stripe contact. The rectangular bar is typically  $380\ \mu\text{m}$  long,  $250\ \mu\text{m}$  wide and  $120\ \mu\text{m}$  thick. The drawing is not to scale in order to show the various layers.

elsewhere (Casey and Panish 1978, Sze 1981, Agrawal and Dutta 1986) and so we shall only dwell upon of the more most recent innovations and achievements.

The simplest contact stripe geometry laser as first introduced (d'Asaro 1973) is shown in figure 8.18. The structure was extensively employed using  $\text{SiO}_2$  or  $\text{Si}_3\text{N}_4$  as an insulating layer to block the electric current outside the stripe and no major changes could be imagined. However, the possibility of forming a high-quality native oxide on the AlGaAs surface was recently reported and a  $20\ \text{mA}$  threshold current was observed for a  $10\ \mu\text{m}$  wide stripe (Dallesasse and Holonyak 1991). The lasers demonstrated high performance capability and a number of promising features of which simplicity of fabrication is the most important advantage. This innovation opens a major pathway to circuit technology for AlGaAs–GaAs similar to that existing for silicon.

In terms of both optical and electrical confinement, buried heterostructures (BH) described by Tsukada (1974) proved to be the most efficient. In this structure the active layer is totally surrounded by a wider-bandgap material giving tight confinement and, therefore, permitting extremely narrow stripe widths (figure 8.19(a)). Recently, submilliampere threshold currents were achieved for AlGaAs–GaAs BH lasers by several groups using MBE-grown lasers with a high-reflectivity coating (Lau *et al* 1988) and MOCVD on a non-planar substrate (Narui *et al* 1992). The latter technique is of special interest since it combines such advantages as an extremely low continuous wave threshold current of  $0.88\ \text{mA}$  without facet coating, high external quantum efficiency of 70%, nearly round beam shape suitable for coupling to optical fibre

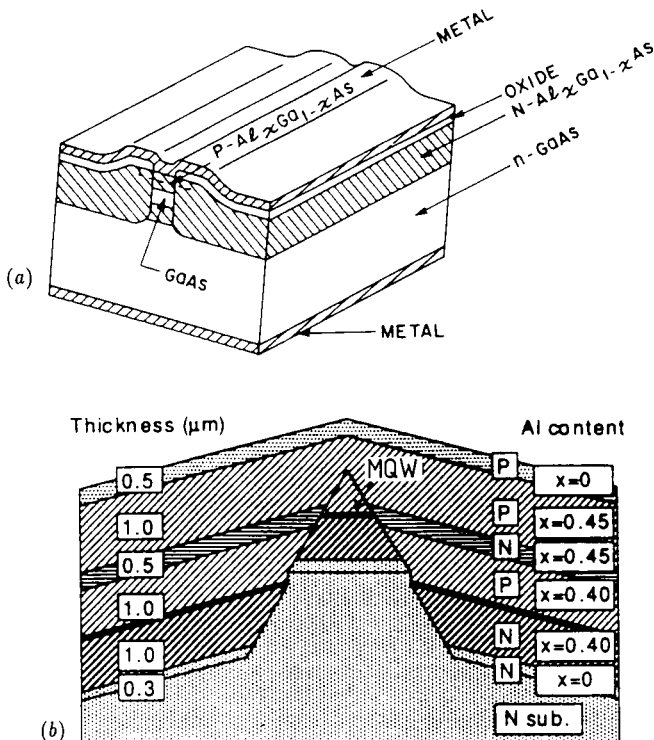


**Figure 8.19** (a) Buried heterostructure laser. The GaAs active region is completely surrounded by  $\text{Al}_x\text{Ga}_{1-x}\text{As}$  (Tsukada 1974). (b) Schematic representation of a separated double-heterostructure (SDH) laser (Narui *et al* 1992).

and relatively simple one-step MOCVD growth. The stripe width in this case is as narrow as  $0.6 \mu\text{m}$ . A schematic view of this unique structure is presented in figure 8.19(b).

Since a thin active layer taken to its ultimate conclusion results in quantum well phenomena, an extremely narrow stripe at some point exhibits carrier quantization in the lateral direction. A one-dimensional structure of this kind is a quantum wire (QWR) promising further progress in perfecting the static and dynamic qualities of lasers. MOCVD growth on V-grooved substrates was successfully used to yield both single-quantum-wire and multiquantum-wire lasers (see figure 8.20) (Simphony *et al* 1991). Low threshold currents were observed for both uncoated (2.5 mA) and coated (0.6 mA) devices. However, even lower threshold current should be achievable in order to guarantee lasing from the fundamental subband and take full advantage of the attractive properties inherent to the new generation of low-dimensional laser structures.

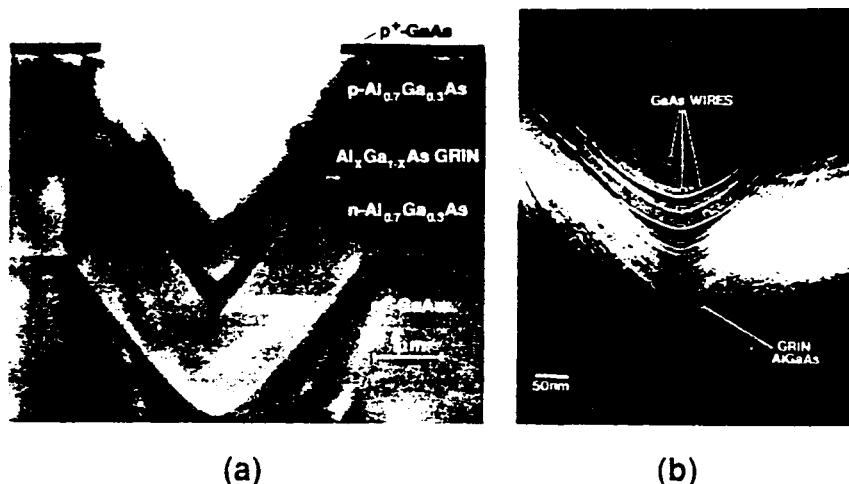


**Figure 8.20** (a) Low-magnification TEM cross-section of the triple-QWR laser, showing the two-dimensional, tapered optical waveguide formed by the growth of the graded-index (GRIN) layers in the V groove ( $x$  linearly graded between 0.2 and 0.7). (b) High-magnification TEM cross-section of the waveguide core, showing the three crescent-shaped QWRs (Simhony *et al* 1991).

#### 8.4 NEW GaAs-BASED MATERIALS FOR LASERS

Most of the results cited earlier in this chapter were obtained in the AlGaAs-GaAs system. This range of solid solutions is attractive due to its perfect lattice match to GaAs substrate for all Al compositions. High-quality material can be readily grown by any known growth technique: LPE, VPE, MBE and MOCVD. Some reports on LPE and MOCVD growth of InGaP and InGaAsP lattice matched to GaAs also appeared (Alferov *et al* 1984, Brunemeir *et al* 1985, Razeghi 1993) and efficient laser devices have been fabricated by this method (Garbuzov *et al* 1990). In recent years, however, new materials have appeared, which essentially require the non-equilibrium growth conditions provided by MBE or MOCVD for controllable layer formation. This includes InGaAs strained layers for the 1  $\mu\text{m}$  wavelength range and AlGaInP for visible range emission. In the following section we shall cover both the major considerations favouring these materials and some new device developments.

##### 8.4.1 Strained InGaAs layer laser structures

Semiconductor lasers emitting in the range 0.8  $\mu\text{m}$  to 1.0  $\mu\text{m}$  are important sources of light for a variety of applications such as pumping erbium-doped optical fibre, pumping solid state lasers and direct frequency doubling for the generation of blue and other visible light lasers. They have a number of attractive

features, including the possibility of fine bandgap adjustment, low threshold current density (Chand *et al* 1991) and large gain permitting high-frequency modulation. Of particular importance is the use of 0.98  $\mu\text{m}$  laser diodes in communication systems for optical fibre pumping.

GaInAs/GaAs strained-layer quantum well structures have been shown to be suitable for the fabrication of laser diodes used for these purposes. In most of the previous works, AlGaAs served for the cladding layers. However, in some recent work GaInP was used in place of GaAlAs (Chen *et al* 1991, Ohkubo *et al* 1992). It was shown that GaInP has advantages over AlGaAs. These advantages include selective chemical etching between  $\text{Ga}_{0.51}\text{In}_{0.49}\text{P}$  and GaAs in addition to less surface oxidation during the fabrication process and device operation due to the absence of Al. Also the growth temperature of GaInP is 510 °C, compared with 700 °C or higher for AlGaAs, which makes this material compatible with monolithic integration for optoelectronic integrated circuits. Finally due to the absence of Al and presence of In, it is expected that these devices will not be affected by dark-line defects causing catastrophic degradation in AlGaAs-based lasers emitting in the same wavelength range.

Extremely low threshold current densities of 45 A cm<sup>-2</sup> have been reported for MBE-grown InGaAs quantum well diodes (Chand *et al* 1991). An example of recent progress in the area of 0.98  $\mu\text{m}$  lasers is the high-quality  $\text{Ga}_{0.8}\text{In}_{0.2}\text{As}/\text{GaAs}/\text{Ga}_{0.51}\text{In}_{0.49}\text{P}$  multiple-quantum-well laser emitting at 0.98  $\mu\text{m}$  that has been grown by low-pressure MOCVD (LP-MOCVD) (Mobarhan *et al* 1992a). Continuous wave operation with an output power of 500 mW per facet was achieved at room temperature for a broad-area laser with 130  $\mu\text{m}$  width and 300  $\mu\text{m}$  cavity length. The external quantum efficiency exceeded 75% with excellent homogeneity and uniformity.

The epitaxial layers were grown on a n<sup>+</sup> silicon-doped GaAs substrate (100) with a 2° misorientation. The process of growth was carried out at a pressure of 76 Torr in a horizontal reactor at a substrate temperature of 510 °C. Trimethylindium (TMI) and triethylgallium (TEG) were used as sources of In and Ga, while pure arsine (AsH<sub>3</sub>) and phosphine (PH<sub>3</sub>) provided As and P, respectively. Hydrogen (H<sub>2</sub>) was used as a carrier gas. SiH<sub>4</sub> and diethylzinc (DEZn) were used as n-type and p-type dopants, respectively. The laser structure consists of (i) 1  $\mu\text{m}$  thick  $\text{Ga}_{0.51}\text{In}_{0.49}\text{P}$ , silicon-doped ( $N_D - N_A \approx 10^{18} \text{ cm}^{-3}$ ) cladding layer, (ii) 500 Å GaAs waveguide layer, (iii) three 40 Å  $\text{Ga}_{0.8}\text{In}_{0.2}\text{As}$  strained-layer quantum wells separated by 100 Å thick GaAs barriers, (iv) a second 500 Å GaAs waveguide layer, (v) 1  $\mu\text{m}$  thick  $\text{Ga}_{0.51}\text{In}_{0.49}\text{P}$ , Zn-doped ( $N_A - N_D \approx 5 \times 10^{17} \text{ cm}^{-3}$ ) cladding layer and (vi) 0.5  $\mu\text{m}$  thick GaAs, Zn-doped ( $N_A - N_D \approx 10^{19} \text{ cm}^{-3}$ ) contact layer. Figure 8.21 shows a typical electrochemical doping profile of the laser structure.

The sample was then thinned down to about 100  $\mu\text{m}$  thickness. The contacts consist, on the p-side, of Pt(1500 Å)/Au(3000 Å) and, on the n-side, AuGe(n)(900 Å)/Mo(2000 Å)/Au(6000 Å). After cleaving individual diodes were mounted p-side down on Au-plated copper heat sinks using In preforms.

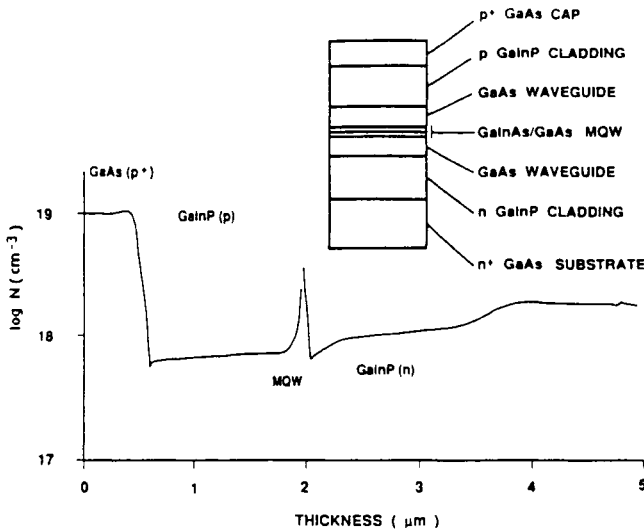


**Figure 8.21** Typical electrochemical profile of  $\text{Ga}_{0.8}\text{In}_{0.2}\text{As}/\text{GaAs}/\text{Ga}_{0.51}\text{In}_{0.49}\text{P}$  strained layer multiple-quantum-well structure grown by LP-MOCVD for  $0.98 \mu\text{m}$  lasers.  $\text{SiH}_4$  and  $\text{DEZn}$  were used as n-type and p-type dopants, respectively (Mobarhan *et al* 1992a).

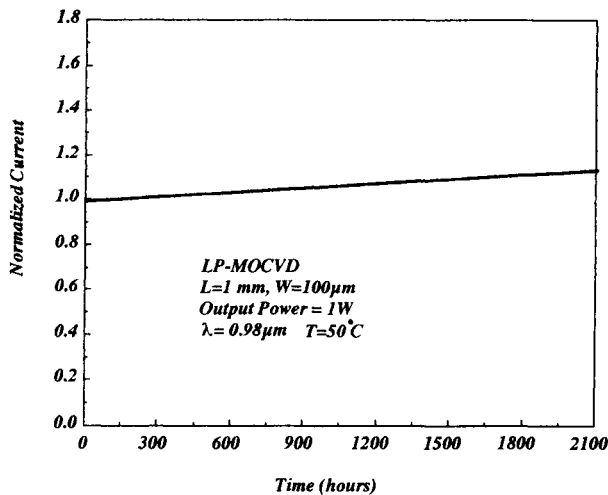


**Figure 8.22** 1 W constant-power CW ageing test at  $50^\circ\text{C}$  for  $\text{In}_{0.20}\text{Ga}_{0.80}\text{As}/\text{GaAs}/\text{In}_{0.49}\text{Ga}_{0.51}\text{P}$  SCH-QW lasers emitting at  $0.98 \mu\text{m}$  ( $T = 50^\circ\text{C}$ ,  $L = 1 \text{ mm}$ , stripe width  $W = 100 \mu\text{m}$ ).

No antireflection or high-reflectivity coatings of any kind were applied on the cleaved mirror facets. Excellent homogeneity of the device was established through a very uniform near-field emission pattern at an injection current just

above threshold. The wavelength of emission was found to be at  $0.98\text{ }\mu\text{m}$  and the device operated in a multilongitudinal mode.

Long time reliability is one of the most critical issues for laser diodes. It is more crucial for the lasers for communication systems such as  $0.98\text{ }\mu\text{m}$  lasers due to the high cost of replacement and/or repair. Operation of InGaAs/InGaP/GaAs lasers for over 2000 h at  $50\text{ }^\circ\text{C}$  with emitting output power of 1 W in CW mode has been reported (Razeghi 1994). After 2000 h of ageing, the increase of the operating current had not exceeded 15% (figure 8.22). Operation at high temperature is a good indicator as to how robust the device is. Operation of Al-free InGaAs/GaAs lasers at  $100\text{ }^\circ\text{C}$  with emitting power of 800 mW was achieved (figure 8.23(a)). The characteristic temperature  $T_0$  was measured up to 350 K in temperature range of  $15\text{--}41\text{ }^\circ\text{C}$  while  $T_0 \sim 250\text{ K}$  overall temperature range (figure 8.23(b)). This is favourably compared with a recent report on an Al-containing counterpart where  $T_0 = 160\text{ K}$  was achieved (Chand *et al* 1994).

A substantial reduction of the threshold current for this kind of laser has been recently achieved by using buried-ridge structures (BRS) very similar to the buried heterostructures described above (Mobarhan *et al* 1992b). The laser structure was grown by two-step LP-MOCVD. Photolithographic and selective chemical etching techniques were used to prepare the ridge. Lateral current localization was obtained by shallow ion implantation. The laser diodes were mounted p-side down on copper heat sinks using In bonding. With this laser, a continuous wave output power of 40 mW has been obtained without any facet coating. The threshold current was 30 mA for a laser with a  $2\text{ }\mu\text{m}$  wide ridge. The laser diodes processed from a  $10\text{ cm}^2$  area of the same wafer showed excellent homogeneity and uniformity. The characteristic temperature  $T_0$  was measured to be about 95 K. Figure 8.24 shows the schematic diagram of this laser.

Submilliampere threshold InGaAs/GaAs/AlGaAs laser array elements grown by single-step MOCVD growth on non-planar substrates have been reported (Zhao *et al* 1994). The epitaxial growths were performed in an atmospheric-pressure MOCVD reactor. The substrate non-planarity is introduced by chemical etching of mesas with (100) tops and (111)A sidewalls. The growth properties of InGaAs/GaAs/AlGaAs on the mesa top and the mesa sidewall are strongly influenced by the sidewall orientation, growth temperature and V/III ratio. By controlling these variables during the lower cladding layer growth, the mesa top width is reduced by 1 to  $2\text{ }\mu\text{m}$  depending on the growth conditions. The InGaAs quantum well growth rate on the (111)A mesa sidewall is four times slower than on the (100) mesa top, resulting in a cathodoluminescence (CL) emission wavelength on the mesa sidewall that is about 100 nm shorter than on the mesa top. The width of this active region is controlled by the starting mesa width and the growth of the  $\text{Al}_{0.6}\text{Ga}_{0.4}\text{As}$  lower cladding layer. Current confinement in this laser is provided by the orientation-selective doping properties of the undoped  $\text{Al}_{0.6}\text{Ga}_{0.4}\text{As}$  cladding layer which results in p-type doping on the (100) mesa top.

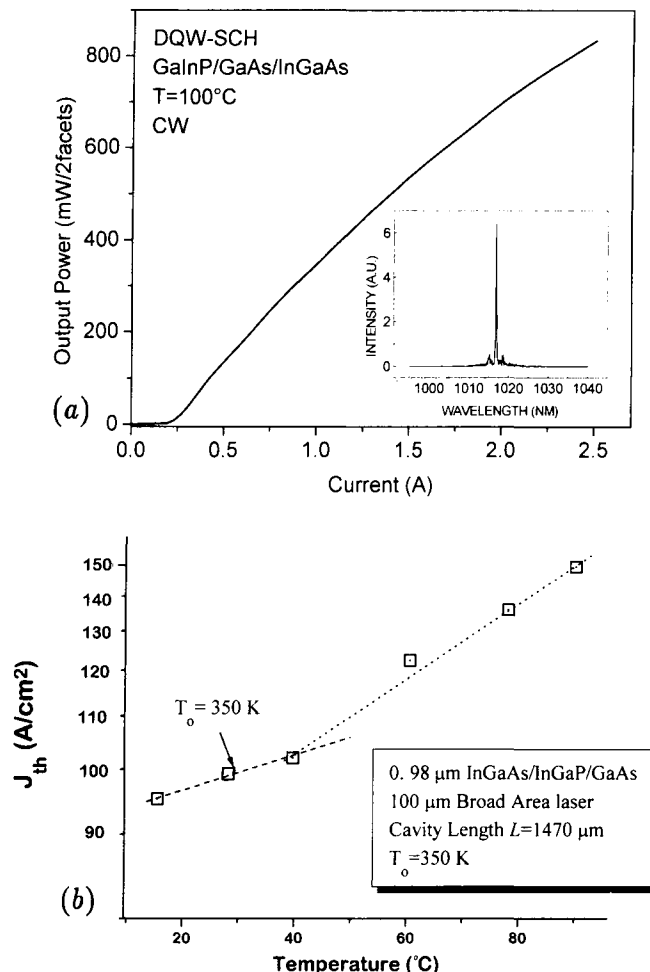


**Figure 8.23** (a) Output power for  $\text{In}_{0.20}\text{Ga}_{0.80}\text{As}/\text{GaAs}/\text{In}_{0.49}\text{Ga}_{0.51}\text{P}$  ( $\lambda = 0.98 \mu\text{m}$ ) double QW-SCH lasers emitting at  $T = 100^\circ\text{C}$ . (b) Temperature dependence of the threshold current density ( $J_{\text{th}}$ ) for a typical  $\text{In}_{0.20}\text{Ga}_{0.80}\text{As}/\text{GaAs}/\text{In}_{0.49}\text{Ga}_{0.51}\text{P}$  ( $\lambda = 0.98 \mu\text{m}$ ) 100  $\mu\text{m}$  broad-area laser ( $L = 1470 \mu\text{m}$ ). The characteristic temperature  $T_0$  is 350 K in the temperature range 15–41  $^\circ\text{C}$  while  $T_0 \sim 250 \text{ K}$  over the whole temperature range.

and n-type doping on the sidewalls. The  $L-I$  curve of a SQW laser with 0.6  $\mu\text{m}$  wide active region is shown in figure 8.25. The room-temperature threshold current for uncoated SQW lasers is 0.7 mA and for uncoated DQW lasers it is 0.5 mA. These lasers have an excellent external quantum efficiency of 80–85%. High reflectance/low reflectance (HR/LR) coated 120  $\mu\text{m}$  long SQW lasers with 0.9  $\mu\text{m}$  wide active regions showed a RT CW threshold current of 0.28 mA. They

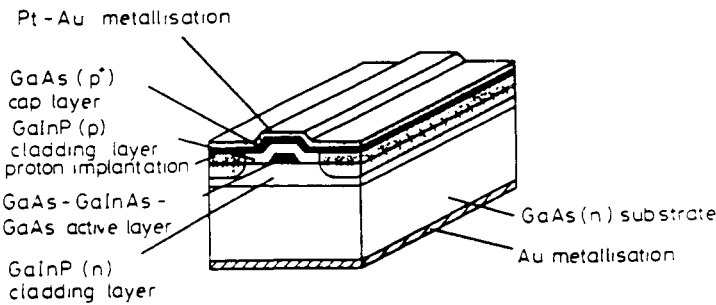


**Figure 8.24** Schematic diagram of a buried ridge structure (BRS),  $\text{Ga}_{0.8}\text{In}_{0.2}\text{As}/\text{GaAs}/\text{Ga}_{0.51}\text{In}_{0.49}\text{P}$  single-quantum-well laser, grown by LP-MOCVD with proton implantation (Mobarhan *et al.* 1992b).

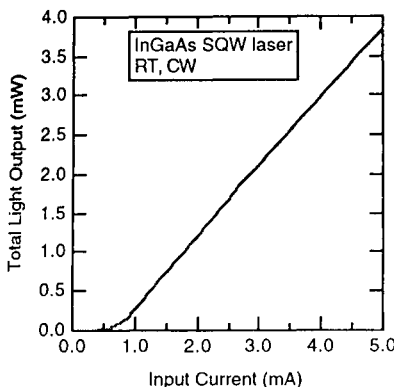


**Figure 8.25** The  $L$ - $I$  curve of a SQW laser with a  $0.6 \mu\text{m}$  wide active region (Zhao *et al.* 1994).

also exhibit excellent threshold and quantum efficiency uniformity and high yield because of the simple growth and processing procedures. Figure 8.26 shows the threshold currents of 1 mA laser array elements on a single bar.

The use of a GaInP/GaAs superlattice as an optical confinement layer (SL-OCL) for a laser has recently been reported for  $0.98 \mu\text{m}$  InGaAs/GaInP lasers (Usami and Matsushima 1994). Figure 8.27 shows the band diagrams for three types of SCH structure for comparison. Figures 8.28–8.30 show the inverse differential quantum efficiency versus cavity length, the threshold current density versus inverse cavity length and temperature dependence of threshold current, respectively. The beneficial effect of SL-OCL is obvious from the figures. An internal quantum efficiency as high as 90% and the threshold current density as low as  $280 \text{ A cm}^{-2}$  are obtained in a laser with a superlattice optical confinement

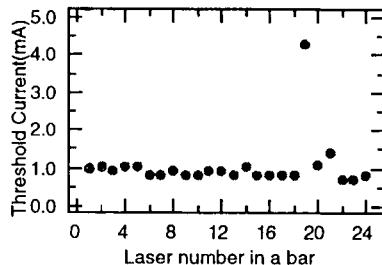


Figure 8.26 Threshold currents of a laser array (Zhao *et al* 1994).

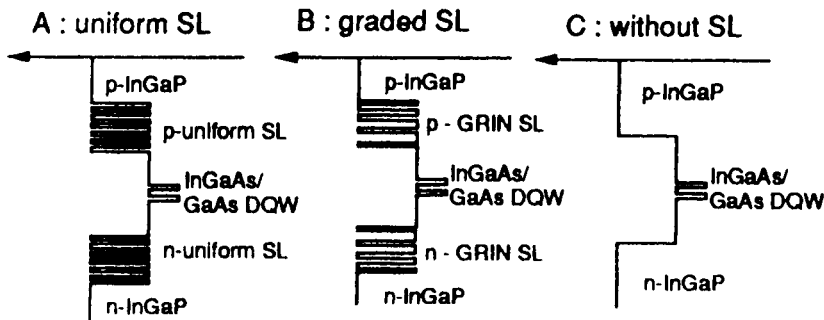


Figure 8.27 Band diagrams of LDs with SL-OCL (type A, type B) and without SL-OCL (type C) (Usami and Matsushima 1994).

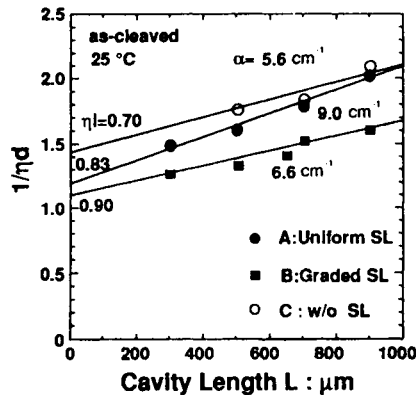


Figure 8.28 Inverse differential quantum efficiency versus cavity length (Usami *et al* 1994).

layer. The SL-OLC structure, in addition to the ordinary graded index (GRIN) effect, is also expected to have the multiple-quantum-barrier (MQB) effect (Iga *et al* 1986), which enhances the confinement of carriers.

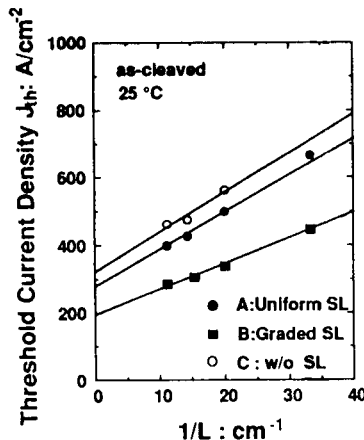


Figure 8.29 Threshold current density versus inverse cavity length (Usami *et al* 1994).

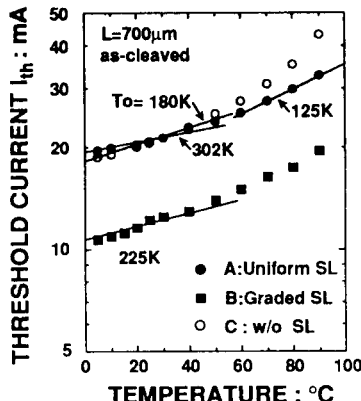


Figure 8.30 Temperature dependence of threshold current (Usami *et al* 1994).

#### 8.4.2 AlGaInP visible lasers

Visible light laser diodes are extremely important light sources having a wide range of applications, including plastic fibre optics, optical recording, high-resolution television, pumping of Cr-doped solid-state lasers, information processing systems, laser printers and bar-code scanners. Shorter-wavelength laser operation is better for obtaining small focused spots and highly luminous light sources for the human eye. It is expected that visible light laser diodes will gradually replace HeNe gas lasers in these fields.

Although the AlGaAs system is the most intensively investigated, the shortest continuous wave lasing wavelength achieved is in the neighbourhood of  $0.68 \mu\text{m}$ , which is very near to the limit for this material system. The AlGaInP system has the potential for the shortest-wavelength emission ( $0.580 \mu\text{m}$ ) of

any III-V semiconductor, with the advantage of complete lattice matching to GaAs substrate. However, the AlGaInP single epitaxial layers are extremely difficult to grow in a controlled manner by any near-equilibrium growth method such as LPE or VPE. This is due to the large Al segregation coefficient. For example, in the growth of the quaternary alloy AlGaInP the Al distribution coefficient from vapour phase to the solid phase is of the order of unity. As a result, MBE and MOCVD (not being equilibrium growth techniques) are the best methods for growing these compounds. The theoretically predicted wavelength region for the AlGaInP double-heterostructure system is  $0.580\text{ }\mu\text{m}$  to  $0.680\text{ }\mu\text{m}$  which, as mentioned, includes the lasing wavelength of HeNe gas lasers ( $0.6328\text{ }\mu\text{m}$ ). However, even for completely lattice-matched GaInP, longer emission wavelengths than theoretically predicted usually result. This can be due to unintentional dopant incorporation into the GaInP causing radiative emission via impurity levels, which have a longer wavelength than that of band to band emission. A slightly excessive In composition in GaInP can also give rise to a smaller bandgap energy. In either case the result is a longer-wavelength emission.

There are different mechanisms available to shorten the wavelength and tailor the bandgap to a specific desired value. One method is by increasing the Al content  $x$  of the  $(\text{Al}_x\text{Ga}_{1-x})_{0.5}\text{In}_{0.5}\text{P}$  active layer. Another way is to use a GaInP quantum well active layer and AlGaInP barrier layers. The application of quantum well structures to laser diodes makes it possible to achieve laser operation at a low threshold current density and high  $T_0$  value, as well as to tailor the bandgap. A reduction in the threshold current density is expected, for example, by optimizing barrier height, barrier layer thickness and well layer numbers as well as the growth conditions. Also, the application of strained-layer quantum well structures to laser diodes can make it possible to achieve laser operation at shorter wavelengths without increasing the Al content, which can give rise to surface oxidation problems and dark-line-induced degradation effects.

High-power continuous wave operation of broad-area InGaAlP (Kobayashi *et al* 1985) and high-power operation of InGaAlP visible lasers using buried ridge waveguide structures have been reported (Fujii *et al* 1987). The performance of these visible lasers is limited by the temperature dependence of the threshold current which is more severe than in AlGaAs lasers. However, 340 mW continuous wave and approximately 1 W pulse output has recently been made possible by reducing the threshold current density to  $425\text{ A cm}^{-2}$  in the GaInP strained-layer single-quantum-well GRIN separate confinement heterostructure (SQW-GRIN-SCH) shown in figure 8.31 (Serreze *et al* 1991). The emission wavelength was 665 nm, which is useful for practical applications. Fundamental transverse-mode operation of a buried heterostructure laser emitting at 600 nm has been achieved with a relatively thick (400 Å) GaInP active layer.

AlGaInP lasers are very susceptible to facet degradation at high-power operation. To overcome this problem, several window structures (Ueno *et al*

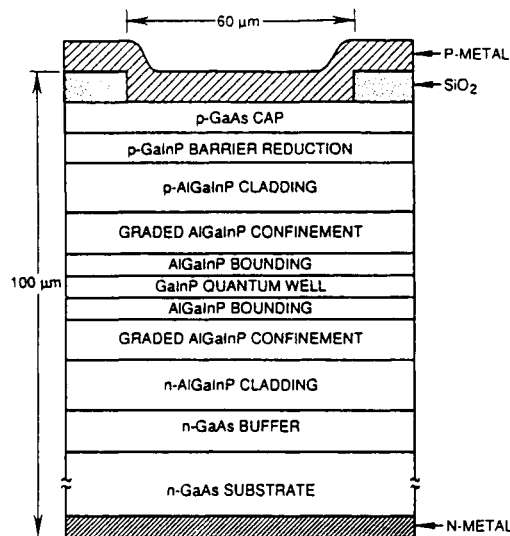


**Figure 8.31** Schematic cross-section (not to scale) of the  $60\text{ }\mu\text{m}$  wide, oxide stripe, strained layer (SQW-GRIN-SCH) visible light laser (Serreze *et al* 1991).

1990, Arimoto *et al* 1993), which reduce optical absorption near the facets, have been reported. Among these window structures, the window grown on a facet structure is rather simple and effective (Sasaki *et al* 1991). The kink-free maximum output of 295 mW was obtained at room temperature, which was about twice as much as that of the conventional one (no window on the facets). The threshold current and the slope efficiency under 150 mW were the same as those of the conventional one, which indicates that the window layers do not affect the laser properties.

#### 8.4.3 GaInAsP/GaAs lasers

##### (a) $0.808\text{ }\mu\text{m}$ GaInAsP/GaAs high-power lasers

Up to now, commercially available diode pumped Nd-YAG solid-state lasers used diode lasers emitting at 808 nm fabricated from materials in the  $\text{Al}_{1-x}\text{Ga}_x\text{As}$  system. However, the lifetime of AlGaAs-based laser diodes limits the reliability of a whole system due to the problem connected with the presence of Al in the diode materials. High interaction of Al with oxygen leads to oxide formation at the mirror facet and enhances the non-radiative recombination of injected carriers near the mirror facet which creates the overheating of the mirror, and decreases the lifetime of the device. Another lifetime limiting factor for AlGaAs-based laser diodes is the formation of dark-line defects, as a consequence of the spreading of the dislocations in the active region during high-power operations.

**Table 8.1** The advantages of Al-free InGaAsP high-power diode allow lower production costs in comparison with AlGaAs lasers.

AlGaAs	InGaAsP
High growth temperature ( $\sim 700^\circ\text{C}$ ) necessary to suppress oxidation of Al during epitaxial growth	Lower growth temperature ( $\sim 500^\circ\text{C}$ ) entails lower consumption of source materials
Ion implantation necessary to achieve high doping level of the p-GaAs contact layer	Lower growth temperature facilitates obtaining high p-doped GaAs ( $N_a \sim 10^{20}\text{cm}^{-3}$ ) with excellent surface morphology
Fabrication of mesa structures and gratings for DFB lasers requires plasma or ion beam etching to avoid the oxidation of AlGaAs	Selective chemical etching is possible for InGaP/GaAs and InGaAsP materials without oxidation
Non-absorbing mirror fabrication necessary to avoid mirror facet overheating and catastrophic damage	Higher ( $\sim 10$ times) COD limit eliminates the necessity of non-absorbing mirror preparation
Pre-selection of diode chips required to eliminate occasionally damaged or defective diodes	Highly uniform defect-free MOCVD material and ruggedness of In-containing compounds provide for the yield of good chips close to 100%
Extreme caution required when handling laser wafers and chips because of material sensitivity to dislocation spreading	Dislocation movement is inhibited by large In atoms and material is insensitive to minor impacts
Burn-in testing and selection required to eliminate diodes demonstrating rapid degradation	Material resistance to dark-line and dark-spot defect formation provides for the yield of good lasers close to 100%

Both of these problems can be solved by the replacement of  $\text{Al}_{1-x}\text{Ga}_x\text{As}$  with the Al-free  $\text{Ga}_x\text{In}_{1-x}\text{As}_y\text{P}_{1-y}$  system (Garbuzov *et al* 1991, Razeghi 1993). It has been demonstrated that the non-radiative recombination velocity near the mirror facet for the GaInAsP system is at least two orders of magnitude less than for the AlGaAs system. On the other hand, due to the presence of big atoms such as In, the dislocation mobility of GaInAsP alloys is much less than for the AlGaAs system. The other advantages of GaInAsP systems include the possibility of selective etching and regrowth which is essential for laser diode processing. Table 8.1 lists the advantages of the GaInAsP/GaAs system over the AlGaAs system based on cost efficiency.

$\text{Ga}_{0.51}\text{In}_{0.49}\text{P}-\text{Ga}_{0.87}\text{In}_{0.13}\text{As}_{0.75}\text{P}_{0.25}-\text{Ga}_{0.51}\text{In}_{0.49}\text{P}-\text{GaAs}$  double-heterostructure (DH) lasers (figure 8.32(a)) emitting at  $0.808\text{ }\mu\text{m}$  have been fabricated by LP-MOCVD (Razeghi 1991). Broad-area contact laser diodes with a stripe width of  $100\text{ }\mu\text{m}$  were prepared by a photolithographic technique. Measurements of the absolute values of external efficiency for spontaneous emission as well as the temperature dependence of the emission efficiency have shown that the

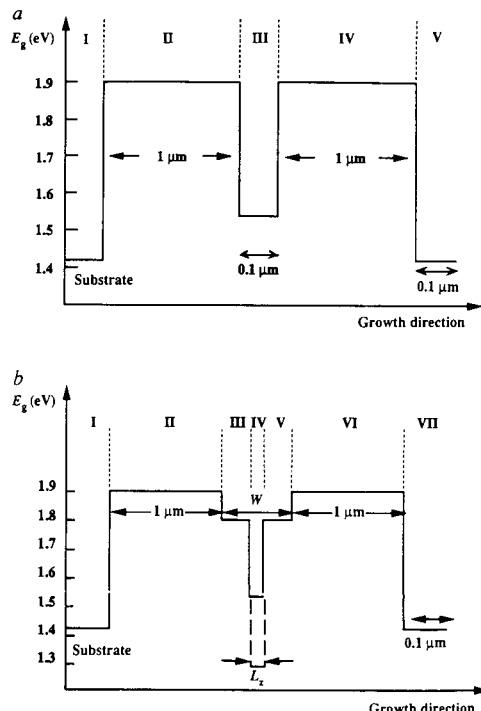


**Figure 8.32** Schematic diagram of the band structure of (a) a double-heterostructure (DH) and (b) separate confinement heterostructure (SCH) single-quantum-well (SQ) GaInAsP lasers emitting at 0.808  $\mu\text{m}$  (Razeghi 1994).

internal efficiency of radiative recombination in the GaInAsP active layer for these laser diodes is close to 100% (Diaz *et al* 1994b). This means that all carriers injected in the  $\text{Ga}_x\text{In}_{1-x}\text{As}_y\text{P}_{1-y}$  active region recombine radiatively at room temperature. In accordance with these results, the threshold current density for these diodes was close to the theoretical limit and better than the data known for the best double-heterostructure AlGaAs/GaAs lasers (Dymant *et al* 1974).

Separate confinement heterostructure quantum well (SCH-QW) laser diodes have been fabricated. The band diagram and details of the structure are shown in figure 8.32(b). By changing the thickness and composition of the GaInAsP active layer, one can vary the emitting wavelength of the lasers between 0.7 and 1  $\mu\text{m}$ . Due to the very thin active region ( $L_z$  in figure 8.32(b)) and quantum size effects, the energy distribution of the carriers is narrower in SCH-QW lasers than for DHs with a thick active layer, which leads to the improvement of the main laser parameters such as the threshold current density ( $J_{\text{th}}$ ), differential efficiency ( $\eta_d$ ), temperature dependence of the threshold current density ( $T_0$ ), etc.

As in the case of DHs, broad-area lasers have been fabricated, and diodes

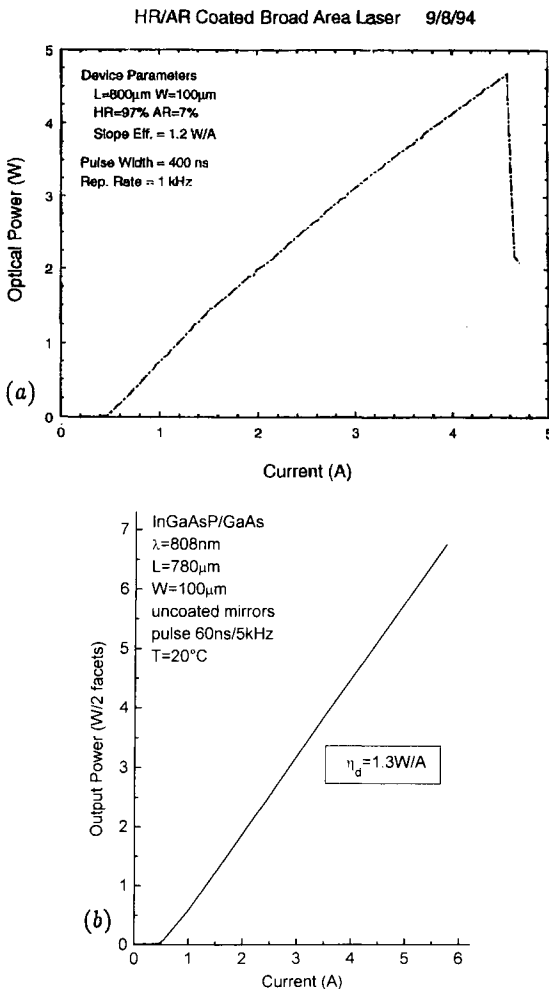


**Figure 8.33** Output power as a function of injection current for GaInP/GaInAsP/GaAs 0.808  $\mu\text{m}$  laser diodes with (a) coated and (b) uncoated facets.

were In bonded onto copper heat sinks. The value of the series resistance measured under the continuous wave (CW) regime for bonded laser diodes with 1 mm cavity length was as low as 0.04  $\Omega$  which is three times less than for similar GaAlAs/GaAs lasers.

An 808 nm GaInAsP laser diode with a facet coating gave out as high as 4.6 W of power from the antireflective- (AR-) coated facet alone (figure 8.33(a)). One laser facet was high reflection (HR) coated to 93% and the other facet was AR-coated to 7%. The differential quantum efficiency from the AR-coated facet was 82%. A slope efficiency of  $1.2\text{ W A}^{-1}$  was obtained from figure 8.33(a).

In fact, a record low of 4.5 A of input current for 4.6 W output power

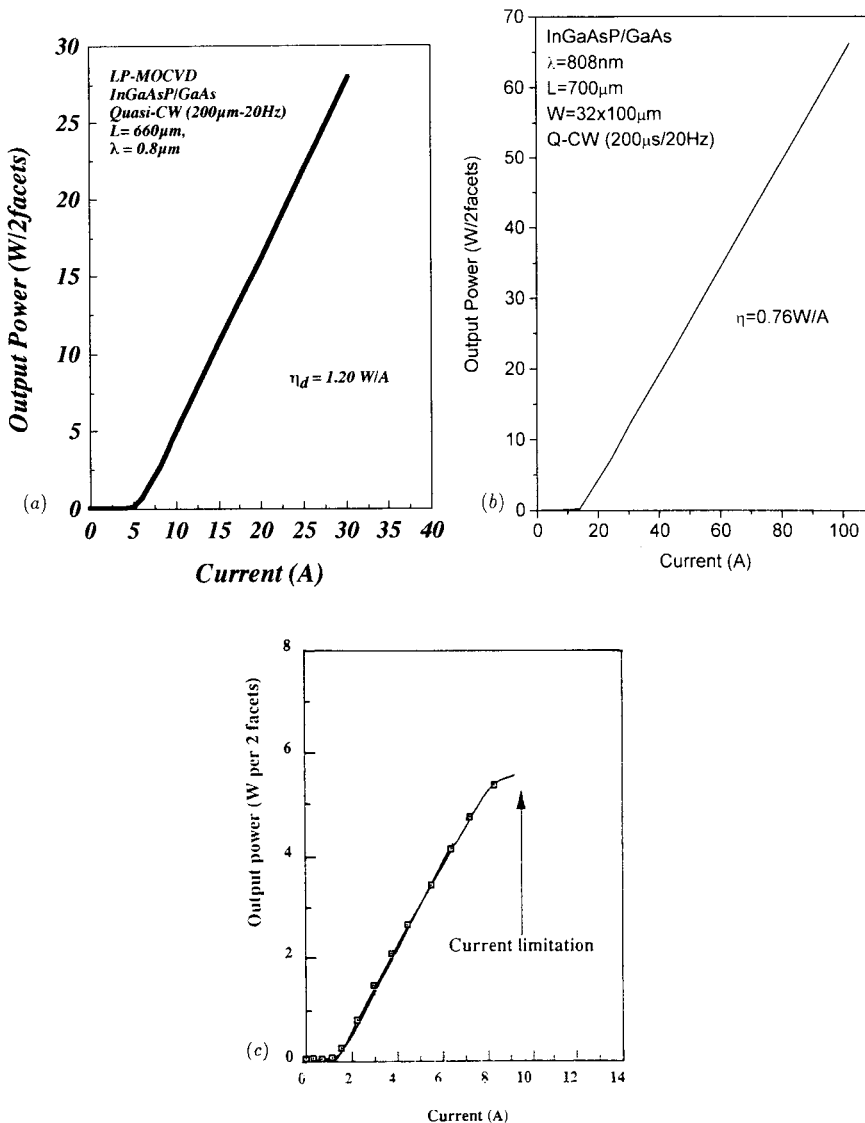


**Figure 8.34** Output power versus injection current for GaInP/GaInAsP/GaAs  $0.808 \mu\text{m}$  laser diodes: (a) quasi-CW, 5 mm wide laser bar; (b) quasi-CW, 1 cm wide laser bar; and (c) CW single laser diode.

was observed. The quantum differential efficiency and output power were even more improved by using more sophisticated ohmic contact formation. When Ti/Pt/Au was used for p-ohmic contact material instead of Au/Zn as used in previous cases, the differential efficiency reached  $1.3 \text{ WA}^{-1}$  (87%) without mirror coating (figure 8.33(b)). It is almost impossible to obtain such high

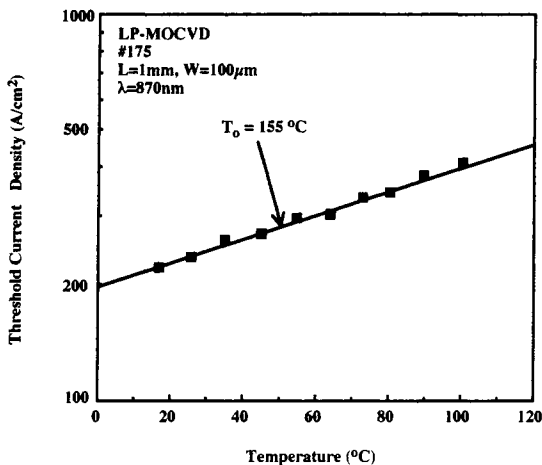


Figure 8.35 Determination of  $T_0$  from  $J(T)-T$  relation (Razeghi *et al* 1994).

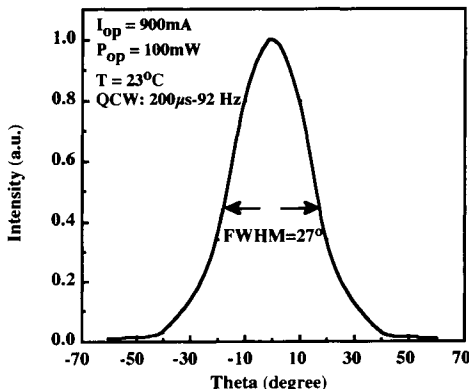
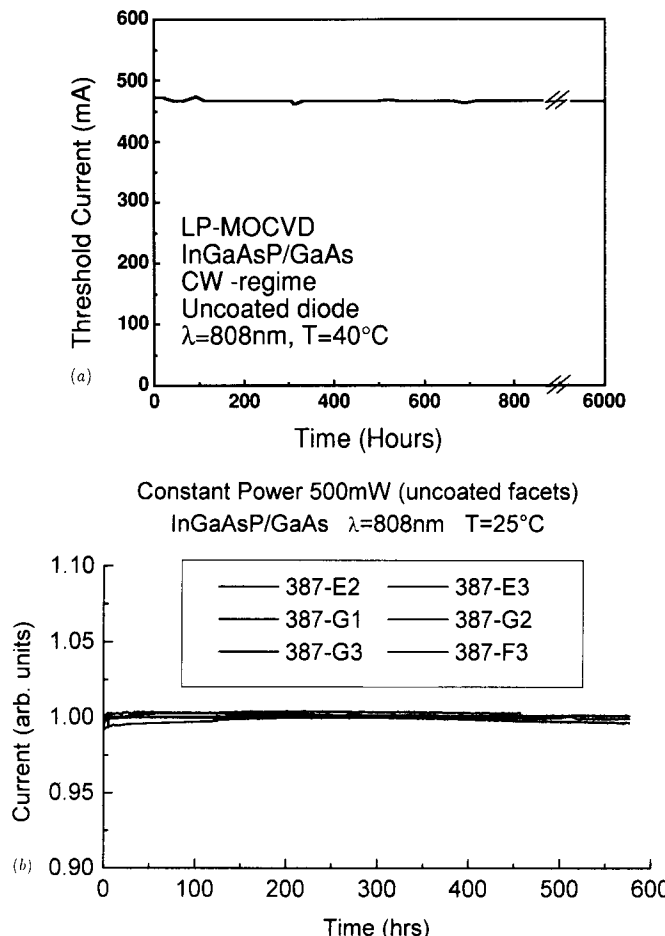


Figure 8.36 Half width of optical beam divergence in the direction perpendicular to the active layer (Razeghi *et al* 1994).

power and efficiency from uncoated AlGaAs/GaAs lasers due to higher non-radiative recombination and degradation related to surface effects.

The laser diodes were tested in the CW regime as well as for the quasi-CW regime (pulse width 200  $\mu$ s, repetition rate 20 Hz), which is typical for a Nd:YAG laser pumping application. In quasi-CW operation the differential efficiency obtained was  $1.2 \text{ W A}^{-1}$  (figure 8.34(a)) at high-power operation of 27 W, while the maximum output could reach up to 67 W (figure 8.34(b)) when a laser bar was made up of 32 diodes. In CW operation, the output power from a single laser diode was up to 6 W, limited by the maximum driving current available in our setup (figure 8.34(c)). All of the lasers used in the quasi-CW and CW operation tests were without mirror coating. The distribution of the



**Figure 8.37** Ageing histories of GaInP/GaInAsP/GaAs 0.808  $\mu\text{m}$  uncoated laser diodes: (a) single laser diode, air ambient; (b) 6 identical laser diodes,  $\text{N}_2$  ambient.

radiation intensity along 100  $\mu\text{m}$  of diode aperture was highly uniform in a wide range of driving current densities.

Typical threshold current densities ( $J_{\text{th}}$ ) were as low as  $220 \text{ A cm}^{-2}$ , with a differential efficiency as high as  $1.2 \text{ W A}^{-1}$  for 1 mm cavity length diodes, with an emitting wavelength of 808 nm. For comparison, the best commercially available AlGaAs-based diodes emitting at 0.808  $\mu\text{m}$  wavelength have  $J_{\text{th}} = 300\text{--}400 \text{ A cm}^{-2}$ , and  $\eta_d = 0.5\text{--}0.8 \text{ W A}^{-1}$ .  $T_0$  reached 155  $^\circ\text{C}$  (figure 8.35) which is comparable with the best results obtained for AlGaAs (130–160  $^\circ\text{C}$ ).

Optical pumping applications impose additional requirements to high-power diodes—primarily the possibility of obtaining a specific emission wavelength. The lasing wavelength may be adjusted precisely to a desired position by varying

**Table 8.2** Comparison of AlGaAs versus aluminium-free InGaAsP high-power laser diodes (aperture 100  $\mu\text{m}$ ).

	AlGaAs	InGaAsP (results of CQD)
$\lambda$ (nm)	800	800
$J_{\text{th}}$ ( $\text{A cm}^{-2}$ )	230 <sup>a</sup> –400 <sup>b</sup>	240–500
$\eta_d$ ( $\text{W A}^{-1}$ )	1.3 <sup>a</sup> –0.8 <sup>b</sup>	1.3
$T_0$ ( $^{\circ}\text{C}$ )	130 <sup>a</sup> –160 <sup>b</sup>	155–175
$R$ ( $\Omega$ )	0.25 <sup>b</sup>	0.1
Thermal resistance ( $\text{K W}^{-1}$ )	10 <sup>b</sup>	1
Transverse beam divergence	32–48 <sup>a,b</sup>	26 <sup>c</sup>
COD limit for uncoated facets ( $\text{MW cm}^{-2}$ )	0.5–1 <sup>c</sup>	6
Lifetime under 1 $\text{MW cm}^{-2}$ (h)	200 (uncoated facets) <sup>d</sup>	> 6000 (uncoated facets)

<sup>a</sup> Yariv A *et al* 1986 *Electron. Lett.* **22** 79.<sup>b</sup> Spectra Diode Labs, 1994 Product Catalogue.<sup>c</sup> Fukuda M 1991 *Reliability and Degradation of Semiconductor Lasers and LEDs* (Boston: Artech House).<sup>d</sup> Tang W C, Altendorf E H, Rosen H J, Webb D J and Vettiger P 1994 *Electron. Lett.* **30** 143.

the cavity length and/or heat-sink temperature of the laser diodes. A spectrum half width as narrow as 2 nm was maintained up to 3–4  $J_{\text{th}}$  under pulse testing.

The half width of the optical beam divergence in the direction perpendicular to the active layer is also another important factor for pumping diodes. The value of the half width for these lasers is 27° (figure 8.36) which is much less than for pumping AlGaAs lasers with a 40–48° divergence for a similar structure. The small difference in refractive indices of the waveguide and cladding layers in the InGaAsP system is the reason for such a narrow half width of beam divergence.

Preliminary lifetesting of GaInAsP (SCH-QW) lasers emitting at 808 nm for uncoated diodes at room temperature for more than 4000 h shows less than 1% decrease of output power (figure 8.37(a)). This device is currently running continuously. Selected laser diodes were tested in a constant-output-power condition (figure 8.37(b)). These devices also did not show any noticeable increase of driving current due to degradation after over 600 h of operation. Equivalent results cannot be obtained with uncoated AlGaAs/GaAs lasers.

The major laser characteristic parameters of GaInAsP/GaAs-based high-power laser diodes, such as  $J_{\text{th}}$ ,  $T_0$  and  $\eta_d$ , as listed in table 8.2, are comparable with the best results obtained with AlGaAs-based laser diodes. On the other hand, the series resistance, beam divergence and resistance to degradation under high-power operation of GaInAsP-based lasers are superior to AlGaAs system.

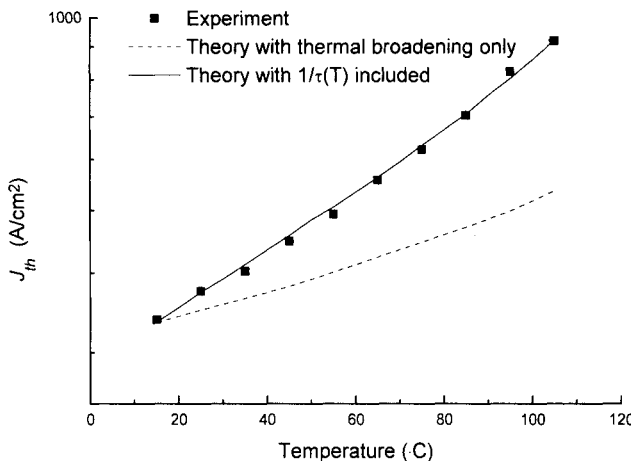


**Figure 8.38** The threshold current density ( $J_{th}$ ) of lasers with cavity length  $L = 1090$  mm for different operating temperatures ( $T$ ) (Yi *et al* 1995).

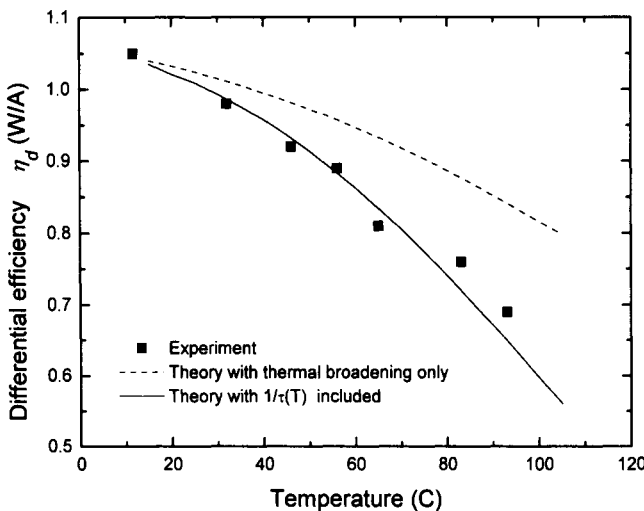


**Figure 8.39** The differential efficiency ( $\eta_d$  (W A<sup>-1</sup>)) of lasers with cavity length  $L = 1090$  mm for different operating temperatures ( $T$ ) (Yi *et al* 1995).

The advantages of the the GaInAsP system mentioned above are sufficient for replacing the AlGaAs-based lasers in present-day high-power laser applications.

(b) *Temperature dependence of the threshold current density  $J_{th}$  and differential efficiency  $\eta_d$  of high-power GaInAsP/GaAs ( $\lambda = 0.8 \mu\text{m}$ ) lasers*

Separate confinement heterostructure (SCH) InGaAsP/GaAs with 300 Å active layer thickness grown on (100)-oriented Si-doped GaAs substrates by low-

pressure MOCVD are used in this study. Undoped quaternary active region  $\text{In}_{0.13}\text{Ga}_{0.87}\text{As}_{0.74}\text{P}_{0.26}$  and waveguide  $\text{In}_{0.37}\text{Ga}_{0.63}\text{As}_{0.25}\text{P}_{0.75}$  were formed between Si-doped ( $N_d \sim 5 \times 10^{17} \text{ cm}^{-3}$ ) and Zn-doped ( $N_a \sim 6 \times 10^{17} \text{ cm}^{-3}$ ) InGaP cladding layers. Broad-area contact laser diodes with a stripe width of 100  $\mu\text{m}$  were fabricated using standard processing methods. The diodes were mounted on copper heat sinks by indium bonding without a mirror coating.

The dependences of  $J_{\text{th}}$  and  $\eta_d$  on temperature were measured under pulse operation (pulse width 100–400 ns, repetition rate 5–2.5 kHz) using an integrating sphere with an Si photodiode for temperatures ranging from 15 °C to 120 °C. The measured data are shown in figure 8.38 and figure 8.39 by full squares.

The variation of  $J_{\text{th}}$  and  $\eta_d$  as a function of cavity length, considering the thermal broadening of the gain spectrum with momentum relaxation rate ( $\hbar/\tau_0, t_0 = 4 \times 10^{-14} \text{ s}$ ) have been calculated (Yi *et al* 1995). The gain thermal broadening effect originates from the microscopic gain expression (Chinn *et al* 1988)

$$g(\hbar\omega) = \frac{q^2|M|^2}{\hbar\omega\varepsilon_0 m^2 c_0 \hbar n L_z} \sum_{ij} m_{r,ij} A_{ij} C_{ij} [\tilde{f}_c - (1 - \tilde{f}_v)] \theta(\hbar\omega - E_{ij}) \quad (8.6)$$

where  $|M|^2$  is the bulk momentum transition matrix element,  $\varepsilon_0$  is the permittivity,  $m$  is the free-electron mass,  $c_0$  is the vacuum speed of light,  $n$  is the effective refractive index,  $i, j$  are conduction-electron valence-heavy-hole quantum numbers,  $m_{r,ij}$  is the reduced mass for transition  $i, j$ ,  $C_{ij}$  is the spatial overlap factor between states  $i$  and  $j$ ,  $\theta(x)$  is the Heaviside step function and  $E_{ij}$  is the transition energy between stages  $i$  and  $j$ .  $A_{ij}$  is the anisotropy factor for transition  $i, j$  given by

$$\begin{aligned} A_{ij} &= (3/4)(1 + \cos^2 \Theta_{ij}) && \text{(for TE)} \\ A_{ij} &= (3/2) \sin^2 \Theta_{ij} && \text{(for TM).} \end{aligned}$$

The angular factor  $\Theta_{ij}$  is given by  $\cos^2 \Theta_{ij} = E_{ij}/E$ .  $\tilde{f}_c(E)$  and  $\tilde{f}_v(E)$  are convoluted quasi-Fermi distribution functions, e.g.

$$\tilde{f}_c(E) = \int_{E_g}^{\infty} d\xi \left[ \frac{1}{\pi} \frac{\hbar/\tau}{(\xi - E)^2 + (\hbar/\tau)^2} \right] \left[ \exp \left( \frac{\xi - E_{fc}}{kT} \right) + 1 \right]^{-1} \quad (8.7)$$

where  $E_{fc}$  is the quasi-Fermi level of electron carriers in an active medium, determined by the injection carrier density, and  $\hbar/\tau$  is the momentum relaxation rate (=scattering rate of carriers).  $\tilde{f}_c(E)$  and  $\tilde{f}_v(E)$  have broader distributions over energy levels at high temperature, causing a broader gain spectrum.

Numerical calculation of  $J_{\text{th}}$  and  $\eta_d$  was carried out, taking into account Auger recombination in the active region, free-carrier absorption in the waveguide and

current leakage to the cladding barriers. The total current through a diode includes the following components

$$J_{\text{total}} = J_{\text{active}} + J_{\text{wg}} + J_{\text{Auger}} + J_{\text{leakage}} \equiv J_{\text{majority}} + J_{\text{leakage}} \quad (8.8)$$

where  $J_{\text{active}}$  and  $J_{\text{wg}}$  represent radiative recombination currents in the active region and waveguide, respectively.  $J_{\text{Auger}}$  is the non-radiative Auger recombination current in the active region and  $J_{\text{leakage}}$  is the current of minority carriers overflowing from the waveguide to the cladding layers.  $J_{\text{leakage}}$  is essentially a current of electrons leaking to the p-cladding layer and eventually recombining on the boundary with the highly doped p-contact layer. The higher effective mass of holes results in a quasi-Fermi level position close to the valence band edge of the active layer so that the hole leakage current may be effectively neglected (Zory 1993). The first three terms in equation (8.8) were calculated according to standard theory (Chinn *et al* 1988) to give  $J_{\text{majority}}$ . Closer attention was paid to the calculation of the leakage current in order to explain the experimental results. In a realistic model, the electric field  $E(x)$  inside the cladding layer should be computed self-consistently with excess electron and hole distributions ( $dn(x)$  and  $dp(x)$ ). In order to perform this analysis, the boundary condition for the electric field  $E_0$  at the interface of the cladding and contact layers was determined from the majority carrier current

$$J_{\text{majority}} = qm_p P_0 E_0 - qD_p \nabla dp \quad (8.9)$$

which gives

$$E_0 \cong \frac{1}{qm_p P_0} (J_{\text{majority}} + qD_p \nabla dn) = \frac{1}{\sigma_p} \left( J_{\text{majority}} + \frac{D_p}{D_n} J_{\text{leakage}} \right). \quad (8.10)$$

Here,  $P_0$ ,  $m_p$  and  $\sigma_p$  are the hole doping concentration, mobility and conductivity in the cladding layer, and  $dn(x) \approx dp(x)$  was used in (8.10).  $dn$  at the interface of the cladding layer and waveguide layer is obtained from the thermal equilibrium distribution:  $\delta n \approx (N_c N_v / P_0) \exp[-\beta(\Delta E_{g,\text{cladding}} - (E_{fc} + E_{fv}))]$ . At the interface of the cladding layer and the contact layer,  $dn = 0$  is satisfied because of surface recombination (Casey 1978). In the above expression,  $N_c$  and  $N_v$  are the density of states for the conduction band and the heavy-hole valence band, and  $\Delta E_{g,\text{cladding}}$  is the difference between the energy gap of the cladding layer and the waveguide layer. Once all the boundary conditions are given,  $E(x)$  and  $dn(x)$  can be determined by numerically solving Poisson's equation and the diffusion-drift equation. With the obtained  $dn(x)$ ,  $J_{\text{leakage}}$  is calculated by  $J_{\text{leakage}} = qD_n \nabla \delta n(x)$ . With reference to parameters such as the internal optical loss  $\alpha_0$  and optical confinement factor  $G$ , the values used by Diaz *et al* (1994c) were employed ( $\alpha_0 = 4 \text{ cm}^{-1}$ ,  $G = 0.050$ ). The theoretical results are shown in figures 8.38 and 8.39, showing that the experimental data have a much

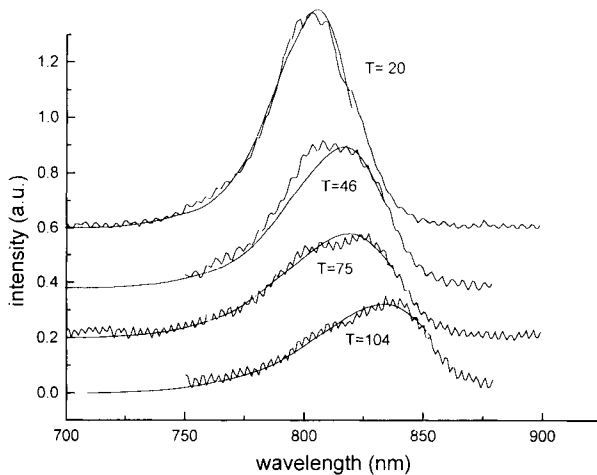


**Figure 8.40** Measured photoluminescence spectra of the studied laser structure at different temperatures (jagged curve). The spectra were reproduced by calculation with best-fit parameters for (i) momentum relaxation rate and (ii) energy gap, at each temperature (full curve) (Yi *et al* 1995).

stronger temperature dependence than this effect alone could explain. This led us to consider the temperature dependence of the momentum relaxation rate  $\hbar/\tau$  and the way it affects  $J_{\text{th}}$  and  $\eta_d$ .

Theoretical calculations (Asada *et al* 1984, Fortini *et al* 1978, Masu *et al* 1983) show that the major mechanisms contributing to the momentum relaxation rate  $\hbar/\tau$  are (i) carrier–carrier scattering (Asada *et al* 1984), (ii) carrier–phonon scattering (Fortini *et al* 1978) and (iii) alloy scattering (Masu *et al* 1983) and their temperature dependences are well known. Since the three major sources of the momentum relaxation have comparable magnitudes in the temperature range of this investigation, it is difficult to theoretically predict the temperature dependence of the relaxation rate  $\hbar/\tau$  when the mechanisms are combined. Yi *et al* (1995) have obtained the temperature dependence of  $\hbar/\tau$  by measuring photoluminescence spectra and comparing them with the theoretically calculated spectrum, as done in Yamada *et al* (1980). The jagged curves in figure 8.40 show the experimental photoluminescence spectrum obtained from the studied laser structure in the temperature range from 15 to 105 °C. The detailed set-up for this measurement was described elsewhere (Diaz *et al* 1994c). The solid curves in figure 8.40 represent the theoretical calculation of the spontaneous emission spectrum  $R(E)$  obtained as follows (Chinn *et al* 1988)

$$R(E) = \frac{16p^2Nq^2E|M|^2}{e_0m^2c_0^3h^4L} \sum_{i,j} m_{r,ij} c_{ij} [\tilde{f}_c \tilde{f}_v] q(E - E_{ij}). \quad (8.11)$$

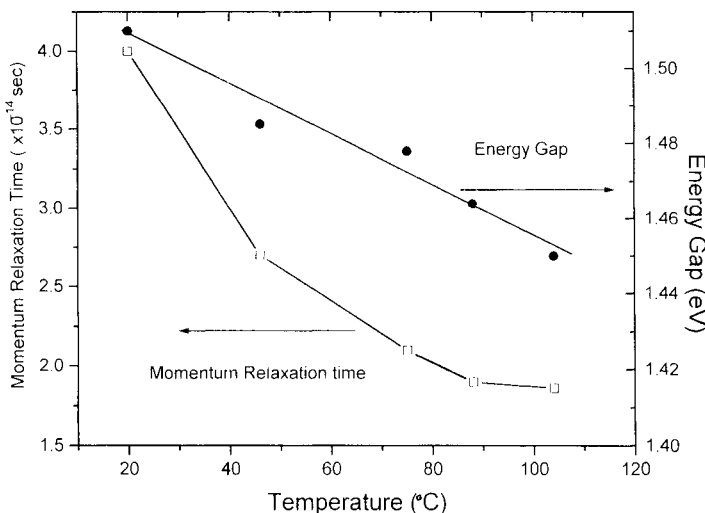


**Figure 8.41** Temperature dependence of the momentum relaxation time and energy gap, obtained from best fitting of the calculated photoluminescence spectrum to the experimental spectrum, as was done in figure 8.40 (Yi *et al* 1995).

At several temperatures between 15 and 105 °C, the theoretical spectrum is fitted to experimental data by adjusting two parameters,  $E_g$  and  $\hbar/\tau$ , as was done in figure 8.40. Roughly speaking,  $E_g$  determines the peak position, and  $\hbar/\tau$  gives the half width of the spectrum. In this way, we obtained  $E_g$  and  $\hbar/\tau$  of the active layer material at each temperature and the results are shown in figure 8.41.

Both  $E_g$  and  $\tau$  decrease from 1.51 eV to 1.45 eV and from  $4 \times 10^{-14}$  s to  $1.8 \times 10^{-14}$  s, respectively, as the temperature varies from 20 to 105 °C. Figure 8.41 shows that  $E_g(T)$  is an almost linear function of temperature, while  $\tau(T)$  has a sublinear dependence approximated by  $T^{-1/2}$ . It is well known that the alloy scattering time (= momentum relaxation time  $\tau$ ) has a  $T^{-1/2}$  dependence from mobility measurements and first-principles calculation (Masu *et al* 1983, Look *et al* 1992), while the polar optical phonon scattering has an approximately  $T^{-2}$  dependence (Fortini *et al* 1978) and carrier-carrier scattering (mainly from hole-hole scattering) has a very small temperature dependence (Asada *et al* 1984). Therefore the photoluminescence experiment data imply that alloy scattering may be the dominant mechanism behind momentum relaxation for the studied active layer material.

The experimental temperature dependence of the momentum relaxation time  $\tau(T)$  given in figure 8.41 is best fitted with the following formula

$$\tau(T) = \tau_0 \left( 1 + \beta \left( \frac{T - T_0}{T_1 - T_0} \right) \right)^{-1} \quad (8.12)$$

where  $T_0 = 15^\circ\text{C}$ ,  $T_1 = 105^\circ\text{C}$ ,  $\beta \approx 1.1$  and  $\tau_0 = 4 \times 10^{-14} \text{ s}$ . With this  $\tau(T)$ , the gain  $g(E)$  was recalculated using (8.6) and (8.7). The decrease of  $\tau(T)$  at high temperature (increase of relaxation rate  $\hbar/\tau$ ) makes  $f_{c(v)}(E)$  and  $g(E)$  broader and reduces their peak heights. Besides the additional gain broadening,  $1/\tau(T)$  affects our theoretical model in two more ways. Firstly, the hole mobility decreases at high temperature because it is inversely proportional to the scattering rate (Look *et al* 1992) (electron mobility does not play a crucial role in the calculation of  $J_{\text{th}}$  and  $\eta_d$  as discussed in Diaz *et al* (1994c))

$$\mu(T) = \mu_0 \left( \frac{\tau_0}{\tau(T)} \right) \quad (8.13)$$

where  $\mu_0 = 300 \text{ cm}^2 \text{ V}^{-1} \text{ s}^{-1}$  was used for the InGaP cladding layer. The mobility of the cladding layer is an important parameter affecting the minority-carrier leakage current which was shown previously to be anomalously large in non-optimized structures (Diaz *et al* 1994a, b). The other effect influences the free-carrier absorption in the waveguide layer. This is because the free-carrier absorption originates from the scattering of photoexcited free carriers, and therefore the absorption rate is linearly proportional to the scattering rate. Thus the free-carrier absorption loss  $\alpha_{\text{fc}}(T)$  is given by

$$\alpha_{\text{fc}}(T) = \alpha_{\text{fc},0} \left( \frac{\tau(T)}{\tau_0} \right) \cong [3N_{\text{wg}} + 7P_{\text{wg}}] \times 10^{-18} \left[ \frac{\tau(T)}{\tau_0} \right] (\text{cm}^{-1}) \quad (8.14)$$

where  $\alpha_{\text{fc},0}$ , the room-temperature free-carrier absorption loss, was obtained from Casey and Panish (1978), and  $N_{\text{wg}}$ ,  $P_{\text{wg}}$  are non-equilibrium electron and hole concentrations in the waveguide layer. All the temperature dependences of  $g(T, \tau(T))$ ,  $m(T)$  and  $\alpha_{\text{fc}}(T)$  which originated from  $\tau(T)$  require  $J_{\text{th}}$  higher and  $\eta_d$  lower than in the case when only thermal broadening  $g(T)$  was considered. The results calculated using (8.6), (8.7), (8.9)–(8.11) are shown in figures 8.38 and 8.39, showing an excellent quantitative agreement.

(c) *Theoretical investigation of minority-carrier leakage of high-power 0.8  $\mu\text{m}$  GaInAP/GaAs laser diodes*

Laser diodes with cavity lengths varying from 200 to 1700  $\mu\text{m}$  were prepared without mirror coating and light-current characteristics were recorded under short-pulse operation (pulse width 400 ns, repetition rate 1250 Hz). Figure 8.42 shows the reciprocal differential efficiency as a function of cavity length ( $L$ ) for the diodes studied. According to conventional theory, assuming constant internal efficiency and internal loss,  $\eta_d$  increases with decreasing  $L$  in the range of cavity lengths longer than 1 mm. However,  $\eta_d$  saturates at the level  $\sim 0.85 \text{ W A}^{-1}$  in the range  $L = 600\text{--}1200 \mu\text{m}$ . A sharp drop in  $\eta_d$  occurs for cavity lengths shorter than 500  $\mu\text{m}$ . Figure 8.43 shows data on threshold current density  $J_{\text{th}}$  as a function of output losses ( $\alpha_m \approx 1/L$ ). Similar to the differential efficiency discussed above,  $J_{\text{th}}$  for long-cavity lasers ( $\alpha_m < 20 \text{ cm}^{-1}$ ) increases linearly

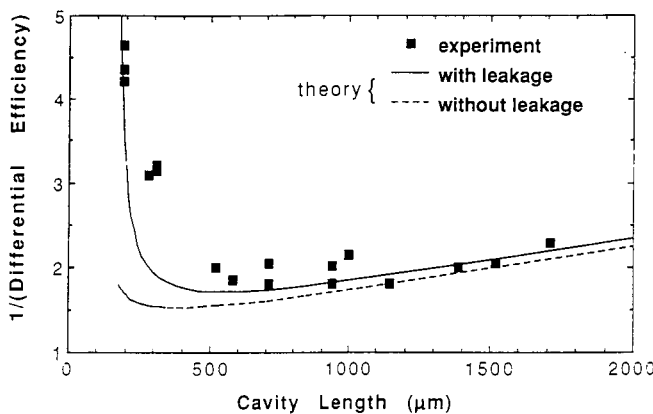


**Figure 8.42** Reciprocal differential efficiency versus cavity length for  $0.8 \mu\text{m}$  InGaAsP/GaAs laser diodes measured in the pulse regime (pulse width 400 ns, repetition rate 1250 Hz). The solid curve is the result of theoretical calculation taking current leakage to the p-cladding layer into account. The dashed curve was calculated neglecting the current leakage (Diaz *et al* 1994b).

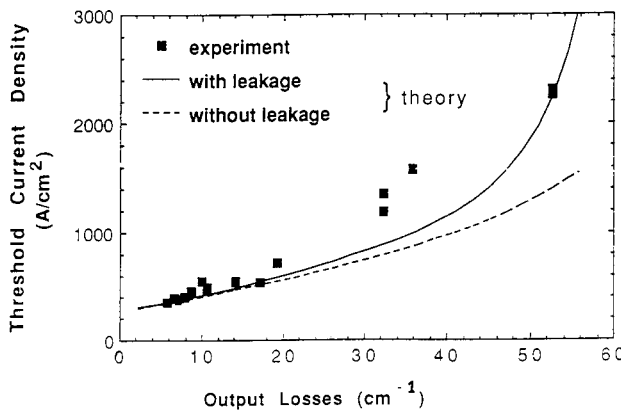


**Figure 8.43** Threshold current density versus output losses ( $\alpha_m \approx 1/L$ ) for  $0.8 \mu\text{m}$  InGaAsP/GaAs laser diodes measured in the pulse regime (pulse width 400 ns, repetition rate 1250 Hz). The solid curve shows the result of calculation taking current leakage to the p-cladding layer into account. The dashed curve was calculated neglecting current leakage (Diaz *et al* 1994b).

with output losses in agreement with conventional theory (Casey and Panish 1978). For shorter cavities, the  $J_{th}$  dependence on output loss deviates from the linearity predicted by conventional theory. Characteristically, the deviation from linear dependence of  $J_{th}$  occurs at the same cavity length as the sharp drop in differential efficiency.

*(d) Comparison of gain and threshold current density for diodes with different QW thicknesses—quantum-size effect of QW lasers*

Here we will demonstrate how the alloy-scattering-induced high relaxation rate discussed in section 8.4.3(b) affects the quantum-size effect to gain and threshold current density. We illustrate this work rather heuristically so that readers without a background in the theoretical frame for the calculation of gain and other laser characteristics easily understand one of the most interesting and sophisticated topics in semiconductor lasers: the quantum-size effect in laser diodes. During the discussion below, for the band-structure calculation based on the Luttinger–Kohn Hamiltonian, and the gain calculation based on their mathematical derivation, see Appendices C and D.

Through experiment and the theoretical model for the leakage current (due to minority-carrier leakage to the p-cladding layer) discussed in section 8.4.3(c), Yi *et al* (1995) revealed that for InGaAsP/GaAs ( $\lambda = 808$  nm) laser diodes, 300 Å is the optimal thickness for the active layer. It was found that laser diodes with active layers thinner than 300 Å had a significantly large minority-carrier leakage to the cladding layer, degrading the threshold condition and internal efficiency. This was primarily due to too small an optical confinement.

Given that 300 Å is the optimal thickness in this case, the question naturally arises as to whether a multiple quantum well with total thickness 300 Å is superior to a single quantum well 300 Å thick. This investigation was motivated by the fact that in AlGaAs/GaAs lasers, narrow QWs are known to have better performance (less temperature dependence and wavelength stability) than thicker active layer lasers (the advantages of quantum well lasers were discussed in section 8.3.1). Arakawa and Yariv (1985) attributed the lower threshold current density of thinner QWs to the lower transparency current (the current at which the gain is zero). They calculated the gains of QW lasers, assuming that the electrons and holes are free particles with masses determined by crystal potential (this approximation is called the effective-mass approximation) as described in detail in Appendix C.

However, their argument (that thinner quantum wells give lower threshold current densities) may not be an accurate conclusion when other factors are considered. Firstly, the effective-mass energy band approximation used in their work fails to describe the mixing of heavy holes and light holes, which has a significant effect on optical transition properties. Since this mixing becomes more prominent in narrow quantum wells, a comparison of optical properties for QWs with different well thickness without considering the mixing effect would not give a valid conclusion. Secondly, a relatively high intraband relaxation rate usually found in the InGaAsP quaternary material due to alloy scattering may deform the gain spectra significantly. Even though lasers with higher relaxation rate are favoured for the single longitudinal mode operation due to the homogeneous broadening of the gain spectrum (Zee 1978), the high relaxation rate may lower the difference of the gain for the lasers with different QW thickness by smoothing the gain spectra.

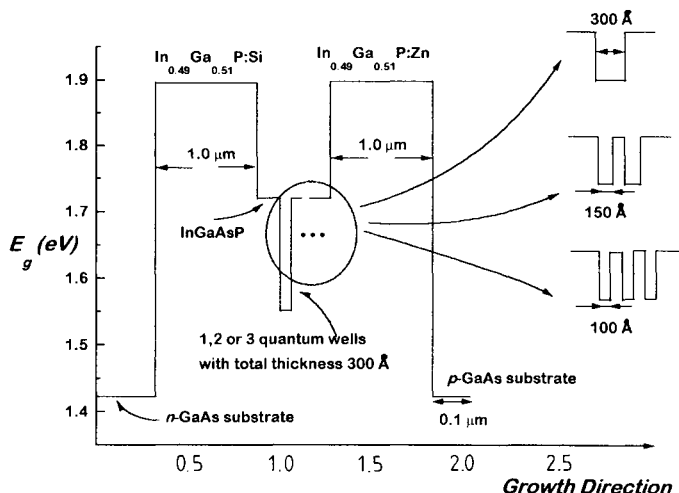


**Figure 8.44** Schematic diagram of the three kinds of laser (a triple 100 Å QW, a double 150 Å QW and a single 300 Å QW) that were used for this experiment.

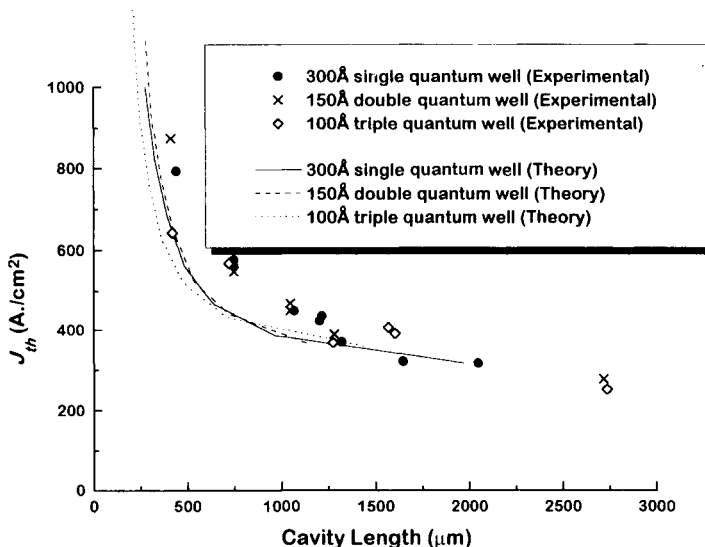


**Figure 8.45** The threshold current densities of the three lasers shown in figure 8.44. The symbols represent experimental results while lines represent theoretical results.

The above question, i.e., whether lasers composed of narrow QWs demonstrate better performance compared with lasers with thicker QWs when the same optical confinement applies (same total active layer thickness), is addressed in this work. Yi *et al* (1995) compared the characteristics of three different QW

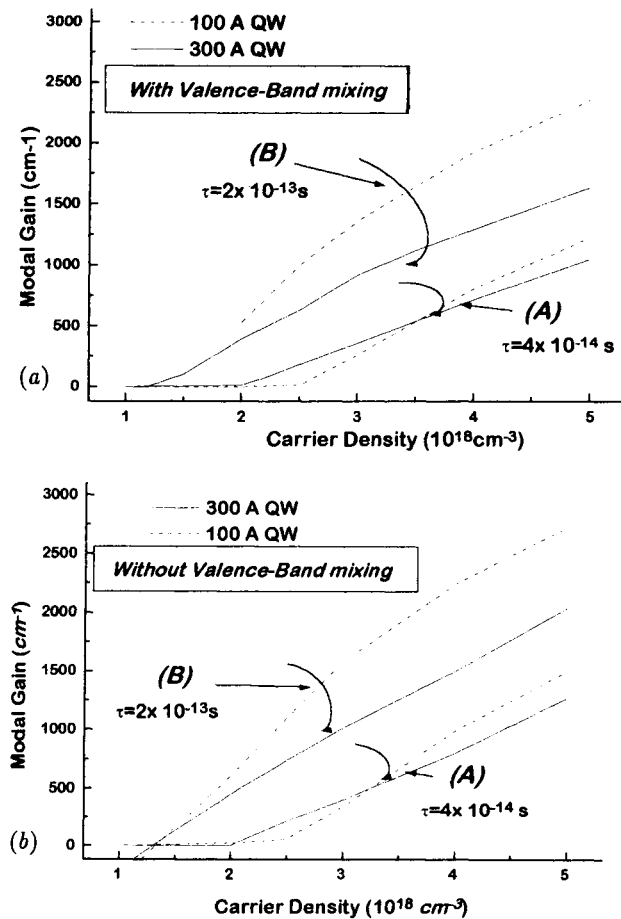


**Figure 8.46** (a) Calculated modal gains for 100 Å QW lasers (dashed lines) and 300 Å QW lasers (solid lines) when valence-band mixing was considered. Curve A is related to the relaxation time  $\tau = 4 \times 10^{-14}$  s, while curve B is for  $\tau = 2 \times 10^{-13}$  s. (b) Same as (a) except that valence-band mixing was not taken into account for the calculation.

structures with the same total QW active layer thickness of 300 Å: (i) triple 100 Å QWs, (ii) double 150 Å QWs, and (iii) a single 300 Å QW for the active layer. A schematic diagram for these structures is shown in figure 8.44. Details of the sample preparation and experimental procedure for measuring  $J_{th}$  and  $\eta_d$  were described in section 8.4.3(a)–(c). The experimental results (symbols) for  $J_{th}$  as a function of the cavity length  $L$  show no significant difference of  $J_{th}$  between the laser structures with one, two and three quantum wells (figure 8.45). The differential efficiency  $\eta_d$  was also found to be independent of the inner structure of the active region.

To determine whether this result comes from intrinsic effects such as valence-

band mixing or a high relaxation rate as mentioned earlier, or from extrinsic effects such as interface-induced degradation, we compared experiment to theory by taking the valence mixing and high relaxation rate into account. The energy levels of the valence bands should be calculated by employing the Luttinger-Kohn Hamiltonian as explained in detail in Appendix D.

Material parameters such as the Luttinger parameter and the energy gap are linearly interpolated from the values of binary materials as in table 8.3. In equation (D.11) in Appendix D, the heavy hole (upper row) and light hole (lower row) are mixed due to the non-zero off-diagonal elements of the Hamiltonian. The space-dependent Hamiltonian was solved using the eigenfunction expansion method (Gershoni *et al* 1993). The energy band and the envelope functions obtained from the Hamiltonian (equation (D.11) of Appendix D) are used in the calculation of the optical gain. In the gain calculation, we used  $\tau = 0.04$  ps for the relaxation time as determined from photoluminescence measurements as in section 8.4.3(b). The calculated gains for the 100 Å QW and 300 Å QW versus injection current density are shown in figure 8.46(a) (curve A). The two curves (in curve A) show a remarkably similar dependence on the injection carrier density. As discussed above, this is quite contrary to the work of Arakawa and Yariv (1985) where a significantly lower transparency carrier density and higher gain were obtained from a thinner QW. The difference may originate from either of two effects considered here: valence-band mixing, or high intraband relaxation rate. To clarify the origin, we recalculated the gain without considering either effect. Curve B in figure 8.46(a) is the gain versus carrier density without considering a high relaxation rate. Instead of  $\tau = 0.04$  ps,  $\tau = 0.2$  ps was assumed. In this case, the quantum-size effect of the QW is evident: the 100 Å QW lasers would have >30% higher gain than the 300 Å QW laser. This difference was almost absent for the  $\tau = 0.04$  ps case.

To estimate the effect of valence-band mixing, the effective-mass approximation (non-mixing) was applied to the gain calculation. For a systematic comparison, we made the following change to the Hamiltonian, while keeping the form of equation (D.11) in Appendix D

$$H_v \rightarrow H_v^{\text{non-mixing}} = \frac{1}{2} \left( \frac{\hbar^2}{m_0} \right) \begin{pmatrix} (\gamma_1 - 2\gamma_2)(k_z^2 + k_\rho^2) & 0 \\ 0 & (\gamma_1 + 2\gamma_2)(k_z^2 + k_\rho^2) \end{pmatrix} + V(z). \quad (8.15)$$

In this way, we could see the difference between mixing and non-mixing directly without being affected by changes in other parameters. Note that equation (D.11) and equation (8.15) would give the same eigenenergies when  $V(z) = 0$  (i.e. for bulk material). Figure 8.46(b) shows the calculated gains when the energies and wavefunction for the holes are calculated with the effective-mass Hamiltonian (equation (8.15)) for  $\tau = 0.04$  ps (curve A) and  $\tau = 0.2$  ps (curve B). This calculation also indicates the absence of a difference in the gains for the 100 Å and 300 Å QW lasers when the relaxation rate is high (curve A). Thus it is

**Table 8.3** Material constant for GaAs, ternary and quaternary materials commonly used for lasers. The effective mass of electrons and Luttinger parameters for quaternary materials are interpolated from the related binary materials (i.e. GaAs, InAs, InP, GaP), using the following equation:

$$A_{(\text{In}_{1-x}\text{Ga}_x\text{As}_y\text{P}_{1-y})} = A_{\text{GaAs}}xy + A_{\text{InAs}}(1-x)y + A_{\text{InP}}(1-x)(1-y).$$

In bulk material, the effective mass of heavy holes ( $m_{\text{hh}}$ ) and light holes ( $m_0$ ) along  $\langle 100 \rangle$  and  $\langle 111 \rangle$  directions are related to the Luttinger parameters by

$$\frac{m_0}{m_{\text{hh}}(\langle 100 \rangle)} = \gamma_1 - 2\gamma_2 \quad \frac{m_0}{m_{\text{hh}}(\langle 100 \rangle)} = \gamma_1 + 2\gamma_2 \quad (\text{T1})$$

$$\frac{m_0}{m_{\text{hh}}(\langle 111 \rangle)} = \gamma_1 - 2\gamma_3 \quad \frac{m_0}{m_{\text{hh}}(\langle 111 \rangle)} = \gamma_1 + 2\gamma_3. \quad (\text{T2})$$

Materials constants						
GaAs	Al <sub>0.50</sub> Ga <sub>0.50</sub> As	Ga <sub>0.49</sub> In <sub>0.51</sub> P	In <sub>0.13</sub> Ga <sub>0.87</sub> As <sub>0.74</sub> P <sub>0.26</sub>	In <sub>0.37</sub> Ga <sub>0.63</sub> As <sub>0.25</sub> P <sub>0.75</sub>	Ga <sub>0.9</sub> In <sub>0.1</sub> As	
Energy gap $E_g$ (eV)	1.42	1.79	1.90	1.52	1.80	1.31
Refractive index $n$	3.655	3.41	3.450	3.58	3.48	3.64
Effective electron mass						
$m_e$ ( $m_0$ unit)	0.067	0.108	0.0794	0.0664	0.072	0.0626
Luttinger parameter $\gamma_1$	6.790	—	5.29	7.428	6.635	8.078
$\gamma_2$	1.924	—	1.541	2.335	2.117	2.568
$\gamma_3$	2.782	—	2.221	3.153	2.847	3.432
Electron affinity $\chi$ (eV)	4.5	—	4.204	4.37	4.231	4.495
Lattice constant $a$ (Å)	5.641	5.65	5.663	5.646	5.652	5.683

not the valence-band mixing that makes the gains for the two QW lasers less different but the high relaxation rate.

In order to directly verify whether the calculated gain correctly models experiment, we performed a calculation of  $J_{\text{th}}$  using the model discussed in section 8.4.3(c). The calculation reveals almost the same threshold current densities for all three laser structures. This result was expected since the three lasers have the same gain, optical confinement, active layer volume, and loss. Figure 8.45 shows the comparison between calculation (lines) and experiment (symbols). The agreement is excellent for the entire range of cavity length investigated.

The excellent match between experiment and theory indicates that the interfaces between well layers and barrier layers do not contribute to loss or non-radiative recombination to a detectable level. If this were not so, the triple 100 Å QW lasers, having 3 times more hetero-interfaces than single 300 Å QW lasers, would have shown a higher threshold current due to the higher loss and non-radiative recombination. The absence of additional loss due to the interface is consistent with recent work on Hall mobility measurements (Mitchel *et al* 1994). In that work, it was shown that the interface roughness should be less than two monolayers. This small fluctuation does not cause any detectable optical loss according to light-scattering calculations (Henry *et al* 1981).

Numerical calculations of the  $\eta_d(L)$  and  $J_{\text{th}}(1/L)$  dependences were performed as described in section 8.4.3(b). Calculated curves for  $\eta_d(L)$  and  $J_{\text{th}}(1/L)$  dependences are shown in figures 8.42 and 8.43 and exhibit good quantitative agreement with experimental data. For comparison, the dashed lines in figures 8.42 and 8.43 demonstrate values of  $\eta_d$  and  $J_{\text{th}}$  calculated without taking the current leakage into account. For short-cavity lasers the leakage current is the single most important factor responsible for the increase in  $J_{\text{th}}$  and drop in  $\eta_d$  for the investigated laser diodes. The leakage current contribution to  $J_{\text{th}}$  increases with output losses because higher threshold gains shift the quasi-Fermi level position to higher energies and thus enhance excess carrier spillover to the waveguide and cladding layers. Leaking excess carriers recombine non-radiatively in the cladding and contact layers and decrease the internal efficiency above the threshold. The comparison of theoretical and experimental data clearly demonstrates that current leakage to the p-cladding layer affects the laser parameters significantly only in the range of cavity lengths below 500 μm. For cavity lengths longer than 500 μm the current leakage results in no more than a 10–15% change in the values of efficiency and threshold. Long-cavity 0.8 μm InGaAsP/GaAs lasers have already been successfully used for high-power operation in the quasi-CW and CW regimes.

## REFERENCES

Adams M J 1973 *Opto-Electron.* **5** 201

- Agrawal G P and Dutta N K 1986 *Long-Wavelength Semiconductor Lasers* (New York: Van Nostrand Reinhold)
- Aigrain P 1958 *Proc. Conf. on Quantum Electronics (Paris, 1963)* p 1762
- Alferov Zh I, Andreev V M, Garbuzov D Z, Zhilyaev Yu V, Morozov E P, Portnoi E L and Trofim V G 1971 *Sov. Phys.-Semicond.* **4** 1573 [Translated from 1970 *Fiz. Tekh. Poluprovodn.* **4** 1826]
- Alferov Zh I, Arsentyev I N, Vavilova L S, Garbuzov D Z and Krasovskyi V V 1984 *Sov. Phys.-Semicond.* **18** 1035
- Alferov Zh I and Kazarinov R F 1963 *Author's Certificate, USSR No 181737* with priority of 30 March
- Arakawa Y and Yariv A 1985 *IEEE J. Quantum Electron.* **QE-21** 1666
- Arimoto S, Yasuda M, Shima A, Kadoiwa K, Kamizato T, Watanabe H, Omura E, Aiga M, Ikeda K and Mitsui S 1993 *IEEE J. Quantum Electron.* **QE-29** 1874
- Arnold G, Pusser P and Petermann K 1982 *Semiconductor Devices for Optical Communications (Springer Topics in Applied Physics 39)* 2nd edn (Berlin: Springer)
- Asada M, Kameyama A and Suematsu Y 1984 *IEEE J. Quantum Electron.* **QE-20** 745
- Brunemeir P E, Hsieh K C, Deppe D G, Brown J M and Holonyak N 1985 *J. Crystal Growth* **71** 705
- Buus J 1991 *Single Frequency Semiconductor Lasers* (Bellingham, WA: SPIE Optical Engineering)
- Casey H C Jr 1978 *J. Appl. Phys.* **49** 3684
- Casey H C Jr and Panish M B 1978 *Heterostructure Lasers* (New York: Academic)
- Casey H C Jr, Panish M B and Merz J L 1973 *J. Appl. Phys.* **44** 5470
- Casey H C Jr, Panish M B, Schlosser W O and Paoli T L 1974 *J. Appl. Phys.* **45** 322
- Chand N, Becker E E, van der Ziel J P, Chu S N G and Dutta N K 1991 *Appl. Phys. Lett.* **58** 1704
- Chand N, Chu S, Dutta N, Geva J, Syrbu A, Mereutza A and Takolev V 1994 *IEEE J. Quantum Electron.* **QE-30** 424
- Chen H Z, Ghaffari A, Morkoc H and Yariv A 1987 *Appl. Phys. Lett.* **51** 2094
- Chen Y K, Wu M C, Kuo J M, Chin M A and Sergent A M 1991 *Appl. Phys. Lett.* **59** 2
- Chin R, Holonyak N Jr, Vojak B A, Hess K, Dupuis R D and Dapkus P D 1980 *Appl. Phys. Lett.* **36** 19
- Chinn K, Zory P and Reisinger A 1988 *IEEE J. Quantum Electron.* **QE-24** 2191
- Dallesasse J M and Holonyak N 1991 *Appl. Phys. Lett.* **58** 394
- d'Asaro L A 1973 *J. Lumin.* **7** 310
- Diaz J, Eliashevich I, He X, Yi H, Kolev E, Garbuzov D and Razeghi M 1994a *Appl. Phys. Lett.* **65** 1004
- Diaz J, Eliashevich I, Yi H, He X, Stanton M, Erdtmann M, Wang L and Razeghi M 1994b *Appl. Phys. Lett.* **65** 2260
- Diaz J, Yi H, Erdtmann M, He X, Kolev E, Garbuzov D, Bigan E and Razeghi M 1994c *J. Appl. Phys.* **76** 700
- Dupuis R D and Dapkus P D 1979 *IEEE J. Quantum Electron.* **QE-15** 128
- Dupuis R D, Dapkus P D, Holonyak N Jr, Rezek E A and Chin R 1978 *Appl. Phys. Lett.* **32** 295
- Dupuis R D, Dapkus P D and Moudy L A 1977 *Tech. Digest 1977 Int. Electron Devices Meeting* p 575
- Dyment J C, Nash F R, Hwang C J, Rozgonyi G A, Hartman R L, Marcos H M and Haszko S E 1974 *Appl. Phys. Lett.* **24** 481
- Esaki L and Tsu R 1970 *IBM J. Res.* **14** 61
- Fortini A, Diguet D and Lugand J 1978 *J. Appl. Phys.* **41** 3121
- Fujii H, Kobayashi K, Kawata S, Gomyo A, Nino I, Hotta H and Suzuki T 1987 *Electron. Lett.* **23** 938

- Fujii T, Yamakoshi S, Nanbu K, Wada O and Hiyamizu S 1984 *J. Vac. Sci. Technol. B* **2** 259
- Garbuzov D Z, Antonishkis N J, Bondarev A D, Gulakov A B, Zhigulin S N, Kotsavets N I, Kochergin A V and Rafailov E V 1991 *IEEE J. Quantum Electron.* **QE-27** 1531
- Garbuzov D Z, Gulakov A B, Kochergin A V, Shkurko A P, Strugov N A, Ter-Martirosyan A L and Chalyi V P 1990 *Tech. Digest Conf. Lasers Electron-Optics (Optical Society of America, Washington, DC)* p 468
- Gershoni D, Henry C H and Baraff G A 1993 *IEEE J. Quantum Electron.* **QE-29** 2433
- Hall D N, Fenner G E, Kingsley J D, Soltys T J and Carlson R O 1962 *Phys. Rev. Lett.* **9** 366
- Hayashi I, Panish M B and Foy P W 1969 *IEEE J. Quantum Electron.* **QE-5** 211
- Henry C H, Logan R and Merritt F 1981 *IEEE J. Quantum Electron.* **QE-17** 2196
- Hersee S D, Baldy M, Assenat P, de Cremoux B and Duchemin J P 1982 *Electron. Lett.* **18** 870
- Hersee S D, de Cremoux B and Duchemin J P 1984 *Appl. Phys. Lett.* **44** 476
- Holonyak N Jr and Bevacqua S F 1962 *Appl. Phys. Lett.* **1** 82
- Iga K, Uenohara H and Koyama F 1986 *Electron. Lett.* **22** 1008
- Itaya K, Watanabe Y, Ishikawa M, Hatakoshi G and Uematsu Y 1991 *Appl. Phys. Lett.* **58** 1718
- Kazarinov R F and Tsarenkov G V 1976 *Sov. Phys.-Semicond.* **10** 178
- Kobayashi K, Kawata S, Gomyo A, Nino I and Suzuki T 1985 *Electron. Lett.* **21** 931
- Kressel H 1980 *Semiconductor Devices for Optical Communication* (Berlin: Springer)
- Kressel H and Nelson H 1969 *RCA Rev.* **30** 106
- Kroemer H 1963 *Proc. IEEE* **51** 1782
- Lau K Y, Derry P L and Yariv A 1988 *Appl. Phys. Lett.* **52** 88
- Look D, Lorance D, Sizelov J, Stutz C, Evans K and Whitson D 1992 *J. Appl. Phys.* **71** 260
- Luttinger J M 1956 *Phys. Rev.* **102** 1030
- Masu K, Tokumitsu El, Konagai M and Takahashi K 1983 *J. Appl. Phys.* **54** 5785
- Mitchel W C, Brown G J, Lo I, Elhamri S, Ahoujja M, Ravindran K, Newrock R S, Razeghi M and He X 1995 *Appl. Phys. Lett.* **65** 1578
- Mobarhan K, Razeghi M and Blondeau R 1992a *Electron. Lett.* **28** 1510
- Mobarhan K, Razeghi M, Marquebielle G and Vassilaki E 1992b *J. Appl. Phys.* **72** 4447
- Narui H, Hirata S and Mori Y 1992 *IEEE J. Quantum Electron.* **QE-28** 4
- Nasledov D N, Rogachev A A, Ryvkin S M and Tsarenkov B V 1962 *Sov. Phys.-Solid State* **4** 782 [Translated from 1962 *Fiz. Tverd. Tela* **4** 1062]
- Nathan M I, Dumke W P, Burns G, Dill F H Jr and Lasher G 1962 *Appl. Phys. Lett.* **1** 62
- Ohkubo M, Ijichi T, Iketani A and Kikata T 1992 *Appl. Phys. Lett.* **60** 23
- Panish M B, Hayashi I and Sumski S 1969 *IEEE J. Quantum Electron.* **QE-5** 210
- Quist T M, Rediker R H, Keyes R J, Krag W E, Lax B, McWhorter A L and Zeiger H J 1962 *Appl. Phys. Lett.* **1** 91
- Razeghi M 1989 *The MOCVD Challenge: Volume 1: A Survey of GaInAsP-InP for Photonic and Electronic Applications* (Bristol: Hilger)
- Razeghi M 1991 *Materials for Photonic Devices, 15* (New Jersey: World Scientific)
- Razeghi M 1993 *InGaAsP Diodes, US Air Force Philips Laboratory, Diode Laser Technology Program Conf. (Albuquerque, 20–22 April)*
- Razeghi M 1994 *Nature* **369** 631
- Razeghi M, Diaz J, Eliashevich I, He X, Yi H, Erdtmann M, Kolev E, Wang L and Garbuzov D 1994 *Conf. Digest IEEE Int. Semiconductor Laser Conf. '94 (Maui, Hawaii, 19–23 September 1994)* p 159

- Sasaki K, Matsumoto M, Kondo M, Ishizumi T, Takeoka T, Yamanoto S and Hijikata T 1991 *Japan. J. Appl. Phys.* **30** L904
- Serreze H B, Chen Y C and Waters R G 1991 *Appl. Phys. Lett.* **58** 3
- Simhony S, Kapon E, Colas E, Hwang D M, Stoffel N G and Worland P 1991 *Appl. Phys. Lett.* **59** 2225
- Sze S M 1981 *Physics of Semiconductor Devices* 2nd edn (New York: Wiley)
- Thompson G H B, Henshall G D, Whiteaway J E A and Kirkby P A 1976 *J. Appl. Phys.* **47** 1501
- Thompson G H B and Kirkby P A 1973 *IEEE J. Quantum Electron.* **QE-9** 311
- Tsang W T 1981a *Appl. Phys. Lett.* **39** 134
- Tsang W T 1981b *Appl. Phys. Lett.* **39** 786
- Tsang W T 1982 *Appl. Phys. Lett.* **40** 217
- Tsang W T 1984 *IEEE J. Quantum Electron.* **QE-20** 1119
- Tsang W T, Weisbuch C, Miller R C and Dingle R 1979 *Appl. Phys. Lett.* **35** 673
- Tsukada T 1974 *J. Appl. Phys.* **45** 4899
- Ueno Y, Fujii H, Kobayashi K, Endo K, Gomyo A, Hara K, Kawata S, Yuasa T and Suzuki T 1990 *Japan. J. Appl. Phys.* **29** L1666
- Usami U and Matsushima Y 1994 *Proc. 14th IEEE Int. Semiconductor Laser Conf. '94 (Maui, Hawaii, 19–23 September 1994)*
- van der Ziel J P, Dingle R, Miller R C, Wiegmann W and Nordlund W A Jr 1975 *Appl. Phys. Lett.* **26** 463
- Wagner D K, Waters R G, Tihanyi P L, Hill D S, Roza A J Jr, Vollmer H J and Leopold M M 1988 *IEEE J. Quantum Electron.* **QE-24** p 1258
- Yamada M, Ishiguro H and Nagato H 1980 *Japan. J. Appl. Phys.* **19** 135
- Yariv A 1989a *IEEE Circuits Devices Mag.* **5**(6) 25
- Yariv A 1989b *Quantum Electron.* 3rd edn (New York: Wiley)
- Yi H Y, Diaz J, Eliashevich I, Stanton M, Erdtmann M, He X, Wang L J and Razeghi M 1995 *Appl. Phys. Lett.* **66** 253
- Yi H Y, Diaz J, Wang L J, Eliashevich I, Kim S, William R, Erdtmann M, He X, Kolev E and Razeghi M 1995 *Appl. Phys. Lett.* **66** 3251
- Yonezu H, Sakuma I, Kobayashi K, Kamejima T, Ueno M and Nannichi Y 1973 *Japan. J. Appl. Phys.* **12** 1585
- Zee B 1978 1978 *IEEE J. Quantum Electron.* **QE-14** 727
- Zhao H, MacDougal M H, Uppal K and Dapkus P D 1994 *Proc. 14th IEEE Int. Semiconductor Laser Conf. '94 (Maui, Hawaii, 19–23 September 1994)*
- Zory P (ed) 1993 *Quantum Well Lasers* (San Diego, CA: Academic) p 315

## GaAs-based heterojunction electron devices grown by MOCVD

### 9.1 INTRODUCTION

In high-speed electronic device applications GaAs and its related compounds are superior to silicon due to their higher carrier mobilities which enhance device speed and current handling capability. Molecular beam epitaxy (MBE) and metallorganic chemical vapour deposition (MOCVD) have been the most important growth techniques in the production of high-quality epilayers for device fabrication. An important problem with MBE is the difficulty in controlling the phosphorus vapour pressure during MBE growth. Therefore phosphorus-based materials are not easy to grow with this technique. Another problem is the low throughput of MBE growth. MOCVD, with its batch capability, is more suitable for volume manufacturing. This chapter will concentrate on the growth, fabrication and characteristics of MOCVD-grown, GaAs-based heterostructure field effect and bipolar transistors which have been the most important devices in digital and microwave applications. It is assumed that the reader is familiar with the basic principles involving the operation of homojunction field effect and bipolar transistors at the level of an undergraduate course on solid-state devices.

#### 9.1.1 Heterojunctions

A heterojunction can be defined as a junction formed between two materials with different electrical properties. Figure 9.1 shows the construction of the band diagram for an n-p heterojunction.

The difference in energy between the vacuum level and the conduction band is defined as the electron affinity  $\chi$  which is the energy necessary to promote an electron from the conduction band to the vacuum level. The work function  $\phi$  is the energy required to take an electron from the Fermi level to the vacuum level. Hence the work function varies with the doping level. When the junction is formed, discontinuities in the conduction and valence bands ( $\Delta E_c$  and  $\Delta E_v$ ) appear due to the difference in the electron affinities. The conduction band

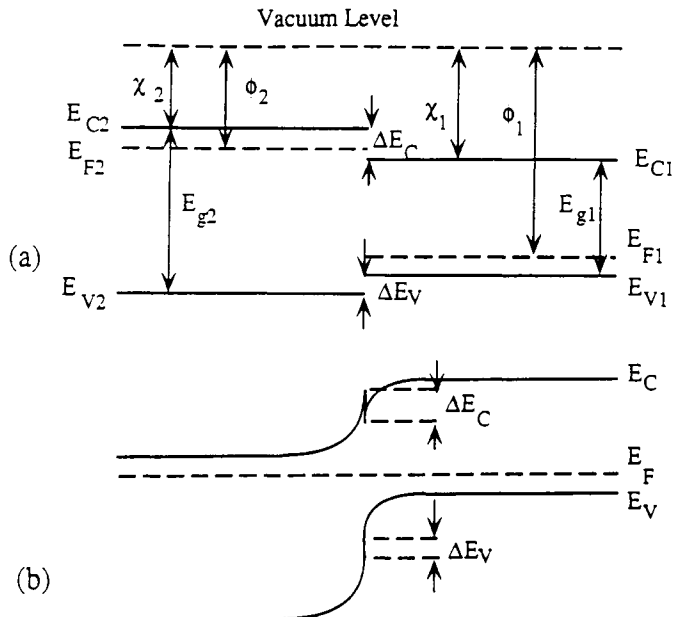


**Figure 9.1** Band diagram of a p-n heterojunction (a) before and (b) after the contact is formed.

discontinuity is given by (Anderson 1962)

$$\Delta E_c = \chi_1 - \chi_2. \quad (9.1)$$

From figure 9.1 it can be seen that the valence band discontinuity can be expressed as

$$\Delta E_v = \Delta E_g - \Delta E_c \quad (9.2)$$

where  $\Delta E_g$  is the difference in bandgaps of two semiconductors.

Due to the initial difference in the Fermi levels in the two semiconductors, band bending is observed at the interface as shown in figure 9.1(b) (similar to homojunctions). The built-in potential is

$$q V_D = E_{F1} - E_{F2}. \quad (9.3)$$

The ratio of the two components of  $V_D$  that drop on p ( $V_{D1}$ ) and n ( $V_{D2}$ ) regions is given by

$$\frac{V_{D1}}{V_{D2}} = \frac{\varepsilon_2 N_2}{\varepsilon_1 N_1} \quad (9.4)$$

where  $N_1, N_2$  are the doping concentrations and  $\varepsilon_1, \varepsilon_2$  are the permittivities in p- and n-type semiconductors, respectively.

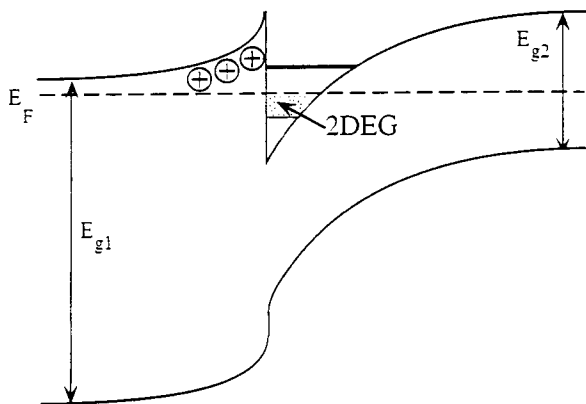


**Figure 9.2** Energy band diagram for a modulation-doped heterostructure.

## 9.2 HETEROSTRUCTURE FIELD-EFFECT TRANSISTORS (HFETS)

One of the promising heterojunction devices in digital and microwave applications is the modulation-doped field effect transistor (MODFET). The transistor has several other names such as HEMT (high-electron-mobility transistor), TEGFET (two-dimensional electron gas field effect transistor) and SDHT (selectively doped heterojunction transistor).

A modulation-doped heterostructure in its simplest form can be defined by a heterojunction between two semiconductors with different bandgaps where only the semiconductor with the larger bandgap is doped. The energy band diagram for a modulation-doped heterostructure is shown in figure 9.2. In order to minimize their energy, electrons are transferred into the lower-bandgap material by diffusion and they form a two-dimensional electron gas confined at the heterojunction interface in a quasitriangular potential well. Since the electrons are separated from the ionized donors, ionized impurity scattering is significantly reduced. This scattering process is the dominant mechanism that scatters electrons at low temperatures where phonon scattering is not significant. The absence of ionized impurity scattering enhances electron mobility and therefore device speed. A combination of the elimination of ionized impurity scattering with the ability to confine a large number of electrons in a thin layer makes it possible to switch large currents rapidly. This is especially important in digital circuits where high current levels are necessary for fast switching of device and interconnection capacitances. The most commonly used material systems are AlGaAs/GaAs, AlGaAs/InGaAs, GaInP/GaAs on GaAs substrate and InAlAs/InGaAs on InP substrate. In the following sections the basics of MODFET operation and the factors affecting its characteristics will be discussed and the performance of devices based on different material systems will be compared.

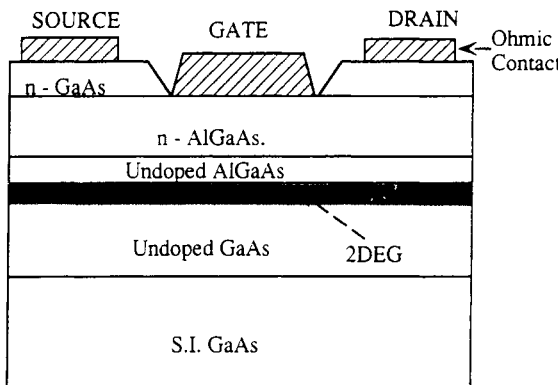


**Figure 9.3** Typical cross-section of an AlGaAs/GaAs MODFET.

### 9.2.1 AlGaAs/GaAs MODFETs

AlGaAs/GaAs has been the most extensively studied material system for modulation-doped field effect transistors.  $\text{Al}_x\text{Ga}_{1-x}\text{As}$  is lattice matched to GaAs over the entire compositional range. This permits the growth of high-quality heterojunctions without misfit dislocations. However, at cryogenic temperatures where a MODFET's superiority over a homojunction field effect transistor becomes significant, abnormal behaviour is observed in AlGaAs/GaAs MODFETs as will be discussed later. Since this system has been the most widely used material system in heterostructures, this section is devoted to the discussion of AlGaAs/GaAs MODFETs.

The cross-sectional structure of an AlGaAs/GaAs MODFET is shown in figure 9.3. The undoped AlGaAs layer (spacer) is used to eliminate remote ionized impurity scattering of the electrons in the GaAs layer by screening the potential of the ionized impurities in the doped AlGaAs layer. The top n-GaAs layer (cap layer) is designed for good ohmic contact formation and for the protection of AlGaAs against oxidation. A widely used metal alloy for ohmic contacts is AuGeNi. During metallization Ge makes contact with the 2DEG channel by diffusing to the AlGaAs/GaAs interface. Due to the excellent lattice match between Ge and GaAs good ohmic contact with a low interface state density is formed. AlTi is commonly used for Schottky barrier contacts.

Since source and drain resistances affect the device performance, these resistances should be minimized. This can be done by ion implantation using a T-bar gate structure. However ion implantation requires subsequent annealing at elevated temperatures for the activation of the implant. An increase in the 2DEG density and a decrease in the mobility have been observed in MBE-grown modulation-doped AlGaAs/GaAs structures during annealing at around 800°C (Ishikawa *et al* 1981). This led to the conclusion that Si impurities in the AlGaAs layer were diffusing into the undoped GaAs layer during annealing.

Later it was reported that rapid thermal annealing, which requires only a few seconds, can reduce Si diffusion (Pearah *et al* 1984).

The operation of a MODFET is similar to that of a homogeneous field effect transistor. The Schottky barrier (gate) on the doped AlGaAs layer modulates the two-dimensional electron gas and the drain-source current by depleting the region under the gate. The doped AlGaAs layer is also depleted at the AlGaAs/GaAs interface due to electron transfer into GaAs. Since the conduction in the doped AlGaAs layer is inferior to the transport in undoped GaAs, it is important that the AlGaAs layer is totally depleted (the two depletion regions overlap) in order to avoid conduction through this layer. Therefore, in a MODFET, the maximum gate voltage is limited. Above a certain value, conduction occurs in the doped AlGaAs layer and a degradation in performance is observed. The limitation in the forward gate voltage also limits the logic swing.

If the AlGaAs layer is sufficiently thin or a large negative bias is applied, the junction depletion region (AlGaAs/GaAs) and gate depletion region (metal/AlGaAs) overlap. Under these conditions, the sheet carrier concentration at the interface can be expressed approximately as (Delagebeaudeuf and Ling 1982, Drummond *et al* 1983)

$$n_s = \frac{\epsilon}{q(d + \Delta d)} (V_g - V_T) \quad (9.5)$$

where  $q$  is the electron charge, and  $d$  is the total thickness of the doped and undoped AlGaAs layers.  $V_g$  is the gate voltage and  $V_T$  is the threshold voltage given by

$$V_T = \Phi_b - \Delta E_c - \frac{q N_d d_d^2}{2\epsilon} + \Delta E_{FO}. \quad (9.6)$$

Here  $\Phi_b$  is the Schottky barrier height,  $N_d$  is the doping density and  $d_d$  is the thickness of the doped AlGaAs layer.  $\Delta d$ ,  $\Delta E_{FO}$  are the fitting parameters ( $\Delta d = 80 \text{ \AA}$  and  $\Delta E_{FO} = 0$  and 25 mV at 300 K and 77 K respectively for the AlGaAs/GaAs system).

The threshold voltage is an important parameter in determining the noise margin of a logic circuit. Large variations in the threshold voltage result in poor logic margins. It is necessary that the sensitivity of the threshold voltage to fabrication process variations be minimized in order to achieve an acceptable yield in the integrated circuits.

A very important characteristic of a field effect transistor is the intrinsic transconductance which is a measure of its gain and is given by

$$g_m = \left. \frac{\partial I_{DS}}{\partial V_{GS}} \right|_{V_{DS}} = \frac{C_G}{\tau} \quad (9.7)$$

where  $I_{DS}$  is the drain-source current,  $V_{GS}$  is the gate-source voltage,  $V_{DS}$  is the drain-source voltage,  $C_G$  is the gate capacitance and  $\tau$  is the transit time of

the carriers through the channel. The maximum intrinsic transconductance of a MODFET is given approximately by (Lee *et al* 1983)

$$g_{m_{\max}} = \frac{q\mu n_s}{L\sqrt{1 + [q\mu n_s(d + \Delta d)/\epsilon v_s L]^2}} \quad (9.8)$$

where  $L$  is the gate length and  $v_s$  is the saturation velocity. For short-gate MODFETs equation (9.8) can be expressed approximately in the form

$$g_{m_{\max}} = \frac{\epsilon v_s}{(d + \Delta d)}. \quad (9.9)$$

Equation (9.9) shows that the maximum transconductance becomes independent of gate length. However, for short-gate devices, electron velocity overshoot effects are important and the carrier velocity depends on the gate length.

The frequency response of a field effect transistor is governed by the transit time of the carriers under the gate ( $\tau$ ). The cut-off frequency of a field effect transistor is given by

$$f_T = \frac{1}{2\pi\tau} \quad (9.10)$$

or if velocity saturation occurs in the channel

$$f_T = \frac{v_s}{2\pi L}. \quad (9.11)$$

Using equations (9.7), (9.10) we obtain

$$f_T = \frac{g_m}{2\pi C_G}. \quad (9.12)$$

$f_T$  sets an upper limit on the operation frequency of a field effect transistor.

(a) *Design considerations for AlGaAs/GaAs MODFETs*

Spacer thickness, Al mole fraction and doping concentration of AlGaAs are the most important parameters in determining the carrier concentration and mobility of a two-dimensional electron gas. The background impurity concentration in GaAs is also an important parameter in determining the mobility of a 2DEG. By decreasing the spacer layer thickness, both the transconductance and drain current can be increased but this lowers the mobility of the 2DEG due to an increase in ionized impurity scattering. Hiyamizu *et al* (1983, 1990) investigated the mobility of a two-dimensional electron gas in MBE-grown AlGaAs/GaAs heterostructures as a function of the spacer layer thickness ( $d_0$ ). They found that the mobility increases with increasing spacer layer thickness for thicknesses less than about 200 Å and decreases with  $d_0$  for spacer layer thicknesses larger than 800 Å. The decrease in mobility for large spacer thicknesses is due to the reduction in the 2DEG density.

Another way to increase the transconductance is to reduce the AlGaAs layer thickness but this calls for an increase in the doping level of this layer in order to obtain an acceptable threshold voltage. However, very high doping levels result in a leaky Schottky barrier which is not desirable for field effect transistors.

Since the conduction-band discontinuity in the AlGaAs/GaAs system, the ionization energy of Si impurities and the trap concentration in AlGaAs depend on the Al mole fraction in AlGaAs, this parameter has to be carefully chosen. We can increase both the conduction-band discontinuity and the Schottky barrier height by increasing this parameter. A large conduction-band discontinuity is desirable since it reduces carrier injection from GaAs into AlGaAs and increases carrier density by providing good carrier confinement at the interface. A large Schottky barrier permits high forward gate voltages and therefore increases logic swing. However for Al mole fractions larger than or around 0.3, DX centres (donor-related traps) become significant and device performance is degraded as will be discussed in the next section. The maximum 2DEG mobility and electron concentration are obtained at Al mole fractions in the range  $0.25 < x < 0.28$ .

(b) *Effect of traps on the performance of AlGaAs/GaAs MODFETs*

Since the diffusion constant of Si in AlGaAs is small, abrupt doping profiles can be obtained by doping AlGaAs with Si; however, Si impurities form deep donor levels called DX centres in AlGaAs. There are three kinds of Si donor in AlGaAs: one shallow and two deep-level donors (Tachikawa *et al* 1985). For Al mole fractions less than about 0.2, almost all the electrons populate shallow donors. For larger  $x$  values, the deep-level donor population increases with  $x$  and a persistent photoconductivity effect is observed due to the presence of DX centres. The trap density in the AlGaAs layer at Al mole fractions of about 0.3 is comparable to the desired shallow-dopant density and the  $I-V$  characteristics of MODFETs with this composition are shown to be a strong function of trap occupancy (Chi *et al* 1984, Drummond *et al* 1983). Under sufficiently high drain-source bias, electrons accelerating through the channel of the device become hot near the drain end and are injected into AlGaAs where traps are present. In dark conditions and at low temperatures, depopulation of the traps by thermal emission progresses at a slow rate and, due to the decrease in the 2DEG density, a collapse in the  $I-V$  characteristics and a degradation of  $g_m$  are observed. Figure 9.4 shows the  $I-V$  characteristics and transconductance versus gate voltage of AlGaAs/GaAs MODFETs before and after bias stress at 77 K in the dark demonstrating a collapse in the drain current and a reduction in the transconductance (Chan *et al* 1990).

Another abnormal behaviour observed in AlGaAs/GaAs MODFETs is a positive shift in the threshold voltage with temperature (0.2 V between 77 K and 300 K) (Valois *et al* 1983). If the gate voltage is low enough, the trap energy level will be above the Fermi level. At sufficiently high temperatures the traps are depopulated by thermal emission. If a positive gate voltage is applied at room temperature, the carriers in the channel are attracted into the doped

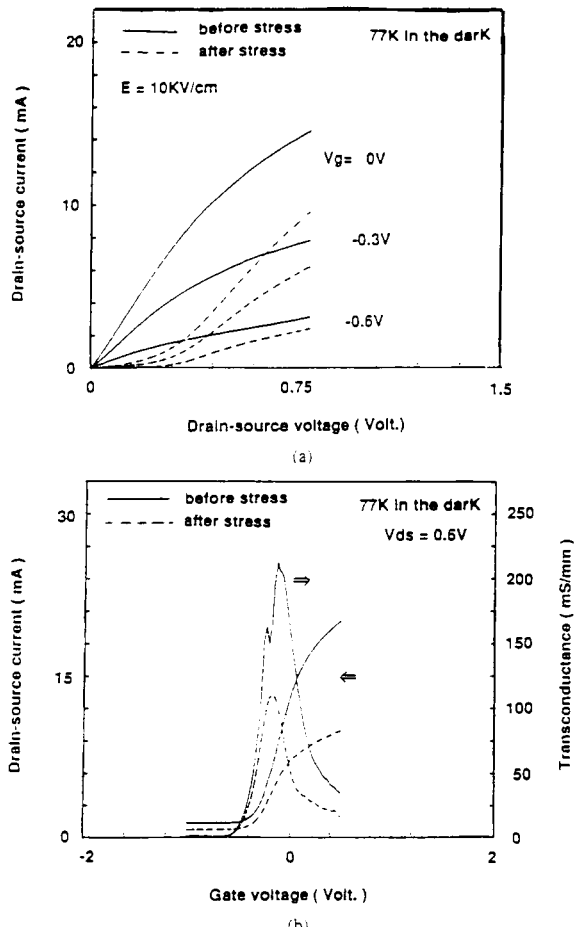


**Figure 9.4** Characteristics of AlGaAs/GaAs MODFETs before and after bias stress at 77 K in the dark (Chan *et al* 1990).

AlGaAs and neutralize the traps. If the gate voltage is subsequently reduced, the trapped carriers return to the channel. If the device is cooled down to 77 K under a positive gate bias, the carriers remain trapped after the gate voltage is lowered. This is due to having insufficient thermal energy to overcome the potential barrier. An increase in the trapped charge density modifies the potential distribution in the AlGaAs layer and therefore the drain current and threshold voltage.

The disadvantages of the AlGaAs/GaAs system can be summarized as follows.

- (i) The sheet carrier concentration at the interface is limited to about  $10^{12}\text{ cm}^{-2}$ . The carrier concentration can be increased by using larger Al mole

fractions, in which case the defect concentration is increased and performance at low temperatures is degraded due to DX centres.

(ii) Diffusion of Si impurities from AlGaAs into GaAs during annealing after ion implantation.

(iii) High reactivity with oxygen causing degradation of the device (Stormer *et al* 1979).

(iv) High-quality AlGaAs is grown at temperatures around 700 °C; this leads to a slight decrease in the semi-insulating properties of the substrate.

### 9.2.2 AlGaAs/InGaAs MODFETs

Because of the disadvantages mentioned in the preceding section, the AlGaAs/GaAs system, although widely used, is not an ideal material system for heterostructure field effect transistors. Therefore researchers have been looking for alternative systems to replace AlGaAs/GaAs. A solution consists of using InGaAs as the undoped narrow-bandgap material and GaAs as the doped large-bandgap material. This approach seems to be promising due to the larger conduction-band discontinuity of this system when compared with low-Al-mole-fraction AlGaAs/GaAs, and because of the good electrical properties of InGaAs (high electron mobility and velocity). If the InGaAs layer is sufficiently thin the mismatch is accommodated as an elastic strain without the formation of misfit dislocations and the structure is called pseudomorphic. Rosenberg *et al* (1985) fabricated pseudomorphic InGaAs/GaAs MODFETs that demonstrated good performance.  $In_{0.15}Ga_{0.85}As$  (200 Å thick) was grown pseudomorphically on a GaAs substrate. An extrinsic transconductance of  $175\text{ mS mm}^{-1}$  for 1 μm gate length devices was obtained at 300 K. Ketterson *et al* (1985) replaced the doped GaAs layer with a low-Al-mole-fraction AlGaAs layer ( $Al_{0.15}Ga_{0.85}As$ ) in order to increase the conduction-band discontinuity and improve carrier confinement at the interface. Since  $x$  was sufficiently low, DX centre effects were not observed. DC transconductances of  $270\text{ mS mm}^{-1}$  at 300 K and  $360\text{ mS mm}^{-1}$  at 77 K were obtained for 1 μm gate devices with a 300 K current gain cut-off frequency of 20 GHz. Later, Nguyen *et al* (1988) reported an  $f_T$  of 120 GHz for 0.2 μm gate length pseudomorphic  $Al_{0.3}Ga_{0.7}As/In_{0.25}Ga_{0.75}As$  MODFETs with high transconductance (peak transconductance of  $550\text{ mS mm}^{-1}$ ). A large indium mole fraction results in a large conduction-band discontinuity and a high two-dimensional electron gas density.

Kikkawa *et al* (1991) fabricated MOCVD-grown AlGaAs/GaAs and pseudomorphic AlGaAs/InGaAs/GaAs MODFETs using tertiarybutylarsine (TBAs). Transconductances of  $324\text{ mS mm}^{-1}$  and  $350\text{ mS mm}^{-1}$  were obtained for 0.5 μm gate n-AlGaAs MODFETs and pseudomorphic AlGaAs/InGaAs/GaAs MODFETs, respectively, verifying that layers grown using TBAs are of device quality.

### 9.2.3 GaInP/GaAs MODFETs

**9.2.3.1 *n*-channel devices.** Using the AlGaAs/InGaAs/GaAs structure instead of AlGaAs/GaAs has permitted the use of low Al mole fractions and avoided DX centre problems. The Al mole fraction in this structure should be less than about 0.15 to completely eliminate the DX centre problem. However, low Al mole fractions result in a small conduction-band discontinuity and poor carrier confinement. Sufficiently large conduction-band discontinuities can be obtained by increasing the indium mole fraction but this results in an increase in the lattice mismatch between AlGaAs and InGaAs.

The DX centre density becomes significant at compositions close to the crossover of direct and indirect conduction bands (at  $x = 0.37$  for  $\text{Al}_x\text{Ga}_{1-x}\text{As}$  and  $x = 0.74$  for  $\text{Ga}_x\text{In}_{1-x}\text{P}$ ). Since  $\text{Ga}_x\text{In}_{1-x}\text{P}$  is lattice matched to GaAs at  $x = 0.51$ , which is far from the crossover point, DX centres are expected to be negligible for this material. DLTS measurements have shown that there are no detectable deep levels in n-doped  $\text{Ga}_{0.51}\text{In}_{0.49}\text{P}$  layers (Watanabe and Ohba 1986, Tanaka *et al* 1987) and the concentration of electron traps is lower than  $1 \times 10^{13} \text{ cm}^{-3}$ .

Initially, the study of two-dimensional electrons in GaInP/GaAs heterostructures suffered from extremely low mobilities when compared to MBE-grown AlGaAs/GaAs heterostructures. Later, Razeghi *et al* (1989) have shown that extremely high mobilities can be obtained with this material system. They have reported a mobility of  $780\,000 \text{ cm}^2 \text{ V}^{-1} \text{ s}^{-1}$  at an electron density of  $4.1 \times 10^{11} \text{ cm}^{-2}$ .

Razeghi *et al* (1991) fabricated lattice-matched ( $\text{Ga}_{0.51}\text{In}_{0.49}\text{P}/\text{GaAs}$ ) and strained ( $\text{Ga}_{0.51}\text{In}_{0.49}\text{P}/\text{Ga}_{0.85}\text{In}_{0.15}\text{As}/\text{GaAs}$ ) modulation-doped field effect transistors by using LP-MOCVD. Growth was carried out at 76 Torr, at a substrate temperature of  $510^\circ\text{C}$ . The growth conditions of GaAs and GaInP are listed in table 9.1. The residual doping of both materials was n-type. The undoped GaAs grown under these conditions had an electron Hall mobility of  $9000 \text{ cm}^2 \text{ V}^{-1} \text{ s}^{-1}$  at 300 K and  $335\,000 \text{ cm}^2 \text{ V}^{-1} \text{ s}^{-1}$  at 40 K for  $12 \mu\text{m}$  thick layers.  $3 \mu\text{m}$  thick GaInP layers grown on GaAs substrates had an electron carrier concentration of  $8 \times 10^{14} \text{ cm}^{-3}$  and a Hall mobility of  $6500 \text{ cm}^2 \text{ V}^{-1} \text{ s}^{-1}$  at 300 K and  $50\,000 \text{ cm}^2 \text{ V}^{-1} \text{ s}^{-1}$  at 77 K.

Figure 9.5 shows the structures of lattice-matched (a) and strained (b) MODFETs after the layers are grown. A  $1 \mu\text{m}$  thick GaAs buffer layer was grown followed by a  $70 \text{ \AA}$  GaInP spacer and a doped GaInP layer  $200 \text{ \AA}$  thick. A  $250 \text{ \AA}$  thick undoped GaInP layer was grown for the purpose of reducing the gate leakage. Finally a  $200 \text{ \AA}$  n<sup>+</sup>-GaAs cap layer was grown to reduce the contact resistance. Figure 9.6 shows the cross-section of the lattice-matched MODFET after the device is fabricated.

Sulphur or silicon are used as n-type dopants for GaInP. Using H<sub>2</sub>S for n-type doping, with the same growth conditions and the same H<sub>2</sub>S flow rate, the probability of sulphur incorporation in the GaInP lattice is an order of

**Table 9.1** Mobility  $\mu$  ( $\text{cm}^2 \text{V}^{-1} \text{s}^{-1}$ ) and sheet carrier density  $n_s$  ( $\text{cm}^{-2}$ ) of lattice-matched (A) and strained (B) Ga(In)As/GaInP heterostructures (Razeghi *et al* 1991).

Device type	Temperature of measurement			Carrier density increases at 77 K
	300 K	77 K (dark)	77 K (light)	
A	$\mu = 3500$ $n_s = 1.89 \times 10^{12}$	$\mu = 21\,300$ $n_s = 1.26 \times 10^{12}$	$\mu = 21\,900$ $n_s = 1.42 \times 10^{12}$	13%
B	$\mu = 5300$ $n_s = 2.45 \times 10^{12}$	$\mu = 78\,500$ $n_s = 9.79 \times 10^{11}$	$\mu = 76\,600$ $n_s = 1.13 \times 10^{12}$	16%

$n + \text{GaAs} > 3 \times 10^{18} \text{ cm}^{-3}$	200 Å
undoped $\text{Ga}_{0.49}\text{In}_{0.51}\text{P}$	250 Å
$n + \text{Ga}_{0.49}\text{In}_{0.51}\text{P} 2 \times 10^{18} \text{ cm}^{-3}$	200 Å
undoped $\text{Ga}_{0.49}\text{In}_{0.51}\text{P}$	70 Å
undoped GaAs	1.0 $\mu\text{m}$
Si-GaAs substrate	

(a)

$n + \text{GaAs} > 3 \times 10^{18} \text{ cm}^{-3}$	200 Å
undoped $\text{Ga}_{0.49}\text{In}_{0.51}\text{P}$	250 Å
$n + \text{Ga}_{0.49}\text{In}_{0.51}\text{P} 2 \times 10^{18} \text{ cm}^{-3}$	200 Å
undoped $\text{Ga}_{0.49}\text{In}_{0.51}\text{P}$	70 Å
undoped $\text{In}_{0.15}\text{Ga}_{0.85}\text{As}$	150 Å
undoped GaAs	1.0 $\mu\text{m}$
Si-GaAs substrate	

(b)

**Figure 9.5** MODFET structures after the layers are grown: (a) lattice-matched n-GaInP/GaAs HEMT, and (b) 15% In strained n-GaInP/GaAs HEMT (Razeghi *et al* 1991).

magnitude higher than in GaAs. Therefore sulphur doping of GaInP is useful in modulation and delta doping. However, sulphur-doped GaInP shows persistent photoconductivity, which is not observed in Si doping. Recently it has been reported (Ginoudi *et al* 1992) that considerable degradation in the  $g_m$  and the drain current of MOMBE-grown S-doped GaInP/GaAs MODFETs is observed at low temperatures while the performance of Si-doped devices remains good. In order to avoid this problem, Si was used as the n-type dopant in the fabrication of the MODFETs (Razeghi *et al* 1991).

MODFETs were fabricated using conventional 1  $\mu\text{m}$  long gate optical lithography.  $\text{NH}_4\text{OH}:\text{H}_2\text{O}_2:\text{H}_2\text{O}$  (10:4:500) and  $\text{H}_3\text{PO}_4:\text{HCl}$  (1:1) were used to etch GaAs and GaInP respectively to define the active regions of the device.  $\text{NH}_4\text{OH}:\text{H}_2\text{O}_2:\text{H}_2\text{O}$  is selective for GaInP and attacks only GaAs, therefore uncontrolled gate recess variation is avoided. Ge/Au/Ni/Ti/Au (700/1400/500/200/1000 Å) was deposited for ohmic contact formation and a rapid thermal annealing at 440 °C for 10 s was carried out. Before depositing

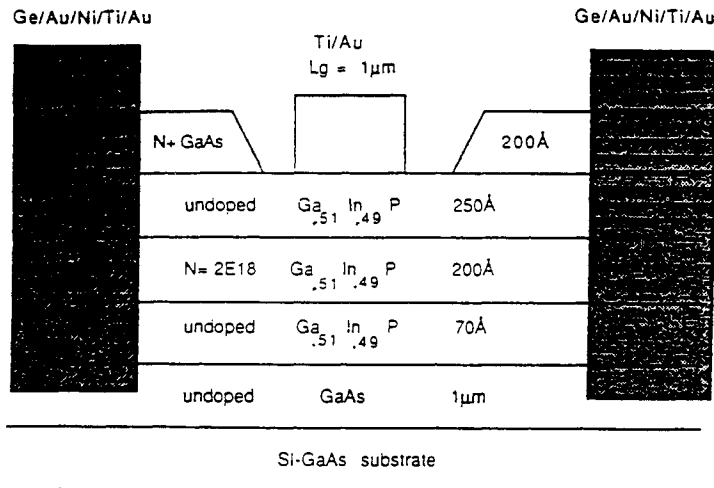


**Figure 9.6** Cross-section of the lattice-matched GaInP/GaAs MODFET (Razeghi *et al* 1991).

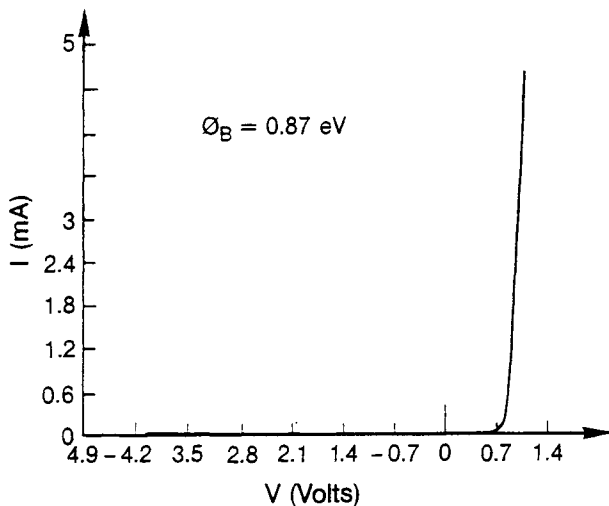


**Figure 9.7**  $I-V$  characteristics of a metal-GaInP Schottky diode (Razeghi *et al* 1991).

the gate metal (Ti/Au 500/3000 Å) a gate recess was made to remove the n<sup>+</sup>-GaAs (200 Å) layer by NH<sub>4</sub>OH:H<sub>2</sub>O<sub>2</sub>:H<sub>2</sub>O (10:4:500) selective etching.

Table 9.1 shows the Hall measurement results for lattice-matched (A) and strained (B) GaInP/GaAs heterostructures. Note that at 300 K, the mobility and carrier concentration change considerably by adding 15% excess In in the channel. It can also be seen that the heterostructures are not light sensitive at low

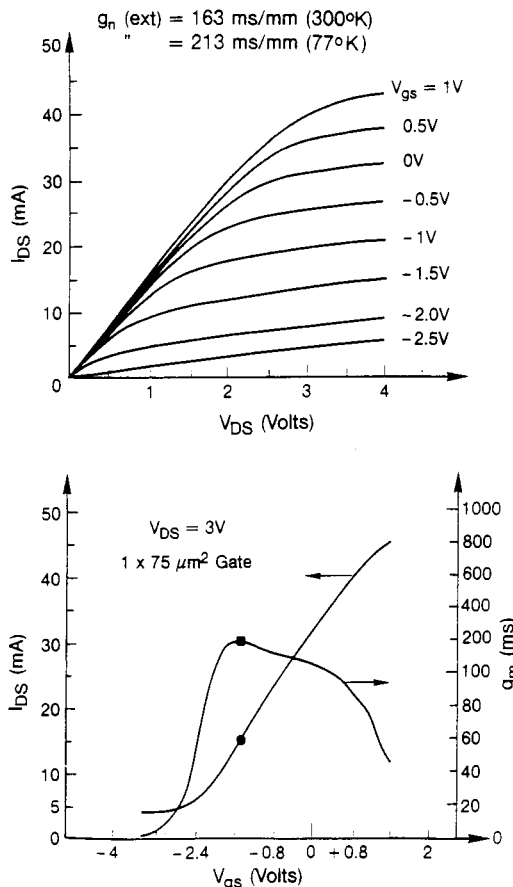


**Figure 9.8** Characteristics of a lattice-matched GaInP/GaAs MODFET (Razeghi *et al* 1991).

temperatures. The carrier density has a slight dependence on the illumination. The mobilities obtained were high, despite the high doping of GaInP.

Figure 9.7 shows the  $I$ - $V$  characteristics of a typical metal-GaInP Schottky diode. The reverse-bias leakage current is very low ( $I_{rev} < 200$  nA at  $V_{GS} = -4$  V) demonstrating the high quality of the undoped GaAs layers. The Schottky barrier height evaluated from  $C$ - $V$  measurements was 0.87 eV.

Figure 9.8 shows  $I_{DS}$ - $V_{DS}$  and  $g_m$ ,  $I_{DS}$ - $V_{GS}$  transfer characteristics for the lattice-matched device. The extrinsic transconductance was  $163 \text{ mS mm}^{-1}$  at 300 K and  $213 \text{ mS mm}^{-1}$  at 77 K. Figure 9.9 shows the measured short-circuit current ( $H_{21}$ ) and power ( $G$ ) gain for lattice-matched MODFETs at  $V_{DS} = 3.5$  V and  $V_{GS} = -1.85$  V which revealed cut-off frequencies  $f_T = 17.8$  GHz and  $f_{max} = 23.5$  GHz.

$I$ - $V$  characteristics and  $g_m$ ,  $I_{DS}$ - $V_{GS}$  transfer characteristics for strained

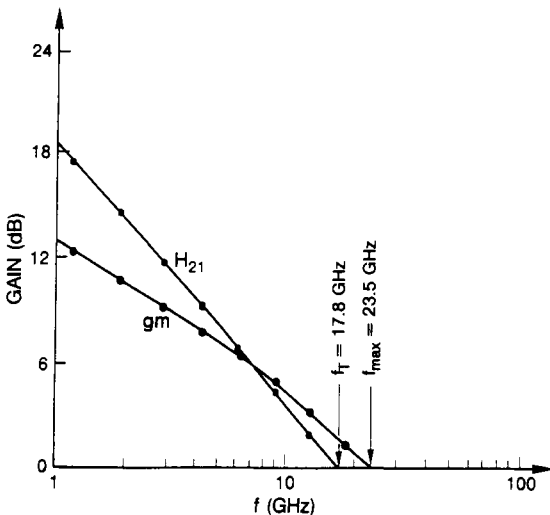
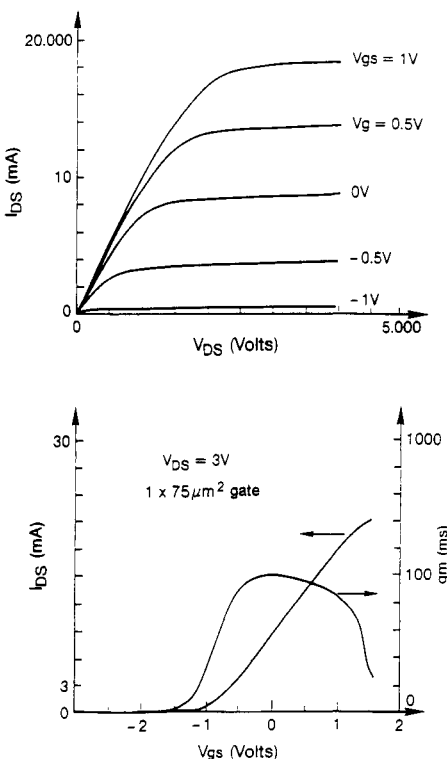


Figure 9.9 Short-circuit current ( $H_{21}$ ) and power ( $g_m$ ) gain for lattice-matched MODFETs (Razeghi *et al* 1991).

devices are shown in figure 9.10. The extrinsic transconductance was  $133 \text{ mS mm}^{-1}$  at 300 K which was lower than for the lattice-matched MODFET. The devices showed very good channel pinch-off behaviour and extremely low output conductance ( $g_{DS} < 2 \text{ mS mm}^{-1}$ ). The cut-off frequency was 11 GHz and  $f_{\max}$  was 23.5 GHz.

Figure 9.11 shows the  $I-V$  characteristics and  $I_{DS}-g_m$  versus gate voltage at 77 K before and after bias stress. As shown in the figure only a slight decrease in the current and transconductance was observed. The threshold voltage of the devices biased in the dark at  $V_{DS} = 3 \text{ V}$  was  $-3.34 \text{ V}$  at 300 K and  $-3.38 \text{ V}$  at 77 K. These results demonstrate that traps in GaInP are negligible and good device characteristics can be maintained at low temperatures.

Takikawa *et al* (1991) reported high-performance MOCVD-grown strained layer GaInP/InGaAs/GaAs MODFETs. They obtained good uniformity for doping concentration, thickness and composition over a 3 inch wafer. The 2DEG concentration and mobility for an n-InGaP-InGaAs-GaAs structure with a 25 Å thick spacer were  $1.5 \times 10^{12} \text{ cm}^{-2}$  and  $7000 \text{ cm}^2 \text{ V}^{-1} \text{ s}^{-1}$  at 300 K and  $1.4 \times 10^{12} \text{ cm}^{-2}$  and  $45\,000 \text{ cm}^2 \text{ V}^{-1} \text{ s}^{-1}$  at 77 K. They have observed that the sheet carrier concentration increases monotonically with InAs mole fraction but the mobility shows a peak at an InAs mole fraction of about 0.15. The mobility and concentration at this composition were higher than those obtained for AlGaAs/InGaAs/GaAs by Ketterson *et al* (1986). They have also observed that short-channel effects are less significant in GaInP/InGaAs/GaAs MODFETs when compared with AlGaAs/GaAs devices.



**Figure 9.10** Characteristics of a strained GaInP/InGaAs/GaAs MODFET (Razeghi *et al* 1991).

**9.2.3.2 *p*-channel devices.** The valence-band discontinuity in the GaInP/GaAs system is larger than that of AlGaAs/GaAs resulting in better carrier confinement when *p*-channel MODFETs are considered. In comparison with *n*-channel devices, the transconductance of *p*-channel lattice-matched MODFETs is inferior due to the lower mobility of holes. For lattice-matched AlGaAs/GaAs MODFETs the best experimentally demonstrated ratio of transconductance between *n*- and *p*-channel lattice-matched devices is  $g_{mn}/g_{mp} = 8$ . The low transconductance of *p*-channel devices can be increased by increasing the width of the device but this is not desirable due to the increase in the chip dimensions. It has been shown that the performance of *p*-channel devices can be increased by introducing strain into the structure (Drummond *et al* 1986, Lee *et al* 1987). Strained *p*-channel MODFETs have been attracting considerable interest in digital applications (Kiehl *et al* 1987). The reduced hole mass and improved transport properties make

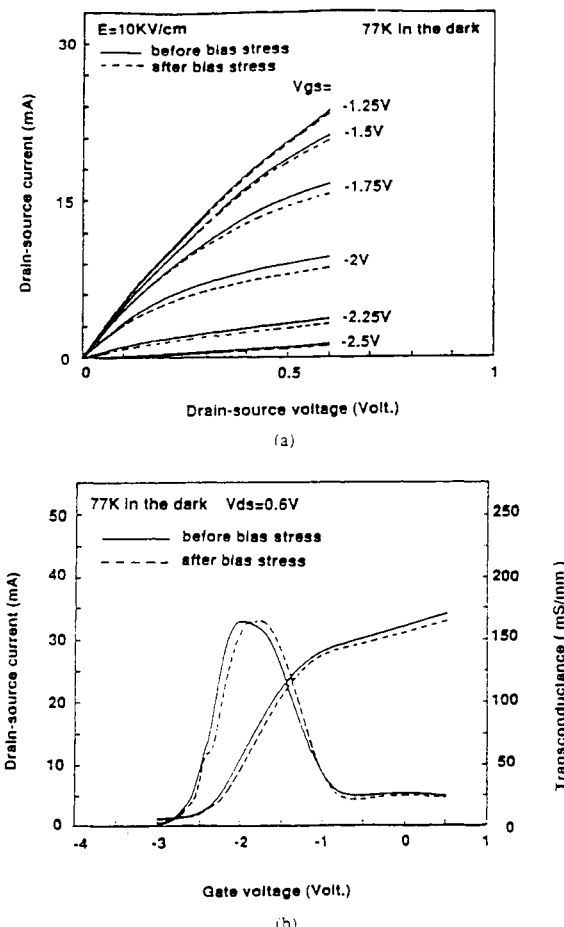


**Figure 9.11** Characteristics of GaInP/GaAs MODFETs at 77 K in the dark before and after bias stress (Chan *et al* 1990).

them useful for complementary logic circuits with small power-delay products.

To study the effect of strained channels, Chan *et al* (1988) carried out a theoretical and experimental study of device performance in both lattice-matched and strained GaInP/GaAs heterostructures. Their simulations have shown that the average density of state mass at room temperature decreases by 30% due to the strain (from  $0.57m_0$  to  $0.36m_0$ ) and the reduction is more dramatic at lower temperatures. The cross-sections of the designed lattice-matched ( $x = 0$ ) and strained ( $x = 0.1$ ) GaInP/InGaAs/GaAs MODFETs are shown in figure 9.12. The channel consists of an undoped GaAs and a strained  $\text{In}_x\text{Ga}_{1-x}\text{As}$  ( $x = 0.1$ ) layer. A 50 Å undoped  $\text{Ga}_{0.51}\text{In}_{0.49}\text{P}$  spacer was grown between the strained channel and the Zn-doped ( $2 \times 10^{18} \text{ cm}^{-3}$ ) p- $\text{Ga}_{0.51}\text{In}_{0.49}\text{P}$  layer. A 200 Å thick undoped

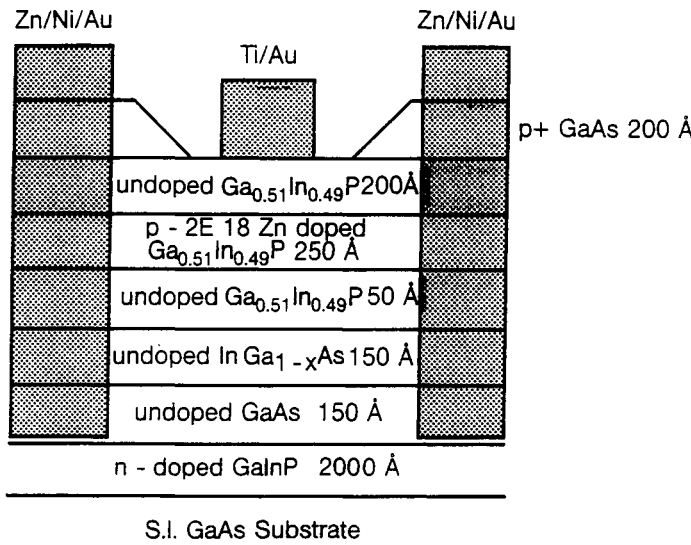


**Figure 9.12** Cross-section of the lattice-matched ( $x = 0$ ) and strained ( $x = 0.1$ ) p-channel GaInP/InGaAs/GaAs MODFETs (Chan *et al.* 1988).

$\text{Ga}_{0.51}\text{In}_{0.49}\text{P}$  layer was grown to reduce the gate leakage current. Finally a  $\text{p}^+$ -GaAs layer was grown to improve the ohmic contacts.

The devices were grown by low-pressure MOCVD. A  $\text{NH}_4\text{OH}/\text{H}_2\text{O}_2/\text{H}_2\text{O}$  solution was used for etching the GaAs cap layer. The etching of GaInP for the mesas was achieved using a  $\text{HCl}:\text{H}_3\text{PO}_4$  solution. ZnNiAu ohmic contacts were deposited by lift off and followed by conventional annealing in  $\text{N}_2$  at  $425^\circ\text{C}$  for 5 min. Ti/Au was used for gate metallization.

The layers were characterized to confirm the hole mobility enhancement by strain. Figure 9.13 shows the gate bias dependence of the mobility for both lattice-matched and strained structures. In the lattice-matched case the reduction in mobility with gate bias is due to a decrease in the sheet carrier density (and therefore a decrease in the screening) and an increase of heavy-hole band occupation. In the strained structure, the HH and LH bands are split and an increase in the gate bias increases the LH population resulting in mobility enhancement. The  $g_m-V_G$  and  $I_D-V_G$  characteristics of a  $1\ \mu\text{m} \times 100\ \mu\text{m}$  MODFET are shown in figure 9.14. It was found that the velocity improvement by strain was 68%.

Significant threshold voltage shifts with temperature have been reported for p-AlGaAs/GaAs MODFETs grown by MBE (Hirano *et al.* 1986). Chan *et al.* (1988) have also found that threshold voltage shifts with temperature are negligible in p-GaInP/InGaAs/GaAs MODFETs making this system very promising for high-speed digital applications.

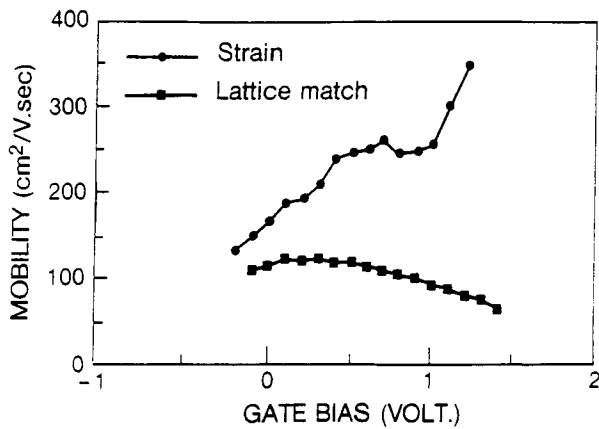


**Figure 9.13** Gate bias dependence of mobility in p-channel GaInP/InGaAs/GaAs MODFETs (Chan *et al* 1988).

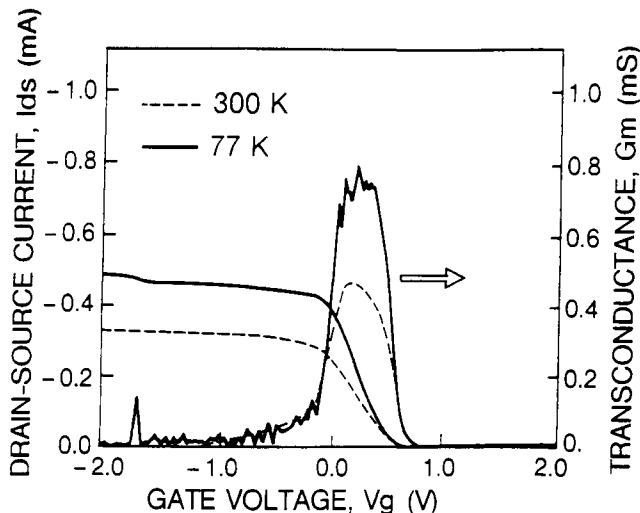


**Figure 9.14** Characteristics of the strained p-channel GaInP/InGaAs/GaAs MODFET (Chan *et al* 1990).

#### 9.2.4 MODFETs on Si substrate

There has been considerable interest in the integration of III-V semiconductors with Si technology using the best aspects of both technologies to produce better performance and cheaper devices. Si technology is mature and Si has a higher thermal conductivity and mechanical strength compared to III-V materials. Also, large-area Si substrates are available. Therefore the growth of III-V-based devices on Si substrates is an important approach for ultralarge-scale integration.

A significant amount of research has been done on GaAs-based materials and devices on Si substrates (Razeghi *et al* 1989, Houdre and Morkoc 1990, Fang *et al* 1990).

Studies on the fabrication of AlGaAs/GaAs MODFETs on Si substrate have shown that their performance is comparable to MODFETs on GaAs substrates (Fischer *et al* 1986, Ren *et al* 1992, Ohari *et al* 1988). Omnes and Razeghi (1991) used low-pressure MOCVD to grow multiquantum-well structures of GaAs/GaInP on GaAs, InP and Si substrates. It was found from x-ray diffraction and photoluminescence measurements that the films grown on Si substrate are of comparable quality to the films grown on GaAs substrate. Suehiro *et al* (1991) fabricated MOCVD-grown  $0.6\text{ }\mu\text{m}$  gate enhancement- and depletion-mode GaInP/InGaAs/GaAs pseudomorphic MODFETs on Si substrate. The performance of the devices on Si substrate ( $g_m = 242\text{ mS mm}^{-1}$ ,  $K = 324\text{ mS V}^{-1}\text{ mm}^{-1}$  for e-mode,  $g_m = 211\text{ mS mm}^{-1}$ ,  $K = 184\text{ mS V}^{-1}\text{ mm}^{-1}$  for d-mode) was comparable to devices built on GaAs substrates under the same conditions ( $g_m = 236\text{ mS mm}^{-1}$ ,  $K = 371\text{ mS V mm}^{-1}$  for e-mode,  $g_m = 224\text{ mS mm}^{-1}$ ,  $K = 265\text{ mS V mm}^{-1}$  for d-mode). The threshold voltage standard deviation for the devices on Si substrate (22 mV) was higher than that for the devices on GaAs substrate (6 mV) but it was still at an acceptable level. These results verify that GaInP/InGaAs/GaAs MODFETs on Si substrates are potential devices for high-speed, low-power ultralarge-scale integration.

### 9.2.5 GaInP/GaAs heterostructure insulated gate field effect transistors

Heterostructure insulated gate field effect transistors (HIGFETs) have demonstrated promising characteristics for high-speed digital circuit applications (Solomon *et al* 1984, Feuer *et al* 1989). This device is similar to a conventional MODFET except that the higher-bandgap material is left undoped. Under flat-band conditions, charge neutrality is preserved throughout the device. If a sufficiently large positive gate voltage is applied, a negative charge (consisting of electrons in a two-dimensional well) is induced in the semiconductor (figure 9.15). Similarly, a two-dimensional hole gas can be formed by applying a negative gate bias. Since the threshold voltage of the device is determined by the material independent of the doping density and thickness, an improved threshold voltage uniformity is achieved. Furthermore, since the active channel is induced under the gate only by the application of a bias, both n- and p-type devices can be fabricated on the same wafer by changing the type of the implant in the source and drain contacts. This allows the realization of complementary logic circuits with low power dissipation.

To date, the most commonly used material system in heterostructure FET applications has been AlGaAs/GaAs, which has major drawbacks as was discussed in the previous sections. Razeghi *et al* (1990a) fabricated MOCVD-grown n- and p-type GaInP/InGaAs/GaAs lattice-matched and strained HIGFETs in order to investigate the potential of this system in HIGFET applications as

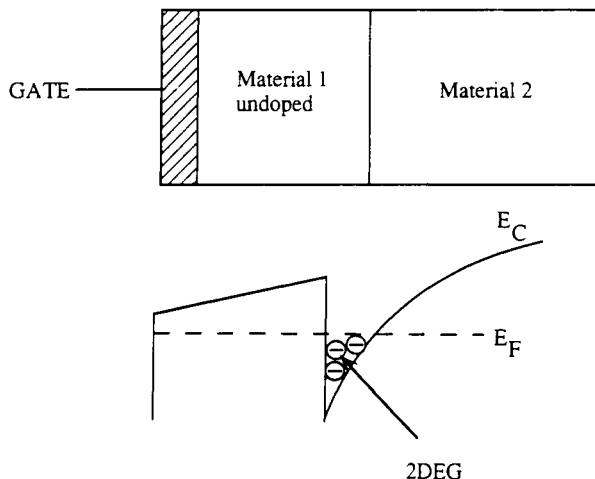


**Figure 9.15** A heterostructure with an undoped semiconductor and its band diagram under a sufficiently large, positive gate bias.

an alternative to the AlGaAs/GaAs system. The device cross-section is shown in figure 9.16. A  $1\ \mu\text{m}$  undoped GaAs layer was used as a buffer followed by  $250\text{ \AA}$  undoped GaInP used as an insulator. The growth conditions of GaInP were optimized in order to obtain a high-purity material (necessary for good insulating properties) lattice matched to GaAs. The growth parameters are the same as those listed in table 6.1. The background doping levels in the GaInP and GaAs layers were  $1 \times 10^{15}\ \text{cm}^{-3}$  and  $1 \times 10^{14}\ \text{cm}^{-3}$  respectively.

A  $1.55\ \mu\text{m}$  long  $\text{WSi}_x$  gate was defined by optical lithography and lift off. Self-aligned Si and Be implantations were used to access n- and p-channels, respectively. In order to activate the implant, the samples were treated by rapid thermal annealing at  $800^\circ\text{C}$  for 5 s. Studies on the implant activation for Si in GaInP showed that activation was 5% at  $800^\circ\text{C}$ , and 36% at  $900^\circ\text{C}$  for 5 s rapid thermal annealing. Very high temperatures necessary for good activation are not compatible with the conditions required to maintain material integrity: phosphorus, for example, evaporates and degrades material stoichiometry.

Following mesa etching, source and drain contacts were defined by depositing and annealing Ge/Au/Ni/Ti/Au ( $700/1400/500/200/1000\text{ \AA}$ ) at  $460^\circ\text{C}$  for 10 s for n-type and Zn/Ni/Au ( $300/500/2500\text{ \AA}$ ) at  $425^\circ\text{C}$  for 2 min for p-type devices.

Figure 9.17 shows the  $I_{\text{DS}}-V_{\text{DS}}$  and  $g_m-I_{\text{DS}}-V_{\text{GS}}$  characteristics of the n-type lattice-matched HIGFETs with  $1.5 \times 75\ \mu\text{m}^2$  gates. The devices showed excellent pinch-off characteristics with enhancement-mode operation ( $V_{\text{th}} = 0.19\ \text{V}$ ). The corresponding characteristics for the strained n-channel HIGFETs are shown in figure 9.18. The improvement in device performance with the introduction of In in the channel is apparent. The improvement is reflected by electron mobility and

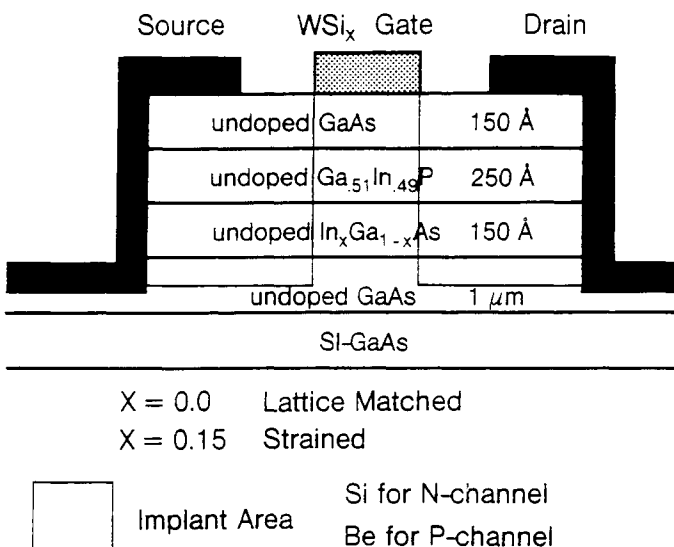


**Figure 9.16** Cross-section of the GaInP/InGaAs/GaAs HIGFET (Razeghi *et al* 1990a).

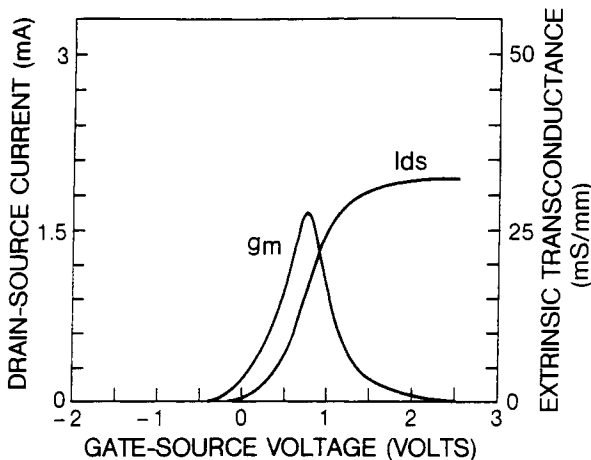


**Figure 9.17** Characteristics of the n-type lattice-matched HIGFET (Razeghi *et al* 1990a).

sheet carrier density enhancement. The full advantages of GaInP/InGaAs/GaAs heterostructures can be obtained by fully optimizing the postimplantation capless rapid-thermal-annealing conditions. This allows the optimization of access regions and therefore larger extrinsic  $g_m$  values. By using sufficiently thick gate metal and high-energy implantation, the access resistances can be minimized.

The threshold voltages for the strained structure at 300 K and 77 K were 0.56

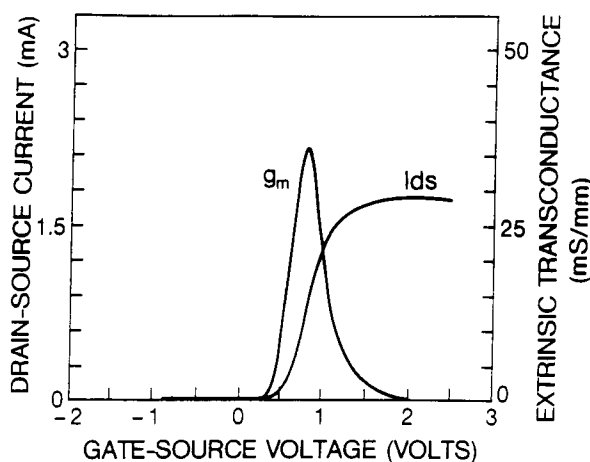


**Figure 9.18** Characteristics of the n-type strained HIGFET (Razeghi *et al* 1990a).

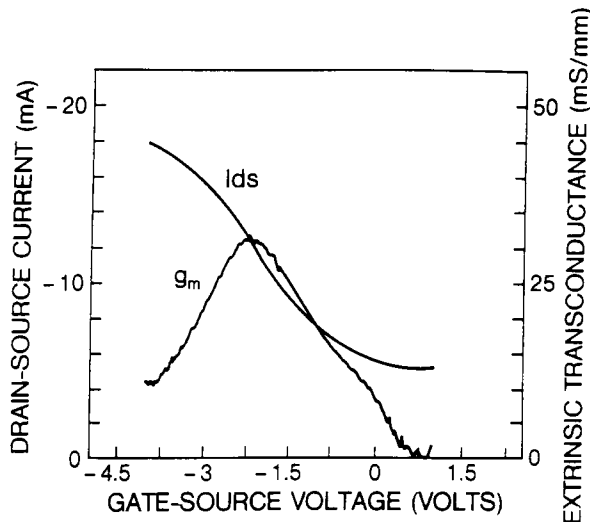


**Figure 9.19** Characteristics of the p-type lattice-matched HIGFET (Razeghi *et al* 1990a).

$V$  and 0.62 V respectively, demonstrating the absence of carrier trapping at low temperatures. The high-bandgap GaInP allows the application of large gate voltages before leakage by thermionic emission through the barrier becomes significant. The gate leakage current at  $V_{GS} = 2$  V was  $250 \text{ mA mm}^{-2}$  on  $520\text{\AA}$  thick GaInP devices. This is small compared with AlGaAs/GaAs or InGaAs/AlInAs where the maximum gate voltage is limited to about 1.5 V.

The  $I_{DS}-V_{DS}$  and  $g_m-I_{DS}-V_{GS}$  characteristics of p-type lattice-matched

devices are shown in figure 9.19. The intrinsic transconductance was  $74 \text{ mS mm}^{-1}$  which is considered to be high for p-type HGFETs. The high channel leakage current at  $V_{GS} = 0 \text{ V}$  is associated with the penetration of Be ions through the thin  $\text{WSi}_x$  gate.

### 9.3 HETEROJUNCTION BIPOLAR TRANSISTORS (HBTS)

#### 9.3.1 Introduction

The bipolar junction transistor, since its invention in 1948 by Bardeen, Brattain and Shockley, has played the most important role in the development of semiconductor electronics. The idea of a heterojunction bipolar transistor (HBT), or, in other words, using wider-bandgap material in the emitter is almost as old as the transistor itself (Kroemer 1957). However, the difficulties in the material processing technologies delayed successful implementation of this idea until the 1970s. Starting in the early 1970s, with the breakthroughs in material technology, especially with the development of MBE and MOCVD, high-performance HBTs have been fabricated and the gain, frequency and power capabilities of the bipolar transistor have increased significantly.

In comparison with field effect transistors, the HBT has the following important advantages. Since it is a vertical device, which means that the electrons travel perpendicular to the wafer surface, the transit time of the carriers is determined by the layer thickness which can be controlled precisely by epitaxy. Therefore, a high-frequency response can be obtained without using sophisticated lithographic techniques required for submicron design. HBTs can handle higher current levels when compared with FETs and the switch-on voltage of the HBT is relatively insensitive to process variations resulting in good uniformity of this parameter over the wafer. In this section, after a basic introduction to the heterojunction bipolar transistor and its advantages over the homojunction bipolar transistor, we will discuss growth, fabrication and performance features of MOCVD-grown, state of the art HBTs based on AlGaAs/GaAs and GaInP/GaAs material systems.

Figure 9.20 shows the energy band diagram and the current components in an n-p-n homojunction transistor biased in the active region. The forward bias at the emitter-base junction reduces the energy barrier for electron flow from the emitter into the base. Electrons that overcome the barrier travel through the base by drift and diffusion and are swept into the collector due to the high electric field in the base-collector depletion region.

Some of the injected electrons from the emitter into the base and some of the injected holes from the base into the emitter are lost due to recombination in the emitter-base space charge region ( $I_{IR}$ ). Depending on the base thickness and the lifetime of the minority carriers in the base, part of the injected electron current ( $I_{EL}$ ) is lost due to recombination with the holes in the quasineutral base

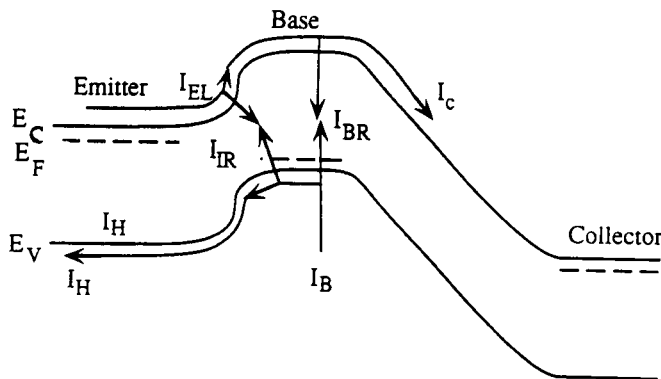


**Figure 9.20** Energy band diagram and current components in an n-p-n homojunction bipolar transistor.

( $I_{BR}$ ). The holes lost due to injection into the emitter ( $I_H$ ) and recombination (in the emitter-base depletion layer ( $I_{IR}$ ) and in the base ( $I_{BR}$ )) are supplied through the base contact which results in the base current  $I_B$ . We have neglected the generation current in the collector-base depletion region. The emitter current is given by

$$I_E = I_{EL} + I_{IR} + I_H \quad (9.13)$$

and the collector current is

$$I_c = I_{EL} - I_{BR}. \quad (9.14)$$

The base current, which is the difference between the emitter and the collector currents, can be expressed as

$$I_B = I_{BR} + I_{IR} + I_H. \quad (9.15)$$

The common emitter current gain  $\beta$  is a figure of merit for a bipolar transistor and is given by

$$\beta = \frac{I_c}{I_B} = \frac{I_{EL} - I_{BR}}{I_H + I_{IR} + I_{BR}}. \quad (9.16)$$

The current transfer ratio of a bipolar transistor  $\alpha$  is the ratio of the collector current to the emitter current which is related to  $\beta$  by

$$\beta = \frac{\alpha}{1 - \alpha}. \quad (9.17)$$

Therefore, in an efficient bipolar transistor with high current gain,  $\alpha$  should be very close to unity.  $\alpha$  is determined by two factors: the ratio of the injected electron current to the total emitter current, which is the emitter injection efficiency  $\gamma$ , and the fraction of the injected electrons which reach the collector without being recombined in the base, which is the base transport factor  $B$ . In

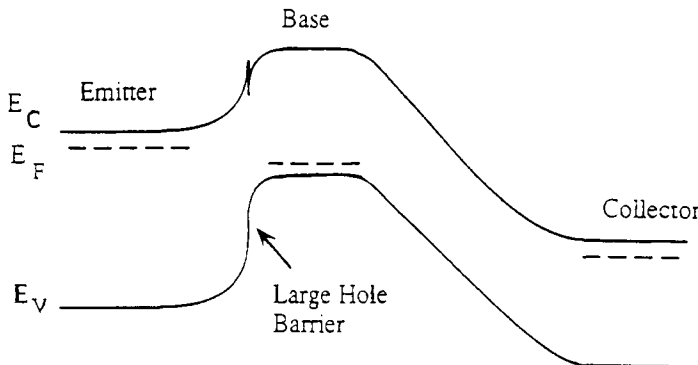


Figure 9.21 Energy band diagram for a heterojunction bipolar transistor.

order to obtain an  $\alpha$  close to unity and therefore high  $\beta$ , both  $\gamma$  and  $B$  should be near unity or in other words the emitter current should be due mostly to electrons (for n-p-n transistors) and the fraction of injected electrons that recombine in the base should be as small as possible.

If we assume that the current gain is limited by the emitter injection efficiency (that is, the recombination currents are negligible), the common emitter current gain  $\beta_{\max}$  is given by the ratio of the injected electron current from the emitter into the base to the injected hole current from the base into the emitter. If the base is doped lightly with respect to the emitter doping level, the hole current injected into the emitter will be small in comparison to the electron current injected into the base from the emitter resulting in a large current gain. However, device performance is very sensitive to the doping level in the base. Low base doping results in high base resistance which degrades device performance by causing parasitic effects such as emitter crowding and reach-through of the base depletion region from the collector to the emitter. A high base resistance also degrades the speed performance of the device as will be discussed later. The main purpose of using a wide-bandgap emitter or, in other words, a heterostructure emitter-base junction is to improve  $\beta_{\max}$  which is an upper limit for the gain. Figure 9.21 shows the energy band diagram of a heterojunction bipolar transistor. Due to the extra barrier for the holes, the hole injection current from the base to the emitter is significantly reduced and a high current gain is achieved even if the base is very highly doped. In this case  $\beta_{\max}$  is given approximately by (Kroemer 1982)

$$\beta_{\max} = \frac{N_E v_{nb}}{P_B v_{pe}} \exp\left(\frac{\Delta E_g}{kT}\right) \quad (9.18)$$

where  $N_E$ ,  $P_B$  are the doping densities in the emitter and base, respectively.  $v_{pe}$  and  $v_{nb}$  are the effective velocities of holes in the base end of the emitter and electrons in the emitter of the base. Noting that  $\Delta E_g$  is zero for a homojunction,

the improvement factor in the current gain is  $\exp(\Delta E_g/kT)$ . Since this factor is quite large, very high values of current gain can be obtained regardless of the ratio of the doping levels in the emitter and base.

### 9.3.2 Frequency response and design considerations

One of the figures of merit for bipolar transistors is the current gain cut-off frequency  $f_T$  where the transistor incremental current gain drops to unity.  $f_T$  is given by

$$f_T = \frac{1}{2\pi \tau_{ec}} \quad (9.19)$$

where  $\tau_{ec}$  is the emitter to collector transit time expressed in the form

$$\tau_{ec} = \tau_e + \tau_b + \tau_{cdl} + \tau_c. \quad (9.20)$$

In this expression,  $\tau_e$  is the emitter charging time which is  $r_e C_e$  where  $r_e$  is the emitter resistance and  $C_e$  is the emitter capacitance.  $\tau_b$  is the base transit time determined by the base thickness, diffusivity of electrons in the base and the drift fields in this region.  $\tau_{cdl}$  is the collector depletion layer transit time given by  $W_c/2v_s$  where  $W_c$  is the collector depletion layer width and  $v_s$  is the saturation-limited electron velocity in the collector.  $\tau_c$  is the collector charging time which is  $r_c C_c$  where  $r_c$  is the collector bulk resistance and  $C_c$  is the collector capacitance.

Another figure of merit is the frequency at which the maximum power gain of the transistor drops to unity, which is called the maximum frequency of oscillation  $f_{max}$  and is given by

$$f_{max} = \left( \frac{f_T}{8\pi r_b C_{bc}} \right)^{1/2} \quad (9.21)$$

where  $r_b$  is the base resistance and  $C_{bc}$  is the base collector capacitance. Due to the  $r_b C_{bc}$  time constant, the base resistance is an important factor in the frequency response of a bipolar transistor. In heterojunction bipolar transistors, the base can be doped very heavily resulting in a very low base resistance without sacrificing the emitter injection efficiency. Since high base doping causes low lifetimes in the base for the injected electrons, it is important that the base region be thin to keep the recombination current  $I_{BR}$  small and the base transport factor close to unity.

Assuming that the base is heavily doped, the emitter capacitance is determined by the doping level in the emitter. In order to keep the emitter depletion layer charging time  $\tau_e$  low, the emitter can be doped lightly to provide a small emitter capacitance and the emitter resistance can be kept low by decreasing the total emitter thickness. A low doping level in the emitter also provides a high emitter reverse breakdown voltage.

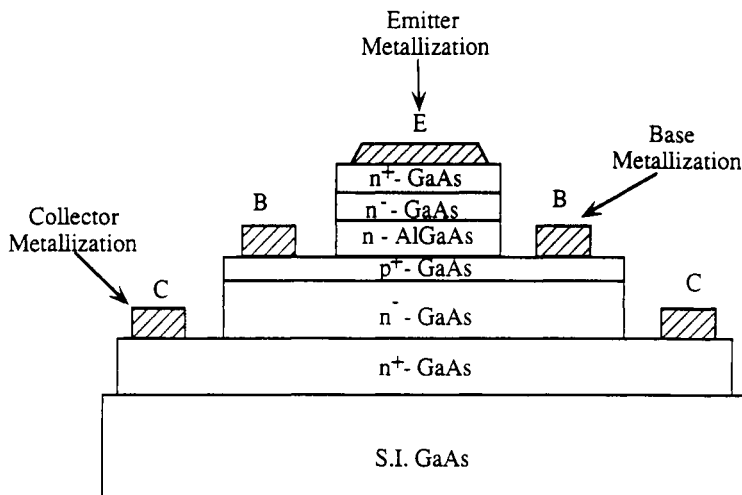


Figure 9.22 Cross-sectional structure of an AlGaAs/GaAs HBT.

The conduction-band discontinuity at the emitter-base junction establishes a barrier for electron flow from the emitter into the base. The emitter injection efficiency can be further increased by compositionally grading the emitter-base junction which eliminates the conduction-band discontinuity. However, the conduction-band discontinuity lowers the base transit time by injecting the electrons into the base with high velocities (Ankri *et al* 1982). The base transit time can be further reduced by compositionally grading the base. The gradual change in the conduction-band energy establishes a quasielectric field in the base. In this case the injected electrons are driven by both diffusion and drift. Figure 9.22 shows the energy band diagrams for graded-junction and graded-base HBTs. The collector depletion layer transit time  $\tau_{cdl}$  plays an important role in determining the total transit time and therefore the frequency response. Using a heavy doping level in the collector results in a low collector depletion layer transit time due to the small depletion layer width, but this results in a low collector-base breakdown voltage and high collector capacitance. Monte Carlo simulations for AlGaAs/GaAs HBTs have shown that the electron velocity may exceed the saturation velocity in the collector depletion layer (Asbeck *et al* 1982). Maziar *et al* (1986) have demonstrated that by using an inverted field structure, velocity overshoot can be extended over a longer portion of the collector space-charge region reducing the transit time through this layer.

In double-heterojunction transistors, wide-bandgap material is used for both emitter and collector. By using a wide-bandgap collector, the breakdown voltage of the collector junction can be increased, and carrier injection from the collector to the base can be suppressed which results in faster operation in digital applications.

### 9.3.3 AlGaAs/GaAs HBTs

Due to the excellent lattice match between  $\text{Al}_x\text{Ga}_{1-x}\text{As}$  and GaAs over the entire compositional range, the AlGaAs/GaAs system has been the most widely used system for heterojunction bipolar transistors. Figure 9.22 shows the cross-sectional structure of an AlGaAs/GaAs HBT. In order to avoid DX centre problems, the Al mole fraction  $x$  in  $\text{Al}_x\text{Ga}_{1-x}\text{As}$  is usually kept around 0.25 which results in a conduction-band discontinuity of 0.2 eV and a valence-band discontinuity of 0.1 eV. Due to the large conduction-band discontinuity, the emitter-base junction is usually compositionally graded.

Device isolation is performed by deep ion implantation to make the layers outside the device semi-insulating or by using a mesa structure. Using composition-selective etches, vias are etched to the base and collector layers to make the corresponding contacts.

In order to obtain good device performance, the contact resistances of the ohmic contacts should be minimized. One of the ways that has been used to reduce the emitter contact resistance is to use lattice-mismatched InGaAs cap layers grown on the emitter. Due to the small metal-semiconductor barrier height good ohmic contacts can be achieved. Commonly used contacts are AuGe/Ni and Ge/Au/Cr. Minimization of the parasitic resistances is also very important in obtaining good device performance. The base-emitter separation should be a few tenths of a micron. This can be accomplished by using self-aligned techniques (Nagata *et al* 1987, Hayama *et al* 1987, Chang *et al* 1987). By using a shallow proton implant into the collector region under the base contacts, extrinsic collector doping and therefore the base-collector capacitance can be reduced (Ginoudi *et al* 1992).

It is important that the base-emitter p-n junction coincide with the heterojunction between AlGaAs and GaAs. Therefore good doping profile and material composition control is required in the growth of the epilayers. Most of the AlGaAs/GaAs HBT research has been done on MBE-grown devices. Since the early 1980s the performance of MOCVD-grown AlGaAs/GaAs HBTs has increased significantly. An  $f_{\max}$  of 94 GHz and an  $f_T$  of 45 GHz have been obtained by Enquist and Hutchby (1989) using a self-aligned structure.

One of the difficulties in HBT fabrication is the diffusion of impurities from the heavily doped GaAs base into the AlGaAs emitter at high temperatures during or subsequent to growth. This causes the p-n junction to move into the AlGaAs layer and the current gain of the device is reduced due to the reduction in the barrier to hole injection. This problem can be avoided by introducing a thin undoped GaAs spacer layer between the base and emitter or by reduction of the growth temperature before the AlGaAs layer is grown. Common p-type dopants in MOCVD are magnesium, zinc and carbon. Mg doping shows abnormal memory effects which requires growth interruptions in order to obtain an abrupt doping profile (Kuech *et al* 1988, Landgren *et al* 1988). Zn has a large diffusion coefficient and carbon doping needs a low growth temperature both of

which are incompatible with the growth of high-quality AlGaAs which requires high temperatures. However, very high base doping levels are possible with carbon doping due to the very low diffusion coefficient of carbon (Ashizawa *et al* 1991). Using carbon doping in the base ( $p = 4 \times 10^{19} \text{ cm}^{-3}$ ), Twynam *et al* (1991) have reported MOCVD-grown AlGaAs/GaAs microwave HBTs with an  $f_T$  of 42 GHz,  $f_{\max}$  of 117 GHz and a current gain of 50.

### 9.3.4 GaInP/GaAs HBTs

As mentioned in the previous chapters, the  $\text{Ga}_{0.51}\text{In}_{0.49}\text{P}/\text{GaAs}$  system has some major advantages over AlGaAs/GaAs. For n-p-n heterojunction bipolar transistors, the GaInP/GaAs system has an additional advantage when compared with the widely used AlGaAs/GaAs structure. The valence-band discontinuity in the  $\text{Ga}_{0.51}\text{In}_{0.49}\text{P}/\text{GaAs}$  system is about 0.28 eV and conduction-band discontinuity is 0.2 eV (Biswas *et al* 1990). A large valence-band discontinuity is an exciting property for n-p-n HBTs. In the AlGaAs/GaAs system, the same amount of valence-band discontinuity requires that the Al mole fraction be about 0.6, in which case there would be a very large conduction-band spike at the emitter-base junction together with an indirect-gap emitter, neither being acceptable. In the AlGaAs/GaAs system, about 60 per cent of the energy gap difference occurs in the conduction band and the emitter-base junction of the device is usually graded to eliminate the conduction-band spike which decreases the emitter injection efficiency and increases the emitter switch-on voltage. However, theoretical investigations (Das and Lundstrom 1988) have shown that grading of the emitter-base junction increases the recombination in the emitter-base junction and therefore the current gain may not be increased considerably by junction grading. Because of the relatively small conduction-band discontinuity and large valence-band discontinuity of  $\text{Ga}_{0.51}\text{In}_{0.49}\text{P}/\text{GaAs}$ , it can be estimated that the current gain of n-p-n HBTs based on this material system will be significantly higher than that of AlGaAs/GaAs HBTs.

Modry and Kroemer (1985) have reported a GaInP/GaAs HBT grown by MBE. The current gain was low at small current densities suggesting a high recombination rate at the emitter-base junction due to a large number of defects at the heterojunction interface. A maximum current gain of 30 was obtained at  $3000 \text{ A cm}^{-2}$ . Later, MOCVD- and chemical-beam-epitaxy-grown GaInP/GaAs HBTs with better performance were reported (Kobayashi *et al* 1989, Razeghi *et al* 1990b, Alexandre *et al* 1990, Bachem *et al* 1992). Razeghi *et al* (1990b) reported a current gain of 400 for a low-pressure MOCVD-grown GaInP/GaAs HBT. Three different HBT structures were grown: (i) conventional, (ii) double heterojunction, (iii) pseudo-graded base. Optimized growth parameters are given in table 6.1. The details of collector, base and emitter thicknesses, carrier concentrations and a typical x-ray diffraction pattern for the structures around the (400) reflection peak are shown in figure 9.23. The signal is very intense and has a full width at half maximum (FWHM) of  $20''$ , demonstrating

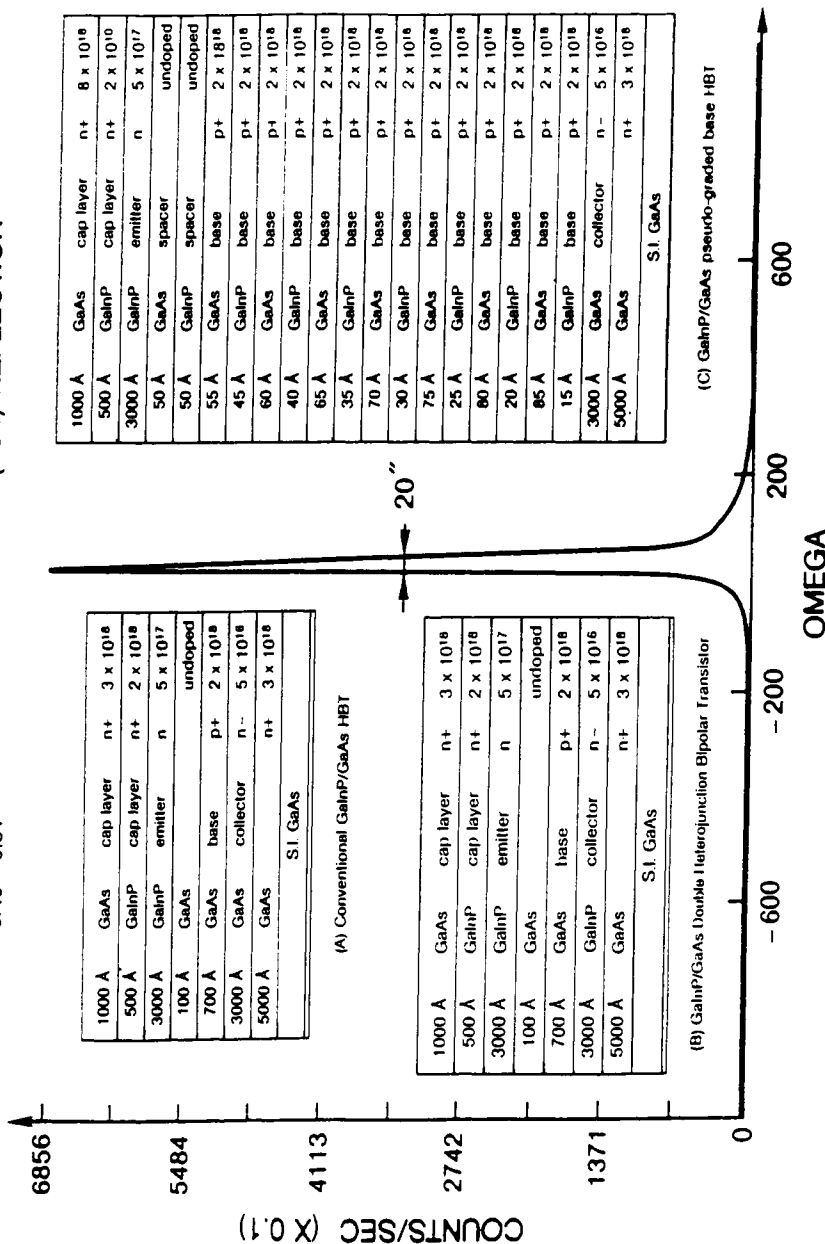
(GaAs - Ga<sub>0.49</sub>In<sub>0.51</sub>P) HBT

Figure 9.23 Typical x-ray double-diffraction pattern of a GaAs-GaInP HBT: (A) conventional, (B) double heterojunction, (C) pseudograded base (Razeghi *et al* 1990b).

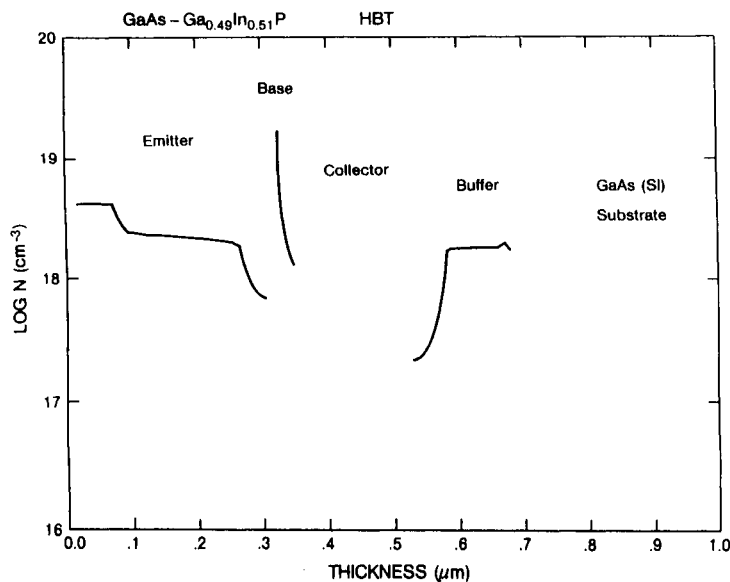


Figure 9.24 Typical doping profile of the HBTs (Razeghi *et al* 1990b).

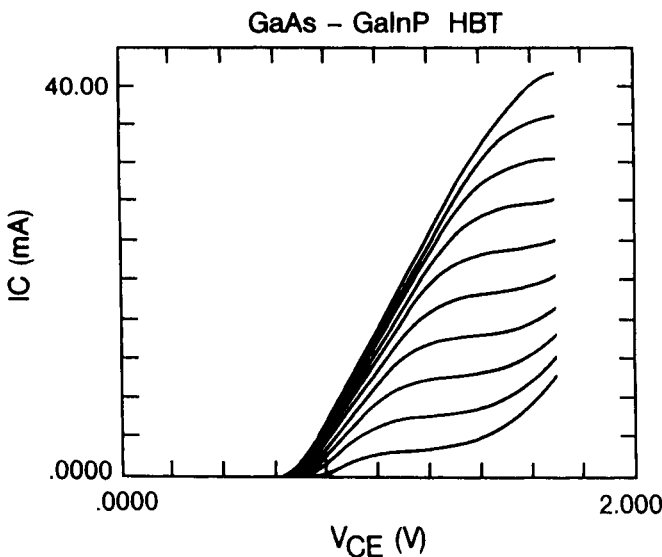


Figure 9.25 Emitter-grounded  $I$ - $V$  characteristics of structure (A) of figure 9.23 (Razeghi *et al* 1990b).

that GaInP is perfectly lattice matched to GaAs and the pseudograded base has excellent crystallographic properties, which is necessary to allow optimal transport properties of the injected minority carriers. Figure 9.24 shows the

doping profile demonstrating an abrupt and perfectly controlled transition from emitter to base and from base to collector. The device structure was a conventional mesa type.  $\text{NH}_4:\text{H}_2\text{O}_2:\text{H}_2\text{O}$  (10:4:500) and  $\text{HCl}:\text{H}_3\text{PO}_4$  (1:1) were used to etch GaAs and GaInP respectively. The emitter and collector contacts were defined by depositing and annealing Ge/Au/Ni/Au. The base contact was defined by the deposition and annealing of Zn/Au. Figure 9.25 shows the emitter-grounded  $I-V$  characteristics of the device which exhibited a current gain of 400 at 20 mA.

The investigations of the potential of the GaInP/GaAs system for use in heterostructure field effect and bipolar transistor applications have shown that this material system deserves much more attention than it is receiving at the time of writing of this book.

## REFERENCES

- Alexandre F, Benchimol J L, Dangla J, Dubon-Chevallier C and Amarger V 1990 *Electron. Lett.* **26** 1753
- Anderson R L 1962 *Solid-State Electron.* **5** 341
- Ankri D, Schaff W, Smith P, Wood C E C and Eastman L F 1982 *IEDM Tech. Digest* p 788
- Asbeck P M, Miller D L, Asatourian R and Kirkpatrick C G 1982 *IEEE Electron Devices Lett.* **EDL-3** 403
- Ashizawa Y, Noda T, Morizuka K, Asaka M and Obara M 1991 *J. Crystal Growth* **107** 903
- Bachem K H, Lauterbach Th, Maier M, Pletschen W and Winkler K 1992 *Gallium Arsenide and Related Compounds 1991 (Inst. Phys. Conf. Ser. 120)* ed G B Stringfellow (Bristol: Institute of Physics) ch 6, p 293
- Biswas D, Debban N, Bhattacharya P, Razeghi M, Defour M and Omnes F 1990 *Appl. Phys. Lett.* **56** 833
- Chan Y-J, Pavlidis D, Razeghi M, Jaffe M and Singh J 1988 *Gallium Arsenide and Related Compounds (Inst. Phys. Conf. Ser. 96)* ed J S Harris (Bristol: Institute of Physics) ch 7, p 459
- Chan Y-J, Pavlidis D, Razeghi M and Omnes F 1990 *IEEE Trans. Electron Devices* **ED-37** 2141
- Chang M F, Asbeck P M, Wang K C, Sullivan C J, Sheng N H, Higgins J A and Miller D L 1987 *IEEE Electron Devices Lett.* **EDL-8** 7
- Chi J Y, Holmstrom R P and Salerno J P 1984 *IEEE Electron Devices Lett.* **EDL-5** 381
- Das A and Lundstrom M S 1988 *IEEE Trans. Electron Devices* **ED-35** 863
- Delagebeaudeuf D and Ling N T 1982 *IEEE Trans. Electron Devices* **ED-29** 955
- Drummond T J, Fischer R, Kopp W, Morkoc H, Lee K and Shur M S 1983 *IEEE Trans. Electron Devices* **ED-30** 1806
- Drummond T J, Masselink W T and Morkoc H 1986 *IEEE Proc.* **74** 773
- Enquist P M and Hutchby J A 1989 *Electron. Lett.* **25** 1124
- Fang S F, Adomi K, Iyer S, Morkoc H and Zabel H 1990 *J. Appl. Phys.* **68** R31
- Feuer M D, Tenant D M, Kuo J M, Shunk S C, Tell B and Chang T Y 1989 *IEEE Electron Devices Lett.* **10** 70
- Fischer R, Morkoc H, Neumann D A, Zabel H, Choi C, Otsuko N, Longerbone M and Erickson L R 1986 *J. Appl. Phys.* **60** 1640

- Ginoudi A, Paloura E C, Kostandinidis G, Kiriakidis G, Maurel Ph, Garcia J C and Christou A 1992 *Appl. Phys. Lett.* **60** 3162
- Hayama N, Okamoto A, Madihan M and Hanjo K 1987 *IEEE Electron Devices Lett.* **EDL-8** 246
- Hirano M, Oe K and Yanagawa F 1986 *IEEE Trans. Electron Devices* **ED-33** 620
- Hiyamuzu S 1990 *Semicond. Semimet.* **30** 53
- Hiyamuzu S, Saito J, Nanbu K and Ishikawa T 1983 *Japan. J. Appl. Phys.* **22** L609
- Houdre R and Morkoc H 1990 *CRC Crit. Rev. Solid State Mater. Sci.* **16** 91
- Ishikawa T, Hiyamuzu S, Mimura T, Saito J and Hashimoto H 1981 *Japan. J. Appl. Phys.* **20** L814
- Ketterson A A, Masselink W T, Gedymin J S, Klem J, Peng C K, Kopp W F, Morkoc H and Gleason K R 1986 *IEEE Trans. Electron Devices* **ED-33** 564
- Ketterson A A, Moloney M, Masselink W T, Klem J, Fischer R, Kopp W and Morkoc H 1985 *IEEE Electron Devices Lett.* **EDL-6** 628
- Kiehl R A, Scontras M A, Widiger D J and Kwapien W M 1987 *IEEE Trans. Electron Devices* **ED-34** 2412
- Kikkawa T, Ohori T, Tanaka H, Kasai K and Komeno J 1991 *J. Crystal Growth* **115** 448
- Kobayashi T, Taira K, Nakamura F and Kawai H 1989 *J. Appl. Phys.* **65** 4898
- Kroemer H 1957 *Proc. IRE* **45** 1535
- Kroemer H 1982 *Proc. IEEE* **70** 13
- Kuech T F, Wang P J, Tischler M A, Potenski R, Scilla G J and Cardone F 1988 *J. Crystal Growth* **93** 624
- Landgren G, Rask M, Anderson S G and Lundberg A 1988 *J. Crystal Growth* **93** 646
- Lee J S, Iwasa Y and Muera N 1987 *Semicond. Sci. Technol.* **2** 675
- Lee K, Shur M, Drummond T J, Su S L, Lyons W G, Fisher R and Morkoc H 1983 *J. Vac. Sci. Technol. B* **1** 186
- Maziar C M, Klausmeier-Brown M E and Lundstrom M S 1986 *IEEE Electron Devices Lett.* **EDL-7** 483
- Modry M J and Kroemer H 1985 *IEEE Electron Devices Lett.* **EDL-6** 175
- Morkoc H and Unlu H 1987 *Semicond. Semimet.* **24** 135
- Nagata K, Nakajima O, Nittono T, Ito H and Ishibashi T 1987 *Electron. Lett.* **23** 64
- Nguyen L D, Radulescu D C, Tasker P J, Schaft W J and Eastman L F 1988 *IEEE Electron Devices Lett.* **EDL-9** 374
- Ohari T, Takechi M, Suzuki M, Takikawa M and Komeno J 1988 *J. Crystal Growth* **93** 905
- Omnès F and Razeghi M 1991 *Appl. Phys. Lett.* **59** 1034
- Pearah P, Henderson T, Klem J, Morkoc H, Nilsson B, Wu O, Swanson A W and Ch'en D R 1984 *J. Appl. Phys.* **56** 1851
- Razeghi M, Defour M, Omnes F, Dobers M, Vieren J P and Guldner Y 1989 *Appl. Phys. Lett.* **55** 457
- Razeghi M, Omnes F, Defour M, Maurel Ph, Bove Ph, Chan Y-J and Pavlidis D 1990a *Semicond. Sci. Technol.* **5** 274
- Razeghi M, Omnes F, Defour M, Maurel Ph, Hu J, Wolk E and Pavlidis D 1990b *Semicond. Sci. Technol.* **5** 278
- Razeghi M, Omnes F, Maurel Ph, Chan Y-J and Pavlidis D 1991 *Semicond. Sci. Technol.* **6** 103
- Ren F, Abernathy C R, Peatton S J, Lothian J R, Chu S N G, Wisk P W, Fullowan T R, Tseng B and Chen Y K 1992 *Electron. Lett.* **28** 2250
- Rosenberg J J, Benlamri M, Kirchner P D, Woodall J M and Pettit J P 1985 *IEEE Electron Devices Lett.* **EDL-6** 491
- Solomon P M, Knoedler C M and Wright S L 1984 *IEEE Electron Devices Lett.* **EDL-5** 379

- Stormer H L, Dingle R, Gossard A C, Wiegmann W and Sturge M D 1979 *Solid State Commun.* **29** 705
- Suehiro M, Hirata T, Maeda M, Hihara M, Yamada N and Hosomatsu H 1991 *Japan. J. Appl. Phys.* **30** 3410
- Tachikawa M, Mizuta M, Kukimoto H and Minomura S 1985 *Japan. J. Appl. Phys.* **24** L821
- Takikawa M, Ohori T, Takechi M, Suzuki M and Komono J 1991 *J. Crystal Growth* **107** 942
- Tanaka H, Kawamura Y, Nojima S, Wakita K and Asahi H 1987 *J. Appl. Phys.* **61** 1713
- Twynam J K, Sato H and Kinoshita T 1991 *Electron. Lett.* **27** 141
- Valois A J, Robinson G Y, Lee K and Shur M S 1983 *J. Vac. Sci. Technol. B* **1** 190
- Watanabe M O and Ohba Y 1986 *J. Appl. Phys.* **60** 1032

## Optoelectronic Integrated Circuits (OEICs)

### 10.1 INTRODUCTION

With the advancements in epitaxial growth techniques such as MOCVD, optoelectronics has been attracting increasing attention in a wide area of applications such as communication systems, optical discs and computers. Most of the optoelectronics research has been focused on improving the speed and reliability of optical communication. Optical fibre communication systems with bit rates in multigigabits s<sup>-1</sup> have been demonstrated and a significant amount of research is in progress to achieve faster, more reliable and lower-cost optical communication. Recently, optoelectronic integration has also received attention in building the optical interconnects in computing systems as will be discussed later.

An optoelectronic integrated circuit (OEIC) includes both optical devices, such as lasers and photodetectors, and electronic devices, such as transistors (which are necessary for driving the lasers), amplification and signal processing (Hirano 1987). Most of the optoelectronic circuits which are commercially available are still fabricated using a hybrid assembly technology, and the interconnections between optical and electronic discrete devices are performed using conventional techniques such as wire bonding. However, as the bit rate is increased, the parasitic capacitances and inductances associated with discrete packaging and bonding wires lead to significant degradations in the performance of the circuit. Therefore, monolithic integration of optical and electronic devices on the same substrate (preferably a semi-insulating one) has received increasing attention since the first demonstration of an optoelectronic integrated circuit by Lee *et al* (1978) which consisted of the integration of a laser diode with a Gunn oscillator. However, present integration techniques are still complicated due to the different structural and material requirements of optical and electronic devices. It looks like the future of optoelectronics relies not only on improvements in the performance of electronic and optical devices, but also on advancements in monolithic integration techniques, which have the advantage of compactness, higher performance and lower cost over conventional hybrid technology.

**Table 10.1** First GaAs-based electronic and optical devices fabricated on Si substrate.

Device	Material	Growth	Reference
LED	GaAs/Ge/Si	MBE	Shinoda <i>et al</i> (1983)
DH laser	GaAs/AlGaAs/Si	MBE	Windhorn <i>et al</i> (1984)
SLS laser	InGaAs/AlGaAs	MOCVD	Choi <i>et al</i> (1991)
PIN photodiode	GaAs/Si	MBE	Paslaski <i>et al</i> (1988)
MESFET	GaAs/Ge/Si	MBE	Choi <i>et al</i> (1984)
MODFET	GaAs/AlGaAs/Si	MBE	Fischer <i>et al</i> (1984)
Bipolar transistor	GaAs/Si	MBE	Fischer <i>et al</i> (1986)
Solar cell	GaAs/Ge/Si	MOCVD	Gale <i>et al</i> (1981)
Modulator	AlGaAs/GaAs/Si	MBE	Dobbelaere <i>et al</i> (1988)
Waveguide	GaAs/AlGaAs/Si	MBE	Kim <i>et al</i> (1990)

**Table 10.2** First InP-based electronic and optical devices fabricated on Si substrate.

Device	Material	Reference
LED at RT	InGaAs/InP/Si (1.15 $\mu\text{m}$ )	Razeghi <i>et al</i> (1988a)
DH laser	GaInAsP/InP/Si (1.3 $\mu\text{m}$ )	Razeghi <i>et al</i> (1988c)
BRS CW laser	GaInAsP/InP/Si (1.3 $\mu\text{m}$ )	Razeghi <i>et al</i> (1988b)
PIN photodiode	GaInAs/InP/Si	Razeghi <i>et al</i> (1989)
Waveguide	MQW GaInAs/InP/Si (1.5 $\mu\text{m}$ )	Razeghi <i>et al</i> (1989)
Solar cell	InP/Si	Yamaguchi <i>et al</i> (1987)
Bipolar transistor	InGaAs/InP/Si	Makimoto <i>et al</i> (1991)
Heterojunction phototransistor	InGaAs/InP/Si	Aina <i>et al</i> (1991)
MQW laser at RT	InGaAs/InGaAsP/Si	Sugo <i>et al</i> (1991)

OEICs on Si substrates. The fabrication of a monolithic photoreceiver on Si using selective growth has been reported (Aboulhouda *et al* 1990). The photoreceiver consists of a GaAs MESFET (0.5  $\mu\text{m}$  wavelength), a long-wavelength (1.3–1.55  $\mu\text{m}$ ) MSM photodetector and an inductor in order to achieve the resonance effect. Figure 10.2 shows the circuit diagram of the receiver. The inductor couples the photodetector and the preamplifier. The load can be either active or passive as indicated on the figure. Figure 10.3 presents a schematic view of the device. The epitaxial layers have been grown by LP-MOCVD on high-resistivity Si substrate. The epilayer structure consists of a 3  $\mu\text{m}$  thick undoped buffer, a 0.2  $\mu\text{m}$  thick n-type layer doped to  $3 \times 10^{17} \text{ cm}^{-3}$  which serves as the channel and a 0.2  $\mu\text{m}$  thick n<sup>+</sup> top layer for ohmic contact formation.

The epilayers for MSM have been deposited with the MOCVD growth technique by using a dielectric mask. The structure includes a 1  $\mu\text{m}$  thick In<sub>0.53</sub>Ga<sub>0.47</sub>As layer for long-wavelength operation and a 100 Å thick GaAs cap layer for Schottky contact formation. In order to achieve a planar structure, the InGaAs/GaAs heteroepitaxy has been embedded into a groove previously

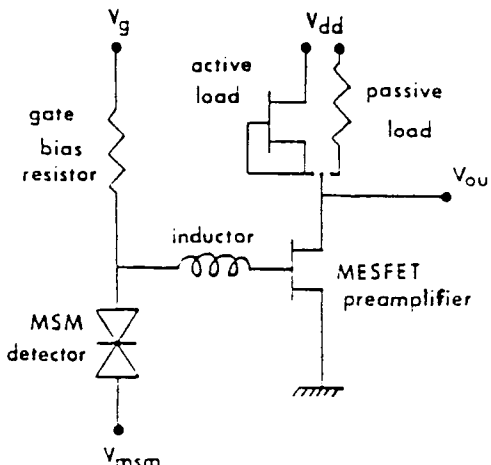


**Figure 10.2** Circuit diagram of the monolithic resonant photoreceiver (Aboulhouda *et al* 1990).

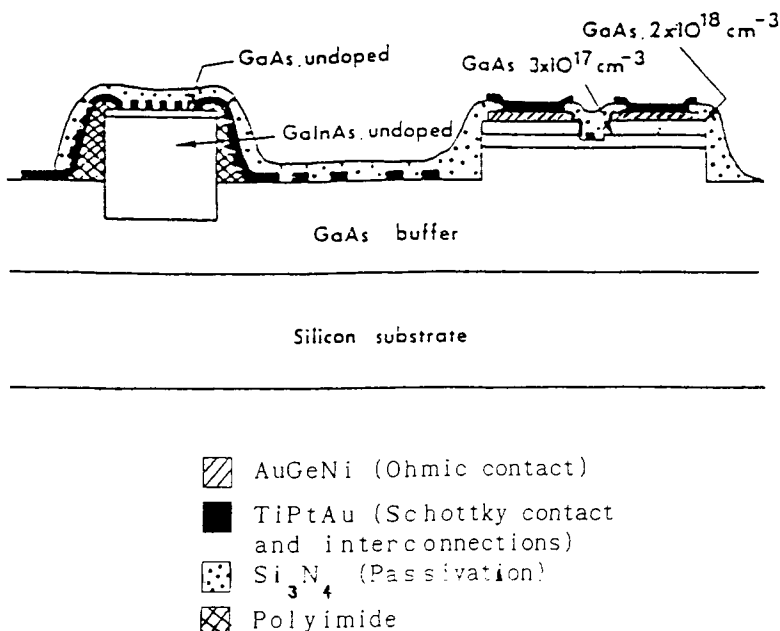


**Figure 10.3** Schematic view of the monolithic resonant receiver (Aboulhouda *et al* 1990).

etched in the GaAs layer. The first step of the local epitaxy is  $\text{SiO}_2$  deposition (1200 Å). After the  $\text{SiO}_2$  is etched where the photodetector will be grown, the

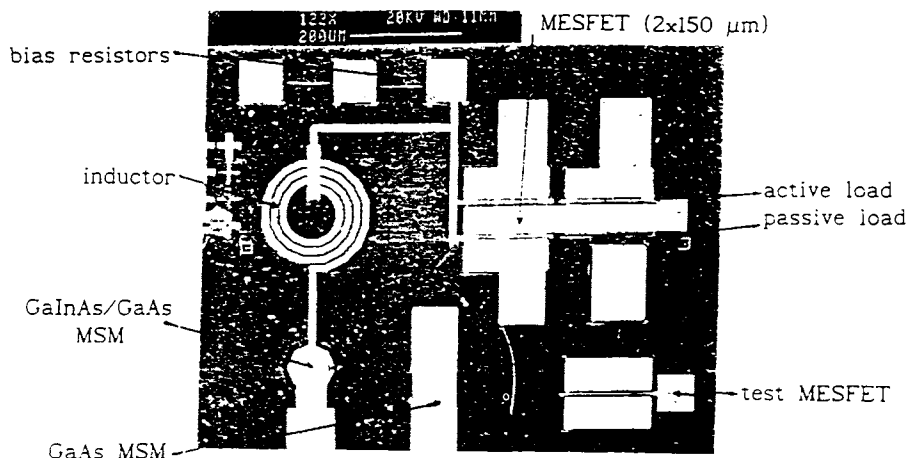


**Figure 10.4** SEM photograph of the integrated resonant receiver (Aboulhouda *et al* 1990).

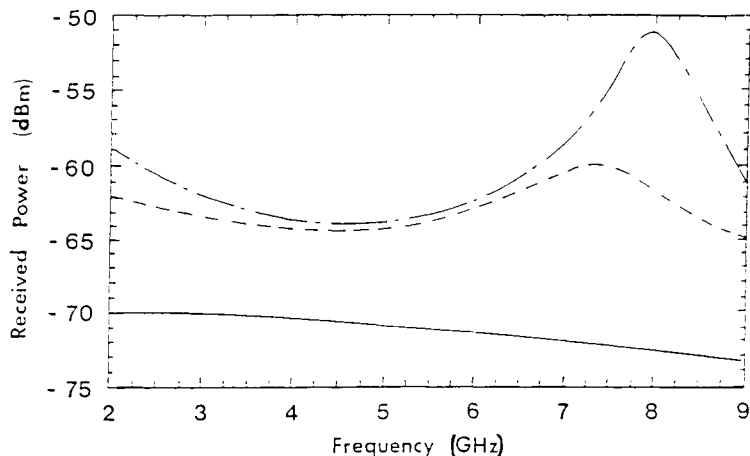


**Figure 10.5** Measured (broken curve) and calculated (chain curve) frequency response of the photoreceiver compared to that of a PIN loaded on a  $50\Omega$  resistor (solid curve) (Aboulhouda *et al* 1990).

groove is made using GaAs wet etching. Following the growth of InGaAs/GaAs layers, the  $\text{SiO}_2$  layer is removed.

A scanning electron microscopy (SEM) photograph of the device is presented in figure 10.4. The spiral inductor has been designed to have an inductance of 3 nH. A GaAs MSM ( $80\mu\text{m}$ – $80\mu\text{m}$ ) has been fabricated for comparison. The GaAs MESFET exhibited transconductance and a cut-off frequency close to 110

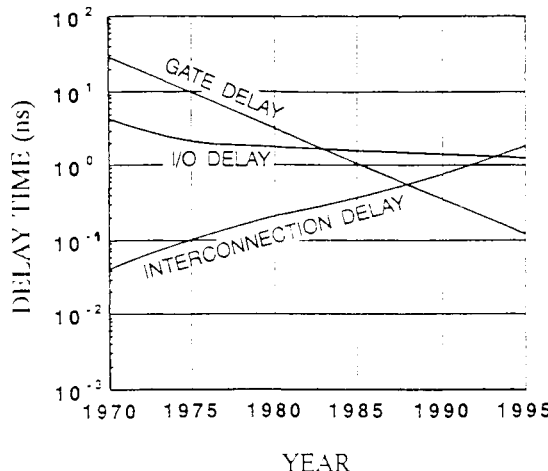


**Figure 10.6** Improvement in the delay time in Si MOS LSI circuits (Hirose *et al* 1990).

$\text{mS mm}^{-1}$  and 14 GHz respectively. The dark current of the InGaAs/GaAs MSM has been found to be lower than  $20 \mu\text{A}$  at 2 V and a capacitance of 0.4 pF has been measured at 500 MHz. Figure 10.5 shows the measured and calculated frequency response of the photoreceiver. Results obtained on a PIN photodiode loaded on a  $50 \Omega$  bias resistor are also shown in the figure for comparison. An improvement of 10 dB at 7.25 GHz has been achieved compared to the response of the PIN photodiode. The results clearly show that selective epitaxy can be a useful technique to combine GaAs electronics and long-wavelength optoelectronics on the same wafer.

#### 10.4 THE ROLE OF OPTOELECTRONIC INTEGRATION IN COMPUTING

A computing system consists of central processing units (CPUs), data storage systems and input/output (I/O) interfaces. Mature Si technology offers low-cost, high-density integration and the complexity of Si VLSI chips used in each subsystem is steadily increasing due to the need for faster and higher-performance computing. Conventional data transfer between Si VLSI chips and different subsystems is performed through electrical transmission lines, which suffer from limited bandwidth, and packaging problems as the scale of integration is increased. The time constant  $RC$  of the wire interconnect increases strongly with decreasing design rule leading to a significant increase in the interconnect delay. This introduces a major obstacle to the improvement of the speed performance of the computing system. Figure 10.6 shows the improvement in delay time in Si MOS large-scale-integration circuits (Hirose *et al* 1990). With the rapid progress in device fabrication, gate delay has been reduced significantly. However, as the length of the interconnects increases with

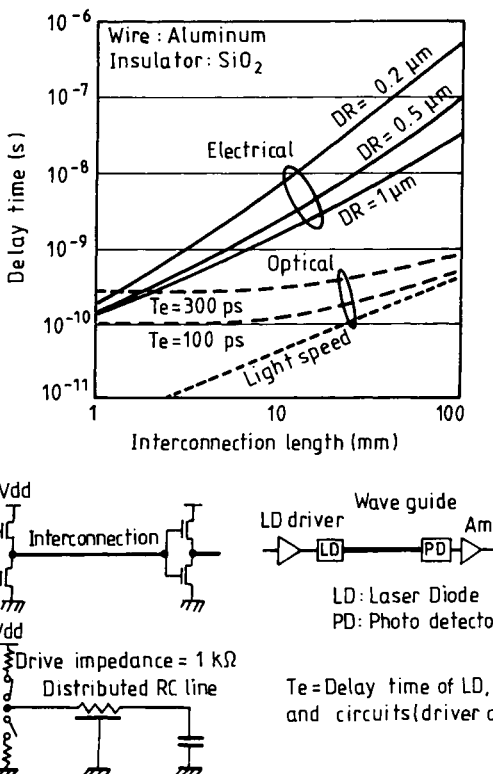


**Figure 10.7** Comparison of the delay time of electrical and optical interconnects (Hayashi 1993).

increasing chip size, an increase in the interconnect delay is seen. It is expected that the interconnection delay will be the major speed degrading mechanism in the future for ultralarge-scale-integration (ULSI) circuits using conventional electrical wiring and sequential data transfer.

Photons have major advantages in signal transfer. Optical interconnects offer high speed, need relatively low power and their large bandwidth and immunity to crosstalk provide a way to decrease the number of interconnects by multiplexing/demultiplexing. Figure 10.7 compares the delay time of electrical and optical interconnects (Hayashi 1993). The speed advantage of optical interconnects becomes more significant as the transmission distance is extended. This is especially important in the clock and bus distribution in ULSI microprocessors. A schematic view of a proposed clock distribution and optical bus are shown in figure 10.8 (Hayashi 1993). Besides the speed advantage, high fan-in and fan-out problems are eliminated since the performances of laser diodes and photodiodes are not considerably affected by fan-out and fan-in.

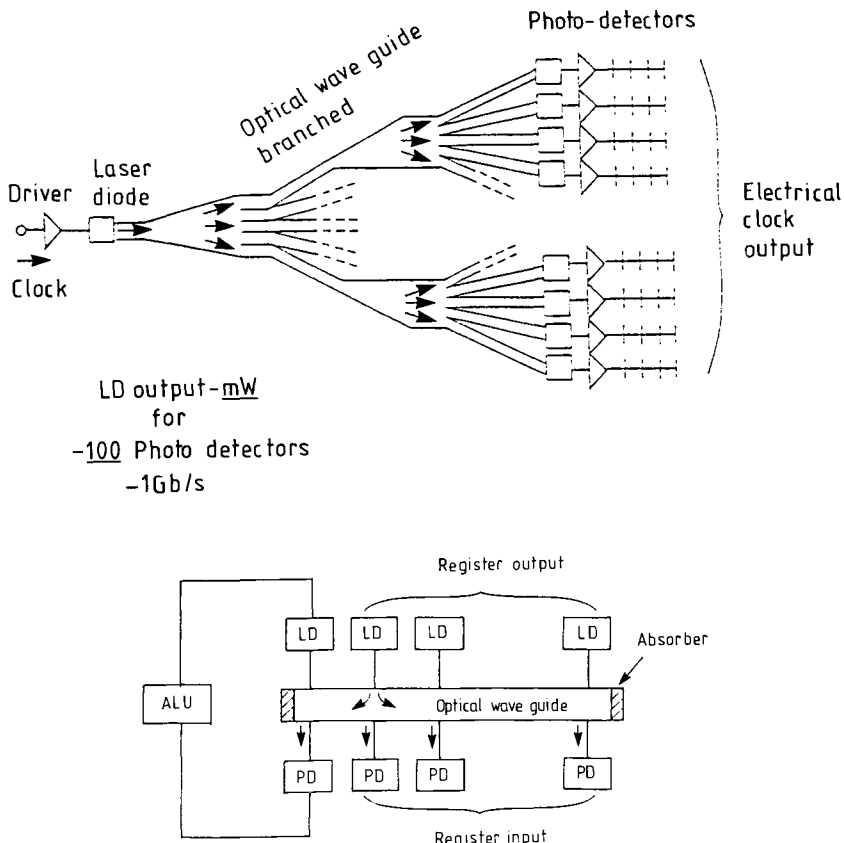


**Figure 10.8** Proposed clock distribution and optical bus line (Hayashi 1993).

The advantages offered by the optical interconnects over conventional electrical wiring open an important application field for optoelectronic integration in the rapidly improving computer industry. It is reasonable to assume that optical interconnection in computers will soon reach the board to board, chip to chip and finally intrachip level. A schematic drawing of a proposed optical interconnection between microprocessor boards is presented in figure 10.9 (Wada 1990). Surface emitting laser and photodiode arrays can be used for parallel interconnection between boards. This makes the two-dimensional integration of lasers, photodiodes and switching circuits an important research field.

A three-dimensional common memory offering ultrafast data transfer has been suggested (Hirose *et al* 1990) as shown schematically in figure 10.10. The two-dimensional silicon memory (static RAM) cell arrays with monolithically integrated light emitting diodes and photoconductors are optically coupled.

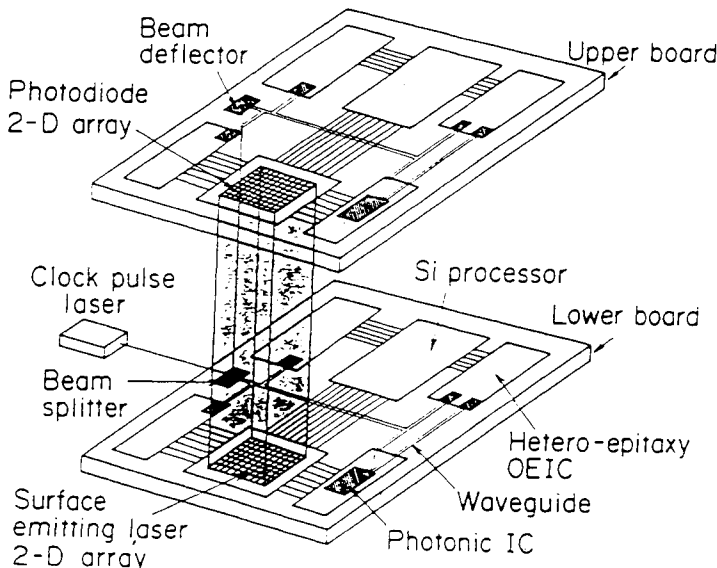


**Figure 10.9** Schematic drawing of a proposed optical interconnection system between processor boards (Wada 1990).

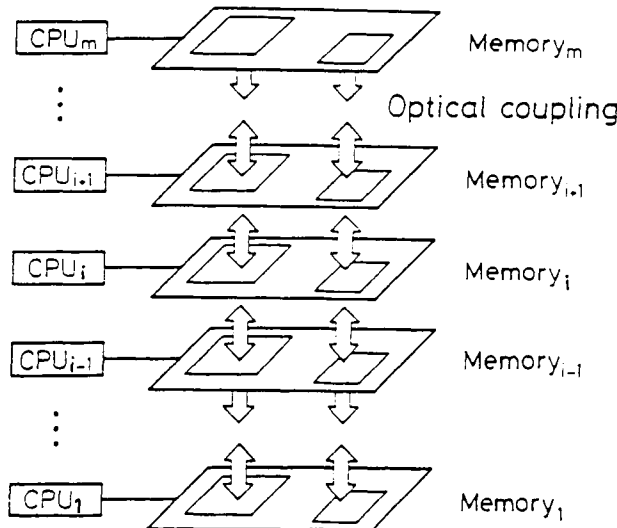


**Figure 10.10** Three-dimensional optically coupled common memory (Hirose *et al* 1990).

Optical data transfer between two memory layers can be performed between individual cells or cell blocks. Data transfer occurs sequentially through the

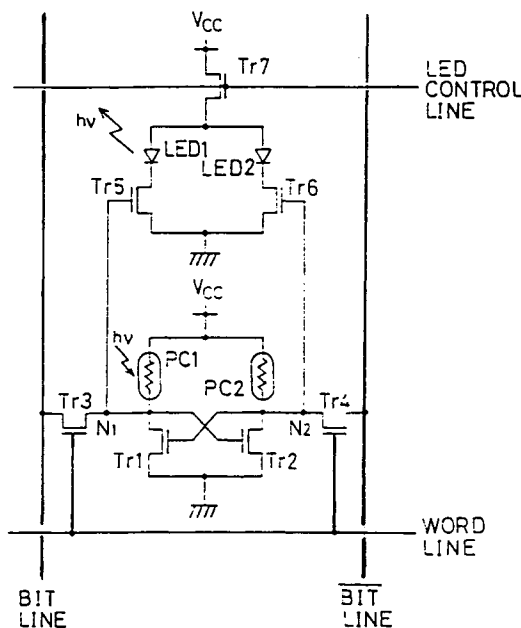


**Figure 10.11** Circuit diagram of the memory cell circuit (Hirose *et al* 1990).

memory layers, and after the transfer is completed, each CPU can execute its individual process by using the common data on the three-dimensional memory. Figure 10.11 presents a diagram of the memory cell circuit. The circuit has a data storage area which is similar to the conventional static RAM cell and a data transfer part. The high resistive load (photoconductor) detects the light signal sent by the following or preceding level memory cell. The flip-flop node with the photoconductor receiving light is set to high. Optical data transfer is started by selecting the LED control line which makes the LED connected to the 'high' node of the flip-flop emit light that is received by the photoconductors in the upper and lower memory cells. The LEDs and photoconductors in memory cells of any layer must face the photoconductors and LEDs of the upper and lower level memory cells as shown in figure 10.12. It is clear that the Si substrate must be thin enough (a few microns) to minimize the optical attenuation of the light signal through the substrate. It has been suggested that each of the memory layers be fabricated by selective epitaxial growth of GaAs on a patterned Si window at low temperatures following the conventional silicon LSI process.

In conclusion, with the developments in heteroepitaxy and monolithic integration techniques, a new era in the semiconductor industry which allows close collaboration of electrons and photons is expected to take place in the

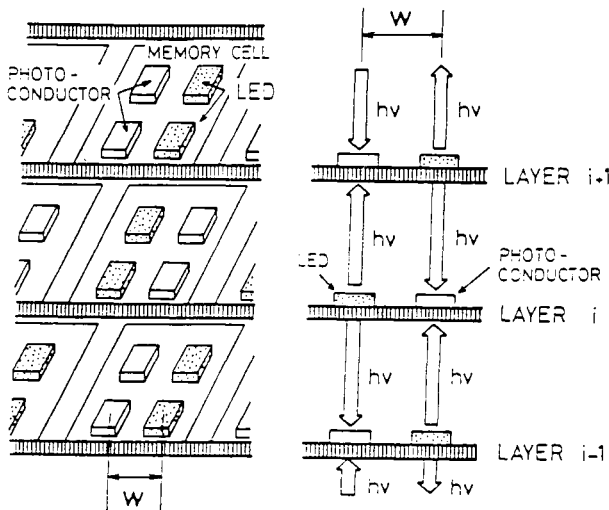


**Figure 10.12** Layout of LEDs and photodetectors in a three-dimensional optically coupled common memory (Hirose *et al* 1990).

near future. The developments in the heteroepitaxy of GaAs- and InP-based materials on Si substrates will facilitate the integration of III-V devices with Si technology using the best aspects of both technologies. Heteroepitaxy on Si substrate will also have a major impact on the computer industry by permitting the fabrication of optical interconnects inside Si ULSI chips. However, there are still many problems to be solved. First of all, to facilitate high-density integration, micron-sized laser diodes with low threshold currents (as low as microamperes) are necessary. Considering the fact that thousands of laser diodes and photodetectors will be needed for optical coupling, very high yield and highly reliable fabrication techniques are necessary which also calls for defectless III-V heteroepitaxy on Si.

## 10.5 EXAMPLES OF OPTOELECTRONIC INTEGRATION BY MOCVD

MOCVD growth technology of GaAs-GaInP, GaAs-GaInAsP, and GaAs-GaInAlP for photonic and electronic devices, as well as on patterned substrates, makes OEIC possible. MOCVD is perfectly suitable for OEIC fabrication since using the local and (in some cases) mismatched epitaxy, it is possible to deposit what we want exactly where we want it, independent of the integration functions and of the type of substrate. This allows separate optimization of each component independently of the others on an OEIC. Since epilayers suitable for lasers, for example, are not optimized for photodetectors, waveguides,

modulators or transistors, such a method would solve the difficult problem of technological compatibility between all the components of an OEIC, which is the key for the development of such devices. This will open the door to mass production, low-cost optoelectronic devices. In this chapter, silicon has been suggested as the common substrate for any monolithic integration for two reasons. First, large-scale electronic integration is now well developed on this material. Second, this material displays a large thermal conductivity which makes it attractive for any application requiring high power dissipation.

In this section we describe four different examples of monolithic integration of optoelectronic devices with different functions.

*Monolithic integration of photodetectors with transistors* (Hosserni *et al* 1988) This can significantly improve the signal to noise ratio by reducing parasitic elements compared to hybrid systems. A GaAs-based photoreceiver has been demonstrated by the monolithic association of a GaAs Schottky photodiode (PD) and a GaAs metal–semiconductor field effect transistor (MESFET). In the first step, the Schottky contact of the photodiode was deposited on an n-type GaAs layer for the MESFET gate leading to a large PD capacitance, and to a low sensitivity. In a second step, in order to optimize separately the transistor and the PD, a special undoped layer for the fabrication of the Schottky PD was grown by molecular beam epitaxy (MBE) on the epilayers suitable for the fabrication of the MESFET. The capacitance of the PD could be reduced and the performance of the photoreceiver increased. In the third step, the MESFET epilayers were replaced by epilayers suitable for high electron mobility transistor (HEMT) fabrication. With the same structure as for the previous device, an improvement of 3 dB m on the sensitivity has been recorded. It should be noted that precise etching processes are needed for such a technology.

A promising technique for the fabrication of OEICs is the use of mismatch epitaxy to fabricate FETs on GaAs-based materials and PDs on InP-based materials. In the first demonstration, a GaInAs photoconductive detector was monolithically associated with a GaAs MESFET. Good performance (sensitivity of  $-28$  dB m at  $250$  Mbit s $^{-1}$ ) has been recorded with this integrated circuit.

*Monolithic integration of photodetectors with optical waveguides* (Mallecot *et al* 1988)

This is suitable for coherent applications since it could reduce the difficult problem of achieving alignment between several optical and optoelectronic components.

Several structures have been proposed, mainly on InP substrate, based on evanescent field coupling or the butt-coupling technique. The evanescent field coupling technique seems more convenient from a technological point of view, since epilayers for photodetection can be deposited on the epilayers of the optical waveguide in a one-step growth. Because of the difference in refractive indices between the absorbing layer and the waveguide layer, part of the light propagating inside the waveguide is detected by the photodetector

(PD). However, in general, the coupling length needed to detect the totality of the light is large and thus increases the capacitance of the PD. A thin and short metal–semiconductor–metal (MSM) PD was integrated with a GaAlAs optical rib waveguide on GaAs semi-insulating substrate by MBE. Two undoped GaAlAs epilayers were deposited to optically isolate the GaAlAs guiding layer from the GaAs semi-insulating substrate. An inverted rib was etched before depositing the guiding layer. A very thin ( $0.2\text{ }\mu\text{m}$ ) undoped GaAs epilayer was grown to form the MSM photodetector. This quasi-planar structure is completely compatible with the fabrication of a MESFET. Experimental results performed at  $0.85\text{ }\mu\text{m}$  wavelength show that only a  $100\text{ }\mu\text{m}$  long GaAs absorbing layer is needed to detect 90% of the light intensity, and that the cut-off frequency is in excess of 15 GHz.

This technique was also applied to long-wavelength applications. In the first device, a GaInAs photoconductor was monolithically integrated with a  $n^-/n^+$  GaAs rib waveguide. In the improved device, a short-length GaInAs photoconductor was monolithically integrated with a GaAs/GaAlAs optical waveguide on a GaAs semi-insulating substrate. As for the previous device, a GaInAs length of only  $100\text{ }\mu\text{m}$  is needed to detect 90% of the light.

#### *Monolithic integration of optical modulator with lasers* (Oe 1991)

This technique offers a solution to overcome the high-speed modulation limit of direction modulation imposed by such phenomena as electron–photon resonance, and increases the modulation frequency up to hundreds of GHz. Among various modulation schemes, an intensity modulator based on electro-absorption effects using the quantum-confined Stark effect in multiple-quantum-well structures provides very efficient modulation because of its higher extinction ratio and smaller driving voltage and power consumption. A new integration scheme for efficient modulation involves depositing two separate electrodes on the same MQW epilayers so that one of them can act as the electrode for the laser while the other acts as the modulator electrode. Then the laser part is biased by the forward voltage and the modulator part is biased by the reverse voltage to provide the electric field needed to change the absorption coefficient. The advantages of this scheme for the modulator are the short modulator length arising thanks to the strong absorption effect, and the very low modulation power consumption since it is under reverse bias. When this device is fabricated on a silicon substrate, heating due to the CW current of the laser part and the light absorption in the modulation part can be easily dissipated.

#### *Surface emitting laser diodes*

These are key components for the development of optoelectronic systems, offering two-dimensional arrays that are suitable for optical signal processing. So far most of the results have been obtained in GaAs/AlGaAs or InGaAs/GaAs heterostructures that are known to suffer from reliability problems related to aluminium-induced oxidation. In this respect, GaInP/GaAs heterostructures which provide much lower surface recombination are an attractive alternative

to surface-emitting lasers. Power dissipation problems resulting from the very small active volume can be solved also by employing Si as the substrate.

## REFERENCES

- Aboulhouda S, Razeghi M, Vilcot J P, Decoster D, Francois M and Maricot S 1990 *Proc. SPIE* **1362** 494
- Aina O, Serio M, Mattingly M, O'Connor J, Shastry S K, Hill D S, Salerno J P and Ferm P 1991 *Appl. Phys. Lett.* **59** 268
- Choi H K 1987 *Optoelectronics* **2** 265
- Choi H K, Tsaur B Y, Metze G M, Turner G W and Fan C C 1984 *IEEE Electron Devices Lett.* **EDL-5** 207
- Choi H K, Wang C A and Karam N H 1991 *Appl. Phys. Lett.* **59** 2634
- Dobbelaere W, Huang D, Unlu M S and Morkoc H 1988 *Appl. Phys. Lett.* **53** 94
- Fischer R, Henderson T, Klem J, Masselink W T, Kopp W, Morkoc H and Litton C W 1984 *Electron. Lett.* **20** 945
- Fischer R, Peng C K, Klem J, Henderson T and Morkoc H 1986 *Solid-State Electron.* **29** 269
- Fukuzawa T, Nakamura M, Hirao M, Kuroda T and Umeda J 1980 *Appl. Phys. Lett.* **36** 181
- Gale R P, Fan C C, Tsaur B Y, Turner G W and Davis G M 1981 *IEEE Electron Devices Lett.* **EDL-2** 169
- Hayashi I 1993 Critical Reviews in Optical Science and Technology *Integrated Optics and Optoelectronics* ed K K Wong and M Razeghi, CR45, 3
- Hirano M 1987 *Optoelectronics* **2** 137
- Hirose M, Takata H and Koyanagi M 1990 *Proc. SPIE* **1362** 316
- Hosserni T A, Decoster D, Vilcot J P and Razeghi M 1988 *J. Appl. Phys.* **64** 2215
- Ito M, Wada O, Nakai K and Sakurai T 1984 *IEEE Electron Devices Lett.* **EDL-5** 531
- Kasahara K, Hayashi J, Makita K, Taguchi K, Suzuki A, Nomura H and Matsushita S 1984 *Electron. Lett.* **20** 314
- Kim Y S, Lee S S, Ramaswamy R V, Sakai S, Kao Y C and Shichijo H 1990 *Appl. Phys. Lett.* **56** 802
- Kolbas R M, Abrokwa J, Carney J K, Bradshaw D H, Elmer B R and Biard J R 1983 *Appl. Phys. Lett.* **43** 821
- Lee C P, Margalit S, Ury I and Yariv A 1978 *Appl. Phys. Lett.* **32** 806
- Makimoto T, Kurishima K, Kobayashi T and Ishibashi T 1991 *Japan. J. Appl. Phys.* **30** 3815
- Mallecot F, Vinchant I E, Razeghi M and Vandermoere D 1988 *Appl. Phys. Lett.* **53** 2522
- Matsueda H, Tanaka T P and Nakamura M 1990 *Semiconductors and Semimetals* vol 30, ed T Ikoma (Boston: Academic) p 231
- Oe K 1991 *Optoelectronic Materials and Device Concepts* ed M Razeghi (Bellingham: SPIE Optical Engineering) p 222
- Paslaski J, Chen H. Z, Morkoc H and Yariv A 1988 *Appl. Phys. Lett.* **52** 1410
- Razeghi M 1989 *Prog. Crystal Growth Charact.* **19** 21
- Razeghi M, Blondeau R, Defour M, Omnes F, Maurel Ph and Brillouet F 1988a *Appl. Phys. Lett.* **53** 854
- Razeghi M, Defour M, Blondeau R, Omnes F, Maurel Ph, Ocher O, Brillouet F, Fan C C and Salerno J 1988b *Appl. Phys. Lett.* **53** 2389
- Razeghi M, Defour M, Omnes F, Maurel Ph, Chazelas J and Brillouet F 1988c *Appl. Phys. Lett.* **53** 725
- Shimomura H, Okada Y and Kawabe M 1992 *Japan. J. Appl. Phys.* **31** L628

- Shinoda Y, Nishioka T and Ohmachi Y 1983 *Japan. J. Appl. Phys.* **22** L450  
Sugo M, Mori H, Itoh Y, Sakai Y and Tachikawa M 1991 *Japan. J. Appl. Phys.* **30** 3876  
Wada O 1990 *Proc. SPIE* **1362** 598  
Windhorn T H, Metze G M, Tsaur B Y and Fan C C 1984 *Appl. Phys. Lett.* **45** 309  
Yamaguchi M, Yamamoto A, Itoh Y and Nishioka T 1987 *Proc. 19th IEEE Photovoltaic Specialists Conf.* p 267

## Appendix A

---

### Effect of Substrate Miscut on the Measured Superlattice Period

A miscut substrate is widely used in crystal growth since the miscut surface provides a step where minimum growth energy is required, and thus growth is easier at this step and better interfacial quality is obtained. The relation between the thickness of the layer  $D$ , the wavelength of the x-rays  $\lambda$ , the separation of the superlattice satellites  $\Delta\theta$ , and the Bragg diffraction angle of the substrate  $\theta_B$  can be described by

$$D = \frac{\lambda}{2 \Delta\theta \cos \theta_B}. \quad (\text{A.1})$$

It appears that the effect of the miscut of the substrate on the measurement result is noticed when about 5% difference in the measured superlattice period between (002) diffraction and (004) diffractions is observed. The observed discrepancy results from the fact that (A.1) is only valid for symmetric geometry. For a miscut substrate, the diffraction results from asymmetric geometry. The real thickness  $D_{\text{asym}}$  is given by

$$D_{\text{asym}} = \lambda \frac{\sin(\theta_B + \alpha)}{\Delta\theta \sin(2\theta_B)} \quad (\text{A.2})$$

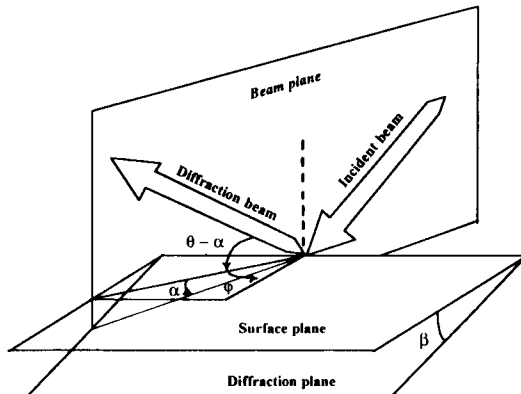
when the separation of the neighbouring peaks,  $\Delta\theta$ , is not too large. In the above equation,  $\alpha$  is the cross-section angle in the beam plane between the diffraction plane and the surface plane, as shown in figure A.1. A relation among  $\alpha$ , the miscut angle  $\beta$ , and the azimuthal angle  $\varphi$  can be obtained from figure A.1 as

$$\tan \alpha = \tan \beta \cos \varphi. \quad (\text{A.3})$$

Combining (A.2) and (A.3) under the limit where the miscut angle  $\beta$  is small, we can obtain the relation between the real superlattice period  $D_{\text{asym}}$  and the period  $D$  calculated from (A.1)

$$D_{\text{asym}} = D(1 + \beta \cot \theta_B \cos \varphi). \quad (\text{A.4})$$

### Effect of Substrate Misorientation



For asymmetric diffraction

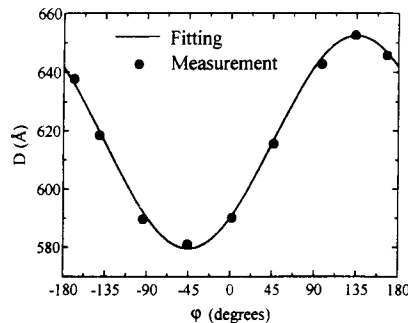
$$D_{\text{asym}} = \frac{\lambda \sin(\theta_B + \alpha)}{\Delta\theta \sin 2\theta_B}$$

$$D = D_{\text{asym}} (1 - \beta \cot \theta_B \cos \varphi)$$

$$D = \frac{\lambda}{\Delta\theta \cos \theta_B}$$

**Figure A.1** A schematic drawing of the x-ray diffraction geometry.

### Effect of Misorientation — Measurement



$$D_{\text{asym}} = 616 \text{ Å}, \quad \beta = 2.2^\circ$$

$$(D_{\max} - D_{\min}) / D_{\text{asym}} = 2\beta \cot \theta_B$$

$$= 12\% \text{ for } (004)$$

$$= 27\% \text{ for } (002)$$

**Sample must be positioned properly  
(α=0) to get correct results.**

**Figure A.2** The relation between measured periods of a GaAs/Ga<sub>0.51</sub>In<sub>0.40</sub>P superlattice and the azimuthal angle.

When  $\beta \cot \theta \ll 1$ , then (A.4) can be approximated as

$$D = D_{\text{asym}} (1 - \beta \cot \theta_B \cos \varphi). \quad (\text{A.5})$$

Figure A.2 shows the variation of  $D$  with azimuthal angle  $\varphi$  measured by HRXRD for a 10-period GaAs/Ga<sub>0.51</sub>In<sub>0.49</sub>P superlattice grown by LPMOCVD on a GaAs(001) substrate misoriented by 2° towards  $\langle 110 \rangle$  (miscut 2°). The nominal well thicknesses and barrier thicknesses are 90 Å and 100 Å, respectively. Figure A.2 indicates that a satisfactory agreement between the measured value of  $D$  and theoretical predictions is obtained.  $\beta$  and  $D_{\text{asym}}$  from the fitting are 2.2°, and the measured superlattice period is also close to the thickness measured from the TEM picture.

The maximum error in  $D$  from incorrect alignment estimated from (A.5) is 25% and 11% at (002) and (004) diffraction, respectively, for a sample grown on a 2° miscut GaAs substrate. This is an extremely significant error for most measurements.

## Appendix B

---

### Optimization of Thickness and In Composition of InGaAs Well for 980 nm Lasers

An InGaAs/GaAs strained quantum well is used as the active layer for lasers lasing at the wavelength 980 nm.

In the biaxially compressed InGaAs quantum well (QW) the normally cubic unit cell deforms elastically, matching to the smaller GaAs lattice in the plane of the QW, while in the plane perpendicular to the QW the unit cell stretches. Such a deformation affects the InGaAs energy band structure.

The strain Hamiltonian for a band at  $k = 0$  is

$$H_\epsilon = -a\epsilon_{ii} - 3b(L_i^2 - \frac{1}{3}L^2)\epsilon_{ij}\delta_{ij} - \sqrt{3}dL_iL_j\epsilon_{ij} \quad (\text{B.1})$$

where  $a$  is the hydrostatic deformation potential and  $b$  and  $d$  are the shear deformation potentials corresponding to strains of tetragonal and rhombohedral symmetries, respectively.  $\epsilon$  is a strain tensor.

In the [100] direction

$$\epsilon_{xx} = \epsilon_{yy} = \epsilon \quad (\text{B.2})$$

$$\epsilon_{zz} = -2\frac{C_{12}}{C_{11}}\epsilon \quad (\text{B.3})$$

$$\epsilon_{ij} = 0 \quad \text{for } i \neq j \quad (\text{B.4})$$

where  $C_{ij}$  is the  $ij$ th component of the stiffness tensor and  $-\epsilon$  is equal to the relaxed mismatch.  $\epsilon > 0$  for tensile strain and  $\epsilon < 0$  for compressive strain.

Applying the wavefunction of the appropriate band to the Hamiltonian in (B.1), the energy of each band under strain is obtained:

$$E(\text{hh}) = E_g + E_{\text{hydr}} - E_{\text{shear}} \quad (\text{B.5})$$

$$E(\text{ll}) = E_g + E_{\text{hydr}} + E_{\text{shear}} \quad (\text{B.6})$$

$$E(\Delta) = E_g + \Delta + E_{\text{hydr}} \quad (\text{B.7})$$

where  $E_g$  is the bandgap energy,  $\Delta$  is the split-off energy, and

$$E_{\text{hydr}} = 2a \frac{C_{11} - C_{12}}{C_{11}} \varepsilon \quad (\text{B.8})$$

$$E_{\text{hydr}} = b \frac{C_{11} + C_{12}}{C_{11}} \varepsilon \quad (\text{B.9})$$

are the hydropressure energy shift and shear strain energy shift, respectively.

The critical thickness of a strained layer is an important parameter for the strained layer. The force balancing model (Matthews and Blakeslee 1974) gives the following equation for critical thickness:

$$h_c = \frac{2}{k\sqrt{2}\pi\varepsilon} \frac{1 - 0.25\gamma}{1 + \gamma} \left[ \ln\left(\frac{h_c\sqrt{2}}{a}\right) + 1 \right] \quad (\text{B.10})$$

where  $a$  is the lattice constant of the substrate,  $\varepsilon$  is the mismatch of the strained layer, and  $\gamma$  is the Poisson ratio, which is defined as

$$\gamma = \frac{C_{12}}{C_{12} + C_{11}}. \quad (\text{B.11})$$

The coefficient  $k$  has a value of unity for a strained layer superlattice, two for a single quantum well, and four for a single strained layer.

The energy balancing model (People and Bean 1985) gives the following equation for the critical thickness of a single strained layer:

$$h_c = \frac{a}{32\sqrt{2}\pi\varepsilon^2} \frac{1 - \gamma}{1 + \gamma} \ln\left(\frac{h_c\sqrt{2}}{a}\right). \quad (\text{B.12})$$

**Table B.1** Material parameters for GaAs, InAs, and  $\text{In}_x\text{Ga}_{1-x}\text{As}$ .

	InAs	GaAs
Lattice constant ( $\text{\AA}$ )	$a_0$	6.0583
Elastic coefficient ( $10^{12}$ dyn $\text{cm}^{-2}$ )	$C_{11}$	0.8329
	$C_{12}$	0.4526
Hydrostatic deformation potential (eV)	$a$	5.9
Shear deformation potential (eV)	$b$	1.7
Electron effective mass	$m_e^*/m_0$	0.023
Heavy-hole effective mass	$m_{hh}^*/m_0$	0.32
Light-hole effective mass	$m_{lh}^*/m_0$	0.027
$\text{In}_x\text{Ga}_{1-x}\text{As}$		
Bandgap energy (eV)	$E_g$	$1.424 - 1.614x$ $+ 0.54x^2$
Exciton binding energy (meV)	$E_{\text{ex}}$	8
Band offset	$\Delta E_c/\Delta E_g$	0.65

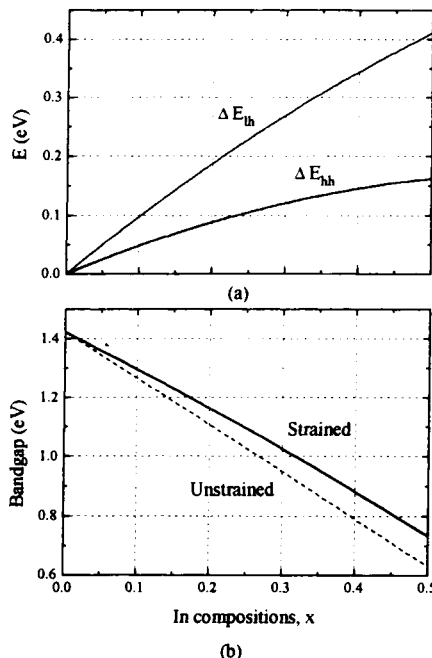


**Figure B.1** (a) Energy shifts in the light-hole valence band edge and heavy-hole valence band edge. (b) The bandgap energies of the strained (solid line) and unstrained  $In_xGa_{1-x}As$  (dashed line) on a GaAs substrate.

Figure B.1(a) shows the energy shifts in the light-hole valence band edge and heavy-hole valence band edge calculated for strained InGaAs on GaAs using (B.5)–(B.9). The necessary parameters in the calculation are listed in table B.1.

Since the energy shift in the light-hole band edge with In composition is much larger than the shift in the heavy-hole valence band edge, recombination in the bulk strained InGaAs layer is dominated by transition from the conduction band to the heavy-hole valence band. There is a strain-induced increase in the bandgap energy with indium composition for InGaAs, which partly offsets the decrease in bandgap energy with composition in unstrained InGaAs. The bandgap energies of strained (solid line) and unstrained InGaAs (dashed curve) on a GaAs substrate are shown in figure B.1(b). Figure B.1 does not take into account the quantum confinement effect, which introduces an extra shift energy. A single-quantum-well calculation is performed to decide the quantum confinement energy shift using the parameters listed in table B.1.

The next figure (figure B.2) shows the equal-energy lines on a composition-well thickness plane together with the critical thickness calculated using (B.10). There are roughly three regions, where the dependence of energy on the In composition or well width varies. At high In composition, peak energy (e.g. observed in photoluminescence spectrum) is sensitive to the variation in well

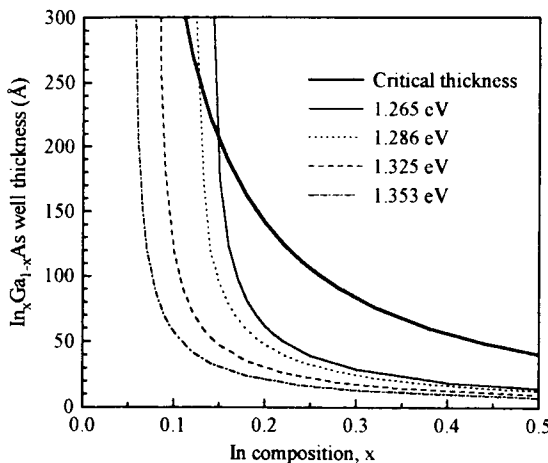


**Figure B.2** Equal-energy lines as functions of well thickness and In composition for strained  $\text{In}_x\text{Ga}_{1-x}\text{As}$  layers on a GaAs substrate.

thickness and relatively insensitive to the In composition. At low In composition, the peak energy is sensitive to the variation in In composition and relatively insensitive to the well thickness. The best region for control of the lasing wavelength is between those two regions, where the peak energy is not sensitive to the In composition or well thickness. For the material lasing at 980 nm (1.265 eV), the best In composition is around 0.19.

Avoidance of misfit dislocation is another important issue. It is observed that being farther away from the critical thickness will improve laser performance. The best In composition is in the range of 0.17–0.22 for 980 nm lasers, where maximum difference between required well width and critical thickness can be maintained.

## REFERENCES

- Matthews J W and Blakeslee A E 1974 *J. Crystal Growth* **27** 118  
 People R and Bean J C 1985 *Appl. Phys. Lett.* **47** 322

## Appendix C

---

### Energy Levels and Laser Gains in a Quantum Well (GaInAsP): the ‘Effective Mass Approximation’

Energy levels for the conduction band for quantum well structures are obtained as below. Wavefunctions in a well (well width,  $L_z$ ; well potential barrier,  $\Delta E_c$ ) are given by

$$\varphi_{cn}^- = A \begin{cases} \cos \\ \sin \end{cases} \left[ \sqrt{2m_{c1}E_{c1}}y/\hbar \right] \quad \text{for } |y| \leq L_z/2 \quad (\text{C.1})$$

$$\varphi_{cn}^+ = B \exp[-\sqrt{2m_{c2}E_{c2}}y/\hbar] \quad \text{for } |y| \geq L_z/2 \quad (\text{C.2})$$

where the upper part of the curly bracket of (C.1) is for odd  $n$ , the lower being for even  $n$ . One can derive the eigenvalue equation for the energy level  $E_{cn}$  for each subband  $n$  using the boundary conditions (continuity of wavefunctions and their derivatives) as

$$(m_{c1}/m_{c2})[(\Delta E_c - E_{cn})/E_{cn}]^{1/2} = \begin{cases} \tan \\ -\cot \end{cases} (L_z \sqrt{2m_{c1}E_{cn}}/2\hbar) \quad (\text{C.3})$$

where  $m_{c1}$  and  $m_{c2}$  are the effective masses of the conduction electrons in the active region and the waveguide region. Energy bands for heavy holes and light holes are obtained in a similar way. Energy levels for intersubbands of InGaAsP( $\lambda = 808$  nm)/GaAs are shown in table C.1.

Material constants such as  $E_g$ ,  $m_c$ ,  $m_{hh}$  and  $m_{lh}$  tabulated in table 8.3 are used for this calculation with the help of the following equations:

$$\frac{m_0}{m_{hh}(100)} = \gamma_1 - 2\gamma_2 \quad \frac{m_0}{m_{lh}(100)} = \gamma_1 + 2\gamma_2 \quad (\text{C.4})$$

$$\frac{m_0}{m_{hh}(111)} = \gamma_1 - 2\gamma_3 \quad \frac{m_0}{m_{lh}(111)} = \gamma_2 + 2\gamma_3. \quad (\text{C.5})$$

The quasi-Fermi energy level is the chemical potential for the electron or hole gas in the active layer at quasiequilibrium during current injection. Since the

**Table C.1**

QW width ( $L_z$ )	Subbands	Energy level (meV)				
		$n = 1$	$n = 2$	$n = 3$	$n = 4$	$n = 5$
150 Å	$E_c$	15.06	57.08			
	$E_{hh}$	2.82	11.24	25.20	44.30	67.68
	$E_{lh}$	12.14	14.83	93.62		
300 Å	$E_c$	4.98	19.74	48.70	75.09	
	$E_{hh}$	0.79	3.15	7.06	12.58	19.62
	$E_{lh}$	3.86	15.44	34.39	59.96	89.64

quasi-Fermi energy level determines not only injection carrier density, but also the laser gain, we calculate the quasi-Fermi energy level from the relation between the carrier density in the active layer ( $n_{act}$ ) and the quasi-Fermi energy level ( $E_{fc}$ ).

$$n_{act} \equiv \int f_D(E_k, E_{fc}) dk = \sum_n kT\rho_n \ln[1 + \exp(\beta(E_{fc} - E_{cn}))] \quad (\text{C.6})$$

where  $f_D(E_k, E_{fc})$  is the Fermi–Dirac distribution for energy  $E_k$ , when the chemical potential is  $E_{fc}$ , and  $\rho_n$ , the density of states for 2D, is given by

$$\rho_n = qmkT/\pi\hbar^2 L_z. \quad (\text{C.7})$$

Quasi-Fermi levels for holes ( $E_{fv}$ ) are obtained in the same way. Once  $E_{fc}$  and  $E_{fv}$  have been determined, the gain spectrum can be calculated from the Fermi golden rule:

$$g(\hbar\omega) = \frac{q^2|M|^2}{\hbar\omega\epsilon_0 m^2 c_0 \hbar n L_z} \sum_{ij} m_{r,ij} A_{ij} C_{ij} [f_c - (1 - f_v)] \theta(\hbar\omega - E_{ij}) \quad (\text{C.8})$$

where

$$A_{ij} = \frac{3}{4}(1 + \cos^2 \Theta_{ij}) \quad (\text{for TE})$$

$$A_{ij} = \frac{3}{2} \sin^2 \Theta_{ij} \quad (\text{for TM}).$$

The angular factor  $\Theta_{ij}$  is given by  $\cos^2 \Theta_{ij} = E_{ij}/E$ . Since  $\Theta_{ij}$  is close to zero at the band edge, TM modes give a very small contribution compared to TE modes and therefore will be neglected below for simplicity. The calculation results for GaAs/AlGaAs lasers when an optical loss for the laser cavity of  $\alpha_{loss} = 10 \text{ cm}^{-1}$  is assumed are shown in figure C.1.

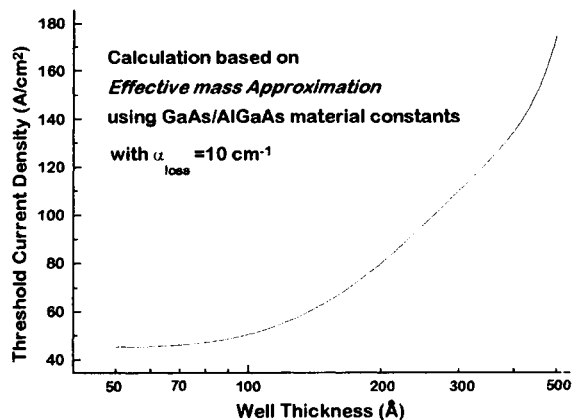


**Figure C.1** The threshold current change as a function of the quantum well thickness  $L_z$  when the total loss of the laser cavity  $\alpha_{\text{loss}}$  is  $10 \text{ cm}^{-1}$  and material constants for GaAs/AlGaAs were used for (C.1)–(C.5).

## Appendix D

---

### Luttinger–Kohn Hamiltonian

#### D.1 $k \cdot p$ THEORY

The general Hamiltonian for electrons in a solid can be written as

$$\left[ \frac{p^2}{2m_0} + V_0 \right] \Psi_{nk}(r) = \varepsilon_{nk} \Psi_{nk}(r). \quad (\text{D.1})$$

By Bloch's theorem,  $\Psi_{nk}(r) = e^{ik \cdot r} \phi_{nk}(r)$ , where  $\phi_{nk}(r)$  is invariant in crystal symmetry translation or rotation. Hence, (D.1) can be written as

$$\left[ \frac{p^2}{2m_0} + V_0 + \frac{\hbar}{m_0} \mathbf{k} \cdot \mathbf{p} \right] \phi_{nk}(r) = \varepsilon_{nk} \phi_{nk}(r). \quad (\text{D.2})$$

This is the basic Hamiltonian for  $k \cdot p$  perturbation theory.

#### D.2 LUTTINGER–KOHN HAMILTONIAN

The Luttinger–Kohn Hamiltonian is a Hamiltonian describing degenerate valence bands. According to the degenerate second-order perturbation theory, energies for  $|X\rangle$ ,  $|Y\rangle$ ,  $|Z\rangle$  states (hole eigenstates with  $x$ ,  $y$ ,  $z$  symmetry) for the  $k \cdot p$  Hamiltonian (D.2) are given by

$$H_{ij} = \frac{\hbar^2 k^2}{2m_0} \delta_{ij} + \sum_m \frac{|\langle i | H_1 | j \rangle|^2}{\varepsilon_i - \varepsilon_m} \quad (\text{D.3})$$

where  $i$ ,  $j$  indicate  $X$ ,  $Y$ ,  $Z$ .  $H_1$  is the  $k \cdot p$  term  $((\hbar/m_0)\mathbf{k} \cdot \mathbf{p})$  in (D.2). Using the equation

$$\frac{m_0^2}{\hbar^2} |\langle X | H_1 | m \rangle|^2 = |\langle X | p_x | m \rangle|^2 k_x^2 + |\langle X | p_y | m \rangle|^2 k_y^2 + |\langle X | p_z | m \rangle|^2 k_z^2 \quad (\text{D.4})$$

(D.3) is rewritten as

$$H = \begin{pmatrix} E_1 + Ak_x^2 + B(k_y^2 + k_z^2) & Ck_xk_y & Ck_xk_z \\ Ck_xk_y & E_1 + Ak_y^2 + B(k_x^2 + k_z^2) & Ck_yk_z \\ Ck_xk_z & Ck_yk_z & E_1 + Ak_z^2 + B(k_x^2 + k_y^2) \end{pmatrix}. \quad (\text{D.5})$$

This is not yet an accurate perturbation theory since the spin-orbit interaction is not included in this way (we have included only crystal potentials, the spin-orbit interaction is a self-interaction of the electrons). The spin-orbit interaction decouples the six states ( $2$  (spin number)  $\times 3$  ( $X, Y, Z$ )) into  $|J = \frac{3}{2}\rangle$  and  $|J = \frac{1}{2}\rangle$ . Since the  $|J = \frac{1}{2}\rangle$  state has much lower energy (by  $\Delta_0 \sim 300$  meV), we consider only  $|J = \frac{3}{2}\rangle$  states. Translating the  $|L = 1\rangle$  states (such as  $|X\rangle$ ) into  $|J = \frac{3}{2}\rangle$  states (using Clebsch-Gordan coefficients), (D.5) can be rewritten as

$$H = \begin{pmatrix} H_{\text{hh}} & -c & -b & 0 \\ -c^* & H_{\text{lh}} & 0 & b \\ -b^* & 0 & H_{\text{hh}} & -c \\ 0 & b^* & -c^* & H_{\text{lh}} \end{pmatrix} \quad (\text{D.6})$$

where

$$H_{\text{hh}} = \frac{\hbar^2}{2m_0} \left\{ (\gamma_1 + \gamma_2)k_\rho^2 + (\gamma_1 - 2\gamma_2)k_z^2 \right\} \quad (\text{D.7})$$

$$H_{\text{lh}} = \frac{\hbar^2}{2m_0} \left\{ (\gamma_1 + \gamma_2)k_z^2 + (\gamma_1 - 2\gamma_2)k_\rho^2 \right\} \quad (\text{D.8})$$

$$c = \frac{\sqrt{3}\hbar^2}{2m_0} \left\{ \gamma_2(k_x^2 - k_y^2) - 2i\gamma_3k_xk_y \right\} \quad (\text{D.9})$$

$$b = \frac{\sqrt{3}\hbar^2}{2m_0} \gamma_3k_z(k_x - ik_y). \quad (\text{D.10})$$

Further simplifications is possible if we assume  $\gamma_2$  and  $\gamma_3$  are close to each other ( $\gamma_2 \sim \gamma_3$ ) (called the axial approximation). Then by a unitary transformation (Brodio and Sham 1985), (D.6) is transformed into decoupled  $2 \times 2$  matrices as

$$H_v = \frac{1}{2} \left( \frac{\hbar^2}{m_0} \right) \begin{pmatrix} (\gamma_1 + \gamma_2)k_\rho^2 + (\gamma_1 - 2\gamma_2)k_z^2 & \sqrt{3}\gamma_2k_\rho(k_\rho + i2k_z) \\ \sqrt{3}\gamma_2k_\rho(k_\rho + i2k_z) & (\gamma_1 - \gamma_2)k_\rho^2 + (\gamma_1 + 2\gamma_2)k_z^2 \end{pmatrix} + V(z) \quad (\text{D.11})$$

where  $V(z)$  is the potential profile of the valence band. This is the Luttinger-Kohn Hamiltonian with the axial approximation.

## REFERENCES

Brodio D A and Sham L J 1985 *Phys. Rev. B* **31** 888

# Appendix E

---

## Infrared Detectors

### E.1 CLASSIFICATION

In general, infrared detectors fall into two categories: photon detectors (also named photodetectors) and thermal detectors (see figure E.1). In photon detectors the incident photons are absorbed within the material by interaction with electrons, either to lattice atoms, or to impurity atoms or with free electrons. The observed electrical signal results from the changed electronic energy distribution. The photon detectors show a selective wavelength dependence of the response per unit incident radiation power. In thermal detectors, the incident radiation is absorbed and raises the temperature of the material. The output signal is observed as a change in some temperature-dependent property of the material. In pyroelectric detectors a change in the internal electrical polarization is measured, whereas in the case of bolometers a change in the electrical resistance is measured. The thermal effects are generally wavelength independent since the radiation can be absorbed in a ‘black’ surface coating.

### E.2 GENERAL THEORY OF PHOTODETECTORS

The photodetector is a slab of homogeneous semiconductor with the actual ‘electrical’ area  $A_e$  which is coupled to the beam of the infrared radiation by its optical area  $A_o$  (figure E.2). Usually, the optical and electrical areas of the device are the same or close. The use of optical concentrators can increase the  $A_o/A_e$  ratio, however.

The current responsivity of the photodetector is determined by the quantum efficiency  $\eta$  and by the photoelectric gain  $g$ . The quantum efficiency value describes how well the detector is coupled to the radiation to be detected. It is usually defined as the number of electron–hole pairs generated per incident photon. The photoelectric gain is the number of carriers passing contacts per pair generated. This value shows how well the generated electron–hole pairs are used to generate the current response of a photodetector. Both values are assumed here as constant over the volume of the device.

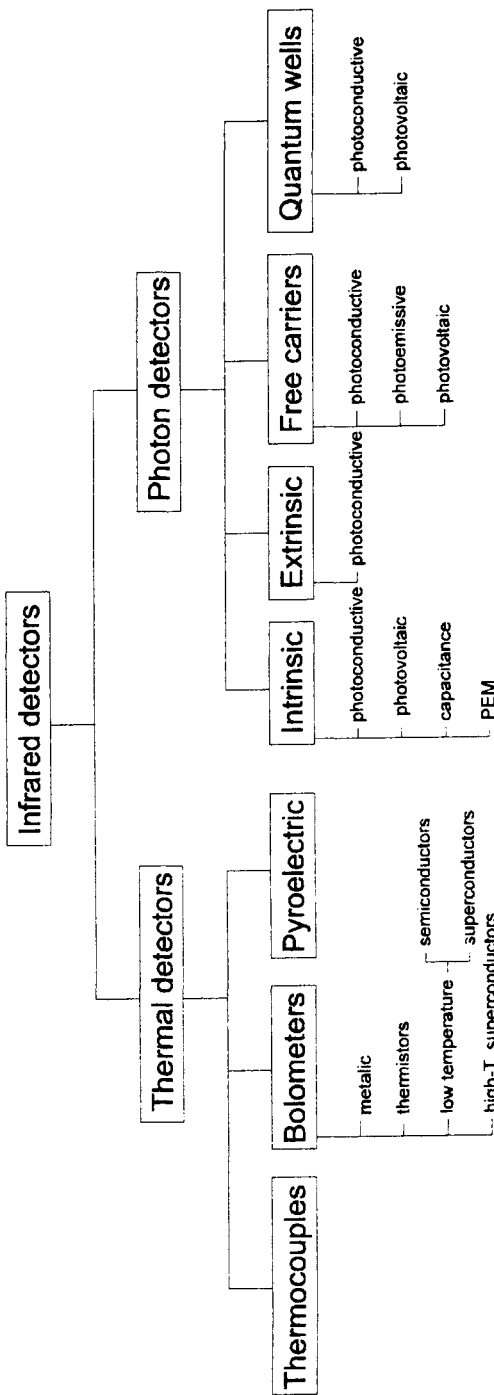


Figure E.1 Classification of infrared detectors.

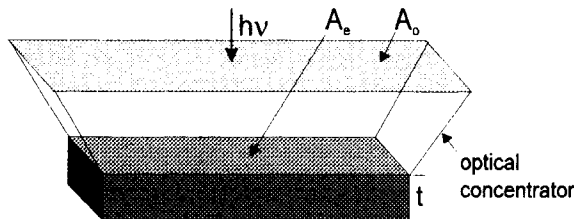


Figure E.2 Model of a photodetector.

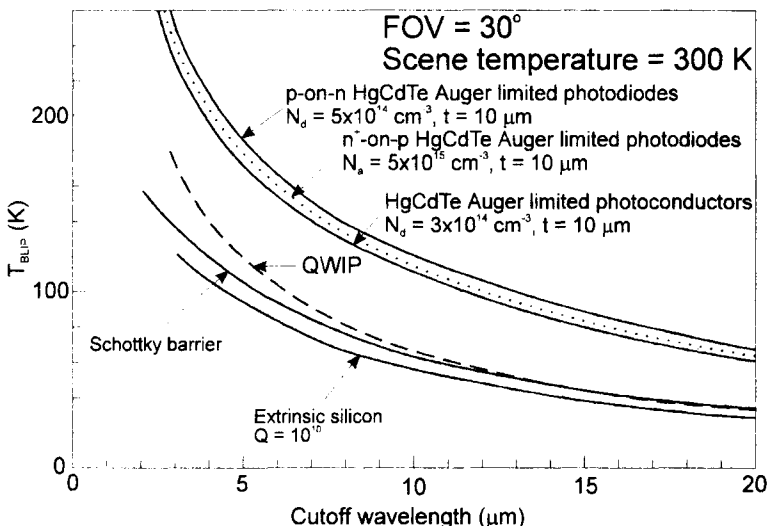


Figure E.3 An estimation of the temperature required for background-limited operation of different types of photon detector. In the calculations  $\text{FOV} = 30^\circ$  and  $T_B = 300 \text{ K}$  are assumed (after Rogalski 1995).

The spectral current responsivity is

$$R_i = \frac{\lambda \eta}{hc} q g \quad (\text{E.1})$$

where  $\lambda$  is the wavelength,  $h$  is the Planck constant,  $c$  is the light velocity,  $q$  is the electron charge, and  $g$  is the photoelectric current gain. Assuming that the current gains for photocurrent and noise current are the same, the current noise due to generation and recombination processes is

$$I_n^2 = 2(G + R)A_e t \Delta f q^2 g^2 \quad (\text{E.2})$$

where  $G$  and  $R$  are the generation and recombination rates,  $\Delta f$  is the frequency band, and  $t$  is the thickness of the slab.

The detectivity  $D^*$  is the main parameter characterizing the normalized signal to noise performance of detectors and can be defined as

$$D^* = \frac{R_i(A_o \Delta f)^{1/2}}{I_n}. \quad (\text{E.3})$$

According to (E.1)–(E.3)

$$D^* = \frac{\lambda}{hc} \left( \frac{A_o}{A_e} \right)^{1/2} \eta [2(G + R)t]^{-1/2}. \quad (\text{E.4})$$

For a given wavelength and operating temperature the highest performance can be obtained by maximizing  $\eta/[t(G + R)]^{1/2}$  which corresponds to the condition of the highest ratio of the sheet optical generation to the square root of sheet thermal generation–recombination.

The effects of a fluctuating recombination can frequently be avoided by arranging for the recombination process to take place in a region of the device where it has little effect due to low photoelectric gain: for example, at the contacts in sweep-out photoconductors or in the neutral regions of diodes. In this case, the noise can be reduced by a factor of  $2^{1/2}$  and detectivity increased by the same factor. The generation process with its associated fluctuation, however, cannot be avoided by any means.

The total generation rate is a sum of the optical and thermal generation

$$G = G_{\text{th}} + G_{\text{op}}. \quad (\text{E.5})$$

The optical generation may be due to the signal or thermal background radiation. Usually thermal background radiation is higher compared to the signal radiation. The optical generation rate is

$$G_{\text{op}} = \frac{A_o \eta \Phi_B}{A_e t} \quad (\text{E.6})$$

where  $\Phi_B$  is the background photon flux density.

If the thermal generation is reduced much below the optical one, the performance of the device is determined by the background radiation (BLIP conditions, for background-limited infrared photodetector).  $T_{\text{BLIP}}$  is the temperature at which the thermally generated current is equal to the background-generated current in the detector. Assuming that recombination does not contribute to the noise

$$D_{\text{BLIP}}^* = \frac{\lambda}{hc} \left( \frac{\eta}{2\Phi_B} \right)^{-1/2}. \quad (\text{E.7})$$

It should be noted that  $D_{\text{BLIP}}^*$  does not depend on the ratio  $A_o/A_e$ .

In figure E.3 plots of the calculated temperature required for BLIP operation in a 30° field of view (FOV) are shown as a function of cut-off wavelength. We can see that the operating temperature for HgCdTe detectors is higher than for other types of photon detector. HgCdTe detectors with background-limited performance operate with thermoelectric coolers in the MWIR range, whereas the LWIR detectors ( $8 \leq \lambda_c \leq 12 \mu\text{m}$ ) operate at  $\approx 100$  K. HgCdTe is characterized by high optical absorption coefficient and quantum efficiency and relatively low thermal generation rate compared to extrinsic detectors, silicide Schottky barriers, and GaAs/AlGaAs quantum well infrared photodetectors (QWIPs). However, the cooling requirements for QWIPs with cut-off wavelengths below 10  $\mu\text{m}$  are less stringent in comparison with extrinsic detectors and Schottky barrier devices.

## REFERENCES

- Rogalski A (ed) 1995 *Infrared Photon Detectors* (Bellingham, WA: SPIE Optical Engineering)



Taylor & Francis  
Taylor & Francis Group  
<http://taylorandfrancis.com>

# Index

---

- III-V binary compounds, 1  
III-V intersubband infrared detectors, 271–279  
  focal plane arrays, 303  
  performance of AlGaAs/GaAs detectors, 300–303  
  performance of GaInP/GaAs detectors, 300–308  
  technology of AlGaAs/GaAs detectors, 271–275  
  technology of GaInP/GaAs detectors, 272–275
- III-V lattice-matched heterojunctions  
  RDS observations of GaInAs/InP heterojunction growth, 75–81  
  RDS observations of GaInAsP/InP heterojunction growth, 71–73
- III-V lattice-mismatched structures  
  3D growth, 99–101, 108–110  
  growth procedure of InAs/InP, 89  
  growth procedure of InP/GaAs/Si, 89  
  optical models, 94–99, 104–106  
  RDS observations of GaInP/GaAs and GaInP/InP growth, 106–107  
  RDS observations of InAs/GaAs/Si growth, 89–93  
  RDS observations of InAs/InP growth, 90–93, 99–104
- III-V quaternary alloys  
  bandgap energy, 4  
  lattice constants, 3
- III-V ternary alloys  
  bandgap energy, 1, 3  
  lattice constants, 3  
  physical constants, 2
- Air-mass-zero (AM0) spectrum, 308  
AlGaAs/GaAs HBTs, 396  
AlGaInP lasers, 343–345  
Auger analysis  
  GaInP/GaAs MOCVD quantum wells and superlattices, 263  
  on chemical bevels, 260–263
- Bandgap diagram  
  of double heterostructure, 347  
  of GaAs/AlGaAs GRIN-SCH laser, 330  
  of HBT, 393  
  of n-p-n HBT, 392  
  of single quantum well, 347
- Band offsets evaluation  
  from  $C-V$  profiling, 215–216  
  from DLTS data, 217–218  
  from  $I-V$  curve of HEMTs, 218–219  
  from collector current of HBTs, 219–220  
  GaAs/GaInP system, 215–220, 264–270  
  theory, 267–270
- Band structure  
  of GaAs, 174, 178  
  of GaInAsP, 177

- Bath revelation, 117–118  
 BLIP conditions, 434  
 Bloch function, 171  
 Bound-state energies, 326  
 Brillouin zone  
     of GaAs-based materials, 172  
 Built-in potential, 165  
 Burnboxes, 28
- Carrier concentration  
     concentration of acceptors, 164  
     concentration of donors, 164  
     intrinsic carrier concentration, 165  
     under non-degenerate conditions, 163
- Charge neutrality, 163
- Chemical beam epitaxy, 47
- Chemical bevel revelation  
     apparatus, 114–117  
     principle of magnification, 114
- Chemical potential, 31
- Classical lifetime  
     in GaInP/GaAs heterojunction, 244–247
- Compensation ratio, 162
- Critical thickness, 423
- Deep levels, 120
- Deep-level transient spectroscopy, 16, 118–128  
     basic concepts, 121–124  
     determination of trap parameters, 125–128
- $\delta$ -doping, 232–233
- Density of states  
     in a quantum well, 326
- Depletion correction, 165
- Depletion layer thickness, 165
- Detectivity, 295, 434
- Diffusion equation, 180–181
- Doping in III–V alloys, 215
- Double-heterostructure laser, 320, 324
- DX centre, 16, 179
- Effective layer thickness, 134
- Effective lifetime, 234
- Effective mass, 174
- Effective mass approximation, 426
- Eigenvalue equation, 173
- Electrochemical capacitance–voltage (ECV) measurements  
     C–V measurements, 149–150  
     electrochemical cell, 151
- Electrolyte electroreflectance, 264
- Electronic devices  
     bipolar devices, 5  
     IMPATT diodes, 5  
     tunnel diodes, 5  
     unipolar devices, 5
- Electronic mass flow controllers, 24–25
- Electron spin resonance  
     in 2DEG of GaInP/GaAs  
     heterostructures, 227–232
- Electro-optical modulators, 282–292  
     applications, 286–289, 292  
     multiple-quantum-well modulators, 284–289  
     perspectives, 292  
     superlattice modulators, 289–292
- Energy gap  
     of GaInP, 18  
     of AlGaAs, 18
- Energy shift, 299, 424
- Enthalpy, 31
- Entropy, 31
- Epitaxial layers  
     atomic layer epitaxy, 13  
     liquid phase epitaxy, 10  
     metallorganic chemical vapour deposition, 12  
     metallorganic molecular beam epitaxy, 13  
     migration enhanced epitaxy, 14  
     molecular beam epitaxy, 11  
     vapour phase epitaxy, 10–11
- Exciton complex, 147
- Exhaust system, 25
- Ex situ* characterization, 114–168

- chemical bevel revelation, 114–118  
 deep-level transient spectroscopy, 118–128  
 electrochemical capacitance–voltage measurements, 149–155  
 Hall measurement, 158–165  
 photoluminescence, 143–148  
 photovoltage spectroscopy, 154–155  
 resistivity measurements, 155–158  
 thickness measurements, 166–168  
 x-ray diffraction, 129–143
- Feedback, 318  
 Fermi level, 164  
 Figures of merit, 292–295  
 detectivity, 295  
 NEI, 294  
 NEP, 294  
 responsivity, 295
- Field effect transistor  
 frequency response, 374  
 transconductance, 373
- Fourier transformation, 145
- Fourier transform spectroscopy, 143–145
- Full width at half maximum (FWHM), 147
- GaAs/AlGaAs quantum well infrared detectors, 200–304  
 advantages, 304  
 focal plane arrays, 303  
 photoconductive detectors, 301–302
- GaAs/GaInP p-type quantum well infrared detectors, 304–308
- GaAs-based lasers, 317–365  
 new materials, 336–365
- GaAs laser structures  
 double-heterostructure lasers, 327  
 graded-index separate confinement heterostructure lasers, 330  
 lateral mode control, 329–332  
 multiquantum-well structures, 330  
 quantum well lasers, 335
- separate confinement heterostructure lasers, 328
- GaAs solar cells, 310–313
- Gain  
 photoconductive gain, 293  
 threshold gain, 320, 360–363
- GaInAsP/GaAs lasers, 343–365  
 advantage, 343–344  
 comparison of gain and threshold current  
 density, 360–365  
 differential efficiency, 353–358  
 minority-carrier leakage, 353–355  
 threshold current density, 358–359  
 0.808  $\mu\text{m}$  high-power lasers, 345–353
- GaInP/GaAs band offsets, 264–270 values, 264
- GaInP/GaAs HBTs, 397–400
- GaInP/GaAs heterostructures, 214–248  
 band offsets, 215–220  
 cyclotron resonance absorption, 225  
 electron spin resonance in 2D  
 electron gas, 227–232  
 high-mobility heterostructures, 223–227  
 magnetotransport measurements, 232–235  
 persistent photoconductivity, 235–242  
 quantum and classical lifetimes, 244–247  
 quantum Hall effect, 247  
 two-dimensional (2D) electron gas, 221–223  
 with  $\delta$ -doping, 232–233
- GaInP/GaAs heterostructure  
 isolated-gate FETs, 387–391
- GaInP/GaAs MOCVD multilayers, 247–252  
 structural properties, 248–250  
 transport properties, 250–252

- GaInP/GaAs MOCVD quantum wells**  
and superlattices, 252–260  
Auger analysis, 260–264  
energy levels, 258  
growth parameters, 253  
photoluminescence spectrum, 254  
x-ray diffraction patterns, 255, 259
- GaInP/GaAs MODFETs**, 378–386  
n-channel devices, 378–382  
p-channel devices, 383–385
- GaInP/GaAs superlattices**  
electrolyte electroreflectance, 268  
structural characterization, 138–143
- GaInP/GaAs three-quantum-well structure**, 270
- Gas flow pattern in MOCVD reactor**, 34–42  
Berkman *et al.*'s model, 39  
flow visualization, 39  
heat effect, 37–38  
holographic interference study, 39  
modelling, 39–40  
numerical simulation, 40
- Gas leak detector**, 29
- Gas source MBE**, 47
- Gibbs free energy**, 30
- Growth of III–V binaries**  
optimization of InAs growth by RDS, 64–71
- Hall measurements**, 159–162  
in  $\delta$ -doped GaInP layers, 232
- Hamiltonian**  
Luttinger–Kohn Hamiltonian, 429  
strain Hamiltonian, 422
- Heterojunction bipolar transistors (HBTs)**  
AlGaAs/GaAs HBTs, 396  
band diagram, 393  
basic parameters, 391–393  
frequency response, 344–395  
GaInP/GaAs HBTs, 397
- Heterojunctions**, 369–370
- Heterostructure, grown**,
- GaAs–GaAlAs, 14  
GaAs–GaInP, 15
- Heterostructure, lasers**,  
double heterostructure, 7  
single heterostructure, 7
- HgCdTe detectors**, 295–297
- HgTe–CdTe superlattice detectors**, 297
- Hydrogen purifier**, 23
- InGaAs lasers**  
buried-ridge structure, 341  
optical confinement layer, 341  
strained layer structures, 336–342
- Incorporation of impurities in MOCVD GaAs**, 188–197  
carbon, 190  
erbium, 196  
magnesium, 195  
selenium, 193  
silicon, 191–192  
sulphur, 193  
zinc, 194
- Incorporation of impurities in MOCVD GaInP**, 207–214  
magnesium, 214  
selenium, 211  
silicon, 209–210  
sulphur, 207–209  
tellurium, 211  
zinc, 212
- In situ characterization**  
reflectance difference spectroscopy (RDS), 54–110
- Infrared detectors**, 431–435  
classification, 431  
general theory, 431–435
- Interference effects**, 82–85
- Interface quality determination**, 131–133
- Intersubband p-type GaInP/GaAs quantum wells**, 275–279  
growth procedure, 276  
transmission spectra, 277

- x-ray diffraction patterns, 276
- $\mathbf{k} \cdot \mathbf{p}$  perturbation theory, 172, 429
- Laminar and turbulent flow, 34–37, 41
- Lasers
  - band diagrams, 322, 328, 337
  - carrier confinement, 322
  - high-speed modulation, 323–325
  - light confinement, 322
  - longitudinal modes, 321
  - optical gain and feedback, 318–319
  - output power, 348
  - quantum size effect, 325–326
  - test, 350
  - threshold current, 321–322
- Laser structures, 326–332
  - buried heterostructure, 335
  - double-heterostructure, 327–328
  - graded-index separate confinement
    - heterostructure, 330
  - homostucture, 320
  - quantum well lasers, 332
  - separate confinement
    - heterostructure, 328, 347
  - stripe geometry, 333
- Laser test
  - ageing test, 350
  - continuous-wave regime, 350
  - quasi-continuous-wave regime, 350
- Lattice parameter of GaInP, 177
- Linear thermal expansion coefficient of GaInP, 177
- Low-pressure MOCVD, 47
- Magnetoemission study in GaInP/GaAs system, 247
- Magnetoresistivity of GaInP/GaAs heterostructure, 226, 229–232
- Manifold, 25
- Mass spectroscopy, 54
- Memory effect, 41
- Metallorganic MBE, 47–49
  - InP-based materials, 48–49
- Michelson interferometer, 144
- Mobility
  - due to acoustic phonon scattering, 159
  - due to ionized impurity scattering, 159
  - in p-channel GaInP/InGaAs/GaAs MODFETs, 386
- MOCVD growth mechanism, 29–34
  - gas flow patterns, 34–37
  - growth rate, 180–181
  - heat effect, 37
  - kinetics, 32–34
  - mass transport, 30
  - physicochemical model, 34
  - thermodynamics, 30–32,
  - uniformity, 40–42
- MOCVD growth mechanism of GaAs
  - DLTS measurements, 186–187
  - experimental procedure, 182–183
  - growth rate, 180
  - photoluminescence results, 187–188
  - residual impurities, 189
  - transport properties, 184–186
- MOCVD growth of GaInP
  - defects, 204–207
  - experimental growth details, 200–202
  - structural ordering, 202–204
- MOCVD growth systems, 23–29
  - exhaust system, 25
  - gas handling system, 22
  - reactor chamber, 22
  - safety apparatus, 24
- MOCVD starting materials, 42–46
  - group III sources, 42–45
  - group V sources, 45–47
- Modulation-doped field effect
  - transistors (MODFET), 371–387
  - AlGaAs/GaAs, 372–377
  - AlGaAs/InGaAs, 377
  - GaInP/GaAs, 378–385
  - on Si substrate, 386–387
  - parameters, 373–374

- Modulation-doped structures  
 GaAs–GaAlAs, 14  
 GaAs–GaInP, 15  
 GaInAsP, 16  
 GaInAsP–InP, 17
- Momentum relaxation time, 357
- Multilayer heterostructures, 9
- Noise, 294, 433
- Non-equilibrium and equilibrium processes, 30
- Non-parabolicity, 174
- Optical devices, 283–313  
 electro-optical modulators, 283–292  
 quantum-well infrared photodetectors, 300–308  
 solar cells, 308–313
- Optical gain, 318
- Optical interconnections, 410
- Optoelectronic devices, 4, 403  
 laser diodes, 6  
 light emitting diodes, 6  
 modulators, 4  
 photodetectors, 6  
 solar cells, 6
- Optoelectronic integrated circuits (OEICs), 403–416
- GaAs-based devices on Si substrate, 405–409  
 in computing, 400–404
- InP-based devices on Si substrate, 406, 413  
 materials, 404  
 OEICs on Si substrate, 405–409  
 receivers, 404  
 transmitters, 404
- Quantum efficiency, 293
- Quantum Hall effect  
 GaInP/GaAs heterostructure, 221
- Quantum lifetime  
 in GaInP/GaAs heterojunction, 245–246
- Quantum size effect, 322
- Quantum well infrared detectors, 297–308
- GaAs/AlGaAs intersubband detectors, 300–304
- GaAs/GaInP p-type intersubband detectors, 304–308
- HgTe–CdTe superlattice detectors, 297
- InAsSb detectors, 298
- InAsSb SLSs detectors, 299
- Quasi-Fermi energy, 427
- Particulate filters, 28
- Pendellosung fringes, 133
- Persistent photoconductivity  
 in GaInP, 207, 222  
 in GaInP/GaAs heterojunctions, 235–243
- Phase diagram, 32
- Photoluminescence, 143
- Photon detectors, 431
- Photovoltage spectroscopy, 154–155
- Physical parameters  
 of AlAs, 175  
 of AlGaAs, 175  
 of GaAs, 175
- Physical properties  
 of GaAs–GaAlAs, 14  
 of GaAs–GaInP, 15  
 of GaInAlP–GaAs, 18  
 of GaInAsP–InP, 17
- Quantum lifetime, 238–240
- Raman scattering, 55
- Rayleigh number, 38
- Reaction in gas phase, 33
- Recombination processes, 146–147
- Reflectance difference spectroscopy (RDS), 57–63  
 application for growth monitoring, 86–89  
 experimental procedure, 61–62  
 optical set-up, 59–61  
 principles of the method, 57–59

- RDS in MOCVD reactor, 62–63  
Relaxation time, 185  
Resistivity measurements  
    four-point method, 156–157  
    Van der Pauw's method, 157–158  
Responsivity, 295, 433  
Reynolds number, 37  
RHEED method, 54  
  
Scattered radiation effect, 134  
Scrubbing systems, 26  
    liquid-based scrubber, 27  
    solid-based scrubber, 28  
Sheet carrier concentration, 373  
Shubnikov–de Haas oscillations  
    GaInP/GaAs heterostructure, 221–223  
Solar cells, 308–313  
    air-mass-zero (AM0) spectrum, 308  
    efficiency, 309  
    fill factor, 310  
    GaAs solar cells, 310–313  
Spin-orbit coupling, 173  
Spontaneous emission, 356  
Stark effect, 285  
Strained layer superlattice, 298  
Substrate miscut, 419  
Superlattice period, 419  
Thermal bath, 23  
Thermal detectors, 431  
Thickness measurements  
    ball polishing, 166  
    surface profiler, 167  
Threshold current density, 327–336,  
    basic theory, 320–321  
    of GaAs–GaAlAs lasers, 8, 17, 428  
    of GaInAsP–InP DH lasers, 17  
    temperature dependence, 353  
    versus output losses, 359  
Transconductance, 373  
Trap parameters,  
    activation energy, 125–126  
    concentration, 126  
    capture cross-section, 127–128  
    capture rate, 128  
Two-dimensional electron gas,  
    in GaInP/GaAs heterojunctions, 221–223  
  
Wannier–Stark localization, 289  
  
X-ray diffraction, 129–138  
    analysis of diffraction, 131–134  
    Bond's method, 131  
    Bragg's law, 129–130  
    diffraction pattern simulation, 136–138  
    dynamical theory of diffraction, 135–136  
X-ray reflectivity, 133–134  
X-ray refraction, 134  
Zincblende lattice, 171



Taylor & Francis  
Taylor & Francis Group  
<http://taylorandfrancis.com>



Taylor & Francis  
Taylor & Francis Group  
<http://taylorandfrancis.com>